

**Density-matrix renormalization group studies of
strongly correlated many-particle systems
in one dimension**

Habilitationsschrift

zur

Erlangung des akademischen Grades

doctor rerum naturalium habilitatus (Dr. rer. nat. habil.)

an der Mathematisch-Naturwissenschaftlichen Fakultät

der

Ernst-Moritz-Arndt-Universität Greifswald

vorgelegt von

Satoshi Ejima

geboren am 12. Oktober 1977

in Saitama, Japan

Greifswald, April 2016

Dekan: _____

1. Gutachter: _____

2. Gutachter: _____

3. Gutachter: _____

Tag der Habilitation: _____

Contents

1	Introduction	1
2	Numerical technique	5
2.1	DMRG algorithms	5
2.1.1	Density matrix projection	5
2.1.2	Infinite-system algorithm	7
2.1.3	Finite-system algorithm	8
2.2	Pseudo-site approach	9
2.3	Dynamical DMRG	11
2.4	Periodic boundary conditions	13
2.5	Parallelization of the DMRG algorithm	15
2.6	Tomonaga–Luttinger liquid parameters	17
2.7	Entanglement analysis	18
3	Excitonic insulators in one dimension	21
3.1	Extended Falicov–Kimball model (EFKM)	21
3.2	BCS-BEC crossover in the EFKM	22
4	Metal-insulator transitions in fermion-boson coupled systems	27
4.1	Electron-phonon coupled systems	27
4.1.1	Spinless Holstein model	27
4.1.2	Hubbard–Holstein model	30
4.2	Edwards transport model	33
4.2.1	Metal-insulator transition at half filling	34
4.2.2	Metal-insulator transition at one-third band filling	37
4.2.3	Phase separation	38
5	Quantum phase transitions of lattice bosons	41
5.1	Superfluid-Mott insulator quantum phase transition	41
5.1.1	Superfluidity in the Bose–Hubbard model	42
5.1.2	Dynamical properties	45
5.2	Haldane insulator in the extended Bose–Hubbard model	49
5.2.1	Symmetry-protected topological order	50
5.2.2	Dynamical structure factor	51
6	Ising quantum phase transition between Feshbach-resonant superfluids	55
6.1	Model and ground-state phase diagram	55

6.2	Field theory predictions for correlation functions	57
6.3	Finite-size scaling for momentum space observables	59
7	Summary and outlook	63
8	Thesis Articles	67
	Article I — Order, criticality, and excitations in the extended Falicov-Kimball model	73
	Article II — Exact-diagonalization study of exciton condensation in electron bilayers	79
	Article III — Excitonic BCS-BEC crossover in double-layer systems	85
	Article IV — Luttinger parameters and momentum distribution function for the half-filled spinless fermion Holstein model: A DMRG approach	91
	Article V — DMRG analysis of the SDW-CDW crossover region in the 1D half-filled Hubbard-Holstein model	97
	Article VI — Quantum phase transition in a 1D transport model with boson-affected hopping: Luttinger liquid versus charge-density-wave behavior	101
	Article VII — Metal-insulator transition in the Edwards model	105
	Article VIII — One-dimensional quantum transport affected by a background medium: Fluctuations versus correlations	109
	Article IX — Anderson localization versus charge-density-wave formation in disordered electron systems	115
	Article X — Charge-density-wave formation in the Edwards fermion-boson model at one-third band filling	121
	Article XI — Phase separation in the Edwards model	127
	Article XII — A Green’s function decoupling scheme for the Edwards fermion-boson model	133
	Article XIII — Dynamic properties of the one-dimensional Bose-Hubbard model	147
	Article XIV — Characterization of Mott-insulating and superfluid phases in the one-dimensional Bose-Hubbard model	153
	Article XV — Dynamic density-density correlations in interacting Bose gases on optical lattices	169
	Article XVI — Dynamical correlation functions for the one-dimensional Bose-Hubbard insulator	173
	Article XVII — One-dimensional Bose-Hubbard model with local three-body interactions	181
	Article XVIII — Spectral and entanglement properties of the bosonic Haldane insulator	187
	Article XIX — Entanglement properties of the nontrivial Haldane insulator in the 1D extended Bose-Hubbard model	195

Article XX — Comparative density-matrix renormalization group study of symmetry-protected topological phases in spin-1 chain and Bose-Hubbard models	201
Article XXI — Ising deconfinement transition between Feshbach-resonant superfluids	211
Article XXII — Discrete symmetry breaking transitions between paired superfluids	215
Article XXIII — Magnetic properties of the second Mott lobe in pairing Hamiltonians	231
Article XXIV — Criticality at the Haldane-insulator charge-density-wave quantum phase transition	245
Bibliography	251
Erklärung	259
Curriculum Vitae	261
Acknowledgments	271

1 Introduction

After the discovery of high-temperature superconductivity in copper oxides in 1986, strongly correlated many-particle systems have attracted much attention. Despite the longstanding search for the origin of an attractive interaction causing fermionic bound states in repulsively interacting particles, possible mechanisms of superconductivity in the cuprates are still the subject of considerable debate and further research. In the field of high- T_c superconductivity the bosonic degrees of freedom play an important role: on the one hand, tightly paired fermions act approximately as bosons, and so can collectively form a quantum coherent state at low temperatures. On the other hand, it is accepted that the nature of the high-temperature superconductivity is controlled not only by the electron-electron interaction but also by the electron-phonon interaction. In order to investigate such a fermionic system with phonons, the bosonic degrees of freedom should be taken into account. However, this makes the numerical simulations much complicated, since an unlimited number of bosons may occupy the same site. Thus, from the theoretical point of view, one-dimensional (1D) systems are of specific interest because there exist exact numerical and analytical techniques which permit deep insights into understanding of the nature of the quantum many-body systems with and without background medium such as the electron-phonon coupling.

The recent rapid progress in cooling atoms to low temperatures and manipulating their interactions has also motivated theorists to explore strongly correlated quantum systems including bosonic degrees of freedom. After achievement of the Bose–Einstein condensations (BEC) in the ultracold dilute gases in 1995, the quantum phase transition between Mott insulating (MI) and superfluid (SF) phases has been observed experimentally using bosonic atoms loaded into an optical lattice. A number of optical lattice experiments have investigated the nature of Bose condensates in disordered traps to answer a fundamental unsolved issue, what is the fate of Anderson localization in the presence of strong quantum correlations. Moreover, the crossover between a molecular BEC and a Bardeen–Cooper–Schrieffer (BCS) pairing state has been realized using Feshbach resonances, which enable one to control the strength of pairing interactions using a magnetic field. Thus, ultracold fermionic/bosonic atoms in optical lattices provide highly controllable quantum systems allowing to probe various quantum many-body phenomena experimentally. Excitation of superfluids in optical lattices have been probed by momentum-resolved Bragg spectroscopy, which motivates theoreticians to compute dynamical quantities for a direct comparison with experiments. Since bosons on a chain are also accessible in optical lattice experiments, it is also of significant interest to study the 1D quantum systems for bosons, while the main numerical obstacle is again caused by the multiple occupancies of bosons on a single site.

The BCS-BEC crossover can also be investigated by considering excitons, i.e., elec-

tron-hole bound pairs. With increasing the magnitude of the Coulomb interaction, which acts as an attraction between an electron and a hole, electron-hole pairs experience the crossover from a weakly bound BCS-like state to a BEC state of tightly bound excitons. Here, the so-called excitonic insulator (EI) is one of the longstanding problems in condensed matter physics. Despite its half a century-old history, the experimental realization of the EI state is still quite challenging. Needless to say, the bosonic degrees of freedom play a significant role in the EI, since (tightly) bound pairs can be regarded approximately as bosons.

Various numerically exact techniques are used to investigate such strongly correlated many-particle systems. The most direct method is (Lanczos) Exact Diagonalization (ED), which allows us to calculate almost all properties of a quantum system. However, ED is restricted to systems (for spinful fermions) with up to about 20 particles because of the exponential increase of the memory capacity with the number of particles. In many cases, such system sizes are too small to extrapolate the physical quantities of interest to the thermodynamic limit. Quantum Monte Carlo (QMC) techniques can be applied to much larger system sizes than ED. QMC is, however, restricted to simple quantum models due to the notorious “minus sign” problem. In (quasi-)1D systems these problems can be overcome by means of the *Density-Matrix Renormalization group* (DMRG) technique. The DMRG can be used to investigate very large systems, $L \sim \mathcal{O}(10^3)$, and is widely applicable not only to fermionic but also to bosonic strongly correlated systems. In the latter case the cut-off should be introduced to restrict the maximum number of bosons per site. Thereby, applying the pseudo-site approach, DMRG allows one to perform accurate simulations in a system with background medium, such as the electron-phonon coupled Holstein model and the Edwards fermion-boson model. Most remarkably, the dynamical DMRG (DDMRG) technique provides a novel opportunity for investigating the dynamical properties of quantum many-body systems for all frequencies in large systems with a few hundred sites. DDMRG is as widely applicable to quantum systems as the standard DMRG method, and thus opens doors for a direct comparison with experimental results in the strongly correlated systems.

In this thesis we investigate the static and dynamical properties of 1D quantum many-body systems including bosonic degrees of freedom. Based on the unbiased large-scale DMRG technique, we perform a careful finite-size scaling analysis combined with field theory when necessary, to characterize each phase and phase boundaries, and to examine the quantum criticality. In order to determine quantum phase transition points, Tomonaga–Luttinger liquid (TLL) parameters and/or central charge are exploited. Dynamical quantities obtained by DDMRG can also be used to characterize different phases and phase boundaries.

The outline of the thesis is as follows. In the next chapter, we introduce the basic ideas and algorithms of the standard DMRG and DDMRG techniques. Then the pseudo-site approach is explained, which is necessary to simulate a system with background medium, as in the Holstein and Edwards models. At the end of Chap. 2 we present accurate numerical methods to estimate TLL parameters and central charge.

In Chap. 3 we explore the BCS-BEC crossover of electron-hole pairs (excitons) in the half-filled Falicov–Kimball model, using the ED and DMRG techniques. So far, the absence of an order parameter has prevented addressing the problem of excitonic condensation in 1D systems by mean-field approaches, despite their success in higher dimensions. In order to overcome this problem, we simulate the off-diagonal anomalous Green function, which is originally introduced for detecting the particle fluctuations of Cooper pairs in 2D systems. The binding energy and coherence length of the electron-hole pairs obtained from the anomalous spectral function and condensation amplitude show a Coulomb interaction driven BCS-BEC crossover.

In Chap. 4 we apply the pseudo-site DMRG technique to 1D quantum many-particle systems with background medium. In order to explore the origin of attractive interactions between electrons we investigate the electron-phonon coupled Holstein model for spinless and spinful cases. As a second example for the system with background medium we study the Edwards transport model with boson-affected hopping, which exhibits a surprisingly rich physics including the metal-insulator quantum phase transitions, the anomalous momentum distribution function triggered by the effective next-nearest-neighbor hopping process at half filling, and even the attractive TLL phase away from half band filling.

In Chap. 5 we investigate the pure bosonic systems in 1D. Exploring first the ground-state phase diagram and the Kosterlitz–Thouless transition between SF and MI phases in the standard 1D Bose–Hubbard model (BHM), we demonstrate the accuracy of DMRG results in comparison to strong-coupling perturbation theory. Analogously, dynamical quantities in the BHM obtained by the DDMRG exhibits excellent agreements with the perturbative results.

Then, including the nearest-neighbor Coulomb interaction in the BHM we examine the entanglement and dynamical properties of the so-called Haldane insulator, which is regarded as a *symmetry-protected topological* (SPT) phase by the lattice inversion symmetry. In order to detect such a Haldane state in optical lattice experiments, we simulate the dynamical structure factor, which exhibits the gapped excitation spectrum in analogy with the spin-1 Heisenberg chain.

Feshbach resonances and molecule formation will also be studied in the bosonic lattice system in Chap. 6. From the theoretical point of view, the BCS-BEC crossover problem for bosons differs markedly from the fermionic case since the carriers themselves may Bose condense. This leads to the possibility of an Ising quantum phase transition occurring between distinct paired superfluids. We characterize the phases and quantum phase transitions of bosons interacting via Feshbach resonant pairing interactions in 1D lattice and provide compelling evidence for an Ising quantum phase transition.

Figure 1.1 summarizes all issues and lattice models addressed in this thesis schematically. Thesis articles are categorized into each lattice model.

A summary and an outlook can be found in Chap. 7, which closes the scientific part of the thesis.

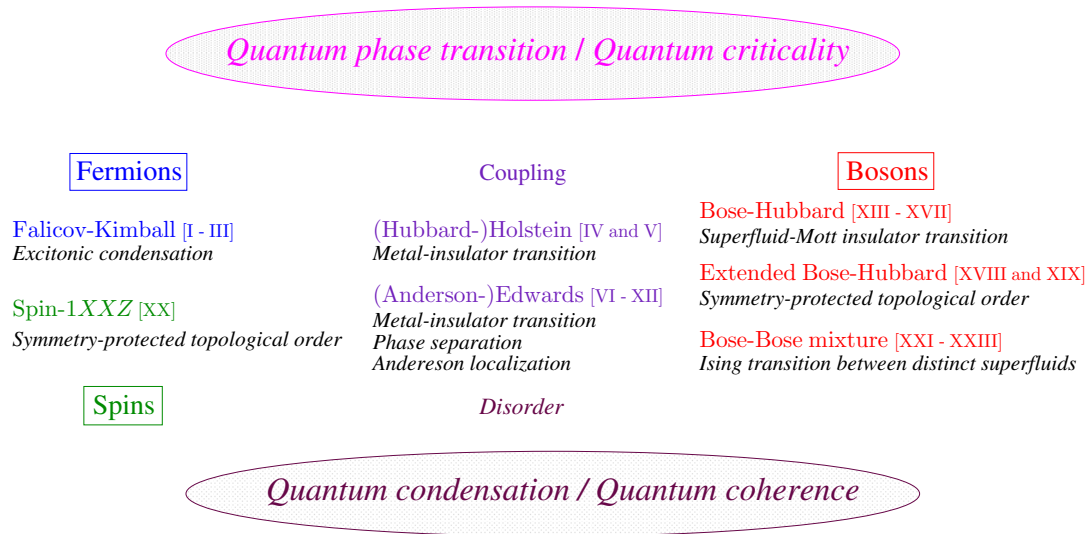


Fig. 1.1: Schematic representation of the lattice models, which will be discussed in this thesis. The roman numbers after each lattice model denote the number of corresponding thesis articles listed in Chap. 8.

2 Numerical technique

The Density-Matrix Renormalisation Group (DMRG) technique was invented in 1992 by Steven R. White [1,2], and is considered now as the most efficient numerical method for investigating the (quasi-) 1D quantum systems. The DMRG allows one to calculate static, dynamic, and spectral properties in the strongly correlated 1D systems with high precision for large system sizes as $L \sim \mathcal{O}(10^3)$. In this chapter we will introduce briefly basic notions of the (dynamical) DMRG which can be applied to the various 1D interacting systems as demonstrated in this thesis later.

2.1 DMRG algorithms

2.1.1 Density matrix projection

We divide the entire system (*superblock*) into the *system block* $|i\rangle$ and *environment block* $|j\rangle$ as shown in Fig. 2.1. Then, the state of the superblock is given by

$$|\psi\rangle = \sum_{i,j} \psi_{i,j} |i\rangle |j\rangle. \quad (2.1)$$

Here, we assume $|\psi\rangle$ to be normalized, $\langle\psi|\psi\rangle = 1$. The reduced density matrix for the system block is defined as

$$\rho_{ii'} = \sum_j \psi_{ij}^* \psi_{i'j}, \quad (2.2)$$

where $\text{Tr}\hat{\rho} = 1$ due to normalization. Then, for any system block operator \hat{A} we have

$$\langle\psi|\hat{A}|\psi\rangle = \text{Tr}\hat{\rho}\hat{A} = \sum_{\alpha} w_{\alpha} \langle u^{\alpha}|\hat{A}|u^{\alpha}\rangle \quad (2.3)$$

with the eigenstates $|u^{\alpha}\rangle$ and eigenvalues $w_{\alpha} \geq 0$ of $\hat{\rho}$. Since $\text{Tr}\hat{\rho} = 1$, we have $\sum_{\alpha} w_{\alpha} = 1$. Eq. (2.3) gives us a way to discard some states from the system block, namely, keeping the states with significant w_{α} and discarding ones with $w_{\alpha} \approx 0$, we obtain a good approximation value of $\langle\hat{A}\rangle$ as

$$\langle\psi|\hat{A}|\psi\rangle_{\text{approx}} = \sum_{\alpha=1}^m w_{\alpha} \langle u^{\alpha}|\hat{A}|u^{\alpha}\rangle \quad (2.4)$$

for a fixed number of m system block states kept.

Let us make this argument more precise. For the moment, we assume that the superblock has been diagonalized and we have obtained one particular state $|\psi\rangle$, e.g.,

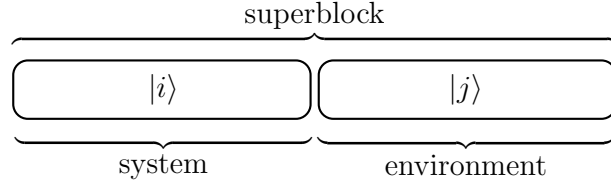


Fig. 2.1: A superblock divided into a system block and an environment block.

the ground state. We desire to construct an accurate approximation state $|\psi'\rangle$ for $|\psi\rangle$, which is given by

$$|\psi\rangle \approx |\psi'\rangle = \sum_j \sum_{\alpha=1}^m a_{\alpha,j} |u^\alpha\rangle |j\rangle, \quad (2.5)$$

where the system block states $|u^\alpha\rangle$ are defined for a fixed number m of states kept as

$$|u^\alpha\rangle = \sum_i u_i^\alpha |i\rangle, \quad \alpha = 1, \dots, m. \quad (2.6)$$

To this end, we minimize

$$\mathcal{D}_m = \|\psi\rangle - |\psi'\rangle\|^2 \quad (2.7)$$

by varying over all $a_{\alpha,j}$ and u^α , with the condition $\langle u^\alpha | u^{\alpha'} \rangle = \delta_{\alpha,\alpha'}$. In general, one can write

$$|\psi'\rangle = \sum_{\alpha} a_{\alpha} |u^\alpha\rangle |v^\alpha\rangle, \quad (2.8)$$

where $v_j^\alpha = \langle j | v^\alpha \rangle = N_{\alpha} a_{\alpha,j}$, with N_{α} chosen to set $\sum_j |v_j^\alpha|^2 = 1$. Then, \mathcal{D}_m is described by

$$\mathcal{D}_m = \sum_{ij} \left(\psi_{ij} - \sum_{\alpha=1}^m a_{\alpha} u_i^{\alpha} v_j^{\alpha} \right)^2, \quad (2.9)$$

and we need to minimize \mathcal{D}_m over all u^α , v^α and a_{α} with the given number of m . Here, ψ is a rectangular matrix. The solution is determined by the singular value decomposition of ψ ,

$$\psi = U D V^T, \quad (2.10)$$

where U is an orthogonal $\ell \times \ell$ matrix and V is a column-orthogonal $\ell \times J$ matrix, where $j = 1, \dots, J$ and we assume $J \geq \ell$. Here, the diagonal matrix D contains the singular values of ψ . The diagonal elements of D are the a_{α} and the corresponding columns of U and V are the u^{α} and v^{α} , respectively. Using Eq. (2.2) we obtain

$$\rho = U D^2 U^T. \quad (2.11)$$

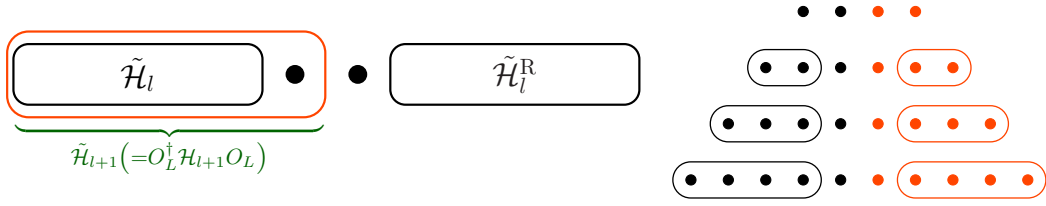


Fig. 2.2: Superblock configuration (left panel) and process (right panel) of the infinite-system algorithm.

The eigenvalues of ρ are $w_\alpha = a_\alpha^2$ and the eigenstates of ρ with the largest eigenvalues are u^α . Each w_α represents the probability of the block being in the state u^α , with $\sum_\alpha w_\alpha$.

More specifically, D_m is the so-called “discarded weight” of the density matrix eigenvalues

$$D_m = \sum_{\alpha=m+1}^{m_{\max}} w_\alpha = 1 - \sum_{\alpha=1}^m w_\alpha, \quad (2.12)$$

where m_{\max} is the size of the density matrix. Since the discarded weight D_m is strongly correlated with the error in the ground-state energy, D_m is often used as a measure of the error. One can calculate the ground-state energy and the discarded weight for several values of m and make an extrapolation $m \rightarrow \infty$. This approach provides a reliable estimate of the error on the ground-state energy [1, 3].

In most cases, the accuracy of the energy for a given number of m is many orders of magnitude better for open boundary conditions (OBC) than for periodic boundary conditions (PBC). Therefore, it is usually better to treat systems with OBC on larger lattices than small systems with PBC. However, sometimes one needs to simulate a specific quantity with PBC, e.g. in order to avoid boundary effects with OBC. In Sec. 2.4 we introduce the so-called folding lattice procedure, which improve the accuracy with PBC drastically.

2.1.2 Infinite-system algorithm

The DMRG procedure starts with the infinite-system algorithm to enlarge the system size in real space up to the desired system size while keeping the maximal dimension of the superblock Hamiltonian constant. The environment block is constructed using a *reflection* of the system block. The superblock configuration is shown in the left panel of Fig. 2.2. Here, $\tilde{\mathcal{H}}_l$ is the Hamiltonian for the system block with the reduced basis, each dot represents a single site, and the environment block $\tilde{\mathcal{H}}_l^R$ is obtained by the reflection of $\tilde{\mathcal{H}}_l$.

The infinite-system algorithm proceeds as follows:

1. Form a superblock with L sites that is small enough to be exactly diagonalized.

2. Diagonalize the superblock Hamiltonian $\mathcal{H}_L^{\text{SB}}$, e.g., by using the Lanczos algorithm, or the more elaborate Lanczos–Davidson [4, 5] algorithm, to find the ground-state eigenvalue E_0 and eigenvector $|\psi\rangle$. Other states could also be kept, such as the first excited ones. They are called “target states”.
3. Form the reduced density matrix $\rho_{ii'}$ for the new system block with l' sites from $|\psi\rangle$ using Eq. (2.2), where $l' = l = L/2 - 1$.
4. Diagonalize $\rho_{ii'}$, and obtain the m eigenvectors u_1, \dots, u_m with the largest eigenvalues.
5. Construct \mathcal{H}_{l+1} and other operators A_{l+1} in the new system block, and transform them to the reduced density matrix eigenbasis as $\tilde{\mathcal{H}}_{l+1} = O_L^\dagger \mathcal{H}_{l+1} O_L$ and $\tilde{A}_{l+1} = O_L^\dagger A_{l+1} O_L$, where $O_L = (u_1, \dots, u_m)$.
6. Form a new superblock $\mathcal{H}_{L+2}^{\text{SB}}$ from $\tilde{\mathcal{H}}_{l+1}$, two single sites, and $\tilde{\mathcal{H}}_{l+1}^{\text{R}}$.
7. Repeat again from step 2 replacing L with $L + 2$.

The superblock size increases by two sites at each step as shown in the right panel of Fig. 2.2. Iterations are continued until a good approximation of an infinite system is obtained.

Note that PBC can be attached to the ends by forming the superblock, and a different block layout should be considered to avoid connecting two big blocks (system and environment) which takes longer to converge. This is the key reason why DMRG prefers OBC.

2.1.3 Finite-system algorithm

The finite-system algorithm is the DMRG procedure to calculate the properties of a finite system most accurately. The environment is chosen so that the size of the superblock is kept fixed at every iteration.

The finite-system algorithm proceeds as follows:

0. Run the infinite-system algorithm until the superblock reaches size L . Store $\tilde{\mathcal{H}}_l$ and the operators needed to connect the blocks at each iteration.
1. Carry out steps 3-5 of the infinite-system algorithm to obtain $\tilde{\mathcal{H}}_{l+1}$, and store it (note that now $l \neq l'$).
2. Form a superblock of size L using $\tilde{\mathcal{H}}_{l+1}$, two single sites and $\tilde{\mathcal{H}}_{l'-1}$.
3. Repeat steps 1 and 2 until the environment size reaches $l' = 1$. This is the *left* to *right* zipping phase of the algorithm.
4. Carry out steps 3-5 of the infinite-system algorithm but with the direction to build up the environment, and store $\tilde{\mathcal{H}}_{l'+1}^{\text{R}}$ at each iteration.

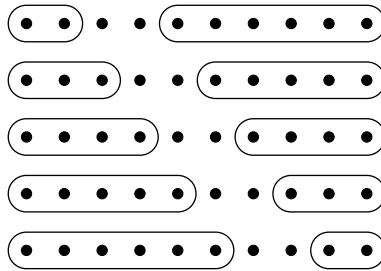


Fig. 2.3: Finite-system algorithm.

5. Form a superblock of size L using $\tilde{\mathcal{H}}_{l-1}$, two single sites and $\tilde{\mathcal{H}}_{l+1}$.
6. Repeat steps 4 and 5 until $l = 1$. This is the *left to right* zipping phase of the algorithm.
7. Repeat again from step 1.

Iterations are continued through every configuration of the superblock for a given number m of the density-matrix eigenstates kept until convergence. This procedure is illustrated in Fig. 2.3. This ensures a self-consistent optimization and thus considerably improves the quality of the results as compared to the infinite-system algorithm.

Before we close this subsection, it should be noted that DMRG can be considered as a variational approach. Namely, the energy functional

$$E(\psi) = \frac{\langle \psi | \hat{H} | \psi \rangle}{\langle \psi | \psi \rangle} \quad (2.13)$$

is minimized in a variational subspace in order to find the ground-state wave function $|\psi_0\rangle$ and energy $E_0 = E(\psi_0)$ whereby the DMRG energy error is proportional to the weight of the density-matrix eigenstates discarded in the renormalisation process. The discarded weight can be reduced systematically by increasing the number m of density-matrix eigenstates kept.

2.2 Pseudo-site approach

In principle, the DMRG algorithm can be adapted directly to the strongly correlated electron systems including bosons, e.g., as background medium in the electron-phonon system. However, the simulations are often not practical, since one has to deal with the infinite dimension of the bosonic Hilbert space even for finite systems. To overcome this difficulty Jeckelmann and White introduced the pseudo-site approach [6] in the usual DMRG procedure. The key idea is to transform each boson site into several artificial two-state sites (pseudo-sites), since the DMRG works much more effective to treat several two-state sites than single many-state site. In this section, we will explain

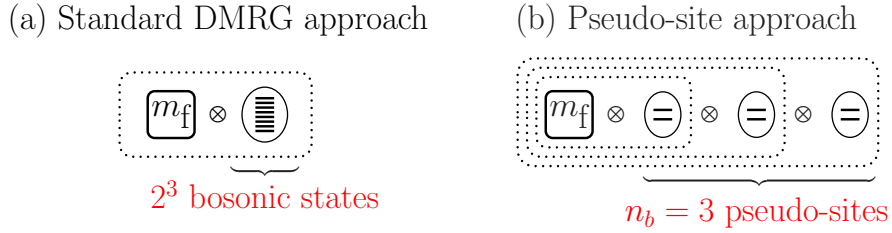


Fig. 2.4: Panel (a): Standard DMRG approach with a block (dotted rectangle) including a fermionic block (solid rectangle) and a bosonic site (oval) with $m_b = 8$ states. Panel (b): Pseudo-site approach with a block made of the previous block and $n_b = 3$ pseudo-sites. It takes n_b steps to build the final block (largest dotted rectangle), which is equivalent to the whole block in panel (a).

the pseudo-site approach, which is essential to investigate the Holstein-type models and the Edwards fermion-boson system.

Let us consider first a simple lattice model, as the Hubbard model for spinful fermions, where the number of states per site is $m_f = 4$. In the case of bosonic systems, however, the number of states on a single site is infinite in principle. For numerical calculations we truncate this number and keep a finite number of states per site m_b . In a standard implementation of the DMRG procedure for bosonic systems, memory and CPU time costs increase roughly as m_b^2 and m_b^3 , respectively. The main difficulty of the fermion-boson coupled systems is the large number of bosonic degrees of freedom. For fermion-boson coupled systems, however, we need to keep a large number of bosonic states per site ($m_b \sim 10 - 100$) in order to reduce errors caused by the truncation of bosonic Hilbert spaces. Thus, such simulations cost much more computational time than DMRG computations, e.g., in the Hubbard model.

To understand the key idea of the pseudo-site approach, it should be emphasized that the computational resources needed by the DMRG increase only linearly with the number of lattice sites. Therefore, individual lattice sites should be defined so that the total number of states per site $m_s = m_f m_b$ is as small as possible, although it brings an increase of the total sites in the lattice. Then, the first step in the fermion-boson coupled system is to separate the fermions and bosons of a site into two sites as shown in Fig. 2.4(a), instead of treating a site with both fermion and boson degrees of freedom. A boson site with $m_b = 2^{n_b}$ states can be further divided into n_b pseudo-sites, where each site is made of a hard-core boson with two states per site, as depicted in Fig. 2.4(b).

To be more precise, let us consider a boson site with a truncated occupation-number basis $\{|\alpha\rangle, \alpha = 0, 1, 2, \dots, 2^{n_b} - 1\}$, where $\hat{b}^\dagger \hat{b} |\alpha\rangle = \alpha |\alpha\rangle$. Here, \hat{b}^\dagger (\hat{b}) is the boson creation (annihilation) operator. In this case, we need to introduce n_b hard-core boson sites (pseudo-sites) with $\{r_j, r_j = 0, 1\}$ for $j = 1, \dots, n_b$ and the creation and annihilation hard-core boson operators $\hat{a}_j^\dagger, \hat{a}_j$, such as $\hat{a}_j^\dagger |0\rangle = |1\rangle$, $\hat{a}_j^\dagger |1\rangle = 0$, and \hat{a}_j is

the Hermitian conjugate of \hat{a}_j^\dagger . A boson level $|\alpha\rangle$ can be mapped one-to-one with the relation

$$\alpha = \sum_{j=1}^{n_b} 2^{j-1} r_j . \quad (2.14)$$

Then, all boson operators should be defined via pseudo-site operators. For instance, the boson number operator is given by

$$\hat{N}_b = \hat{b}^\dagger \hat{b} = \sum_{j=1}^{n_b} 2^{j-1} \hat{a}_j^\dagger \hat{a}_j . \quad (2.15)$$

Other boson operators can be determined from the one-to-one mapping (2.14) and the properties of the boson and hard-core boson operators. As an example, \hat{b}^\dagger can be obtained as follows. We first define $\hat{b}^\dagger = \hat{B}^\dagger \sqrt{N_b + 1}$ with $\hat{B}^\dagger |\alpha\rangle = |\alpha + 1\rangle$, where $\sqrt{N_b + 1}$ and \hat{B}^\dagger are given by

$$\sqrt{N_b + 1} = \sum_{\alpha=0}^{m_b-1} \sqrt{\alpha + 1} \hat{P}_1(r_1) \hat{P}_2(r_2) \cdots \hat{P}_{n_b}(r_{n_b}) , \quad (2.16)$$

$$\hat{B}^\dagger = \hat{a}_1^\dagger + \hat{a}_2^\dagger \hat{a}_1 + \hat{a}_3^\dagger \hat{a}_2 \hat{a}_1 + \cdots + \hat{a}_{n_b}^\dagger \hat{a}_{n_b-1} \hat{a}_{n_b-2} \cdots \hat{a}_1 . \quad (2.17)$$

Here, $\hat{P}_j(1) = \hat{a}_j^\dagger \hat{a}_j$, $\hat{P}_j(0) = \hat{a}_j \hat{a}_j^\dagger$, and r_j can be obtained from the relation (2.14). More concretely, for $n_b = 2$ pseudo-sites,

$$\hat{b}^\dagger = \hat{a}_1^\dagger + \sqrt{2} \hat{a}_2^\dagger \hat{a}_1 + (\sqrt{3} - 1) \hat{a}_1^\dagger \hat{a}_2^\dagger \hat{a}_2 . \quad (2.18)$$

Other boson operators can also be determined in a similar manner.

By substituting each boson site in the lattice with $n_b = \log_2(m_b)$ pseudo-sites and rewriting the Hamiltonian and other operators in terms of the pseudo-sites operators, DMRG algorithms can be proceeded to simulate the physical properties in the system.

2.3 Dynamical DMRG

In this section we will describe the variational principle in order to simulate a dynamical correlation function, which allows us to investigate the linear response of a quantum system.

The zero-temperature dynamic response of a quantum system to a time-dependent perturbation can be described by dynamical correlation functions as

$$G_{\hat{A}}(\omega + i\eta) = -\frac{1}{\pi} \langle \psi_0 | \hat{A}^\dagger \frac{1}{E_0 + \omega + i\eta - \hat{H}} \hat{A} | \psi_0 \rangle . \quad (2.19)$$

Here, \hat{H} is the time-independent Hamiltonian of the system, \hat{A} denotes the operator of the physical quantity to be analyzed, and \hat{A}^\dagger is the Hermitian conjugate of \hat{A} . The

small real number $\eta > 0$ shifts the poles of the correlation function in the complex plane. The imaginary part of the correlation function corresponding to the spectral function is obtained as

$$I_{\hat{A}}(\omega + i\eta) = \text{Im } G_{\hat{A}}(\omega + i\eta) \quad (2.20)$$

$$= \frac{1}{\pi} \langle \psi_0 | \hat{A}^\dagger \frac{\eta}{(E_0 + \omega - \hat{H})^2 + \eta^2} \hat{A} | \psi_0 \rangle, \quad (2.21)$$

which can be calculated by the correction vector method [7]. The correction vector is defined by

$$|\psi_A(\omega + i\eta)\rangle = \frac{1}{E_0 + \omega + i\eta - \hat{H}} |A\rangle, \quad (2.22)$$

where $|A\rangle = \hat{A}|\psi_0\rangle$. In order to determine a correction vector one solves an inhomogeneous linear equation

$$\left[(E_0 + \omega - \hat{H})^2 + \eta^2 \right] |\psi\rangle = -\eta |A\rangle, \quad (2.23)$$

which always has a unique solution $|\psi\rangle = |Y_A(\omega + i\eta)\rangle$ for $\eta \neq 0$. Then, the correction vector is calculated as

$$|\psi_A(\omega + i\eta)\rangle = |X_A(\omega + i\eta)\rangle + i|Y_A(\omega + i\eta)\rangle \quad (2.24)$$

with

$$|X_A(\omega + i\eta)\rangle = \frac{\hat{H} - E_0 - \omega}{\eta} |Y_A(\omega + i\eta)\rangle. \quad (2.25)$$

Minimizing the following functional

$$W_{A,\eta}(\omega, \psi) = \langle \psi | (E_0 + \omega - \hat{H})^2 + \eta^2 | \psi \rangle + \eta \langle A | \psi \rangle + \eta \langle \psi | A \rangle, \quad (2.26)$$

which has a well-defined and nondegenerate minimum for any $\eta \neq 0$ and a fixed frequency ω , the solution of Eq. (2.23) can be simulated as

$$|\psi_{\min}\rangle = |Y_{\hat{A}}(\omega + i\eta)\rangle. \quad (2.27)$$

The value of the minimum corresponds to the imaginary part of the dynamical correlation function as

$$W_{A,\eta}(\omega, \psi_{\min}) = -\pi\eta I_{\hat{A}}(\omega + i\eta). \quad (2.28)$$

Thus, the simulation of spectral functions ends up in a minimization problem. In order to determine $I_{\hat{A}}(\omega + i\eta)$ for any frequency ω and $\eta > 0$ one minimizes the corresponding functional $W_{A,\eta}(\omega, \psi_{\min})$. This is the variational principle of the dynamical DMRG procedure [8, 9].

This variational formulation is completely equivalent if $|Y_A(\omega+i\eta)\rangle$ can be determined exactly. However, in an approximate calculation with an error of the order $\epsilon \ll 1$, $|\psi\rangle = |Y_A(\omega+i\eta)\rangle + \epsilon|\phi\rangle$ with $\langle\phi|\phi\rangle = 1$, the variational procedure is more accurate. In the correction vector method the error in the spectrum $I_{\hat{A}}(\omega+i\eta) = -\frac{1}{\pi}\langle A|bY_A(\omega+i\eta)\rangle$ is of the order of ϵ . In the variational formulation the error in $W_{A,\eta}(\omega, \psi_{\min})$, thus in $I_{\hat{A}}(\omega+i\eta)$, is of the order of ϵ^2 as can be shown easily from Eq. (2.26).

This minimization process of the functional $W_{A,\eta}(\omega, \psi)$ can be easily integrated into the DMRG algorithm, which is used to minimize the energy functional $E(\psi)$ in Eq. (2.13). At every step of a DMRG sweep, the following processes are performed in the superblock subspace:

0. Run the infinite-system algorithm until the superblock reaches size L .
1. Minimize the energy functional $E(\psi)$ to obtain the ground-state wave function $|\psi_0\rangle$ and its energy E_0 .
2. Calculate $|A\rangle = \hat{A}|\psi_0\rangle$.
3. Minimize the functional $W_{A,\eta}(\omega, \psi)$ to determine the part of the correction vector $|Y_A(\omega+i\eta)\rangle$ and the imaginary part of the correlation function $I_{\hat{A}}(\omega+i\eta)$.
4. Calculate the other part of the correction vector $|X_A(\omega+i\eta)\rangle$ via Eq. (2.25).
5. Build a new superblock including the four states $|\psi_0\rangle$, $|A\rangle$, $|Y_A(\omega+i\eta)\rangle$, and $|X_A(\omega+i\eta)\rangle$ as targets in the density-matrix renormalization. Repeat from step 1 until the minimum of both functionals $E(\psi)$ and $W_{A,\eta}(\omega, \psi)$ converge.

Note that in the practical calculations, it is of great importance in the first place to determine the ground state with high precision. Therefore, we keep larger number of eigenstates m during first few DMRG sweeps, and afterwards use the slightly reduced number of m for the calculations of dynamical properties in order to reduce the computational time.

2.4 Periodic boundary conditions

As mentioned above, the DMRG will encounter a severe problem by carrying out the 1D simulations with PBC due to the structural issue. By imposing PBC with an open-ended 1D shape as shown in Fig. 2.5(a), the nearest-neighbor interaction/hopping between site 1 and site L becomes an effective long-range process proportional to the distance L , so that the simulations lose accuracy drastically as the system size L increases.

Applying the so-called *folding lattice* approach [10] as demonstrated in Fig. 2.5(b), this issue can be eliminated, in which the nearest-neighbor interactions/hoppings can be considered as the combination of nearest-neighbor and next-nearest-neighbor processes. While the larger number of m is still necessary to carry out simulations with high accuracy comparing with OBC, the obtained results with PBC show often much less system-size dependence and are free from the boundary effect like Friedel oscillations.

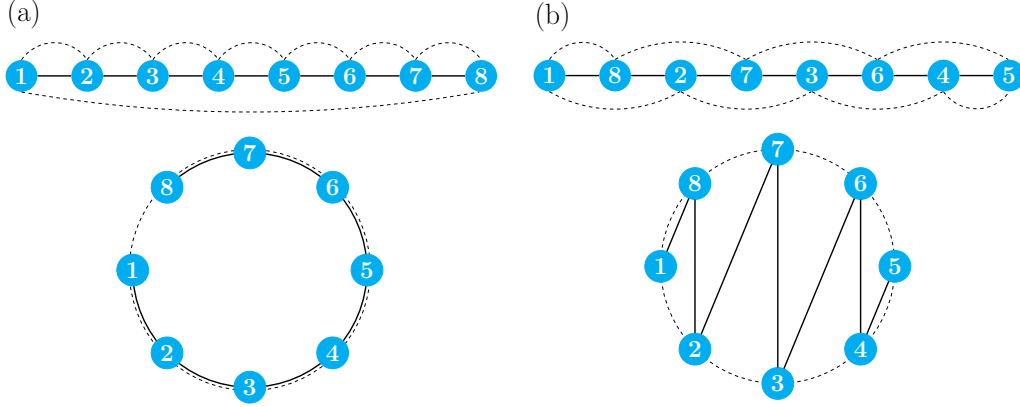


Fig. 2.5: Implementation of PBC in the DMRG technique for the system size $L = 8$. Solid lines denote the actual sites configurations in the DMRG simulations, dotted ones (effective) interaction/hopping processes. (a): The standard approach including a long-range process proportional to the system size L . (b): The reconfigured *folding lattice* approach, in which the nearest-neighbor interactions/hopping are replaced with the nearest- and next-nearest-neighbor processes effectively.

In the following, we demonstrate the accuracy of the DMRG ground-state energy in the half-filled Hubbard model as a paradigm of the strongly correlated electron systems. The Hamiltonian of the Hubbard model is defined as

$$\hat{H} = -t \sum_{\langle i,j \rangle \sigma} \hat{c}_{i\sigma}^\dagger \hat{c}_{j\sigma} + U \sum_i \hat{n}_{i\uparrow} \hat{n}_{i\downarrow}, \quad (2.29)$$

where $\hat{c}_{i\sigma}^\dagger$ ($\hat{c}_{i\sigma}$) creates (annihilates) an electron with spin $\sigma = \uparrow, \downarrow$ in a Wannier orbital centered around site i , and $\hat{n}_i = \hat{c}_{i\sigma}^\dagger \hat{c}_{i\sigma}$. Here, i and j refer to the sites of a one- or higher-dimensional lattice, and $\langle i, j \rangle$ represents nearest-neighbors. In Table 2.1, we compare the DMRG ground-state energy $E_{\text{DMRG}}^{(\text{folding})}$ for PBC with the exact values E_{exact} from Bethe Ansatz. For small system sizes $L \sim \mathcal{O}(10)$ the standard configuration in Fig. 2.5(a) provides still the accurate results and the numerical error can be reduced with increasing the number of the density-matrix states m kept (see the results for $L = 30$ in Table 2.1). The accuracy of the DMRG results with the folding lattice approach is similar to these with the standard configuration. On the other hand, for the system size $L \gtrsim \mathcal{O}(10^2)$, the accuracy of the energy with the standard configuration can not be improved any more even for $m = 4000$ states as shown in the results for $L = 130$, while the magnitude of the discarded weight is erroneously decreased. The DMRG ground state gets stuck into wrong minimum. Applying the folding lattice approach in Fig. 2.5(b) this issue can be eliminated. With increasing m the accuracy of the ground-state energy is improved, so that the DMRG can be regarded as numerically exact technique again.

L	m	$ E_{\text{ex}} - E_{\text{DMRG}} $	D_m for E_{DMRG}	$ E_{\text{ex}} - E_{\text{DMRG}}^{\text{folding}} $	D_m for $E_{\text{DMRG}}^{\text{folding}}$
30	100	1.97×10^{-1}	6.36×10^{-6}	4.13×10^{-2}	2.64×10^{-5}
30	1000	2.84×10^{-5}	2.72×10^{-8}	3.31×10^{-5}	3.43×10^{-8}
30	2000	1.46×10^{-6}	1.49×10^{-9}	1.62×10^{-6}	1.62×10^{-9}
130	1000	3.14×10^{-1}	4.62×10^{-13}	4.12×10^{-3}	6.99×10^{-7}
130	2000	3.14×10^{-1}	3.14×10^{-15}	6.94×10^{-4}	1.20×10^{-7}
130	4000	3.14×10^{-1}	2.48×10^{-17}	7.19×10^{-5}	1.43×10^{-8}

Table 2.1: Ground-state energy difference between exact values E_{ex} and numerical ones E_{DMRG} ($E_{\text{DMRG}}^{\text{folding}}$) in the 1D half-filled Hubbard model for $U/t = 5$ with L sites using the DMRG with PBC (applying the folding lattice approach). m is the number of density-matrix states kept, D_m the discarded weight in Eq. (2.12).

2.5 Parallelization of the DMRG algorithm

The accuracy of physical observables as the ground-state energy depends strongly on the number of density-matrix states m kept. For a particular problem the discarded weight D_m in Eq. (2.12) provides us some hint for choosing the proper m . In order to compute the complex systems accurately, it is important to compute the system with large m as much as possible. Simultaneously, the system size should also be enough large to perform the finite-size scaling. Thus, in the case of the 1D system with background medium, e.g., the Holstein–Hubbard model, a sequential DMRG run for the system size $L \sim \mathcal{O}(10^2)$ and $m \sim 2000$ immediately takes more than a week. The parallelization of the DMRG technique is therefore essential to reduce the actual wall time, since a single node in the modern computer consists of a few cores.

The most time-consuming part of the DMRG algorithm is the diagonalization process of the superblock Hamiltonian $\hat{\mathcal{H}}$, which is carried out by a Davidson procedure. Thus, repeated multiplications of $\hat{\mathcal{H}}$ with superblock wavefunctions ψ have to be carried out. Thereby, a Hamiltonian consisting of two blocks can be described as

$$\hat{\mathcal{H}}_{ij;i'j'} = \sum_{\alpha} \hat{A}_{ii'}^{\alpha} \hat{B}_{jj'}^{\alpha}, \quad (2.30)$$

where \hat{A} and \hat{B} are operators in two blocks and α indicates different terms in $\hat{\mathcal{H}}$. Due to double indices the matrix-vector multiplication (MVM) for $\hat{\mathcal{H}}\psi$ is at the end of the matrix-matrix type:

$$\sum_{i'j'} \hat{\mathcal{H}}_{ij;i'j'} \psi_{i'j'} = \sum_{\alpha} \sum_{i'} \hat{A}_{ii'}^{\alpha} \sum_{j'} \hat{B}_{jj'}^{\alpha} \psi_{i'j'}. \quad (2.31)$$

Since many operators have non-zero matrix elements between states only with specific quantum numbers, it is sufficient to store only the non-zero blocks. Those blocks are

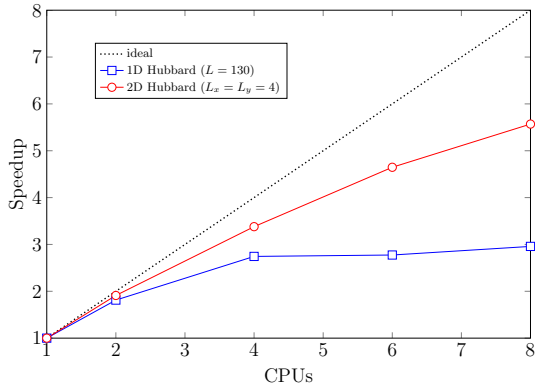


Fig. 2.6: Timing of OpenMP DMRG simulations on Intel Xeon E5-2637 v3 machine (3.5GHz) in the half-filled Hubbard model with PBC. Squares (circles) denote the scaling in 1D (2D) system with $L = 130$ ($L_x = L_y = 4$) and PBC. A speedup of S indicates that the calculation using n cores was S times faster than the same calculation using only single core.

labeled by indices $R(k)$ [$L(k)$] on the RHS (LHS). Omitting the normal matrix indices and adding sum over quantum numbers, Eq. (2.31) can be rewritten as

$$\hat{\mathcal{H}}\psi = \sum_{\alpha} \sum_k (\hat{\mathcal{H}}\psi)_{L(k)}^{\alpha} = \sum_{\alpha} \sum_k \hat{A}_k^{\alpha} \psi_{R(k)} \left[\hat{B}^T \right]_k^{\alpha}. \quad (2.32)$$

In this equation there exists three loops, which can be performed in parallel: the innermost matrix-matrix multiplication (twice), the sum over quantum numbers and the sum over terms in the Hamiltonian. In Ref. [11] Hager *et al.* presented a efficient parallelization strategy on shared-memory systems via OpenMP by setting up an array of OpenMP locks in order to describe loops in Eq. (2.32) as a single loop.

The efficiency of this OpenMP parallelized DMRG program depends strongly on the model, the system size, and the number of density-matrix states m kept. In Fig. 2.6 we demonstrate the OpenMP scaling of the parallelized DMRG code with up to 8 CPUs comparing the wall time of a whole simulation in the 1D and 2D half-filled Hubbard model. As a first benchmark we compare the results for the 1D system at $U/t = 5$ with $L = 130$ sites and PBC for $m = 4000$, applying the folding lattice approach as explained in Sec. 2.4 (the accuracy of the ground-state energy is shown in Table 2.1). Increasing the number of CPU cores, the computational time can successfully be reduced up to four CPUs in this case. Simulating with more than 4 cores speedups between 2 and 3 are achievable, so that in practice it is often most reasonable in 1D systems to carry out the OpenMP parallelized calculations with 4 CPUs. Much better efficiency of the parallelized code has been achieved in the second benchmark case for the 2D Hubbard model at $U/t = 4$ with 4×4 sites and PBC including $m = 15000$ states, which is a default benchmark system in Ref. [11] while m was chosen to be up to 2000 there. Note that with $m = 15000$ the numerical error $|E_{\text{ED}} - E_{\text{DMRG}}|$ is reduced to be 3.1×10^{-4} . As shown in Fig. 2.6, increasing the number of cores up to 8 we observe the much better efficiency and the simulation with 8 CPUs can be finished five times faster than the ones with a single core.

2.6 Tomonaga–Luttinger liquid parameters

The physical properties of the metallic state in 1D interacting fermionic systems are described by the Tomonaga–Luttinger liquid (TLL) theory. In the TLL picture the space- and time-dependent correlation functions display unusual power-law decays, determined by nonuniversal coefficients, K_ρ and K_σ . These so-called TLL parameters can be used to identify not only the properties of the TLL phase, but also the phase boundaries to the insulating states [12, 13]. In this section we revisit shortly, how the TLL parameters can be computed by the DMRG technique.

Let us first define the density-density correlation function as

$$S_\rho(r) = \frac{1}{L} \sum_l \{ \langle \hat{n}_{l+r} \hat{n}_l \rangle - \langle \hat{n}_{l+r} \rangle \langle \hat{n}_l \rangle \}, \quad (2.33)$$

where $\hat{n}_j = \hat{n}_{j\uparrow} + \hat{n}_{j\downarrow}$ counts the electrons on site j .

Using conformal field theory it can be shown [14, 15] that the asymptotic behavior for $1 \ll r \ll L$ is given by

$$S_\rho(r) \sim -\frac{K_\rho}{\pi r^2} + \frac{A \cos(2k_F r)}{r^{1+K_\rho}} \ln^{-3/2}(r) + \dots, \quad (2.34)$$

where $k_F = n\pi/2$ is the Fermi wave number, and A is a constant. For spinless fermions, the first term should be multiplied by $1/2$. In order to extract K_ρ , we introduce the Fourier transform

$$\tilde{S}_\rho(q) = \sum_{r=1}^L e^{-iqr} S_\rho(r) \quad (2.35)$$

with $0 \leq q < 2\pi$. By construction, $\tilde{S}_\rho(q=0) = 0$. Then, K_ρ is proportional to the slope of the charge-structure factor in the long-wavelength limit $q \rightarrow 0^+$ [16]:

$$K_\rho = \alpha\pi \lim_{q \rightarrow 0^+} \frac{\tilde{S}_\rho(q)}{q}, \quad q = \frac{2\pi}{L}, \quad L \rightarrow \infty, \quad (2.36)$$

where $\alpha = 2$ ($\alpha = 1$) in the 1D spinless (spinfull) fermionic systems. From this relation K_ρ can be determined accurately using the DMRG technique [17].

Similarly, we define the spin-spin correlation function in order to extract K_σ in the 1D spinful systems as

$$S_\sigma(r) = \frac{1}{L} \sum_l \{ \langle \hat{s}_{l+r}^z \hat{s}_l^z \rangle - \langle \hat{s}_{l+r}^z \rangle \langle \hat{s}_l^z \rangle \}, \quad (2.37)$$

where $\hat{s}_j^z = \hat{n}_{j\uparrow} - \hat{n}_{j\downarrow}$. Then, K_σ can be determined from the Fourier transform $\tilde{S}_\sigma(q)$ as

$$K_\sigma = \pi \lim_{q \rightarrow 0^+} \frac{\tilde{S}_\sigma(q)}{q}, \quad q = \frac{2\pi}{L}, \quad L \rightarrow \infty. \quad (2.38)$$

In this way we can investigate the properties of TLL parameters very accurately in any quasi-1D systems using the DMRG technique with OBC. Its accuracy can be checked in the Hubbard model and the spinless fermion model with nearest-neighbor interaction V by comparing with the exact results from the Bethe-ansatz solutions. The agreement between both results is excellent [17].

In Chap. 4, we apply this method to the fermion-boson Edwards model and to the Holstein model for both spinless and spinfull fermions in order to determine the metal-insulator transition points accurately and especially to discuss the possible existence of an attractive TLL phase indicated by $K_\rho > 1$.

2.7 Entanglement analysis

In last decade it has been shown that an entanglement analysis can be used to detect and locate quantum phase transitions in low-dimensional systems.

As explained above, in the DMRG algorithms we divide a system with L sites into two sub-blocks and the reduced density matrix $\rho_\ell = \text{Tr}_{L-\ell}[\rho]$ of a sub-block of arbitrarily length ℓ is calculated during each DMRG sweeps. Adding up the weights λ_α of the reduced density matrix ρ_ℓ during the simulation, we have direct access to the von Neumann entropy $S_L(\ell) = -\text{Tr}_\ell[\rho_\ell \ln \rho_\ell]$. From conformal field theory [18] it follows that in the case of a periodic system the von Neumann entropy takes the form

$$S_L(\ell) = \frac{c}{3} \ln \left[\frac{L}{\pi} \sin \left(\frac{\pi \ell}{L} \right) \right] + s_1, \quad (2.39)$$

where s_1 is a non-universal constant. In order to determine the quantum phase transition point accurately, Läuchli and Kollath have suggested to determine the central charge from the entropy difference [19]

$$\Delta S(L) \equiv S_L(L/2) - S_{L/2}(L/4) = \frac{c}{3} \ln(2) + \dots . \quad (2.40)$$

However, $\Delta S(L)$ includes the effect of the nonuniversal constant s_1 , and the values of the critical point cannot be extrapolated systematically. Since the most precise data of $S_L(\ell)$ are obtained when the length ℓ of the sub-block equals half the system size L , the relation [20]

$$c^*(L) \equiv \frac{3[S_L(L/2 - 1) - S_L(L/2)]}{\ln[\cos(\pi/L)]} \quad (2.41)$$

is much better suited for determining the central charge than expression Eq. (2.39), or evaluating the entropy difference $\Delta S(L)$ via Eq. (2.40). As will be shown in this thesis, the numerically obtained central charge $c^*(L)$ not only determines the universality class the system belongs to, but also provides an alternative way of precisely determining the phase boundaries, e.g., at metal-insulator transitions, accurately.

In the framework of the DMRG, entanglement analysis provides further information especially for the SPT phases. Li and Haldane [21] pointed out that it is also useful

to examine the full entanglement spectrum $\xi_\alpha \equiv -2 \ln \lambda_\alpha$ rather than just representing entanglement by a single number, e.g., as the von Neumann entropy $S_L(\ell)$. Namely, the low-lying entanglement spectrum can be used as a “fingerprint” to identify topological order. Pollmann *et al.* demonstrated that in the topological Haldane phase the lowest entanglement levels show a characteristic degeneracy reflecting the symmetry protection of the system [22, 23].

In Sec. 5.2, we investigate the entanglement properties of the Haldane insulator phase in the 1D extended Bose–Hubbard model and demonstrate that the bosonic Haldane phase also reveals a characteristic degeneracy of the entanglement spectrum.

3 Excitonic insulators in one dimension — Article I

The formation and condensation of excitonic bound states between electrons and holes have been a continuously studied problem in condensed matter physics for 5 decades. The attractive Coulomb interaction between oppositely charged particles can trigger their pairing, and can even build up a macroscopic phase-coherent quantum state under certain conditions. Quite recently, quasi-1D Ta₂NiSe₅ has raised as a candidate for the excitonic insulator (EI) state and attracted much experimental attention [24]. An extremely flat valence-band top was observed by angle-resolved photoemission spectroscopy and taken as a strong signature for the EI state to be formed out of “condensed” bound Ni 3*d*–Se 4*p* holes and Ta 5*d* electrons. This detection of the EI state in the quasi-1D material has brought renewed attention to the formation and possible condensation of excitons in 1D systems. However, in 1D, it has been unable to capture the EI state by mean-field based approaches despite their success in higher dimensions, since spontaneous breaking of continuous systems is generally impossible in 1D even at zero temperature.

In this chapter we investigate the nature of excitonic bound states and the development of exciton coherence in the 1D system using exact numerical techniques. Adopting a technique introduced for detecting the particle fluctuations of Cooper pairs in 2D systems [25, 26] we compute the off-diagonal anomalous exciton Green function, which exhibits a Coulomb interaction driven crossover from BCS-like electron-hole pairing fluctuations to BEC-like tightly bound excitons.

3.1 Extended Falicov–Kimball model

A minimal lattice fermion model to address the problem of exciton condensation is the so-called extended Falicov–Kimball model (EFKM) [27–30]:

$$\hat{H} = -t_c \sum_{\langle i,j \rangle} \hat{c}_i^\dagger \hat{c}_j - t_f \sum_{\langle i,j \rangle} \hat{f}_i^\dagger \hat{f}_j + U \sum_i \hat{c}_i^\dagger \hat{c}_i \hat{f}_i^\dagger \hat{f}_i + \frac{D}{2} \sum_i (\hat{c}_i^\dagger \hat{c}_i - \hat{f}_i^\dagger \hat{f}_i). \quad (3.1)$$

Here, $\hat{\alpha}_i^\dagger$ ($\hat{\alpha}_i$) denotes the creation (annihilation) operator of a spinless fermion in the $\alpha = c, f$ orbital at site i . The transfer amplitude between f (c) orbitals on nearest-neighbor sites is denoted by t_f (t_c). $U (> 0)$ parameterizes the on-site Coulomb attraction between f holes and c electrons, and D is the level splitting between different α orbitals. Increasing the magnitude of D in the EFKM we expect to find the staggered orbital ordered (SOO) phase which corresponds to the antiferromagnetic phase in the

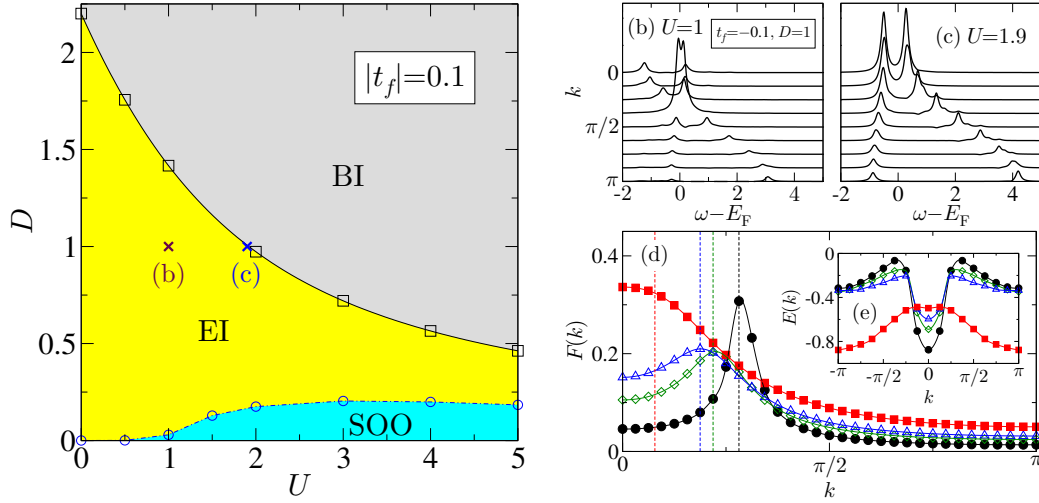


Fig. 3.1: (a): Ground-state phase diagram of the half-filled 1D EFKM with $|t_f| = 1$. Squares (circles) denote the EI-BI (EI-SOO) transition points D_{c_2} (D_{c_1}). The solid line gives the analytical solution (3.2) for the EI-BI boundary. Anomalous spectral function $F(k, \omega)$ with $U = 1$ (b) and $U = 1.9$ (c), where $t_f = -0.1$, $D = 1$. Data are obtained by ED using $\eta = 0.1$, $L = 16$, and PBC. Numerical results for $F(k)$ (d) and $E(k)$ (e) are also shown for $U = 1$ (circles), 1.5 (diamonds), 1.7 (triangles), and 1.9 (squares). $E(k)$ is extracted from the lowest peaks of single-particle spectra $A(k, \omega)$ calculated by ED for $L = 16$ (PBC). Dashed lines in the panel (d) mark the corresponding Fermi momenta $k_F = \pi N_c/L$ in the noninteracting limit. Adapted from Article I.

spin-1/2 XXZ chain, the EI phase with finite excitonic binding energy, and the band insulator (BI) state characterized by a filled (empty) f (c) band. The EI-BI phase boundary is exactly known to be [31]

$$D_{c_2} = \sqrt{4(|t_f| + |t_c|)^2 + U^2} - U. \quad (3.2)$$

Using DMRG, BI-EI and EI-SOO transition points can be obtained from the energy differences

$$D_{c_2}(L) = E_0(L, 0) - E_0(L - 1, 1) = -E_0(L - 1, 1), \quad (3.3)$$

$$D_{c_1}(L) = E_0(L/2 + 1, L/2 - 1) - E_0(L/2, L/2), \quad (3.4)$$

in the course of a finite-size scaling. The DMRG ground-state phase diagram is presented in Fig. 3.1(a). In this chapter we take t_c as the energy unit.

3.2 BCS-BEC crossover in the EFKM

In 1D system the $\langle \hat{c}^\dagger \hat{f} \rangle$ expectation value is always zero in the absence of an explicit f - c -band hybridization. For the 1D EFKM, power-law excitonic correlations were observed

instead [29]. Mean-field-based approaches are unable to capture the EI state in 1D due to the lack of an order parameter associated with the breaking of the $U(1)$ symmetry.

In order to examine the BCS-BEC crossover, we therefore adopt a technique introduced for detecting the particle fluctuations of Cooper pairs in 2D systems [25, 26]. That is, we consider the off-diagonal anomalous Green function

$$G_{cf}(k, \omega) = \left\langle \psi_1 \left| \hat{c}_k^\dagger \frac{1}{\omega + i\eta - \hat{H} + E_0} \hat{f}_k \right| \psi_0 \right\rangle, \quad (3.5)$$

where $|\psi_0\rangle$ is the ground state $|N_f, N_c\rangle$ with fixed numbers of f - and c -electrons, $|\psi_1\rangle$ is the excited state $|N_f - 1, N_c + 1\rangle$, E_0 is the averaged energy of $|\psi_0\rangle$ and $|\psi_1\rangle$, and η is a broadening. Then we determine the corresponding spectral function

$$F(k, \omega) = -\frac{1}{\pi} \Im G_{cf}(k, \omega) \quad (3.6)$$

that gives the condensation amplitude

$$F(k) = \langle \psi_1 | \hat{c}_k^\dagger \hat{f}_k | \psi_0 \rangle. \quad (3.7)$$

$F(k)$ can be directly computed by the ground-state DMRG method taking into account an extra target state $|\psi_1\rangle$. From $F(k)$ the coherence length characterizing the excitonic condensate follows as

$$\xi^2 = \sum_k |\nabla_k F(k)|^2 / \sum_k |F(k)|^2. \quad (3.8)$$

The binding energy of the excitons E_B can be also determined from diverse ground-state energies (see also Article II):

$$E_B = E_0(N_f - 1, N_c + 1) + E_0(N_f, N_c) - E_0(N_f - 1, N_c) - E_0(N_f, N_c + 1). \quad (3.9)$$

Figures 3.1(a) and (b) show the anomalous spectral function $F(k, \omega)$ for $U = 1$ and $U = 1.9$, respectively, where $t_f = -0.1$ and $D = 1$. In the former case the EI arises from a semimetallic phase. As a consequence most of the spectral weight of the quasiparticle excitations is located around the Fermi points $k = \pm k_F$, again indicating a BCS-type pairing of electrons and holes. Obviously, Fermi surface effects play no role for large U where the Hartree shift drives the system in the semiconducting regime. Here the excitation gap occurs at $k = 0$. Note that the gap between the lowest energy peaks in $F(k, \omega)$ is equal to the binding energy E_B given by Eq. (3.9). Figure 3.1(d) displays the frequency-integrated quantity $F(k)$. At $U = 1$, $F(k)$ exhibits a sharp peak at the Fermi momentum. Increasing U the peak weakens and shifts to smaller momenta. Close to the EI-BI transition point $U = 1.9 \lesssim U_{c_2} = 1.92$, $F(k)$ has a maximum at $k = 0$ but is spread out in momentum space, indicating that the radius of electron-hole pairs becomes small in real space. Panel (e) gives the quasiparticle dispersion $E(k)$ derived from $A(k, \omega)$. Driving the BCS-BEC crossover by increasing U , the peaks

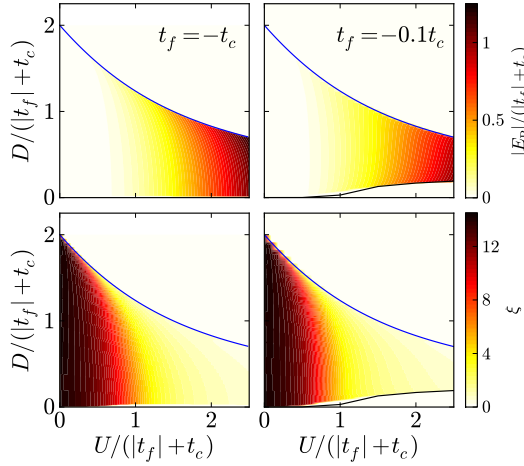


Fig. 3.2: Intensity plots of the binding energy E_B (upper panels; $L = 128$, OBC) and the correlation length ξ (lower panels; $L = 64$, PBC) in the rescaled $U/(|t_f|+t_c) - D/(|t_f|+t_c)$ plane, using DMRG for $N_f > L/2$. Solid lines denote the SOO-EI and EI-BI transition points in the thermodynamic limit. Adapted from Article I.

around $k = \pm k_F$ disappear as well as the notch around $k = 0$. Instead a valence band with a flat top around $k = 0$ develops, just as observed e.g. in quasi-1D Ta_2NiSe_5 [24].

Figure 3.2 shows the variation of the coherence length and the binding energy in the EI phase of the 1D EFKM with $|t_f| = 1$ (left panels) and 0.1 (right panels). At small U the excitonic state is composed of electron-hole pairs having large spatial extension, leading to large values of ξ . E_B , on the other hand, is rather small, but increases exponentially with U . This typifies a BCS pairing mechanism. At large U , the binding energy increases linearly with U . Here, tightly bound spatially confined excitons acquire quantum coherence (with $\xi \ll 1$) in a Bose-Einstein condensation process.

At last we address the influence of a mass imbalance between f - and c -band quasi-particles. As suggested by the EI-BI transition lines (3.2), both the U and D axes in Fig. 3.2 have been rescaled by $(|t_f| + t_c)$. Indeed we find that EI phase shrinks as $|t_f|$ decreases. That is, the mass anisotropy gets stronger, which is simply a bandwidth effect, however, leading to a stronger Ising anisotropy. This, on their part, enlarges the SOO region, while the EI-BI phase boundary basically is unaffected. Importantly, the location of the BCS-BEC crossover, which can be derived from the intensity plots for E_B and ξ , does not change in this presentation.

To conclude this chapter, adopting the numerically exact ED and DMRG techniques, we examined the excitonic insulator states in the 1D half-filled EFKM. The complete ground-state phase diagram was derived, in which besides the EI to BI transition, the EI-SOO phase boundary was determined with high accuracy. The whole phase diagram of the 1D EFKM could be scaled by $|t_f| + t_c$; the SOO phase appears only for small mass-imbalance ratios $|t_f|/t_c$. The absence of an order parameter prevents addressing the problem of excitonic condensation in 1D systems by usual mean-field approaches. That is why we exploited the off-diagonal anomalous Green function. The related anomalous spectral function elucidates the different nature of the electron-hole pairing and condensation process at weak and strong couplings. At fixed level

splitting the binding energy between c electrons and f holes is exponentially small in the weak-coupling regime. It strongly increases as the Coulomb attraction increases. Concomitantly the coherence length of the electron-hole pair condensate shortens. This unambiguously demonstrates a crossover from BCS-like electron-hole pairing to a Bose-Einstein condensation of preformed excitons. The quasiparticle band dispersion in the BEC regime exhibits a rather dispersionless valence band near $k = 0$. This result further supports the EI scenario for quasi-1D Ta₂NiSe₅, where the flat valence-band top was detected by angle-resolved photoemission spectroscopy experiments.

In Articles II and III the formation of excitons in electron-hole double-layer systems has been studied in the two-dimensional EFKM. Most notably, we have provided strong evidence for exciton condensation and a BCS-BEC crossover scenario at zero temperature, again by exploiting the anomalous Green's function using the unbiased Lanczos ED technique.

4 Metal-insulator transitions in fermion-boson coupled systems

In solid state physics it is one of the most fundamental problems to investigate how a material evolves from a metallic to an insulating state. Except for band structure and disorder effects, metal-insulator quantum phase transitions stem quite often from electron-electron and electron-phonon interactions in many cases. A subtle competition between Mott–Hubbard transition caused by the strong Coulomb correlations and Peierls transition driven by the coupling to vibrational excitations of the crystal triggers even a quantum insulator-insulator transition. The challenge of understanding such metal-insulator or insulator-insulator quantum phase transitions has attracted broad attention on generic microscopic models with interacting electrons and phonons. Especially, in the high- T_c cuprate superconductivity, the importance of the electron-phonon interaction is indicated by angle-resolved photoemission spectroscopy [32] and optical conductivity [33] measurements.

In this chapter, we introduce the 1D fermion-boson coupled systems in order to explore the role of background medium such as the electron-phonon coupling. Thereby, the large-scale pseudo-site DMRG method plays an essential role due to the large dimension of the bosonic Hilbert space.

4.1 Electron-phonon coupled systems

In this section we study the ground-state properties of the Holstein model for both spinless and spinfull fermions at half band filling. At the commensurate fillings, the lattice degrees of freedom trigger charge ordering, so that a quantum phase transition is expected between a metallic and a charge-ordered insulating phases. In the following, we demonstrate that the metal-insulator transition point in the Holstein model can be extracted from the Tomonaga–Luttinger liquid (TLL) parameters accurately. Moreover, in the metallic phase, the coupling to the lattice might make the system even attractive, indicated by the TLL charge exponent $K_\rho > 1$. It is of particular interest to prove the existence of such an attractive TLL phase.

4.1.1 Spinless Holstein model — Article IV

Let us first neglect the spin degrees of freedom in the 1D electron-phonon system. The resulting 1D Holstein model for spinless fermions is given by

$$\hat{H} = -t \sum_j (\hat{c}_j^\dagger \hat{c}_{j+1} + \text{h.c.}) - g\omega_0 \sum_j (\hat{b}_j^\dagger + \hat{b}_j) \hat{n}_j + \omega_0 \sum_j \hat{b}_j^\dagger \hat{b}_j, \quad (4.1)$$

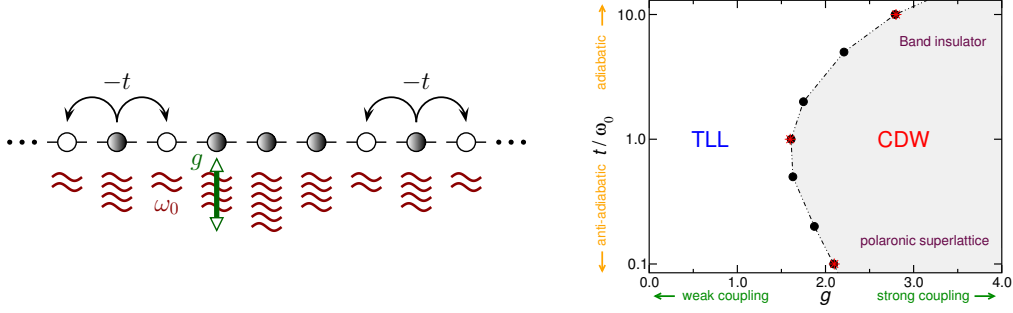


Fig. 4.1: Left: Schematic representation of the 1D spinless half-filled Holstein Hamiltonian. Right: Ground-state phase diagram according to Refs. [34–37]. Stars denote the phase transition points obtained from $K_\rho = 1/2$ via Eq. (2.36) as shown in Fig. 4.3(a).

where b_j^\dagger (b_j) is the creation (annihilation) operator for a dispersionless phonon with frequency ω_0 . It accounts for a tight-binding electron band ($\propto t$), a local electron-phonon interaction ($\propto g$), and the energy of the phonon subsystem in harmonic approximation. The schematic representation of the model (4.1) is shown in the left panel of Fig. 4.1. Despite its simplicity, the model (4.1) is not exactly solvable. However, it is generally accepted that the model exhibits a quantum phase transition from metal to a CDW insulator at half filling ($N = L/2$) [38], when the electron-phonon coupling g increases at fixed $\omega_0 > 0$. During the last three decades various analytical and numerical techniques have been applied to figure out the ground-state phase diagram in the half-filled spinless Holstein model [34–41]. In the anti-adiabatic limit ($\omega_0 \rightarrow \infty$), the model can be mapped onto the exactly solvable spin-1/2 XXZ model [38], which shows a Kosterlitz–Thouless-type transition. In the adiabatic limit ($\omega_0 \rightarrow 0$) the CDW phase above the critical coupling $g_c(\omega_0)$ vanishes.

Since a 1D gapless metallic system of interacting fermions should belong to the TLL universality class, the correlation exponent K_ρ can be used to characterize the metallic phase. In the past, K_ρ in the spinless Holstein model were determined via the charge

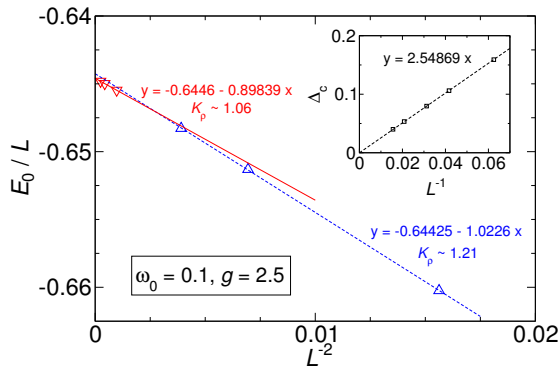


Fig. 4.2: Finite-size scaling of the ground-state energy $E_0(L)$ and the single-particle charge excitation gap Δ_c (inset) for $\omega_0 = 0.1$ and $g = 2.5$ in the spinless Holstein model at half-filling. The linear equations give the coefficients of a straight-line fit to the scaling relations (4.2). Adopted from Article IV.

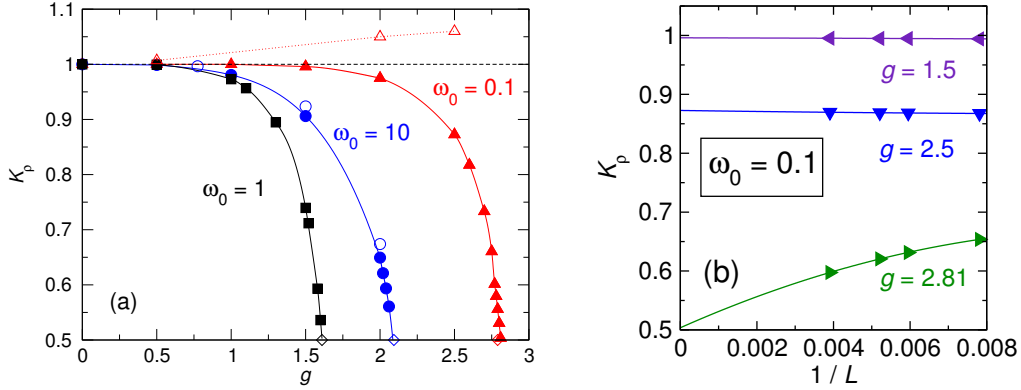


Fig. 4.3: (a): TLL parameter K_ρ in the spinless Holstein model at half filling. Closed symbols are obtained from Eq. (2.36) via $S_c(q)$ for $\omega_0/t = 0.1$ (triangles), 1 (squares), and 10 (circles). K_ρ obtained from the scaling relations (4.2) are included as open symbols. (b): K_ρ as a function of the inverse system size at $g/t = 1.5, 2.5$, and 2.81 for $\omega_0 = 0.1$ (adiabatic regime). Lines are polynomial fits. Adopted from Article IV.

velocity u_ρ and the single-particle gap Δ_{c_1} as

$$\begin{aligned} \frac{E_0(L)}{L} &= \epsilon(\infty) - \frac{\pi u_\rho}{3} \frac{1}{L^2}, \\ \Delta_{c_1}(L) &= E_0^\pm(L) - E_0(L) = \pi \frac{u_\rho}{2} \frac{1}{K_\rho L}. \end{aligned} \quad (4.2)$$

Here, $\epsilon(\infty)$ denotes the energy density of the infinite system at half filling, $E_0^\pm(L)$ are the ground-state energies with $N = L/2 \pm 1$ fermions. Simulating K_ρ from Eqs. (4.2) on finite clusters using the exact numerical methods, $g_c(\omega_0)$ can be determined with K_ρ reaching $1/2$ from above the transition point. Moreover, the TLL phase seemed to split into two different regions: for large phonon frequencies the effective fermion-fermion interaction is repulsive ($K_\rho < 1$), while it is attractive ($K_\rho > 1$) for small frequencies [34, 35].

However, the existence of an attractive TLL ($K_\rho > 1$) in the half-filled spinless Holstein model is by no means free from doubts. Although retardation effects might lead to an effective attraction between electrons at small ω_0/t it has been pointed out that such an interaction is ineffective in the case of spinless fermions due to the Pauli exclusion principles [38, 42]. This issue arises from the determination of K_ρ via the relations (4.2). Namely, Eqs. (4.2) are leading-order expressions so that one has to take nonlinear correction terms into account, e.g., in order to obtain accurate data for $g_c(\omega_0)$ especially in the adiabatic region. In particular, the $g_c(\omega_0)$ determined with and without nonlinear correction terms adds up to more than 3% for $\omega_0/t = 0.1$ whereas it is only 0.4% for $\omega_0 = 10$. In Article IV it is also demonstrated that the charge velocity u_ρ depends strongly on the system size as shown in Fig. 4.2, using the pseudo-site

DMRG method. Extrapolating the ground-state energies $E(L)$ for $L = 8, 12$ and 16 , u_ρ can be estimated as $u_\rho/2 \sim 0.977$, so that $K_\rho \sim 1.21$ from the finite-size scaling of Δ_{c_1} , while taking the ground-state energies for $L = 32, 48$ and 64 , the extracted values of K_ρ reduces to 1.06 ($u_\rho/2 \sim 0.858$).

As explained in Sec. 2.6, K_ρ can be determined via Eq. (2.36) more accurately. Figure 4.3(a) presents K_ρ in the thermodynamic limit ($L \rightarrow \infty$) for various phonon frequencies in the spinless Holstein Model. For intermediate-to-large phonon frequencies, we find $K_\rho(g) < 1$ for all g , and the values of K_ρ via Eq. (2.36) agree reasonably with those determined by the scaling relations (4.2) [see Fig. 4.3(a), filled and open symbols for $\omega_0/t = 10$]. Furthermore, our values for the critical coupling, g_c , confirm previous results as can be seen by inserting the points where $K_\rho(g_c) = 1/2$ (stars) into the existing phase diagram [34–37], see the right panel of Fig. 4.1.

The situation changes dramatically, when we enter the adiabatic regime. Figure 4.3(b) shows the finite-size scaling of K_ρ via Eq. (2.36) with OBC and up to $L = 256$ sites. Surprisingly, K_ρ scales to values smaller than unity for any electron-phonon coupling (filled symbols). This holds for other adiabatic phonon frequencies $\omega_0 < 1$ as well. Thus, we arrive at the conclusion that the half-filled spinless Holstein model does not exhibit an attractive TLL phase.

4.1.2 Hubbard–Holstein model — Article V

The Holstein–Hubbard model (HHM) is archetypal for exploring the complex interplay of electron-electron and electron-phonon interactions especially in quasi-1D materials. The Hamiltonian is given by

$$\hat{H} = -t \sum_{j\sigma} (\hat{c}_{j\sigma}^\dagger \hat{c}_{j+1\sigma} + \text{h.c.}) + U \sum_j \hat{n}_{j\uparrow} \hat{n}_{j\downarrow} - g\omega_0 \sum_{j\sigma} (\hat{b}_j^\dagger + \hat{b}_j) \hat{n}_{j\sigma} + \omega_0 \sum_j \hat{b}_j^\dagger \hat{b}_j, \quad (4.3)$$

where $\hat{c}_{j\sigma}^\dagger$ ($\hat{c}_{j\sigma}$) creates (annihilates) a spin- σ electron at Wannier site j of an 1D lattice with L sites and $\hat{n}_{j\sigma} = \hat{c}_{j\sigma}^\dagger \hat{c}_{j\sigma}$. The electron itinerancy ($\propto 4t$) competes with electron-electron ($\propto u = U/4t$) and electron-phonon ($\propto \lambda = g^2\omega_0/2t$) interactions. The left panel of Fig. 4.4(a) shows a schematic representation of the HHM (4.3). Hereafter, we consider the half-filled case, $\frac{1}{L} \sum_{j\sigma} \hat{n}_{j\sigma} = 1$, and take t as energy unit.

Based on ED data for the staggered static charge/spin structure factor, $S_{\rho/\sigma}(\pi)$, it has been argued that the HHM shows a crossover between Mott and Peierls insulating phases near $u/\lambda \simeq 1$ [43]. But this only holds in the strong-coupling adiabatic-to-intermediate phonon frequency regime. Later on the ground-state phase diagram of the HHM was explored in more detail, also for weak interaction strengths and large phonon frequencies. In this regime, variational displacement Lang-Firsov [44], stochastic series expansion QMC [45, 46], and DMRG [47–49] methods give strong evidence that, if λ is enhanced at fixed u and ω_0 , the SDW-CDW transition splits into two subsequent SDW-TLL and TLL-CDW transitions at λ_{c_1} and λ_{c_2} , respectively [see Fig. 4.4(b), dashed and dot-dashed lines].

The TLL parameters, K_ρ and K_σ , can be used to examine the properties of the metallic phase and the phase boundaries to the insulating states. $K_\rho > 1$ corresponds

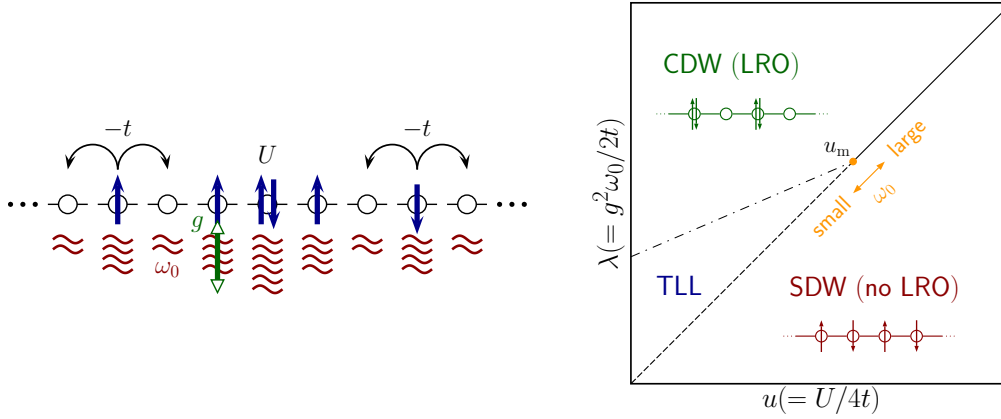


Fig. 4.4: Left: Schematic representation of the 1D Hubbard–Holstein Hamiltonian. Right: Qualitative phase diagram. The ground state is metallic at $u = 0$ for $\omega_0 > 0$ and this TLL phase continues to exist between the SDW and CDW phases for $u > 0$. With increasing ω_0 the region of the intervening TLL phase increases, and the tricritical point u_m moves to larger u . The SDW state shows no long-range order (LRO) and is characterized by a vanishing spin gap Δ_s but a finite charge gap Δ_{c1} , whereas the CDW phase exhibits true LRO and $\Delta_s = \Delta_{c1} > 0$.

to attractive charge correlations in the TLL and $K_\rho = 0$ signals an insulating phase. Moreover, at half filling the repulsive metallic phase can be realized only for $K_\rho = 1$. Hence one expects that K_ρ jumps from $1 \rightarrow 0$ at the metal-SDW/CDW transitions. The spin-exponent takes the value $K_\sigma = 0$ in a spin-gapped phase and $K_\sigma = 1$ everywhere else in the thermodynamic limit. For finite systems the situation is more involved, in particular for the spin exponent K_σ . First, the convergence $K_\sigma \rightarrow 0$ is slow-going as $L \rightarrow \infty$ in the spin-gapped phase. Second, logarithmic corrections prevent $K_\sigma \rightarrow 1$ in the spin-gapless (SDW) phase. On the other hand, these logarithmic corrections vanish at the critical point, where the spin gap opens, and we can utilize that K_σ (K_ρ) crosses 1 from above (below) at some λ_{c1} (as the electron-phonon coupling increases for fixed u), in order to determine the SDW-metal phase boundary itself. Increasing λ further, K_ρ should cross 1 once again, this time from above, at another critical coupling strength, λ_{c2} , which pins the metal-CDW transition point down.

In order to characterize the SDW-CDW-intervening metallic phase, K_ρ and K_σ are intensively studied in Ref. [46], comparing with the numerical data in the half-filled negative- U Hubbard model. Specifically, QMC data up to $L = 64$ appear to show $K_\rho > 1$ in the intermediate region, which corresponds to attractive charge correlations. However, the authors argued that $K_\rho > 1$ might be the finite-size effects and the true K_ρ should be equal to unity, considering the numerical *wrong* results of $K_\rho > 1$ in the negative- U Hubbard model instead of the exact value, $K_\rho = 1$.

In Article V, we investigated TLL parameters, various excitation energies and the binding energy, using the large-scale boson pseudo-site DMRG approach. Figure 4.5

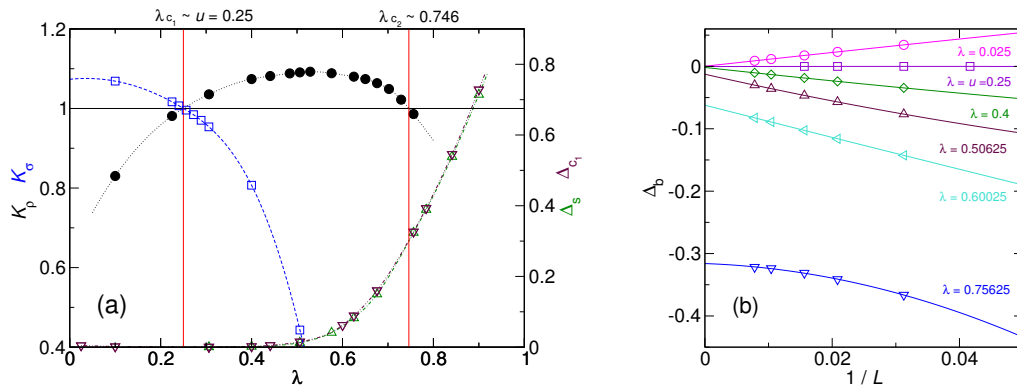


Fig. 4.5: DMRG results for the half-filled HHM with $u = 0.25$ and $\omega_0 = 5$. (a): charge (K_ρ , filled circles) and spin (K_σ , open squares) TLL exponents as functions of λ . Open triangles up (triangles down) give the spin (charge) gap Δ_s (Δ_{c_1}). Data shown are extrapolated values for the infinite systems, using open boundary conditions. (b): Finite-size scaling of the binding energy Δ_b for different λ . Lines are polynomial fits. Adapted from Article V.

corroborates the scenario mentioned above for the anti-adiabatic regime ($\omega_0 = 5$) of the HHM. The values of two critical points λ_{c_1} and λ_{c_2} are in accord with the phase diagram obtained by QMC [45, 46]. $K_\sigma < 1$ and $K_\rho > 1$ earmark the intervening metallic phase. Here we inspect the finite-size scaling of the spin and single-particle charge excitation gaps,

$$\Delta_s(L) = E_0(1) - E_0(0), \quad (4.4)$$

$$\Delta_{c_1}(L) = E_0^{1+}(1/2) + E_0^{1-}(-1/2) - 2E_0(0), \quad (4.5)$$

respectively, as well as that of the two-particle binding energy

$$\Delta_b(L) = E_0^{2-}(0) + E_0(0) - 2E_0^{1-}(-1/2), \quad (4.6)$$

where $E_0^{[\delta N \pm]}(S^z)$ denotes the ground-state energy at [away from] half filling with $N_e = N[\pm \delta N]$ particles in the sector with total spin- z component S^z . Figure 4.5(a) demonstrates that both spin and charge gaps open at λ_{c_1} (but there is no long-range order). For $u < u_m$, the transition at λ_{c_1} seems to be of Kosterlitz–Thouless type, i.e. just above λ_{c_1} the gaps are exponentially small and therefore their magnitude is difficult to determine numerically. In this region, we find $\Delta_{c_1} \sim \Delta_s$, and the binding energy Δ_b is also extremely small, or maybe even zero [see the data for $\lambda = 0.4$ (triangles up) in Fig. 4.5(b)]. As λ increases, we obtain a crossover to a metallic regime with a noticeable two-particle binding energy $\Delta_b < 0$, where $\Delta_{c_1} \sim \Delta_s$. In the CDW phase, which typifies a bipolaronic superlattice at large phonon frequencies, we have, besides $\Delta_s = \Delta_{c_1} > 0$ and $\Delta_b < 0$, whereas in the SDW state $\Delta_{c_1} > 0$ but $\Delta_b(L \rightarrow \infty) \rightarrow 0$. While the basic scenario discussed so far persists in the adiabatic regime, the metallic region shrinks as the phonon frequency ω_0 becomes smaller [45, 46, 49]. Furthermore,

the CDW state rather behaves as a normal Peierls insulator and consequently there is a weaker tendency towards bipolaron formation in the metallic state for small λ , and $u < u_m$.

In this way the QMC results of the TLL parameter $K_\rho > 1$ in Refs. [45, 46] can be confirmed by using the large-scale DMRG technique. However, we still can not exclude the possibility that $K_\rho > 1$ in the half-filled HHM arises from the finite-size effect. It is desired to establish a numerical technique, which provides $K_\rho = 1$ in the half-filled negative- U Hubbard model, and to apply it to the intermediate metallic region in the HHM. The infinite-system DMRG [50, 51] might be a strong candidate.

4.2 Edwards transport model

The nature of charge transport within a correlated background medium can be described by spinless fermions coupled to bosons in the model introduced by Edwards [52, 53]. Although the physically interesting regime with respect to superconductivity is for low to moderate fermion density, the Edwards model has interesting properties over the whole density range.

The Hamiltonian of the 1D fermion-boson coupled Edwards model is given by

$$\hat{H}_E = \hat{H}_{fb} - \lambda \sum_j (\hat{b}_j^\dagger + \hat{b}_j) + \omega_0 \sum_j \hat{b}_j^\dagger \hat{b}_j, \quad (4.7)$$

where a boson-affected nearest-neighbor hopping ($\propto t_b$) of spinless fermions is

$$\hat{H}_{fb} = -t_b \sum_{\langle j,l \rangle} \hat{c}_l^\dagger \hat{c}_j (\hat{b}_j^\dagger + \hat{b}_l). \quad (4.8)$$

Every time a fermion $\hat{c}_j^{(\dagger)}$ hops, it creates or absorbs a boson $\hat{b}_j^{(\dagger)}$ of energy ω_0 at the sites it leaves or enters. Such an excitation or deexcitation corresponds to a local distortion of the background medium. Due to quantum fluctuations the distortions are able to relax ($\propto \lambda$). Performing the unitary transformation $\hat{b}_j \mapsto \hat{b}_j + \lambda/\omega_0$ eliminates the boson relaxation term in favor of a second fermion hopping channel:

$$\hat{H}_E = \hat{H}_{fb} - t_f \sum_{\langle j,l \rangle} \hat{c}_l^\dagger \hat{c}_j + \omega_0 \sum_j \hat{b}_j^\dagger \hat{b}_j, \quad (4.9)$$

with a strongly reduced energy scale, $t_f = 2\lambda t_b/\omega_0$. We would like to emphasize that coherent propagation of a fermion is possible even in the limit $\lambda = t_f = 0$ by means of a six-step vacuum-restoring hopping process [53]

$$\hat{R}_j^{(6)} = \hat{L}_{j+2}^\dagger \hat{L}_{j+1}^\dagger \hat{R}_j^\dagger \hat{L}_{j+2} \hat{R}_{j+1} \hat{R}_j, \quad (4.10)$$

where $\hat{R}_j^\dagger = \hat{c}_j^\dagger \hat{c}_{j+1} \hat{b}_j$ and $\hat{L}_j^\dagger = \hat{c}_j^\dagger \hat{c}_{j-1} \hat{b}_j$. Note that $\hat{R}_j^{(6)}$ acts as direct next-nearest-neighbor transfer “ $\hat{c}_{j+2}^\dagger \hat{c}_j$ ”, in complete analogy to the “Trugman path” of a hole in a 2D Néel-ordered spin background [54].

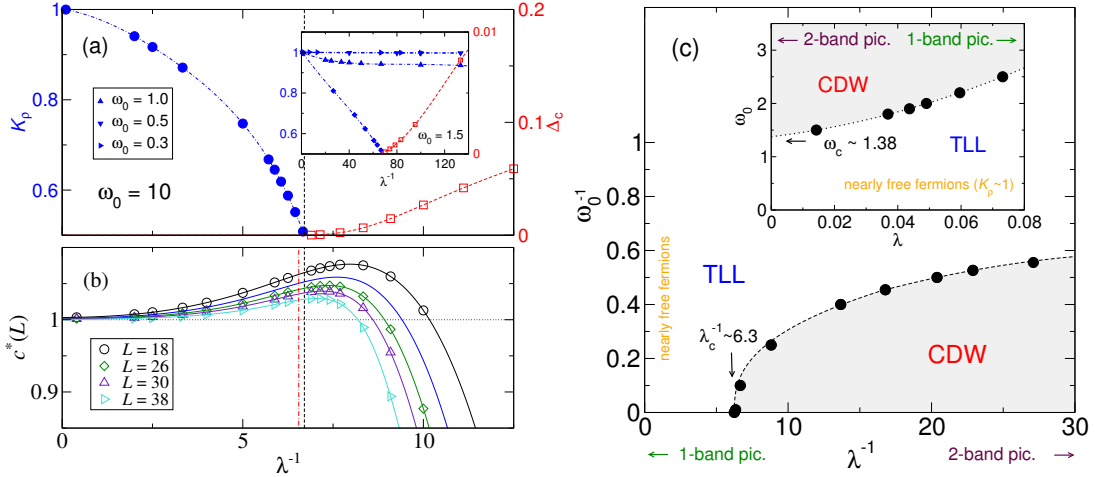


Fig. 4.6: (a): TLL parameter K_ρ (circles) and single-particle gap Δ_{c1} (open squares) as a function of λ^{-1} for $\omega_0 = 10$ (main panel). The inset displays results for smaller ω_0 . (b): Central charge c^* at $\omega_0 = 10$ for different system sizes with PBC. The red dashed-dotted line gives the metal-insulator transition point determined by extrapolating the maximum of $c^*(L)$ in reasonable agreement with the value obtained from K_ρ (black dashed line) in panel (a). (c): DMRG phase diagram of the Edwards model at half filling. The inset gives the phase diagram in the λ - ω_0 plane. Adapted from Articles VI and VII.

Albeit the simplicity of the Hamiltonian, the Edwards model displays a rich physics, e.g., a metal to CDW insulator quantum phase transitions at commensurate fillings, an attractive TLL phase with $K_\rho > 1$ and phase-separated regimes similar to the t - J model. In the following, we introduce part of the numerical results for the Edwards fermion-boson model obtained by the large-scale boson pseudo-site DMRG approach. Note that in this section we take $t_b = 1$ as the energy unit.

4.2.1 Metal-insulator transition at half filling — Articles VI - IX

As in the case of the Holstein model, the most fundamental problem is to prove the existence of a metal-insulator transition. At half filling evidence for such a quantum phase transition in the Edwards model has been found first in a ED study [55]. Calculating the photoemission spectra up to the system size $L = 16$ sites, the opening of a single-particle excitation gap has been observed at $k_F = \pm\pi/2$ as λ decreases at relatively large $\omega_0 = 2$. Of course, this is not a unambiguous proof of the existence of a metal-insulator transition which should be confirmed in the thermodynamic limit $L \rightarrow \infty$.

In the absence of disorder, the formation of a CDW state is the only possibility for a metal-insulator transition. In the 1D spinless fermion model at half filling one expects that the metal-CDW insulator transition occurs when the TLL charge exponent

K_ρ reaches $1/2$. In Article VI we extract the TLL parameter K_ρ via Eq. (2.36) in order to figure out the ground-state phase diagram at half filling. Lowering λ at fixed values of $\omega_0 = 10$, the extrapolated values of K_ρ actually decreases from $1 \rightarrow 1/2$ as shown in Fig. 4.6(a). The point where $K_\rho = 1/2$ is reached marks the critical coupling $\lambda_c^{-1}(\omega_0 = 10) \sim 6.7$ at the metal-insulator transition. We expect that the single-particle gap Δ_c becomes finite in the insulating phase, which is given by

$$\Delta_c(L) = E(N+1) + E(N-1) - 2E(N), \quad (4.11)$$

where $E(N)$ and $E(N\pm 1)$ are the ground-state energies in the N - and $(N\pm 1)$ -fermionic-particle sectors, respectively, with $L = N/2$. Actually, Δ_c opens exponentially when entering the insulating phase, indicating the Kosterlitz–Thouless-type transition. This collaborates with the numerically obtained central charge via Eq. (2.41), where we find $c^*(L \rightarrow \infty) \sim 1$ for $\lambda^{-1} < \lambda_c^{-1}$, as shown in Fig. 4.6(b). Furthermore, extrapolating the value of $\lambda_c(L)$ where $c^*(L)$ shows maximum to the thermodynamic limit $L \rightarrow \infty$, the metal-insulator transition point λ_c can be also determined and matches the critical value obtained from K_ρ surprisingly well as show in Fig. 4.6(b). Note that at half filling we find only a repulsive particle interaction ($K_\rho \leq 1$) in the metallic phase even for small boson frequencies [see the inset of Fig. 4.6(a)]; i.e., in 1D there is no indication for a pairing instability at half band filling.

Figure 4.6(c) represents the ground-state phase diagram of the 1D half-filled Edwards model in the λ^{-1} - ω_0^{-1} plane. The phase space is divided into two regimes, the repulsive TLL phase ($K_\rho \leq 1$) and the $2k_F$ -CDW phase with long-range order. Let us first consider how the CDW state is realized in the limit of large ω_0 at half filling. The CDW is a few-boson state that typifies rather a correlated (Mott-Hubbard-type) insulator than a Peierls state with many bosons (phonons) involved. Since in the limit $\omega_0 \gg 1 \gg \lambda$ background fluctuations are energetically costly, charge transport is hindered and an effective Hamiltonian with nearest-neighbor fermion repulsion results. To leading order, in a reduced (zero-boson) Hilbert space, we obtain

$$\hat{H}_{tV} = -t_f \sum_{\langle j,l \rangle} \hat{c}_l^\dagger \hat{c}_j + V \sum_j \hat{n}_j^f \hat{n}_{j+1}^f \quad (4.12)$$

with $V = t_b^2/\omega_0$. This so-called t - V model can be mapped onto the integrable spin-1/2 XXZ model, and exhibits also a TLL-CDW quantum phase transition at half filling for $V/t_f = 2$, i.e., for $\lambda_c^{-1} = 4$. This value is slightly smaller than those obtained in the Edwards model, $\lambda_c^{-1} \simeq 6.3$ in the limit $\omega_0 \ll 1$ [see Fig. 4.6], because already three-site and next-nearest-neighbor hopping terms of the effective model were neglected in Eq. (4.12). In the opposite limit of small ω_0 , the background medium is easily disturbed by particle motion. Therefore the rate of bosonic fluctuations ($\propto \omega_0^{-1}$) is high. Now we enter the fluctuation dominated regime, and consequently CDW order is suppressed. The inset of Fig. 4.6(c) shows that even for $\lambda = 0$, i.e., if the explicit λ -relaxation channel is closed, a metallic state may exist below a finite critical energy $\omega_0(\lambda = 0) \sim 1.38$.

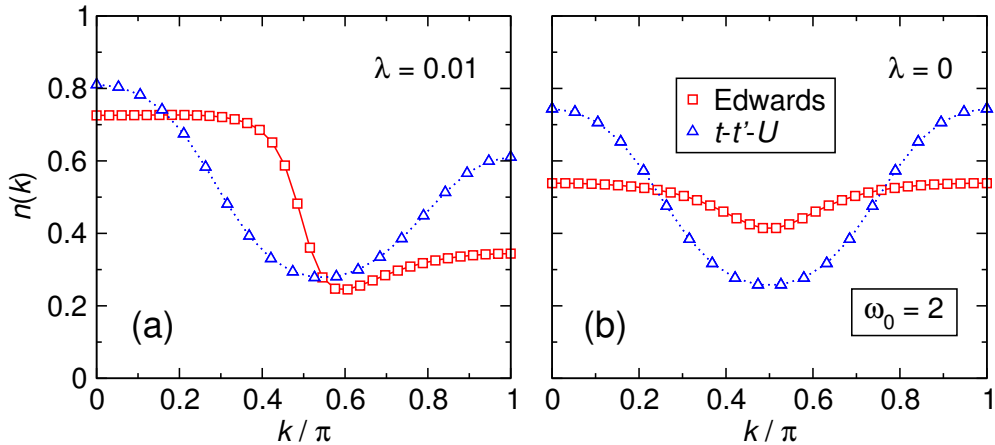


Fig. 4.7: Momentum distribution function $n(k)$ in the CDW phase of the half-filled Edwards model with PBC, for $\lambda = 0.01$ (a) and $\lambda = 0$ (b) at $\omega_0 = 2$ (squares). Triangles show $n(k)$ in the half-filled t - t' - U model for $U = 10t'$ with $t = t'$ [panel (a)] and $t = 0$ [panel (b)]. Adapted from Article VIII.

The different transport behavior in the Edwards model becomes apparent in the momentum distribution function

$$n(k) = \frac{1}{L} \sum_{j,l} e^{ik(j-l)} \langle \hat{c}_j^\dagger \hat{c}_l \rangle. \quad (4.13)$$

By means of DMRG the correlation function $\langle \hat{c}_j^\dagger \hat{c}_l \rangle$ can be easily calculated with PBC. Figure 4.7 displays $n(k)$ for two characteristic boson energies. In the CDW phase the periodicity of $n(k)$ doubles at $\lambda = 0$, since only a $\hat{R}^{(6)}$ next-nearest-neighbor hopping channel, Eq. (4.10), survives. To substantiate this reasoning we have included in Fig. 4.7 $n(k)$ data calculated in the 1D Hubbard model with additional next-nearest-neighbor transfer t' . We see that $n(k)$ of the Edwards model is in qualitative agreement with our data and those for the t - t' - U Hubbard model [56], in particular, for the case $t = 0$.

In Article IX, the interplay of disorder and interaction effects is also studied in the framework of the Anderson–Edwards model at half filling. Adding the disorder induced by random on-site potentials, the Anderson localized state replaces the TLL phase of the half-filled Edwards model. It will be shown that the nature of the Anderson insulator state can still be understood in terms of scaling relations containing the charge susceptibility and the TLL parameter K_ρ of the metallic phase in the absence of disorder only. However, the Anderson–Edwards model reveals a complex interrelation between disorder and CDW correlations due to additional scattering channels, involving bosonic excitation and annihilation processes.

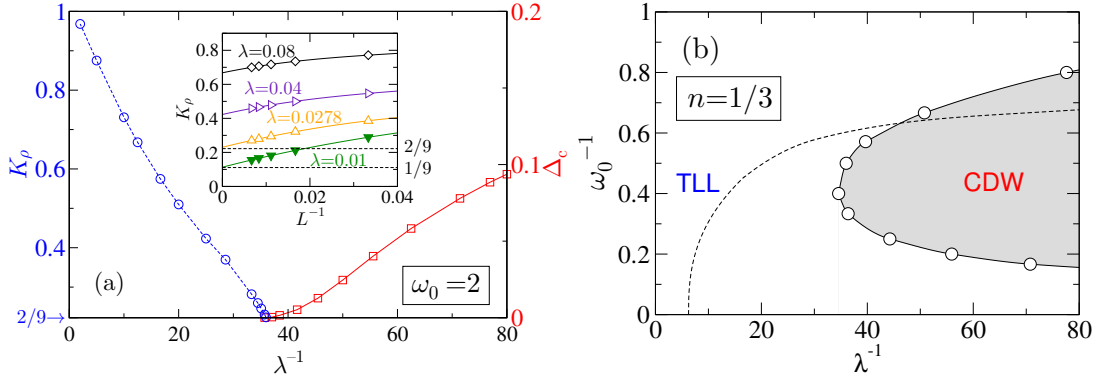


Fig. 4.8: (a): $L \rightarrow \infty$ extrapolated K_ρ (circles) and Δ_c (squares) as functions of λ^{-1} for $\omega_0 = 2$ in the one-third filled Edwards model. The inset shows the finite-size scaling of K_ρ for various values of $\lambda (> \lambda_c)$ (open symbols) in the TLL phase and for $\lambda = 0.01$ with $n = 1/3 - 1/L$ (filled symbols) in the infinitesimally doped CDW insulator. (b): DMRG ground-state phase diagram of the 1D Edwards model at one-third filling. The dashed line denotes the MI transition points at half filling from Article VI. Adopted from Article X.

4.2.2 Metal-insulator transition at one-third band filling — Article X

Surprisingly, the Edwards fermion-boson model displays a metal-to-insulator quantum phase transition also at one-third band filling ($n = 1/3$). Determining the single-particle gap Δ_c and the TLL parameter K_ρ via Eq. (2.36), the quantum phase transition points can be examined as in the case of half band filling. For a spinless-fermion system with one-third band filling, bosonization theory yields $K_\rho^* = 2/9$ at the metal-insulator transition point and $K_\rho^{\text{CDW}} = 1/9$ for an infinitesimally doped three-period CDW insulator [12, 57]. At fixed $\omega_0 = 2$ the values of K_ρ decreases with increasing λ^{-1} and becomes equal to $K_\rho^* = 2/9$ at the Kosterlitz–Thouless transition point $\lambda_c^{-1} \sim 36$; see Fig. 4.8(a). For $\lambda^{-1} > \lambda_c^{-1}$ the system embodies a $2k_F$ -CDW insulator with finite charge gap Δ_c . Furthermore, calculating $K_\rho(L)$ for $N = L/3 - 1$ particles deep in the CDW phase, K_ρ approaches $1/9$ in the thermodynamic limit [cf. the $\lambda = 0.01$ data (filled symbols) in the inset of Fig. 4.8(a)] as expected from bosonization.

Figure 4.8(b) represents the ground-state phase diagram of the one-third filled Edwards model. Analogous to the half-filled case, the $L \rightarrow \infty$ extrapolated K_ρ values determine the metal-insulator transition point. The repulsive TLL phase ($2/9 < K_\rho < 1$) appears at large λ , when any distortion of the background medium readily relaxes ($\propto \lambda$), or in the opposite limit of small λ , when the rate of the bosonic fluctuations ($\propto \omega_0^{-1}$) is sufficiently high. At half filling the CDW phase with $\Delta_c > 0$ and long-range order appears for small λ and by trend large ω_0 (see dashed lines); $\lambda_c \simeq 0.16$ for $\omega_0 \rightarrow \infty$, see Fig. 4.6(b). Interestingly, for $n = 1/3$, we observe that the CDW will be suppressed again if the energy of a background distortion becomes larger than a certain λ -dependent value [see Fig 4.8(b)]. In stark contrast to the half-filled band

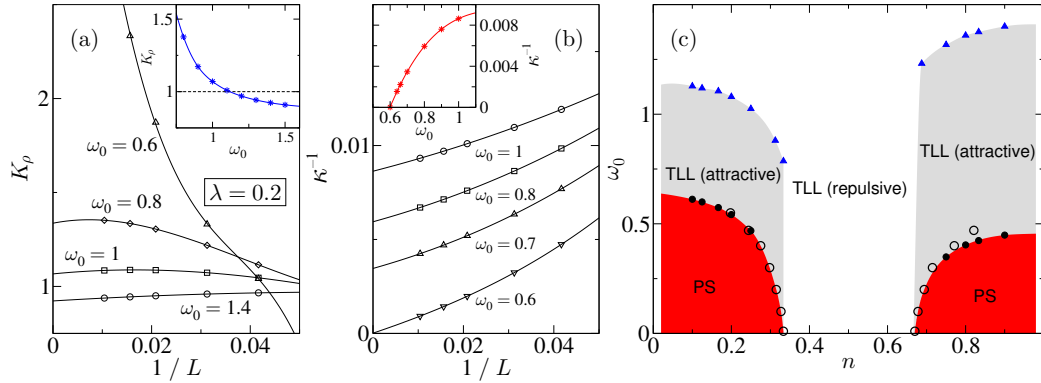


Fig. 4.9: Finite-size scaling of the TLL parameter K_ρ (a) and inverse compressibility κ^{-1} (b) for $\lambda = 0.2$ at $n = 1/8$. Insets show the variation with ω_0 of the $L \rightarrow \infty$ extrapolated values. Panel (c) represents the ground-state phase diagram of the Edwards model, showing repulsive TLL ($K_\rho < 1$), attractive TLL ($K_\rho > 1$), and phase separated ($\kappa^{-1} = 0$) regions. The phase boundaries were obtained by DMRG (filled symbols) and by projective renormalization method [41, 58] (open symbols). Adopted from Article XI.

case, at $n = 1/3$ it seems that the TLL is stable $\forall \lambda$, when $\omega_0 \rightarrow \infty$. This is because in this limit not only a nearest-neighbor Coulomb repulsion V but also a substantial next-nearest-neighbor interaction V_2 is needed to derive the metal-to-CDW transition in the corresponding spinless model (4.12) at $n = 1/3$. Again in the limit $\omega_0/t_b \gg 1 \gg \lambda/t_b$, the Edwards model at one-third filling can be described by the effective t - V - V_2 model with $V = 2t_b^2/3\omega_0$ and $V_2 = 2t_b^4/\omega_0^3$, i.e., $V_2/t_f = t_b^3/\lambda\omega_0^2$, which clearly explains the absence of the CDW phase for $\omega_0 \gg 1$.

4.2.3 Phase separation — Article XI

The situation away from half-band filling is much less understood. By analogy with the t - J model, one might expect that the system is metallic for $0 < n < 1/2$, at least if the background is not too stiff. If so, the next question will be whether there might exist an attractive TLL phase ($K_\rho > 1$) in a certain parameter regime (λ, ω_0) of the Edwards model. Apparently, a second electron, following the path of a first one, can take advantage of the background excitations (bosons) left behind by the first electron. This acts like an effective attractive interaction. If this attraction completely dominates the kinetic energy, the system might even phase-separate into particle-enriched and particle-depleted regions.

To address these problems, we analyze again the TLL parameter K_ρ and the charge compressibility κ away from the half-band filling. The latter quantity can be obtained as

$$\kappa = \frac{L}{N^2} \left[\frac{E_0(N+2) + E_0(N-2) - 2E_0(N)}{4} \right]^{-1}. \quad (4.14)$$

An infinite compressibility signals the formation of a phase separated state.

Figures 4.9(a) and (b) demonstrate the finite-size-scaling of the TLL exponent K_ρ and the inverse compressibility κ^{-1} at various ω_0 . The transition point between a repulsive and an attractive TLL phases at smaller ω_0 can be read off from the inset [depicting the extrapolations $K_\rho(L \rightarrow \infty)$] as $\omega_{0,c1}(\lambda = 0.2) \simeq 1.118$. Reducing ω_0 further, in the attractive TLL phase, a dramatic increase in K_ρ is observed at $\omega_{0,c2} \simeq 0.6$. Our inverse compressibility data indicate that at this point, the attraction among the particles becomes so strong that the system shows phase separation, i.e., $\kappa^{-1} = 0$ for $\omega_0 < \omega_{0,c2}$.

Proceeding in the same manner for different values of n and ω_0 for a fixed value of λ , we can map out the phase diagram of the Edwards model in the n - ω_0 space as shown in Fig. 4.9(c). Let us consider the case of a not too small boson relaxation, $\lambda = 0.2$, which ensures that the system is metallic for large ω_0 in the whole density regime. Then, depending on n we find up to three different regimes: For small and large particle densities, an attractive TLL, and a phase separated state appear in sequence as the energy of the bosons is lowered. In contrast, around half band filling only the repulsive TLL phase exists. Note that the behavior in the low-density regime is consistent with what is found for the 1D t - J model [59, 60], where the holes correspond to the spinless fermions in the Edwards model.

To summarize this section, the Edwards fermion-boson model has been intensively studied using the large-scale DMRG technique combined with the boson pseudo-site approach. At half- and one-third-band fillings the system realizes a TLL or a truly long-range ordered CDW state. Depending on the properties of the background medium, the TLL might be repulsive or attractive away from half filling. In the low- and high-density regions, the attraction between the particles mediated by the bosonic degrees of freedom representing the background medium might become so strong that electronic phase separation sets in. Thus, the Edwards model captures important features of Holstein-, t - J -, and Hubbard-type models.

The dynamical properties of the Edwards model have also been investigated using the dynamical DMRG technique, but will not be discussed here. We only like to note that the simple Green's function approximation is proposed for the Edwards model in Article XII, showing excellent agreements with the DDMRG results.

5 Quantum phase transitions of lattice bosons

At very low temperatures, bosonic atoms which are loaded into an optical lattice realize a superfluid (SF) for a shallow optical potential or a Mott insulator (MI) for a deep optical potential. The SF-MI transition has been observed experimentally [61, 62]. Since bosons on a chain are also accessible experimentally [63], it attracts increasing attention for studying the 1D lattice model for bosons. The physics of 1D bosonic systems is rather peculiar. For instance, the state with the lowest kinetic energy is not macroscopically occupied in the “superfluid” but it is characterized by an algebraic divergence of the momentum distribution [13]. Moreover, the Mott gap is exponentially small in the Mott insulator close to the phase transition. Therefore, it is very difficult to determine the critical interaction strength numerically.

The minimal model of the strongly interacting bosons on a lattice is the so-called Bose–Hubbard model (BHM), which exhibits a SF-MI phase transition, induced by the competition between the on-site repulsion and the hopping integral. In order to determine this quantum phase transition point the BHM has been intensively studied both by analytical [64, 65] and numerical [66, 67] methods at zero temperature. In Sec. 5.1 we demonstrate that the quantum phase transition point can be determined with high accuracy not only by the TLL parameter as in Ref. [66, 67] but also the numerically obtained central charge, showing an excellent agreement between both results. Moreover, comparing the static and dynamical quantities obtained from the (D)DMRG method with those by the strong-coupling perturbation theory, we show the accuracy of DMRG simulations in the bosonic systems.

In Sec. 5.2, we further apply the (D)DMRG technique to the extended model with the longer-range repulsion. Namely, we investigate the entanglement and dynamical properties of the so-called Haldane insulator, which is now categorized as a *symmetry-protected topological phase*.

5.1 Superfluid-Mott insulator quantum phase transition

The Bose–Hubbard Hamiltonian \hat{H}_{BH} on a chain with L sites is defined by

$$\begin{aligned}\hat{H}_{\text{BH}} &= -t\hat{T} + U\hat{D}, \\ \hat{T} &= \sum_{j=1}^L (\hat{b}_j^\dagger \hat{b}_{j+1} + \hat{b}_{j+1}^\dagger \hat{b}_j),\end{aligned}\tag{5.1}$$

$$\hat{D} = \frac{1}{2} \sum_{j=1}^L \hat{n}_j (\hat{n}_j - 1).$$

Here, \hat{b}_j^\dagger (\hat{b}_j) is the boson creation (annihilation) operator on site j and $\hat{n}_j = \hat{b}_j^\dagger \hat{b}_j$. The physics of the BHM is governed by the ratio between kinetic energy and interaction energy, $x = t/U$. If x is larger than a critical value x_c the bosons are superfluid. Below x_c the system becomes Mott insulating with an integer filling factor ρ . In experiments, x can be varied over several orders of magnitude by modifying the depth of the lattice through quantum optical techniques whereby SF and MI phases can be realized.

A detailed theoretical understanding of the BHM requires the calculations of (dynamical) correlation functions which poses a hard problem since the model for $U < \infty$ (soft-core bosons) is not integrable. From the analytical point of view, in the SF phase weakly interacting boson at low energies are well described as a Tomonaga–Luttinger liquid [68, 69]. In the MI phase, the strong-coupling expansions in x give reliable analytical results. For instance, the ground-state energy of all Mott lobes was determined to second order by Freericks and Monien [64], and was improved up to order x^{14} for the first Mott lobe by Damski and Zakrzewski [70]. The results for the momentum distribution $n(k)$ to third order in x were obtained for $\rho = 1$ in Refs. [70, 71]. From the numerical point of view, the (D)DMRG technique permits the calculation of ground-state and dynamical properties in the 1D BHM at zero temperature with excellent accuracy for large systems [67]. Again, the main obstacle thereby is related to the fact that, in principle, each lattice site can be occupied by infinitely many bosonic particles. Therefore, one has to introduce a cutoff n_b^{\max} , the maximum number of bosons per site taken into account. The DMRG results are nonetheless unbiased and numerically exact, if the dependence on n_b^{\max} can be proven to be negligible.

In this section we demonstrate the ground-state and dynamical results of the 1D BHM obtained by the large-scale (D)DMRG technique comparing with the perturbative results, which give reliable analytical estimations especially in the MI phase. While in the past DMRG has been successfully applied to investigate the ground-state properties of the BHM [66, 67] DMRG results for dynamical properties are rare, but highly desirable because superfluids in optical lattices can be studied by momentum-resolved Bragg spectroscopy [72].

5.1.1 Superfluidity — Articles XIII and XIV

Ground-state energy

The ground-state energy E_0 of the 1D BHM has been determined analytically in the weak- and strong-coupling cases. For weak interactions, the ground-state energy in Bogoliubov theory is given by

$$\frac{E_0^B(U)}{L} = -3t + \frac{\sqrt{2Ut}}{\pi} + \frac{U + 2t}{\pi} \arccos \left(\sqrt{\frac{U}{U + 2t}} \right). \quad (5.2)$$

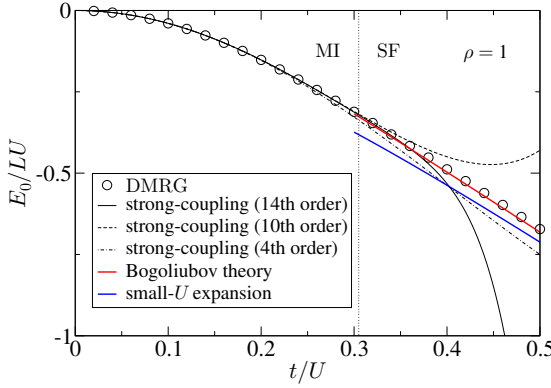


Fig. 5.1: Ground-state energy E_0/LU as a function of interaction strength t/U for the first Mott lobe. Weak- and strong-coupling results are compared with the $L \rightarrow \infty$ extrapolated DMRG data. Adapted from Article XIV.

The small- U expansion yields

$$\frac{E_0^B(U \ll t)}{Lt} = -2 + \frac{U}{2t} - \frac{\sqrt{2}(U/t)^{3/2}}{3\pi}. \quad (5.3)$$

For strong interactions, an expansion up to 14th order in $x = t/U$ was obtained by Damski and Zakrzewski [70]

$$\begin{aligned} \frac{E_0^{[14]}}{4UL} &= -x^2 + x^4 + \frac{68}{9}x^6 - \frac{1267}{81}x^8 + \frac{44171}{1458}x^{10} - \frac{4902596}{6561}x^{12} \\ &\quad - \frac{8020902135607}{2645395200}x^{14} + \mathcal{O}(x^{16}). \end{aligned} \quad (5.4)$$

Figure 5.1 compares these perturbative results with DMRG data. The strong-coupling series expansion is in accordance with the numerical exact data, surprisingly even beyond the Kosterlitz–Thouless transition point (i.e., for $t/U \simeq 0.4$). Clearly, the quality of the strong-coupling approximation improves as higher-order corrections are taken into account. Figure 5.1 also shows the range of validity of the corresponding weak-coupling approaches.

Ground-state phase diagram

At integer filling $\rho = N/L$, the 1D BHM describes a Mott transition between the SF phase, characterized by a divergence of the momentum distribution at momentum $k = 0$, and a MI phase, characterized by a finite gap for single-particle excitations. The latter is defined by the energy difference between the chemical potentials which are given by

$$\begin{aligned} \Delta(L) &= \mu^+(L) - \mu^-(L), \\ \mu^+(L) &= E_0(L, N+1) - E_0(L, N), \\ \mu^-(L) &= E_0(L, N) - E_0(L, N-1), \end{aligned} \quad (5.5)$$

where $E_0(L, N)$ is the ground-state energy for L sites and N particles. In the thermodynamical limit, $N, L \rightarrow \infty$ and $\rho = N/L$ integer, the gap is finite for the Mott insulator,

$\Delta = \lim_{N,L \rightarrow \infty} \Delta(L) > 0$, so that the system becomes incompressible when we go from the SF phase to the MI phase. The Mott transition lines in the μ - U ground-state phase diagram have been previously determined by various analytical and numerical methods, e.g., strong-coupling expansions [64, 65], QMC [73, 74], and DMRG [66, 67], as also shown in Fig. 5.2(a) for the first Mott lobe ($\rho = 1$) and the second Mott lobe ($\rho = 2$) by DMRG.

At the tip of each Mott lobe, the model is in the universality class of XY spin model with central charge $c = 1$ so that there is a Kosterlitz–Thouless phase transition with the TLL parameter $K_b = 1/2$, and the gap is exponentially small in the vicinity of $(t/U)_c$. In the following we explain how the critical interactions $(t/U)_c$ in the BHM can be determined via the TLL parameter K_b and numerically obtained central charge c^* using the DMRG technique.

As in the case of 1D fermionic systems the TLL parameter K_b determines the asymptotic behavior of the correlation functions in the SF phase, and various correlation functions have been used to extract K_b . Similar to the TLL parameter in 1D fermionic systems explained in Sec. 2.6 we consider the density-density correlation function

$$S(r) = \frac{1}{L} \sum_l \{ \langle \hat{n}_{l+r} \hat{n}_l \rangle - \langle \hat{n}_{l+r} \rangle \langle \hat{n}_l \rangle \}. \quad (5.6)$$

Asymptotically, it behaves like

$$S(r \rightarrow \infty) \sim -\frac{1}{2K_b} \frac{1}{(\pi r)^2} + \frac{A\rho^2 \cos(2\pi\rho r)}{(\rho r)^{2/K_b}} + \dots \quad (5.7)$$

Thus, we can extract K_b from the derivative of its Fourier transformation $\tilde{S}(q)$,

$$\frac{1}{2K_b} = \lim_{L \rightarrow \infty} \frac{\tilde{S}(q)}{q}. \quad (5.8)$$

In order to treat finite systems in numerical calculations, we translate Eq. (5.8) into

$$\frac{1}{2K_b(L)} = \lim_{L \rightarrow \infty} \frac{L}{2} \tilde{S}\left(\frac{2\pi}{L}\right), \quad (5.9)$$

and extrapolate $K_b(L)$ to the thermodynamic limit. As shown in Fig. 5.2(b), $K_b(L)$ can be reliably extrapolated to the thermodynamic limit using polynomial functions in $1/L$. When we extrapolate our data for up to $L = 1024$ lattice sites for $\rho = 1$, we find $K_b(t/U = 0.304) > 1/2$ and $K_b(t/U = 0.306) < 1/2$. Therefore, we locate the transition point at $(t/U)_c = 0.305 \pm 0.001$ for the first Mott lobe. In the same way we find the transition point for the second Mott lobe at $(t/U)_c = 0.180 \pm 0.001$ (not shown) for the restricted BHM with $n_b^{\max} \leq 5$.

Alternatively the SF-MI transition point can be extracted from the numerically obtained central charge c^* , since the SF phase is described by the TLL. Figure 5.2(c) displays $c^*(L)$ via Eq. (2.41) for the 1D BHM. By extrapolating the position of the maximum in c^* to the thermodynamic limit [see Fig. 5.2(d)], $(t/U)_c$ can be determined reliably. In this way we again get the cone point of the Mott lobes $(t/U)_c = 0.305(3)$ for $\rho = 1$ and $(t/U)_c = 0.179(7)$ for $\rho = 2$ (not shown), in excellent agreement with the previous estimates from the finite-size scaling of K_b .

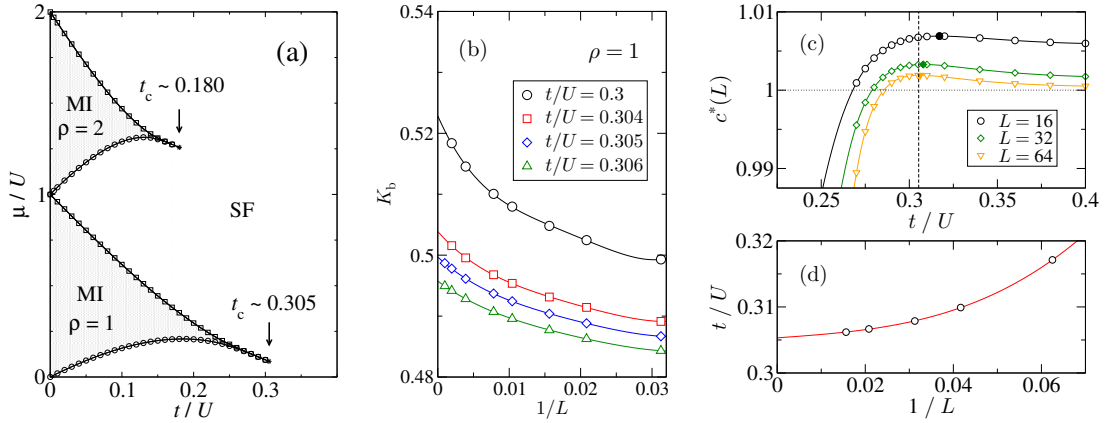


Fig. 5.2: (a): Phase diagram of the 1D Bose–Hubbard model, showing superfluid (SF) and Mott-insulating (MI) regions as a function of the chemical potential μ/U and the tunneling amplitude t/U . (b): Finite-size scaling for the Tomonaga–Luttinger liquid parameter K_b in the 1D constrained BHM ($n_b^{\max} = 5$) for the first Mott lobe ($\rho = 1$). (c): Central charge $c^*(L)$ from Eq. (2.41). The closed symbols indicate the maximum value in c^* for each system size. (d): An extrapolation of the t/U values at maxima from panel (c) to the thermodynamic limit provides the Kosterlitz–Thouless transition point for $\rho = 1$, $(t/U)_c = 0.305(3)$. Adapted from Articles XIII and XIV.

5.1.2 Dynamical properties — Articles XIII, XIV and XV

In the following, we present the dynamical properties for the first Mott lobe ($\rho = 1$) in the 1D BHM at zero temperature using the numerically exact dynamical DMRG technique explained in Sec. 2.3.

Photoemission spectra

Single-particle excitations associated with the injection or emission of a boson with wave vector k and frequency ω , $A^+(k, \omega)$ or $A^-(k, \omega)$, are described by the spectral functions

$$A^\pm(k, \omega) = \sum_n \left| \langle \psi_n^\pm | \hat{b}^\pm(k) | \psi_0 \rangle \right|^2 \delta(\omega \mp \omega_n^\pm), \quad (5.10)$$

where $\hat{b}^+(k) = \hat{b}^\dagger(k)$ [$\hat{b}^-(k) = \hat{b}(k)$] create [annihilate] particles with momentum k . Moreover, $|\psi_0\rangle$ is the ground state of a L -site system in the N -particle sector while $|\psi_n^\pm\rangle$ denote the n th excited states in the $(N \pm 1)$ -particle sectors with excitation energies $\omega_n^\pm = E_n^\pm - E_0$.

Figures 5.3(a), (b) and (c) display the results for the Mott insulator with $\rho = 1$ in the 1D BHM. The spectra $A(k, \omega) = A^+(k, \omega) + A^-(k, \omega)$ for fixed k consist of two Lorentzians of width $\eta = 0.04$; the size of broadening introduced in the DDMRG

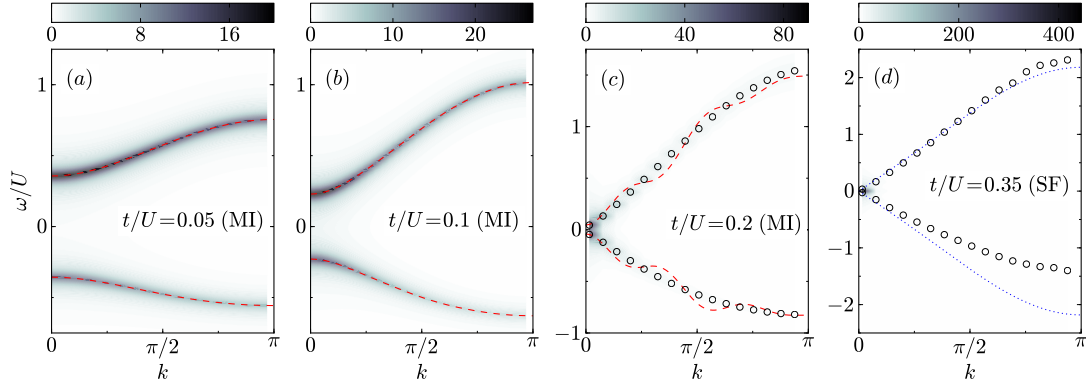


Fig. 5.3: Intensity of the single-boson spectral functions $A(k, \omega)$ for different t/U where $\rho = 1$. The dashed lines denote the strong-coupling dispersions for the propagation of a hole and a double occupancy $\omega_{h,p}(k)$, Eqs. (5.11) and (5.12). Circles in panels (c) and (d) mark the positions of the peaks in each k sector. The dotted lines in panel (d) show the dispersion of the condensate excitations $E(k)$ from Bogoliubov theory. Adapted from Article XIV.

procedure. For comparison, we also include strong-coupling result of the quasi-particle dispersions (dashed lines). From strong-coupling perturbation theory the single-hole and single-particle energies are given by

$$\begin{aligned} \frac{\omega_h(k)}{t} &= 8x - \frac{512}{3}x^5 + \left(-2 + 12x^2 - \frac{224}{3}x^4\right) \cos(k) \\ &+ \left(-4x + 64x^3 - \frac{1436}{3}x^5\right) \cos(2k) + \left(-12x^2 + 276x^4\right) \cos(3k) \\ &+ \left(-44x^3 + 1296x^5\right) \cos(4k) - 180x^4 \cos(5k) - 792x^5 \cos(6k) + \mathcal{O}(x^6) , \end{aligned} \quad (5.11)$$

and

$$\begin{aligned} \frac{\omega_p(k)}{t} &= \frac{1}{x} + 5x - \frac{513}{20}x^3 - \frac{80139}{200}x^5 + \left(-4 + 18x^2 - \frac{137}{150}x^4\right) \cos(k) \\ &+ \left(-4x + 64x^3 - \frac{426161}{1500}x^5\right) \cos(2k) + \left(-12x^2 + 276x^4\right) \cos(3k) \\ &+ \left(-44x^3 + 1296x^5\right) \cos(4k) - 180x^4 \cos(5k) - 792x^5 \cos(6k) + \mathcal{O}(x^6) . \end{aligned} \quad (5.12)$$

Because of the large Mott gap separating single-particle and single-hole quasiparticle band in the strong-coupling regime ($x \lesssim 0.15$), the perturbative results are in perfect agreement with the DDMRG data. In fact, for large interactions, each site is singly occupied in the ground state. As a consequence, a hole or doubly occupied site can move almost freely through the system. From this consideration, the leading-order expression for the quasiparticle dispersions results, see Eqs. (5.11) and (5.12). Note that the simple mean-field approach by van Oosten *et al.* [75] fails to reproduce the quasiparticle dispersion already for $x = 0.1$, see Article XIII.

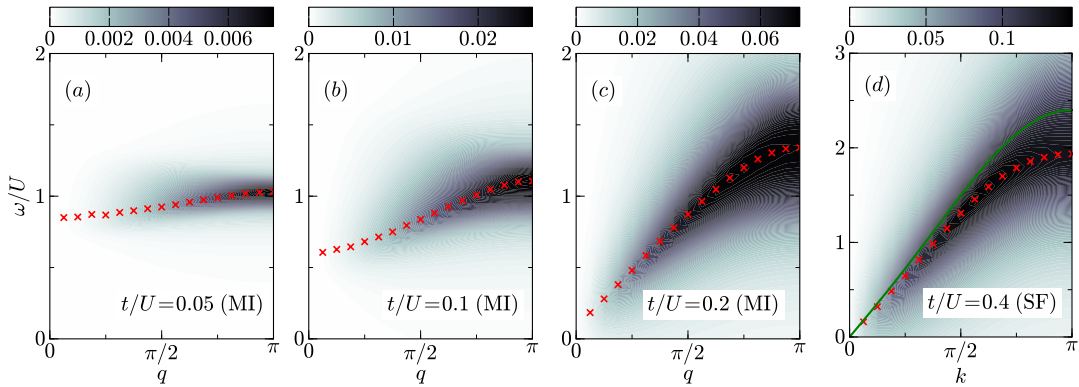


Fig. 5.4: Intensity of the dynamical structure factor $S(q, \omega)$ for different t/U where $\rho = 1$. Crosses mark the positions of the peaks in each k sector. The solid line in panel (d) shows the dispersion of the condensate excitations $E(k)$ from Bogoliubov theory. Adapted from Articles XIV and XV.

As the on-site interaction further weakens, the Mott gap gradually closes. Obviously, strong-coupling theory becomes imprecise at $x \simeq 0.2$ as shown in Fig. 5.3 and completely fails at $x \gtrsim 0.25$.

In the SF phase, the elementary excitations concentrate around the region ($k = 0$, $\omega = 0$), which indicates the formation of a “condensate”. In accordance with Bogoliubov theory and field theory [76, 77], the low-energy, low-momentum excitations dominate the single-particle spectrum. As can be seen from Fig. 5.3(d), our spectral function indeed exhibits a phonon mode whose excitation energy is linear in k and gapless at $k = 0$ for a system in the thermodynamic limit. Yet, for finite-size systems a gap is present whose magnitude is inversely proportional to the system size. Our DDMRG data demonstrate that the gap almost vanishes already for a OBC system with 64 sites.

Dynamic density-density correlations

Let us now turn to the dynamical structure factor

$$S(q, \omega) = \sum_n |\langle \psi_n | \hat{n}_q | \psi_0 \rangle|^2 \delta(\omega - \omega_n), \quad (5.13)$$

where $|\psi_0\rangle$ and $|\psi_n\rangle$ denote the ground and n -th excited state, respectively, and $\omega_n = E_n - E_0$ gives the corresponding excitation energy. We compare the large-scale DDMRG results with the fourth-order strong-coupling theory by keeping the states to fifth order in x .

Figure 5.4 illustrates the change of the intensity distribution of $S(q, \omega)$ in the q - ω plane as $x = t/U$ increases. For small x , deep in the MI phase, the spectral weight is concentrated around $\omega \sim U$ in the region $q > \pi/2$. In this regime the structure factor is dominated by the primary band. When x increases, the maximum of $S(q, \omega)$ acquires an appreciable dispersion; simultaneously the overall intensity of the density-density

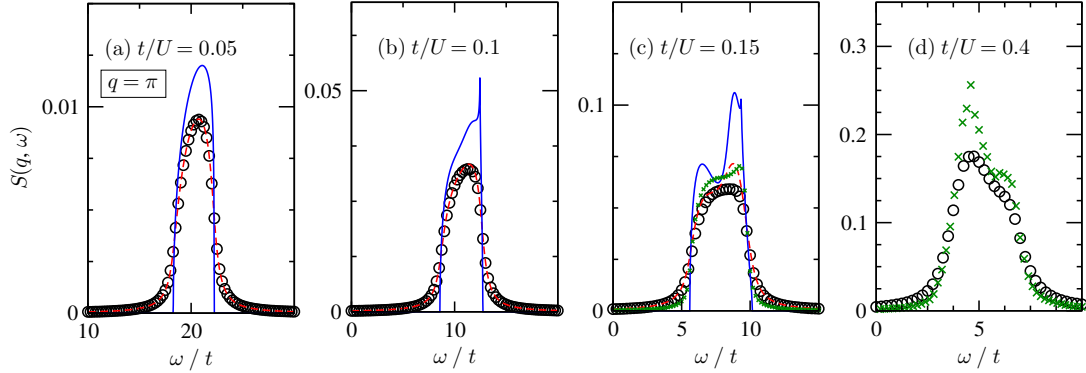


Fig. 5.5: $S(q, \omega)$ at fixed momentum $q = \pi$. Circles (green crosses) mark the DDMRG results for $L = 64$, PBC, and $\eta = 0.5t$ ($L = 128$, PBC, and $\eta = 0.2t$). Blue solid (red dashed) lines give the corresponding results of the strong-coupling theory with $\eta = 0$ ($\eta = 0.5t$). Adapted from Article XIV.

response strengthens [see, e.g., Fig.5.4(c) and also Fig. 5.5]. As the system approaches the MI-SF transition point, the excitation gap closes. Concomitantly, we find a significant redistribution of the spectral weight to smaller q values [see Fig. 5.4(c)]. At small momenta in the SF phase [Fig. 5.4(d)], Bogoliubov theory gives the correct slope of the dispersion which we derive from the maximum of the DDMRG data for $S(q, \omega)$. Bogoliubov's dispersion overestimates the DDMRG maxima for larger momenta and higher energies, as observed experimentally for a three-dimensional setup [72].

In Fig. 5.5 we show constant-moment scans of $S(q, \omega)$ at $q = \pi$. For $x = 0.05$ and $x = 0.1$, the agreement between the broadened strong-coupling results and the DDMRG data for $S(q, \omega)$ is excellent. As x becomes larger than $x \simeq 0.1$, the strong-coupling theory yields a double-peak structure in $S(q = \pi, \omega)$. When we increase the lattice size and reduce η , this feature also appears in DDMRG data for $x = 0.15$. Therefore, this feature is not an artifact of the strong-coupling approach even though the strong-coupling expansion overestimates the double-peak structure for $x = 0.15$. Interestingly, in the SF phase we also find a shoulder in $S(q = \pi, \omega)$ as shown in Fig. 5.5(d), which may form a double peak as $L \rightarrow \infty$, $\eta \rightarrow 0$. This high-energy double peak in the SF phase resembles the structure seen in the MI phase. In our opinion, this rules out an interpretation of the second peak as signature of a massive Higgs mode [78].

Summary

In this section, we provided extensive numerical (D)DMRG data for static and dynamical quantities of the 1D BHM at integer filling (mostly for $\rho = 1$), comparing mainly with the analytical strong-coupling perturbation theory to explore merits and limitations in the most demanding case of one dimension.

Calculating the central charge via von Neumann entropy we confirmed the critical values for the SF-to-MI transition obtained from the Tomonaga-Luttinger liquid

parameter for integer filling.

We simulated the dynamical quantities such as the single-particle spectral function and the dynamical structure factor. The comparison in the photoemission spectra (dynamical structure factor) between DDMRG data and the strong-coupling expansions shows that the latter are reliable for $x = t/U \lesssim 0.15$ ($x \lesssim 0.1$). In the SF phase, the response at low energies is dominated by the quasicondensate, in agreement with predictions from field theory and Bogoliubov theory. In Article XVI we further examined the dynamical current and kinetic-energy correlation functions for $\rho = 1$ by means of the DDMRG and the strong-coupling theory, showing again excellent agreement between both methods in the interaction and frequency regimes where they are applicable.

Thus, the (D)DMRG technique provide us reliable ground-state and dynamical estimations in both insulating and superfluid phases of the 1D Bose–Hubbard-type systems. We demonstrated high accuracy of the (D)DMRG techniques comparing mainly with the perturbations theory. Advantageously, further extensions of the Hamiltonians are easily possible in (D)DMRG. For instance, in Article XVII, we investigated the static and dynamical properties of the Bose–Hubbard model with local three-body interaction W . Surprisingly, physical quantities in the second Mott lobe ($\rho = 2$) such as the gap and the dynamical structure factor scale almost perfectly in $t/(U + W)$, even close to the Mott transition. Strong-coupling theory shows that there is no true scaling but deviations from it are quantitatively small in the strong-coupling limit. Therefore, this observation should remain true also in higher dimensions.

5.2 Haldane insulator in the extended Bose–Hubbard model — Articles XVIII and XIX

A quarter-century after Haldane’s conjecture of an appearance of finite gap in the integer-spin chain [79], the so-called Haldane phase attracts renewed attention from a topological point of view. Such a topological protected state, characterized by symmetries and a finite bulk gap, is termed now a symmetry-protected topological (SPT) ordered phase [23, 80]. To analyze SPT states in interacting systems it has been proposed that the entanglement spectrum can be used as a fingerprint of topological order [21]. Namely, the lowest entanglement level reflects the degree of degeneracy corresponding to symmetries and the edge states of the system, as demonstrated in various spin chains [22, 23, 81]. It is important to notice that the odd Haldane (OH) phase in odd-integer-spin chains is a SPT phase, because the odd- S AKLT state [82] cannot be adiabatically connected to another trivial state without undergoing a phase transition. On the other hand, the even Haldane (EH) state in the even-integer-spin systems is a trivial state, since the even- S AKLT state is adiabatically connected to a trivial state without a bulk phase transition [23].

Interestingly, a hidden SPT phase was also found in interacting boson systems with long-range repulsion [83]. This phase resembles the Haldane gapped phase of the quantum spin-1 Heisenberg chain. Indeed, assuming that the site occupation of an 1D Bose–

Hubbard model (EBHM) with nearest-neighbor repulsion is restricted to $n_j = 0, 1$ or 2 , the system can be described by an effective spin-1 model with $S_j^z = n_j - \rho$ for $\rho = 1$. The Hamiltonian of the EBHM is defined as

$$\hat{H}_{\text{eBH}} = \hat{H}_{\text{BH}} + V \sum_j \hat{n}_j \hat{n}_{j+1}, \quad (5.14)$$

where V parameterizes the nearest-neighbor Coulomb repulsion. The Haldane insulator (HI) appears between the conventional Mott insulator (MI) and the density wave (DW) phases at intermediate couplings [83, 84]. Field theory predicts the MI-HI transition to be in the Luttinger liquid universality class with central charge $c = 1$, whereas the HI-DW transition belongs to the Ising universality class with $c = 1/2$ [84].

In this section we focus on the characterization of the EBHM's ground-state and spectral properties comparing with those in the corresponding effective spin-1 XXZ model, which is given by

$$\begin{aligned} \hat{H}_{\text{eBH}}^{\text{eff}} &= \hat{H}_{XXZ} + \hat{H}', & (5.15) \\ \hat{H}_{XXZ} &= \sum_j [J(\hat{S}_j^x \hat{S}_{j+1}^x + \hat{S}_j^y \hat{S}_{j+1}^y) + J_z \hat{S}_j^z \hat{S}_{j+1}^z] + D \sum_j (\hat{S}_j^z)^2, & (5.16) \end{aligned}$$

where \hat{S}_j denotes a spin-1 operator and the parameter D represents the uniaxial single-ion anisotropy. Here, \hat{H}' contains further terms which breaks the particle-hole symmetry of \hat{H}_{XXZ} . The MI, HI, and DW phases of the EBHM correspond to the EH, OH, and antiferromagnetic (AFM) phases of the spin-1 XXZ model, respectively. In the following, we apply the (D)DMRG technique to the EBHM and show that the lowest entanglement level in the topological HI phase is actually degenerate. The universality classes of the MI-HI and HI-DW transitions are determined from the central charge in accordance with what is obtained from field theory. Most notably we demonstrate that the dynamical structure factor $S(q, \omega)$ can be used to unambiguously discriminate the HI from the MI and DW phases.

5.2.1 Symmetry-protected topological order

Figure 5.6(a) illustrates the ground-state phase diagram of the EBHM with a maximum number of bosons per site $n_b = 2$ and $\rho = 1$, showing three different insulating phases as well as a superfluid state in the weak-coupling regime. As demonstrated in Fig. 5.6(b) at fixed $U/t = 5$, the MI-HI (HI-DW) quantum phase transitions can be easily determined from the numerically obtained central charge $c^*(L)$ via Eq. (2.41) in the intermediate-coupling region ($3t \lesssim U \lesssim 8t$), since the system becomes critical only at the transition points with $c = 1$ ($1/2$). With increasing system size L two sharp peaks develop, indicating the MI-HI and HI-DW transition points. For $L = 128$, we found $c^* \simeq 0.999$ in the former case and $c^* \simeq 0.494$ in the latter, showing an excellent agreement with those from field theory.

Let us now discuss the entanglement properties of the SPT state in the intermediate-coupling region. Since we divide the system in halves when calculating the entanglement

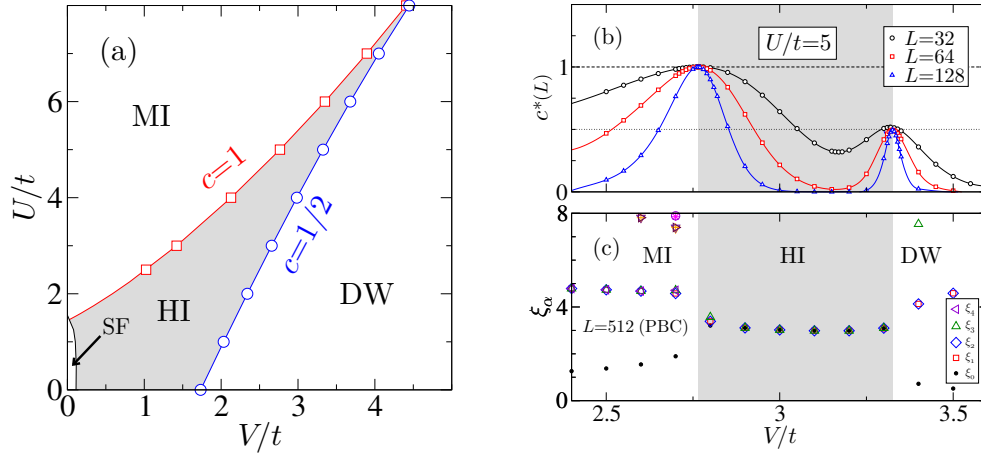


Fig. 5.6: (a): Ground-state phase diagram of the constrained extended Bose–Hubbard model for $n_b^{\max} = 2$ and $\rho = 1$, showing the Mott insulator (MI), Haldane insulator (HI), density wave (DW), and superfluid (SF) phases. (b): Central charge $c^*(L)$ for $U/t = 5$, indicating the MI-HI (HI-DW) transition point with $c = 1$ ($c = 1/2$). (c): Entanglement spectrum ξ_α with $U/t = 5$, exhibiting a characteristic degeneracy in the HI phase. Adapted from Article XVIII.

spectrum ξ_α using the DMRG with PBC, one of the block with $L/2$ possesses two edges. Thus, the ξ_α in the HI phase is expected to be at least fourfold degenerate, reflecting the broken $\mathbb{Z}_2 \times \mathbb{Z}_2$ symmetry. Figure 5.6(c) shows the DMRG data for ξ_α obtained at $U/t = 5$ for $L = 512$ and PBC. Indeed, almost all HI states exhibit this degeneracy. By contrast, in the trivial MI and DW phases the lowest entanglement level is always nondegenerate. Note that the HI phase is protected by the inversion symmetry of the lattice. Adding an appropriate perturbation [84] to the Hamiltonian (5.14), this symmetry can be broken. In fact, by turning on any finite perturbation, the fourfold degeneracy in the HI phase will be dissolved, see Fig. 3 in Article XVIII.

5.2.2 Dynamical structure factor

Since the EBHM (5.14) can be realized by ultracold bosonic atoms loaded in optical lattices it is highly desirable to study dynamical correlation functions which are accessible by experiments. For this purpose, we suggest the dynamical structure factor $S(q, \omega)$ [Eq. (5.13)]—which can be directly measured by momentum resolved Bragg spectroscopy [72, 85]—to be indicative of a SPT state.

Figure 5.7 reveals DDMRG results for $S(q, \omega)$ obtained for the EBHM with $U/t = 5$ inside the three insulating phases, as well as at the quantum phase transition points in between. In the MI phase [Fig. 5.7(a) at $V/t = 1$], a gap opens at $q = 0$ and most of the spectral weight is concentrated in the momentum range $q > \pi/2$, around $\omega/U \simeq 1$, just as for the MI phase in the BHM [see Fig. 5.4]. The dispersion of the maximum in $S(q, \omega)$ behaves cosine-like for small-to-intermediate momenta, and is flattened close to

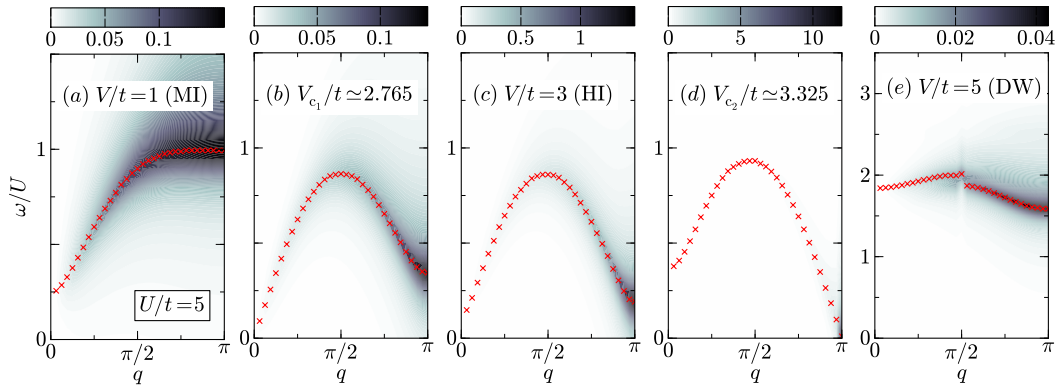


Fig. 5.7: Intensity plots of the dynamical structure factor $S(q, \omega)$ for fixed $U/t = 5$ for different V/t in the EBHM. Crosses give the maximum value of $S(q, \omega)$ at fixed momenta $q = 2\pi j/L$ with $j = 1, \dots, L/2$. Adapted from Article XVIII.

the Brillouin zone boundary (above $k \geq 3\pi/4$). With increasing V/t , the MI-HI transition occurs at $V/t = V_{c_1}/t \simeq 2.765$, where the excitation gap closes at the momentum $q = 0$, as shown in Fig. 5.7(b). Deep in the HI phase, the situation changes dramatically [see Fig. 5.7(c) for $V/t = 3$]. Now the dispersion of the maximum in $S(q, \omega)$ takes a sine-like form. Again there are finite excitation gap at $k = 0$ and π . Here the spectral weight exclusively concentrates at $k \approx \pi$ and finite but small $\omega \ll U$. The question is whether the gap in $S(q, \omega)$ again closes at the HI-DW transition point if V/t is increased further. Figure 5.7(d) shows that the gap indeed closes, at $V/t = V_{c_2}/t \simeq 3.325$, but this time at momentum $q = \pi$, reflecting the lattice-period doubling in the DW phase. In the DW phase [Fig. 5.7(e) at $V/t = 5$], the dispersion becomes flattened with a large excitation gap that opens at $k = \pi$. In every sense, $S(q, \omega)$ behaves very differently in the MI, DW, and HI states and might therefore be used to discriminate these insulating phases.

In summary, we studied the topologically nontrivial Haldane insulator in the intermediate-coupling region of the 1D EBHM. The MI-HI (HI-DW) quantum phase transition is determined with high precision from the central charge c^* obtained from the von Neumann entropy. We furthermore established a characteristic fourfold degeneracy of the lowest entanglement level in the SPT Haldane phase. Finally, we analyzed the dynamical structure factor $S(q, \omega)$ for the EBHM and demonstrated that $S(q, \omega)$ can be used to distinguish the Haldane insulator, exhibiting a gapped excitation spectrum similar to the spin-1 isotropic Heisenberg model, from conventional Mott and density-wave states.

In Article XX, (D)DMRG results for the spin-1 XXZ model (5.16) are also demonstrated. The phase boundaries between the nontrivial OH phase and EH/AFM phase are determined numerically with high precision again via the central charge. The ground-state phase diagram resembles those of the restricted EBHM with $n_b^{\max} = 2$. The degeneracy of the lowest entanglement level in the OH phase can be observed by

finite-system DMRG simulations. Interestingly, the results of the dynamical spin structure factor in the EH, OH, and AFM phases are similar to those for $S(q, \omega)$ in the MI, HI, and DW phases of the EBHM. These results corroborate that the spin-1 model can be taken as an effective model for the EBHM with $n_{\text{b}}^{\text{max}} = 2$.

6 Ising quantum phase transition between Feshbach-resonant superfluids — Articles XXI and XXII

The recent rapid progress in cooling atoms to low temperatures and controlling their interactions allows to realize Bose–Einstein condensates (BEC), Bardeen–Cooper–Schrieffer (BCS) pairing in Fermi gases, and strongly correlated Mott insulators. In particular, the BEC-BCS crossover between a molecular BEC and a weakly bound BCS pairing state has played a significant role. This has been achieved through the use of Feshbach resonances, which enable us to control the strength of pairing interactions via a magnetic field. Feshbach resonances and molecule formation have also been studied in bosonic systems experimentally [86]. On the theoretical side, the BEC-BCS “crossover” for bosons is strikingly different from the fermionic case since both atoms and molecules may undergo Bose–Einstein condensation. This leads to the possibility of an Ising quantum phase transition occurring between distinct molecular (MC) and atomic plus molecular (AC+MC) condensates [87–89].

In this chapter, we consider the 1D lattice model for bosons interacting via Feshbach resonant pairing. Using DMRG and field theory techniques, we first characterize the phases and quantum phase transitions of this model and provide strict evidence of an Ising quantum phase transition separating distinct paired superfluids, including results for the energy gaps, correlation functions, and entanglement entropy. We further demonstrate that the visibility is in accordance with the absence of a purely atomic superfluid phase. Thereby, the careful finite-size scaling of DMRG data by means of field theory analysis plays a significant role. A polynomial extrapolation leads erroneously to a purely atomic superfluid phase reported in Ref. [90].

6.1 Model and ground-state phase diagram

In order to establish the presence of such novel \mathbb{Z}_2 transitions, we explore the atomic and molecular correlations in the 1D bosonic Feshbach systems considering the pairing Hamiltonian

$$\hat{H} = \sum_{i\alpha} \epsilon_\alpha \hat{n}_{i\alpha} - \sum_{\langle ij \rangle} \sum_{\alpha} t_\alpha (\hat{b}_{i\alpha}^\dagger \hat{b}_{j\alpha} + \text{H.c.}) + \sum_{i\alpha\alpha'} \frac{U_{\alpha\alpha'}}{2} : \hat{n}_{i\alpha} \hat{n}_{i\alpha'} : + \hat{H}_F, \quad (6.1)$$

where $\alpha = a, m$ labels atoms and molecules and ϵ_α are on-site potentials. Normal ordering yields $: \hat{n}_{i\alpha} \hat{n}_{i\alpha'} : = \hat{n}_{i\alpha} (\hat{n}_{i\alpha} - 1)$ for like species and $: \hat{n}_{i\alpha} \hat{n}_{i\alpha'} : = \hat{n}_{i\alpha} \hat{n}_{i\alpha'}$ for

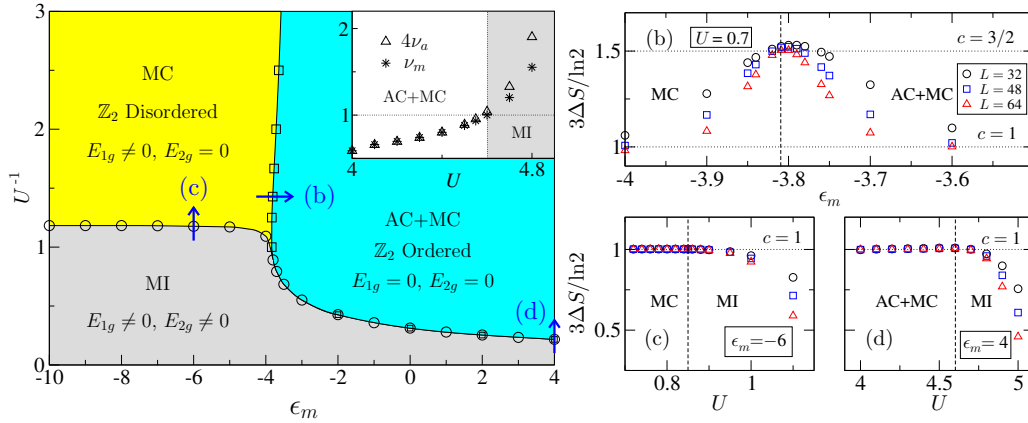


Fig. 6.1: (a): Phase diagram of the 1D lattice model (6.1), showing a Mott insulator (MI), a molecular condensate (MC), and a coupled atomic plus molecular condensate (AC+MC). The squares and circles indicate the vanishing of the single- and two-particle gaps, E_{1g} and E_{2g} , as $L \rightarrow \infty$. Inset: AC+MC to MI transition at $\epsilon_m = 4$. The atomic and molecular exponents, ν_a and ν_m , are locked up to the MI boundary where $\nu_m = 1$, indicating the absence of an AC phase. The remaining panels (b), (c), and (d) show the numerically obtained central charge on transiting across the phase boundaries in panel (a). Adapted from Articles XXI and XXII.

distinct species. Molecules are formed by the Feshbach resonance term

$$\hat{H}_F = g \sum_i (\hat{m}_i^\dagger \hat{a}_i \hat{a}_i + \text{H.c.}), \quad (6.2)$$

where $\hat{m}_i \equiv \hat{b}_{im}$ and $\hat{a}_i \equiv \hat{b}_{ia}$. The number of atoms and molecules are not conserved separately, but the total $N_T \equiv \sum_i (\hat{n}_{ia} + 2\hat{n}_{im})$ is preserved. To make contact with previous quantum Monte Carlo (QMC) simulations [90] we choose parameters $\epsilon_a = 0$, $U_{aa}/2 = U_{mm}/2 = U_{am} = g = U$, $t_a = 1$ and $t_m = 1/2$.

The phase boundaries of the model (6.1) correspond to the vanishing of the single- and two-particle excitation gaps, $E_{1g} \equiv \mu_{1p}(L) - \mu_{1h}(L)$ and $E_{2g} \equiv \mu_{2p}(L) - \mu_{2h}(L)$, respectively. Here

$$\mu_{np} = [E_0(L, N_T + n) - E_0(L, N_T)]/n, \quad (6.3)$$

$$\mu_{nh} = [E_0(L, N_T) - E_0(L, N_T - n)]/n, \quad (6.4)$$

where $E_0(L, N)$ is the ground-state energy for a system of size L and a total number N of atoms and molecules. The phase diagram in Fig. 6.1(a) consists of three distinct phases: a Mott insulator (MI) with gaps for both excitations $E_{1g} \neq 0$ and $E_{2g} \neq 0$, a MC phase with a single-particle gap $E_{1g} \neq 0$ and $E_{2g} = 0$, and a AC+MC phase with $E_{1g} = 0$ and $E_{2g} = 0$. In contrast to the QMC phase diagram in Ref. [90], we find no evidence for a single-component AC phase. This is supported by direct evaluation of

the correlation function. Namely, throughout the AC+MC phase we find power laws for atoms *and* molecules with related exponents; see inset of Fig.6.1(a). The conclusion of Ref. [90] is attributed by the finite-size effects when simulating the zero-momentum molecular occupation number as will be discussed in Sec. 6.3.

Let us now concentrate on the transition between the MC and AC+MC superfluids. In order to understand the origin of the proposed Ising transitions it is useful to consider that the Hamiltonian (6.1) is invariant under $U(1) \times \mathbb{Z}_2$ transformations:

$$\hat{m} \rightarrow e^{i\theta} \hat{m}, \quad \hat{a} \rightarrow e^{i(\theta/2 \pm \pi)} \hat{a}, \quad (6.5)$$

where $\theta \in \mathbb{R}$. In higher dimensions, the MC phase has $\langle \hat{m} \rangle \neq 0$ and $\langle \hat{a} \rangle = 0$. This only breaks the $U(1)$ contribution and leaves \mathbb{Z}_2 symmetry, $\hat{a} \rightarrow -\hat{a}$, intact. This leads to the disordered phase of an Ising model, coexisting with molecular superfluidity. On the other hand, the AC+MC phase has $\langle \hat{m} \rangle \neq 0$ and $\langle \hat{a} \rangle \neq 0$. This breaks the $U(1) \times \mathbb{Z}_2$ symmetry completely and corresponds to the ordered phase of an Ising model, coexisting with atomic and molecular superfluidity. However, in 1D the spontaneous formation of expectation values $\langle \hat{a} \rangle$ and $\langle \hat{m} \rangle$ is prohibited, since continuous $U(1)$ symmetry is absent. Instead, superfluid order is characterized by long-range power law correlations, and the nature of the phases and transitions requires closer inspection.

Let us first examine the MC to AC+MC transition via the central charge c obtained from the entanglement entropy (2.40). As shown in Fig. 6.1(b), the numerically extracted central charge of the MC phase yields $c = 1$ as expected for a free boson with coexisting gapped degrees of freedom. In addition, the AC+MC phase has also $c = 1$. Close to the MC to AC+MC transition, where the Ising gap closes, one expects the central charge to increase to $c = 3/2$, due to *additional* critical Ising degrees of freedom with $c = 1/2$. The evolution with increasing L is consistent with this prediction. Moreover, the MI to superfluid transitions yields $c = 1$ close to the MI boundary, suggesting XY behavior; see Figs. 6.1(c) and (d).

6.2 Field theory predictions for correlation functions

In the \mathbb{Z}_2 disordered MC phase, the atomic correlation function decays exponentially with a power law prefactor,

$$\langle \hat{a}^\dagger(x) \hat{a}(0) \rangle \sim x^{-1/2 - \nu_m/4} e^{-x/\xi}, \quad (6.6)$$

where ξ is the Ising correlation length. On the other hand, pairs of atoms condense and exhibit power law correlations,

$$\langle \hat{a}^\dagger(x) \hat{a}^\dagger(x) \hat{a}(0) \hat{a}(0) \rangle \sim \langle \phi^2 \rangle^2 x^{-\nu_m}, \quad (6.7)$$

with the same exponent ν_m as the molecular two-point function,

$$\langle \hat{m}^\dagger(x) \hat{m}(0) \rangle \sim x^{-\nu_m}. \quad (6.8)$$

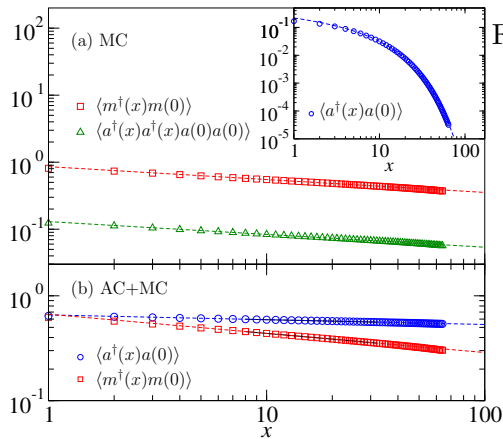


Fig. 6.2: Correlation functions with $U = 0.7$ using DMRG. (a): MC phase with $\epsilon_m = -4$, revealing power laws for molecules and atomic bilinears with the same exponent. Inset: Atomic correlations decay exponentially. (b): AC+MC phase with $\epsilon_m = -3$. Atoms and molecules exhibit power law exponents locked by a factor of 4; the fits are $y = 0.667x^{-0.1827}$ and $y = 0.657x^{-0.0456}$. Adapted from Article XXI.

This behavior is well supported by DMRG simulations in Fig. 6.2(a), which reveal identical power laws for molecules and atomic bilinears.

In contrast, in the \mathbb{Z}_2 ordered AC+MC phase, both molecules and atoms have power law correlations,

$$\langle \hat{m}^\dagger(x)\hat{m}(0) \rangle \sim x^{-\nu_m}, \quad \langle \hat{a}^\dagger(x)\hat{a}(0) \rangle \sim \langle \phi \rangle^2 x^{-\nu_a}, \quad (6.9)$$

with locked exponents, $\nu_m = 4\nu_a$, that differ by a factor of 4. Again, these features can be readily seen in DMRG simulations as shown in Fig. 6.2(b). In addition these robust features persist into the large- U regime where field theoretical arguments are no longer strictly valid. In particular, the molecular correlation function remains a power law throughout the AC+MC phase and close to the Mott boundary shown in Fig. 6.1. Carrying out the scaling collapse of the DMRG data for different system sizes, the atomic and molecular exponents ν_a and ν_m can be extracted. We find that the atomic exponent ν_a reaches the value of $\nu_a = 1/4$ at the AC+MC to MI transition. At the same time, the molecular exponent ν_m reaches the value of $\nu_m = 1$ consistent with the aforementioned exponent locking; see Fig. 6.3. The presence of this molecular superfluid close to the MI boundary clearly supports the absence of an AC phase in contrast to Ref. [90]. This is also compatible with mean-field theory in higher dimensions [87–89] where atomic condensation is always accompanied by molecular condensation due to the structure of the Feshbach term \hat{H}_F .

The DMRG results of the atomic and molecular correlation functions also yield valuable information about the critical exponents extracted from the correlation length ξ and the order parameter $\langle \phi \rangle$, showing excellent agreement with Ising critical exponents ($\nu = 1$ and $\beta = 1/8$), see Articles XXI and XXII.

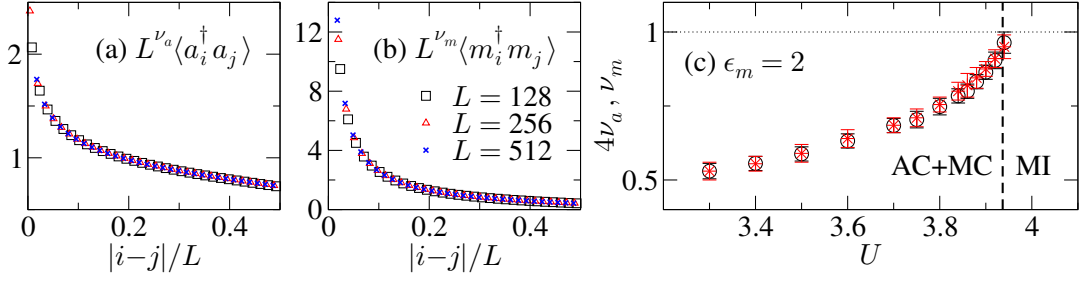


Fig. 6.3: DMRG results for the two-point functions of (a) atoms and (b) molecules in the AC+MC phase. Carrying out the scaling collapse of the data for different system sizes we extract the exponents ν_a and ν_b . In (c) we show the resulting evolution of $4\nu_a$ (circles) and ν_m (stars) as determined in (a) and (b) for fixed values of $\epsilon_m = 2$. The vertical dashed lines correspond to the location of the AC+MC to MI transition obtained from the gap data. The data confirm the locking of the atomic and molecular exponents, $\nu_m = 4\nu_a$. The exponents reach the values of $\nu_a = 1/4$ and $\nu_m = 1$ at the MI boundary, indicating the absence of the AC phase. Adapted from Article XXII.

6.3 Finite-size scaling for momentum space observables

In the previous section we have focused directly on the superfluid correlation functions due to the absence of continuous symmetry breaking in 1D. However, the authors of Ref. [90] rather examined the divergence of the occupation number

$$n_\alpha(k) = \frac{1}{L} \sum_{i,j=1}^L e^{ik(i-j)} \langle \alpha_i^\dagger \alpha_j \rangle \quad (6.10)$$

and its corresponding visibility,

$$\mathcal{V}_\alpha \equiv \frac{n_\alpha^{\max}(k) - n_\alpha^{\min}(k)}{n_\alpha^{\max}(k) + n_\alpha^{\min}(k)}, \quad (6.11)$$

where n_α^{\max} (n_α^{\min}) is the maximum (minimum) in the momentum space occupation number distribution. In the present context this is identified as

$$\mathcal{V}_\alpha = \frac{n_\alpha(0) - n_\alpha(\pi)}{n_\alpha(0) + n_\alpha(\pi)}. \quad (6.12)$$

In a SF phase where $n_\alpha(0)$ diverges with increasing system size, \mathcal{V}_α approaches unity as $L \rightarrow \infty$. In Ref. [90] it was argued that the molecular visibility within the AC+MC phase failed to saturate at this value close to the MI boundary. In order to gain a quantitative handle on this issue we need to exploit the finite-size dependence of the

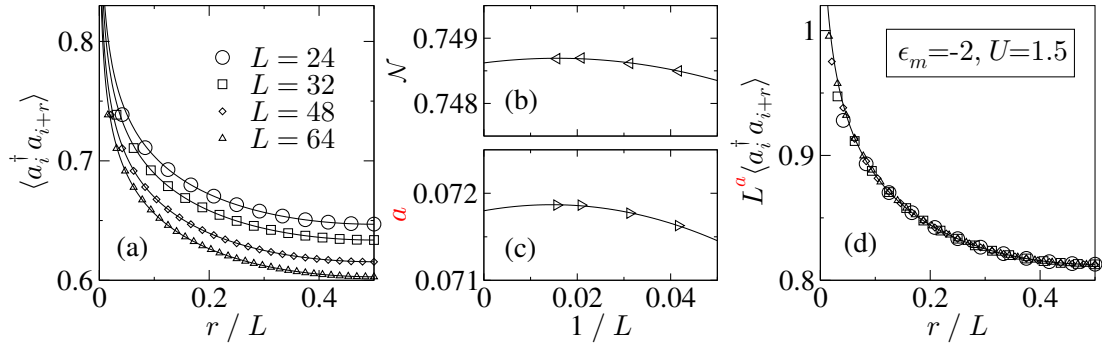


Fig. 6.4: Atomic correlation functions within the AC+MC phase. (a) $\langle a_i^\dagger a_{i+r} \rangle$ as a function of the reduced separation r/L for different system sizes. (b) Normalization factor \mathcal{N} obtained from panel (a) using Eq. (6.13). (c) Correlation exponent a obtained from panel (a) using Eq. (6.13). (d) Rescaling the data in panel (a) using the extracted exponent a leads to data collapse. This confirms the applicability of the conformal result (6.13) within the AC+MC phase. This corresponds to power-law atomic correlations for separations $r \gtrsim 3a_0$. Adapted from Article XXII.

superfluid correlations within the AC+MC phase. In a system with PBC the two-point function of a primary field $\mathcal{O}(r)$ at position r can be obtained by conformal transformation [91]

$$\langle \mathcal{O}(r_1) \mathcal{O}(r_2) \rangle_L = \mathcal{N} \left[\frac{\pi}{L \sin(\frac{\pi r}{L})} \right]^a, \quad (6.13)$$

where a is the critical exponent in the thermodynamic limit, $r = |r_1 - r_2|$ is the separation, and \mathcal{N} is a constant prefactor. It follows that the rescaled combination $L^a \langle \mathcal{O}(r_1) \mathcal{O}(r_2) \rangle_L$ is a prescribed scaling function of the reduced separation r/L . The confirmation of this behavior for the atomic correlation functions within the AC+MC phase is demonstrated in Fig. 6.4. Note that the exponent for molecules can also be determined in a similar manner. Given this agreement we may substitute the conformal result (6.13) into Eq. (6.10) in order to obtain formal expressions for the finite-size dependence of the atomic and molecular visibilities in Eq. (6.11). In Figs. 6.5(a) and (b) we show the results of this conformal extrapolation, where we further incorporate the exact DMRG results for the short distance behavior with $r \leq 3a_0$, where a_0 is the lattice spacing. It is readily seen from the solid lines in left panels of Fig. 6.5 that both the atomic and molecular visibilities extrapolate to unity in the thermodynamic limit. In particular, close to the MI boundary [panel (b) for $U = 2.2$] there are strong deviations from the results that would be obtained by naive polynomial extrapolation as indicated by the dashed lines which *erroneously* suggests that the molecular visibility is less than unity. We use the conformal extrapolation procedure to track the atomic and

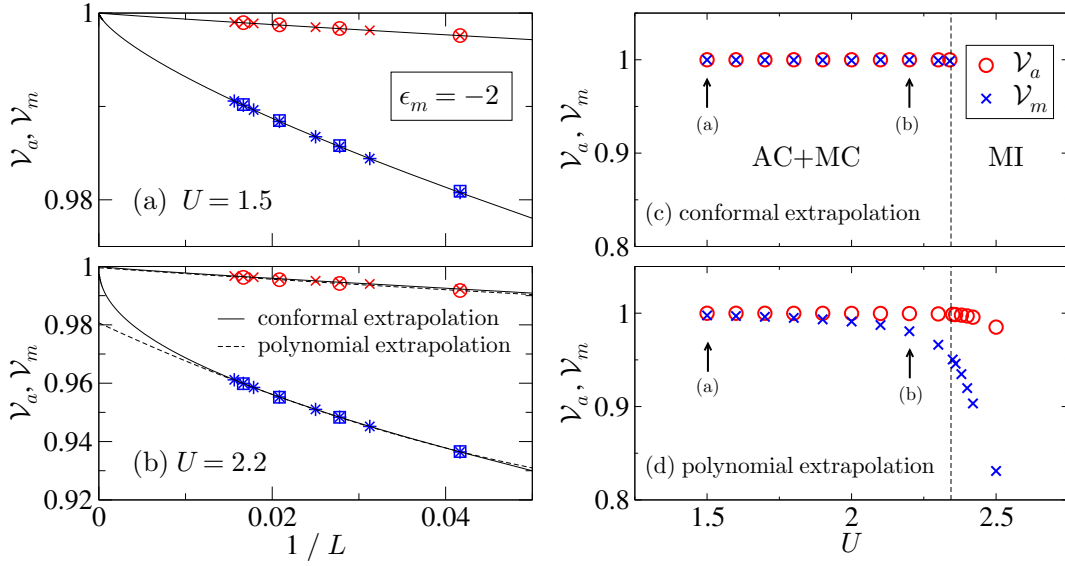


Fig. 6.5: Atomic and molecular visibilities within the AC+MC phase for $\epsilon_m = -2$. Left panels: Finite-size scaling of the visibilities for (a) $U = 1.5$ and (b) $U = 2.2$. The circles correspond to \mathcal{V}_a and the squares to \mathcal{V}_m obtained by DMRG directly. The crosses and stars correspond to Fourier transformation of the conformal result (6.13) supplemented by exact DMRG results for the correlators at small separations $r \leq 3a_0$. The solid line indicates the results of conformal extrapolation (described in the text and justified by the scaling collapse in Fig. 6.4) supplemented by the exact DMRG results for small separations $r \leq 3a_0$. Right panels: Atomic and molecular visibilities in the thermodynamic limit obtained by (c) conformal and (d) polynomial extrapolation procedures. Adapted from Article XXII.

molecular visibilities within the AC+MC phase. The results are consistent with unity right up to the MI boundary. For comparison, in Fig. 6.5(d) we show the results that would be inferred using a naive polynomial extrapolation. The results are in accordance with those of Ref. [90], but differ markedly from the asymptotic visibilities obtained by conformal extrapolation as shown in Fig. 6.5(c). Thus, within the AC+MC phase the finite-size dependence of the atomic and molecular momentum space diagnostics is in complete agreement with power-law correlations for both the atoms and the molecules. This behavior persists right up to the MI boundary and provides further evidence for the absence of a purely AC phase.

Summary

To summarize this chapter, we explored the phase diagram of the bosons interacting via Feshbach resonant pairing in a 1D optical lattice. Strong evidence for an Ising

quantum phase transition between distinct superfluids can be obtained by combining the large-scale DMRG and field theoretical techniques. In particular, we demonstrated that it is of significant importance to carry out the appropriate finite-size scaling close to the (AC+MC)-MI quantum phase transition. Our numerical results are consistent with an Ising quantum phase transition approaching both a molecular KT transition and an atomic KT transition, compatible with mean-field theory predictions for the continuum model in higher dimensions.

In Article XXIII, the Mott insulating state of bosonic pairing Hamiltonians is further investigated using analytical and numerical techniques and the results are consistent with the absence of super-Mott behavior within the second Mott lobe, which is indicated by the QMC in Ref. [90].

7 Summary and outlook

In this thesis, we investigated fermionic, bosonic and fermion-boson coupled systems in one dimension (1D), using the unbiased density-matrix renormalization-group (DMRG) technique, in order to identify and characterize possible quantum phases of matter, as well as the quantum phase transitions between these phases. The low-dimensional setting enables us to study these exactly non-solvable systems by means of the exact numerical technique.

In Chap. 2 we first reviewed the DMRG technique in a traditional manner as introduced by S. White in 1992. The pseudo-site approach was then introduced, which is essential in DMRG to simulate the fermion-boson coupled systems such as the Holstein-type models. The dynamical DMRG (DDMRG) technique provides us an unique opportunity to compute the dynamical quantities in the various (quasi-)1D systems both with and without background medium. Due to the structural reason of the lattices used, the numerical precision of DMRG is better for open boundary conditions comparing with periodic boundary conditions (PBC), in general. However, simulations with PBC provide us often less system-size dependent results. Thereby, applying the folding lattice configuration the accuracy can be drastically improved, so that the calculations with system sizes up to $\mathcal{O}(10^2)$ become possible. Furthermore, parallelization scheme via OpenMP also helps to reduce the practical wall time of (D)DMRG simulations. As explained in last two sections of this chapter the Tomonaga–Luttinger liquid (TLL) parameter and the central charge can be estimated in high accuracy by DMRG taking the advantage of above explained procedures. Quantum phase transition points in the 1D strongly correlated systems can thus be determined by these characteristic quantities as also demonstrated in this thesis.

In Chap. 3, we considered the excitonic insulator states of the 1D half-filled extended Falicov–Kimball model. In 1D, the absence of an order parameter prevents addressing the problem of excitonic condensation by means of the mean-field based approaches, despite their success for $D > 1$. Considering the off-diagonal anomalous Green function instead of calculating the $\langle c^\dagger f \rangle$ expectation value, we demonstrated that the different nature of the electron-hole pairing and condensation process at weak and strong couplings can be clarified by the related anomalous spectral function. The binding energy and the correlation length provided a clear evidence for a Coulomb interaction driven crossover from BCS-like electron-hole pairing fluctuations to tightly bound excitons. Within the Bose–Einstein condensation regime, the quasiparticle dispersion develops a characteristic flat valence-band top, in accord with the experimental findings for quasi-1D Ta_2NiSe_5 .

In Chap. 4 we applied the pseudo-site DMRG technique to the fermion-boson coupled systems. In the first two sections we investigated the fermionic systems with

background medium in order to explore the conditions for the metal-insulator quantum phase transitions and the metallic phase with attractive interactions where TLL parameter K_ρ is larger than unity. In the half-filled spinless Holstein model, in which $K_\rho > 1$ has been reported in former studies, the reexamined TLL parameters by the large-scale DMRG are always less than unity, indicating that there exists no attractive TLL phase. On the other hand, $K_\rho > 1$ was obtained in the intermediate metallic regime of the spinfull Holstein-Hubbard model at half filling, as also reported by the quantum Monte Carlo (QMC) method. Due to the strong system size dependence of K_ρ , however, the existence of the attractive TLL phase is still unclear. Further studies by more recent numerical techniques would be highly desirable to examine the character of the intermediate metallic regime in this model.

In Sec. 4.2, we demonstrated that the 1D spinless fermion Edwards transport model with boson-affected hopping displays an incredibly rich physics despite its simplicity. At half-band filling the metal-insulator quantum phase transition occurs in the case of strong background correlations. The characteristic six-step hopping process is reflected in the momentum distribution function, showing a qualitative agreement with the one in the Hubbard model with the next-nearest-neighbor hopping transfer. Even away from half filling (e.g., at one-third band filling) the Edwards model exhibits a quantum phase transition between TLL and charge-density-wave (CDW) phases without taking longer-range Coulomb interactions into account. If the charge carriers are coupled to slow quantum bosons away from half filling, the TLL parameter becomes clearly attractive ($K_\rho > 1$) and even forms a phase-separated state. Thus, the 1D Edwards model for spinless fermions exhibits the nature not only of the system with longer-range interactions but also of the t - J -like system. It would, therefore, be of significant interest to study this model further in higher dimensions to elucidate the origin of the attractive interactions of Cooper pairs in the superconducting phase.

In Chap. 5 we focused on various Bose-Hubbard-type models which might directly be compared with the experimental results in the optical lattices. By investigating the ground-state and dynamical properties of the pure Bose-Hubbard model (BHM), we developed the fundamental understanding how the bosonic systems should be treated by DMRG. The quantum phase transition between superfluid (SF) and Mott insulator (MI) phases can be successfully determined by the TLL parameter and the central charge. Dynamical quantities estimated by DDMRG agree perfectly with those by the strong-coupling perturbation theory for the appropriate parameter regime.

On this background, in Sec. 5.2 we then included the nearest-neighbor repulsion into the BHM. This extended BHM (EBHM) attracts much attentions from the topological point of view. Namely, the topologically nontrivial Haldane insulator (HI) appears in the midst of the MI, density-wave, and SF phases for the intermediate coupling regime. We approved the universality class of the phase boundaries predicted by the field theory and established the characteristic degeneracy of the lowest entanglement level in the symmetry-protected topological HI phase. Moreover, we demonstrated that the dynamical density structure factor can be used to distinguish the HI, exhibiting a gapped excitation spectrum similar to the spin-1 XXZ chain, from conventional MI

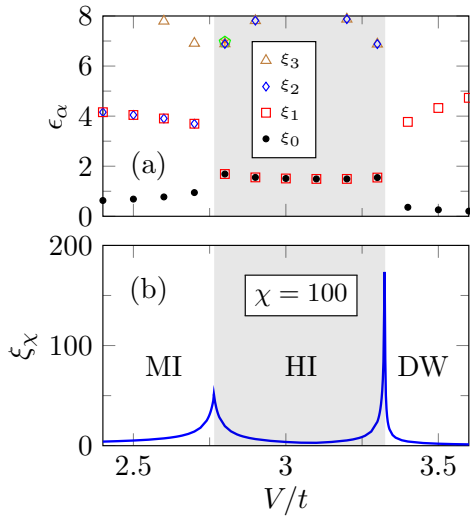


Fig. 7.1: (a) Entanglement spectra ϵ_α and (b) correlation length ξ_χ in the EBHM (5.14) for $n_b = 2$ and $U/t = 5$ obtained by iDMRG with bond dimensions $\chi = 100$. The lowest entanglement level in the Haldane insulator (HI) phase displays the characteristic double degeneracy, while in the Mott insulator (MI) and density wave (DW) phases it is non-degenerate. The correlation length exhibits peaks at both MI-HI and HI-DW transition points, reflecting the criticality with $c = 1$ and $c = 1/2$, respectively.

and DW states.

In the final chapter for the numerical results, we explored the zero-temperature ground-state phase diagram of bosons interacting via Feshbach resonant pairing interactions. Combining the DMRG and field theoretical techniques the phases and quantum phase transitions in this low-dimensional settings were successfully characterized. Thereby, we demonstrated that the careful finite-size scaling by the field theoretical analysis is essential. Naive polynomial extrapolation leads to an atomic superfluid phase erroneously as reported by the QMC method. Finally, we provided a broad evidence in support of an Ising quantum phase transition separating distinct paired superfluids.

By giving an outlook on future developments we close this thesis. In this study, we discussed various 1D quantum many-particle systems (with background medium) by means of the large-scale (D)DMRG technique. Treating finite systems only, however, one always has to perform an additional careful finite-size scaling analysis, as demonstrated in Chap. 6 with the help of field theory. In order to overcome this problem, the matrix-product-states (MPS) based tensor network algorithms (see, e.g., Ref. [51]) have been developed recently and the so-called infinite DMRG (iDMRG) technique [50] based on the MPS scheme enables us to simulate the ground-state properties directly in the thermodynamic limit. Figure 7 displays the advantage of the iDMRG technique. Characteristic degeneracy of the Haldane phase in the EBHM can be proved immediately by iDMRG with bond dimensions $\chi = 100$ [Fig.7(a)], while the system-size dependence should be considered in the case of finite system calculations especially close to the quantum phase transition points [see, Fig. 5.6(c) for comparison with $L = 512$ by DMRG]. Moreover, the correlation length ξ_χ can be extracted from the second largest eigenvalue of the transfer matrix by iDMRG. When the system is critical, ξ_χ diverges

for $\chi \rightarrow \infty$. In the EBHM the system becomes critical only at quantum phase transitions, so that the values of transition points can be determined simply by calculating ξ_χ . The positions of maxima in Fig. 7 are in perfect agreement with the DMRG results, see Fig. 5.6(b). Note that iDMRG helps to reduce the computational cost (CPU time and memory requirements). For instance, each simulation for Fig. 7 with $\chi = 100$ finished in less than 1 hour, while the DMRG calculations with $L = 512$ and PBC for Fig. 5.6 took a few days.

In our most recent work, Article XXIV, we have implemented a MPS-based iDMRG program and applied this efficient code to the extended Hubbard model supplemented by a ferromagnetic spin coupling term for the half-filled band case, in order to study topological phase transitions. The Haldane phase exhibits again the double degeneracy and phase boundaries between HI and CDW phases can be determined via the correlation length ξ_χ analogous to the case in the EBHM demonstrated in Fig. 7. Using the so-called “infinite boundary conditions” [92], the excitation gaps and the dynamical quantities can be simulated directly in the thermodynamic limit. Hence we do not suffer from the usual finite-size and boundary effects in 1D. Again as in the case of the Ising transition point in the EBHM, only neutral gaps closes at the HI-CDW Ising transition and the dynamical density structure factor reflects this behavior.

In this manner, the MPS-based algorithm and the iDMRG technique allow us to explore the quantum phase transitions in the (quasi-)1D strongly correlated systems more precisely. The iDMRG technique might be applied to the systems with the background medium such as the Holstein model and to the Feshbach systems such as the Hamiltonian (6.1). It would be desirable to adopt the iDMRG technique to the 1D half-filled Holstein–Hubbard model (4.3). Reexamining the ground-state character of the intermediate metallic regime, the existence of an attractive TLL might be proved by means of iDMRG, where the strong finite-size effects prevent us from exploring the nature of this phase. Simulating atomic and molecular correlation functions in the 1D lattice model (6.1) and extracting their exponents using iDMRG, the absence of the atomic superfluid phase might be proved directly in the thermodynamic limit.

The tensor network algorithms can be applied to quasi-1D systems, e.g., a ladder system, or a cylindrical system even in the thermodynamic limit. Recent targets are true two-dimensional (2D) systems. In the case of simple spin models, static quantities can be simulated successfully by tensor network algorithms. It is desirable, e.g., to verify the existence of the superconducting phase in the 2D Edwards model introduced in Sec. 4.2 by such a technique, since we found an attractive TLL phase in the 1D Edwards model. Bosonic topological insulators in 2D are another fascinating candidates to be simulated by tensor network algorithms [93].

8 Thesis Articles

Author contribution

Article I:

“*Order, criticality, and excitations in the extended Falicov-Kimball model*”

S. Ejima, T. Kaneko, Y. Ohta, and H. Fehske, *Phys. Rev. Lett.* **112**, 026401 (2014). Copyright (2014) by the American Physical Society.

All authors outlined the scope and strategy of the calculation. The numerical calculation was performed by S. Ejima. S. Ejima and H. Fehske wrote the manuscript which was edited by all authors.

Article II:

“*Exact-diagonalization study of exciton condensation in electron bilayers*”

T. Kaneko, S. Ejima, H. Fehske, and Y. Ohta, *Phys. Rev. B* **88**, 035312 (2013). Copyright (2013) by the American Physical Society.

S. Ejima and T. Kaneko outlined the scope and strategy of the calculation. The numerical calculation was performed by T. Kaneko. H. Fehske, T. Kaneko and Y. Ohta wrote the manuscript which was edited by all authors.

Article III:

“*Excitonic BCS-BEC crossover in double-layer systems*”

T. Kaneko, S. Ejima, H. Fehske, and Y. Ohta, *JPS Conf. Proc.* **3**, 017006 (2014). Copyright (2014) by the Physical Society of Japan.

S. Ejima and T. Kaneko outlined the scope and strategy of the calculation. The numerical calculation was performed by T. Kaneko. H. Fehske, T. Kaneko and Y. Ohta wrote the manuscript which was edited by all authors.

Article IV:

“*Luttinger parameters and momentum distribution function for the half-filled spinless fermion Holstein model: A DMRG approach*”

S. Ejima and H. Fehske, *EPL* **87**, 27001 (2009). Copyright (2009) by the IOP Publishing.

S. Ejima and H. Fehske outlined the scope and strategy of the calculation. The calculation was performed by S. Ejima. S. Ejima and H. Fehske wrote the manuscript.

Article V:

“DMRG analysis of the SDW-CDW crossover region in the 1D half-filled Hubbard-Holstein model”

S. Ejima and H. Fehske, *J. Phys.: Conf. Ser.* **200**, 012031 (2010). Copyright (2010) by the IOP Publishing.

S. Ejima and H. Fehske outlined the scope and strategy of the calculation. The numerical calculation was performed by S. Ejima. S. Ejima and H. Fehske wrote the manuscript.

Article VI:

“Quantum phase transition in a 1D transport model with boson-affected hopping: Luttinger liquid versus charge-density-wave behavior”

S. Ejima, G. Hager and H. Fehske, *Phys. Rev. Lett* **102**, 106404 (2009). Copyright (2009) by the American Physical Society.

All authors outlined the scope and strategy of the calculation. The calculation was performed by S. Ejima. S. Ejima and H. Fehske wrote the manuscript which was edited by all authors.

Article VII:

“Metal-insulator transition in the Edwards model”

H. Fehske, S. Ejima, G. Wellein, and A. R. Bishop, *J. Phys.: Conf. Ser.* **391**, 012152 (2012). Copyright (2012) by the IOP Publishing.

All authors outlined the scope and strategy of the calculation. The numerical calculation was performed by S. Ejima. H. Fehske wrote the manuscript which was edited by all authors.

Article VIII:

“One-dimensional quantum transport affected by a background medium: Fluctuations versus correlations”

S. Ejima and H. Fehske, *Phys. Rev. B* **80**, 155101 (2009). Copyright (2009) by the American Physical Society.

S. Ejima and H. Fehske outlined the scope and strategy of the calculation. The calculation was performed by S. Ejima. S. Ejima and H. Fehske wrote the manuscript.

Article IX:

“Anderson localization versus charge-density-wave formation in disordered electron systems”

S. Nishimoto, S. Ejima, and H. Fehske, *Phys. Rev. B* **87**, 045116 (2013). Copyright (2013) by the American Physical Society.

All authors outlined the scope and strategy of the calculation. The numerical calculation was performed by S. Ejima and S. Nishimoto. S. Nishimoto and H. Fehske wrote the manuscript which was edited by all authors.

Article X:

“Charge-density-wave formation in the Edwards fermion-boson model at one-third band filling”

S. Ejima and H. Fehske, *JPS Conf. Proc.* **3**, 013006 (2014). Copyright (2014) by the Physical Society of Japan.

S. Ejima and H. Fehske outlined the scope and strategy of the calculation. The numerical calculation was performed by S. Ejima. S. Ejima and H. Fehske wrote the manuscript.

Article XI:

“Phase separation in the Edwards model”

S. Ejima, S. Sykora, K. W. Becker, and H. Fehske, *Phys. Rev. B* **86**, 155149 (2012). Copyright (2012) by the American Physical Society.

All authors outlined the scope and strategy of the calculation. The numerical calculation was performed by S. Ejima and S. Sykora. S. Ejima and H. Fehske wrote the manuscript which was edited by all authors.

Article XII:

“A Green’s function decoupling scheme for the Edwards fermion-boson model”

D. M. Edwards, S. Ejima, A. Alvermann and H. Fehske, *J. Phys.: Condens. Matter* **22**, 435601 (2010). Copyright (2010) by the IOP Publishing.

All authors outlined the scope and strategy of the calculation. The calculation was performed by D. M. Edwards and S. Ejima. D. M. Edwards wrote the manuscript which was edited by all authors.

Article XIII:

“*Dynamic properties of the one-dimensional Bose-Hubbard model*”

S. Ejima, H. Fehske, and F. Gebhard, *EPL* **93**, 30002 (2011). Copyright (2011) by the IOP Publishing.

All authors outlined the scope and strategy of the calculation. The numerical calculation was performed by S. Ejima. All authors wrote the manuscript.

Article XIV:

“*Characterization of Mott-insulating and superfluid phases in the one-dimensional Bose-Hubbard model*”

S. Ejima, H. Fehske, F. Gebhard, K. zu Münster, M. Knap, E. Arrigoni, and W. von der Linden, *Phys. Rev. A* **85**, 053644 (2012). Copyright (2012) by the American Physical Society.

All authors outlined the scope and strategy of the calculation. The numerical calculation was performed by S. Ejima, M. Knap and K. zu Münster. S. Ejima, H. Fehske, F. Gebhard and M. Knap wrote the manuscript which was edited by all authors.

Article XV:

“*Dynamic density-density correlations in interacting Bose gases on optical lattices*”

S. Ejima, H. Fehske, and F. Gebhard, *J. Phys.: Conf. Ser.* **391**, 012143 (2012). Copyright (2012) by the IOP Publishing.

All authors outlined the scope and strategy of the calculation. The numerical calculation was performed by S. Ejima and F. Gebhard. All authors wrote the manuscript.

Article XVI:

“*Dynamical correlation functions for the one-dimensional Bose-Hubbard insulator*”

K. zu Münster, F. Gebhard, S. Ejima, and H. Fehske, *Phys. Rev. A* **89**, 063623 (2014). Copyright (2014) by the American Physical Society.

All authors outlined the scope and strategy of the calculation. The numerical calculation was performed by S. Ejima and K. zu Münster. All authors wrote the manuscript.

Article XVII:

“*One-dimensional Bose-Hubbard model with local three-body interactions*”

S. Ejima, F. Lange, H. Fehske, F. Gebhard, and K. zu Münster, *Phys. Rev. A* **88**, 88, 063625 (2013). Copyright (2013) by the American Physical Society.

S. Ejima and F. Gebhard outlined the scope and strategy of the calculation. The numerical calculation was performed by S. Ejima, F. Lange, and K. zu Münster. S. Ejima, H. Fehske and F. Gebhard wrote the manuscript which was edited by all authors.

Article XVIII:

“*Spectral and entanglement properties of the bosonic Haldane insulator*”

S. Ejima, F. Lange, and H. Fehske, *Phys. Rev. Lett.* **113**, 020401 (2014). Copyright (2014) by the American Physical Society.

S. Ejima and H. Fehske outlined the scope and strategy of the calculation. The numerical calculation was performed by S. Ejima and F. Lange. S. Ejima and H. Fehske wrote the manuscript which was edited by all authors.

Article XIX:

“*Entanglement properties of the nontrivial Haldane insulator in the 1D extended Bose-Hubbard model*”

S. Ejima and H. Fehske, *J. Phys.: Conf. Ser.* **592**, 012134 (2015).

S. Ejima and H. Fehske outlined the scope and strategy of the calculation. The numerical calculation was performed by S. Ejima. S. Ejima and H. Fehske wrote the manuscript.

Article XX:

“*Comparative density-matrix renormalization group study of symmetry-protected topological phases in spin-1 chain and Bose-Hubbard models*”

S. Ejima and H. Fehske, *Phys. Rev. B* **91**, 045121 (2015). Copyright (2015) by the American Physical Society.

S. Ejima outlined the scope and strategy of the calculation. The numerical calculation was performed by S. Ejima. S. Ejima and H. Fehske wrote the manuscript.

Article XXI:

“*Ising Deconfinement Transition between Feshbach-Resonant Superfluids*”

S. Ejima, M. J. Bhaseen, M. Hohenadler, F. H. L. Essler, H. Fehske, and B. D. Simons *Phys. Rev. Lett.* **106**, 015303 (2011). Copyright (2011) by the American Physical Society.

All authors outlined the scope and strategy of the calculation. The numerical calculation was performed by S. Ejima. M. J. Bhaseen wrote the manuscript which was edited by all authors.

Article XXII:

“Discrete symmetry breaking transitions between paired superfluids”

M. J. Bhaseen, S. Ejima, F. H. L. Essler, H. Fehske, M. Hohenadler, and B. D. Simons, *Phys. Rev. A* **85**, 033636 (2012). Copyright (2012) by the American Physical Society.

All authors outlined the scope and strategy of the calculation. The numerical calculation was performed by S. Ejima. M. J. Bhaseen wrote the manuscript which was edited by all authors.

Article XXIII:

“Magnetic properties of the second Mott lobe in pairing Hamiltonians”

M. J. Bhaseen, S. Ejima, M. Hohenadler, A. O. Silver, F. H. L. Essler, H. Fehske, and B. D. Simons, *Phys. Rev. A* **84**, 023635 (2011). Copyright (2011) by the American Physical Society.

All authors outlined the scope and strategy of the calculation. The numerical calculation was performed by S. Ejima, M. Hohenadler and A. O. Silver. M. J. Bhaseen wrote the manuscript which was edited by all authors.

Article XXIV:

“Criticality at the Haldane-insulator charge-density-wave quantum phase transition”

F. Lange, S. Ejima, and H. Fehske, *Phys. Rev. B* **92**, 041120(R) (2015). Copyright (2015) by the American Physical Society.

All authors outlined the scope and strategy of the calculation. The numerical calculation was performed by S. Ejima and F. Lange. S. Ejima and H. Fehske wrote the manuscript which was edited by all authors.

Confirmed:

(Prof. Dr. Holger Fehske)

Greifswald, April 2016

(Dr. Satoshi Ejima)

Greifswald, April 2016

Order, Criticality, and Excitations in the Extended Falicov-Kimball Model

S. Ejima,¹ T. Kaneko,² Y. Ohta,² and H. Fehske¹

¹*Institut für Physik, Ernst-Moritz-Arndt-Universität Greifswald, 17489 Greifswald, Germany*

²*Department of Physics, Chiba University, Chiba 263-8522, Japan*

(Received 1 August 2013; published 13 January 2014)

Using exact numerical techniques, we investigate the nature of excitonic (electron-hole) bound states and the development of exciton coherence in the one-dimensional half-filled extended Falicov-Kimball model. The ground-state phase diagram of the model exhibits, besides band-insulator and staggered orbital ordered phases, an excitonic insulator (EI) with power-law correlations. The criticality of the EI state shows up in the von Neumann entropy. The anomalous spectral function and condensation amplitude provide the binding energy and coherence length of the electron-hole pairs which, on their part, point towards a Coulomb interaction driven crossover from BCS-like electron-hole pairing fluctuations to tightly bound excitons. We show that while a mass imbalance between electrons and holes does not affect the location of the BCS-BEC crossover regime, it favors staggered orbital ordering to the disadvantage of the EI. Within the Bose-Einstein condensation (BEC) regime, the quasiparticle dispersion develops a flat valence-band top, in accord with the experimental finding for Ta₂NiSe₅.

DOI: 10.1103/PhysRevLett.112.026401

PACS numbers: 71.35.-y, 71.10.Hf

The formation and condensation of excitonic bound states of electrons and holes in semimetallic or semiconducting systems possessing a small band overlap or band gap is still—half a century after its theoretical prediction [1]—a topical issue in condensed matter physics [2–4]. If the binding energy of the excitons exceeds the overlap or gap, they may spontaneously condensate at low temperatures and drive the system into an excitonic insulator (EI) state. It has been pointed out that the semimetal-EI transition can be discussed in close analogy to the BCS superconductivity, whereas the semiconductor-EI transition is described in terms of a Bose-Einstein condensation (BEC) of preformed excitons [5]. Quite recently, as a candidate for the EI state, quasi-one-dimensional (1D) Ta₂NiSe₅ has raised and attracted much experimental attention [6]. Most notably, by angle-resolved photoemission spectroscopy, an extremely flat valence-band top at 40 K was observed and taken as a strong signature for the EI state to be formed out of “condensed” bound Ni 3*d* – Se 4*p* holes and Ta 5*d* electrons.

The detection of the EI state in Ta₂NiSe₅ has spurred multifaceted research activities with regard to the formation and possible condensation of excitons in 1D systems [7]. The minimal theoretical model in this respect is of the Falicov-Kimball type. While the original Falicov-Kimball model (FKM) describes localized *f* electrons interacting via a local Coulomb repulsion (*U*) with itinerant *c* electrons (*t_c*) if residing at the same Wannier site [8], an extended version takes into account also the direct nearest-neighbor *f*-electron hopping (*t_f*) [9]:

$$\mathcal{H} = -t_c \sum_{\langle i,j \rangle} c_i^\dagger c_j - t_f \sum_{\langle i,j \rangle} f_i^\dagger f_j + U \sum_i c_i^\dagger c_i f_i^\dagger f_i + \frac{D}{2} \sum_i (c_i^\dagger c_i - f_i^\dagger f_i). \quad (1)$$

Here, α_i^\dagger (α_i) denotes the creation (annihilation) operator of a spinless fermion in the $\alpha = \{c, f\}$ orbital at site *i*, and *D* is the level splitting between different α orbitals. In regard to the modeling of Ta₂NiSe₅, the half-filled-band case is of particular importance, and it has been shown theoretically that a direct *f*-*c* hopping (hybridization) is prohibited by symmetry reasons, at least between the valence-band top and conduction-band bottom [7].

For the original FKM, rigorous results were obtained only in infinite spatial dimensions by dynamical mean-field theory; see, e.g., reviews in Refs. [10,11]. The extended FKM (EFKM) [Eq. (1)] has been studied extensively in the context of EI formation for *D* > 1, using dynamical mean-field theory [12], random phase approximation [13], slave-boson [14], projective renormalization [15], and variational cluster [16] techniques, or purely numerical diagonalization procedures [17]. At the same time, the problem of electronic ferroelectricity, which is equivalent to the appearance of the EI in some theoretical models, has also attracted much attention [18,19]. This phenomenon was confirmed for the 2D EFKM by constrained path Monte Carlo simulations [20]. In 1D, however, true ferroelectric long-range order (the equivalent of a nonvanishing $\langle c^\dagger f \rangle$ expectation value in the limit of vanishing *c*-*f*-band hybridization) is not possible. This was demonstrated for the 1D FKM [21]. For the 1D EFKM, power-law critical (excitonic) correlations were observed instead [20]. Mean-field-based approaches [22] are unable to capture the EI state in 1D (despite their success for *D* > 1), mainly due to the lack of an order parameter associated with the breaking of the *U*(1) symmetry. On this note, a thorough investigation of the ground-state and spectral properties of the 1D EFKM is still missing.

In this paper, we present a comprehensive numerical analysis of the 1D EFKM at half-filling. At first, we

determine the ground-state phase diagram from large-scale density-matrix renormalization group (DMRG) [23] calculations and identify—depending on the orbital level splitting—staggered orbital ordered (SOO) and band-insulator (BI) phases as well as an intervening critical EI state. Then, within the EI, we detect a crossover between BCS- and Bose-Einstein-type condensates monitoring the exciton-exciton correlation and exciton momentum distribution functions. Note that in our 1D setting, we use the term “condensate” to indicate a critical phase with power-law correlation decay. Finally, combining DMRG, Lanczos exact diagonalization (ED), and Green functions techniques [24], we study the anomalous spectral function and extract the correlation length and binding energy of the electron-hole pairs. This allows us to comment on the nature of the excitonic bound states preceding the condensation process and to discuss the effect of a mass imbalance between (*c*) electrons and (*f*) holes.

Examining the (large-*U*) strong-coupling regime gives a first hint of which phases might be realized in the 1D EFKM at zero temperature. To leading order, the EFKM can be mapped onto the exactly solvable spin-1/2 XXZ-Heisenberg model in a magnetic field $h = D$ aligned in the *z* direction [25]: $\mathcal{H}_{XXZ} = J \sum_j \{ \Delta S_j^z S_{j+1}^z + (1/2) (S_j^+ S_{j+1}^- + S_j^- S_{j+1}^+) \} - h \sum_j S_j^z$, with $J = 4|t_f|t_c/U$ and $\Delta = (t_f^2 + t_c^2)/(2|t_f|t_c)$. The XXZ model exhibits three phases: the gapped antiferromagnetic (AF) phase, the critical gapless XY phase with central charge $c = 1$, and the ferromagnetic (FM) phase, where both transition lines, those between the AF and XY phases (h_{c_1}/J) and those between the XY and FM phases (h_{c_2}/J), follow from the Bethe ansatz [26]. Correspondingly, increasing the magnitude of the *f*-*c* level splitting *D* in the EFKM, we expect to find the following sequence of phases: (i) the SOO phase that matches the Ising-like AF phase in the XXZ model, (ii) an intermediate critical EI phase with finite excitonic binding energy, and (iii) a BI state, which is characterized by a filled (empty) *f* (*c*) band and related to the FM phase of the XXZ model. The phase boundary separating the EI and BI states is exactly known to be [27]

$$D_{c_2} = \sqrt{4(|t_f| + |t_c|)^2 + U^2} - U. \quad (2)$$

The complete phase diagram of the 1D EFKM is presented in Fig. 1. Symbols denote the DMRG BI-EI and EI-SOO transition points, which can be obtained from the energy differences

$$D_{c_2}(L) = E_0(L, 0) - E_0(L-1, 1) = -E_0(L-1, 1) \quad (3)$$

and

$$D_{c_1}(L) = E_0(L/2 + 1, L/2 - 1) - E_0(L/2, L/2), \quad (4)$$

respectively, in the course of a finite-size scaling analysis (see the inset). Here, $E_0(N_f, N_c)$ denotes the ground-state

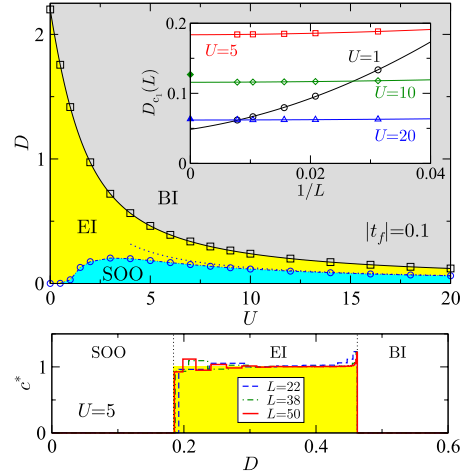


FIG. 1 (color online). Upper panel: Ground-state phase diagram of the half-filled 1D EFKM with $|t_f| = 0.1$. Here and in what follows, we take t_c as the unit of energy. Squares (circles) denote the EI-BI (EI-SOO) transition points D_{c_2} (D_{c_1}) obtained by the DMRG method with up to $L = 128$ sites and OBCs. The solid line gives the analytical solution (2) for the EI-BI boundary; the dotted line shows the strong-coupling result for the EI-SOO boundary. The finite-size scaling of $D_{c_1}(L)$ is illustrated by the inset (open symbols); here, the corresponding strong-coupling data are given by filled symbols. Lower panel: Central charge obtained at $U = 5$ for various L and PBCs. Criticality $c^* \sim 1$ is observed for the EI.

energy for a system with N_f *f* and N_c *c* electrons at $D = 0$. Note that Eq. (3) holds for both open and periodic boundary conditions (OBCs and PBCs), whereas Eq. (4) has to be evaluated with PBCs (if here OBCs were used, an extra factor 2 results: $D_{c_1}^{\text{OBC}} = 2D_{c_1}$). For the DMRG runs performed in this work, we keep at least $m = 3200$ density-matrix eigenstates, which ensures a discarded weight smaller than 1×10^{-6} . The $D_{c_2}(L \rightarrow \infty)$ values demonstrate the accuracy of our DMRG calculations. Exact results for $D_{c_1}(L \rightarrow \infty)$ can only be obtained numerically, where a comparison with the dotted line reveals the limits of the strong-coupling approach [25]; see Fig. 1. The criticality of the EI phase—corresponding to the critical XY phase in the XXZ model with central charge $c = 1$ —can be confirmed by the von Neumann entanglement entropy $S_L(\ell) = -\text{Tr}_\ell(\rho_\ell \ln \rho_\ell)$ [with reduced density matrix $\rho_\ell = \text{Tr}_{L-\ell}(\rho)$]. Numerically, the central charge is best estimated from the entropy difference [28,29]:

$$c^*(L) \equiv 3[S_L(L/2 - 1) - S_L(L/2)] / \ln [\cos(\pi/L)]. \quad (5)$$

Our results for c^* , displayed in the lower panel of Fig. 1 for $|t_f| = 0.1$ at $U = 5$, give clear evidence that $c^* \rightarrow 1$ in the EI, whereas we find $c^* = 0$ in the BI and SOO phases. Regrettably, $c^*(L)$ is strongly system size dependent near the EI-SOO transition.

Let us now discuss the nature of the EI state in more detail. For simplicity, we consider the case $t_f t_c < 0$, where two Fermi points ($\pm k_F$) exist for $U = 0$, provided D is sufficiently small (otherwise, a direct band gap emerges). As a signature of an excitonic Bose-Einstein condensate in 1D, one expects (i) a power-law decay of the correlations $\langle b_i^\dagger b_j \rangle$ with $b_i^\dagger = c_i^\dagger f_i$ and (ii) a divergence of the excitonic momentum distribution $N(q) = \langle b_q^\dagger b_q \rangle$ with $b_q^\dagger = (1/\sqrt{L}) \sum_k c_{k+q}^\dagger f_k$ for the state with the lowest possible energy (in the direct gap case at $q = 0$) due to the absence of true long-range order. Figure 2 supports these expectations: Whereas in the weak-coupling BCS regime ($U = 1$), $\langle b_i^\dagger b_j \rangle$ decays almost exponentially and $N(q)$ shows only a marginal system-size dependence (for all momenta), in the strong-coupling BEC regime close to the EI-BI transition ($U = 1.9$), $\langle b_i^\dagger b_j \rangle$ exhibits a rather slow algebraic decay of the excitonic correlations and $N(q = 0)$ becomes divergent as $L \rightarrow \infty$.

We note that the $\langle c^\dagger f \rangle$ expectation value is always zero for a 1D system in the absence of an explicit f - c -band hybridization. To examine the BCS-BEC crossover, we adopt a technique introduced for detecting the particle fluctuations of Cooper pairs in 2D systems [24]. That is, we consider the off-diagonal anomalous exciton Green function

$$G_{cf}(k, \omega) = \left\langle \psi_1 \left| c_k^\dagger \frac{1}{\omega + i\eta - \mathcal{H} + E_0} f_k \right| \psi_0 \right\rangle, \quad (6)$$

where $|\psi_0\rangle$ is the ground state $|N_f, N_c\rangle$ with fixed numbers of f and c electrons, $|\psi_1\rangle$ is the excited state $|N_f - 1, N_c + 1\rangle$, E_0 is the averaged energy of $|\psi_0\rangle$ and $|\psi_1\rangle$, and η is a broadening, and determine the corresponding spectral function $F(k, \omega) = (-1/\pi) \Im G_{cf}(k, \omega)$ that gives the condensation amplitude $F(k) = \langle \psi_1 | c_k^\dagger f_k | \psi_0 \rangle$. $F(k)$ can be directly computed by the ground-state DMRG method, taking into account an extra target state $|\psi_1\rangle$. From $F(k)$, the coherence length characterizing the excitonic condensate follows as

$$\xi^2 = \sum_k |\nabla_k F(k)|^2 / \sum_k |F(k)|^2. \quad (7)$$

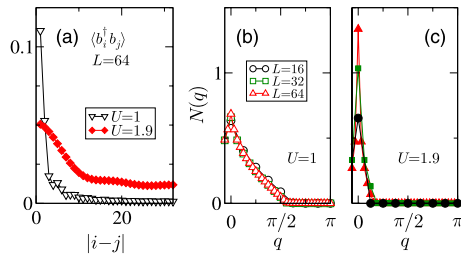


FIG. 2 (color online). (a) Exciton-exciton correlation function $\langle b_i^\dagger b_j \rangle$ and excitonic momentum distribution function $N(q)$ at (b) $U = 1$ and (c) $U = 1.9$ for $t_f = -0.1$, $D = 1$. Data are obtained by the DMRG for 1D L -site lattices with PBCs.

The binding energy of the excitons E_B can be also determined from diverse ground-state energies [17]:

$$E_B = E_0(N_f - 1, N_c + 1) + E_0(N_f, N_c) - E_0(N_f - 1, N_c) - E_0(N_f, N_c + 1). \quad (8)$$

Figures 3(a) and 3(b) show the anomalous spectral function $F(k, \omega)$ in the weak-coupling ($U = 1$) and strong-coupling ($U = 1.9$) regimes, respectively, where $D = 1$. In the former case, the EI arises from a semimetallic phase. As a consequence, most of the spectral weight of the quasiparticle excitations is located around the Fermi points $k = \pm k_F$, again indicating a BCS-type pairing of electrons and holes. Obviously, Fermi surface effects play no role for large U , where the Hartree shift drives the system in the semiconducting regime. Here, the excitation gap occurs at $k = 0$. Note that the gap between the lowest energy peaks in $F(k, \omega)$ is equal to the binding energy E_B given by Eq. (8). Figure 3(c) displays the frequency-integrated quantity $F(k)$. At $U = 1$, $F(k)$ exhibits a sharp peak at the Fermi momentum. Increasing U , the peak weakens and shifts to smaller momenta. Close to the EI-BI transition point $U = 1.9 \lesssim U_{c2} = 1.92$, $F(k)$ has a maximum at $k = 0$ but is spread out in momentum space, indicating that the radius of electron-hole pairs becomes small in real space. Figure 3(d) gives the quasiparticle dispersion $E(k)$ derived from $A(k, \omega)$. Driving the BCS-BEC crossover by

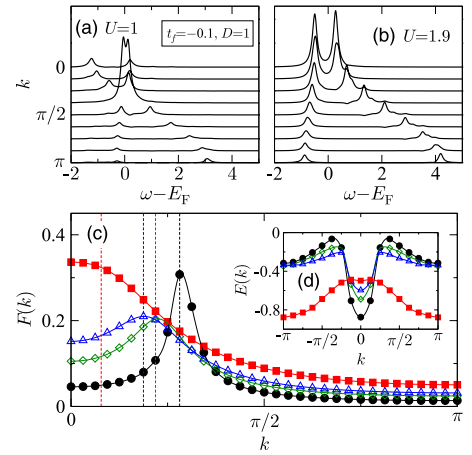


FIG. 3 (color online). Anomalous spectral function $F(k, \omega)$ in the 1D EFKM with (a) $U = 1$ and (b) $U = 1.9$, where $t_f = -0.1$, $D = 1$. Data are obtained by ED using $\eta = 0.1$, $L = 16$, and PBCs. Numerical results for (c) $F(k)$ and (d) $E(k)$ are shown for $U = 1$ (circles), 1.5 (diamonds), 1.7 (triangles), and 1.9 (squares). $F(k)$ is determined by the DMRG for $L = 64$ (PBC), whereas $E(k)$ is extracted from the lowest peaks of single-particle spectra $A(k, \omega)$ calculated by ED for $L = 16$ (PBC). Dashed lines in (c) mark the corresponding Fermi momenta $k_F = \pi N_c / L$ in the noninteracting limit.

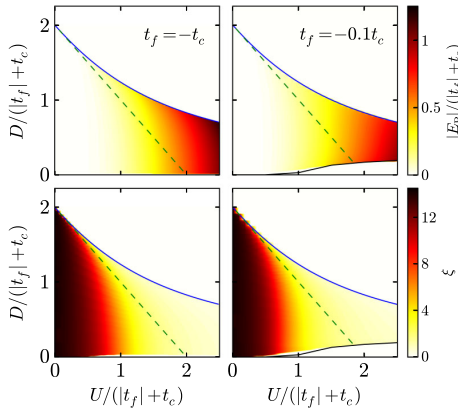


FIG. 4 (color online). Intensity plots of the binding energy E_B (upper panels; $L = 128$, OBC) and the coherence length ξ (lower panels; $L = 64$, PBC) in the rescaled $U/(|t_f| + t_c) - D/(|t_f| + t_c)$ plane. Data were calculated by the DMRG for $N_f > L/2$ (to avoid the AF state in the Hubbard model limit $|t_f| = 1, D = 0$). Solid lines denote the SOO-EI and EI-BI transition points in the thermodynamic limit (in the lower panels, the small uncolored slot just above the SOO-EI appears because $|E_B|$ and ξ are obtained here for a fixed finite system size). The dashed line $[U_{\text{BI}}(D)]$ would separate the semimetallic and semiconducting phases if the EI is assumed to be absent.

increasing U , the peaks around $k = \pm k_F$ disappear as well as the notch around $k = 0$. Instead, a valence band with a flattop around $k = 0$ develops, just as observed, e.g., in quasi-1D Ta_2NiSe_5 [6].

Figure 4 shows the variation of the coherence length and the binding energy in the EI phase of the 1D EFKM with $|t_f| = 1$ (left panels) and 0.1 (right panels). At small U , the excitonic state is composed of electron-hole pairs having large spatial extension, leading to large values of ξ . E_B , on the other hand, is rather small, but increases exponentially with U . This typifies a BCS pairing mechanism. At large U , the binding increases linearly with U . Here, tightly bound spatially confined excitons acquire quantum coherence (with $\xi \ll 1$) in a Bose-Einstein condensation process.

We finally address the influence of a mass imbalance between f - and c -band quasiparticles. The EI phase is absent for $t_f = 0$. In the mass-symmetric case $|t_f| = t_c$, the 1D Hubbard model results for $D = 0$. Here, we cannot distinguish between the AF (with vanishing spin gap) and EI phases because both phases are critical. Therefore, in this limit, we have examined the 1D EFKM for $N_f > L/2$. To this end, both the U and D axes in Fig. 4 have been rescaled by $(|t_f| + t_c)$, as suggested by the EI-BI transition lines [Eq. (2)]. Indeed, we find that the EI phase shrinks as $|t_f|$ decreases. That is, the mass anisotropy gets stronger, which is simply a bandwidth effect, however, leading to a stronger Ising anisotropy. This, on their part, enlarges the SOO region, while the EI-BI phase boundary basically is unaffected. Importantly, the location of the BCS-BEC

crossover, which can be derived from the intensity plots for E_B and ξ , does not change in this presentation. To expose correlation effects, we included in Fig. 4 the semimetallic-to-semiconducting transition line, assuming that the EI phase is absent. $U_{\text{BI}}(D)$ can be obtained from the band gap Δ_c that depends linearly on U for fixed D : $\Delta_c(D) = U + 2(|t_f| + t_c) + U_{\text{BI}}(D)$ [i.e., $U_{\text{BI}}(D)$ scales again with $|t_f| + t_c$]. Apparently in the BCS-BEC crossover regime, a strong renormalization of the band structure due to the incipient f - c hybridization takes place.

To conclude, adopting the numerically exact density-matrix renormalization group technique, we examined the 1D EFKM and, most notably, proved the EI state shown to be critical. The complete ground-state phase diagram was derived and put into perspective, with the Bethe ansatz results obtained in the strong-coupling limit for the spin-1/2 XXZ chain. Besides the EI-to-band-insulator transition, the boundary between the EI and a phase with staggered orbital ordering was determined with high accuracy. The whole phase diagram of the 1D EFKM could be scaled by $|t_f| + t_c$; staggered orbital ordering appears only for small mass-imbalance ratios $|t_f|/t_c$. The absence of an order parameter prevents addressing the problem of excitonic condensation in 1D systems by the usual mean-field approaches. That is why we exploited the off-diagonal anomalous Green function. The related anomalous spectral function elucidates the different nature of the electron-hole pairing and condensation process at weak and strong couplings. At fixed level splitting, the binding energy between c electrons and f holes is exponentially small in the weak-coupling regime. It strongly increases as the Coulomb attraction increases. Concomitantly, the coherence length of the electron-hole pair condensate shortens. This unambiguously demonstrates a crossover from BCS-like electron-hole pairing to a Bose-Einstein condensation of preformed excitons. The quasiparticle band dispersion in the BEC regime exhibits a rather dispersionless valence band near $k = 0$, despite the fact that the expectation value $\langle c^\dagger f \rangle$ is zero because of the 1D setting. This result further supports the EI scenario for quasi-1D Ta_2NiSe_5 , where the flat valence-band top was detected by angle-resolved photoemission spectroscopy experiments.

The authors would like to thank Y. Fuji, F. Göhmann, S. Nishimoto, K. Seki, T. Shirakawa, and B. Zenker for valuable discussions. S. E. and H. F. acknowledge funding by the DFG through SFB 652 Project B5. T. K. was supported by a JSPS Research Fellowship for Young Scientists. Y. O. acknowledges the Japanese Kakenhi Grant No. 22540363.

- [1] N. F. Mott, *Philos. Mag.* **6**, 287 (1961); L. V. Keldysh and H. Y. V. Kopaev, *Sov. Phys. Solid State* **6**, 2219 (1965); D. Jérôme, T. M. Rice, and W. Kohn, *Phys. Rev.* **158**, 462 (1967).

- [2] J. Neuenchwander and P. Wächter, *Phys. Rev. B* **41**, 12693 (1990); P. Wächter, B. Bucher, and J. Malar, *Phys. Rev. B* **69**, 094502 (2004).
- [3] H. Cercellier, C. Monney, F. Clerc, C. Battaglia, L. Despont, M. G. Garnier, H. Beck, P. Aebi, L. Patthey, H. Berger, and L. Forró, *Phys. Rev. Lett.* **99**, 146403 (2007); C. Monney, C. Battaglia, H. Cercellier, P. Aebi, and H. Beck, *Phys. Rev. Lett.* **106**, 106404 (2011).
- [4] H. Min, R. Bistritzer, J. J. Su, and A. H. MacDonald, *Phys. Rev. B* **78**, 121401(R) (2008); T. Stroucken, J. H. Grönqvist, and S. W. Koch, *J. Opt. Soc. Am. B* **29**, A86 (2012).
- [5] F. X. Bronold and H. Fehske, *Phys. Rev. B* **74**, 165107 (2006).
- [6] Y. Wakisaka, T. Sudayama, K. Takubo, T. Mizokawa, M. Arita, H. Namatame, M. Taniguchi, N. Katayama, M. Nohara, and H. Takagi, *Phys. Rev. Lett.* **103**, 026402 (2009).
- [7] T. Kaneko, T. Toriyama, T. Konishi, and Y. Ohta, *Phys. Rev. B* **87**, 035121 (2013); T. Kaneko, T. Toriyama, T. Konishi, and Y. Ohta, *Phys. Rev. B* **87**, 199902(E) (2013).
- [8] L. M. Falicov and J. C. Kimball, *Phys. Rev. Lett.* **22**, 997 (1969); P. Farkašovský, *Eur. Phys. J. B* **20**, 209 (2001).
- [9] C. D. Batista, *Phys. Rev. Lett.* **89**, 166403 (2002).
- [10] T. Kennedy, *Rev. Math. Phys.* **06**, 901 (1994).
- [11] J. K. Freericks and V. Zlatić, *Rev. Mod. Phys.* **75**, 1333 (2003).
- [12] A. Taraphder, S. Koley, N. S. Vidhyadhiraja, and M. S. Laad, *Phys. Rev. Lett.* **106**, 236405 (2011).
- [13] B. Zenker, D. Ihle, F. X. Bronold, and H. Fehske, *Phys. Rev. B* **85**, 121102(R) (2012).
- [14] P. M. R. Brydon, *Phys. Rev. B* **77**, 045109 (2008); B. Zenker, D. Ihle, F. X. Bronold, and H. Fehske, *Phys. Rev. B* **81**, 115122 (2010).
- [15] V. N. Phan, K. W. Becker, and H. Fehske, *Phys. Rev. B* **81**, 205117 (2010).
- [16] K. Seki, R. Eder, and Y. Ohta, *Phys. Rev. B* **84**, 245106 (2011); T. Kaneko, K. Seki, and Y. Ohta, *Phys. Rev. B* **85**, 165135 (2012).
- [17] T. Kaneko, S. Ejima, H. Fehske, and Y. Ohta, *Phys. Rev. B* **88**, 035312 (2013).
- [18] T. Portengen, T. Östreich, and L. J. Sham, *Phys. Rev. Lett.* **76**, 3384 (1996).
- [19] U. K. Yadav, T. Maitra, I. Singh, and A. Taraphder, *Europhys. Lett.* **93**, 47013 (2011).
- [20] C. D. Batista, J. E. Gubernatis, J. Bonča, and H. Q. Lin, *Phys. Rev. Lett.* **92**, 187601 (2004).
- [21] P. Farkašovský, *Phys. Rev. B* **59**, 9707 (1999); P. Farkašovský, *Phys. Rev. B* **65**, 081102 (2002).
- [22] C. Schneider and G. Czycholl, *Eur. Phys. J. B* **64**, 43 (2008); P. Farkašovský, *Phys. Rev. B* **77**, 155130 (2008).
- [23] S. R. White, *Phys. Rev. Lett.* **69**, 2863 (1992).
- [24] Y. Ohta, T. Shimoza, R. Eder, and S. Maekawa, *Phys. Rev. Lett.* **73**, 324 (1994); Y. Ohta, A. Nakauchi, R. Eder, K. Tsutsui, and S. Maekawa, *Phys. Rev. B* **52**, 15617 (1995).
- [25] G. Fáth, Z. Domański, and R. Lemański, *Phys. Rev. B* **52**, 13910 (1995).
- [26] J. des Cloizeaux and M. Gaudin, *J. Math. Phys. (N.Y.)* **7**, 1384 (1966); M. Takahashi, *Thermodynamics of One-Dimensional Solvable Models* (Cambridge University Press, Cambridge, England, 1999).
- [27] A. N. Kocharian and J. H. Sebold, *Phys. Rev. B* **53**, 12804 (1996).
- [28] P. Calabrese and J. Cardy, *J. Stat. Mech.* (2004) P06002.
- [29] S. Nishimoto, *Phys. Rev. B* **84**, 195108 (2011).

Exact-diagonalization study of exciton condensation in electron bilayers

T. Kaneko,¹ S. Ejima,² H. Fehske,² and Y. Ohta¹

¹*Department of Physics, Chiba University, Chiba 263-8522, Japan*

²*Institut für Physik, Ernst-Moritz-Arndt-Universität Greifswald, 17489 Greifswald, Germany*

(Received 30 May 2013; revised manuscript received 4 July 2013; published 23 July 2013)

We report on small-cluster exact-diagonalization calculations which prove the formation of electron-hole pairs (excitons) as a prerequisite for spontaneous interlayer phase coherence in double-layer systems described by the extended Falicov-Kimball model. Evaluating the anomalous Green's function and momentum distribution function of the pairs, and thereby analyzing the dependence of the exciton binding energy, condensation amplitude, and coherence length on the Coulomb interaction strength, we demonstrate a crossover between a BCS-like electron-hole pairing transition and a Bose-Einstein condensation of tightly bound preformed excitons. We furthermore show that a mass imbalance between electrons and holes tends to suppress the condensation of excitons.

DOI: [10.1103/PhysRevB.88.035312](https://doi.org/10.1103/PhysRevB.88.035312)

PACS number(s): 73.21.-b, 71.35.-y, 71.10.Fd

I. INTRODUCTION

The formation of excitonic quantum condensates is an intensively studied continuous problem in condensed matter physics.¹⁻⁴ In a two-component (electron-hole) many-particle system, the attractive Coulomb interaction between oppositely charged electrons and holes can trigger their pairing and—under certain conditions—build up a macroscopic phase-coherent quantum state.

A variety of experimental attempts have been made to observe the condensed state of excitons in quasithermal equilibrium, e.g., in photoexcited semiconductors such as Cu₂O,⁵⁻⁹ or in unconventional semiconductor and bilayer graphene systems subject to electric and/or magnetic fields.¹⁰⁻¹⁴ Quite recently, the emergence of spontaneous coherence in a gas of indirect excitons in an electrostatic trap has been reported.¹⁵ Neutral electron-ion quantum plasmas are other promising candidates for exciton condensates.^{16,17}

From a theoretical point of view, a possible continuous transition between a Bardeen-Cooper-Schrieffer (BCS) electron-hole pair condensate and a Bose-Einstein condensate (BEC) of preformed excitons has been of topical interest.^{4,18-23} However, exact results for the ground-state properties of strongly correlated electron-hole (excitonic) systems are rare. Gas (or fluid) models have recently been studied, e.g., by the diffusion quantum Monte Carlo method.^{24,25} Lattice fermion models with short-range Coulomb interaction, such as multiband Hubbard-like models,²⁶⁻²⁸ should be capable of describing the physics of exciton condensation as well, but they have not yet been thoroughly explored using unbiased numerical techniques.

Motivated by this situation, in this paper we made an attempt to address the problem of exciton condensation in electron-hole bilayers in terms of a minimal lattice fermion model, the so-called extended Falicov-Kimball model (EFKM).²⁹⁻³³ Originally the EFKM described a two-band electron system with local Coulomb interaction between f - and c -band electrons, and it has been used to study electronic ferroelectricity,^{30,31,34} excitonic resonances,³⁵ or the excitonic insulator state.^{33,36-40} Different from these problems, in our double-layer (DL) system, the numbers of f and c particles are separately conserved, however, because charge transfer

between the two layers is assumed to be impossible. This mimics the generic situation in semiconductor electron-hole double quantum wells,^{12,41,42} bilayer quantum antiferromagnets,⁴³ and double-monolayer^{44,45} or double-bilayer graphene.⁴⁶

II. MODEL

The EFKM for an electron-hole DL takes the form

$$\mathcal{H} = -t_f \sum_{(i,j)} (f_i^\dagger f_j + \text{H.c.}) - t_c \sum_{(i,j)} (c_i^\dagger c_j + \text{H.c.}) - \mu_f \sum_i n_i^f - \mu_c \sum_i n_i^c + U \sum_i n_i^f n_i^c, \quad (1)$$

where f_i^\dagger (f_i) creates (annihilates) an electron in the f orbital at site i of the hole (or valence-band) layer, and $n_i^f = f_i^\dagger f_i$ is the f -particle number operator. The transfer amplitude between f orbitals on nearest-neighbor sites is denoted by t_f . Corresponding definitions apply for the c orbital of the electron (or conduction-band) layer. U (> 0) parametrizes the on-site interlayer (on-site) Coulomb attraction between f holes and c electrons. The spin degrees of freedom have been ignored for simplicity. Furthermore, we assume a band structure with a direct band gap ($t_c t_f < 0$) as shown in Fig. 1.

Taking into account the experimental situation,^{5-13,17,45} we assume that the excited electrons and holes have an infinite lifetime, that the number of excited electrons is equal to the number of excited holes, and that the number of bound pairs (excitons) can be viewed as an input parameter, independent of the interaction strength. In practice, we adjust the chemical potentials μ_f and μ_c to maintain the number of electrons in the f and c layer separately, thereby fixing the average f - and c -particle density per site as n^f and n^c , respectively. Due to this simplified description Eq. (1), issues such as the exciton Mott transition and biexciton formation¹⁶ are beyond the scope of this work.

III. THEORETICAL APPROACH

We employ a Lanczos exact-diagonalization technique for a finite square lattice with periodic boundary conditions (see Fig. 1) and calculate the anomalous Green's function for

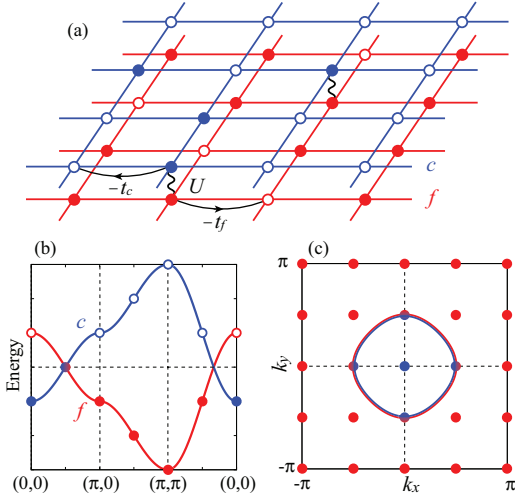


FIG. 1. (Color online) (a) Schematic representation of the DL EFKM cluster model with $N_s = 16$ sites (32 orbitals). (b) Noninteracting tight-binding band structure and (c) square lattice Brillouin zone. Dots indicate the allowed momenta of the 4×4 lattice with periodic boundary conditions. Throughout this work, we assume filling factors $n^f = 0.75$ and $n^c = 0.25$, i.e., $(N_f, N_c) = (12, 4)$, which means $n^h = n^e = 0.25$, irrespective of U . The red and blue lines in (c) show the perfectly matching hole and electron Fermi surfaces, respectively, with finite-lattice Fermi momenta \mathbf{k}_F located at $\mathbf{k} = (\pm\pi/2, 0)$ and $(0, \pm\pi/2)$.

exciton condensation,

$$G^{cf}(\mathbf{k}, \omega) = \langle \psi_0^N | c_k^\dagger \frac{1}{\omega + i0^+ - \mathcal{H} + E_0} f_k | \psi_0^N \rangle, \quad (2)$$

in the momentum (\mathbf{k}) and frequency (ω) space, where $|\psi_0^N\rangle$ is the ground-state wave function and E_0 is the ground-state energy of a system with N electrons. We define the anomalous spectral function

$$F(\mathbf{k}, \omega) = -\frac{1}{\pi} \text{Im} G^{cf}(\mathbf{k}, \omega) \quad (3)$$

and denote its frequency integral by F_k . Clearly, the anomalous Green's function vanishes in finite systems without long-range phase coherence. We therefore have to assume the presence of the state $|\psi_0^N\rangle$, which is a coherent superposition of states with different numbers of excited electrons and holes (or excitons) at a given number N , just as for the BCS wave function of superconductors where the number of electrons is also not conserved. To detect particle fluctuations of the exciton condensate, we adopt a technique introduced for the evaluation of the superconducting anomalous Green's function on small clusters,^{47,48} which allows for the calculation of the off-diagonal Green's functions with respect to varying particle numbers [see Eq. (4)]. We thus monitor the excitonic pairing instability via the anomalous excitation spectrum (corresponding to the Bogoliubov quasiparticle spectrum in superconductors). Note that the term ‘‘anomalous’’ is used to indicate that the number of electrons on each of the f and c bands is not conserved in the course of exciton condensation

(or spontaneous c - f hybridization) although the total number of electrons N is conserved.

Having $G^{cf}(\mathbf{k}, \omega)$ determined, we can calculate the condensation amplitude F_k (following Refs. 47 and 48) from

$$F_k = \langle N_f - 1, N_c + 1 | c_k^\dagger f_k | N_f, N_c \rangle, \quad (4)$$

where $|N_f, N_c\rangle$ is the ground state with the fixed numbers of f and c electrons, and subsequently we will be able to determine the order parameter,

$$\Delta = \frac{U}{N_s} \sum_k F_k, \quad (5)$$

and the coherence length,

$$\xi = \sqrt{\frac{\sum_k |\nabla_k F_k|^2}{\sum_k |F_k|^2}}, \quad (6)$$

for the excitonic condensate (N_s denotes the number of lattice sites).

The binding energy of an exciton E_B should be equal to twice the order parameter Δ in the weak-coupling limit and deviate largely from this value in the strong-coupling regime. Within our finite-cluster approach, E_B may be obtained representing the orbital flavor by electron-hole variables, i.e., $f_i^\dagger \rightarrow h_i$ and $c_i^\dagger \rightarrow e_i^\dagger$. As a result, the interaction term of the DL EFKM takes the form $U \sum_i n_i^f n_i^c \rightarrow -U \sum_i n_i^h n_i^e + U \sum_i n_i^e$, where, in addition to the attractive electron-hole interaction, an extra on-site energy term appears. Due to this term, we should first determine the energy for the addition and removal of an electron:

$$E_B^+ = E_0(N_f - 1, N_c + 1) + E_0(N_f, N_c) - 2E_0(N_f, N_c + 1) + U, \quad (7)$$

$$E_B^- = E_0(N_f - 1, N_c + 1) + E_0(N_f, N_c) - 2E_0(N_f - 1, N_c) - U, \quad (8)$$

where $E_0(N_f, N_c)$ is the ground-state energy of the system with (N_f, N_c) electrons. Then, if $|t_f| = t_c$, the exciton binding energy E_B equals $E_B^+ = E_B^-$. For the mass-asymmetric case $|t_f| \neq t_c$, however, $E_B^+ \neq E_B^-$ because $E_0(N_f, N_c + 1) - U \neq E_0(N_f - 1, N_c)$. Hence, E_B should be defined as the average of E_B^+ and E_B^- , i.e., in general the exciton binding energy is given by

$$E_B = E_0(N_f - 1, N_c + 1) + E_0(N_f, N_c) - E_0(N_f - 1, N_c) - E_0(N_f, N_c + 1). \quad (9)$$

Finally, introducing a creation operator $b_q^\dagger = (1/\sqrt{N_s}) \sum_k c_{k+q}^\dagger f_k$ of an excitonic quasiparticle with momentum \mathbf{q} , the momentum distribution function of excitons can be obtained from

$$N_q = \langle N_f, N_c | b_q^\dagger b_q | N_f, N_c \rangle. \quad (10)$$

IV. NUMERICAL RESULTS

A. Mass-symmetric case

We now present the results of our exact-diagonalization study. Let us first examine the DL EFKM without mass

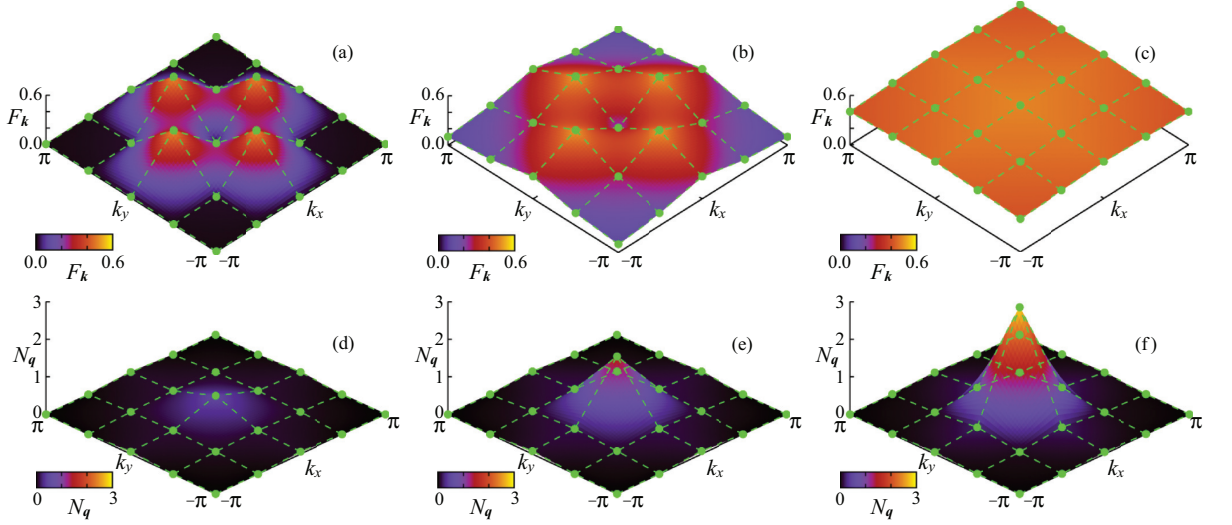


FIG. 2. (Color online) Condensation amplitude F_k (upper panels) and momentum distribution function N_q of excitons (lower panels) in the mass-symmetric DL EFKM with $U/t = 0.5$ (left), 5 (middle), and 50 (right).

imbalance, i.e., $|t_f| = t_c \equiv t$. Figure 2 shows the corresponding data for the condensation amplitude F_k and the exciton momentum distribution N_q , in a wide parameter range of U/t . In the weak-coupling regime [panels (a) and (d)], F_k exhibits pronounced maxima at the Fermi momenta, $\mathbf{k}_F = (\pm\pi/2, 0)$, $(0, \pm\pi/2)$, and decreases rapidly away from the “Fermi surface,” pointing toward a BCS-type instability of weakly bound electron-hole pairs with s -wave symmetry. As U/t increases, F_k broadens in momentum space [panel (b)], indicating that the radius of the bound electron-hole objects becomes smaller in real space. Accordingly, N_q is enhanced at momentum $\mathbf{q} = (0, 0)$; see Fig. 2(e). In the strong-coupling regime [panels (c) and (f)], F_k is homogeneously spread over the entire Brillouin zone, whereas N_q is sharply peaked at $\mathbf{q} = (0, 0)$, which is a sign of a BEC of tightly bound excitons. That is to say, as the attraction between electrons and holes increases in the DL EFKM, we get evidence for a BCS-BEC crossover scenario.

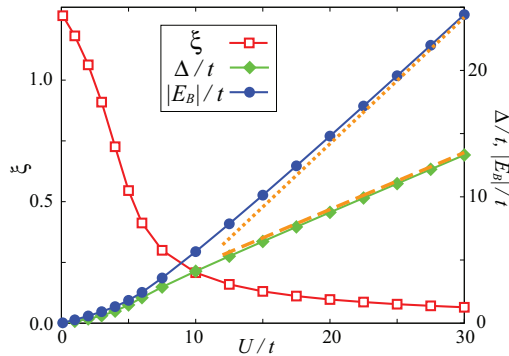


FIG. 3. (Color online) Coherence length ξ (squares), order parameter Δ (diamonds), and exciton binding energy $|E_B|$ (circles) for the mass-symmetric DL EFKM as functions of U/t . For comparison, the asymptotics in the strong-coupling limit $\Delta \propto 0.45U$ (dashed line) and $|E_B| \propto U$ (dotted line) have been inserted.

The behavior of the coherence length depicted in Fig. 3 as a function of the Coulomb attraction corroborates this finding. The spatial coherence of the excitonic state decreases with increasing U/t , indicating that the character of the condensate changes from BCS-like to BEC-like. That ξ stays finite as $U/t \rightarrow 0$ is an obvious artifact of our small cluster calculation. Figure 3 also displays the functional dependence of both the exciton order parameter and the exciton binding energy on U/t . The results may be compared with those of the BCS mean-field theory,^{21,22} which gives Δ and E_B as a solution of the self-consistent equations

$$1 = \frac{U}{2N_s} \sum_k \frac{1}{\sqrt{(\varepsilon_k - \bar{\mu})^2 + \Delta^2}}, \quad (11)$$

$$2n = 1 - \frac{1}{N_s} \sum_k \frac{\varepsilon_k - \bar{\mu}}{\sqrt{(\varepsilon_k - \bar{\mu})^2 + \Delta^2}}, \quad (12)$$

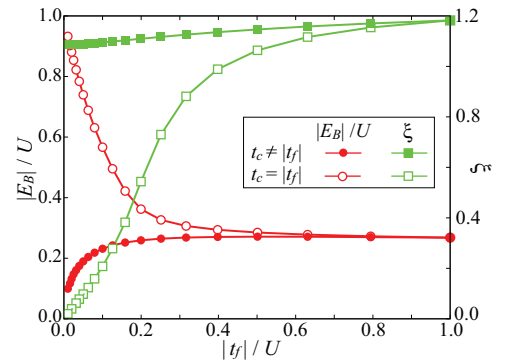


FIG. 4. (Color online) Binding energy $|E_B|/U$ (left ordinate) and coherence length ξ (right ordinate) for the mass-asymmetric (filled symbols) and mass-symmetric (open symbols) DL EFKM as functions of $|t_f|/U$ at $t_c/U = 1$.

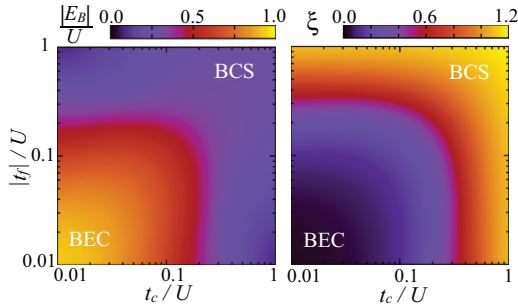


FIG. 5. (Color online) Exciton binding energy E_B/U (left panel) and coherence length ξ (right panel) of the DL EFKM in the t_c/U - $|t_f|/U$ plane.

where $\varepsilon_k = 2t(\cos k_x + \cos k_y)$, $n = n^e = n^h$, $\bar{\mu} = \mu - U(n - 1/2)$, and $\mu_f = -\mu_c = \mu$.

In the weak-coupling limit, we should recover the usual BCS picture. Δ should therefore increase exponentially with U : $\Delta \propto \exp[-1/\rho(\varepsilon_F)U]$, thereby satisfying the relation $|E_B| = 2\Delta$, with $\rho(\varepsilon_F)$ being the density of states at the Fermi level. In the strong-coupling limit, on the other hand, the BCS equations yield the asymptotic behavior: $\Delta = U\sqrt{n(1-n)} = \sqrt{3}U/4 \simeq 0.433U$ and $|E_B| = 2\sqrt{\bar{\mu}^2 + \Delta^2} = U$. The numerical results obtained for Δ and $|E_B|$ show that we find the BCS relation $|E_B| = 2\Delta$ at weak couplings. In the strong-coupling limit, Δ and $|E_B|$ are found to be $\propto 0.45U$ and $\propto U$, respectively, which matches the BEC of composite bosons, where $\Delta = 0.433U$ and $|E_B| = U$ for $U/t \rightarrow \infty$.

B. Mass-asymmetric case

We finally address the effects of a mass imbalance between f holes and c electrons. Since $|t_f| \neq t_c$, it makes sense to use U as the unit of energy and determine the exciton binding energy E_B and coherence length ξ in dependence on $|t_f|/U$. Figure 4 shows the results for $t_c/U = 1$ in comparison to the mass-symmetric case where a BCS-to-BEC transition occurs with decreasing $|t_f|/U$. In contrast, ξ is not reflective of such a crossover for $t_c \neq |t_f|$, and the exciton binding energy even weakens at strong couplings, $|t_f|/U \ll 1$.

In the strong-coupling region, where both $|t_f|/U$ and t_c/U are small, the EFKM can be mapped onto the XXZ quantum spin-1/2 model in a magnetic field,³⁰

$$\mathcal{H}_{\text{eff}} = J \sum_{(i,j)} [\boldsymbol{\tau}_i \cdot \boldsymbol{\tau}_j + \delta \tau_i^z \tau_j^z] - B_z \sum_i \tau_i^z \quad (13)$$

with $\boldsymbol{\tau}_i = (1/2) \sum_{\alpha,\beta} \alpha_i^\dagger \boldsymbol{\sigma}_{\alpha\beta} \beta_i$ ($\alpha, \beta = f, c$; $\boldsymbol{\sigma}$ is the vector of Pauli matrices), $J = 4|t_f|t_c/U$, and $\delta = (|t_f| - t_c)^2 / (2|t_f|t_c)$. $B_z = 2\mu$ is determined in order to maintain $\sum_i \tau_i^z = 1/4$. The

effective model is isotropic in spin space for the case of $|t_f| = t_c$, and it exhibits antiferromagnetic order in the x - y plane at zero temperature. This long-range ordered state corresponds to an exciton condensate in the original EFKM. Different hopping parameters $t_c \neq |t_f|$ give rise to an Ising anisotropy δ , which tends to suppress the x - y antiferromagnetic order. Accordingly, the exciton binding energy $|E_B|$ (excitonic condensate) is suppressed as $|t_f|/U \rightarrow 0$.

Figure 5 compiles our E_B (left panel) and ξ (right panel) data by two contour plots in the t_c/U - $|t_f|/U$ plane. For the mass-symmetric case $t_c = |t_f|$, i.e., on the diagonals of Fig. 5, both $|E_B|/U$ and ξ indicate a smooth crossover from BCS to BEC as U increases. On the other hand, at sufficiently weak Coulomb interactions, $t_c/U \gtrsim 0.3$, we stay in the BCS-like state as $|t_f|/U$ is varied by changing the absolute value of t_f/t_c . Note that a strong mass imbalance between electrons and holes acts in a ‘‘pair-breaking’’ way in both the BCS⁴⁹ and BEC^{26,50} limits.

V. SUMMARY

Based on unbiased exact-diagonalization calculations for the two-dimensional extended Falicov-Kimball model, we have studied the formation of excitons in both mass-symmetric and mass-asymmetric electron-hole double-layer systems (bilayers) and provided, most notably, strong evidence for exciton condensation and a BCS-BEC crossover scenario at zero temperature. Thereby, the properties of the excitonic quasiparticles and the nature of the condensation process were analyzed, exploiting the anomalous Green’s function in order to determine the order parameter of the condensate and coherence length, as well as the binding energy and momentum distribution function of excitons. The weak and strong correlation limits are discussed and put into perspective to approximative analytical approaches. We corroborated previous analytical^{26,49,50} and numerical¹⁷ findings to the effect that a mass imbalance between electrons and holes might suppress the condensation of excitons. This holds even in the strong-coupling regime. We hope that the presented results will stimulate further experimental studies of exciton condensation in bilayer systems with strong electronic correlations.

ACKNOWLEDGMENTS

The authors would like to thank K. Seki, Y. Tomio, and B. Zenker for enlightening discussions. T.K. acknowledges support from JSPS Research Fellowship for Young Scientists. This work was supported in part by the Kakenhi Grant No. 22540363 of Japan and by the Deutsche Forschungsgemeinschaft through SFB 652 B5. Part of the computations have been carried out at the Research Center for Computational Science, Okazaki Research Facilities, Japan.

¹J. M. Blatt, K. W. Böer, and W. Brandt, *Phys. Rev.* **126**, 1691 (1962).

²L. V. Keldysh and Y. V. Kopayev, *Sov. Phys. Solid State* **6**, 2219 (1965).

³S. A. Moskalenko and D. W. Snoke, *Bose-Einstein Condensation of Excitons and Biexcitons* (Cambridge University Press, Cambridge, 2000).

⁴P. B. Littlewood, P. R. Eastham, J. M. J. Keeling, F. M. Marchetti, B. D. Simons, and M. H. Szymanska, *J. Phys. Condens. Matter* **16**, S3597 (2004).

⁵D. W. Snoke, J. P. Wolfe, and A. Mysyrowicz, *Phys. Rev. B* **41**, 11171 (1990).

⁶J. L. Lin and J. P. Wolfe, *Phys. Rev. Lett.* **71**, 1222 (1993).

- ⁷N. Naka and N. Nagasawa, *J. Lumin.* **112**, 11 (2005).
- ⁸K. Yoshioka, E. Chae, and M. Kuwata-Gonokami, *Nat. Commun.* **2**, 328 (2011).
- ⁹H. Stolz, R. Schwartz, F. Kieseling, S. Som, M. Kaupisch, S. Sobkowiak, D. Semkat, N. Naka, T. Koch, and H. Fehske, *New J. Phys.* **14**, 105007 (2012).
- ¹⁰L. V. Butov, A. C. Gossard, and D. S. Chemla, *Nature (London)* **418**, 751 (2002).
- ¹¹D. Snoke, S. Denev, Y. Liu, L. Pfeiffer, and K. West, *Nature (London)* **418**, 754 (2002).
- ¹²J. P. Eisenstein and A. H. MacDonald, *Nature (London)* **432**, 691 (2004).
- ¹³A. H. Castro Neto, F. Guinea, N. M. R. Peres, K. S. Novoselov, and A. K. Geim, *Rev. Mod. Phys.* **81**, 109 (2009).
- ¹⁴R. Nandkishore and L. Levitov, *Phys. Rev. Lett.* **104**, 156803 (2010).
- ¹⁵A. A. High, J. R. Leonard, M. Remeika, L. V. Butov, M. Hanson, and A. C. Gossard, *Nano Lett.* **12**, 2605 (2012).
- ¹⁶V. S. Filinov, H. Fehske, M. Bonitz, V. E. Fortov, and P. R. Levashov, *Phys. Rev. E* **75**, 036401 (2007).
- ¹⁷J. Schleede, A. Filinov, M. Bonitz, and H. Fehske, *Contrib. Plasma Phys.* **52**, 819 (2012).
- ¹⁸L. V. Keldysh and A. N. Kozlov, *Zh. Eksp. Teor. Fiz.* **54**, 978 (1968) [*Sov. Phys. JETP* **27**, 521 (1968)], <http://www.jetp.ac.ru/cgi-bin/e/index/e/27/3/p521?a=list>.
- ¹⁹C. Comte and P. Nozières, *J. Phys. (France)* **43**, 1069 (1982).
- ²⁰P. Nozières and C. Comte, *J. Phys. (France)* **43**, 1083 (1982).
- ²¹P. Nozières and S. Schmitt-Rink, *J. Low Temp. Phys.* **59**, 195 (1985).
- ²²R. Micnas, J. Ranninger, and S. Robaszkiewicz, *Rev. Mod. Phys.* **62**, 113 (1990).
- ²³P. Pieri, D. Neilson, and G. C. Strinati, *Phys. Rev. B* **75**, 113301 (2007).
- ²⁴S. De Palo, F. Rapisarda, and G. Senatore, *Phys. Rev. Lett.* **88**, 206401 (2002).
- ²⁵R. Maezono, P. Lopez Rios, T. Ogawa, and R. J. Needs, *Phys. Rev. Lett.* **110**, 216407 (2013).
- ²⁶Y. Tomio, K. Honda, and T. Ogawa, *Phys. Rev. B* **73**, 235108 (2006).
- ²⁷T. Ogawa and Y. Tomio, *J. Lumin.* **129**, 1478 (2009).
- ²⁸Y. Tomio and T. Ogawa, *J. Phys. Soc. Jpn.* **79**, 104707 (2010).
- ²⁹L. M. Falicov and J. C. Kimball, *Phys. Rev. Lett.* **22**, 997 (1969).
- ³⁰C. D. Batista, *Phys. Rev. Lett.* **89**, 166403 (2002).
- ³¹P. Farkašovský, *Phys. Rev. B* **77**, 155130 (2008).
- ³²C. Schneider and G. Czycholl, *Eur. Phys. J. B* **64**, 43 (2008).
- ³³D. Ihle, M. Pfäfferott, E. Burovski, F. X. Bronold, and H. Fehske, *Phys. Rev. B* **78**, 193103 (2008).
- ³⁴C. D. Batista, J. E. Gubernatis, J. Bonča, and H. Q. Lin, *Phys. Rev. Lett.* **92**, 187601 (2004).
- ³⁵N. V. Phan, H. Fehske, and K. W. Becker, *Europhys. Lett.* **95**, 17006 (2011).
- ³⁶B. Zenker, D. Ihle, F. X. Bronold, and H. Fehske, *Phys. Rev. B* **81**, 115122 (2010).
- ³⁷B. Zenker, D. Ihle, F. X. Bronold, and H. Fehske, *Phys. Rev. B* **83**, 235123 (2011).
- ³⁸B. Zenker, D. Ihle, F. X. Bronold, and H. Fehske, *Phys. Rev. B* **85**, 121102R (2012).
- ³⁹K. Seki, R. Eder, and Y. Ohta, *Phys. Rev. B* **84**, 245106 (2011).
- ⁴⁰V. A. Apinyan and T. K. Kopeć, [arXiv:1211.4735](https://arxiv.org/abs/1211.4735).
- ⁴¹X. Zhu, P. B. Littlewood, M. S. Hybertsen, and T. M. Rice, *Phys. Rev. Lett.* **74**, 1633 (1995).
- ⁴²J. A. Seamons, C. P. Morath, J. L. Reno, and M. P. Lilly, *Phys. Rev. Lett.* **102**, 026804 (2009).
- ⁴³L. Rademaker, K. Wu, H. Hilgenkamp, and J. Zaanen, *Europhys. Lett.* **97**, 27004 (2012).
- ⁴⁴H. Min, R. Bistritzer, J.-J. Su, and A. H. MacDonald, *Phys. Rev. B* **78**, 121401(R) (2008).
- ⁴⁵N. V. Phan and H. Fehske, *New J. Phys.* **14**, 075007 (2012).
- ⁴⁶A. Perali, D. Neilson, and A. R. Hamilton, *Phys. Rev. Lett.* **110**, 146803 (2013).
- ⁴⁷Y. Ohta, T. Shimozato, R. Eder, and S. Maekawa, *Phys. Rev. Lett.* **73**, 324 (1994).
- ⁴⁸Y. Ohta, A. Nakauchi, R. Eder, K. Tsutsui, and S. Maekawa, *Phys. Rev. B* **52**, 15617 (1995).
- ⁴⁹F. X. Bronold and H. Fehske, *Phys. Rev. B* **74**, 165107 (2006).
- ⁵⁰K. Mizoo, T. J. Inagaki, Y. Ueshima, and M. Aihara, *J. Phys. Soc. Jpn.* **74**, 1745 (2005).

Excitonic BCS-BEC crossover in double-layer systems

T. Kaneko¹, S. Ejima², H. Fehske², and Y. Ohta¹

¹*Department of Physics, Chiba University, Chiba 263-8522, Japan*

²*Institute of Physics, Ernst Moritz Arndt University Greifswald, 17489 Greifswald, Germany*

E-mail: tatsuya-kaneko@chiba-u.jp

(Received September 23, 2013)

We investigate electron-hole pair condensation in electron bilayers described by the square-lattice extended Falicov-Kimball model. Using exact diagonalization and variational cluster approximation techniques we first calculate the anomalous Green's function to clarify the character of the excitons in momentum space. We then evaluate the coherence length ξ (in unit of the lattice constant a) from the corresponding condensation amplitude and demonstrate the smooth crossover between a BCS state of weakly paired electrons and holes ($\xi/a \gg 1$) and a BEC state of tightly bound excitons ($\xi/a \ll 1$) as the Coulomb attraction increases. Overcoming the finite-size effects of exact diagonalization while still taking into account the essential correlation effects we show that the variational cluster approximation provides an advantageous description of exciton condensation in strongly correlated electron systems.

KEYWORDS: exciton condensation, BCS-BEC crossover, Falicov-Kimball model, exact diagonalization, variational cluster approximation

1. Introduction

The formation of excitonic quantum condensates are intensively studied during the last half century [1–4]. Experimentally, multifaceted attempts have been made to observe the condensed state of excitons, e.g., in photoexcited semiconductors [5–9], unconventional semiconductor/graphene systems [10–14], electrostatic traps [15], or neutral electron-ion quantum plasmas [16]. Theoretically, a possible crossover between a Bardeen-Cooper-Schrieffer (BCS) electron-hole pair condensate and a Bose-Einstein condensate (BEC) of preformed excitons has been of topical interest [4, 17–23].

In order to get unbiased results for the problem of exciton condensation in electron-hole double-layer systems, in previous work [24], we investigated a minimal lattice fermion model, the so-called extended Falicov-Kimball model (EFKM) [25–29], by exact diagonalization (ED) of small clusters. To pinpoint the finite-size effects and affirm the main conclusions of [24] in the thermodynamic limit, in the present work, we employ the variational cluster approximation (VCA), based on the self-energy functional theory [30–33], to the square-lattice double-layer EFKM. Thereby we will corroborate the excitonic BCS-BEC crossover scenario suggested previously for strongly correlated electron-hole systems [34–36]. Calculating the anomalous excitation spectra and the condensation amplitude, we are able to extract the coherence length and order parameter of the condensate in both limits. Methodically, we will compare the VCA results with the corresponding ED and mean-field (MF) data to point out the range of applicability of the different approaches.

2. Model and Method

2.1 Extended Falicov-Kimball model

The EFKM for an electron-hole double layer is defined by the Hamiltonian

$$\mathcal{H} = - \sum_{\alpha=c,f} t_{\alpha} \sum_{\langle i,j \rangle} (\alpha_i^{\dagger} \alpha_j + \text{H.c.}) + U \sum_i n_i^f n_i^c - \sum_{\alpha=c,f} \mu_{\alpha} \sum_i n_i^{\alpha}, \quad (1)$$

where α_i^{\dagger} (α_i) creates (annihilates) an electron in the α ($= c, f$) orbital at site i , and $n_i^{\alpha} = \alpha_i^{\dagger} \alpha_i$. The transfer amplitude of electrons between the α orbitals on nearest-neighbor sites is denoted by t_{α} . We assume a band structure with a direct band gap ($t_c t_f < 0$). Without loss of generality the f orbitals were assigned to the hole (or valence-band) layer and the c orbitals to the electron (or conduction-band) layer. U (> 0) parametrizes the on-site interlayer Coulomb repulsion between f and c electrons that allows for an on-site interlayer Coulomb attraction between f hole and c electrons. Note that in our double-layer system the numbers of f and c particles are separately conserved because charge transfer between the two layers is assumed to be impossible. This mimics the generic situation in semiconductor electron-hole double quantum wells [12, 37, 38], and double-monolayer [39, 40] or double-bilayer graphene systems [41]. We furthermore assume that the excited electrons and holes have infinite lifetime and that the number of excited electrons is equal to the number of excited holes. This is in accord with the experimental situation in the majority of cases [5–13, 23, 40]. In practice, we adjust the chemical potentials μ_f and μ_c to maintain the number of electrons in the f and c layers independently. Throughout this work, we assume that the effective mass of the f band is equal to that of the c band (or $|t_f| = t_c = t$). Then we have the chemical potentials $\mu_f = -\mu_c = \mu$. Let us stress that the exciton condensation state in the double-layer EFKM can be mapped onto the superconducting (superfluid) state in the attractive Hubbard model in the mass-balanced case [42].

2.2 Exact diagonalization and variational cluster approximation

Within the ED investigation of the double-layer EFKM we use finite-size square lattices of $L_c = 4 \times 4 = 16$ sites (32 orbitals) with periodic boundary conditions (PBC). The particle densities are fixed to be $n_f = 0.75$ and $n_c = 0.25$, i.e., $(N_f, N_c) = (12, 4)$, which realizes a quarter-filled electron and hole band: $n^e = n^h = 0.25$. For the 4×4 lattice considered, the Fermi momenta are $\mathbf{k}_F = (\pm\pi/2, 0)$ and $\mathbf{k}_F = (0, \pm\pi/2)$.

To accomplish the thermodynamic limit, we employ the VCA based on the variational principle for the grand potential as a functional of the self-energy [30–33]. The trial self-energy for the variational method is generated from the exact self-energy of the disconnected finite clusters which act as a reference system. The Hamiltonian of the reference system is defined as $\mathcal{H}' = \mathcal{H} + \mathcal{H}_{\text{pair}} + \mathcal{H}_{\text{local}}$ with

$$\mathcal{H}_{\text{pair}} = \Delta' \sum_i (c_i^{\dagger} f_i + \text{H.c.}) \quad \text{and} \quad \mathcal{H}_{\text{local}} = \varepsilon'_f \sum_i n_i^f + \varepsilon'_c \sum_i n_i^c, \quad (2)$$

where the Weiss field for the s -wave pairing Δ' and the on-site potentials ε'_{α} ($\alpha = f, c$) are variational parameters. Note that the ε'_{α} , fulfilling for the mass-balanced case $\varepsilon'_f = -\varepsilon'_c = \varepsilon'$, were introduced to determine the particle density correctly. Provided $(\partial\Omega/\partial\Delta', \partial\Omega/\partial\varepsilon'_{\alpha}) = (0, 0)$ is guaranteed, the particle density n_{α} follows from $n_{\alpha} = -\partial\Omega/\partial\mu_{\alpha}$, and the chemical potential μ_{α} is determined to maintain $n_f = 0.75$ and $n_c = 0.25$. The Fermi momentum \mathbf{k}_F is defined via $\varepsilon_{\mathbf{k}_F} = \mu$ (at $U = 0$), where $\varepsilon_{\mathbf{k}} = -2t(\cos k_x + \cos k_y)$. Note that in the space of the cluster reference system all electronic correlations were exactly taken into account. We use $L_c = 2 \times 2 = 4$ (8 orbitals) in what follows.

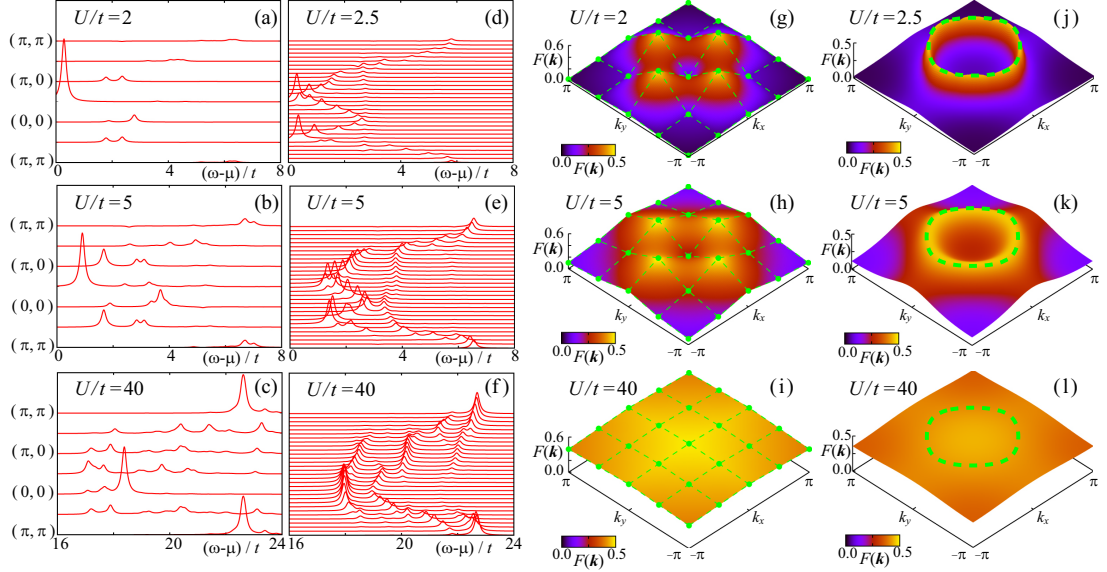


Fig. 1. (Color online) Left panel: Anomalous spectral function $F(\mathbf{k}, \omega)$ as obtained by ED [(a)-(c)] and VCA [(d)-(f)] with a Lorentzian broadening of $\eta/t = 0.1$. Right panel: Exciton condensation amplitude $F(\mathbf{k})$ calculated by ED [(g)-(i)] and VCA [(j)-(l)]. In panels (j)-(l) the green dashed lines indicate the Fermi surface.

3. Numerical results

3.1 Anomalous Green's function

Let us first discuss the anomalous Green's function. Using ED, the anomalous Green's function is obtained from

$$G_{\text{ED}}^{cf}(\mathbf{k}, \omega) = \langle N_f - 1, N_c + 1 | c_{\mathbf{k}}^\dagger \frac{1}{\omega + i\eta - \mathcal{H} + E_0} f_{\mathbf{k}} | N_f, N_c \rangle, \quad (3)$$

where $|N_f, N_c\rangle$ is the ground state of the EFKM with fixed numbers of c and f electrons. In Eq. (3), E_0 is the average energy of the states $|N_f, N_c\rangle$ and $|N_f - 1, N_c + 1\rangle$ [24, 43, 44]. Within VCA, the anomalous Green's function is calculated by cluster perturbation theory (CPT) [45], $G_{\text{CPT}}^{cf}(\mathbf{k}, \omega)$, making use of optimized variational parameters. From $G^{cf}(\mathbf{k}, \omega)$, we can immediately deduce the anomalous spectral function: $F(\mathbf{k}, \omega) = -\frac{1}{\pi} \text{Im} G^{cf}(\mathbf{k}, \omega)$.

Figure 1 (a)-(f) gives an intensity plot of $F(\mathbf{k}, \omega)$ in the square-lattice Brillouin zone. First of all we note that the VCA spectra basically agree with the ED spectra at the wave vectors allowed for a 4×4 cluster with PBC. In the weak-coupling regime [see Fig. 1 (a) and (d)], $F(\mathbf{k}, \omega)$ has a sharp peak at the Fermi momentum \mathbf{k}_F whose intensity rapidly decreases as soon as the momentum deviates from \mathbf{k}_F . With increasing U/t , the lowermost peak of $F(\mathbf{k}, \omega)$ shifts to higher energies, indicating an enhancement of the exciton's binding energy $|E_B|$, which may also be evaluated by the ground-state energies [24]. For $U/t = 5$ [see Fig. 1 (b) and (e)], $F(\mathbf{k}, \omega)$ still exhibits a pronounced peak around \mathbf{k}_F , but to compare to the $U/t = 2.5$ spectrum, $F(\mathbf{k}, \omega)$ acquires substantial weight at momenta away from \mathbf{k}_F . In the strong-coupling limit [cf. Fig. 1 (c) and (f) for $U/t = 40$], the spectral weight of $F(\mathbf{k}, \omega)$ is redistributed to higher energies and spread over the entire Brillouin zone.

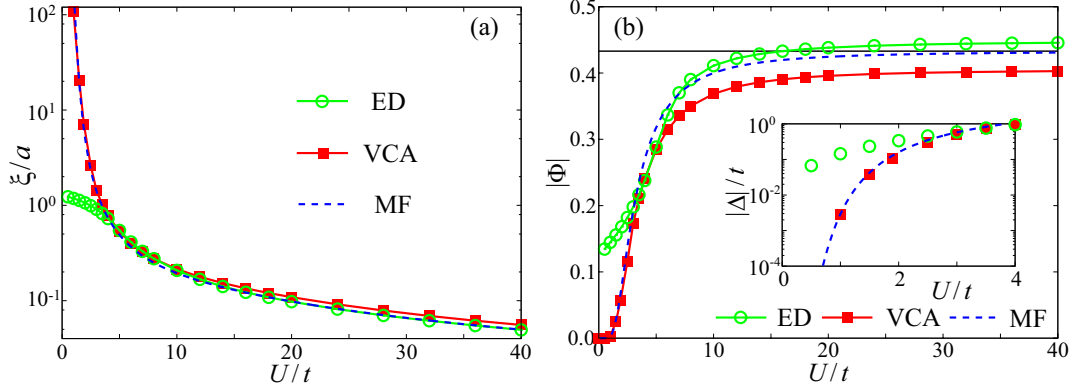


Fig. 2. (Color online) (a) Coherence length ξ in unit of the lattice constant a and (b) anomalous expectation value Φ for the double-layer EFKM, as obtained by ED (open green circles), VCA (full red squares), and MF (dashed blue lines). In (b), the horizontal line indicates $|\Phi| = \sqrt{3}/4$ and the inset gives the order parameter $\Delta = U\Phi$ in the weak-coupling regime.

3.2 Exciton condensation amplitude

To elucidate the nature of excitons in momentum space we now consider the condensation amplitude $F(\mathbf{k})$. Within ED the condensation amplitude can be directly calculated from

$$F(\mathbf{k}) = \langle N_f - 1, N_c + 1 | c_{\mathbf{k}}^\dagger f_{\mathbf{k}} | N_f, N_c \rangle. \quad (4)$$

In VCA the amplitude emanates from the anomalous CPT Green's function

$$F(\mathbf{k}) = \oint_C \frac{dz}{2\pi i} G_{\text{CPT}}^{cf}(\mathbf{k}, z), \quad (5)$$

where the contour C encloses the negative real axis in frequency space.

The results for $F(\mathbf{k})$ are shown in Fig. 1 (g)-(l). Again ED and VCA data agree insofar as comparable. The finite-size limitations of ED become obvious however. At weak couplings [cf. Fig. 1 (g) and (j)], the importance of Fermi surface effects are reflected in the corral-like shape of \mathbf{k}_F with $|F(\mathbf{k}_F)| \simeq 0.5$. The sharply peaked $F(\mathbf{k})$ in momentum space indicates that the radius of the exciton is large in real space, i.e., we observe a weakly bound electron-hole pair. Increasing U/t , $F(\mathbf{k})$ broadens in momentum space, indicating a spatially more confined exciton. In the strong-coupling regime displayed by Fig. 1 (i) and (l), $F(\mathbf{k})$ is (almost) homogeneously distributed over the whole Brillouin zone. Hence the excitons are tightly bound and small in real space.

3.3 Coherence length

The coherence length ξ gives valuable information as to the nature of the exciton condensate. Coming from $F(\mathbf{k})$, this quantity may be defined as

$$\xi^2 = \frac{\sum_{\mathbf{r}} r^2 |F(\mathbf{r})|^2}{\sum_{\mathbf{r}} |F(\mathbf{r})|^2} = \frac{\sum_{\mathbf{k}} |\nabla_{\mathbf{k}} F(\mathbf{k})|^2}{\sum_{\mathbf{k}} |F(\mathbf{k})|^2}, \quad (6)$$

where $F(\mathbf{r}) = \frac{1}{\sqrt{L}} \sum_{\mathbf{r}'} \langle c_{\mathbf{r}'}^\dagger f_{\mathbf{r}+\mathbf{r}'} \rangle$ is the condensation amplitude in real space for the electron-hole pairs with distance \mathbf{r} [24, 35, 42, 44]. The results obtained by ED, VCA, and MF are shown in Fig. 2 (a) in dependence on U/t . We find that ξ calculated by ED stays finite as $U/t \rightarrow 0$. This is clearly a finite-size effect caused by the small number of available momenta in the Brillouin zone. In the

intermediate-to-strong coupling regime, the coherence lengths calculated by ED, VCA, and MF are even in quantitative agreement. They rapidly decrease as U/t increases. At small U/t , the coherence length is much larger than the lattice constant a , in consequence of the weakly bound electron-hole pairs [cf. the behavior of $F(\mathbf{k})$ shown in Fig. 1 (g)-(l)]. This is the BCS limit. Increasing U/t , ξ decreases and firstly becomes comparable and finally much smaller than the lattice constant (for very strong couplings). As a result the excitons become manifest in a BEC. Altogether we observe a smooth crossover from a BCS state of weakly paired electrons and holes ($\xi/a \gg 1$) to a BEC state of tightly bound pairs ($\xi/a \ll 1$). This crossover behavior is consistent with the calculated spectral properties of the system shown in Fig. 1.

3.4 Order parameter

Finally let us discuss the order parameter for exciton condensation $\Delta = U\Phi$, which again can be obtained from the anomalous Green's function since

$$\Phi = \frac{1}{L} \sum_{\mathbf{k}} \langle c_{\mathbf{k}}^{\dagger} f_{\mathbf{k}} \rangle = \frac{1}{L} \sum_{\mathbf{k}} F(\mathbf{k}). \quad (7)$$

The results for Φ and Δ are shown in Fig. 2 (b). The MF theory predicts that the order parameter Δ_{MF} increases exponentially with increasing U/t in the weak-coupling limit ($\log \Delta_{\text{MF}} \propto -1/U$), and Φ_{MF} saturates at $\sqrt{3}/4$ for $n^e = n^h = 0.25$ in the strong-coupling limit. Obviously ED fails in reproducing the correct weak-coupling behavior: Φ_{ED} stays finite as $U/t \rightarrow 0$ and Δ_{ED} does not show the exponential increase at $U/t \gtrsim 0$. Clearly this can be attributed to finite-size effects within our small cluster calculation. Remarkably the VCA yields the exponential increase expected in the weak-coupling limit [see inset of Fig. 2 (b)]. We furthermore note that Φ_{VCA} is in qualitative accordance with the ED and MF results in the intermediate to strong coupling regime. For $U/t \gtrsim 5$, Φ_{VCA} is reduced in comparison to the MF result. This may be due to the effects of quantum fluctuations of exciton condensation included in VCA but not in MF.

4. Conclusions

To summarize, we have investigated the formation and condensation of excitons in the mass-balanced double-layer extended Falicov-Kimball model using—besides ED (exact diagonalization)—VCA (variational cluster approximation) and MF (mean-field) based approaches. We have analyzed the nature of excitonic bound states in dependence on the strength of the Coulomb interaction between electrons and holes and showed—evaluating the anomalous Green's function—that the excitonic condensation amplitude, coherence length, and order parameter function signal a smooth BCS-BEC crossover in the condensed phase. Our comparative numerical study reveals the need for taking control of both correlation and finite-size effects. In this respect the VCA turns out to be especially advantageous in the weak-to-intermediate coupling regime.

Acknowledgments

The authors would like to thank K. Seki, Y. Tomio, and B. Zenker for enlightening discussions. T.K. was supported by a JSPS Research Fellowship for Young Scientists. S.E. and H.F. were funded by DFG through SFB 652 project B5. Y.O. acknowledges the Kakenhi Grant No. 22540363.

References

- [1] J. M. Blatt, K. W. Böer, and W. Brandt: Phys. Rev. **126** (1962) 1691.
- [2] L. V. Keldysh and H. Y. V. Kopaev: Sov. Phys. Sol. State **6** (1965) 2219.
- [3] S. A. Moskalenko and D. W. Snoke: *Bose-Einstein Condensation of Excitons and Biexcitons* (Cambridge Univ. Press, Cambridge, 2000).

- [4] P. B. Littlewood, P. R. Eastham, J. M. J. Keeling, F. M. Marchetti, B. D. Simons, and M. H. Szymanska: *J. Phys. Condens. Matter* **16** (2004) S3597.
- [5] D. W. Snoke, J. P. Wolfe, and A. Mysyrowicz: *Phys. Rev. B* **41** (1990) 11171.
- [6] J. L. Lin and J. P. Wolfe: *Phys. Rev. Lett.* **71** (1993) 1222.
- [7] N. Naka and N. Nagasawa: *J. Lumin.* **112** (2005) 11.
- [8] K. Yoshioka, E. Chae, and M. Kuwata-Gonokami: *Nature Commun.* **2** (2011) 328.
- [9] H. Stolz, R. Schwartz, F. Kieseling, S. Som, M. Kaupisch, S. Sobkowiak, D. Semkat, N. Naka, T. Koch, and H. Fehske: *New J. Phys.* **14** (2012) 105007.
- [10] L. V. Butov, A. C. Gossard, and D. S. Chemla: *Nature* **418** (2002) 751.
- [11] D. Snoke, S. Denev, Y. Liu, L. Pfeiffer, and K. West: *Nature* **418** (2002) 754.
- [12] J. P. Eisenstein and A. H. MacDonald: *Nature* **432** (2004) 691.
- [13] A. H. Castro Neto, F. Guinea, N. M. R. Peres, K. S. Novoselov, and A. K. Geim: *Rev. Mod. Phys.* **81** (2009) 109.
- [14] R. Nandkishore and K. Levitov: *Phys. Rev. Lett.* **104** (2010) 156803.
- [15] A. A. High, J. R. Leonard, M. Remeika, L. V. Butov, M. Hanson, and A. C. Gossard: *Nano Lett.* **12** (2012) 2605.
- [16] Z. Donko, P. Hartmann, and D. Neilson (Eds.): *Proceedings of the Conference on Strongly Coupled Coulomb systems*, *Contrib. Plasma Phys.* **52**, (2012) 1.
- [17] L. V. Keldysh and A. N. Kozlov: *Sov. Phys. JETP* **27** (1968) 521.
- [18] C. Comte and P. Nozières: *J. Phys. (France)* **43** (1982) 1069.
- [19] P. Nozières and C. Comte: *J. Phys. (France)* **43** (1982) 1083.
- [20] P. Nozières and S. Schmitt-Rink: *J. Low Temp. Phys.* **59** (1985) 195.
- [21] R. Micnas, J. Ranninger, and S. Robaszkiewicz: *Rev. Mod. Phys.* **62** (1990) 113.
- [22] P. Pieri, D. Neilson, and G. C. Strinati: *Phys. Rev. B* **75** (2007) 113301.
- [23] J. Schleede, A. Filinov, M. Bonitz, and H. Fehske: *Contrib. Plasma Phys.* **52** (2012) 819.
- [24] T. Kaneko, S. Ejima, H. Fehske, and Y. Ohta: *Phys. Rev. B* **88** (2013) 035312.
- [25] L. M. Falicov and J. C. Kimball: *Phys. Rev. Lett.* **22** (1969) 997.
- [26] C. D. Batista: *Phys. Rev. Lett.* **89** (2002) 166403.
- [27] P. Farkašovský: *Phys. Rev. B* **77** (2008) 155130.
- [28] C. Schneider and G. Czycholl: *Eur. Phys. J. B* **64** (2008) 43.
- [29] D. Ihle, M. Pfafferoth, E. Burovski, F. X. Bronold, and H. Fehske: *Phys. Rev. B* **78** (2008) 193103.
- [30] M. Potthoff: *Eur. Phys. J. B* **32** (2003) 429.
- [31] M. Potthoff: *Eur. Phys. J. B* **36** (2003) 335.
- [32] C. Dahnken, M. Aichhorn, W. Hanke, E. Arrigoni, and M. Potthoff: *Phys. Rev. B* **70** (2004) 245110.
- [33] M. Potthoff: in *Strongly Correlated Systems - Theoretical Methods*, ed. A. Avella and F. Mancini (Springer, Berlin, 2012), pp. 303–339.
- [34] F. X. Bronold and H. Fehske: *Phys. Rev. B* **74** (2006) 165107.
- [35] K. Seki, R. Eder, and Y. Ohta: *Phys. Rev. B* **84** (2011) 245106.
- [36] B. Zenker, D. Ihle, F. X. Bronold, and H. Fehske: *Phys. Rev. B* **85** (2012) 121102R.
- [37] X. Zhu, P. B. Littlewood, M. S. Hybertsen, and T. M. Rice: *Phys. Rev. Lett.* **74** (1995) 1633.
- [38] J. A. Seamons, C. P. Morath, J. L. Reno, and M. P. Lilly: *Phys. Rev. Lett.* **102** (2009) 026804.
- [39] H. Min, R. Bistritzer, J. J. Su, and A. H. MacDonald: *Phys. Rev. B* **78** (2008) 121401(R).
- [40] V.-N. Phan and H. Fehske: *New J. Phys.* **14** (2012) 075007.
- [41] A. Perali, D. Neilson, and A. R. Hamilton: *Phys. Rev. Lett.* **110** (2013) 146803.
- [42] T. Kaneko and Y. Ohta: arXiv:1308.0664v1 (2013).
- [43] Y. Ohta, T. Shimozato, R. Eder, and S. Maekawa: *Phys. Rev. Lett.* **73** (1994) 324.
- [44] Y. Ohta, A. Nakauchi, R. Eder, K. Tsutsui, and S. Maekawa: *Phys. Rev. B* **52** (1995) 15617.
- [45] D. Sénéchal, D. Perez, and M. Pioro-Ladrière: *Phys. Rev. Lett.* **84** (2000) 522.



Luttinger parameters and momentum distribution function for the half-filled spinless fermion Holstein model: A DMRG approach

S. EJIMA and H. FEHSKE^(a)*Institut für Physik, Ernst-Moritz-Arndt-Universität Greifswald - 17489 Greifswald, Germany, EU*

received 8 May 2009; accepted in final form 6 July 2009

published online 22 July 2009

PACS 71.10.Hf – Non-Fermi-liquid ground states, electron phase diagrams and phase transitions in model systems

PACS 71.38.-k – Polarons and electron-phonon interactions

Abstract – We reexamine the nature of the metallic phase of the one-dimensional half-filled Holstein model of spinless fermions. To this end, we determine the Tomonaga-Luttinger-liquid correlation parameter K_ρ by large-scale density matrix renormalisation group (DMRG) calculations, exploiting i) the leading-order scaling relations between the ground-state energy and the single-particle excitation gap and ii) the static charge structure factor in the long-wavelength limit. While both approaches give almost identical results for intermediate-to-large phonon frequencies, we find contrasting behaviour in the adiabatic regime: i) $K_\rho > 1$ (attractive) *vs.* ii) $K_\rho < 1$ (repulsive). The latter result for the correlation exponent is corroborated by data obtained for the momentum distribution function $n(k)$, which puts the existence of an attractive metallic state in the spinless fermion Holstein model into question. We conclude that the scaling relation must be modified in the presence of electron-phonon interactions with noticeable retardation.

Copyright © EPLA, 2009

During the last three decades we have seen a constant growth of experimental realizations of one-dimensional (1D) materials. Nowadays the progress in nanotechnology allows to manufacture isolated carbon nanotubes or quantum wires [1]. But there are also bulk materials with quasi-1D structures inside. Famous examples are conjugated polymers, charge transfer salts, halogen-bridged transition metal complexes, ferroelectric perovskites, spin Peierls compounds, molecular metals or organic superconductors [2]. The apparent diversity of physical properties observed for different material classes has its seeds in the strong competition between the itinerancy of the electronic charge carriers on the one hand and the electron-electron and electron-lattice interactions on the other hand. The latter tend to establish insulating spin-density-wave or charge-density-wave (CDW) ground states, respectively, at least for commensurate band fillings [3–8]. Interactions have drastic effects in 1D systems compared to higher dimensions. Most notably one observes a “collectivisation” of any excitation. As a consequence, for fermionic systems, the usual Fermi-liquid description breaks down [9]. Luttinger-liquid theory provides an adequate compensation [10]. It tells us that all ground-state, spectral and thermodynamic properties

of a Luttinger liquid are basically controlled by a few (non-universal) parameters. This result can be used in the following way. Starting from a specific microscopic model, one can try to compute certain (thermodynamic) quantities exactly, *e.g.* for finite systems by elaborate numerical techniques, and afterwards extract the Luttinger-liquid parameters, *e.g.* the charge correlation exponent K_ρ and charge velocity u_ρ , out of them. Advantageously these parameters, describing the overall low-energy physics of our system, are much less sensitive to finite-size effects than the correlation functions themselves. Of course, the concept of a Luttinger liquid has to be taken as a starting point to study more complex situations, comprising *e.g.* the lattice degrees of freedom or disorder effects. Then the Luttinger parameters become effective parameters, which characterise very basic properties of the system, such as an attractive ($K_\rho > 1$) or repulsive ($K_\rho < 1$) interaction between the particles [9,11].

In this respect, focusing on the coupling of charge carriers to the vibrations of a deformable lattice, the so-called Holstein model of spinless fermions (HMSF) [12],

$$\mathcal{H} = -t \sum_j (c_j^\dagger c_{j+1} + \text{h.c.}) + \omega_0 \sum_j b_j^\dagger b_j - g\omega_0 \sum_j (b_j^\dagger + b_j) \left(n_j - \frac{1}{2} \right), \quad (1)$$

^(a)E-mail: holger.fehske@physik.uni-greifswald.de

is particularly rewarding to study. It accounts for a tight-binding electron band ($\propto t$), a local electron-phonon (EP) interaction ($\propto g$), and the energy of the phonon subsystem in harmonic approximation. In eq. (1), c_j^\dagger (c_j) creates (annihilates) an electron at Wannier site j of a 1D lattice with N sites, b_j^\dagger (b_j) are the corresponding bosonic operators for a dispersionless optical phonon, and ω_0 is the frequency of such an internal (*e.g.* molecular) vibration.

Despite its seemingly simplicity, the 1D HMSF is not exactly solvable. It is generally accepted, however, that the model exhibits a quantum phase transition from a metal to a CDW insulator at half-filling, when the EP coupling g increases at fixed $\omega_0 > 0$ (see footnote ¹). The CDW phase above $g_c(\omega_0)$ is connected to a (Peierls) distortion of the lattice, and can be classified as traditional band insulator and polaronic superlattice, respectively, in the adiabatic ($\omega_0 \ll 1$) and anti-adiabatic ($\omega_0 \gg 1$) regimes [13,14]. A wide range of analytical and numerical methods have been applied to map out the phase diagram of the HMSF in the whole $g - \omega_0$ plane [13,15–19], with significant differences in the region of small-to-intermediate phonon frequencies. The results agree in the anti-adiabatic strong EP coupling limit ($\omega_0 \rightarrow \infty$, $g > 1$), where the HMSF possesses XXZ-model physics. There a Kosterlitz-Thouless-type transition [20] occurs at the spin isotropy point, with K_ρ reaching $1/2$ from above at the transition point [15,18].

In the first instance, however, the correlation exponent K_ρ can be used to characterise the metallic phase itself. According to Haldane’s conjecture [21], a 1D gapless (metallic) system of interacting fermions should belong to the Tomonaga-Luttinger-liquid (TLL) universality class [10,22]. For a TLL of spinless fermions, the ground-state energy $E(N)$ and the one-particle charge excitation gap Δ_{c_1} of a finite system with N sites scale to leading order as [11,23]:

$$\frac{E(N)}{N} = \varepsilon(\infty) - \frac{\pi u_\rho}{3} \frac{1}{2 N^2}, \quad (2)$$

$$\Delta_{c_1} = E^\pm(N) - E(N) = \pi \frac{u_\rho}{2} \frac{1}{K_\rho N}. \quad (3)$$

Here, $\varepsilon(\infty)$ denotes the energy density of the infinite system with $N/2$ electrons, $E^\pm(N)$ are the ground-state energies with ± 1 fermion away from half-filling, and u_ρ is the renormalised charge velocity². Using these equations from field theory, in the past, K_ρ and u_ρ were determined for the HMSF on finite clusters by various exact numerical techniques [13,17,18,26]. Interestingly the TLL phase seems to split into two different regions: for large phonon frequencies the effective fermion-fermion interaction is repulsive ($K_\rho < 1$), while it

is attractive ($K_\rho > 1$) for small frequencies [13,26]. In the former (anti-adiabatic) regime the kinetic energy ($\propto u_\rho$) is strongly reduced and the charge carriers behave like (small) polarons [27,28]. By contrast the mass renormalisation is rather weak in the adiabatic regime [26]. The size of the phonon frequency also significantly affects the electron and phonon spectral functions [14,19,29].

The existence of an attractive TLL ($K_\rho > 1$) in the HMSF is by no means obvious however. Although retardation effects might lead to an effective attraction between electrons at small ω_0/t (*i.e.*, a second electron may take the advantage of the lattice distortion left by the first one), it has been pointed out that such an interaction is ineffective in the case of spinless fermions for small EP couplings because of the Pauli exclusion principle [15]³. Furthermore, if K_ρ would increase with increasing EP coupling at small ω_0 , as indicated by different numerical studies [13,26] exploiting eqs. (2) and (3), how could we detect the phase transition from $K_\rho \rightarrow 1/2$ in the adiabatic regime? Of course, eqs. (2) and (3) are leading-order expressions only, and nonlinear correction terms have to be taken into account in order to obtain accurate data for g_c [18]. This particularly applies to the adiabatic region. According to table III in ref. [18] the difference between the g_c determined with and without nonlinear correction terms adds up to more than 3% for $\omega_0 = 0.1$, whereas it is only 0.4% for $\omega_0 = 10$. Actually the charge velocity u_ρ depends strongly on the system’s size as shown in fig. 1 obtained by a density matrix renormalisation group (DMRG) calculation. Extrapolating the ground-state energies $E(N)$ for $N = 8, 12$ and 16 , the charge velocity u_ρ can be estimated as $u_\rho/2 \sim 0.977$, so that $K_\rho \sim 1.21$ from the finite-size scaling of Δ_{c_1} , while taking the ground-state energies for $N = 32, 48$ and 64 , the extracted value of K_ρ reduces to 1.06 ($u_\rho/2 \sim 0.858$). Moreover we are faced with the difficulty that the single-particle excitation gap seems to scale to zero (see inset of fig. 1 for $\omega_0 = 0.1$, $g = 2.5$), *i.e.* Δ_{c_1} gives no signal for a pairing instability. Because of this situation it is highly desirable to find a reliable and numerical efficient method for calculating the correlation exponent K_ρ with high precision in the whole TLL regime.

Recently Ejima *et al.* [30] have shown that K_ρ can be determined for fermionic models accurately in an alternative way: by a DMRG calculation of the charge structure factor for systems with open boundary conditions. The approach was extended to coupled fermion-boson systems and has been used, *e.g.*, to analyse the metal-insulator transition points in a model with boson affected transport, for both small and large boson frequencies [31].

In this work we adapt this calculation scheme to the 1D Holstein model of spinless fermions (1) and reexamine, in particular, the possible existence of a metallic phase with attractive interaction. To this end we compute, in a first

¹We consider the half-filled band case hereafter, *i.e.*, $\frac{1}{N} \sum_j (c_j^\dagger c_j) = \frac{1}{2}$, and take $t = 1$ as energy unit.

²The TLL scaling relations (2) and (3) were also derived for spinful systems [24], and, *e.g.*, used in order to compute the central charge in the framework of the t - J model [25].

³Note this argument does not hold for the spinful Holstein model.

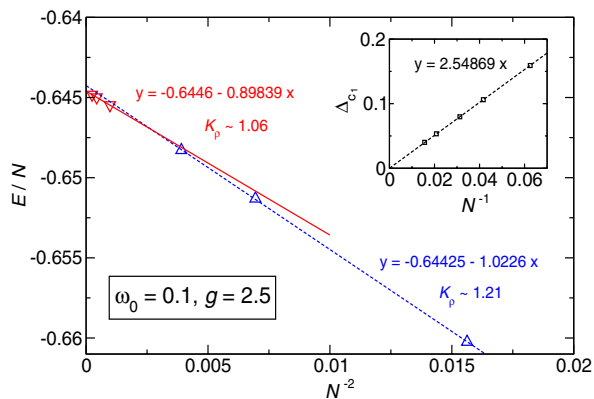


Fig. 1: (Colour on-line) Finite-size scaling of the ground-state energy $E(N)$ and the one-particle charge excitation gap Δ_{c_1} (inset) in the spinless Holstein model at half-filling. Results are obtained by DMRG for $\omega_0 = 0.1$ and $g = 2.5$. The linear equations give the coefficients of a straight-line fit to the scaling relations (2) and (3).

step, the static charge structure factor

$$S_c(q) = \frac{1}{N} \sum_{j,l} e^{iq(j-l)} \left\langle \left(c_j^\dagger c_j - \frac{1}{2} \right) \left(c_l^\dagger c_l - \frac{1}{2} \right) \right\rangle, \quad (4)$$

and extract, in a second step, the TLL correlation exponent K_ρ , being proportional to the slope of $S_c(q)$ in the long-wavelength limit [7,30,32]:

$$K_\rho = \pi \lim_{q \rightarrow 0^+} \frac{S_c(q)}{q}, \quad q = \frac{2\pi}{N}, \quad N \rightarrow \infty. \quad (5)$$

Moreover we calculate the momentum distribution function for the HMSF and, having accurate data for K_ρ at hand, analyse the results within a TLL description, also in relation to the corresponding results for the half-filled spinless t - V model. When treating coupled 1D fermion-boson systems by DMRG we employ the pseudo-site approach [33] which maps a bosonic site, containing 2^{n_b} states, exactly to n_b pseudo-sites. For the numerics presented below we have taken into account up to $n_b = 5$ pseudo-sites, so that the n_b -th local boson density is always smaller than 10^{-8} . In addition we kept $m = 1200$ density matrix eigenstates. Then the discarded weight was always smaller than 1.0×10^{-10} .

Figure 2(a) presents K_ρ obtained from eq. (5) for various phonon frequencies. Note that data points in (a) represent K_ρ -values extrapolated to the infinite system at fixed (g, ω_0) (cf., e.g., panel (c)). For intermediate-to-large phonon frequencies we find $K_\rho(g) < 1$ for all g , but an appreciable reduction of K_ρ takes place above $g = 1$ only. The strong decrease of K_ρ and u_ρ (not shown) for $g > 1$ is closely connected to polaron formation, which appears at about $g \simeq 1$ in the non-to-anti-adiabatic regime [28]. There the TLL typifies a (repulsive) polaronic metal [14]. We emphasise that in this frequency region the values of K_ρ , computed from eq. (5) via the static charge

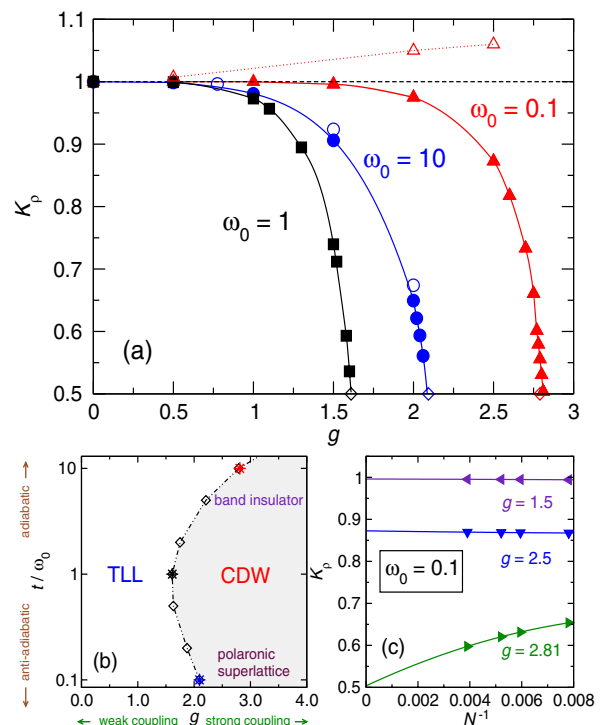


Fig. 2: (Colour on-line) Panel (a): TLL parameter K_ρ in the spinless Holstein model at half-filling. Closed symbols are obtained via $S_c(q)$ from eq. (5) for $\omega_0 = 0.1$ (triangles), 1 (squares), and 10 (circles). K_ρ obtained from the scaling relations (2) and (3) are included as open symbols. Lines are guides to the eye. Panel (b): ground-state phase diagram of the 1D half-filled spinless Holstein model according to refs. [13,14,18]. Stars denote the phase transition points obtained from $K_\rho = 1/2$ in (a). Panel (c): K_ρ as a function of the inverse system size at various EP couplings $g = 1.5, 2.5$, and 2.81 for $\omega_0 = 0.1$ (adiabatic regime). Lines are polynomial fits.

structure factor, reasonably agree with those determined by the scaling relations (2), (3) (see panel (a), filled and open symbols for $\omega_0 = 10$). Furthermore, our values for the critical coupling, g_c , confirm previous results (although a Kosterlitz-Thouless transition is difficult to detect because the gap opens exponentially slow), as can be seen by inserting the points where $K_\rho(g_c) = 1/2$ (stars) into the existing phase diagram of the HMSF [13,14,18] (cf. panel (b)).

Let us now look whether the situation changes when the phonon frequency becomes smaller, i.e., when we enter the adiabatic regime. Figure 2(c) shows the scaling of K_ρ at $\omega_0 = 0.1$, based on the relation (5), for up to $N = 256$ sites, using open boundary conditions. The lines are second-order polynomial fits. Surprisingly, we find that K_ρ scales to values smaller than unity for any EP coupling (filled symbols). This holds for other adiabatic phonon frequencies $\omega_0 < 1$ as well. Taking this result seriously, we arrive at the conclusion that the HMSF does not

exhibit a metallic TLL phase with attractive interaction, which is in strong contradiction to the reasonings based on the leading-order energy scaling laws (2) and (3) (see open symbols in fig. 2(a)). We would like to point out, however, that our $S_c(q)$ -based approach gives apparently the correct value of the critical coupling for the TLL-CDW metal-insulator transition in the adiabatic HMSF. In previous work, g_c was estimated as $g_c(\omega_0 = 0.1) \sim 2.8$ [18], which is in accordance with our DMRG-results for $K_\rho(N)$ at $g = 2.81$ that clearly extrapolate to $K_\rho = 1/2$ in the thermodynamic limit. This means that the TLL-CDW transition at small $\omega_0 = 0.1$ seems to be of Kosterlitz-Thouless type as well.

To substantiate these findings, we investigate another quantity of interest, the so-called momentum distribution function,

$$n(k) = \frac{1}{N} \sum_{j,l} e^{ik(j-l)} \langle c_j^\dagger c_l \rangle. \quad (6)$$

Basically $n(k)$ is the Fourier transform of the equal time Green's function [9] and therefore gives the occupation of fermionic states carrying momentum k . For free fermions, at $T=0$, all states up to the Fermi energy, E_F , are occupied, so that $n(k)$ has a discontinuity ($Z=1$) at the corresponding Fermi momentum k_F (see footnote 4). For a 1D TLL, instead of the (Fermi-liquid archetypical) jump of $n(k)$ at k_F , one finds an essential power law singularity, corresponding to a vanishing quasiparticle weight $Z=0$,

$$n(k) = n_{k_F} - C|k - k_F|^\alpha \text{sgn}(k - k_F), \quad (7)$$

where $n_{k_F} = 1/2$ for the half-filled band case. For spinless fermions, again the critical exponent α is given by the TLL parameter K_ρ :

$$\alpha = \frac{1}{2}(K_\rho + K_\rho^{-1}) - 1. \quad (8)$$

The relation (7) with (8) was first derived in [10,34], and afterwards many analytical [35] and numerical [36] calculations were performed in order to determine the momentum distribution in the weak- and strong-coupling regimes. By means of DMRG, $n(k)$ can be computed directly from the Fourier transformed $\langle c_j^\dagger c_l \rangle$ correlator, $n(k) = \frac{1}{N} \sum_{j,l=1}^N \cos(k(j-l)) \langle c_j^\dagger c_l \rangle$, where $k = \frac{2\pi}{N}m$ with $m=0, \dots, N/2$. In the following, we calculate $n(k)$ for a linear chain with periodic boundary conditions, and $N = 66$ sites.

Before we discuss $n(k)$ for the HMSF, let us consider a somewhat simpler, purely fermionic model, however, the spinless t - V model,

$$\mathcal{H} = -t \sum_j \left(c_j^\dagger c_{j+1} + \text{h.c.} \right) + V \sum_j n_j n_{j+1}, \quad (9)$$

where V is the nearest-neighbour Coulomb interaction. This is of avail because the t - V model can also be mapped

⁴In an interacting Fermi-liquid system there is still a discontinuity, but $Z < 1$.

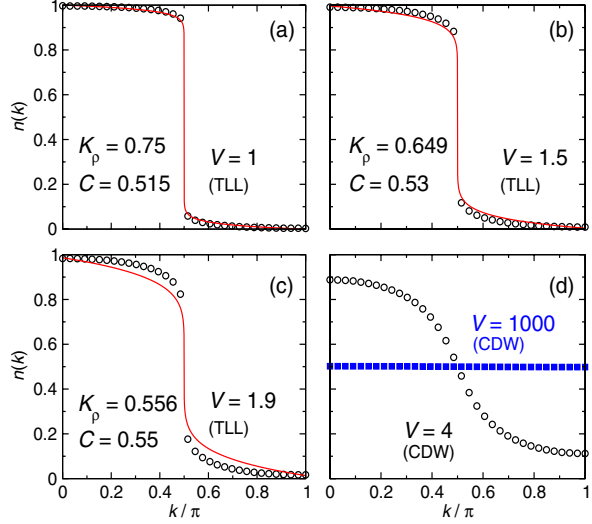


Fig. 3: (Colour on-line) Momentum distribution function $n(k)$ for the half-filled spinless t - V model. Lines are fit to eq. (7) with K_ρ taken from eq. (10).

onto the exactly solvable XXZ-Heisenberg model (*i.e.*, it should exhibit the same asymptotic behaviour as the strong-coupling anti-adiabatic HMSF). For the t - V model the analytical form of K_ρ in the thermodynamic limit is known,

$$K_\rho = \frac{\pi}{2 \arccos[-V/(2t)]}. \quad (10)$$

Hence, the results obtained for $n(k)$ by DMRG can be fitted by the relation (7), with K_ρ taken from eq. (10) [37]. Clearly, since eq. (7) is a weak-coupling result, the DMRG data for $n(k)$ are fitted almost perfectly for small V . This is demonstrated by figs. 3(a) and (b). Figure 3(c) shows that the agreement becomes worse for larger Coulomb interaction ($V = 1.9$). In the insulating phase ($V > 2$), the power law singularity does not exist anymore (cf. the smooth curves in fig. 3(d)). As $V \rightarrow \infty$, the system becomes a “perfect” CDW, and consequently $n(k) = 1/2$ for all momenta k . *De facto* this situation is realized for $V = 1000$ already where, according to fig. 3(d), $n(k)$ is almost constant.

Turning now to the HMSF, we discuss at first the case of large phonon frequencies. Figure 4 gives the $n(k)$ DMRG data obtained for $\omega_0 = 10$ (symbols). Obviously, the momentum distribution is a monotonously decreasing function as k changes from the centre ($k=0$) to the boundary of the Brillouin zone ($k=\pi$), with a power law singularity at $k=k_F$ in the metallic phase (panels (a) to (c)). Quite different from the t - V model, however, the momentum distribution becomes renormalised for all momenta k , as soon as the EP coupling is switched on, where $n(k)$ decreases (increases) almost uniformly for $0 \leq k < \pi/2$ ($\pi/2 < k \leq \pi$). Although there is no jump in $n(k)$ at k_F , as for an ordinary Fermi liquid, for finite

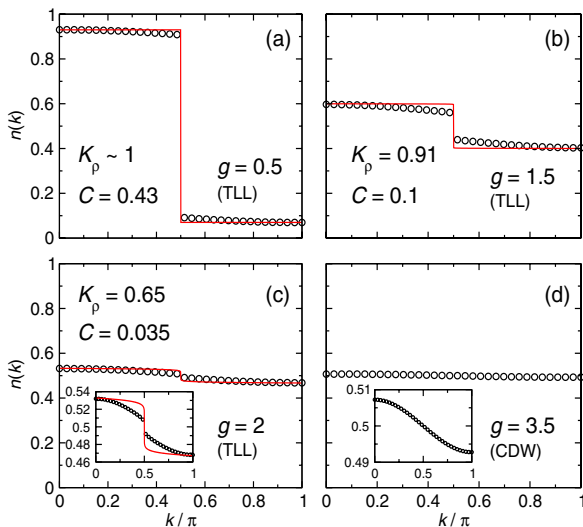


Fig. 4: (Colour on-line) Momentum distribution function $n(k)$ in the anti-adiabatic regime ($\omega_0 = 10$) of the half-filled spinless Holstein model. Lines are a fit to eq. (7) with K_ρ calculated by the DMRG. Insets give $n(k)$ with magnified axis of ordinate.

TLL systems the difference $\Delta = n(k_F - \delta) - n(k_F + \delta)$ is finite (with $\delta = \pi/N = \pi/66$ in our case), and rapidly decreases with increasing EP interaction g . As can be seen from the solid lines in figs. 4(a)–(c), the momentum distribution can be surprisingly well fitted to the weak-coupling result (7), just by adjusting the constant C . Thereby we take the K_ρ -values extracted from eq. (5). Of course, around $k \simeq k_F$ the agreement becomes worse as g increases, but we observe a power law singularity even close to the CDW transition point. Approaching the insulating CDW state this singularity vanishes, and $\Delta \rightarrow 0$ as $g \rightarrow g_c$ (cf. the insets in panels (c) and (d)). In the CDW phase, $n(k) \simeq 1/2$ for all k (see panel (d)). In the anti-adiabatic regime, the CDW state basically constitutes a polaronic superlattice, *i.e.* the electrons are heavily dressed by phonons and, in addition, ordered in a A-B structure. Since the polarons are self-trapped, the system tends to be a perfect CDW, as in the limit $V \rightarrow \infty$ of the t - V model.

Finally, we investigate the behaviour of $n(k)$ in the adiabatic regime of the HMSF (see fig. 5 for $\omega_0 = 0.1$). In this case, $n(k)$ is well approximated by eq. (7) with $C = 0.5$ for all $g < g_c$ (see panels (a) and (b)). This means the weak-coupling result $K_\rho \lesssim 1$, $\Delta \lesssim 1$, holds in (almost) the entire metallic region, where the system can be considered as to be composed of nearly free electrons. The momentum distribution starts to deviate from eq. (7) just in the neighbourhood of the metal insulator transition point $g \simeq g_c$, but even there $n(k)$ differs near $k \sim k_F = \pi/2$ only. Note that Δ (C) is still very large in the transition region. Of course, very close to the critical point, where a strong renormalisation of K_ρ takes place (indicating the formation of a TLL with strong repulsive interactions),

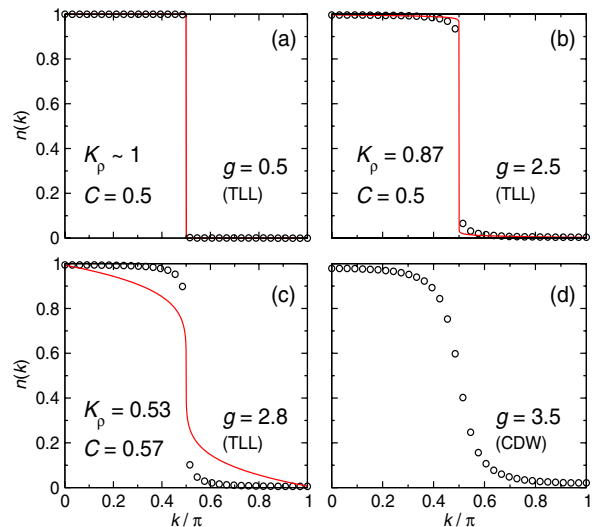


Fig. 5: (Colour on-line) Momentum distribution function $n(k)$ in the adiabatic regime ($\omega_0 = 0.1$) of the half-filled spinless Holstein model. Lines are a fit to eq. (7) with K_ρ calculated by the DMRG.

the fit of our DMRG data to the weak-coupling relation (7) fails. In the insulating state, $n(k)$ is given by a smooth curve (without power law singularity), which—in contrast to the anti-adiabatic case—exhibits a significant curvature because the EP coupling used in fig. 5(d) is small if compared to the half-electronic bandwidth $2t$ (see footnote ⁵). Therefore system now typifies rather a Peierls band insulator than a polaronic superlattice.

To summarise, we investigated the properties of the metallic phase and the metal insulator transition in the spinless fermion Holstein model by means of a boson pseudo-site DMRG technique supplemented by a careful finite-size scaling analysis. In particular we determined the Tomonaga-Luttinger correlation exponent K_ρ from the long-wavelength limit of the static charge structure factor. This approach yields reliable data for K_ρ in the whole range of electron-phonon interaction strengths g and phonon frequencies ω_0 . We compare our results with new and previous data extracted in an alternative way from leading-order scaling relations for the ground-state energy and single-particle excitation gap. In striking contrast to the latter data we find $K_\rho < 1$ for all phonon frequencies, *i.e.*, the metallic state of the HMSF represents a repulsive Tomonaga-Luttinger liquid, even in the adiabatic regime. Therefore we conclude that in one dimension we have to include the spin degrees of freedom [7,8,15] in order to obtain, *e.g.*, a phase with attractive interactions ($K_\rho > 1$), or even dominant superconducting correlations. Furthermore, since the metal insulator phase boundary in the g - ω_0^{-1} plane obtained from the $K_\rho(g, \omega_0) = 1/2$ line is in

⁵Recall that in the adiabatic regime $\lambda = g^2\omega_0/2t$ is the appropriate dimensionless EP interaction parameter in order to discriminate weak- ($\lambda \ll 1$) and strong-coupling ($\lambda \gg 1$) situations.

excellent agreement with previous results [13,14,18], we suppose that the TLL-CDW transition in the HMSF is always of Kosterlitz-Thouless type. Comparing the behaviour of the momentum distribution function with the weak-coupling TLL result reveals, however, significant differences regarding the nature of the metallic and insulating phases in the adiabatic and anti-adiabatic regimes of the HMSF. Whereas the metallic state is a weakly renormalised TLL and the CDW phase typifies a Peierls band insulator at small phonon frequencies, a polaronic metal and a polaronic superlattice are formed at large phonon frequencies. This is in accord with the electron and phonon spectral properties detected in refs. [14,29]. In the strong-coupling anti-adiabatic regime the momentum distribution function indicates perfect CDW behaviour as in the $V \rightarrow \infty$ limit of the t - V model.

The authors would like to thank G. HAGER, E. JECKELMANN, V. MEDEN, and S. NISHIMOTO for valuable discussions. This work was supported by SFB 652.

REFERENCES

- [1] PLOOG K. H. and NÖTZEL R. (Editors), *New Concepts to Fabricate Semiconductor Quantum Wire and Quantum Dot Structures*, in *Lect. Notes Phys.*, Vol. **419** (Springer-Verlag, Berlin/Heidelberg) 1985.
- [2] ISHIGURO T., YAMAJI K. and SAITO G., *Organic Superconductors* (Springer-Verlag, New York) 1973; TSUDA N., NASU K., YANASE A. and SIRATORI K., *Electronic Conduction in Oxides* (Springer-Verlag, Berlin) 1991; BISHOP A. R. and SWANSON B. I., *Los Alamos Sci.*, **21** (1993) 133; HASE M., TERASAKI I. and UCHINOKURA K., *Phys. Rev. Lett.*, **70** (1993) 3651; WELLEIN G., FEHSKE H. and KAMPF A. P., *Phys. Rev. Lett.*, **81** (1998) 3956; TOYOTA N., LANG M. and MÜLLER J., *Low-dimensional Molecular Metals* (Springer-Verlag, Berlin/Heidelberg) 2007.
- [3] MOTT N. F., *Metal-Insulator Transitions* (Taylor & Francis, London) 1990; MONCEAU P., *Fiz. Tverd. Tel.*, **41** (1999) 759.
- [4] PEIERLS R., *Quantum Theory of Solids* (Oxford University Press, Oxford) 1955; GRÜNER G., *Density Waves in Solids* (Addison Wesley, Reading, Mass.) 1994.
- [5] TAKADA Y. and CHATTERJEE A., *Phys. Rev. B*, **67** (2003) 081102(R).
- [6] FEHSKE H., WELLEIN G., HAGER G., WEISSE A. and BISHOP A. R., *Phys. Rev. B*, **69** (2004) 165115; FEHSKE H., HAGER G. and JECKELMANN E., *EPL*, **84** (2008) 57001.
- [7] CLAY R. T. and HARDIKAR R. P., *Phys. Rev. Lett.*, **95** (2005) 096401; HARDIKAR R. P. and CLAY R. T., *Phys. Rev. B*, **75** (2007) 245103.
- [8] TEZUKA M., ARITA R. and AOKI H., *Phys. Rev. Lett.*, **95** (2005) 226401; *Phys. Rev. B*, **76** (2007) 155114.
- [9] GIAMARCHI T., *Quantum Physics in One Dimension* (Oxford University Press, Oxford) 2003.
- [10] LUTTINGER J. M., *J. Math. Phys.*, **4** (1963) 1154.
- [11] VOIT J., *Rep. Prog. Phys.*, **58** (1995) 977.
- [12] HOLSTEIN T., *Ann. Phys. (N.Y.)*, **8** (1959) 325; 343.
- [13] FEHSKE H., HOLICKI M. and WEISSE A., *Adv. Solid State Phys.*, **40** (2000) 235; WEISSE A. and FEHSKE H., *Phys. Rev. B*, **58** (1998) 13526.
- [14] HOHENADLER M., WELLEIN G., BISHOP A. R., ALVERMANN A. and FEHSKE H., *Phys. Rev. B*, **73** (2006) 245120.
- [15] HIRSCH J. E. and FRADKIN E., *Phys. Rev. Lett.*, **49** (1982) 402; *Phys. Rev. B*, **27** (1983) 4302.
- [16] ZHENG H., FEINBERG D. and AVIGNON M., *Phys. Rev. B*, **39** (1989) 9405.
- [17] MCKENZIE R. H., HAMER C. J. and MURRAY D. W., *Phys. Rev. B*, **53** (1996) 9676.
- [18] BURSILL R. J., MCKENZIE R. H. and HAMER C. J., *Phys. Rev. Lett.*, **80** (1998) 5607.
- [19] SYKORA S., HÜBSCH A., BECKER K. W., WELLEIN G. and FEHSKE H., *Phys. Rev. B*, **71** (2005) 045112.
- [20] KOSTERLITZ J. M. and THOULESS D. J., *J. Phys. C*, **6** (1973) 1181.
- [21] HALDANE F. D. M., *Phys. Rev. Lett.*, **45** (1980) 1358.
- [22] TOMONAGA S., *Prog. Theor. Phys.*, **5** (1950) 544.
- [23] CARDY J. L., *J. Phys. A*, **17** (1984) L385.
- [24] FRAHM H. and KOREPIN V. E., *Phys. Rev. B*, **42** (1990) 10553; KAWAKAMI N. and YANG S. K., *Phys. Lett. A*, **148** (1990) 359.
- [25] OGATA M., LUCHINI M. U., SORELLA S. and ASSAAD F. F., *Phys. Rev. Lett.*, **66** (1991) 2388.
- [26] WEISSE A., FEHSKE H., WELLEIN G. and BISHOP A. R., *Phys. Rev. B*, **62** (2000) R747; FEHSKE H., WELLEIN G., HAGER G., WEISSE A., BECKER K. W. and BISHOP A. R., *Physica B*, **359-361** (2005) 699.
- [27] FIRSOV Y. A., *Polarons* (Izd. Nauka, Moscow) 1975.
- [28] FEHSKE H. and TRUGMAN S. A., *Numerical solution of the Holstein polaron problem*, in *Polarons in Advanced Materials*, edited by ALEXANDROV A. S. in *Springer Ser. Mater. Sci.*, Vol. **103** (Canopus/Springer Publishing, Dordrecht) 2007, pp. 393–461.
- [29] SYKORA S., HÜBSCH A. and BECKER K. W., *Europhys. Lett.*, **76** (2006) 644.
- [30] EJIMA S., GEBHARD F. and NISHIMOTO S., *Europhys. Lett.*, **70** (2005) 492.
- [31] EJIMA S., HAGER G. and FEHSKE H., *Phys. Rev. Lett.*, **102** (2009) 106404.
- [32] CLAY R. T., SANDVIK A. W. and CAMPBELL D. K., *Phys. Rev. B*, **59** (1999) 4665.
- [33] WHITE S. R., *Phys. Rev. Lett.*, **69** (1992) 2863; JECKELMANN E. and WHITE S. R., *Phys. Rev. B*, **57** (1998) 6376; JECKELMANN E. and FEHSKE H., *Riv. Nuovo Cimento*, **30** (2007) 259.
- [34] MATTIS D. C. and LIEB E. H., *J. Math. Phys.*, **6** (1965) 304.
- [35] SÓLYOM J., *Adv. Phys.*, **28** (1979) 201; OGATA M. and SHIBA H., *Phys. Rev. B*, **41** (1990) 2326; PRUSCHKE T. and SHIBA H., *Phys. Rev. B*, **44** (1991) 205.
- [36] QIN S., LIANG S., SU Z. and YU L., *Phys. Rev. B*, **52** (1995) 5475.
- [37] MEDEN V., METZNER M., SCHOLLWÖCK U., SCHNEIDER O., STAUBER T. and SCHÖNHAMMER K., *Eur. Phys. J. B*, **16** (2000) 631.

DMRG analysis of the SDW-CDW crossover region in the 1D half-filled Hubbard-Holstein model

S. Ejima and H. Fehske

Institut für Physik, Ernst-Moritz-Arndt-Universität Greifswald, 17489 Greifswald, Germany

Abstract. In order to clarify the physics of the crossover from a spin-density-wave (SDW) Mott insulator to a charge-density-wave (CDW) Peierls insulator in one-dimensional (1D) systems, we investigate the Hubbard-Holstein Hamiltonian at half filling within a density matrix renormalisation group (DMRG) approach. Determining the spin and charge correlation exponents, the momentum distribution function, and various excitation gaps, we confirm that an intervening metallic phase expands the SDW-CDW transition in the weak-coupling regime.

The Hubbard-Holstein model (HHM) [1] is archetypal for exploring the complex interplay of electron-electron and electron-phonon interactions especially in quasi-1D materials, such as halogen-bridged transition metal complexes, charge transfer salts, or organic superconductors [2]. It accounts for a tight-binding electron band ($\propto 2t$), an intra-site Coulomb repulsion between electrons of opposite spin ($\propto u = U/4t$), a local coupling of the charge carriers to optical phonons ($\propto \lambda = g^2\omega_0/2t$), and the energy of the phonon subsystem in harmonic approximation ($\propto \omega_0/t$):

$$\mathcal{H} = -t \sum_{j\sigma} (c_{j\sigma}^\dagger c_{j+1\sigma} + \text{h.c.}) + U \sum_j n_{j\uparrow} n_{j\downarrow} - g\omega_0 \sum_{j\sigma} (b_j^\dagger + b_j) n_{i\sigma} + \omega_0 \sum_j b_j^\dagger b_j. \quad (1)$$

Here $c_{i\sigma}^\dagger$ ($c_{i\sigma}$) creates (annihilates) a spin- σ electron at Wannier site i of an 1D lattice with N sites, $n_{i\sigma} = c_{i\sigma}^\dagger c_{i\sigma}$, and b_i^\dagger (b_i) are the corresponding creation (annihilation) operators for a dispersionless phonon. We consider the case $\frac{1}{N} \sum_{i\sigma} n_{i\sigma} = 1$ hereafter, and take t as energy unit.

Based on exact diagonalisation data for the staggered static spin/charge structure factor, $S_{\sigma/\rho}(q) = \frac{1}{N} \sum_{j,\ell} e^{iq(j-\ell)} \langle (\hat{n}_{j\uparrow} \pm \hat{n}_{j\downarrow})(\hat{n}_{\ell\uparrow} \pm \hat{n}_{\ell\downarrow}) \rangle$, it has been argued that the HHM shows a crossover between Mott and Peierls insulating phases near $u/\lambda \simeq 1$ [3]. But this only holds in the strong-coupling adiabatic-to-intermediate phonon frequency regime. Later on the ground-state phase diagram of the HHM was explored in more detail, also for weak interaction strengths and large phonon frequencies. In this regime, variational displacement Lang-Firsov [4], stochastic series expansion QMC [5], and DMRG [6] methods give strong evidence that, if λ is enhanced at fixed u and ω_0 , the SDW-CDW transition splits into two subsequent SDW-metal and metal-CDW transitions at λ_{c1} and λ_{c2} , respectively (see fig. 1, dashed and dot-dashed lines). Very recent DMRG data indicated that in the anti-adiabatic regime of very large phonon frequencies the metallic phase might be even more extended than the one obtained by QMC and is subdivided into regions with a normal 1D metallic (I) and a bipolaronic-liquid (II) behaviour [7].

In this work, we will re-examine the weak-coupling SDW-CDW transition regime by calculating the ground-state properties of the HHM in the framework of a large-scale numerical (boson pseudo-site) DMRG approach supplemented by a finite-size scaling analysis [8].

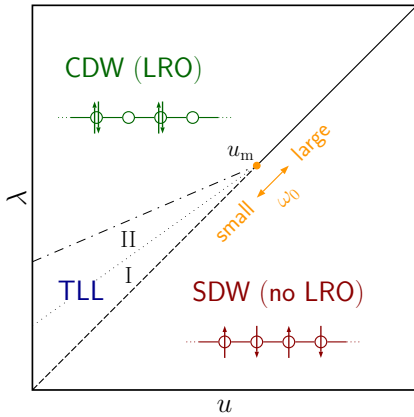


Figure 1. Qualitative phase diagram of the 1D Hubbard-Holstein model. Given that in the half-filled HHM model the ground-state is metallic at $u = 0$ for $\omega_0 > 0$ provided that $g < g_c$, it was proposed that this metallic phase continues to exist between the SDW and CDW states for $u > 0$ [4, 5, 6, 7]. With increasing ω_0 the region of the intervening metallic state increases, and the tricritical point u_m moves to larger u [5]. The SDW state shows no long-range order (LRO) and is characterised by a vanishing spin gap Δ_s but a finite charge gap Δ_{c1} , whereas the CDW phase exhibits true LRO and $\Delta_s = \Delta_{c1} > 0$.

Characterising the SDW-CDW-intervening metallic phase of the HHM, we presume that for the metallic state a Tomonaga-Luttinger-liquid (TLL) description holds. In the TLL picture, nonuniversal coefficients, K_ρ and K_σ , determine the decay of correlation functions and therefore can be used to identify the properties of the TLL phase [9], but also the phase boundaries to the insulating states [5]. In practice, we can extract the TLL correlation exponents from the slope of the corresponding structure factors in the long-wavelength limit [5, 10]: $K_{\rho/\sigma} = \pi \lim_{q \rightarrow 0} S_{\rho/\sigma}(q)/q$, where $q = 2\pi/N$ for $N \rightarrow \infty$.

Specifically, $K_\rho > 1$ ($K_\rho < 1$) corresponds to attractive (repulsive) charge correlations in the TLL and $K_\rho = 0$ signals an insulating phase. Hence K_ρ jumps from $1 \rightarrow 0$ at the metal-SDW/CDW transitions. The spin exponent takes the value $K_\sigma = 0$ in a spin-gapped phase and $K_\sigma = 1$ everywhere else in the thermodynamic limit [11]. For finite systems the situation is more involved, in particular for the spin exponent K_σ . First, the convergence $K_\sigma \rightarrow 0$ is slow-going as $N \rightarrow \infty$ in the spin-gapped phase. Second, logarithmic corrections prevent $K_\sigma \rightarrow 1$ in the spin-gapless (SDW) phase. On the other hand, these logarithmic corrections vanish at the critical point, where the spin gap opens, and we can utilise that K_σ (K_ρ) crosses 1 from above (below) at some λ_{c1} (as the electron-phonon coupling increases for fixed u), in order to determine the SDW-metal phase boundary itself. Increasing λ further, K_ρ should cross 1 once again, this time from above, at another critical coupling strength, λ_{c2} , which pins the metal-CDW transition point down.

Figure 2 corroborates this scenario for the anti-adiabatic regime of the HHM. The two critical values λ_{c1} and λ_{c2} are in accord with the phase diagram obtained by QMC [5]. $K_\sigma < 1$ and $K_\rho > 1$ earmark the intervening metallic phase. In terms of the TLL framework, a metallic phase with $K_\rho > 1$ exhibits dominant superconducting correlations. Recent DMRG calculations of the the (s -, p -, and d -wave) superconducting correlation functions of the half-filled HHM indicate, however, that these correlations are only sub-dominant against CDW correlations [6], while QMC investigations attributed the $K_\rho > 1$ to finite-size effects and suggest that $K_\rho(N \rightarrow \infty) = 1$, i.e., superconducting and CDW correlations are exactly degenerate.

Here we inspect the finite-size scaling of the spin and single-particle charge excitation gaps, $\Delta_s(N) = E_0(1) - E_0(0)$ and $\Delta_{c1}(N) = E_0^+(1/2) + E_0^-(-1/2) - 2E_0(0)$, respectively, as well as that of the two-particle binding energy $\Delta_b(N) = E_0^{2-}(0) + E_0(0) - 2E_0^-(-1/2)$, where $E_0^{(L\pm)}(S^z)$ is the ground-state energy at or away from half-filling with $N_e = N \pm L$ particles in the sector with total spin- z component S^z . The left panel of fig. 2 shows that both spin and charge gaps open at λ_{c1} (but there is no LRO). For $u < u_m$, the transition at λ_{c1} seems to be of Kosterlitz-Thouless type, i.e. just above λ_{c1} the gaps are exponentially small and therefore their magnitude is difficult to determine. In this region, denoted by (I) in fig. 1, we find $\Delta_{c1} \sim \Delta_s$,

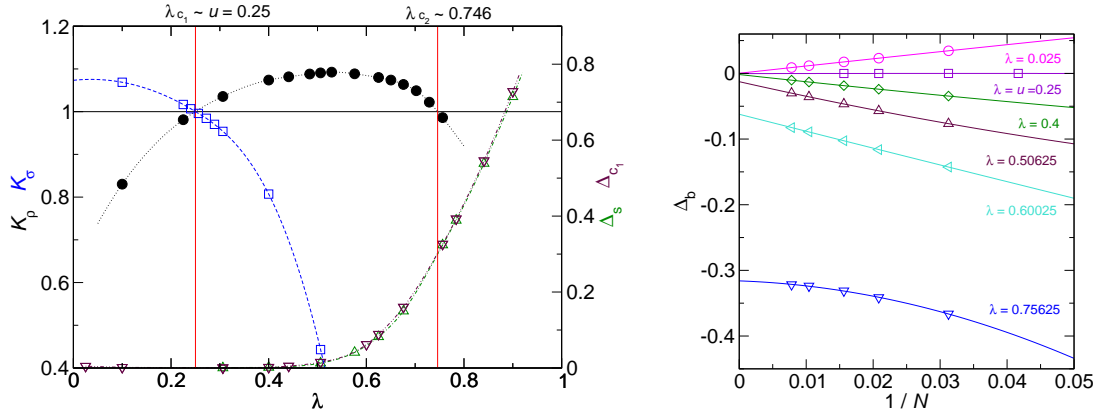


Figure 2. DMRG results for the half-filled HHM with $u = 0.25$ and $\omega_0 = 5$. Left panel: charge (K_ρ , filled circles) and spin (K_σ , open squares) TLL exponents as functions of λ [left-hand axis of ordinate]. Open triangles up (triangles down) give the spin (charge) gap Δ_s (Δ_{c_1}) [right-hand axis of ordinate]. Data shown are extrapolated values for the infinite systems, using open boundary conditions. Right panel: Finite-size scaling of the binding energy Δ_b for different λ ; lines are polynomial fits. In the numerical calculations we use up to five pseudo-sites and keep 2400 density-matrix eigenstates; then, for all parameters studied, the local boson density is less than 10^{-8} and the discarded weight is smaller than 10^{-9} .

and the binding energy Δ_b is also extremely small, or maybe even zero (see triangles up, right-hand panel of fig. 2). As λ increases, we obtain a (smooth) crossover to a metallic regime with a noticeable two-particle binding $\Delta_b < 0$ (region (II) in fig. 1), where $\Delta_{c_1} \sim \Delta_s$. This is in accord with the very recent findings of Ref. [7], where a subdivision of the metallic phase into a weakly renormalised TLL (I) and a bipolaronic liquid¹ (II) was suggested. In the latter phase, the two-particle excitation gap $\Delta_{c_2}(N) = E_0^{2+}(0) + E_0^{2-}(0) - 2E_0(0)$ was shown to scale to zero. In the CDW phase, which typifies a bipolaronic superlattice at large phonon frequencies, we have, besides $\Delta_s = \Delta_{c_1} > 0$, $\Delta_{c_2} > 0$ and $\Delta_b < 0$, whereas in the SDW state $\Delta_{c_2} > 0$ but $\Delta_b(N \rightarrow \infty) \rightarrow 0$. While the basic scenario discussed so far persists in the adiabatic regime, the metallic region shrinks as the phonon frequency ω_0 becomes smaller [5, 7]. Furthermore, the CDW state rather behaves as a normal Peierls insulator and consequently there is a weaker tendency towards bipolaron formation in the metallic state for small λ , and $u < u_m$.

Finally, let us investigate the behaviour of the momentum distribution function, $n_\sigma(k) = \frac{1}{N} \sum_{j,l=1}^N \cos(k(j-l)) \langle c_{j,\sigma}^\dagger c_{l,\sigma} \rangle$, $k = 2\pi m/N$, $m = 0, \dots, N/2$, which can be obtained by DMRG for a system with periodic boundary conditions.

Figure 3 shows the variation of $n(k)$ for weak (circles) and intermediate (stars) Hubbard interactions in the SDW (a), TLL (b)-(c), and CDW (d) phases. The momentum distribution is a monotonously decreasing function as k changes from the centre ($k = 0$) to the boundary of the Brillouin zone ($k = \pi$). Since we consider the weak-coupling regime, $n(k)$ is only weakly renormalised away from the Fermi momentum k_F . For a 1D TLL, instead of the Fermi liquid typical jump of $n(k)$ at k_F , one finds an essential power-law singularity [9], corresponding to a vanishing quasiparticle weight $Z = 0$. For finite TLL systems, the difference $\Delta = n(k_F - \delta) - n(k_F + \delta)$ is finite (with $\delta = \pi/N = \pi/66$ in our case), and rapidly decreases with increasing couplings λ , u . Approaching the insulating SDW/CDW states $n(k)$ becomes a smooth curve, i.e. the singularity vanishes and $\Delta \rightarrow 0$. At very large λ , the system develops a

¹ Note that the polaronic two-particle bound states are not necessarily small (i.e. on-site).

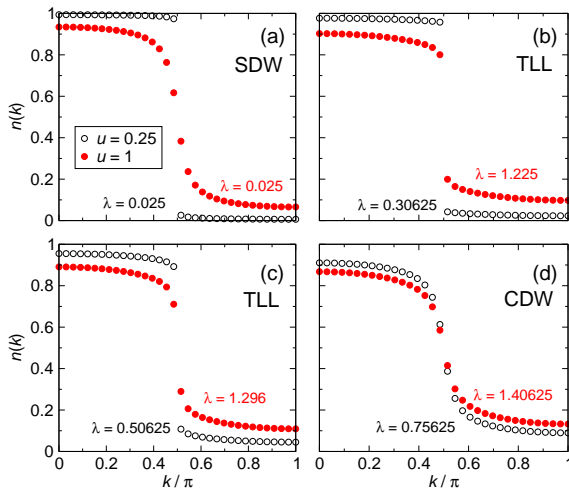


Figure 3. Momentum distribution of the half-filled HHM in the anti-adiabatic regime ($\omega_0 = 5$). Open (closed) circles give DMRG results at $u = 0.25$ ($u = 1$) for a system with $N = 66$ sites and periodic boundary conditions. The occupation of fermionic states carrying momentum k is given by $n(k) = \frac{1}{2} \sum_{\sigma} n_{\sigma}(k)$, and we have $k_F = \pi/2$, $n_{k_F} = 1/2$ for the half-filled band case. In the intermediate metallic phase, $n(k)$ exhibits a power-law singularity at k_F [see panels (b) and (c)]. At weak and strong electron-phonon couplings insulating SDW [panel (a)] and CDW [panel (d)] are realised, respectively.

“perfect” CDW with $n(k) = 1/2$ for all momenta k .

To summarise, we validated the existence of an intervening metallic phase in the SDW-CDW transition regime of the 1D half-filled Hubbard-Holstein model for $u < u_m$ by large-scale DMRG calculations. Spin and charge gaps open exponentially slowly at the SDW-TLL transition point, λ_{c1} , but no long-range order develops. $\lambda_{c1}(u, \omega_0)$ can be determined from the “1”-crossing of the spin and charge TLL parameters. In the TLL, the momentum distribution function exhibits a power-law singularity at k_F . As the electron-phonon coupling increases, a crossover to a bipolaronic metal, indicated by negative binding energy, takes place, before the systems enters the long-range ordered insulating CDW phase at a second critical coupling λ_{c2} . We would like to point out that fixing the metal-CDW phase boundary quantitatively is a difficult issue.

Acknowledgements. The authors would like to thank G. Hager and E. Jeckelmann for valuable discussions. This work was supported by KONWIHR Bavaria, and DFG through SFB 652.

References

- [1] Hirsch J E and Fradkin E 1983 *Phys. Rev. B* **27** 4302; Trapper U *et al.* 1994 *Z. Phys. B* **93** 465; Berger E, Valášek P and von der Linden W 1995 *Phys. Rev. B* **52** 4806; Koller W *et al.* 2004 *Europhys. Lett.* **66** 559; Tam K -M *et al.* 2007 *Phys. Rev. B* **75** 161103(R); Assaad F F and Lang T C 2007 *Phys. Rev. B* **76** 035116; Barone P *et al.* 2007 *Europhys. Lett.* **79** 47003
- [2] Tsuda N, Nasu K, Yanase A and Siratori K 1991 *Electronic Conduction in Oxides* (Berlin: Springer-Verlag); Bishop A R and Swanson B I 1993 *Los Alamos Sciences* **21** 133
- [3] Hotta T and Takada Y 1997 *Physica B* **230-232** 1037; Fehske H *et al.* 2003 *Eur. Phys. Jour. B* **31** 11; Fehske H *et al.* 2004 *Phys. Rev. B* **69** 165115; Hager G *et al.* 2004 *J. of Comp. Phys.* **194** 795-808
- [4] Takada Y and Chatterjee A 2003 *Phys. Rev. B* **67** 081102(R)
- [5] Clay R T and Hardikar R P 2005 *Phys. Rev. Lett.* **95** 096401; Hardikar R P and Clay R T 2007 *Phys. Rev. B* **75**, 245103
- [6] Tezuka M, Arita R and Aoki H 2005 *Phys. Rev. Lett.* **95** 226401; 2007 *Phys. Rev. B* **76** 155114
- [7] Fehske H, Hager G and Jeckelmann E 2008 *Europhys. Lett.* **84** 57001
- [8] White S R 1992 *Phys. Rev. Lett.* **69** 2863; Jeckelmann E and White S R 1998 *Phys. Rev. B* **57** 6376; Jeckelmann E and Fehske H 2007 *Rivista del Nuovo Cimento* **30** 259
- [9] Giamarchi T 2004 *Quantum Physics in One Dimension* (Oxford: Oxford University Press)
- [10] Ejima S, Gebhard F and Nishimoto S 2005 *Europhys. Lett.* **70** 492; Ejima S and Fehske H 2009 *Europhys. Lett.* **87** 27001
- [11] Nishimoto S, Sano K and Ohta Y 2008 *Phys. Rev. B* **77** 085119

Quantum Phase Transition in a 1D Transport Model with Boson-Affected Hopping: Luttinger Liquid versus Charge-Density-Wave Behavior

S. Ejima,¹ G. Hager,² and H. Fehske¹

¹*Institut für Physik, Ernst-Moritz-Arndt-Universität Greifswald, 17489 Greifswald, Germany*

²*Regionales Rechenzentrum Erlangen, Universität Erlangen-Nürnberg, 91058 Erlangen, Germany*

(Received 5 November 2008; published 10 March 2009)

We solve a very general two-channel fermion-boson model describing charge transport within some background medium by means of a refined pseudosite density-matrix renormalization group technique. Performing a careful finite-size scaling analysis, we determine the ground-state phase diagram and convincingly prove that the model exhibits a metal-insulator quantum phase transition for the half-filled band case. In order to characterize the metallic and insulating regimes we calculate, besides the local particle densities and fermion-boson correlation functions, the kinetic energy, the charge-structure factor, the Luttinger liquid charge exponent, and the single-particle excitation gap for a one-dimensional infinite system.

DOI: 10.1103/PhysRevLett.102.106404

PACS numbers: 71.10.Hf, 71.10.Fd, 71.30.+h

The proof of the existence of metal-insulator transitions (MITs) in generic model Hamiltonians is one of the most fundamental problems in solid state theory. While the mechanisms that can drive a MIT, such as band structure effects [1], disorder [2], Coulomb correlations [3], or the coupling to the lattice degrees of freedom [4], are accepted in general, there is only a very small number of microscopic models which have rigorously been shown to indeed exhibit such a transition. Examples are the three-dimensional (3D) Anderson tight-binding (disorder) model, for which an analytical proof of particle localization exists [5], or the 1D spinless fermion Holstein (electron-phonon) model, where the Tomonaga-Luttinger-liquid (TLL) charge-density-wave (CDW) MIT has been confirmed numerically by the density-matrix renormalization group (DMRG) [6]. Zero-temperature MITs triggered by Coulomb interaction are more difficult to assess; the prototype half-filled 1D Hubbard model, e.g., is insulating for all $U > 0$ [7], and only on introducing a (particular) long-range hopping does the MIT take place at finite interaction strength [8]. In the 1D half-filled extended Hubbard (U - V) model, there exists at most a metallic line at the bond-order-wave CDW insulator-insulator transition [9]. If Coulomb and electron-phonon interactions compete, an extended intervening metallic phase may occur between Mott and Peierls insulating states, which allows for a MIT. This has been demonstrated for the 1D Holstein-Hubbard model at half filling [10].

Quite recently a novel quantum transport Hamiltonian has been proposed [11] which describes regimes of quasi-free, correlation or fluctuation dominated transport. In a sense this model parametrizes the correlations inherent to a fermionic many-particle system, but also the couplings to phonon or bath degrees of freedom, by a “background medium” that controls the particle’s transport properties. Thus the model captures basic aspects of more complicated Hubbard or Holstein Hamiltonians. Then it is a legitimate

question to ask whether the interaction with the background may even drive a MIT.

Consider the Hamiltonian [11]

$$H = H_b - \lambda \sum_i (b_i^\dagger + b_i) + \omega_0 \sum_i b_i^\dagger b_i + \frac{N\lambda^2}{\omega_0}, \quad (1)$$

where $H_b = -t_b \sum_{\langle i,j \rangle} f_j^\dagger f_i (b_i^\dagger + b_j)$ describes a boson-affected nearest-neighbor hopping ($\propto t_b$) of spinless fermionic particles ($f_i^{(\dagger)}$). A fermion emits (or absorbs) a local boson b_j^\dagger (b_j) every time it hops between lattice sites i, j . This way the particle creates local distortions of certain energy in the background. In the case of an antiferromagnetic spin background the distortions correspond to local spin deviations (cf. the motion of a hole in the t - J model [12]). If the background medium is a deformable lattice, they are basically lattice fluctuations (phonons). Other situations such as doped CDWs or exciton transport in molecular aggregates might be envisaged. In any case the distortions of the background can be parametrized as bosons [11,13]. The distortions are able to relax (compare λ with J_\perp in the t - J model), which is described by the second term in (1). The third term gives the energy of the bosons; the constant energy shift $N\lambda^2/\omega_0$ guarantees finite energy for $N \rightarrow \infty$. Performing the unitary transformation $b_i \mapsto b_i + \lambda/\omega_0$ eliminates the boson relaxation term in favor of a second, free-fermion hopping channel, $H \rightarrow H = H_b + H_f + \omega_0 \sum_i b_i^\dagger b_i$, where $H_f = -t_f \sum_{\langle i,j \rangle} f_j^\dagger f_i$ with $t_f = 2\lambda t_b/\omega_0$. Hereafter we focus on the 1D half-filled band case, i.e., fermion number $N_f/N = 1/2$, and take $t_b = 1$ as the energy unit.

In our model (1), the particles have only a charge degree of freedom. Then, for a tight-binding band structure and in the absence of disorder, the formation of a CDW is the only possibility for a MIT. The CDW might be induced by strong correlations in the background, which exist for large

ω_0 because (i) coherent transport ($\propto t_f$) takes place on a strongly reduced energy scale only and (ii) incoherent transport is energetically costly [11]. Hence, in the limit $\omega_0 \gg 1$, an effective Hamiltonian with nearest-neighbor fermion repulsion results. By contrast, if the local distortions of the background relax readily (i.e., $\lambda \gg 1$) and/or the energy of the bosons is small (i.e., $\omega_0 \ll 1$), the free hopping channel can act efficiently against any correlation-induced charge ordering.

Evidence for a MIT comes from a very recent exact diagonalization (ED) study of (1): Through calculating the wave-vector-resolved photoemission and inverse photoemission spectra, the opening of a single-particle excitation gap has been observed at $K_F = \pm\pi/2$ as λ decreases at relatively large $\omega_0 = 2$ [14]. Of course, dealing with lattices of up to 16 sites, this does not unambiguously prove the existence of a true phase transition which may occur in the thermodynamic limit $N \rightarrow \infty$ only.

In this Letter, we carry out the first large-scale DMRG investigation of the two-channel transport model (1). In combination with a finite-size scaling analysis this allows us to map out the ground-state phase diagram for the 1D half-filled band case and to characterize the different phases involved. The DMRG is one of the most powerful and accurate numerical techniques for studying 1D fermionic many-body systems [15]. It can be easily generalized to treat systems including bosons. Within the pseudosite approach an exact mapping of a boson site, containing 2^{n_b} states, to n_b pseudosites is performed [16]. Here we take into account up to $n_b = 5$ pseudosites, so that the n_b th local boson density is always smaller than 10^{-8} . In addition, we keep $m = 1200$ to 2000 density-matrix eigenstates and extrapolate various quantities to the $m \rightarrow \infty$ limit. To test our DMRG implementation we compared data obtained for small systems with previous ED results [14] and got very good agreement: The relative error of the ground-state energy $|E_{ED} - E_{DMRG}|$ was always smaller than 10^{-7} (for all λ at $\omega_0 = 2$); the discarded weight was smaller than 5×10^{-8} .

As indicated by small cluster EDs [14], at $\omega_0 = 2.0$, where fermions and bosons are strongly correlated for small λ , a MIT might occur in the range of $0.01 < \lambda < 5$. This is confirmed by DMRG for much larger systems: Figs. 1(a) and 1(b), showing the variation of the local densities of fermions $\langle f_i^\dagger f_i \rangle$ and bosons $\langle b_i^\dagger b_i \rangle$, respectively, point towards the existence of a homogeneous state (CDW state) for rather large (small) λ . Using open boundary conditions (OBCs), the system is obviously not translation invariant; i.e., the local density is inhomogeneous in any case. In the CDW phase, there are two degenerate ground states. Within an OBC DMRG calculation, one of these ground states is picked out by initializing the DMRG algorithm, so that the CDW state is directly observable in the local density. In the metallic regime, on the other hand, the open boundaries reveal (strong) Friedel oscillations, which will be algebraically reduced, however, as we move to-

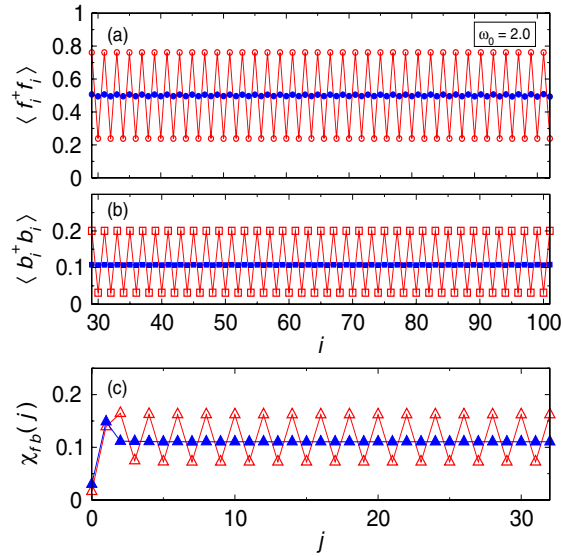


FIG. 1 (color online). Local densities of fermions $\langle f_i^\dagger f_i \rangle$ (a) and bosons $\langle b_i^\dagger b_i \rangle$ (b) for a 128-site system with OBCs. Open symbols are for $\lambda = 0.01$ (CDW regime); filled ones for $\lambda = 0.5$ (metallic regime). The fermion-boson correlation function $\chi_{fb}(j)$ is given in panel (c) for a 64-site system with APBCs [here the discarded weight is 1.4×10^{-10} (7.9×10^{-10}) for $\lambda = 0.01$ ($\lambda = 0.50$)]. In all cases $\omega_0 = 2.0$.

wards the interior. Thus for large enough system sizes, within the central part of the chain, the local density becomes constant [see filled symbols in Figs. 1(a) and 1(b)] [17].

The CDW structure of the insulating state shows up also in the fermion-boson correlation function

$$\chi_{fb}(j) = \frac{1}{N_f} \sum_i \langle f_i^\dagger f_i b_{i+j}^\dagger b_{i+j} \rangle. \quad (2)$$

Calculating $\chi_{fb}(j)$ at $\omega_0 = 2.0$ for $N = 64$ with antiperiodic boundary conditions (APBCs) [18], we find a distinctive alternation for $\lambda = 0.01$ and a constant value away from the “central site” for $\lambda = 0.50$, which again supports the MIT scenario [see Fig. 1(c)]. Note that in the latter case there is still a large boson density at the particle’s nearest-neighbor site, locally enhancing the mobility of the carrier.

Whether the pronounced CDW correlations observed for small λ and large ω_0 are signatures of true long-range order remains an open issue yet. To answer this question, we explore the static charge-structure factor,

$$S_c(q) = \frac{1}{N} \sum_{j,k} e^{iq(j-k)} \left\langle \left(f_j^\dagger f_j - \frac{1}{2} \right) \left(f_k^\dagger f_k - \frac{1}{2} \right) \right\rangle, \quad (3)$$

where $0 \leq q < 2\pi$. If $S_c(\pi)/N$ stays finite in the thermodynamic limit, CDW long-range order exists. Figure 2(a) demonstrates that this is the case for $\lambda = 0.01$, i.e., when the distortions of the background relax poorly. By contrast, $\lim_{N \rightarrow \infty} S(\pi)/N = 0$ for $\lambda = 0.5$. This means the model (1) undergoes a quantum phase transition from a metal to

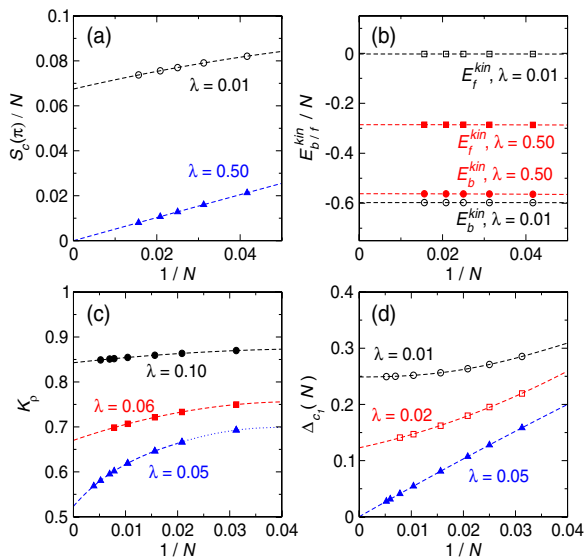


FIG. 2 (color online). Finite-size scaling of several physical quantities: (a) static charge-structure factor $S_c(q)$ at $q = \pi$, (b) kinetic energy parts $E_{b/f}^{\text{kin}}$, (c) Luttinger liquid parameter K_ρ , and (d) single-particle excitation gap Δ_{c_1} . Data obtained for $\omega_0 = 2$ with APBCs [(a), (b)] and OBCs [(c), (d)] applied.

an insulator as the relaxation parameter λ decreases at fixed ω_0 .

Next we investigate the relative importance of the different transport mechanisms by calculating the kinetic energy parts

$$E_{b/f}^{\text{kin}} = \langle \psi_0 | H_{b/f} | \psi_0 \rangle \quad (4)$$

($|\psi_0\rangle$ denotes the ground state). Figure 2(b) shows that E_f^{kin} tends to zero at small λ , indicating the suppression of the coherent transport channel. Note that boson-assisted transport is possible for both small and large λ [E_b^{kin} stays close to -0.6 ; see panel (b)], and even becomes more pronounced in the CDW phase.

Finally we determine the TLL charge exponent K_ρ and the single-particle excitation gap Δ_{c_1} [which, for the model (1), equals the charge gap]. K_ρ is proportional to the slope of the charge-structure factor in the long-wavelength limit $q \rightarrow 0^+$ [19]:

$$K_\rho = \pi \lim_{q \rightarrow 0} \frac{S_c(q)}{q}, \quad q = \frac{2\pi}{N}, \quad N \rightarrow \infty. \quad (5)$$

From this relation we can calculate K_ρ quite accurately using DMRG techniques. As is well-known the 1D spinless fermion model with the nearest-neighbor Coulomb interaction V at half filling can be mapped onto the exactly solvable XXZ model. There the TLL charge exponent decreases from $K_\rho = 1$, as V is enhanced, and finally reaches $1/2$ at the MIT point [20]. We expect that this holds also for the 1D spinless fermion transport model (1) at half band filling, even though there are only a few

analytical or numerical results referring to this for coupled fermion-boson systems [for the (Hubbard-)Holstein model see [6,10]]. The single-particle (charge) gap can be obtained from

$$\Delta_{c_1}(N) = E(N_f + 1) + E(N_f - 1) - 2E(N_f), \quad (6)$$

where $E(N_f)$ and $E(N_f \pm 1)$ are the ground-state energies in the N_f - and $(N_f \pm 1)$ -particle sectors, respectively, with $N_f = N/2$. Figures 2(c) and 2(d) illustrate the finite-size scaling analysis for the TLL parameter (c) and the charge gap (d) at $\omega_0 = 2.0$. Both physical quantities can be extrapolated by performing a least-squares fit to a second-order polynomial in $1/N$. Note that close to the MIT points we need larger system sizes, because a strong finite-size dependence evolves. In this regime, we use chains from $N = 32$ to 256 sites and higher order polynomial functions (up to fourth order) to extrapolate the data. In doing so, we determine the nonuniversal exponents $K_\rho(\lambda) > 0.5$ in the metallic TLL phase where $\Delta_{c_1} = 0$, and the finite charge gap $\Delta_{c_1} > 0$ in the CDW phase [see panels (c) and (d)].

In Fig. 3 we display the extrapolated values of the TLL exponent and the charge gap as a function of λ at fixed $\omega_0 = 2.0$. Lowering λ , K_ρ decreases from $1 \rightarrow 1/2$. The point where $K_\rho = 1/2$ is reached marks the critical coupling for the MIT [$\lambda_c^{-1}(\omega_0 = 2) \sim 20.4$]. From the extrapolated DMRG data it seems that the charge gap opens exponentially on entering the insulating phase and afterwards rises almost linearly. This result is similar to what is observed for the TLL-CDW transition in the anti-adiabatic strong-coupling limit of the spinless fermion Holstein model, which there possesses XXZ-model physics (i.e., a Kosterlitz-Thouless transition at the spin isotropy point). But note that we find a repulsive particle interaction ($K_\rho \leq 1$) in the metallic phase for small boson frequencies as well; i.e., there is no indication for a pairing instability in the half-filled band case.

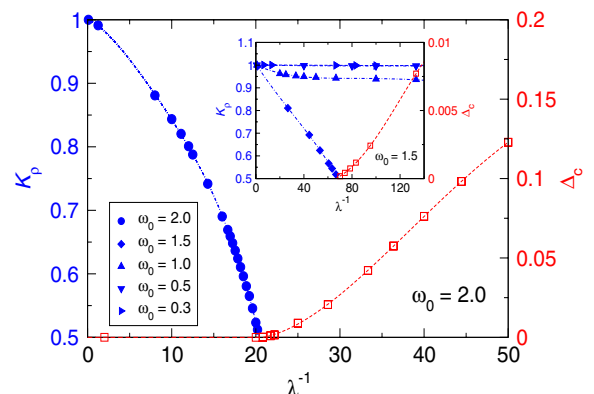


FIG. 3 (color online). Single-particle gap Δ_{c_1} (open squares) and TLL parameter K_ρ as a function of λ^{-1} for $\omega_0 = 2.0$ (main panel). The inset displays results for smaller ω_0 and shows that (i) no CDW state is found for $\omega_0 < \omega_c$ and (ii) $K_\rho < 1$ for all ω_0 , where $K_\rho \rightarrow 1$ as $\omega_0 \rightarrow 0$ and/or $\lambda^{-1} \rightarrow 0$.

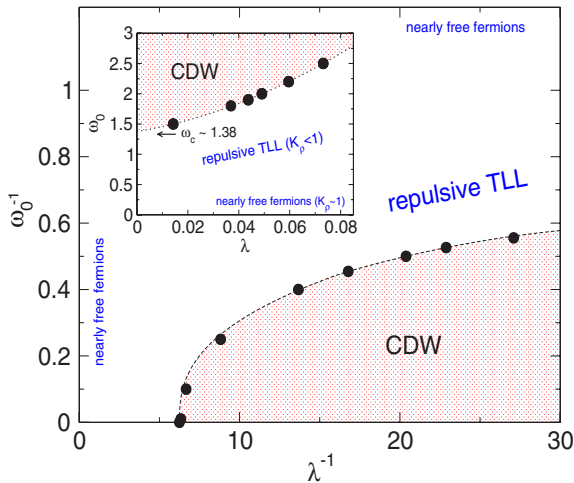


FIG. 4 (color online). DMRG phase diagram of the two-channel transport model (1) for the 1D half-filled band case (the dashed line is a guide to the eye). The inset gives the phase diagram in the λ - ω_0 plane. The MIT point for $\lambda = 0$, $\omega_0(0) \sim 1.38$, is obtained from a quadratic fit (dotted line).

Figure 4 represents the main result of our work: the ground-state phase diagram of the 1D half-filled fermion-boson model (1) in the λ^{-1} - ω_0^{-1} plane. Obviously the phase space is divided into two regimes, the metallic TLL phase and the insulating CDW phase with long-range order. We first discuss the limit of large ω_0 . In this regime background fluctuations, which are intimately connected with any particle hop, are energetically costly. As a result the itinerancy of the particles is suppressed to a large extent, and charge ordering becomes favorable. Nevertheless, we find a metallic state even for $\omega_0 = \infty$, provided that $\lambda^{-1} < \lambda_c^{-1}$ ($\omega_0 = \infty$) (numerically we proved the TLL to exist for $\lambda^{-1} < \lambda_c^{-1} \approx 6.3$ at $\omega_0 = 1000$). In this case the system's ability for relaxation ($\propto \lambda$) is strong enough to prevent long-range charge order. This is reminiscent of the existence of a finite critical coupling strength g_c ($g^2 = \varepsilon_p/\omega_0$) in the antiadiabatic limit ($\omega_0 \rightarrow \infty$) of the spinless fermion Holstein model, where the TLL phase is realized for $g < g_c(\omega)$ [6]. In contrast to the TLL-CDW transition in the Holstein model, however, the symmetry-broken CDW state is a few-boson state [14] (i.e., not a Peierls phase with many phonons involved). In the opposite limit of small ω_0 , the background medium is easily disturbed by particle motion. Therefore the rate of bosonic fluctuations ($\propto \omega_0^{-1}$) is high. Now we enter the fluctuation dominated regime [11], and consequently CDW order is suppressed. The inset of Fig. 4 shows that even for $\lambda = 0$, i.e., if the explicit λ -relaxation channel is closed, a metallic state may exist below a finite critical energy $\omega_0(0)$.

To conclude, using an unbiased numerical (DMRG) technique, we proved that the very general fermion-boson transport model (1) displays a correlation-induced metal-insulator transition at half filling in 1D. The metallic phase typifies a repulsive Luttinger liquid, while the insulating

phase shows CDW long-range order. The phase boundary between these states is nontrivial. It would be highly desirable to verify the numerical results of this Letter by an analytical (field theoretical or algebraic) approach.

The authors would like to thank A. Alvermann, D. M. Edwards, E. Jeckelmann, S. Nishimoto, and G. Wellein for valuable discussions. This work was supported by DFG through SFB 652, and the KONWIHR project HQS@HPC. S. E. acknowledges funding by Ministerium für Bildung, Wissenschaft und Kultur Mecklenburg-Vorpommern, Grant No. 0770/461.01.

- [1] F. Bloch, Z. Phys. **57**, 545 (1929); A. H. Wilson, Proc. R. Soc. A **133**, 458 (1931).
- [2] P. W. Anderson, Phys. Rev. **109**, 1492 (1958).
- [3] N. F. Mott, *Metal-Insulator Transitions* (Taylor & Francis, London, 1990); F. Gebhard, *The Mott Metal-Insulator Transition*, Springer Tracts in Modern Physics Vol. 137 (Springer, New York, 1997).
- [4] R. Peierls, *Quantum Theory of Solids* (Oxford University Press, Oxford, 1955).
- [5] J. Fröhlich, F. Martinelli, E. Scoppola, and T. Spencer, Commun. Math. Phys. **101**, 21 (1985).
- [6] R. J. Bursill, R. H. McKenzie, and C. J. Hamer, Phys. Rev. Lett. **80**, 5607 (1998); M. Hohenadler, G. Wellein, A. R. Bishop, A. Alvermann, and H. Fehske, Phys. Rev. B **73**, 245120 (2006).
- [7] F. H. L. Essler, H. Frahm, F. Göhmann, A. Klümper, and V. E. Korepin, *The One-Dimensional Hubbard Model* (Cambridge University Press, Cambridge, 2005).
- [8] F. Gebhard and A. E. Ruckenstein, Phys. Rev. Lett. **68**, 244 (1992).
- [9] S. Ejima and S. Nishimoto, Phys. Rev. Lett. **99**, 216403 (2007).
- [10] M. Tezuka, R. Arita, and H. Aoki, Phys. Rev. Lett. **95**, 226401 (2005); R. T. Clay and R. P. Hardikar, Phys. Rev. Lett. **95**, 096401 (2005); H. Fehske, G. Hager, and E. Jeckelmann, Europhys. Lett. **84**, 57001 (2008).
- [11] D. M. Edwards, Physica B (Amsterdam) **378-380**, 133 (2006); A. Alvermann, D. M. Edwards, and H. Fehske, Phys. Rev. Lett. **98**, 056602 (2007).
- [12] S. A. Trugman, Phys. Rev. B **37**, 1597 (1988).
- [13] G. Martinez and P. Horsch, Phys. Rev. B **44**, 317 (1991).
- [14] G. Wellein, H. Fehske, A. Alvermann, and D. M. Edwards, Phys. Rev. Lett. **101**, 136402 (2008).
- [15] S. R. White, Phys. Rev. Lett. **69**, 2863 (1992).
- [16] E. Jeckelmann and S. R. White, Phys. Rev. B **57**, 6376 (1998); E. Jeckelmann and H. Fehske, Riv. Nuovo Cimento **30**, 259 (2007).
- [17] The use of smooth boundary conditions opens another possibility to reduce oscillatory finite-size effects; see M. Vekić and S. R. White, Phys. Rev. Lett. **71**, 4283 (1993).
- [18] Note that APBCs give the lowest energy for our spinless fermion model with $N_f = 4n$ particles and $2N_f$ sites.
- [19] M. Dzierzawa, in *The Hubbard Model*, edited by D. Baeriswyl *et al.*, NATO Advanced Study Institutes, Ser. B Vol. 343 (Plenum, New York, 1995).
- [20] S. Ejima, F. Gebhard, and S. Nishimoto, Europhys. Lett. **70**, 492 (2005).

Metal-insulator transition in the Edwards model

H. Fehske¹, S. Ejima¹, G. Wellein² and A. R. Bishop³

¹Institut für Physik, Ernst-Moritz-Arndt-Universität Greifswald, 17489 Greifswald, Germany

²RRZE, Friedrich-Alexander-Universität Erlangen-Nürnberg, 91058 Erlangen, Germany

³Los Alamos National Laboratory, Los Alamos, New Mexico 87545, U.S.

E-mail: <fehsk, ejima>@physik.uni-greifswald.de

Abstract. To understand how charge transport is affected by a background medium and vice versa we study a two-channel transport model which captures this interplay via a novel, effective fermion-boson coupling. By means of (dynamical) DMRG we prove that this model exhibits a metal-insulator transition at half-filling, where the metal typifies a repulsive Luttinger liquid and the insulator constitutes a charge density wave. The quantum phase transition point is determined consistently from the calculated photoemission spectra, the scaling of the Luttinger liquid exponent, the charge excitation gap, and the entanglement entropy.

The way a system evolves from a metallic to an insulating state is one of the most fundamental problems in solid state theory. Electron-electron and electron-phonon interactions are the driving forces behind metal-insulator transitions (MITs) in the majority of cases. For example, the Mott-Hubbard MIT [1] is caused by strong Coulomb correlations, whereas the Peierls MIT [2] is triggered by the coupling to vibrational excitations of the crystal. Theoretically the MIT problem can be addressed by the investigation of generic Hamiltonians for interacting electrons and phonons such as Hubbard or Holstein models [3]. In one dimension (1D), these models exhibit a MIT at half-filling, where on the insulating side of the MIT a spin-density-wave (SDW) or a charge-density-wave (CDW) broken-symmetry ground state appears, respectively. On the metallic side, near the MIT, charge transport then takes place within a strongly correlated “background” that anticipates the developing SDW, respectively CDW, order. Since the particles responsible for charge transport and the background order phenomena are the same, the problem is very complex.

A path forward might be the construction of simplified transport models, which capture the basic mechanisms of quantum transport in a background medium in a rather effective way. Along this line a novel quantum transport model has been proposed recently [4],

$$\mathcal{H} = -t_b \sum_{\langle i,j \rangle} f_j^\dagger f_i (b_i^\dagger + b_j) - \lambda \sum_i (b_i^\dagger + b_i) + \omega_0 \sum_i b_i^\dagger b_i. \quad (1)$$

This so-called Edwards model mimics the correlations inherent to a spinfull fermionic many-particle systems by a boson affected hopping of spinless particles (see Fig. 1). For the half-filled band case, the model describes a repulsive Tomonaga-Luttinger liquid (TLL), provided the excitations of the background are energetically inexpensive ($\omega_0 < \omega_{0,c}$) or will readily relax ($\lambda > \lambda_c(\omega_0)$). This defines the fluctuation dominated regime. By contrast, strong background correlations, which will develop for large ω_0 and small $\lambda \ll t_b$ tend to immobilize the charge carriers and may even drive a MIT by establishing CDW long-range order [5].

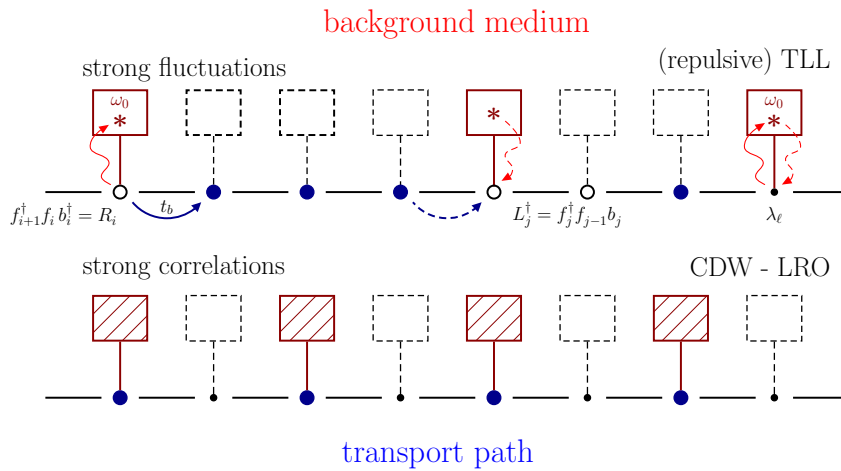


Figure 1. The Edwards model (1) describes a very general situation: As a charge carrier (\bullet) moves along a 1D transport path it creates an excitation with energy ω_0 ($*$) in the background at the site it leaves or annihilates an existing excitation at the site it enters. The background medium may represent, e.g., a magnetically, orbitally or charge ordered lattice. One assumes that the (de)excitation of the background can be parameterized as a bosonic degree of freedom. Any distortion of the background can heal by quantum fluctuations. Accordingly the λ -term allows for spontaneous boson creation and annihilation processes.

In the present work, we employ density-matrix renormalization group (DMRG) and dynamical DMRG methods [6] to analyse the ground-state properties of the Edwards model and the charge carrier dynamics for the limiting case of high-energy background fluctuations.

Let us start with the discussion of the photoemission (PE) spectra. The single-particle spectral function probed by angle-resolved [inverse] PE reads

$$A(k, \omega) = A^-(k, \omega) + A^+(k, \omega), \quad \text{with} \quad A^\pm(k, \omega) = \sum_n |\langle \psi_n^\pm | f_k^\pm | \psi_0 \rangle|^2 \delta[\omega \mp \omega_n^\pm]. \quad (2)$$

Here $A^-(k, \omega)$ [$A^+(k, \omega)$] is associated with the emission [injection] of an electron with wave vector k , i.e. $f_k^- = f_k$ and $f_k^+ = f_k^\dagger$. $|\psi_0\rangle$ is the ground state of a N -site system in the N_f -particle sector, while $|\psi_n^\pm\rangle$ denote the n -th excited states in the $N_f \pm 1$ -particle sectors with excitation energies $\omega_n^\pm = E_n^\pm - E_0$. For the half-filled Edwards model we have $N_f = N/2$.

Figure 2 shows $A(k, \omega)$ for a stiff background, i.e. the distortions induced by particle hopping are energetically costly. In this regime the bosons will strongly affect particle transport: The quasiparticle mass is sizeably enhanced and a renormalized band structure appears but—if λ is large enough—the system remains metallic, as can be seen from the finite spectral weight at the Fermi energy E_F (left panel). As the system's ability for relaxation decreases, i.e., at fixed ω_0 , λ falls below a certain critical value, a gap opens in the single-particle spectrum at $k_F = \pi/2$ (middle panel). Evidently the system has become an insulator. We note the internal feedback mechanism: The collective boson excitations originate from the motion of the charge carriers and have to persist long enough to finally inhibit particle transport, thereby completely changing the nature of the many-particle ground state. The collective boson-particle dynamics leads to an asymmetric band structure for $k \leq k_F$ and $k \geq k_F$ (see inset). While the induced hole probed by PE can only move coherently by a six-step process with three bosons first excited and afterwards consumed, an additional electron can easily move by a two-step process even if strong CDW correlations exist in the background [5]. We note that the (I)PE spectra exhibit weak

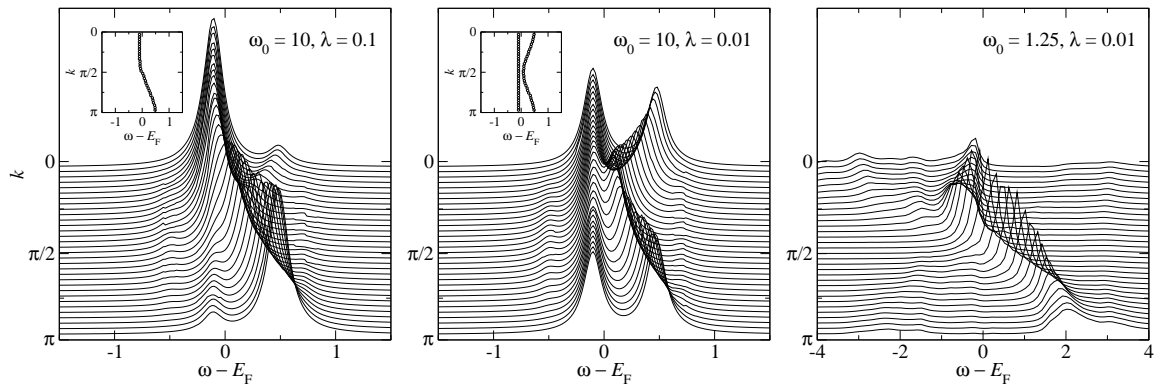


Figure 2. Line-shape of the single-particle spectral $A(k, \omega)$ in the half-filled band sector of the 1D Edwards model. The insets show the dispersion of the absorption/emission maximum. For the numerics, we consider an $N = 32$ -site chain with open boundary conditions (BC) and map a boson site, containing 2^{n_b} states, to n_b pseudosites. We take up to 4 pseudosites, keep $m = 500$ density-matrix eigenstates, and use a broadening $\eta = 0.1$. All energies are given in units of t_b .

signals around the bare boson energies $\pm\omega_0$ (not shown). The interrelation of charge dynamics and background fluctuation becomes apparent again, if we decrease ω_0 keeping λ fixed (right panel). Now the fluctuations overcome the correlations and the system returns to a metallic state which is different in nature, however, from the state we started with: $A(k, \omega)$ shows sharp absorption features near k_F only and is “overdamped” at the Brillouin zone boundaries, where the spectrum is dominated by bosonic excitations.

In order to determine more precisely the phase boundary between the metallic and insulating ground states, typifying a Tomonaga-Luttinger liquid (TLL) and a CDW, respectively, we analyse the limiting ($N \rightarrow \infty$) behaviour of the TLL charge exponent

$$K_\rho = \pi \lim_{q \rightarrow 0} \frac{S_c(q)}{q}, \quad \text{with} \quad S_c(q) = \frac{1}{N} \sum_{i,j} e^{iq(j-k)} \langle (n_j - \frac{1}{2})(n_k - \frac{1}{2}) \rangle, \quad q = \frac{2\pi}{N}, \quad (3)$$

as well as those of the single-particle (charge) gap, $\Delta_c(N) = E_0^+ + E_0^- - 2E_0$, and monitor the finite-size scaling of the entanglement entropy difference [7]

$$\Delta S_N = S_N(N/2) - S_N(N/2 - 1) = -\frac{c^*}{3} \ln \cos \left[\frac{\pi}{N} \right], \quad (4)$$

where $S_N(l) = -\text{Tr}[\rho_l \ln \rho_l] = \frac{c^*}{3} \ln \left[\frac{N}{\pi} \sin \left(\frac{\pi l}{N} \right) \right] + s_1$. We expect that the TLL charge exponent decreases from $K_\rho = 1$, as λ is lowered, and finally reaches $1/2$ at the MIT point, if the transition is of Kosterlitz-Thouless type [8, 9]. The central charge c^* should scale to unity in the metallic TLL regime [10].

Figure 3 demonstrates that the $N \rightarrow \infty$ extrapolated K_ρ indeed becomes $1/2$ at some critical value, where $\lambda_c^{-1}(\omega_0 = 10) \simeq 5.89$, indicating the MIT. In the metallic phase we find a repulsive particle interaction, $K_\rho \leq 1$. Our DMRG results point towards an exponential opening of the charge gap entering the insulating state, which corroborates the Kosterlitz-Thouless transition scenario. Note that the CDW state of the Edwards model is a few boson state, in contrast to the Peierls CDW phase of the Holstein model [5]. That means the MIT in the Edwards model is driven by strong correlations, as for the Mott-Hubbard transition. To extract the central charge c^* we use the entanglement entropy difference, Eq. (4), rather than directly exploiting $S_N(l)$.

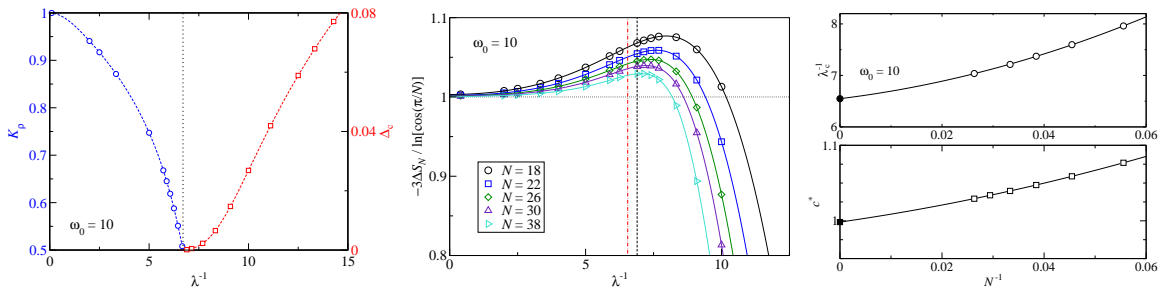


Figure 3. Left panel: $N \rightarrow \infty$ extrapolated value of the TLL parameter K_ρ , respectively of the charge gap Δ_c , as a function of λ^{-1} for $\omega_0 = 10$ (open BC). Middle panel: Entanglement entropy differences ΔS_N for different system sizes (periodic BC). The red dashed-dotted line gives the MIT transition point in reasonable agreement with the value obtained from K_ρ (black dashed line). Right panels: Critical value of λ_c^{-1} (filled circle, top panel) and central charge $c^* \simeq 1$ (filled square, bottom panel), both extrapolated from the maxima of ΔS_N . Here we use $m = 2000$, $n_b = 2$, and ensure a discarded weight less than 10^{-10} .

For a model with spinless fermions this is advantageous because we can work with a fixed system size, thereby avoiding antiperiodic BC that give rise to complex phase factors [7]. As can be seen from the middle panel of Fig. 3, for $\lambda^{-1} < \lambda_c^{-1}$, the rescaled quantity $-3\Delta S_N / \ln[\cos(\pi/N)]$ extrapolates to unity as $N \rightarrow \infty$. This opens an alternative route to detect the MIT point. We find that the $\lambda_c^{-1}(\omega_0)$ determined by extrapolating the maximum of ΔS_N , i.e. in a completely different manner, matches the critical value obtained from K_ρ surprisingly well. Simultaneously, indeed $c^* \rightarrow 1$ (see right panel).

To summarise, we have studied the spectral and ground-state properties of the 1D Edwards fermion-boson transport model by large-scale (dynamical) DMRG numerics. We showed that strong correlations within the background medium will not only affect the charge-carrier's dynamics by enhancing the quasiparticle mass but may even trigger a metal-insulator quantum phase transition. The MIT transition point has been determined in good agreement both from the TLL charge exponent and the entanglement entropy difference. We stress that to date only a very small number of microscopic model exists which have been rigorously shown to exhibit a MIT.

Acknowledgements. The authors would like to thank A. Alvermann, D. M. Edwards, G. Hager and S. Nishimoto for valuable discussions, and the RRZE for providing computer resources. This work is supported by DFG SFB 652 and, at Los Alamos, by CINT and the USDoE.

References

- [1] Mott N F 1990 *Metal-Insulator Transitions* (London: Taylor & Francis)
- [2] Peierls R 1955 *Quantum theory of solids* (Oxford: Oxford University Press)
- [3] Hubbard J 1963 *Proc. Roy. Soc. London, Ser. A* **276** 238; Holstein T 1959 *Ann. Phys. (N.Y.)* **8** 325
- [4] Edwards D M 2006 *Physica B* **378-380** 133; Alvermann A, Edwards D M and Fehske H 2007 *Phys. Rev. Lett.* **98** 056602
- [5] Wellein G, Fehske H, Alvermann A and Edwards D M 2008 *Phys. Rev. Lett.* **101** 136402; Ejima S, Hager G and Fehske H 2009 *Phys. Rev. Lett.* **102** 106404; Ejima S and Fehske H 2009 *Phys. Rev. B* **80** 155101
- [6] White S R 1992 *Phys. Rev. Lett.* **69** 2863; Jeckelmann E 2002 *Phys. Rev. B* **66** 045114
- [7] Nishimoto S 2011, private communication
- [8] Kosterlitz J M and Thouless D J 1973 *J. Phys. C* **6** 1181
- [9] Bursill R J, McKenzie R H and Murray D W 1998 *Phys. Rev. Lett.* **80** 5607; Ejima S, Gebhard F and Nishimoto S *EPL* **70** 492; Ejima S and Fehske H 2009 *EPL* **87** 27001
- [10] Calabrese P and Cardy J 2004 *J. Stat. Mech.* P06002; Laflorencie N, Sørensen E S, Chang M S and Affleck I 2006 *Phys. Rev. Lett.* **96** 100603

One-dimensional quantum transport affected by a background medium: Fluctuations versus correlations

S. Ejima and H. Fehske

Institut für Physik, Ernst-Moritz-Arndt-Universität Greifswald, 17489 Greifswald, Germany

(Received 17 July 2009; revised manuscript received 31 August 2009; published 1 October 2009)

We analyze the spectral properties of a very general two-channel fermion-boson transport model in the insulating and metallic regimes and the signatures of the metal-insulator quantum phase transition in between. To this end we determine the single-particle spectral function related to angle-resolved photoemission spectroscopy, the momentum distribution function, the Drude weight, and the optical response by means of a dynamical (pseudosite) density-matrix renormalization group technique for the one-dimensional half-filled band case. We show how the interplay of correlations and fluctuations in the background medium controls the charge dynamics of the system, which is a fundamental problem in a great variety of advanced materials.

DOI: [10.1103/PhysRevB.80.155101](https://doi.org/10.1103/PhysRevB.80.155101)

PACS number(s): 71.10.Fd, 71.30.+h, 71.10.Hf

I. INTRODUCTION

Charge transport normally takes place in some background medium. To understand how the environment affects the moving carrier and vice versa is a difficult question and in this generality at present perhaps one of the most heavily debated issues in condensed matter physics. Here the term “background” describes a variety of situations. We can think of the motion of a hole through an ordered insulator.¹ Examples are the high- T_c cuprates and the colossal magnetoresistive manganates, with a background of spins and orbitals, respectively, forming a pattern of alternating order. Then, as the hole moves, it disrupts the order of the background, which on its part hinders the particle transfer. Nevertheless coherent particle transport may occur but on a strongly renormalized energy scale. The new quasiparticles formed in the cuprates and manganates are spin or orbital polarons.^{2–4} Another situation concerns a charge carrier coupled to a deformable background. Here, if the interaction with phonons is strong, the particle has to carry a phonon cloud through the medium. The outcome might be a “self-trapped” small lattice polaron.⁵ In this case hopping transport, accompanied by phonon emission and absorption processes, evolves as the dominant transport channel.

So far we have considered a single particle only. It is quite obvious that the problem becomes even more involved if the particle density increases. Then the interrelation between charge carriers and background medium may drive quantum phase transitions. The appearance of ferromagnetism in the three-dimensional manganates, superconductivity in the quasi-two-dimensional (2D) cuprates, or charge-density-wave (CDW) states in one-dimensional (1D) halogen-bridged transition-metal complexes are prominent examples.⁶ In the theoretical description of these strongly correlated systems an additional difficulty arises: the particles which are responsible for charge transport and the order phenomena of the background are the same. As a consequence, on a microscopic level, rather involved many-particle models result, which incorporate the coupling between charge, spin, orbital, and lattice degrees of freedom.^{4,7} Naturally this prevents an exact solution of the problem even in reduced dimensions.

II. MODEL AND METHOD

A way out might be the construction of simplified transport models, which capture the basic mechanisms of quantum transport in a background medium in an effective way. Along this line a quantum transport model has been proposed recently^{8,9}

$$H = -t_b \sum_{\langle i,j \rangle} f_j^\dagger f_i (b_i^\dagger + b_j) - \lambda \sum_i (b_i^\dagger + b_i) + \omega_0 \sum_i b_i^\dagger b_i, \quad (1)$$

which mimics the correlations inherent to a spinful fermionic many-particle system by a boson-affected hopping of spinless particles $\propto t_b$ (see Fig. 1). In the model (1), a fermion $f_i^{(\dagger)}$ creates (or absorbs) a local boson $b_i^{(\dagger)}$ every time it hops, which corresponds to a local excitation in the background with a certain energy ω_0 . Because of quantum fluctuations the distortions are able to relax $\propto \lambda$. A unitary transformation $b_i \rightarrow b_i + \lambda / \omega_0$ replaces this term by second transport channel $H_f = -t_f \sum_{\langle i,j \rangle} f_j^\dagger f_i$, describing unaffected fermionic transfer, however with a renormalized amplitude $t_f = 2\lambda t_b / \omega_0$. It has been shown⁹ that coherent propagation of a fermion is possible even in the limit $\lambda = t_f = 0$ by means of a six-step vacuum-restoring hopping process

$$R_i^{(6)} = L_{i+2}^\dagger L_{i+1}^\dagger R_i^\dagger L_{i+2} R_{i+1} R_i, \quad (2)$$

where $R_i^\dagger = f_i^\dagger f_{i+1} b_i$ and $L_i^\dagger = f_i^\dagger f_{i-1} b_i$. Note that $R_i^{(6)}$ acts as direct next-nearest-neighbor (NNN) transfer “ $f_{i+2}^\dagger f_i$,” in complete analogy to the “Trugman path” of a hole in a 2D Néel-ordered spin background.¹⁰

The model (1) has been solved in the single-particle sector ($N_e = 1$) by exact diagonalization,⁹ using a basis construction for the fermion-boson (many-particle) Hilbert space that is variational for an infinite lattice ($N = \infty$).¹¹ The transport behavior was found to be surprisingly complex, reflecting the properties of both spin and lattice polarons in t - J - and Holstein-type models.

For the 1D half-filled band sector ($N_e = N/2$), evidence for a metal insulator transition comes from small cluster diagonalizations.¹² Quite recently the ground-state phase diagram of the model (1) has been mapped out in the whole $\lambda - \omega_0$ plane,¹³ using a density-matrix renormalization group (DMRG) technique.¹⁴ A quantum phase transition between a

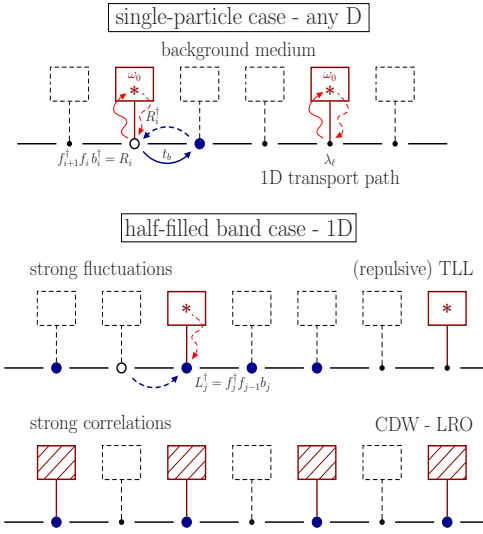


FIG. 1. (Color online) Schematic of quantum transport in a background medium. The background could represent a magnetically, orbitally, or charge ordered lattice but also a heat bath or certain chemical side groups. Then the proposed transport model (1) describes a very general situation: as a charge carrier (●) moves along a 1D transport path it creates an excitation with energy ω_0 (*) in the background medium at the site it leaves or annihilates an existing excitation at the site it enters. It is a plausible assumption that the (de)excitation of the background can be parameterized as a bosonic degree of freedom. In the case of spin deviations, orbital fluctuations, or lattice vibrations, the bosons might be viewed as a Schwinger-bosons, orbitons or phonons. Of course, any distortion of the background can heal out by quantum fluctuations. Accordingly the λ term allows for spontaneous boson creation and annihilation processes. The upper panel displays the single-particle case. Depending on the model parameters quasifree, diffusive, or boson-assisted transport takes place (Ref. 9). The latter case corresponds, e.g., to the motion of a hole through an ordered antiferromagnetic insulator. The lower panel shows the half-filled band case. Here, for spinless fermions in 1D, a repulsive Tomonaga-Luttinger liquid evolves, provided the excitations of the background are energetically inexpensive ($\omega_0 < \omega_{0,c}$) or will readily relax [$\lambda > \lambda_c(\omega_0)$]. This defines the fluctuation dominated regime. By contrast, strong background correlations, which develop for large ω_0 and small $\lambda \ll t_b$ tend to immobilize the charge carriers and even may drive a metal-insulator transition by establishing CDW long-range order (Refs. 12 and 13).

Tomonaga-Luttinger liquid (TLL) and CDW was proven to exist. A complementary study of the dynamical properties of the system is therefore desirable.

In the present work, we employ the dynamical DMRG (DDMRG) method¹⁵ in order to investigate the effects of background fluctuations and correlations on the dynamics of charge carriers in the framework of the 1D half-filled fermion-boson model (1). Thereby the focus is on the wave-vector resolves single-particle spectral function probed by angle-resolved photoemission spectroscopy (ARPES) and on the optical conductivity probed, e.g., by reflectivity measurements.

In general the dynamic response of a quantum system described by a time-independent Hamiltonian H is given by

the imaginary part of correlation functions of type

$$A_O(\omega) = \lim_{\eta \rightarrow 0} \frac{1}{\pi} \langle \psi_0 | O^\dagger \frac{\eta}{(E_0 + \omega - H)^2 + \eta^2} O | \psi_0 \rangle, \quad (3)$$

where the operator O identifies the physical quantity of interest. $|\psi_0\rangle$ and E_0 give the ground-state wave function and energy of H . The small $\eta > 0$ shifts the poles of the related Green's function $G_O(\omega + i\eta)$ into the complex plane.

Single-particle excitations associated with the injection or emission of an electron with wave vector k , $A^+(k, \omega)$ or $A^-(k, \omega)$, can be written in the spectral form

$$A^\pm(k, \omega) = \sum_n |\langle \psi_n^\pm | f_k^\pm | \psi_0 \rangle|^2 \delta[\omega \mp \omega_n^\pm], \quad (4)$$

where $f_k^+ = f_k^\dagger$ and $f_k^- = f_k$. $|\psi_0\rangle$ is the ground state of a N -site system in the N_e -particle sector while $|\psi_n^\pm\rangle$ denote the n th excited states in the $N_e \pm 1$ -particle sectors with excitation energies $\omega_n^\pm = E_n^\pm - E_0$.

Optical excitations, on the other hand, connect states in the same particle sector with a site-parity change. For a system with open boundary conditions (OBC) the regular part of the optical absorption

$$\sigma_{reg}(\omega) = \frac{\pi}{N} \sum_n \omega_n |\langle \psi_n | P | \psi_0 \rangle|^2 \delta[\omega - \omega_n] \quad (5)$$

is related to the dynamical polarizability, $\sigma_{reg}(\omega) = \omega \alpha(\omega)$, where $P = -\sum_{j=1}^N j(f_j^\dagger f_j - 1)$ is the dipole operator (in units of e) and $\omega_n = (E_n - E_0)$. Then the current operator is obtained from $J = i[H, P]$. Applying periodic boundary conditions (PBC), the optical conductivity can be calculated from

$$\sigma_{reg}(\omega) = \frac{\pi}{N} \sum_n \frac{|\langle \psi_n | J | \psi_0 \rangle|^2}{\omega_n} \delta[\omega - \omega_n]. \quad (6)$$

Note that for our fermion-boson model (1), the current operator has two contributions, $J = J_f + J_b$, where $J_f = it_f \sum_j f_{j+1}^\dagger f_j - f_j^\dagger f_{j+1}$ and $J_b = it_b \sum_j f_{j+1}^\dagger f_j b_j^\dagger - f_j^\dagger f_{j+1} b_j + f_{j-1}^\dagger f_j b_j^\dagger - f_j^\dagger f_{j-1} b_j$. The f -sum rule

$$S_{reg}(\infty) + \pi D = -\pi E_{kin}/2 \quad (7)$$

connects the frequency-integrated optical response $S_{reg}(\omega) = \int_0^\omega \sigma_{reg}(\omega') d\omega'$ to the kinetic energy $E_{kin} = \frac{1}{N} \langle 0 | H - \omega_0 \sum_i b_i^\dagger b_i | 0 \rangle$, where the Drude part $\propto D$ serves as a measure for coherent transport. For OBC, only a D precursor exists in the metallic region.

In the actual DDMRG calculation of spectral functions the required CPU time increases rapidly with the number of the density-matrix eigenstates m . Since the DDMRG approach is based on a variational principle,¹⁵ we first of all have to prepare a good "trial function" for the ground state with as many density-matrix eigenstates as possible. As a rule we keep $m \sim 500$ states to obtain the true ground state in the first five DDMRG sweeps and afterwards take $m \sim 200$ states for the calculation of the various spectra from Eq. (3) with a broadening $\eta = 0.1$. In order to save CPU time in the DDMRG runs we take into account just $n_b = 3$ pseudositers. In this case the n_b th local boson pseudosite density is smaller than 10^{-5} . Using $n_b = 4$ this value can be reduced to 10^{-8}

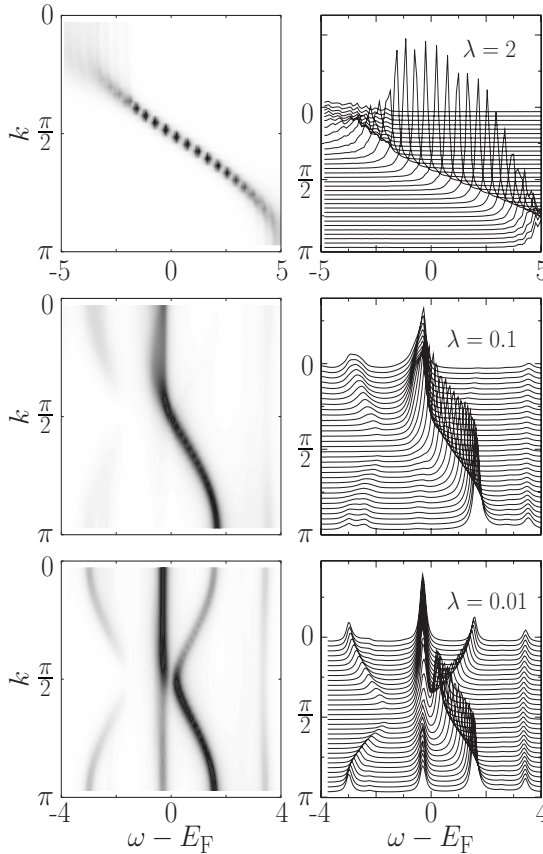


FIG. 2. Intensity (left panels) and line-shape (right panels) of the single-particle spectral function $A(k, \omega)$ in the half-filled band sector of the fermion-boson transport model (1) on a $N=32$ -site chain. The upper two rows (lower row) give DDMRG data for $\lambda=2$ and 0.1 in the metallic regime ($\lambda=0.01$, insulating regime), where $\omega_0=2$. All energies are measured in units of t_b . Since we apply OBC, we use quasimomenta $k=\pi l/(N+1)$ with integers $1 \leq l \leq N$.

which leads, however, not to visible change in the spectra because the discarded weight in the DDMRG calculations is $\sim 10^{-3}$ (i.e., three orders of magnitude larger than for the DMRG ground-state calculations).

III. RESULTS

A. Photoemission spectrum

Let us first discuss the single-particle spectra of the transport model (1) in the regime where the background is stiff, i.e., the distortions induced by the particle hopping process are energetically costly ($\omega_0=2$).

For very large λ the free transport channel nevertheless dominates and an almost particle-hole symmetric spectrum [$A^+(k, \omega - E_F) \sim A^-(k - \pi, E_F - \omega)$] results (see Fig. 2 upper panels). As λ decreases, the background distortions hardly relax. Consequently, the bosonic degrees of freedom will strongly affect the transport. The middle panels of Fig. 2 show how, at $\lambda=0.1$, strong correlations develop in the occupied states probed by photoemission (PE) for $\omega < E_F$. The introduced hole can only move coherently by the six-step

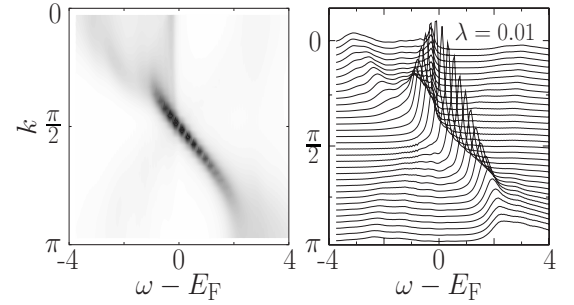


FIG. 3. Density (left) and line-shape (right) plot of the $A(k, \omega)$ spectra. Again $N=32$ (OBC), $\lambda=0.01$, but now $\omega_0=1$.

process [Eq. (2)], where in steps one-three, three bosons were excited, which are consumed in steps four-six afterward. In this way the collective particle-boson dynamics leads to a flattening of the “coherent” band for $k \leq k_F$. By contrast an additional electron, which probes the unoccupied states in an inverse (I)PE experiment ($\omega > E_F$), can more easily move by a two-step process, even if pronounced CDW correlations exist in the background medium.¹² The incoherent parts of $A(k, \omega)$ far away from the Fermi energy E_F are caused by excitations with additional bosons involved (bear in mind that the ground state with N_e electrons is a multiphonon state and the wave vector of the $N_e \pm 1$ target state corresponds to the total momentum of electrons and bosons).

While for $\lambda=0.1$, $A(k_F, \omega)$ has finite spectral weight at E_F , i.e., the system is still metallic (albeit the TLL charge exponent K_ρ is noticeably reduced from one¹³), an excitation gap opens in the PE spectrum as λ falls below a certain critical value, provided that $\omega_0 > \omega_{0,c}(\lambda=0)$.¹³ We find $\lambda_c(\omega_0=2) \approx 0.05$. The lower panels of Fig. 2 show $A(k, \omega)$ for $\lambda=0.01$, in the insulating regime, where a CDW with true long-range order exists. The TLL-CDW quantum phase transition is driven by the correlations that might evolve in the background medium at commensurate fillings. Let us emphasize the dynamical aspect of this process: the (collective) bosonic excitations are intimately connected to the motion of the particles, and themselves have to persist long enough in order to affect the many-particle state.

The ARPES spectrum for the insulating state clearly shows the doubling of the Brillouin zone. The remaining asymmetry with regard to the spectral weight of the absorption signals as $k \leftrightarrow (\pi - k)$ vanishes for $\lambda \rightarrow 0$. Most notably the widths of the highest PE and lowest IPE coherent bands differ by a factor of about $(t_b/\omega_0)^4$ since the CDW order is restored if the injected hole [electron] is transferred to a NNN site by a process of order $O(t_b^6/\omega_0^5)$ [$O(t_b^2/\omega_0)$]. Hence the CDW state exhibits a correlation-induced asymmetric band structure.¹²

The strong interrelation of charge dynamics and background fluctuations becomes obvious if we decrease ω_0 below $\omega_{0,c}$ keeping $\lambda=0.01$ fixed. Of course, in passing the accompanied insulator-metal transition the PE spectrum changes completely but the “nature” of the TLL at $\omega_0=1$ is different compared to that of the metallic state realized at larger ω_0 and λ as well (cf. Fig. 3 and upper panels of Fig. 2). The single-particle spectrum for $\omega_0=1$ shows sharp ab-

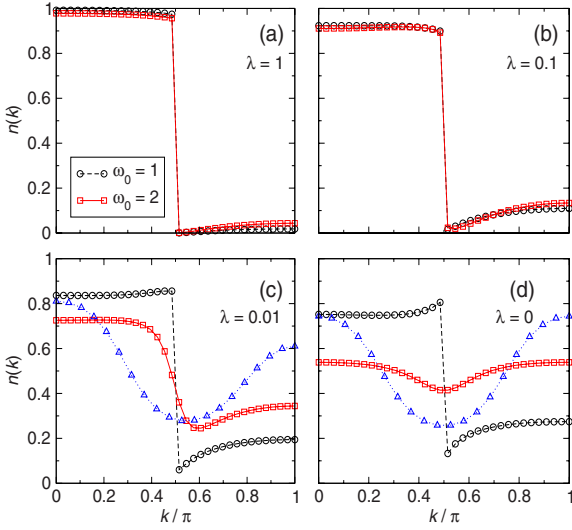


FIG. 4. (Color online) Momentum distribution function $n(k)$ for the half-filled two-channel transport model (1) with 66 sites and PBC, as λ decreases from one (a) to zero (d) at $\omega_0=1$ (circles) and 2 (squares). Triangles show $n(k)$ for a half-filled t - t' - U model (38 sites, PBC) with $U=10t'$, $t=t'$ [panel (c)], and $t=0$ [panel (d)] (see text). In order to obtain more accurate ground-state data we use $n_b=4$ pseudospins.

sorption signals in the vicinity of k_F only. In a wide k -space region emanating from $k=0$ ($k=\pi$) the PE (IPE) spectrum is smeared out (overdamped), i.e., here the dynamics of the system is dominated by bosonic fluctuations.

B. Momentum distribution function

The different transport behavior becomes also apparent in the momentum distribution function

$$n(k) = \frac{1}{N} \sum_{j,l} e^{ik(j-l)} \langle c_j^\dagger c_l \rangle. \quad (8)$$

By means of DMRG, the ground-state correlation function $\langle c_j^\dagger c_l \rangle$ can be easily calculated for PBC. Figure 4 displays $n(k)$ for two characteristic boson energies, above and below $\omega_{0,c}$.

In the former case, the TLL-CDW transition causes significant changes in the functional form of $n(k)$. For $\lambda > \lambda_c$, one expects an essential power law singularity at k_F , corresponding to a vanishing quasiparticle weight. For finite TLL systems the difference $\Delta = n(k_F - \delta) - n(k_F + \delta)$ is finite (with $\delta = \pi/66$ in our case).¹⁶ Δ rapidly decreases approaching the CDW transition point with decreasing λ [see data for $\omega_0=2$ (red squares)]. In the CDW phase the singularity at k_F vanishes. Note that the periodicity of $n(k)$ doubles at $\lambda=0$, in accordance with a $R^{(6)}$ NNN-only hopping channel. To substantiate this reasoning we have included in Fig. 4 $n(k)$ data calculated for the 1D Hubbard model with additional NNN transfer t' . We see that $n(k)$ of the fermion-boson model (1) is in qualitative agreement with our data and previous results for the t - t' Hubbard model.¹⁷ In particular, for the case $t=0$. The upturn in $n(k)$ for $k > k_F$ persists even in the metallic

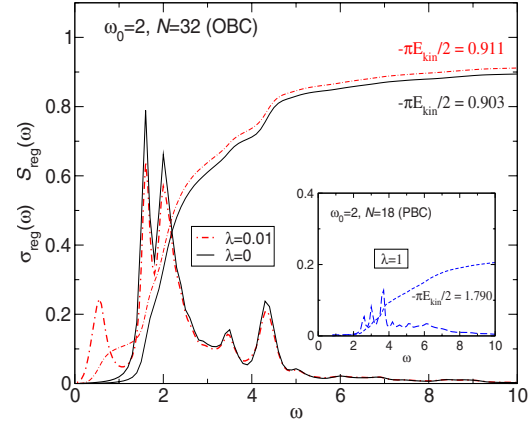


FIG. 5. (Color online) Optical conductivity $\sigma_{reg}(\omega)$ and integrated spectral weight $S_{reg}(\omega)$ in the half-filled transport model (1). The main panel (inset) displays DDMRG data for $\omega_0=2$ at $\lambda < \lambda_c$ ($\lambda > \lambda_c$), i.e., in the insulating (metallic) region, applying OBC (PBC).

regime as long as NNN-hopping processes triggered by the (CDW) correlations in the background are of importance.

For $\omega_0=1$ the system stays metallic for all λ . Besides the usual renormalization of $n(k)$ with increasing correlations (i.e., decreasing λ) we find a slight upturn in $n(k)$ for $k \lesssim k_F$. This might be attributed to the fact that in our model (1) a particle injected with $k = \pm \pi$ is almost unaffected by bosonic fluctuations (which holds also for the single-particle case⁹). So to speak the system behaves as a nearly perfect metal at this point. It is worth mentioning that an increase in $n(k)$ for both $k \lesssim k_F$ and $k \gtrsim k_F$ has also been found for the momentum distribution function of the Hubbard model (with and without magnetization) using the Gutzwiller variational wave function.¹⁸

C. Optical response

Finally we consider the evolution of the optical conductivity going from the correlated TLL to the CDW phase at $\omega_0=2$. The corresponding optical absorption spectra are depicted in Fig. 5. In the metallic state most of the spectral weight resides in the coherent Drude part. At $\lambda=1$ (see inset), we find $\pi D/N \approx 1.6$, which has to be compared with $S_{reg}(\infty) \approx 0.2$ (of course D decreases as λ gets smaller). In this case the wave-vector resolved single-particle spectra roughly extends from $\omega = -6$ to $\omega = 6$. The regular part of the conductivity is mainly due to excitations to the phononic side bands appearing in the sectors with momenta far away from k_F . In the insulating region (see main panel), the first peak at about $\omega \approx 0.5$ can be assigned to an optical excitation across the gap in the (coherent) two-band structure. These excitations are only accessible for $\lambda > 0$. Additional excitations with higher energy occur around multiples of the boson frequency, where $\omega \approx \omega_0=2$ sets an absorption threshold for the $\lambda=0$ case. As expected for an insulating system with OBC, the whole spectral weight is contained in $S_{reg}(\infty) \approx -\pi E_{kin}/2$. We emphasize that the CDW state in our model contains less than one boson per site on average, unlike, e.g.,

the Peierls insulating state in the Holstein model. That is the CDW phase typifies rather as a correlated insulator—such as the Mott-Hubbard insulator—and no divergence occurs at the optical absorption threshold.¹⁹

IV. SUMMARY

In conclusion, we have determined the spectral properties of a highly nontrivial two-channel fermion-boson transport model for the 1D half-filled band case, using an unbiased DDMRG technique. The background medium, parameterized by bosonic degrees of freedom, strongly influences the charge-carrier dynamics, as it happens in many novel materials. If the background fluctuations dominate we find diffusive transport. In opposite case of strong background correlations coherent quantum transport may evolve on a reduced

energy scale. These correlations can also trigger a metal-insulator transition. The insulating CDW state has an asymmetric band structure, leading to characteristic signatures in the ARPES and optical response. Whether an extended model with spinful fermions gives rise to an attractive metallic phase like in the Holstein-Hubbard model²⁰ would be an interesting question for further research.

ACKNOWLEDGMENTS

The authors would like to thank A. Alvermann, K. W. Becker, D. M. Edwards, F. Gebhard, G. Hager, E. Jeckelmann, S. Sykora, L. Tincani, S. A. Trugman, and G. Wellein for valuable discussions. This work was supported by DFG under Grant No. SFB 652 and the KONWIHR project HQS@HPC.

-
- ¹M. Berciu, *Phys.* **2**, 55 (2009).
²C. L. Kane, P. A. Lee, and N. Read, *Phys. Rev. B* **39**, 6880 (1989).
³G. Martinez and P. Horsch, *Phys. Rev. B* **44**, 317 (1991).
⁴K. Wohlfeld, A. M. Oleś, and P. Horsch, *Phys. Rev. B* **79**, 224433 (2009).
⁵*Polarons in Advanced Materials*, Springer Series in Material Sciences Vol. 103, edited by A. S. Alexandrov (Springer, Dordrecht, 2007).
⁶N. Tsuda, K. Nasu, A. Fujimori, and K. Siratori, *Electronic Conduction in Oxides* (Springer-Verlag, Berlin, 2000).
⁷A. Weiße and H. Fehske, *New J. Phys.* **6**, 158 (2004).
⁸D. M. Edwards, *Physica B (Amsterdam)* **378-380**, 133 (2006).
⁹A. Alvermann, D. M. Edwards, and H. Fehske, *Phys. Rev. Lett.* **98**, 056602 (2007).
¹⁰S. A. Trugman, *Phys. Rev. B* **37**, 1597 (1988).
¹¹J. Bonča, S. A. Trugman, and I. Batistić, *Phys. Rev. B* **60**, 1633 (1999).
¹²G. Wellein, H. Fehske, A. Alvermann, and D. M. Edwards, *Phys. Rev. Lett.* **101**, 136402 (2008); H. Fehske, A. Alvermann, and G. Wellein, in *High Performance Computing in Science and Engineering*, edited by S. Wagner, M. Steinmetz, A. Bode, and M. Brehm (Springer-Verlag, Berlin, 2009), pp. 649–668.
¹³S. Ejima, G. Hager, and H. Fehske, *Phys. Rev. Lett.* **102**, 106404 (2009).
¹⁴S. R. White, *Phys. Rev. Lett.* **69**, 2863 (1992).
¹⁵E. Jeckelmann, *Phys. Rev. B* **66**, 045114 (2002); E. Jeckelmann and H. Fehske, *Riv. Nuovo Cimento* **30**, 259 (2007).
¹⁶S. Ejima and H. Fehske, *Europhys. Lett.* **87**, 27001 (2009).
¹⁷C. Gros, K. Hamacher, and W. Wenzel, *Europhys. Lett.* **69**, 616 (2005).
¹⁸W. Metzner and D. Vollhardt, *Phys. Rev. Lett.* **59**, 121 (1987); M. Kollar and D. Vollhardt, *Phys. Rev. B* **65**, 155121 (2002).
¹⁹E. Jeckelmann, F. Gebhard, and F. H. L. Essler, *Phys. Rev. Lett.* **85**, 3910 (2000).
²⁰M. Tezuka, R. Arita, and H. Aoki, *Phys. Rev. Lett.* **95**, 226401 (2005).

Anderson localization versus charge-density-wave formation in disordered electron systems

S. Nishimoto,¹ S. Ejima,² and H. Fehske²

¹*Institute for Theoretical Solid State Physics, IFW Dresden, 01171 Dresden, Germany*

²*Institute of Physics, Ernst Moritz Arndt University Greifswald, 17489 Greifswald, Germany*

(Received 3 August 2012; revised manuscript received 10 January 2013; published 18 January 2013)

We study the interplay of disorder and interaction effects including bosonic degrees of freedom in the framework of a generic one-dimensional transport model: the Anderson-Edwards model. Using the density-matrix-renormalization group technique, we extract the localization length and the renormalization of the Tomonaga-Luttinger-liquid parameter from the charge-structure factor by an elaborate sample-average finite-size scaling procedure. The properties of the Anderson localized state can be described in terms of scaling relations of the metallic phase without disorder. We analyze how disorder competes with the charge-density-wave correlations triggered by the bosons and give evidence that disorder will destroy the long-range charge-ordered state.

DOI: [10.1103/PhysRevB.87.045116](https://doi.org/10.1103/PhysRevB.87.045116)

PACS number(s): 71.23.An, 71.27.+a, 71.30.+h, 71.45.Lr

I. INTRODUCTION

Disorder is an inherent part of any solid-state system.¹ Low-dimensional materials are exceedingly susceptible to disorder. In one dimension (1D), theory predicts that all carriers are strongly localized for arbitrary energies and arbitrarily weak disorder. This holds for Anderson's noninteracting tight-binding Hamiltonian with a diagonal (i.e., on-site) random potential.^{2,3} The coherent backscattering from the randomly distributed impurities thereby transforms the metal into an insulator.

In 1D, the mutual interaction of the particles is likewise of significance; here even weak interactions can cause strong correlations. The instantaneous Coulomb repulsion between the electrons, for instance, tends to immobilize the charge carriers as well. As a consequence, at half filling, a Mott insulating (spin-density-wave) phase is energetically favored over the metallic state.⁴ The retarded electron-phonon coupling, on the other hand, may lead to structural distortions accompanied by polaron formation,⁵ and is the driving force behind the metal-to-Peierls transition, establishing a charge-density-wave (CDW) order.⁶

An understanding of how disorder and interaction act together is of vital importance not only to discuss the metal-insulator itself but also to analyze the electronic properties of many quasi-1D materials of current interest, such as conjugated polymers, organic charge-transfer salts, ferroelectric perovskites, halogen-bridged transition-metal complexes, TMT[SF,TF] chains, Qn(TCNQ)₂ compounds, or, e.g., the quite recently studied vanadium dioxide Peierls-Mott insulator.^{7–10} Carbon nanotubes¹¹ and organic semiconductors¹² are other examples where disorder and bosonic degrees of freedom are of importance. Regarding interacting bosons, ultracold atoms trapped in optical lattices offer the unique possibility to tune both the disorder and interaction strength.¹³

Unfortunately, the subtle interplay of disorder and interaction effects is one of the most challenging problems in solid-state theory and—despite 50 years of intense research—is still an area of uncertainty; see Ref. 14 and references therein. In the limit of vanishing charge-carrier density, only the interaction with the lattice vibrations matters. Then Anderson disorder may affect the polaron self-trapping in

a highly nontrivial way.¹⁵ This has been demonstrated for the Anderson-Holstein model within the statistical dynamical mean-field and momentum-average approximations.^{16,17} At finite carrier density, the Mott-Anderson transition for Coulomb correlated electrons was investigated by self-consistent mean-field theory in $D = \infty$ and $D = 3$,^{18–20} as well as by variational Gutzwiller-ansatz-based approaches.²¹ Electron-electron interactions may screen the disorder potential in strongly correlated systems, thereby stabilizing metallicity.²² Exact results are rare, however. In 2D, Lanczos and quantum Monte Carlo data suggest a disorder-induced stabilization of the pseudogap, also away from half filling.²³ The density-matrix-renormalization group (DMRG)²⁴ allows the numerical exact calculation of ground-state properties of disordered, interacting fermion systems in 1D, on fairly large systems. Exploiting this technique, the properties of disordered Luttinger liquids have been analyzed in the framework of the spinless fermion Anderson- t - V model (AtVM)²⁵ and the spinful Anderson-Hubbard model.²⁶

In this paper, we address how many-body Anderson localization competes with CDW formation triggered by bosonic degrees of freedom in the framework of the Anderson-Edwards model (AEM).

II. MODEL

The Edwards model²⁷ represents a very general two-channel fermion-boson Hamiltonian, describing quantum transport in a background medium. Its fermion-boson interaction part

$$H_{fb} = -t_b \sum_{(i,j)} f_j^\dagger f_i (b_i^\dagger + b_j) \quad (1)$$

mimics the correlations/fluctuations inherent to a spinful fermion many-particle system by a boson-affected transfer of spinless charge carriers. In Eq. (1), a fermion $f_i^{(\dagger)}$ creates (or absorbs) a local boson $b_i^{(\dagger)}$ every time it hops to a nearest-neighbor (NN) site j . Thereby it creates a local excitation in the background with energy ω_0 : $H_b = \omega_0 \sum_i b_i^\dagger b_i$. Because of quantum fluctuations, the background distortions should be able to relax with a certain rate λ . The entire Edwards

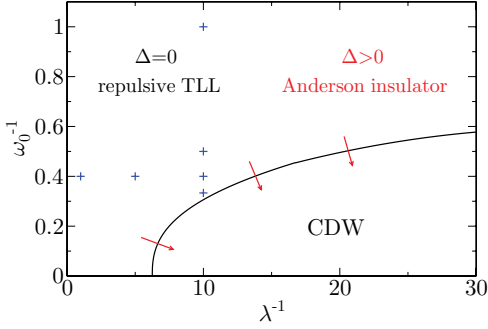


FIG. 1. (Color online) DMRG metal-insulator phase boundary for the 1D half-filled Edwards model without disorder (solid line). CDW order is suppressed if the background fluctuations dominate [$\omega_0 < 1$] or if the system's ability for relaxation is high [$\lambda > \lambda_c(\omega_0)$]. The blue crosses denote the parameter sets considered in this paper for the disordered Edwards model.

Hamiltonian then reads

$$H_E = H_{fb} - \lambda \sum_i (b_i^\dagger + b_i) + H_b. \quad (2)$$

A unitary transformation $b_i \mapsto b_i + \lambda/\omega_0$ eliminates the boson relaxation term in favor of a second fermion hopping channel:

$$H_E = H_{fb} - t_f \sum_{(i,j)} f_j^\dagger f_i + H_b. \quad (3)$$

We like to emphasize that (i) this free-fermion transfer, however, takes place on a strongly reduced energy scale, $t_f = 2\lambda t_b/\omega_0$, and (ii) coherent propagation of a fermion is possible even in the limit $\lambda = t_f = 0$ by means of a six-step vacuum-restoring hopping process,²⁸ acting as a direct next-NN transfer “ $f_{i+2}^\dagger f_i$.” The Edwards model reveals a surprisingly rich physics. Depending on the relative strengths t_f/t_b of the two transport mechanisms and the rate of bosonic fluctuations t_b/ω_0 , it reproduces Holstein and t - J model-like lattice- and spin-polaron transport, respectively, in the single-particle sector.^{28,29} For the half-filled band case, a metal-insulator quantum phase transition from a repulsive Tomonaga-Luttinger-liquid (TLL) to a CDW has been reported,^{30,31} see Fig. 1. Note that the CDW is a few-boson state that typifies rather a correlated (Mott-Hubbard-type) insulator than a Peierls state with many bosons (phonons) involved.^{30,31} Since in the limit $\omega_0 \gg 1 \gg \lambda$ (here, and in what follows, t_b is taken as the unit of energy) background fluctuations are energetically costly, charge transport is hindered and an effective Hamiltonian with NN fermion repulsion results. To leading order, in a reduced (zero-boson) Hilbert space, we get

$$H_{tV} = -t_f \sum_{(i,j)} f_j^\dagger f_i + V \sum_i n_i^f n_{i+1}^f, \quad (4)$$

with $V = t_b^2/\omega_0$. This so-called t - V model can be mapped onto the exactly solvable XXZ model, which exhibits a TLL-CDW quantum phase transition at $V/t_f = 2$, i.e., at $\lambda_c^{-1} = 4$. This value is smaller than those obtained for the Edwards model in the limit $\omega_0^{-1} \ll 1$, where $\lambda_c^{-1} \simeq 6.3$ (see Fig. 1 and Ref. 31),

because already three-site and effective next-NN hopping terms were neglected in the derivation of the tV model.

We now employ the DMRG technique,²⁴ which can be easily generalized to treat systems including bosons,³² in order to obtain unbiased results for the full AEM,

$$H_{AE} = \Delta \sum_i \varepsilon_i n_i^f + H_E, \quad (5)$$

and the related $AtVM$, $H_{AtV} = \Delta \sum_i \varepsilon_i n_i^f + H_{tV}$, where disorder of strength Δ is induced by independently distributed random on-site potentials ε_i , drawn from the box distribution $P(\varepsilon_i) = \theta(1/2 - |\varepsilon_i|)$. Within the pseudosite approach, a boson is mapped to n_b pseudosites.^{32,33} In the numerical study of the AEM, we take into account up to $n_b = 4$ pseudosites and determine n_b by the requirement that local boson density of the last pseudosite is less than 10^{-7} for all i . Furthermore, we keep up to $m = 1200$ density-matrix eigenstates in the renormalization steps to ensure that the discarded weight is smaller than 10^{-8} . The calculations are performed for finite systems with lengths $L = 16$ to 128 and open boundary conditions (OBC). For the simpler effective $AtVM$, we reach $L = 192$ with OBC. Here the use of $m = 1000$ density-matrix eigenstates makes the discarded weight negligible. To gain representative results for our disordered systems, we proceed as follows. We first compute the physical quantity of interest at fixed L for numerous samples $\{\varepsilon_i\}$, then set up an appropriate statistical average, and finally perform a careful finite-size scaling.

III. FINITE-SIZE SCALING

An important question is, of course, which physical quantity to use in the finite-size scaling of the Anderson transition. For this purpose, the localization length ξ seems to be promising because it is sensitive to the nature, localized or extended, of the electron's eigenstate.^{34,35} So far, ξ has been determined from the phase sensitivity of the ground-state energy.^{17,25} Quite recently, Berkovits demonstrates that the entanglement entropy can also be used to extract the localization length.³⁶ However, in both methods, the system size L should be always larger than ξ .

Advantageously, the localization length can be extracted by a finite-size scaling analysis of the charge-density-structure factor even for $L \ll \xi$, which works equally well for interacting systems,²⁶ and therefore allows us to discuss the interplay between Anderson localization and CDW formation in a consistent manner. The charge structure is defined as

$$\tilde{C}(q) = \frac{1}{L} \sum_{i,r=1}^L [(n_i^f n_{i+r}^f) - \langle n_i^f \rangle \langle n_{i+r}^f \rangle] e^{iqr}. \quad (6)$$

Assuming an exponential decay of the equal-time density-density correlations in the Anderson insulating phase,³⁷ the structure factor scales with

$$\tilde{C}(q) = -\frac{K_\rho^*}{2\pi^2} \frac{e^{-\frac{\pi^2 L}{6\xi}} - 1}{e^{\frac{\pi^2}{6\xi}} - 1} q^2, \quad (7)$$

where $q = 2\pi/L \ll 1$.²⁶ Equation (7) contains two unknown parameters: the localization length ξ and the disorder-modified

TLL interaction coefficient K_ρ^* . Hence, if the charge-structure factor is determined numerically, then ξ and K_ρ^* can be easily derived by fitting the numerical data with Eq. (7). For vanishing disorder, $\Delta \rightarrow 0$, ξ diverges and K_ρ^* becomes the ordinary TLL parameter K_ρ . We are aware that a disordered 1D system is no longer a TLL and, consequently, the TLL parameter is ill defined in the strict sense. Nevertheless, if the localization length significantly exceeds the lattice constant, then the short-range correlation functions should still show a power-law decay. Therefore, we might gain some valuable information about the local motion of fermions from K_ρ^* .

IV. DMRG RESULTS

Figure 2 demonstrates that the finite-size scaling of the averaged charge-structure factor $\tilde{C}_{av}(q)$ by means of (7) works best and equally well for the 1D AEM and $AtVM$ (this applies to all parameter values discussed below). To accommodate the missing correlations owing to the OBC, we have plotted $\tilde{C}_{av}(q)$ as a function of $1/(L - \delta)$ instead of $1/L$ (this way of plotting the data is nonessential but gives a quantitative refinement of the fit). The parameter δ is adjusted to reproduce $K_\rho^* = K_\rho$ and $\xi = \infty$ at $\Delta = 0$. We note the general tendency that the charge correlations arising at finite L will be suppressed as Δ becomes larger.

In a next step, we extract the localization length ξ and the modified TLL parameter for the disordered Edwards and t - V models. Figure 3 shows the dependence of ξ and K_ρ^* on the disorder strength Δ . First of all, we find a power-law decay of ξ with $1/\Delta$ in the whole $(\lambda, \omega_0; V)$ parameter regime:

$$\xi/\xi_0 = \Delta^{-\gamma} \quad (8)$$

[note that Δ is given in units of t_b (t_f) in Fig. 3 for the AEM ($AtVM$)]. The estimated values of the (bare) decay length ξ_0 and the exponent γ are given in the caption of Fig. 3 for characteristic model parameters. As expected, the localization length decreases with increasing disorder strength. Stronger electronic correlations, i.e., smaller λ or larger ω_0 (larger V) in the AEM ($AtVM$), also tend to reduce ξ . In any case, ξ turns out to be finite as soon as $\Delta > 0$, indicating that

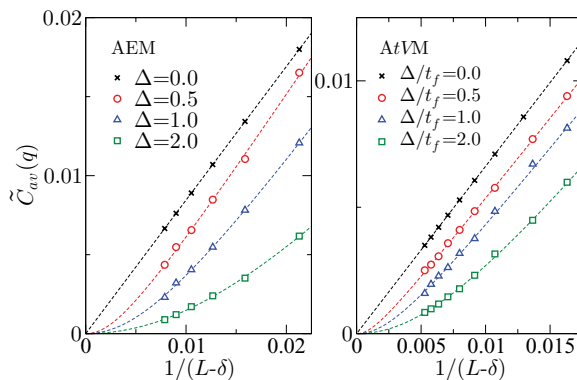


FIG. 2. (Color online) Charge-structure factor of the AEM with $\lambda = 0.1$ and $\omega_0 = 2$ (left panel) and the $AtVM$ with $V/t_f = 1.5$ (right panel) sampled over 300 and 500 disorder realizations, respectively. Dashed lines give the finite-size scaling of $\tilde{C}_{av}(q)$ according to (7).

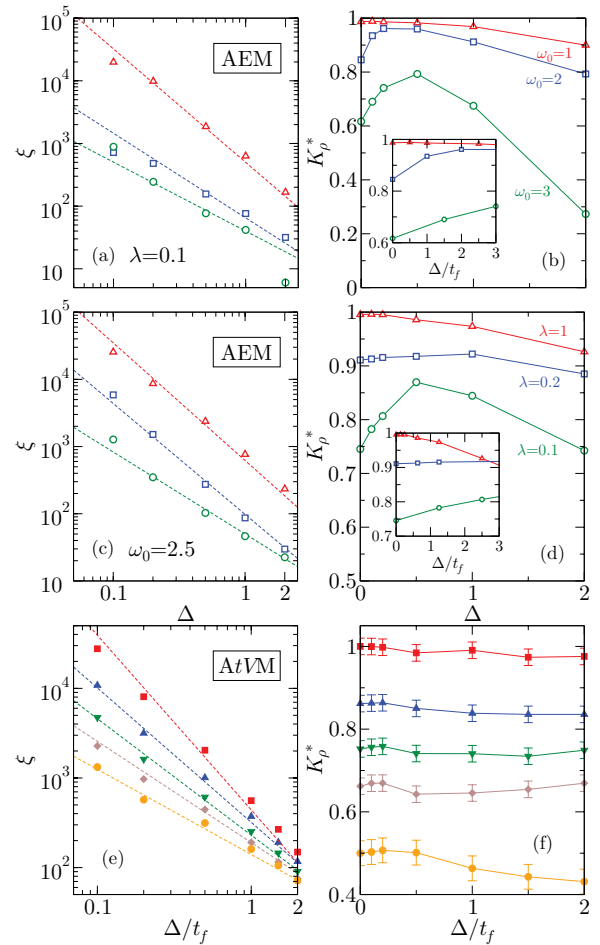


FIG. 3. (Color online) Left panels: Log-log plot of the localization length vs disorder strength for the AEM at (a) fixed $\lambda = 0.1$, (c) fixed $\omega_0 = 2.5$, and (e) for the $AtVM$. Dashed lines are fits to Eq. (8) with (a) $\xi_0 = 620, 98, 50$ and $\gamma = 1.75, 1.65, 1.22$ for $\lambda = 1, 0.2, 0.1$; (c) $\xi_0 = 500, 65, 40$ and $\gamma = 1.81, 1.35, 1.1$ for $\omega_0 = 1, 2, 3$; and (e) $\xi_0 = 440, 350, 230, 190, 150$ and $\gamma = 1.95, 1.5, 1.3, 1.1, 0.95$ for $V/t_f = 0, 0.5, 1, 1.5, 2$ (from top to bottom), respectively. Right panels: Corresponding results for the modified TLL parameter K_ρ^* in the (b), (d) AEM and (f) $AtVM$.

the repulsive TLL, if realized for $\Delta = 0$, makes way for an Anderson insulator. Thereby the localization length becomes comparable to the lattice spacing at $\Delta = 2$ in the AEM with $\lambda = 0.1$, $\omega_0 = 2.5$, while it is still about 10^2 for the $AtVM$ with $V/t_f = 2$.

The right-hand panels display striking differences in the Δ dependence of K_ρ^* for the models under consideration. These can be attributed to the fact that the Edwards model contains two energy scales λ and ω_0 , while the physics of the t - V model is merely governed by the ratio $V/t_f = t_b/2\lambda$, i.e., ω_0 drops out. Far away from the CDW instability, however, both models describe a weakly correlated TLL with $K_\rho \lesssim 1$, and K_ρ^* slowly decays as the disorder Δ increases (see the red open triangles in Fig. 3; to make the comparison with the t - V model data

easy, we have shown K_ρ^* versus Δ/t_f in the insets). If we move towards the CDW instability by decreasing λ at fixed $\omega_0 > \omega_{0,c}$ or increase ω_0 at $\lambda < \lambda_c$ (cf. Fig. 1), then a nonmonotonous behavior develops. At small Δ , K_ρ^* is significantly enhanced as the disorder increases. Obviously, weak disorder destabilizes the $2k_F$ -CDW correlations locally, since disorder-induced second- (and higher-) order boson-assisted (inelastic) hopping processes are possible in the AEM, even for $\omega_0 \gg 1$. This in sharp contrast to the $AtVM$, where only elastic scattering takes place and the intersite Coulomb repulsion is hardly affected by Δ . As a result, in the disordered t - V model, the CDW correlations will be stronger and more robust. Hence, for the $AtVM$, K_ρ^* appears to be nearly independent from Δ for $0.5 \lesssim V/t_f \lesssim 2$. This also notably differs from the behavior found for the disordered Hubbard model,²⁶ where the umklapp scattering is effectively enhanced by the formation of Mott plateaus appearing due to disorder.³⁸ If Δ exceeds a certain value in the AEM, then K_ρ^* starts to decrease and, finally, the whole scaling procedure breaks down when $\xi \gtrsim 1$ (see the point at $\Delta = 2$ in the upper right panel with K_ρ^* well below 0.5). In this regime, the wave functions of the particles are strongly localized and the TLL behavior is as much suppressed as the CDW correlations. Let us point out that the enhancement of K_ρ^* triggered by the bosonic degrees of freedom might serve as an explanation for the observed increasing charge velocity near a negatively charged defect in the single-wall carbon nanotubes,¹¹ since the TLL parameter K_ρ is proportional to the charge velocity.

We now focus on the localization behavior at large distances [$O(\xi \gg 1)$], and therefore make an attempt to analyze the decay length ξ_0 and the exponent γ , for both the AEM and $AtVM$, in terms of the interaction exponent K_ρ and the charge susceptibility χ_c of standard TLL theory.³⁷ We expect that ξ_0 is strongly influenced by the strength of the charge fluctuations quantified by χ_c , which is given—for the t - V model—as

$$\chi_c = \frac{2K_\rho}{\pi v_c} = \frac{4}{\pi \sqrt{1 - (\frac{V}{2t_f})^2}} \left[\frac{\pi}{\arccos(-\frac{V}{2t_f})} - 1 \right], \quad (9)$$

with charge velocity v_c . Figure 4 shows that ξ_0 nicely scales with V/t_f , i.e., $\xi_0 \propto \chi_c$, in fact (see upper panel). The same holds—perhaps surprisingly—for the AEM when ξ_0/t_f^γ is

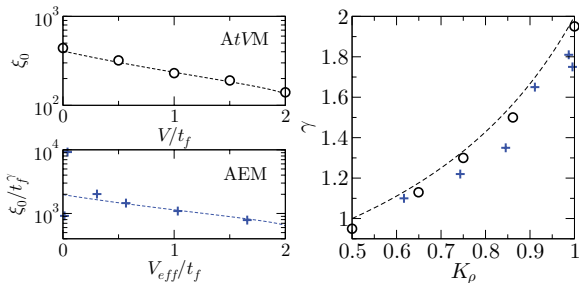


FIG. 4. (Color online) Left panels: Decay length ξ_0 as a function of the (effective) Coulomb repulsion V_{eff} for the $AtVM$ and AEM. Right panel: Corresponding γ exponent vs K_ρ , in comparison to the scaling relation (10) (dashed line). For further explanation, see text.

plotted versus an effective intersite repulsion estimated from $V_{\text{eff}}/t_f = -2 \cos(\pi/2K_\rho)$ (see lower panel). Moreover, for the disordered t - V model, the exponent γ is connected to K_ρ of the (spinless fermion) TLL system without disorder via the renormalization equation: $d(\Delta^2)/dl = (3 - 2K_\rho)\Delta^2$ (with scale quantity l). This causes the scaling relation^{37,39,40}

$$\gamma = 2/(3 - 2K_\rho). \quad (10)$$

The right panel of Fig. 4 displays that γ basically depends on K_ρ , as predicted by Eq. (10). This means that the long-range localization properties of the AEM can be understood in the framework of $AtVM$ with an effective intersite interaction induced by the bosonic degrees of freedom. Since the (effective) Coulomb repulsion tends to result in a lesser K_ρ , γ decreases with increasing V_{eff} (cf. Fig. 4). In this way, the $2k_F$ -CDW fluctuations triggered by V tend to weaken Anderson localization. While $\gamma = 2$ in the free-fermion limit ($V, 1/\lambda \rightarrow 0$), it scales to unity approaching the CDW transition point located, e.g., at $\lambda_c \simeq 0.07$ for $\omega_0 = 2.5$, respectively, at $\omega_{0,c} \simeq 3.1$ for $\lambda = 0.1$.

The question of how disorder affects the insulating CDW state could not be addressed by the above TLL-based scaling. In particular, we cannot assess by our numerical approach whether the CDW phase survives *weak* disorder (as experimentally observed for disordered Peierls-Mott insulators).¹⁰ If the Imry-Ma argument for disordered (low-D) interacting systems⁴¹ holds, then CDW long-range order should be destroyed by any finite Δ . Figure 5, showing the spatial variation of the local fermion/boson densities for a specific but typical disorder realization (note that any real experiment is performed on a particular sample), illustrates the situation deep inside the (former) CDW phase ($\lambda^{-1} = 100$, $\omega_0^{-1} = 0.4$; cf. Fig. 1). One realizes that long-range charge order ceases to exist but short-range CDW correlations locally persist whenever neighboring on-site potentials do not differ much (see, e.g., the region $i = 45, \dots, 55$ in the lower panel of Fig. 5).

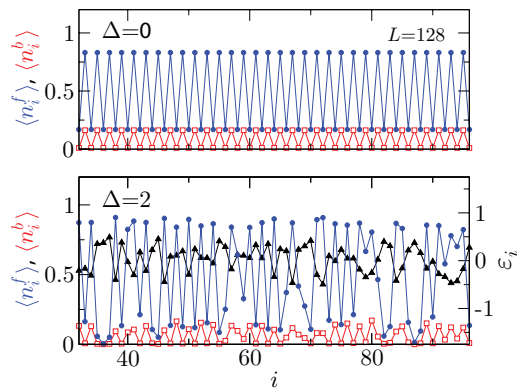


FIG. 5. (Color online) Local densities of fermions $\langle f_i^\dagger f_i \rangle$ (blue circles) and bosons $\langle b_i^\dagger b_i \rangle$ (red open squares) in the central part of an open AEM chain without ($\Delta = 0$) and with ($\Delta = 2$) disorder. Results are given for a single realization $\{\epsilon_i\}$ (black triangles). Model parameters are $\lambda = 0.01$, $\omega_0 = 2.5$, and $L = 128$ (OBC).

V. CONCLUSIONS

To summarize, using an unbiased numerical DMRG approach, we investigated the interplay of disorder and interaction effects including bosonic degrees of freedom in the framework of the 1D spinless fermion Anderson-Edwards model. Although the TLL phase disappears owing to the disorder, the localization properties of the Anderson insulator state can be understood in terms of scaling relations containing the charge susceptibility and the Luttinger liquid parameter of the metallic phase without disorder only, as in the case of the spinless fermion Anderson- t - V model. However, the

Anderson-Edwards model reveals a more complex interrelation between disorder and CDW correlations because additional scattering channels, involving bosonic excitation and annihilation processes, appear. This offers a promising route for adapting the description of low-dimensional transport in many disordered materials. Disorder also affects the CDW state in that true long-range order vanishes although local CDW correlations survive.

ACKNOWLEDGMENT

This work was supported by DFG through SFB 652.

- ¹V. F. Gantmakher, in *Electrons And Disorder in Solids*, International Series of Monographs on Physics Vol. 130 (Clarendon, Oxford, 2005).
- ²P. W. Anderson, *Phys. Rev.* **109**, 1492 (1958).
- ³J. Fröhlich, F. Martinelli, E. Scoppola, and T. Spencer, *Commun. Math. Phys.* **101**, 21 (1985).
- ⁴N. F. Mott, *Metal-Insulator Transitions* (Taylor & Francis, London, 1990).
- ⁵L. D. Landau, *Phys. Z. Sowjetunion* **3**, 664 (1933).
- ⁶R. Peierls, *Quantum Theory of Solids* (Oxford University Press, Oxford, 1955).
- ⁷N. Tsuda, K. Nasu, A. Yanase, and K. Siratori, *Electronic Conduction in Oxides* (Springer-Verlag, Berlin, 1991).
- ⁸A. R. Bishop and B. I. Swanson, *Los Alamos Sci.* **21**, 133 (1993).
- ⁹D. Jérôme and H. J. Schulz, *Adv. Phys.* **31**, 299 (1982).
- ¹⁰C. Weber, D. D. O'Regan, N. D. M. Hine, M. C. Payne, G. Kotliar, and P. B. Littlewood, *Phys. Rev. Lett.* **108**, 256402 (2012).
- ¹¹I. O. Maciel, N. Anderson, M. A. Pimenta, A. Hartschuh, H. Qian, M. Terrones, H. Terrones, J. Campos-Delgado, A. M. Rao, L. Novotny *et al.*, *Nature Mater.* **7**, 878 (2008).
- ¹²S. Ciuchi and S. Fratini, *Phys. Rev. Lett.* **106**, 166403 (2011).
- ¹³Z. Ristivojevic, A. Petković, P. Le Doussal, and T. Giamarchi, *Phys. Rev. Lett.* **109**, 026402 (2012).
- ¹⁴E. Abrahams, *50 Years of Anderson Localization* (World Scientific, Singapore, 2010).
- ¹⁵P. W. Anderson, *Nature (London)* **235**, 163 (1972).
- ¹⁶F. X. Bronold and H. Fehske, *Phys. Rev. B* **66**, 073102 (2002).
- ¹⁷H. Ebrahimnejad and M. Berciu, *Phys. Rev. B* **85**, 165117 (2012).
- ¹⁸M. A. Tusch and D. E. Logan, *Phys. Rev. B* **48**, 14843 (1993).
- ¹⁹V. Dobrosavljević and G. Kotliar, *Phys. Rev. Lett.* **78**, 3943 (1997).
- ²⁰K. Byczuk, W. Hofstetter, and D. Vollhardt, *Phys. Rev. Lett.* **94**, 056404 (2005).
- ²¹A. Farhoodfar, R. J. Gooding, and W. A. Atkinson, *Phys. Rev. B* **84**, 205125 (2011).
- ²²D. Tanasković, V. Dobrosavljević, E. Abrahams, and G. Kotliar, *Phys. Rev. Lett.* **91**, 066603 (2003).
- ²³S. Chiesa, P. B. Chakraborty, W. E. Pickett, and R. T. Scalettar, *Phys. Rev. Lett.* **101**, 086401 (2008).
- ²⁴S. R. White, *Phys. Rev. Lett.* **69**, 2863 (1992).
- ²⁵P. Schmitteckert, T. Schulze, C. Schuster, P. Schwab, and U. Eckern, *Phys. Rev. Lett.* **80**, 560 (1998).
- ²⁶S. Nishimoto and T. Shirakawa, *Phys. Rev. B* **81**, 113105 (2010).
- ²⁷D. M. Edwards, *Physica B* **378–380**, 133 (2006).
- ²⁸A. Alvermann, D. M. Edwards, and H. Fehske, *Phys. Rev. Lett.* **98**, 056602 (2007).
- ²⁹M. Berciu and H. Fehske, *Phys. Rev. B* **82**, 085116 (2010).
- ³⁰G. Wellein, H. Fehske, A. Alvermann, and D. M. Edwards, *Phys. Rev. Lett.* **101**, 136402 (2008).
- ³¹S. Ejima, G. Hager, and H. Fehske, *Phys. Rev. Lett.* **102**, 106404 (2009).
- ³²E. Jeckelmann and S. R. White, *Phys. Rev. B* **57**, 6376 (1998).
- ³³E. Jeckelmann and H. Fehske, *Riv. Nuovo Cimento* **30**, 259 (2007).
- ³⁴E. Abrahams, P. W. Anderson, D. C. Licciardello, and T. V. Ramakrishnan, *Phys. Rev. Lett.* **42**, 673 (1979).
- ³⁵B. Kramer and A. Mac Kinnon, *Rep. Prog. Phys.* **56**, 1469 (1993).
- ³⁶R. Berkovits, *Phys. Rev. Lett.* **108**, 176803 (2012).
- ³⁷T. Giamarchi and H. J. Schulz, *Phys. Rev. B* **37**, 325 (1988).
- ³⁸M. Okumura, S. Yamada, N. Taniguchi, and M. Machida, *Phys. Rev. Lett.* **101**, 016407 (2008).
- ³⁹F. Woynarovich and H. P. Eckerle, *J. Phys. A* **20**, L97 (1987).
- ⁴⁰C. J. Hamer, C. R. W. Quispel, and M. T. Batchelor, *J. Phys. A* **20**, 5677 (1987).
- ⁴¹Y. Imry and S. Ma, *Phys. Rev. Lett.* **35**, 1399 (1975).

Charge-density-wave formation in the Edwards fermion-boson model at one-third band filling

Satoshi Ejima* and Holger Fehske†

Institut für Physik, Ernst-Moritz-Arndt-Universität Greifswald, 17489 Greifswald, Germany

(Received September 26, 2013)

We examine the ground-state properties of the one-dimensional Edwards spinless fermion transport model by means of large-scale density-matrix renormalization-group calculations. Determining the single-particle gap and the Tomonaga-Luttinger liquid parameter (K_ρ) at zero temperature, we prove the existence of a metal-to-insulator quantum phase transition at one-third band filling. The insulator—established by strong correlation in the background medium—typifies a charge density wave (CDW) that is commensurate with the band filling. $K_\rho = 2/9$ is very small at the quantum critical point, and becomes $K_\rho^{\text{CDW}} = 1/9$ in the infinitesimally doped three-period CDW, as predicted by the bosonization approach.

KEYWORDS: Edwards model, metal-insulator transition, DMRG

1. Introduction

Strong correlations can affect the transport properties of low-dimensional systems to the point of insulating behavior. Prominent examples are broken symmetry states of quasi one-dimensional (1D) metals, where charge- or spin-density waves brought about by electron-phonon or by electron-electron interactions [1]. These interactions can be parametrized by bosonic degrees of freedom, with the result that the fermionic charge carrier becomes “dressed” by a boson cloud that lives in the particle’s immediate vicinity and takes an active part in its transport [2]. A paradigmatic model describing quantum transport in such a “background medium” is the Edwards fermion-boson model [3, 4]. The model exhibits a surprisingly rich phase diagram including metallic repulsive and attractive Tomonaga-Luttinger-liquid (TLL) phases, insulating charge-density-wave (CDW) states [5–8], and even regions where phase separation appears [9].

The part of the Edwards Hamiltonian that accommodates boson-affected transport is

$$H_{fb} = -t_b \sum_{\langle i,j \rangle} f_j^\dagger f_i (b_i^\dagger + b_j). \quad (1)$$

Every time a spinless fermion hops between nearest-neighbor lattice sites i and j it creates (or absorbs) a local boson b_j^\dagger (b_i). As to $H_b = \omega_0 \sum_i b_i^\dagger b_i$ this enhances (lowers) the energy of the background by ω_0 . Moving in one direction only, the fermion creates a string of local bosonic excitations that will finally immobilize the particle (just as for a hole in a classical Néel background). Because of quantum fluctuations any distortion in the background should be able to relax however. Incorporating this effect the entire Edwards model takes the form

$$H = H_{fb} - \lambda \sum_i (b_i^\dagger + b_i) + H_b, \quad (2)$$

*E-mail address: ejima@physik.uni-greifswald.de

†E-mail address: fehske@physik.uni-greifswald.de

where λ is the relaxation rate. The unitary transformation $b_i \rightarrow b_i + \lambda/\omega_0$ replaces the second term in (2) by a direct, i.e., boson-unaffected, fermionic hopping term $H_f = -t_f \sum_{\langle i,j \rangle} f_j^\dagger f_i$. In this way the particle can move freely, but with a renormalized transfer amplitude $t_f = 2\lambda t_b/\omega_0$. We note that coherent propagation of a fermion is possible even in the limit $\lambda = t_f = 0$, by means of a six-step vacuum-restoring hopping being related to an effective next-nearest-neighbor transfer. This process takes place on a strongly reduced energy scale (with weight $\propto t_b^6/\omega_0^5$), and is particularly important in the extreme low-density regime ($n^f \ll 1$), where the Edwards model mimics the motion of a single hole in a quantum antiferromagnet [10].

At low-to-intermediate particle densities $n^f \leq 0.3$ the 1D Edwards model system stays metallic. If here the fermions couple to slow (low-energy) bosons ($\omega_0/t_b \lesssim 1$), the primarily repulsive TLL becomes attractive, and eventually even phase segregation into particle-enriched and particle-depleted regions takes place at small λ [9]. No such particle attraction is observed, however, for densities $0.3 \lesssim n^f \leq 0.5$. Perhaps, in this regime, the repulsive TLL might give way to an insulating state with charge order if the background is “stiff”, i.e., for small λ/t_b and fast (high-energy) bosons $\omega_0/t_b > 1$. So far, a correlation induced TLL-CDW metal-insulator transition like that has been proven to exist for the half-filled band case ($n^f = 0.5$) [5, 6]. In the limit $\omega_0/t_b \gg 1 \gg \lambda/t_b$ the Edwards model can be approximated by an effective t - V model, $H_{tV} = H_f + V \sum_i n_i^f n_{i+1}^f$, with nearest-neighbor Coulomb interaction $V = t_b^2/\omega_0$ [11]. The spinless fermion t - V model on his part can be mapped onto the exactly solvable XXZ -Heisenberg model, which exhibits a Kosterlitz-Thouless [12] (TLL-CDW) quantum phase transition at $(V/t_f)_c = 2$, i.e., at $(\lambda/t_b)_{tV,c} = 0.25$. The critical value is in reasonable agreement with that obtained for the half-filled Edwards model in the limit $\omega_0 \rightarrow \infty$: $(\lambda/t_b)_c \simeq 0.16$ [6]. At lower densities, however, for example at $n^f = 1/3$, a CDW instability occurs in 1D t - V -type models only if (substantially large) longer-ranged Coulomb interactions were included, such as a next-nearest-neighbor term V_2 [13].

In order to clarify whether the 1D Edwards model by itself shows a metal-to-insulator transition off half-filling at large ω_0 and what is the reason for the absence of phase separation for small ω_0 , in this work, we investigate the model at one-third band filling, using the density matrix renormalization group (DMRG) technique [14] combined with the pseudo-site approach [15, 16] and a finite-size analysis. This allows us to determine the ground-state phase diagram of the 1D Edwards model in the complete parameter range.

2. Theoretical approach

To identify the quantum phase transition between the metallic TLL and insulating CDW phases we inspect—by means of DMRG—the behavior of the local fermion/boson densities $n_i^{f/b}$, of the single-particle gap Δ_c , and of the the TLL parameter K_ρ . In doing so, we take into account up to four pseudo-sites, and ensure that the local boson density of the last pseudo-site is always less than 10^{-7} for all real lattice sites i . We furthermore keep up to $m = 1200$ density-matrix eigenstates in the renormalization process to guarantee a discarded weight smaller than 10^{-8} .

For a finite system with L sites the single-particle charge gap is given by

$$\Delta_c(L) = E(N+1) + E(N-1) - 2E(N), \quad (3)$$

where $E(N)$ and $E(N \pm 1)$ are the ground-state energies in the N - and $(N \pm 1)$ -particle sectors, respectively. In the CDW state Δ_c is finite, but will decrease exponentially across the MI transition point if the transition is of Kosterlitz-Thouless type as for the t - V model. This hampers an accurate determination of the TLL-CDW transition line.

In this respect the TLL parameter K_ρ is more promising. Here bosonization field theory predicts how K_ρ should behave at a quantum critical point. In order to determine K_ρ accurately by DMRG,

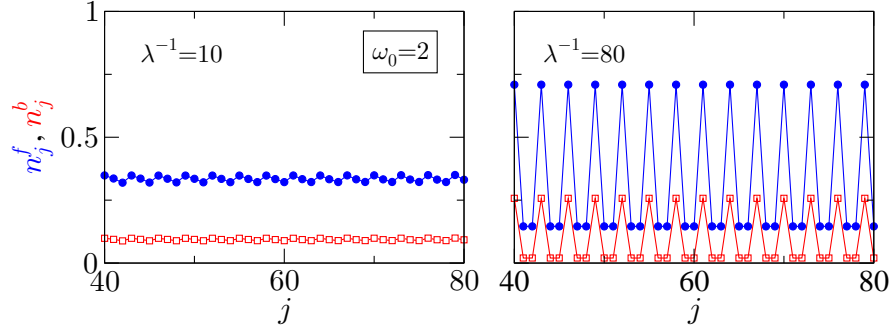


Fig. 1. (Color online) Local fermion (n_j^f – filled blue circles) and boson (n_j^b – open red squares) densities in the central part of an Edwards model chain with $L = 120$ sites and OBC. DMRG data shown in the left-hand (right-hand) panel indicate a homogeneous TLL (CDW) state for $n^f = 1/3$ and $\lambda^{-1} = 10$ ($\lambda^{-1} = 80$), where $\omega_0 = 2$. In what follows all energies are measured in units of t_b .

we first have to calculate the static (charge) structure factor

$$S_c(q) = \frac{1}{L} \sum_{j,l} e^{iq(j-l)} \langle (f_j^\dagger f_j - n)(f_l^\dagger f_l - n) \rangle, \quad (4)$$

where the momenta $q = 2\pi m/L$ with integers $0 < m < L$ [17]. The TLL parameter K_ρ is proportional to the slope of $S_c(q)$ in the long-wavelength limit $q \rightarrow 0^+$:

$$K_\rho = \pi \lim_{q \rightarrow 0} \frac{S_c(q)}{q}. \quad (5)$$

For a spinless-fermion system with one-third band filling, the TLL parameter should be $K_\rho^* = 2/9$ at the metal-insulator transition point. For an infinitesimally doped three-period CDW insulator, on the other hand, bosonization theory yields $K_\rho^{\text{CDW}} = 1/9$ [18, 19].

3. Numerical results

First evidence for the formation of a CDW state in the one-third filled Edwards model comes from the spatial variation of the local densities of fermions $n_i^f \equiv \langle f_i^\dagger f_i \rangle$ and bosons $n_i^b \equiv \langle b_i^\dagger b_i \rangle$. Fixing $\omega_0 = 2$, we find a modulation of the particle density commensurate with the band filling factor 1/3 for very small $\lambda = 0.0125$ (see Fig. 1, right panel). Thereby, working with open boundary conditions (OBC), one of the three degenerate ground states with charge pattern (... 100100100 ...), (... 010010010 ...), or (... 001001001 ...) is picked up by initializing the DMRG algorithm. As a result the CDW becomes visible in the local density. Note that also in the metallic state, which is realized already for λ 's as small as 0.1 (cf. Fig. 1, left panel), a charge modulation is observed. Those, however, can be attributed to Friedel oscillations, which are caused by the OBC and will decay algebraically in the central part of the chain as L increases. Thus, for $\omega_0 = 2$, a metal-to-insulator transition is expected to occur in between $10 < \lambda^{-1} < 80$.

To localize the point where—at given ω_0 and λ —the quantum phase transition takes place, we first compute the single-particle gap Δ_c and TLL charge exponent K_ρ for finite chains with up to $L = 150$ sites and OBC. Then we perform a finite-size scaling as illustrated for K_ρ by Fig. 2, left panel. Here open symbols give K_ρ as a function of the inverse system size L^{-1} . The DMRG data can be extrapolated to the thermodynamic limit by third-order polynomial functions. Decreasing λ

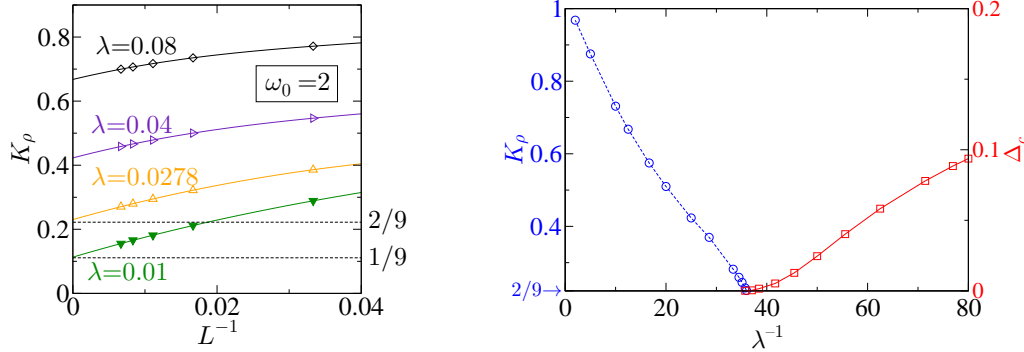


Fig. 2. (Color online) Left panel: $K_\rho(L)$ in the one-third filled Edwards model as a function of the inverse system size for various values of λ at $\omega_0 = 2$ (open symbols). The finite-size interpolated DMRG data at the metal-insulator transition point and for the infinitesimally doped CDW insulator [$n^f = 1/3 - 1/L$ (filled symbols)] are in perfect agreement with the bosonization results $K_\rho^* = 2/9$ and $K_\rho^{\text{CDW}} = 1/9$, respectively. Right panel: $L \rightarrow \infty$ extrapolated K_ρ (circles) and Δ_c (squares), as functions of λ^{-1} for $\omega_0 = 2$, indicate a TLL-CDW transition at $\lambda^{-1} \sim 36$.

at fixed $\omega_0 = 2$ the values of K_ρ decreases too and becomes equal to $K_\rho^* = 2/9$ at the Kosterlitz-Thouless transition point $(\lambda^{-1})_c \sim 36$; see Fig. 2, right panel. For $\lambda^{-1} > 36$ the system embodies a $2k_F$ -CDW insulator with finite charge gap Δ_c . Furthermore, calculating $K_\rho(L)$ for $N = L/3 - 1$ particles, we can show that the infinitesimally doped CDW insulator has $K_\rho^{\text{CDW}} = 1/9$ at $n^f = 1/3$. Deep in the CDW phase, K_ρ approaches $1/9$ in the thermodynamic limit [cf. the $\lambda = 0.01$ data (filled symbols) in the left panel of Fig. 2].

Our final result is the ground-state phase diagram of the one-third filled Edwards model shown in Fig. 3. The TLL-CDW phase boundary is derived from the $L \rightarrow \infty$ extrapolated K_ρ values. Within the TLL region $2/9 < K_\rho < 1$. Of course, the TLL appears at large λ , when any distortion of the background medium readily relaxes ($\propto \lambda$), or, in the opposite limit of small λ , when the rate of the bosonic fluctuations ($\propto \omega_0^{-1}$) is sufficiently high. Below $\omega_{0,c} \simeq 0.93$ the metallic state is stable $\forall \lambda$, because the background medium is easily disturbed and therefore does not hinder the particle's motion much. Note that this value is smaller than the corresponding one for the half-filled band case, where $\omega_{0,c} \simeq 1.38$. On the other hand, the $2k_F$ -CDW phase with $\Delta_c > 0$ and long-range order appears, at half-filling, for small λ and by trend large ω_0 (see dashed lines); $\lambda_c \simeq 0.16$ for $\omega_0 \rightarrow \infty$ [6]. Interestingly, for $n^f = 1/3$, we observe that the CDW will be suppressed again if the energy of a background distortion becomes larger than a certain λ -dependent value (see Fig. 3, left panel). In stark contrast to the half-filled band case, at $n^f = 1/3$, it seems that the TLL is stable $\forall \lambda$, when $\omega_0 \rightarrow \infty$. This is because in this limit in the corresponding one-third filled t - V model not only a nearest-neighbor Coulomb repulsion V but also a substantial next-nearest-neighbor interaction V_2 is needed to drive the TLL-to-CDW transition [13]. Again in the limit $\omega_0/t_b \gg 1 \gg \lambda/t_b$, the Edwards model at one-third filling can be described by the effective t - V - V_2 model with $V = 2t_b^2/3\omega_0$ and $V_2 = 2t_b^4/\omega_0^3$, i.e., $V_2/t_f = t_b^3/\lambda\omega_0^2$, which clearly explains the absence of the CDW phase for $\omega_0 \gg 1$.

4. Conclusions

To summarize, using an unbiased numerical (density matrix renormalization group) technique, we investigated the one-dimensional fermion-boson Edwards model at one-third band filling. We proved that the model displays a metal-insulator quantum phase transition induced by correlations in

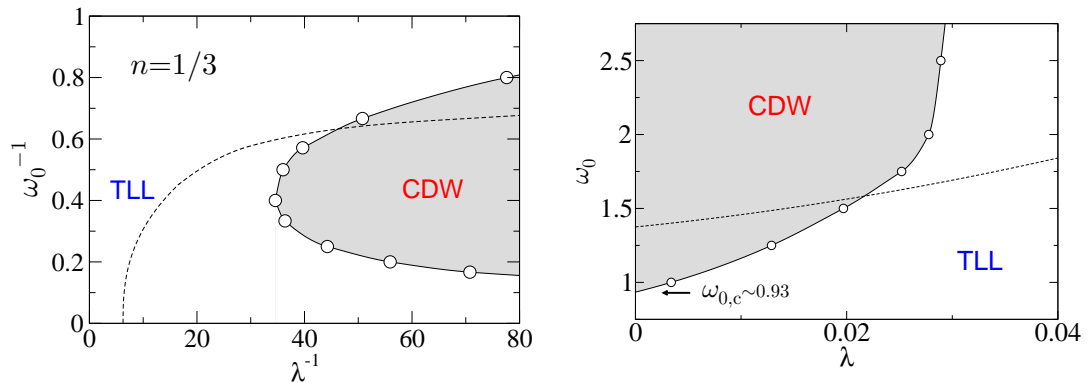


Fig. 3. (Color online) DMRG ground-state phase diagram of the 1D Edwards model at one-third band filling, showing the stability regions of metallic TLL and insulating CDW phases in the λ^{-1} - ω_0^{-1} (left panel) and λ - ω_0 (right panel) plane. The dashed line denotes the MI transition points at half band filling from Ref. [6].

the background medium. The metallic phase is a Tomonaga-Luttinger liquid with $2/9 < K_\rho < 1$. The insulator represents a $2k_F$ charge density wave with $K_\rho^{\text{CDW}} = 1/9$ deep inside the long-range ordered state. Performing a careful finite-size scaling analysis, the phase transition point can be precisely determined by K_ρ . If the background medium is stiff, we can conclude—by analogy with the ground-state phase diagram of the one-third filled t - V - V_2 model—that the Edwards model incorporates the effects of both effective nearest-neighbor and next-nearest-neighbor Coulomb interactions between the fermionic charge carriers. The effect of the latter one is reduced when the energy of a local distortion in the background is very large, which maintains metallic behavior—different from the half-filled band case—even for weak boson relaxation.

Acknowledgements

The authors would like to thank S. Nishimoto for useful discussions. This work was supported by the Deutsche Forschungsgemeinschaft through SFB 652, project B5.

References

- [1] G. Grüner: *Density Waves in Solids* (Addison Wesley, Reading, MA, 1994).
- [2] M. Berciu: *Physics* **2** (2009) 55.
- [3] D. M. Edwards: *Physica B* **378-380** (2006) 133.
- [4] A. Alvermann, D. M. Edwards, and H. Fehske: *Phys. Rev. Lett.* **98** (2007) 056602.
- [5] G. Wellein, H. Fehske, A. Alvermann, and D. M. Edwards: *Phys. Rev. Lett.* **101** (2008) 136402.
- [6] S. Ejima, G. Hager, and H. Fehske: *Phys. Rev. Lett.* **102** (2009) 106404.
- [7] S. Ejima and H. Fehske: *Phys. Rev. B* **80** (2009) 155101.
- [8] H. Fehske, S. Ejima, G. Wellein, and A. R. Bishop: *J. Phys.: Conference Series* **391** (2012) 012152.
- [9] S. Ejima, S. Sykora, K. W. Becker, and H. Fehske: *Phys. Rev. B* **86** (2012) 155149.
- [10] D. M. Edwards, S. Ejima, A. Alvermann, and H. Fehske: *J. Phys. Condens. Matter* **22** (2010) 435601.
- [11] S. Nishimoto, S. Ejima, and H. Fehske: *Phys. Rev. B* **87** (2013) 045116.
- [12] J. M. Kosterlitz and D. J. Thouless: *J. Phys. C* **6** (1973) 1181.
- [13] P. Schmitteckert and R. Werner: *Phys. Rev. B* **69** (2004) 195115.
- [14] S. R. White: *Phys. Rev. Lett.* **69** (1992) 2863.
- [15] E. Jeckelmann and S. R. White: *Phys. Rev. B* **57** (1998) 6376.
- [16] E. Jeckelmann and H. Fehske: *Rivista del Nuovo Cimento* **30** (2007) 259.
- [17] S. Ejima, F. Gebhard, and S. Nishimoto: *Europhys. Lett.* **70** (2005) 492.

- [18] H. J. Schulz: in *Strongly Correlated Electronic Materials*, ed. K. S. Bedell, Z. Wang, and D. E. Meltzer (Addison-Wesley, Reading, MA, 1994), pp. 187; cond-mat/9412036.
- [19] T. Giamarchi: *Quantum Physics in One Dimension* (Clarendon Press, Oxford, 2003).

Phase separation in the Edwards model

S. Ejima,¹ S. Sykora,² K. W. Becker,³ and H. Fehske¹

¹*Institut für Physik, Ernst-Moritz-Arndt-Universität Greifswald, 17487 Greifswald, Germany*

²*Institute for Theoretical Solid State Physics, IFW Dresden, 01069 Dresden, Germany*

³*Institut für Theoretische Physik, Technische Universität Dresden, 01062 Dresden, Germany*

(Received 13 August 2012; published 25 October 2012)

The nature of charge transport within a correlated background medium can be described by spinless fermions coupled to bosons in the model introduced by Edwards. Combining numerical density matrix renormalization group and analytical projector-based renormalization methods, we explore the ground-state phase diagram of the Edwards model in one dimension. Below a critical boson frequency, any long-range order disappears and the system becomes metallic. If the charge carriers are coupled to slow quantum bosons, the Tomonaga-Luttinger liquid is attractive and finally makes room for a phase separated state, just as in the t - J model. The phase boundary separating the repulsive from the attractive Tomonaga-Luttinger liquid is determined from long-wavelength charge correlations, whereas fermion segregation is indicated by a vanishing inverse compressibility. On approaching phase separation, the photoemission spectra develop strong anomalies.

DOI: 10.1103/PhysRevB.86.155149

PACS number(s): 71.10.Hf, 71.30.+h, 71.10.Fd

I. PROBLEM

The Edwards fermion-boson model^{1,2} constitutes a paradigmatic model for the theoretical description of quantum transport in solids. Charge transport normally takes place in the presence of some background medium.³ Examples for such a “background” could be a spin-, charge-, or orbital-ordered lattice,^{4,5} but also a sequence of chemical side groups along the transport path, a deformable medium, or even a heat bath might be possible. In all these cases, the transfer of the charge carriers will be strongly influenced by fluctuations, which may exist in the background medium. The other way around, the properties of the background are quite often determined by the motion of the particle itself.

Correlations inherent in such a complex interactive system are mimicked by a boson-affected hopping of spinless fermionic particles in the Edwards model. It reads

$$H = -t_b \sum_{(i,j)} f_j^\dagger f_i (b_i^\dagger + b_j) - \lambda \sum_i (b_i^\dagger + b_i) + \omega_0 \sum_i b_i^\dagger b_i. \quad (1)$$

Every time a fermion $f_i^{(\dagger)}$ hops, it creates or absorbs a boson $b_i^{(\dagger)}$ of energy ω_0 at the sites it leaves or enters. Such an excitation or deexcitation corresponds to a local “distortion” of the background. Because of quantum fluctuations, the distortions are able to relax ($\propto \lambda$). The physically most interesting regimes in this setting are those of vanishing fermion density and of a half-filled band, representing doped Mott insulators, polaronic organics, and charge-density-wave (CDW) systems^{6–9} with possible relevance to high- T_c superconductors,^{10,11} colossal magnetoresistive manganites,^{12–14} carbon nanotubes,^{15,16} graphene,^{17,18} and CDW transition metal complexes,^{19,20} respectively. However, the Edwards model also reveals fascinating properties over the whole density range.

On these grounds, the main goal of the present work is to pinpoint the ground-state phase diagram of the one-dimensional (1D) Edwards model as a function of the band filling n . Thereby, we demonstrate that this model indeed captures a number of very interesting phenomena, including,

e.g., electronic phase separation (PS). To obtain reliable information about the ground-state and spectral properties of the model in the thermodynamic limit, we employ numerical pseudosite density-matrix renormalization group (DMRG) and dynamical DMRG (DDMRG) techniques (supplemented by a careful finite-size scaling procedure; for details, see Refs. 9 and 21–24), in combination with the analytical projective renormalization method (PRM).^{25,26}

So far the 1D Edwards model has been solved exactly by numerical approaches for two cases.^{22,24,27} The first, in no way trivial, case concerns just a single particle on an infinite lattice, where—depending on the model parameters—transport appears to be quasifree, diffusive, or boson-assisted.^{6,28} When strong correlations develop at small λ and large ω_0 , the background becomes “stiff” and the spinless particle’s motion resembles those of a hole in an antiferromagnetic spin background,^{29,30} as known from the t - J model. Interestingly, the Edwards model allows for so-called Trugman paths³¹ in a 1D setting (Trugman paths usually unwind the string of misaligned spins a mobile hole leaves behind in two dimensions). The second case is half-filling, $n = 1/2$. Here a metal-insulator transition has been proven to exist: For small λ and large ω_0 , the repulsive Tomonaga-Luttinger liquid (TLL) gives way to a CDW.^{7,8} The CDW constitutes a few-boson state that typifies a Mott-Hubbard insulator rather than a Peierls state (normally established by the softening of a boson mode).

II. THEORETICAL RESULTS

A. Ground-state properties

The situation at finite density n ($n \neq 1/2$) is much less understood. By analogy with the t - J model, one might expect that the system is metallic for $0 < n < 1/2$, at least if the background is not too stiff. If so, the next question will be whether the Edwards model might support the pairing of electrons in a certain parameter regime (λ, ω_0). Apparently a second electron, following the path of a first one, can take advantage of the background excitations (bosons) left behind

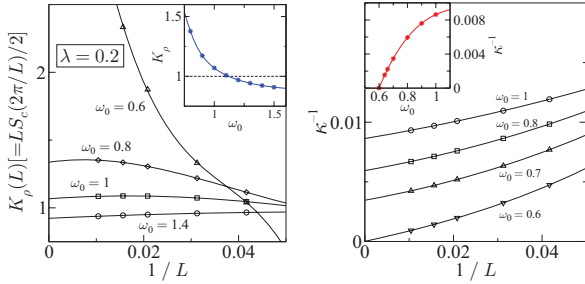


FIG. 1. (Color online) Finite-size scaling of the TLL parameter K_ρ (left panel) and inverse compressibility κ^{-1} (right panel) for the 1D Edwards model with $\lambda = 0.2$ at $n = 1/8$. Insets show the variation with ω_0 of the $L \rightarrow \infty$ extrapolated values. Results are obtained by DMRG for a lattice with L sites and OBC. In all DMRG runs, we take into account up to $n_b = 4$ bosonic pseudospins and determine n_b by the requirement that the local boson density of the last pseudospin is less than 10^{-6} for all j . Using selectively $n_b = 5$, we controlled that convergence is truly achieved. Furthermore, we keep up to $m = 1200$ density-matrix eigenstates in the renormalization steps to ensure that the discarded weight is smaller than 10^{-8} .

by the first electron. This acts like an effective attractive interaction. If this attraction completely dominates the kinetic energy, the system might even phase-separate into particle-enriched and particle-depleted regions.³² Since the Edwards model is not particle-hole symmetric, it is a moot point whether a corresponding hole pairing mechanism is at play also for $1/2 < n < 1$.

To address these problems, we analyze the charge correlations existing in the ground state of the 1D Edwards model. First, we calculate the charge structure factor

$$S_c(q) = \frac{1}{L} \sum_{j,l} e^{iq(j-l)} \langle (f_j^\dagger f_j - n)(f_l^\dagger f_l - n) \rangle \quad (2)$$

for a system with N fermions, L sites, and open boundary conditions (OBCs). So the particle density is $n = N/L$ and the momenta $q = 2\pi s/L$ with integers $0 < s < L$. The TLL charge exponent is proportional to the slope of $S_c(q)$ in the long-wavelength limit $q \rightarrow 0^+$ (cf. Refs. 33 and 34):

$$K_\rho = \pi \lim_{q \rightarrow 0} \frac{S_c(q)}{q}. \quad (3)$$

Then, $K_\rho > 1$ ($K_\rho < 1$) characterizes an attractive (repulsive) TLL for our spinless fermion transport model (1), and $K_\rho = 1/2$ will define a metal-insulator transition point at $n = 1/2$.³⁵ That the finite-size scaling of $S_c(q)$ and K_ρ works well has been demonstrated for the half-filled band case.⁸ Secondly, in order to comprise potential PS, we determine the finite-size equivalent of the charge compressibility,³⁶

$$\kappa = \frac{L}{N^2} \left[\frac{E_0(N+2) + E_0(N-2) - 2E_0(N)}{4} \right]^{-1}, \quad (4)$$

with $E_0(N)$ being the ground-state energy for N electrons on L sites. An infinite compressibility signals the formation of a PS state.

Figure 1 demonstrates that all this works in practice. Exemplarily choosing $n = 1/8$ and $\lambda = 0.2$, we show how the

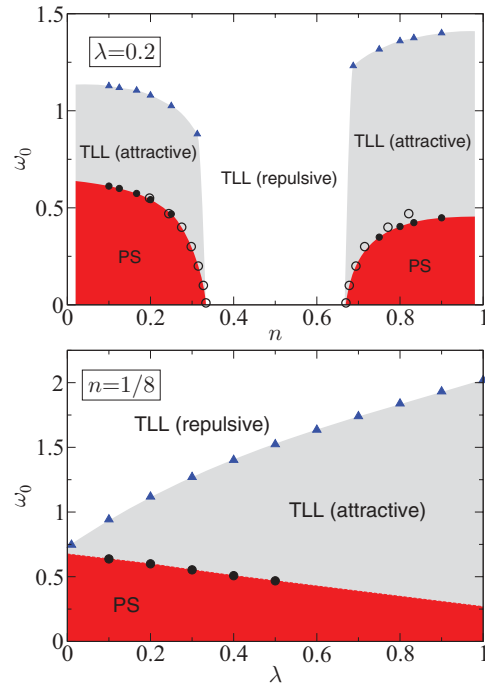


FIG. 2. (Color online) Ground-state phase diagram of the 1D Edwards model, showing repulsive TLL ($K_\rho < 1$), attractive TLL ($K_\rho > 1$), and PS ($\kappa^{-1} = 0$) regions. The phase boundaries were obtained by DMRG (filled symbols) in the course of a careful finite-size scaling analysis and for the infinite system directly by PRM (open symbols). The upper panel displays the phase diagram as a function of n , varying ω_0 at fixed $\lambda = 0.2$; the lower panel gives the phase diagram in the λ - ω_0 plane for fixed density $n = 1/8$.

TLL exponent K_ρ and the inverse compressibility κ^{-1} scale with increasing system size at various ω_0 . The transition point between a repulsive TLL—obviously realized at $\omega_0 > \omega_{0,c1}$ when excitations of the background are energetically rather costly—and an attractive TLL at smaller ω_0 can be read off from the inset [depicting the extrapolations $K_\rho(L \rightarrow \infty)$] to be $\omega_{0,c1}(\lambda = 0.2) \simeq 1.118$. Reducing ω_0 further, in the attractive TLL phase, a dramatic increase in K_ρ is observed at $\omega_{0,c2} \simeq 0.6$. Our inverse compressibility data indicate that at this point, the attraction among the particles becomes so strong that the system shows PS, i.e., $\kappa^{-1} = 0$ for $\omega_0 < \omega_{0,c2}$.

Proceeding in the same manner for different values of n and λ , and, respectively, ω_0 , we can map out the phase diagram of the 1D Edwards model. The outcome is displayed in Fig. 2. Let us first consider the case of a not too small boson relaxation ($\propto \lambda$), which ensures that the system is metallic for large ω_0 in the whole density regime. Then, as the upper panel of Fig. 2 shows, depending on n we find up to three different regimes: For small and large particle densities, a repulsive TLL, an attractive TLL, and a PS state appear in sequence as the energy of the bosons is lowered. In contrast, around half-filling only the repulsive TLL exists. At this point, we would like to remind the reader that at half-filling, for smaller values of λ ($\lambda < \lambda_c$), a CDW is formed for $\omega_0 > \omega_{0,c}$.⁸ Our unbiased DMRG calculations give no evidence for any other phases. Note that

the behavior in the low-density regime is consistent with what is found for the 1D t - J model,^{36,37} where the holes correspond to the spinless fermions in the Edwards model. As mentioned before, the phase diagram is not symmetric with respect to $n = 1/2$. This is because the hopping of a hole (missing electron) to a neighboring site creates in the Edwards model a boson at the arrival site and not on the departure site, as in the motion of a single particle. Since this boson can be destroyed immediately when the hole makes a further hop, there is no string effect and a few holes propagate more easily than a few electrons. Hence the background at fixed ω_0 and λ appears to be less stiff for $n \lesssim 1$ than for $n \gtrsim 0$ and, as a result, the boundary between the repulsive and attractive TLL is shifted to larger values of $\omega_{0,c1}$. Contrariwise, since carriers will be less mobile in a state with charge separation, the boundary between the attractive TLL and the PS state $\omega_{0,c2}$ is shifted to smaller values if one compares the corresponding results at high and low carrier density.

We next consider a fixed particle density $n = 1/8$ and track the phase boundaries in the λ - ω_0 plane; see the lower panel of Fig. 2. The repulsive TLL established for large ω_0 is strongly renormalized if the ability of the background to relax is low. For example, we find $K_\rho = 0.527$ for $\omega_0 = 2$ at $\lambda = 0.01$. Lowering ω_0 for such a stiff background, the transition to the PS state happens almost instantaneously with a narrow intervening attractive TLL state; at $\lambda = 0.01$ we have $\omega_{0,c1} \simeq 0.747$ and $\omega_{0,c2} \simeq 0.672$. If we fix, on the other hand, $\omega_0 = 2$ and increase λ , we observe a strong enhancement of K_ρ in the interval $0 < \lambda < 0.3$ ($K_\rho = 0.767, 0.879$, and 0.932 for $\lambda = 0.1, 0.2$, and 0.3 , respectively), followed by a very gradual increase until the transition to the attractive TLL takes place at about $\lambda_{c1} \simeq 1$. Obviously, the region where the attractive TLL (PS state) constitutes the ground state expands (shrinks) as λ gets larger, which can be traced back to the subtle competition between kinetic energy and charge segregation effects.

To gain deeper insight into the different mechanisms at play, we analyze the variation of the local fermion [$n_j^f = \langle f_j^\dagger f_j \rangle$] and boson [$n_j^b = \langle b_j^\dagger b_j \rangle$] densities in real space. In Fig. 3, we show both density profiles for $n = 1/8$ and characteristic values of λ and ω_0 , implementing repulsive TLL, attractive TLL, and PS states. In the metallic regime, the OBCs lead to Friedel oscillations in the particle density. These oscillations are especially pronounced for the repulsive TLL [Fig. 3(a)], and they will be even stronger for $\omega_0 = 2$ (not shown), where the number and fluctuations of the bosons is reduced. Note that the Friedel oscillations caused by the OBC will be algebraically reduced if we move for very large systems toward the central part of the chain. If we enter the attractive TLL regime by increasing λ at fixed ω_0 , the Friedel oscillation will be smeared out [Fig. 3(b)]. Thereby, the number of oscillations stays constant, which means that a pairing of electrons does not occur. This is an important difference from the spinful 1D t - J model, where a recent DMRG study reveals that the number of Friedel oscillations is halved (by increasing J), corresponding to half the number of particles, which indicates pairing.³⁷ Next, lowering ω_0 to a point where PS sets in, the particle density oscillations vanish; see Fig. 3(c). There, just above the PS boundary, no evidence is found for the clustering of multiple particles in several groups. This agrees with the findings for the 1D t - J model.³⁷ Once we are deep inside the

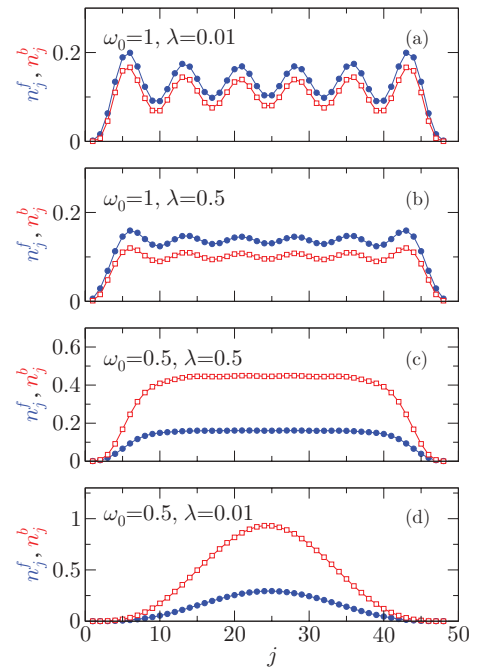


FIG. 3. (Color online) Local particle (filled circles) and boson (open squares) densities for the 1D Edwards model with $n = 1/8$, calculated for a 48-site system with OBC at various λ and ω_0 .

PS region, a density distribution results, where a single island of particles at the central part of the system appears, leaving a sizable number of almost empty sites at both ends of the chain [see Fig. 3(d)]. Looking at the bosonic degrees of freedom, we see that the strong attraction among these particles is mediated by a boson cloud covering the electron-rich region. As a result, the kinetic fluctuations will be strongly quenched.

It is all but impossible to comprise by DMRG the large number of bosons and the strong bosonic fluctuations, which appear at still smaller ω_0 in the Edwards model, simply because the dimension of the Hilbert space increases dramatically. To access the low- ω_0 regime and reconfirm the DMRG phase boundaries obtained for the 1D Edwards model at larger values of ω_0 , we employ the analytical PRM approach.²⁵ The basic idea of the PRM approach is to construct—performing a sequence of discrete unitary transformations and eliminating all transitions with energy larger than a given cutoff energy—an effective noninteracting Hamiltonian \tilde{H} with renormalized parameters (in the limit of vanishing cutoff energy). For the metallic state of the Edwards model, in momentum space, it takes the form

$$\tilde{H} = \sum_k \tilde{\epsilon}_k f_k^\dagger f_k + \sum_q \tilde{\omega}_q b_q^\dagger b_q + \tilde{E}, \quad (5)$$

where the renormalization equations for $\tilde{\epsilon}_k$ and $\tilde{\omega}_q$ have been derived in Ref. 26 (for the half-filled band case). To fix the boundary between metallic and PS states, we (i) solve the renormalization equations at a given E_F in the TLL phase, (ii) determine the corresponding fermion density n , and (iii) slightly vary E_F (to get closer to the PS instability), determine n , and repeat the whole procedure self-consistently

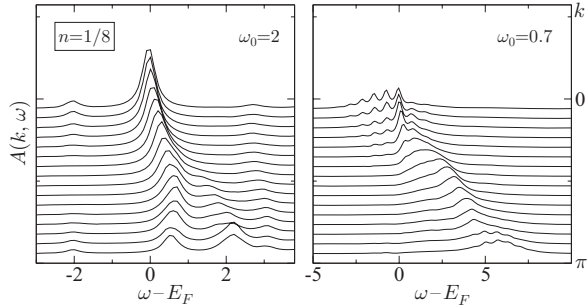


FIG. 4. Line-shape of the single-particle spectral function $A(k, \omega)$ for the 1D Edwards model with $\lambda = 0.2$ at $n = 1/8$. Results are obtained by DDMRG for a 16-site chain with quasimomenta $k = \pi s/(L + 1)$, using a broadening $\eta = 0.2$.

until the functional dependence of n on E_F is established. A vanishing inverse compressibility can then be read off from a sudden jump of n under a tiny variation of E_F or, the other way around, if a plateau in the E_F versus n plot appears. The transition points, determined in the manner described, were inserted in Fig. 2 to complete the ground-state phase diagram in the n - ω_0 plane. Whenever points can be compared, we find a remarkable agreement between our DMRG and PRM data. The deviation of the PRM data at larger particle densities $n \gtrsim 0.75$ results from uncertainties in fixing the jump of n under E_F variation. Here we should trust in the DMRG phase boundary.

B. Spectral properties

Let us finally discuss the single-particle spectrum of the 1D Edwards model. The single-particle excitations associated with the injection (+) or emission (-) of an electron with wave vector k ,

$$A^\pm(k, \omega) = \sum_m |\langle \psi_m^\pm | f_k^\pm | \psi_0 \rangle|^2 \delta(\omega \mp \omega_m^\pm), \quad (6)$$

can be computed by DDMRG,^{23,24} where $f_k^+ = f_k^\dagger$, $f_k^- = f_k$, $|\psi_0\rangle$ is the ground state of an L -site system in the N -particle sector, and $|\psi_m^\pm\rangle$ denotes the m th excited states in the $(N \pm 1)$ -particle sectors with excitation energies $\omega_m^\pm = E_m^\pm - E_0$.

Within PRM, we find for the photoemission part

$$\begin{aligned} A^-(k, \omega) = & \tilde{\alpha}_k^2 \tilde{n}_k^f \delta(\omega - \tilde{\epsilon}_k) \\ & + \sum_q \tilde{\beta}_{k,q}^2 (1 + \tilde{n}_q^b) \tilde{n}_{k+q}^f \delta(\omega + \tilde{\omega}_q - \tilde{\epsilon}_{k+q}) \\ & + \sum_q \tilde{\gamma}_{k,q}^2 \tilde{n}_q^b \tilde{n}_{k-q}^f \delta(\omega - \tilde{\omega}_q - \tilde{\epsilon}_{k-q}), \end{aligned} \quad (7)$$

where \tilde{n}_q^f (\tilde{n}_q^b) are the fermion (boson) occupation numbers in momentum space calculated with the renormalized Hamiltonian \tilde{H} . The coefficients $\tilde{\alpha}_k^2$, $\tilde{\beta}_{k,q}^2$, and $\tilde{\gamma}_{k,q}^2$ follow from renormalization equations.²⁶ Taking the corresponding expression for $A^+(k, \omega)$, the sum rule $\int_{-\infty}^{\infty} d\omega [A^+(k, \omega) + A^-(k, \omega)] = 1$ is fulfilled.

Figure 4 gives the combined photoemission spectrum, $A(k, \omega) = A^+(k, \omega) + A^-(k, \omega)$, as obtained by DDMRG for quasimomenta k . In the repulsive TLL regime (left panel,

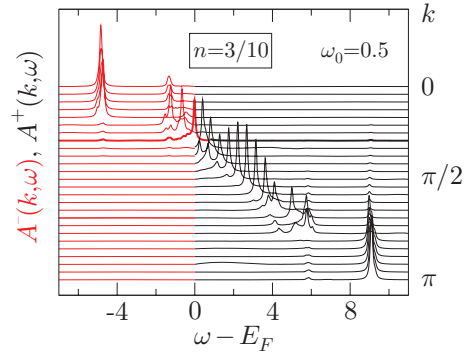


FIG. 5. (Color online) PRM (inverse) photoemission spectrum $[A^+(k, \omega), A^-(k, \omega)]$ for the Edwards model with $\lambda = 0.2$, $n = 3/10$. The bold line marks the signal at the Fermi momentum $k_F = 0.3\pi$.

$\omega_0 = 2$), we find a rather coherent signal with comparable spectral weight for all k values $k \lesssim \pi/2$. For larger k , excitations with at least one additional ω_0 boson involved become important (recall that both initial N -particle- and target $(N \pm 1)$ -particle states are multiboson states with a momentum being the total momentum of electrons and bosons). The spectrum in the attractive TLL phase (right panel, $\omega_0 = 0.7$) shows a sharp absorption signal in the vicinity of k_F only. Here the (inverse) photoemission spectrum for $k < k_F$ ($k > k_F$) exhibits a few absorption maxima at multiples of the boson energy. Obviously, due to the smaller ω_0 , here the dynamics of the system becomes dominated by bosonic fluctuations.

The (inverse) photoemission close to the transition to the PS state is depicted in Fig. 5, as calculated by PRM for $\omega_0 = 0.5$. Here the almost dispersionless signal for $k \leq 0.212\pi$ ($k \geq 0.788\pi$) is a precursor of the PS instability. As we noted above, E_F does not show any variation with n if n is smaller (larger) than the lower (upper) critical density n_{c2} for PS. Since in the PRM derivation of $A^\pm(k, \omega)$ terms with two (and more) bosonic creation or annihilation operators were neglected,²⁶ the photoemission spectrum of Fig. 5 does not feature the multiboson related signatures found within a DDMRG treatment.

III. CONCLUSIONS

To summarize, the combination of analytical (PRM) and numerical (DMRG) approaches permits the precise determination of the ground-state phase diagram of the 1D Edwards model in the whole parameter regime. In the low- and high-density regions, the attraction between the particles mediated by the bosonic degrees of freedom representing the background medium might become so strong that electronic PS sets in. In the remaining region, the system realizes a TLL or, at $n = 1/2$, possibly even a truly long-range ordered CDW state. Depending on the properties of the background medium, the TLL might be attractive or repulsive. The richness of the phase diagram is remarkable. The model captures important features of Holstein, t - J , Hubbard, and Falicov-Kimball type models.^{6-9,38} Since the Edwards model is one of the simplest models for studying transport in low-dimensional systems,

an inspection of its predictions with ultracold fermion/boson quantum gases,³⁹ as, e.g., carried out for the 1D t - J model,⁴⁰ would be of great interest.

ACKNOWLEDGMENT

This work was supported by DFG through SFB 652.

- ¹D. M. Edwards, *Physica B* **378-380**, 133 (2006).
²D. M. Edwards, S. Ejima, A. Alvermann, and H. Fehske, *J. Phys.: Condens. Matter* **22**, 435601 (2010).
³M. Berciu, *Physics* **2**, 55 (2009).
⁴L. G. L. Wegener and P. B. Littlewood, *Phys. Rev. B* **66**, 224402 (2002).
⁵K. Wohlfeld, A. M. Oleś, and P. Horsch, *Phys. Rev. B* **79**, 224433 (2009).
⁶A. Alvermann, D. M. Edwards, and H. Fehske, *Phys. Rev. Lett.* **98**, 056602 (2007).
⁷G. Wellein, H. Fehske, A. Alvermann, and D. M. Edwards, *Phys. Rev. Lett.* **101**, 136402 (2008).
⁸S. Ejima, G. Hager, and H. Fehske, *Phys. Rev. Lett.* **102**, 106404 (2009).
⁹S. Ejima and H. Fehske, *Phys. Rev. B* **80**, 155101 (2009).
¹⁰L. G. Bednorz and K. A. Müller, *Z. Phys. B* **64**, 189 (1986).
¹¹E. Dagotto, *Rev. Mod. Phys.* **66**, 763 (1994).
¹²G. H. Jonker and J. H. van Santen, *Physica* **16**, 337 (1950).
¹³E. Dagotto, *Nanoscale Phase Separation and Colossal Magnetoresistance: The Physics of Manganites and Related Compounds* (Springer, Heidelberg, 2003).
¹⁴A. Weiße and H. Fehske, *New J. Phys.* **6**, 158 (2004).
¹⁵R. Saito, G. Dresselhaus, and M. S. Dresselhaus, *Physical Properties of Carbon Nanotubes* (Imperial College, London, 1998).
¹⁶H. Mousavi and M. Bagheri, *Physica E* **44**, 1722 (2012).
¹⁷K. S. Novoselov, A. K. Geim, S. V. Morozov, D. Jiang, Y. Zhang, S. V. Dubonos, I. V. Grigorieva, and A. A. Firsov, *Science* **306**, 666 (2004).
¹⁸T. Stauber and N. M. R. Peres, *J. Phys.: Condens. Matter* **20**, 055002 (2008).
¹⁹R. J. H. Clark, in *Advances in Infrared and Raman Spectroscopy*, edited by R. J. H. Clark and R. E. Hester (Wiley Heyden, New York, 1984), Vol. 11, p. 95.
²⁰D. Baeriswyl and A. R. Bishop, *Phys. Scr.*, T **19**, 239 (1987).
²¹S. R. White, *Phys. Rev. Lett.* **69**, 2863 (1992).
²²E. Jeckelmann and S. R. White, *Phys. Rev. B* **57**, 6376 (1998).
²³E. Jeckelmann, *Phys. Rev. B* **66**, 045114 (2002).
²⁴E. Jeckelmann and H. Fehske, *Riv. Nuovo Cimento* **30**, 259 (2007).
²⁵K. W. Becker, A. Hübsch, and T. Sommer, *Phys. Rev. B* **66**, 235115 (2002); S. Sykora, A. Hübsch, K. W. Becker, G. Wellein, and H. Fehske, *Phys. Rev. B* **71**, 045112 (2005).
²⁶S. Sykora, K. W. Becker, and H. Fehske, *Phys. Rev. B* **81**, 195127 (2010).
²⁷J. Bonča, S. A. Trugman, and I. Batistić, *Phys. Rev. B* **60**, 1633 (1999).
²⁸A. Alvermann, D. M. Edwards, and H. Fehske, *J. Phys. Conf. Ser.* **220**, 012023 (2010).
²⁹C. L. Kane, P. A. Lee, and N. Read, *Phys. Rev. B* **39**, 6880 (1989).
³⁰G. Martinez and P. Horsch, *Phys. Rev. B* **44**, 317 (1991).
³¹S. A. Trugman, *Phys. Rev. B* **37**, 1597 (1988).
³²V. J. Emery, S. A. Kivelson, and H. Q. Lin, *Phys. Rev. Lett.* **64**, 475 (1990).
³³M. Dzierzawa, in *The Hubbard Model*, edited by D. Baeriswyl, Vol. 343 of NATO Advanced Study Institute Series B: Physics (Plenum, New York, 1995).
³⁴S. Ejima, F. Gebhard, and S. Nishimoto, *Europhys. Lett.* **70**, 492 (2005).
³⁵T. Giamarchi, *Quantum Physics in One Dimension* (Clarendon, Oxford, 2003).
³⁶M. Ogata, M. U. Luchini, S. Sorella, and F. F. Assaad, *Phys. Rev. Lett.* **66**, 2388 (1991).
³⁷A. Moreno, A. Muramatsu, and S. R. Manmana, *Phys. Rev. B* **83**, 205113 (2011).
³⁸M. Berciu and H. Fehske, *Phys. Rev. B* **82**, 085116 (2010).
³⁹I. Bloch, J. Dalibard, and W. Zwerger, *Rev. Mod. Phys.* **80**, 885 (2008).
⁴⁰A. Eckardt and M. Lewenstein, *Phys. Rev. A* **82**, 011606 (2010).

A Green's function decoupling scheme for the Edwards fermion–boson model

D M Edwards¹, S Ejima², A Alvermann² and H Fehske²

¹ Department of Mathematics, Imperial College London, London SW7 2BZ, UK

² Institute of Physics, Ernst Moritz Arndt University, D-17489 Greifswald, Germany

E-mail: d.edwards@imperial.ac.uk

Received 8 July 2010, in final form 10 September 2010

Published 7 October 2010

Online at stacks.iop.org/JPhysCM/22/435601

Abstract

Holes in a Mott insulator are represented by spinless fermions in the fermion–boson model introduced by Edwards. Although the physically interesting regime is for low to moderate fermion density, the model has interesting properties over the whole density range. It has previously been studied at half-filling in the one-dimensional (1D) case by numerical methods, in particular using exact diagonalization and the density matrix renormalization group (DMRG). In the present study the one-particle Green's function is calculated analytically by means of a decoupling scheme for the equations of motion, valid for arbitrary density in 1D, 2D and 3D with fairly large boson energy and zero boson relaxation parameter. The Green's function is used to compute some ground state properties, and the one-fermion spectral function, for fermion densities $n = 0.1, 0.5$ and 0.9 in the 1D case. The results are generally in good agreement with numerical results obtained using the DMRG and dynamical DMRG, and new light is shed on the nature of the ground state at different fillings. The Green's function approximation is sufficiently successful in 1D to justify future application to the 2D and 3D cases.

1. Introduction

Hubbard-like models provide a paradigm for a large class of strongly correlated systems. A general form for the Hubbard Hamiltonian is

$$\mathcal{H}_{\text{Hu}} = \mathcal{T} + \mathcal{U} = - \sum_{\mathbf{r}, \rho, a, b} t_{\rho ab} c_{\mathbf{r}+\rho b}^\dagger c_{\mathbf{r}a} + U \sum_{\mathbf{r}} n_{\mathbf{r}+} n_{\mathbf{r}-} \quad (1)$$

and the system is strongly correlated when the repulsive on-site interaction U is considerably larger than the hopping parameters t . Here $c_{\mathbf{r}a}$ destroys an electron in state a on lattice site \mathbf{r} and $c_{\mathbf{r}+\rho b}^\dagger$ creates an electron in state b on a nearest-neighbour site $\mathbf{r} + \rho$. The state indices a, b are summed over two states denoted by $+$ and $-$, and the occupation numbers $n_{\mathbf{r}\pm} = c_{\mathbf{r}\pm}^\dagger c_{\mathbf{r}\pm}$. In general we consider bipartite lattices in one, two and three dimensions. The standard Hubbard model [1] corresponds to the case of a single orbital on each site with states \pm corresponding to spin $\pm 1/2$ and with hopping parameter

$$t_{\rho ab} = t_0 \delta_{ab}. \quad (2)$$

This model with a 2D square lattice is frequently used to describe the copper–oxygen plane of high- T_c systems such as

doped La_2CuO_4 , where the orbital corresponds to a Cu $d_{x^2-y^2}$ orbital. A related model on a 2D square lattice in the xy plane describes a ferromagnetic system in which the on-site states all have the same spin and the states $+$ and $-$ correspond to $d_{z^2-x^2}$ and $d_{z^2-y^2} t_{2g}$ orbitals respectively. This ‘ t_{2g} model’ describes ferromagnetic planes in Sr_2VO_4 and also in fluorides such as K_2CuF_4 and Cs_2AgF_4 , where in this case a crystal field converts e_g orbitals into an effective t_{2g} system [2–6]. In the t_{2g} model one considers only the dominant hopping processes in which hopping between $+$ states occurs along the x axis and hopping between $-$ states occurs along the y axis. Thus in the t_{2g} model

$$t_{\rho ab} = t_0 \delta_{ab} |\hat{\rho} \cdot \mathbf{e}_a|, \quad (3)$$

where \mathbf{e}_+ and \mathbf{e}_- are unit vectors along the x and y directions respectively and $\hat{\rho}$ is a unit vector in the nearest-neighbour direction ρ .

In the large- U limit we can approximate the Hamiltonian \mathcal{H}_{Hu} by an effective Hamiltonian \mathcal{H}_{eff} which is defined to act only within a subspace where there is no double occupation of any site. \mathcal{H}_{eff} takes the form

$$\mathcal{H}_{\text{eff}} = \mathcal{T} - \mathcal{T}_1^2 / U, \quad (4)$$

where \mathcal{T}_1 is that part of \mathcal{T} which has matrix elements linking states of no double occupation with states having a single doubly occupied site. If three-site terms are neglected it is straight-forward to write the second term of equation (4) in terms of spin (pseudospin for the t_{2g} model) operators $S_r^z = (n_{r+} - n_{r-})/2$, $S_r^\pm = S_r^x \pm S_r^y = c_{r\pm}^\dagger c_{r\mp}$ and number operator $n_r = n_{r+} + n_{r-}$. Then, for the Hubbard model, \mathcal{H}_{eff} becomes

$$\mathcal{H}_{t-J} = \mathcal{T}_{t-J} + \frac{1}{2}J \sum_{\mathbf{r}, \boldsymbol{\rho}} [S_r^z S_{r+\boldsymbol{\rho}}^z + \frac{1}{2}(S_r^+ S_{r+\boldsymbol{\rho}}^- + S_r^- S_{r+\boldsymbol{\rho}}^+) - \frac{1}{4}n_r n_{r+\boldsymbol{\rho}}] = \mathcal{T}_{t-J} + \frac{1}{2}J \sum_{\mathbf{r}, \boldsymbol{\rho}} (\mathbf{S}_r \cdot \mathbf{S}_{r+\boldsymbol{\rho}} - \frac{1}{4}n_r n_{r+\boldsymbol{\rho}}), \quad (5)$$

where $J = 4t_0^2/U$ and \mathcal{T}_{t-J} contains the hopping parameters of equation (2) [7]. For the t_{2g} model the corresponding Hamiltonian is

$$\mathcal{H}_{t_{2g}} = \mathcal{T}_{t_{2g}} + \frac{1}{4}J \sum_{\mathbf{r}, \boldsymbol{\rho}} (S_r^z S_{r+\boldsymbol{\rho}}^z - \frac{1}{4}n_r n_{r+\boldsymbol{\rho}}), \quad (6)$$

where $\mathcal{T}_{t_{2g}}$ contains the hopping parameters of equation (3) [2]. \mathcal{H}_{t-J} is known as the t-J model and if the transverse exchange terms in equation (5) are omitted we have the t- J^z model. This differs from $\mathcal{H}_{t_{2g}}$ where + and - spins only hop along the x and y axes respectively. For the case of one electron per site, the undoped case for the oxides being modelled, \mathcal{T} drops out and the system is a Mott insulator. In the Hubbard case the insulator is a Heisenberg antiferromagnet and in the t_{2g} case it is an Ising antiferromagnet with alternating orbital order in the ground state. The transverse exchange terms in equation (5) are not present in equation (6) owing to the directional hopping of the orbitals in the t_{2g} case.

When a hole is introduced into the lattice its motion disturbs the spin or orbital order of the ground state. At each hop through the ordered lattice the hole leaves a spin, or orbital, deviation at the site it vacates. Thus as the hole hops through the lattice the energy of the system increases linearly and the hole is bound to its starting point. This is known as the string effect and it exists in dimensions higher than one [8]. In 1D the spin deviation created by a hole at its first hop, from some initial position, increases the energy but subsequent hops in the same direction merely shift the ordered spin configuration by a lattice spacing without further increase in energy. There is therefore no string effect in the 1D t-J or t- J^z models. Furthermore in the 2D or 3D t-J models the string effect is relaxed by the $S_r^+ S_{r+\boldsymbol{\rho}}^-$ terms in equation (5) which exchange spin directions between lattice sites and can lead to a healing of the spin deviations created by the hole. Thus the hole can move at a speed determined by the healing rate, which leads to a quasiparticle band of width proportional to the exchange parameter J [9]. This way of relaxing the string effect is not possible in the t- J^z or the $\mathcal{H}_{t_{2g}}$ model owing to the absence of the $S_r^+ S_{r+\boldsymbol{\rho}}^-$ terms. In these models a relaxation mechanism can be introduced by including in the Hamiltonian a term of the form

$$\sum_{\mathbf{r}} (S_r^+ + S_r^-) = 2 \sum_{\mathbf{r}} S_r^x \quad (7)$$

so that the spin part of equation (6) becomes a transverse-field Ising antiferromagnet. In the physical case of the t_{2g} model this

transverse field corresponds to an on-site crystal field which mixes the two t_{2g} orbitals just as the transverse magnetic field mixes + and - spins. In both the t- J^z and the $\mathcal{H}_{t_{2g}}$ model inclusion of three-site terms mentioned earlier also relaxes the string effect [2] but we shall not include them here. A hole in the 2D t- J^z model can also propagate by means of a Trugman path [10] which consists of six hops around a four-site square plaquette. The hole moves to a next-nearest-neighbour site and leaves the antiferromagnetic spin arrangement undisturbed. This cannot occur in the $\mathcal{H}_{t_{2g}}$ model owing to the directional hopping [2]. We shall here concentrate on the t-J model and the t- J^z model in a transverse field although there should be no difficulty in treating the directional hopping of the $\mathcal{H}_{t_{2g}}$ model.

Our reference state has one electron on each site with spins (or pseudospins) ordered as in an antiferromagnet. We follow Martinez and Horsch [11] in introducing a spinless fermion operator f_r^\dagger which creates a hole in the reference state at site \mathbf{r} and a boson operator b_r^\dagger which creates a spin reversal on site \mathbf{r} . Thus $b_r^\dagger = S_r^-$ for site \mathbf{r} on the + spin sublattice and $b_r^\dagger = S_r^+$ for \mathbf{r} on the - sublattice. Clearly each nearest-neighbour hop of the hole through the ordered lattice reverses the spin on the site vacated by the hole. Thus the hopping operator \mathcal{T}_{t-J} may be written as

$$\mathcal{T}_{t-J} = -t_0 \sum_{\mathbf{r}, \boldsymbol{\rho}} (f_{r+\boldsymbol{\rho}}^\dagger f_r b_r^\dagger + \text{H.c.}). \quad (8)$$

For the t_{2g} model the corresponding hopping operator $\mathcal{T}_{t_{2g}}$ is

$$\mathcal{T}_{t_{2g}} = -t_0 \sum_{\mathbf{r}, \boldsymbol{\rho}} (f_{r+\boldsymbol{\rho}}^\dagger f_r b_r^\dagger + \text{H.c.}) |\hat{\boldsymbol{\rho}} \cdot \mathbf{e}_a|. \quad (9)$$

Since $S_r^\pm = \pm(\frac{1}{2} - b_r^\dagger b_r)$ for \mathbf{r} on the \pm spin sublattice we may write the Ising part of the exchange term, in the presence of a hole, as

$$\begin{aligned} & -\frac{1}{8}J \sum_{\mathbf{r}, \boldsymbol{\rho}} (1 - h_r)(1 - 2b_r^\dagger b_r)(1 - 2b_{r+\boldsymbol{\rho}}^\dagger b_{r+\boldsymbol{\rho}})(1 - h_{r+\boldsymbol{\rho}}) \\ & = \frac{1}{2}J \sum_{\mathbf{r}, \boldsymbol{\rho}} b_r^\dagger b_r (1 - h_{r+\boldsymbol{\rho}} - b_{r+\boldsymbol{\rho}}^\dagger b_{r+\boldsymbol{\rho}}), \end{aligned} \quad (10)$$

where $h_r = f_r^\dagger f_r$ and an irrelevant constant term has been dropped. Here we have used $h_r b_r^\dagger b_r = 0$ since the hole and a spin deviation cannot occupy the same site. A spin deviation created on site \mathbf{r} when the hole vacates that site will in general have one neighbouring site $\mathbf{r} + \boldsymbol{\rho}$ occupied by the hole and another by a spin deviation created when the hole arrived on site \mathbf{r} . Thus the expression in equation (10) may be written as

$$\frac{1}{2}J(z-2) \sum_{\mathbf{r}} b_r^\dagger b_r, \quad (11)$$

where z is the number of nearest-neighbours. $z = 2$ in 1D so that the above term is zero, which is consistent with the absence of the string effect in the 1D t- J^z model. Apart from an additive constant the t-J Hamiltonian equation (5) becomes

$$\begin{aligned} \mathcal{H}_{t-J} & = -t_0 \sum_{\mathbf{r}, \boldsymbol{\rho}} (f_{r+\boldsymbol{\rho}}^\dagger f_r b_r^\dagger + \text{H.c.}) \\ & + \frac{1}{4}J \sum_{\mathbf{r}, \boldsymbol{\rho}} (b_{r+\boldsymbol{\rho}}^\dagger b_{r+\boldsymbol{\rho}} + b_r b_{r+\boldsymbol{\rho}}) + \frac{1}{2}J(z-2) \sum_{\mathbf{r}} b_r^\dagger b_r. \end{aligned} \quad (12)$$

Note that the derivation of this Hamiltonian in [11] gives additional constraints which we will not discuss here.

The relaxation of the string effect occurs when bosons, created by fermion hopping, are spontaneously destroyed in nearest-neighbour pairs by the terms $b_r b_{r+\rho}$. Edwards [12] introduced a simplified model Hamiltonian of the form

$$\mathcal{H}_{\text{Ed}} = -t_0 \sum_{r\rho} (f_{r+\rho}^\dagger f_r b_r^\dagger + \text{H.c.}) - \lambda \sum_{\mathbf{r}} (b_{\mathbf{r}}^\dagger + b_{\mathbf{r}}) + \omega_0 \sum_{\mathbf{r}} b_{\mathbf{r}}^\dagger b_{\mathbf{r}} + N\lambda^2/\omega_0 \quad (13)$$

in which boson relaxation terms $b_r b_{r+\rho}$ are replaced by the simpler linear ones b_r . A unitary transformation $\tilde{\mathcal{H}}_{\text{Ed}} = e^{\mathcal{S}} \mathcal{H}_{\text{Ed}} e^{-\mathcal{S}}$, $\mathcal{S} = (\lambda/\omega_0) \sum_{\mathbf{r}} (b_{\mathbf{r}} - b_{\mathbf{r}}^\dagger)$, resulting in $b_{\mathbf{r}} \rightarrow b_{\mathbf{r}} + \lambda/\omega_0$, yields

$$\tilde{\mathcal{H}}_{\text{Ed}} = -\frac{2t_0\lambda}{\omega_0} \sum_{r\rho} f_{r+\rho}^\dagger f_r - t_0 \sum_{r\rho} (f_{r+\rho}^\dagger f_r b_r^\dagger + \text{H.c.}) + \omega_0 \sum_{\mathbf{r}} b_{\mathbf{r}}^\dagger b_{\mathbf{r}}. \quad (14)$$

Thus the second term in \mathcal{H}_{Ed} is eliminated in favour of the first term in $\tilde{\mathcal{H}}_{\text{Ed}}$ which introduces a coherent hopping channel in addition to the original incoherent one. In the ground state $|\tilde{0}\rangle$ of the Hamiltonian $\tilde{\mathcal{H}}_{\text{Ed}}$, in the absence of fermions, there are no bosons, so that $b_{\mathbf{r}}|\tilde{0}\rangle = 0$. Thus for the ground state $|0\rangle$ of \mathcal{H}_{Ed} we have $(b_{\mathbf{r}} - \lambda/\omega_0)|0\rangle = 0$ and hence $\langle 0|b_{\mathbf{r}}^\dagger b_{\mathbf{r}}|0\rangle = \lambda^2/\omega_0^2$.

From the above discussion it is clear that in 2D the Edwards model corresponds, within a certain range of parameters, to an underlying t-J^z type of model with Hamiltonian

$$-t_0 \sum_{r\rho\sigma} c_{r+\rho}^\dagger c_{r\sigma} + \frac{1}{2}\omega_0 \sum_{r\rho} S_r^z S_{r+\rho}^z - 2\lambda \sum_{\mathbf{r}} S_{\mathbf{r}}^x, \quad (15)$$

since $2S_{\mathbf{r}}^x = S_{\mathbf{r}}^+ + S_{\mathbf{r}}^- = b_{\mathbf{r}}^\dagger + b_{\mathbf{r}}$. This corresponds to a doped antiferromagnetic Ising model in a transverse magnetic field, but this correspondence is only valid for low hole density (low fermion density in the \mathcal{H}_{Ed} model) and $\lambda \ll \omega_0$. In this case, since $|\langle 0|S_r^z|0\rangle| = \frac{1}{2} - \langle 0|b_r^\dagger b_r|0\rangle = \frac{1}{2} - \lambda^2/\omega_0^2$, the holes move in a background medium which is close to a saturated antiferromagnet. For $\lambda \gtrsim \omega_0$ the transverse-field Ising model no longer exhibits antiferromagnetic order [13]. In 1D the correspondence breaks down completely since if $\lambda = 0$ and $\omega_0 \neq 0$ the \mathcal{H}_{Ed} model exhibits the string effect which is absent in the 1D t-J^z model. In fact the 1D \mathcal{H}_{Ed} model has an interesting similarity to the 2D t-J^z model. Even for $\lambda = 0$ the string effect is relaxed by an analogue of the Trugman path [14]. This is again a six-step process in which the fermion propagates to a next-nearest-neighbour site with the background medium left undisturbed, i.e. no bosons excited. During the process the fermion excites three bosons which are subsequently destroyed. Unfortunately the model \mathcal{H}_{Ed} does not represent precisely any physical system that we know of. The underlying Ising exchange is characteristic of the t_{2g} model for vanadates and fluorides but the directional hopping of that model is not included, although this could be remedied in the 2D model. However if the model is considered over the whole $\lambda/t_0, \omega_0/t_0$ -space it is found, even in the 1D case, to exhibit

a surprising number of different physical regimes reminiscent of some found in realistic strongly correlated electron systems and strongly coupled electron-phonon systems. This was first demonstrated for the case of a single fermion ($N_f = 1$) at temperature $T = 0$ by the method of variational Lanczos diagonalization [14]. A great advantage of the model is that the simple treatment of the background medium, in terms of local bosons, makes it possible to obtain essentially exact results in the thermodynamic limit, at least in the 1D case. More recently the half-filled case, with $N_f = N/2$ where N is the number of lattice sites, has been investigated [15–17]. The ground state phase diagram has been mapped out in the whole λ - ω_0 plane, using a density matrix renormalization group (DMRG) technique [18, 19]. A quantum phase transition between a metallic Tomonaga-Luttinger liquid and an insulating charge density wave (CDW) was shown to exist.

It is desirable to complement these numerical results with some more analytical approaches. Nearly all analytical work on t-J-like or polaronic models is confined to the case of a single fermion. However very recently the projective renormalization method [20] has been applied to the half-filled 1D \mathcal{H}_{Ed} model in a study of CDW formation at $T = 0$ [21]. Our initial analytical work on the \mathcal{H}_{Ed} model was confined to the one-fermion case in 1D at $T = 0$ with the additional restriction $\lambda = 0$ [22]. The latter restriction means that the fermion can only propagate as a coherent quasiparticle by the Trugman-like process discussed above. This requires the coexistence of at least three bosons during the particle's motion and in [22] the one-fermion Green's function was calculated within a three-boson approximation. The spectral functions agree well with exact numerical results for $\omega_0/t_0 \gtrsim 1$. In this paper we extend the analytical approach for $\lambda = 0$ to finite fermion density and to higher dimension, 2D and 3D. This is achieved within a two-boson approximation and comparison with exact numerical results in 1D shows that the range of validity is thereby reduced to $\omega_0/t_0 \gtrsim 3$. No Trugman-like processes exist in the two-boson approximation but they are unimportant to understand CDW formation at finite density. Relaxation of the string effect does not depend on them because bosons created by one fermion can be destroyed by other fermions. Near half-filling a CDW state is found, in good agreement with 1D numerical results, and the CDW transition temperature can be calculated formally. However, within the two-boson approximation, the transition is mean-field-like, with no short-range order in the disordered state. This is clearly not realistic in 1D but finite-temperature calculations should certainly be relevant in 3D. In this paper we concentrate on the calculation of spectral functions in 1D at $T = 0$ with various fermion densities and compare with some new DMRG results.

In section 2 we determine the one-fermion Green's function for $\lambda = 0$ within the two-boson approximation in the cases of one particle ($N_f = 1$) and one hole ($N_f = N - 1$). The method used is different from that previously employed for $N_f = 1$ [22] and provides a wavefunction as a byproduct. In section 3 we study the hierarchy of equations of motion for the Green's function at arbitrary density and devise a decoupling which leads to the correct Green's function in the two-boson approximation for $N_f = 1$ and $N - 1$. This two-boson Green's

function is valid for any bipartite lattice in 1D, 2D or 3D and allows for two distinct sublattices so that the CDW state can be investigated. In section 4 spectral functions and ground state properties calculated from the two-boson Green's function are compared with those calculated numerically by the DMRG method. In section 5 we draw conclusions and consider the outlook for future work.

2. Limiting cases of the Green's function within the two-boson approximation

We now derive expressions for the one-fermion Green's function in the special cases of a single fermion ($N_f = 1$) and a single hole ($N_f = N - 1$). For these single-particle cases the Green's function may be calculated by direct solution of the Schrödinger equation, which also yields the wavefunction.

2.1. The case $N_f = 1$

For $\lambda = 0$ the Hamiltonian equation (13), written in \mathbf{k} -space, takes the form

$$\mathcal{H}_{\text{Ed}} = \frac{1}{\sqrt{N}} \sum_{\mathbf{k}\mathbf{k}'} f_{\mathbf{k}}^\dagger f_{\mathbf{k}'} [\gamma(\mathbf{k}) b_{\mathbf{k}'-\mathbf{k}}^\dagger + \gamma(\mathbf{k}') b_{\mathbf{k}-\mathbf{k}'}] + \omega_0 \sum_{\mathbf{q}} b_{\mathbf{q}}^\dagger b_{\mathbf{q}}, \quad (16)$$

where

$$f_{\mathbf{k}} = \frac{1}{\sqrt{N}} \sum_{\mathbf{r}} e^{i\mathbf{k}\cdot\mathbf{r}} f_{\mathbf{r}}, \quad b_{\mathbf{q}} = \frac{1}{\sqrt{N}} \sum_{\mathbf{r}} e^{i\mathbf{q}\cdot\mathbf{r}} b_{\mathbf{r}}, \quad (17)$$

$$\gamma(\mathbf{k}) = -t_0 \sum_{\rho} e^{i\mathbf{k}\cdot\rho}.$$

The ρ -summation is over z nearest-neighbours in a 1D, 2D or 3D bipartite lattice. In the two-boson approximation the wavefunction for a single fermion is of the form

$$\Psi_{\mathbf{k}} = \left[f_{\mathbf{k}}^\dagger + \sum_{\mathbf{q}_1} a(\mathbf{q}_1) f_{\mathbf{k}-\mathbf{q}_1}^\dagger b_{\mathbf{q}_1}^\dagger + \sum_{\mathbf{q}_1} \sum_{\mathbf{q}_2} a(\mathbf{q}_1, \mathbf{q}_2) f_{\mathbf{k}-\mathbf{q}_1-\mathbf{q}_2}^\dagger b_{\mathbf{q}_1}^\dagger b_{\mathbf{q}_2}^\dagger \right] |\text{vac}\rangle, \quad (18)$$

where $|\text{vac}\rangle$ is the vacuum state and $a(\mathbf{q}_1, \mathbf{q}_2) = a(\mathbf{q}_2, \mathbf{q}_1)$. On substituting this in the Schrödinger equation $\mathcal{H}\Psi_{\mathbf{k}} = E\Psi_{\mathbf{k}}$, and multiplying on the left by $\langle \text{vac} |$, $\langle \text{vac} | b_{\mathbf{q}_1} f_{\mathbf{k}-\mathbf{q}_1}^\dagger$ and $\langle \text{vac} | b_{\mathbf{q}_1} b_{\mathbf{q}_2} f_{\mathbf{k}-\mathbf{q}_1-\mathbf{q}_2}^\dagger$ we obtain equations of the form

$$-E + \frac{1}{\sqrt{N}} \sum_{\mathbf{q}_1} \gamma(\mathbf{k} - \mathbf{q}_1) a(\mathbf{q}_1) = 0, \quad (19)$$

$$\frac{1}{\sqrt{N}} \gamma(\mathbf{k} - \mathbf{q}_1) + a(\mathbf{q}_1)(\omega_0 - E) + \frac{2}{\sqrt{N}} \sum_{\mathbf{q}_2} a(\mathbf{q}_1, \mathbf{q}_2) \gamma(\mathbf{k} - \mathbf{q}_1 - \mathbf{q}_2) = 0, \quad (20)$$

$$\frac{1}{\sqrt{N}} \gamma(\mathbf{k} - \mathbf{q}_1 - \mathbf{q}_2) [a(\mathbf{q}_1) + a(\mathbf{q}_2)] + 2a(\mathbf{q}_1, \mathbf{q}_2)(2\omega_0 - E) = 0. \quad (21)$$

On solving equation (21) for $a(\mathbf{q}_1, \mathbf{q}_2)$, and substituting in equation (20), we find

$$a(\mathbf{q}_1) \left[\omega_0 - E - \frac{z t_0^2}{2\omega_0 - E} \right] = -\frac{1}{\sqrt{N}} \gamma(\mathbf{k} - \mathbf{q}_1) + \frac{1}{N} \sum_{\mathbf{q}_2} \frac{[\gamma(\mathbf{k} - \mathbf{q}_1 - \mathbf{q}_2)]^2 a(\mathbf{q}_2)}{2\omega_0 - E}. \quad (22)$$

It is easily shown that for a bipartite lattice the last term in this equation vanishes when $a(\mathbf{q}) \propto \gamma(\mathbf{k} - \mathbf{q})$. Hence a solution for $a(\mathbf{q}_1)$ is obtained by omitting the last term and, on substituting this solution in equation (19), we find

$$E + \frac{z t_0^2}{\omega_0 - E - \frac{z t_0^2}{2\omega_0 - E}} = 0. \quad (23)$$

The solutions of this equation are the energies of single fermion eigenstates, which are the poles of the one-fermion Green's function $G_{\mathbf{k}}(E)$. The left-hand side of equation (23) is $G_{\mathbf{k}}^{-1}(E)$. The absence of \mathbf{k} -dependence in this expression shows that the single fermion eigenstates are localized. This is due to the string effect which is not relaxed in the two-boson approximation.

2.2. The case $N_f = N - 1$

The motion of a single hole in the present model is quite different from that of a single particle. To avoid confusion it should be stressed that the hole discussed here does not correspond to a hole in a t-J-like model, the latter being represented by a fermion in the present model. Clearly when the hole considered here hops to a neighbouring site a boson is created on the arrival site, not on the departure site as in the motion of a single particle. This boson can be destroyed immediately when the hole makes a further hop. There is therefore no string effect and the hole propagates easily. To find the Green's function in this case we use the Schrödinger equation as in the case of a single particle. The wavefunction for the hole is of the form

$$\Phi_{\mathbf{k}} = \left[f_{\mathbf{k}} + \sum_{\mathbf{q}_1} c(\mathbf{q}_1) f_{\mathbf{k}+\mathbf{q}_1} b_{\mathbf{q}_1}^\dagger + \sum_{\mathbf{q}_1} \sum_{\mathbf{q}_2} c(\mathbf{q}_1, \mathbf{q}_2) f_{\mathbf{k}+\mathbf{q}_1+\mathbf{q}_2} b_{\mathbf{q}_1}^\dagger b_{\mathbf{q}_2}^\dagger \right] |F\rangle, \quad (24)$$

where $|F\rangle$ is the state with every site occupied by a fermion and $c(\mathbf{q}_1, \mathbf{q}_2) = c(\mathbf{q}_2, \mathbf{q}_1)$. The equations corresponding to equations (19)–(21) in the previous case are

$$-E - \frac{1}{\sqrt{N}} \gamma(\mathbf{k}) \sum_{\mathbf{q}_1} c(\mathbf{q}_1) = 0, \quad (25)$$

$$-\frac{1}{\sqrt{N}} \gamma(\mathbf{k}) + c(\mathbf{q}_1)(\omega_0 - E) - \frac{2}{\sqrt{N}} \gamma(\mathbf{k} + \mathbf{q}_1) \sum_{\mathbf{q}_2} c(\mathbf{q}_1, \mathbf{q}_2) = 0, \quad (26)$$

$$-\frac{1}{\sqrt{N}} [c(\mathbf{q}_1) \gamma(\mathbf{k} + \mathbf{q}_1) + c(\mathbf{q}_2) \gamma(\mathbf{k} + \mathbf{q}_2)] + 2c(\mathbf{q}_1, \mathbf{q}_2)(2\omega_0 - E) = 0. \quad (27)$$

From equations (26) and (27) we find that for a bipartite lattice and

$$c(\mathbf{q}_1) = \frac{1}{\sqrt{N}} \frac{\gamma(\mathbf{k})}{\omega_0 - E - \frac{[\gamma(\mathbf{k}+\mathbf{q}_1)]^2}{2\omega_0 - E}}. \quad (28)$$

Hence, from equation (25),

$$-E - [\gamma(\mathbf{k})]^2 \frac{1}{N} \sum_{\mathbf{q}} \frac{1}{\omega_0 - E - \frac{[\gamma(\mathbf{q})]^2}{2\omega_0 - E}} = 0. \quad (29)$$

The solutions of this equation are the energies of single hole eigenstates and, as expected, they depend on the wavevector \mathbf{k} , being functions of $[\gamma(\mathbf{k})]^2$. This type of \mathbf{k} dependence arises from the fact that the hole propagates through the lattice, leaving behind no excited bosons, by means of double hops, as discussed at the beginning of this section. As in the one-particle case we deduce that for one hole ($N_f = N - 1$) the one-fermion Green's function is given by

$$[G_{\mathbf{k}}(E)]^{-1} = E - [\gamma(\mathbf{k})]^2 \frac{1}{N} \sum_{\mathbf{q}} \frac{1}{\omega_0 + E - \frac{[\gamma(\mathbf{q})]^2}{2\omega_0 + E}}. \quad (30)$$

The sign of E has been changed since in equation (29) the energy refers to a hole state.

3. The Green's function at finite fermion density

In this section we study the hierarchy of equations of motion of the one-fermion Green's function and find a decoupling which is consistent with the results derived in section 2 for the limiting cases of low ($N_f = 1$) and high ($N_f = N - 1$) fermion density. We allow for two distinct sublattices with different occupation so that the CDW state can be investigated.

The Fourier transform of the one-fermion retarded Green's function is defined by [23]

$$G_{\mathbf{k}}(E) = \langle\langle f_{\mathbf{k}}; f_{\mathbf{k}}^\dagger \rangle\rangle = -i \int_{-\infty}^{\infty} dt \theta(t) \langle [f_{\mathbf{k}}(t), f_{\mathbf{k}}^\dagger]_+ \rangle e^{iEt}, \quad (31)$$

where $f_{\mathbf{k}}(t) = e^{iHt} f_{\mathbf{k}} e^{-iHt}$ and $\theta(t)$ is the unit step function. We may write $f_{\mathbf{k}}$, defined by equation (17), as a sum of two-sublattice components. Thus

$$f_{\mathbf{k}} = \frac{1}{\sqrt{2}} (f_{\mathbf{k}1} + f_{\mathbf{k}2}), \quad (32)$$

where

$$f_{\mathbf{k}l} = \sqrt{\frac{2}{N}} \sum_{\mathbf{r}_l} e^{i\mathbf{k}\cdot\mathbf{r}_l} f_{\mathbf{r}_l}. \quad (33)$$

Here the summation is over sites \mathbf{r}_l which belong to sublattice l ($l = 1, 2$). It follows from equations (31) and (32) that

$$G_{\mathbf{k}}(E) = \frac{1}{2} \sum_{l=1}^2 \sum_{m=1}^2 G_{\mathbf{k}}^{lm}(E), \quad (34)$$

where

$$G_{\mathbf{k}}^{lm} = \langle\langle f_{\mathbf{k}l}; f_{\mathbf{k}m}^\dagger \rangle\rangle = \frac{2}{N} \sum_{\mathbf{r}_l, \mathbf{r}_m} e^{i\mathbf{k}\cdot(\mathbf{r}_l - \mathbf{r}_m)} G_{\mathbf{r}_l, \mathbf{r}_m}, \quad (35)$$

$$G_{\mathbf{r}_l, \mathbf{r}_m} = \langle\langle f_{\mathbf{r}_l}; f_{\mathbf{r}_m}^\dagger \rangle\rangle. \quad (36)$$

The equation of motion for the Green's function $\langle\langle A; B \rangle\rangle$ is [23]

$$E \langle\langle A; B \rangle\rangle = \langle\langle [A, B]_+ \rangle\rangle + \langle\langle [A, \mathcal{H}]; B \rangle\rangle. \quad (37)$$

Hence, noting that \mathcal{H} is given by equation (13) with $\lambda = 0$, we find

$$E G_{\mathbf{r}_l, \mathbf{r}_m} = \delta_{\mathbf{r}_l, \mathbf{r}_m} - t_0 \sum_{\rho} H_{\mathbf{r}_l + \rho, \mathbf{r}_m}^{\mathbf{r}_l} - t_0 \sum_{\rho} I_{\mathbf{r}_l + \rho, \mathbf{r}_m}^{\mathbf{r}_l + \rho}, \quad (38)$$

where

$$H_{\mathbf{r}_l + \rho, \mathbf{r}_m}^{\mathbf{r}_l} = \langle\langle f_{\mathbf{r}_l + \rho} b_{\mathbf{r}_l}; f_{\mathbf{r}_m}^\dagger \rangle\rangle, \quad (39)$$

$$I_{\mathbf{r}_l, \mathbf{r}_m}^{\mathbf{r}_l + \rho} = \langle\langle f_{\mathbf{r}_l} b_{\mathbf{r}_l + \rho}^\dagger; f_{\mathbf{r}_m}^\dagger \rangle\rangle. \quad (40)$$

Here \mathbf{r}_l is a general site on the sublattice \bar{l} which complements the sublattice l ($\bar{l} = 2, 1$ for $l = 1, 2$ respectively). $\mathbf{r}_l + \rho$ is a particular site on the sublattice \bar{l} but it is necessary to define I more generally in order to close the equations of motion. However we first calculate the second term on the right of equation (38).

The equation of motion for H is

$$\begin{aligned} (E - \omega_0) H_{\mathbf{r}_l + \rho, \mathbf{r}_m}^{\mathbf{r}_l} &= \delta_{\mathbf{r}_l + \rho, \mathbf{r}_m} \langle b_{\mathbf{r}_l} \rangle \\ &- t_0 \sum_{\rho'} \langle\langle f_{\mathbf{r}_l + \rho} f_{\mathbf{r}_l + \rho'}^\dagger; f_{\mathbf{r}_m}^\dagger \rangle\rangle \\ &- t_0 \sum_{\rho'} \langle\langle f_{\mathbf{r}_l + \rho + \rho'} (b_{\mathbf{r}_l + \rho} + b_{\mathbf{r}_l + \rho + \rho'}^\dagger) b_{\mathbf{r}_l}; f_{\mathbf{r}_m}^\dagger \rangle\rangle. \end{aligned} \quad (41)$$

The last term of this equation is produced by a process in which a fermion hops from $\mathbf{r}_l + \rho$ to $\mathbf{r}_l + \rho + \rho'$ with either the creation of a boson on the vacated site $\mathbf{r}_l + \rho$ or destruction of a boson on the arrival site $\mathbf{r}_l + \rho + \rho'$. The latter boson must have been created by another fermion so that the term involving $b_{\mathbf{r}_l + \rho + \rho'}^\dagger b_{\mathbf{r}_l}$ corresponds to a dynamical interaction between fermions. This should only be included if we consider two-fermion interactions consistently which goes beyond the effective Hartree-Fock treatment introduced below. We therefore neglect this term. In the second term on the right of equation (41) we retain only the part involving fermions on two sites, thus taking $\rho' = \rho$, and then make a Hartree-Fock type of approximation. Thus the second term becomes

$$- t_0 \langle\langle (1 - n_{\mathbf{r}_l + \rho}) f_{\mathbf{r}_l}; f_{\mathbf{r}_m}^\dagger \rangle\rangle \simeq - t_0 (1 - \langle n_{\mathbf{r}_l + \rho} \rangle) G_{\mathbf{r}_l, \mathbf{r}_m}, \quad (42)$$

where $n_{\mathbf{r}_l} = f_{\mathbf{r}_l}^\dagger f_{\mathbf{r}_l}$. Also we write the average fermion occupation for sites on sublattice l as $n_l = \langle n_{\mathbf{r}_l} \rangle$ so that $\langle n_{\mathbf{r}_l + \rho} \rangle = n_{\bar{l}}$. Following this discussion equation (41) becomes

$$\begin{aligned} (E - \omega_0) H_{\mathbf{r}_l + \rho, \mathbf{r}_m}^{\mathbf{r}_l} &= \delta_{\mathbf{r}_l + \rho, \mathbf{r}_m} \langle b_{\mathbf{r}_l} \rangle - t_0 (1 - n_{\bar{l}}) G_{\mathbf{r}_l, \mathbf{r}_m} \\ &- t_0 \sum_{\rho'} J_{\mathbf{r}_l + \rho + \rho', \mathbf{r}_m}^{\mathbf{r}_l + \rho}, \end{aligned} \quad (43)$$

where

$$J_{\mathbf{r}_l + \rho + \rho', \mathbf{r}_m}^{\mathbf{r}_l + \rho} = \langle\langle f_{\mathbf{r}_l + \rho + \rho'} b_{\mathbf{r}_l + \rho} b_{\mathbf{r}_l}; f_{\mathbf{r}_m}^\dagger \rangle\rangle. \quad (44)$$

In the equation of motion for J the terms arising from $[f_{\mathbf{r}_l + \rho + \rho'}, \mathcal{H}]$ involve three boson operators and we neglect

them. The terms arising from $[b_{\mathbf{r}_l+\boldsymbol{\rho}}b_{\mathbf{r}_l}, \mathcal{H}]$ may be treated in the Hartree–Fock-like way used to obtain equation (42). Hence

$$(E - 2\omega_0)J_{\mathbf{r}_l+\boldsymbol{\rho}+\boldsymbol{\rho}',s_m}^{\mathbf{r}_l+\boldsymbol{\rho},\mathbf{r}_l} = \delta_{\mathbf{r}_l+\boldsymbol{\rho}+\boldsymbol{\rho}',s_m} \langle b_{\mathbf{r}_l+\boldsymbol{\rho}}b_{\mathbf{r}_l} \rangle - t_0(1 - n_l)H_{\mathbf{r}_l+\boldsymbol{\rho},s_m}^{\mathbf{r}_l}. \quad (45)$$

We approximate $\langle b_{\mathbf{r}_l+\boldsymbol{\rho}}b_{\mathbf{r}_l} \rangle$ by $b_l b_l$, where $b_l = \langle b_{\mathbf{r}_l} \rangle$. Furthermore it is shown below that $b_l = 0$ for the present model, with $\lambda = 0$. Hence $\langle b_{\mathbf{r}_l+\boldsymbol{\rho}}b_{\mathbf{r}_l} \rangle$ may be neglected. On substituting for J in equation (43), using equation (45), and summing over $\boldsymbol{\rho}$, we find

$$\sum_{\boldsymbol{\rho}} H_{\mathbf{r}_l+\boldsymbol{\rho},s_m}^{\mathbf{r}_l} = C(E, n_l) \left[b_l \sum_{\boldsymbol{\rho}} \delta_{\mathbf{r}_l+\boldsymbol{\rho},s_m} - z t_0(1 - n_l) G_{\mathbf{r}_l,s_m} \right], \quad (46)$$

where

$$C(E, n_l) = \frac{1}{E - \omega_0 - \frac{z t_0^2(1-n_l)}{E-2\omega_0}}. \quad (47)$$

The second term on the right of equation (38) has therefore been determined and to find the third term we must consider the equation of motion of the Green's function I defined by equation (40). This takes the form

$$(E + \omega_0)I_{\mathbf{r}_l,s_m}^{\mathbf{r}_l+\boldsymbol{\rho}} = \delta_{\mathbf{r}_l,s_m} \langle b_{\mathbf{r}_l+\boldsymbol{\rho}}^\dagger \rangle + t_0 \sum_{\boldsymbol{\rho}'} \langle \langle f_{\mathbf{r}_l} f_{\mathbf{r}_l+\boldsymbol{\rho}}^\dagger f_{\mathbf{r}_l+\boldsymbol{\rho}+\boldsymbol{\rho}'}^\dagger; f_{s_m}^\dagger \rangle \rangle - t_0 \sum_{\boldsymbol{\rho}'} \langle \langle f_{\mathbf{r}_l+\boldsymbol{\rho}'} (\delta_{\mathbf{r}_l,\mathbf{r}_l+\boldsymbol{\rho}} + b_{\mathbf{r}_l+\boldsymbol{\rho}}^\dagger b_{\mathbf{r}_l} + b_{\mathbf{r}_l+\boldsymbol{\rho}}^\dagger b_{\mathbf{r}_l+\boldsymbol{\rho}}^\dagger); f_{s_m}^\dagger \rangle \rangle. \quad (48)$$

We now make similar approximations to those used to obtain equation (43). Thus we make an effective Hartree–Fock approximation to the second term on the right of equation (48), retaining it only when $\mathbf{r}_l = \mathbf{r}_l + \boldsymbol{\rho}$, and we neglect the $b_{\mathbf{r}_l+\boldsymbol{\rho}}^\dagger b_{\mathbf{r}_l}$ term in the third term. Hence

$$(E + \omega_0)I_{\mathbf{r}_l,s_m}^{\mathbf{r}_l+\boldsymbol{\rho}} = \delta_{\mathbf{r}_l,s_m} b_l^* - t_0 n_l \delta_{\mathbf{r}_l,\mathbf{r}_l+\boldsymbol{\rho}} \sum_{\boldsymbol{\rho}'} G_{\mathbf{r}_l+\boldsymbol{\rho}',s_m} - t_0 \sum_{\boldsymbol{\rho}'} K_{\mathbf{r}_l+\boldsymbol{\rho}',s_m}^{\mathbf{r}_l+\boldsymbol{\rho},\mathbf{r}_l+\boldsymbol{\rho}}, \quad (49)$$

where

$$K_{\mathbf{r}_l+\boldsymbol{\rho}',s_m}^{\mathbf{r}_l+\boldsymbol{\rho},\mathbf{r}_l+\boldsymbol{\rho}} = \langle \langle f_{\mathbf{r}_l+\boldsymbol{\rho}'} b_{\mathbf{r}_l+\boldsymbol{\rho}'}^\dagger b_{\mathbf{r}_l+\boldsymbol{\rho}}^\dagger; f_{s_m}^\dagger \rangle \rangle. \quad (50)$$

We treat the equation of motion of K in a similar way to that of J . A slight difference is that instead of neglecting all the terms arising from $[f_{\mathbf{r}_l+\boldsymbol{\rho}'}, H]$ we retain one which leads to a factor $b_{\mathbf{r}_l+\boldsymbol{\rho}'} b_{\mathbf{r}_l+\boldsymbol{\rho}'}^\dagger$. This equals $[1 + b_{\mathbf{r}_l+\boldsymbol{\rho}'}^\dagger b_{\mathbf{r}_l+\boldsymbol{\rho}'}]$ which we approximate by 1, neglecting the boson occupation number. Hence, neglecting a $\langle b^\dagger b^\dagger \rangle$ correlation function as before, we find

$$(E + 2\omega_0)K_{\mathbf{r}_l+\boldsymbol{\rho}',s_m}^{\mathbf{r}_l+\boldsymbol{\rho},\mathbf{r}_l+\boldsymbol{\rho}} = -t_0 n_l \sum_{\boldsymbol{\rho}''} I_{\mathbf{r}_l+\boldsymbol{\rho}'+\boldsymbol{\rho}'',s_m}^{\mathbf{r}_l+\boldsymbol{\rho}}. \quad (51)$$

Thus, from equations (49) and (51),

$$(E + \omega_0)I_{\mathbf{r}_l,s_m}^{\mathbf{r}_l+\boldsymbol{\rho}} = \delta_{\mathbf{r}_l,s_m} b_l^* - t_0 n_l \delta_{\mathbf{r}_l,\mathbf{r}_l+\boldsymbol{\rho}} \sum_{\boldsymbol{\rho}'} G_{\mathbf{r}_l+\boldsymbol{\rho}',s_m} + \frac{t_0^2 n_l}{E + 2\omega_0} \sum_{\boldsymbol{\rho}'} \sum_{\boldsymbol{\rho}''} I_{\mathbf{r}_l+\boldsymbol{\rho}'+\boldsymbol{\rho}'',s_m}^{\mathbf{r}_l+\boldsymbol{\rho}}. \quad (52)$$

To solve this equation for I we introduce the Fourier transform

$$\bar{I}_{\mathbf{k}\mathbf{q}}^{\bar{m}} = \left(\frac{2}{N} \right)^{\frac{3}{2}} \sum_{\mathbf{r}_l, \mathbf{r}_l, s_m} I_{\mathbf{r}_l, s_m}^{\mathbf{r}_l+\boldsymbol{\rho}} e^{i[(\mathbf{k}+\mathbf{q})\cdot\mathbf{r}_l - \mathbf{k}\cdot s_m - \mathbf{q}\cdot(\mathbf{r}_l+\boldsymbol{\rho})]} \quad (53)$$

so that

$$\left(E + \omega_0 - \frac{n_l [\gamma(\mathbf{k} + \mathbf{q})]^2}{E + 2\omega_0} \right) \bar{I}_{\mathbf{k}\mathbf{q}}^{\bar{m}} = \sqrt{\frac{N}{2}} \delta_{\mathbf{q}0} \delta_{\bar{m}} b_l^* + \sqrt{\frac{2}{N}} n_l \gamma(\mathbf{k}) G_{\mathbf{k}}^{\bar{m}}. \quad (54)$$

By taking the Fourier transform of equation (38), and using equation (46), we find

$$E G_{\mathbf{k}}^{\bar{m}} = \delta_{\bar{m}} - C(E, n_l) [b_l \gamma(\mathbf{k}) \delta_{\bar{m}} - z t_0^2 (1 - n_l) G_{\mathbf{k}}^{\bar{m}}] + \gamma(\mathbf{k}) \bar{I}_{\mathbf{k}}^{\bar{m}}, \quad (55)$$

where

$$\bar{I}_{\mathbf{k}}^{\bar{m}} = \frac{2}{N} \sum_{\mathbf{r}_l, s_m} e^{i[\mathbf{k}\cdot(\mathbf{r}_l - s_m)]} I_{\mathbf{r}_l, s_m}^{\mathbf{r}_l} = \sqrt{\frac{2}{N}} \sum_{\mathbf{q}} \bar{I}_{\mathbf{k}\mathbf{q}}^{\bar{m}}. \quad (56)$$

By combining the last three equations we obtain

$$G_{\mathbf{k}}^{\bar{m}} [E - z t_0^2 (1 - n_l) C(E, n_l) - [\gamma(\mathbf{k})]^2 n_l \bar{D}(E, n_l)] = \delta_{\bar{m}} - [C(E, n_l) b_l + D(E, \mathbf{k}, n_l) b_l^*] \delta_{\bar{m}} \gamma(\mathbf{k}), \quad (57)$$

where

$$D(E, \mathbf{k}, n_l) = \frac{1}{E + \omega_0 - \frac{n_l [\gamma(\mathbf{k})]^2}{E + 2\omega_0}}, \quad (58)$$

and

$$\bar{D}(E, n_l) = \frac{2}{N} \sum_{\mathbf{q}} D(E, \mathbf{q}, n_l). \quad (59)$$

It remains to explain why, as indicated following equation (45), $b_l = 0$. This may be shown using

$$b_l = \langle b_{\mathbf{r}_l} \rangle = \frac{1}{z} \sum_{\boldsymbol{\rho}} \langle [b_{\mathbf{r}_l} f_{\mathbf{r}_l+\boldsymbol{\rho}}, f_{\mathbf{r}_l+\boldsymbol{\rho}}^\dagger]_+ \rangle = \frac{i}{2\pi z} \sum_{\boldsymbol{\rho}} \int_{-\infty}^{\infty} [H_{\mathbf{r}_l+\boldsymbol{\rho},\mathbf{r}_l+\boldsymbol{\rho}}^{\mathbf{r}_l}(E + i\eta) - H_{\mathbf{r}_l+\boldsymbol{\rho},\mathbf{r}_l+\boldsymbol{\rho}}^{\mathbf{r}_l}(E - i\eta)] dE. \quad (60)$$

Equations (46) and (57) may be used to show that the above expression is a linear combination of b_l and b_l^* . Thus b_l, b_l^* ($l = 1, 2$) satisfy a set of linear homogeneous equations so that in general $b_l = 0$. This result is consistent with the symmetry of the transverse-field t-J^z model (equation (15)) which underlies the present model for low fermion density. When $\lambda = 0$, as assumed here, the transverse magnetic field vanishes so that by symmetry the expected value of the transverse spin moment $\langle S_{\mathbf{r}}^x \rangle = \langle b_{\mathbf{r}}^\dagger + b_{\mathbf{r}} \rangle / 2 = 0$. The properties $b_l = 0$ and the characteristic periodicity in \mathbf{k} are shown in the appendix to be generally true for the model with $\lambda = 0$ for all values of ω_0/t_0 . As soon as $\lambda \neq 0$ we shall in general have $b_l \neq 0$ so that, from equation (57), the \mathbf{k} dependence of the Green's function will involve $\gamma(\mathbf{k})$ and not only $[\gamma(\mathbf{k})]^2$ as is the case for $\lambda = 0$.

The final result for the Green's function in the case $\lambda = 0$ is

$$G_{\mathbf{k}}^{lm}(E) = \delta_{lm} [E - zt_0^2(1 - n_l)C(E, n_l) - \gamma(\mathbf{k})^2 n_l \bar{D}(E, n_l)]^{-1} \quad (61)$$

where C and \bar{D} are given by equations (47) and (59) respectively. Also, from equation (34),

$$G_{\mathbf{k}}(E) = \frac{1}{2} [G_{\mathbf{k}1}(E) + G_{\mathbf{k}2}(E)], \quad (62)$$

where $G_{\mathbf{k}l} = G_{\mathbf{k}}^{ll}$. In the homogeneous case, where there is no CDW, $n_1 = n_2 = n$, where $n = N_f/N$ is the fermion density, and $G_{\mathbf{k}1} = G_{\mathbf{k}2} = G_{\mathbf{k}}$. For $n = 0$ we recover the $N_f = 1$ result for $G_{\mathbf{k}}^{-1}$, given by the left-hand side of equation (23), and for $n = 1$ we recover the $N_f = N - 1$ result given by equation (30). Thus $G_{\mathbf{k}}$ is correct in these two limits within the two-boson approximation. The factor δ_{lm} in equation (61) shows that within the present approximation fermions propagate, by means of double hops, within a single sublattice. The dimension of the bipartite lattice (1, 2 or 3) enters only through the band energy $\gamma(\mathbf{k})$ (equation (17)) and the function \bar{D} , which may be written as

$$\bar{D}(E, n_l) = \int \frac{N_0(\gamma)}{E + \omega_0 - \gamma^2 n_l / (E + 2\omega_0)} d\gamma, \quad (63)$$

where $N_0(\gamma)$ is the density of states per site for the band energy $\gamma(\mathbf{k})$.

To complete the present formulation we require the equations which determine the chemical potential μ and the self-consistent sublattice densities n_1, n_2 for a given fermion density n . The density of states per site on sublattice l is given by

$$N_l(E) = -\frac{1}{N\pi} \sum_{\mathbf{k}} \text{Im} G_{\mathbf{k}l}(E + i\eta) \quad (64)$$

and

$$n_l = \int N_l(E) f(E, \mu) dE, \quad (65)$$

where $f(E, \mu) = [e^{\beta(E-\mu)} + 1]^{-1}$ is the Fermi function with chemical potential μ and $\beta = (k_B T)^{-1}$. The chemical potential and the CDW order parameter P are determined by

$$\frac{1}{2}(n_1 + n_2) = n, \quad \frac{1}{2}(n_1 - n_2) = nP. \quad (66)$$

If the system is ordered ($P \neq 0$) at $T = 0$ the CDW temperature T_c , where $P \rightarrow 0$, can be calculated. In the present mean-field-like approximation this will not be the true T_c but a higher temperature where short-range order substantially disappears. The calculated T_c should be a reasonable approximation to the true value in 3D. In general, if quantities such as the spectral functions discussed below are calculated assuming $P = 0$, the results will be valid in the high-temperature limit where there is truly no short-range order.

The spectral function for states projected onto the sublattice l is given by

$$S_l(\mathbf{k}, E) = -\frac{1}{\pi} \text{Im} G_{\mathbf{k}l}(E + i\eta) \quad (67)$$

and the total spectral function is

$$S(\mathbf{k}, E) = -\frac{1}{\pi} \text{Im} G_{\mathbf{k}}(E + i\eta) = \frac{1}{2} [S_1(\mathbf{k}, E) + S_2(\mathbf{k}, E)]. \quad (68)$$

These spectral functions may be used to calculate the occupation number $n(\mathbf{k}) = \langle f_{\mathbf{k}}^\dagger f_{\mathbf{k}} \rangle$ and the related quantity $d(\mathbf{k}) = \langle f_{\mathbf{k}}^\dagger f_{\mathbf{k}+\mathbf{Q}/2} \rangle$, where \mathbf{Q} is a basis vector of the reciprocal lattice. $f_{\mathbf{k}}$ is given by equation (32) and it follows from equation (33) that $f_{\mathbf{k}+\mathbf{Q}/2} = (f_{\mathbf{k}1} - f_{\mathbf{k}2})/\sqrt{2}$. Hence we find

$$n(\mathbf{k}) = \frac{1}{2} \int_{-\infty}^{\mu} [S_1(\mathbf{k}, E) + S_2(\mathbf{k}, E)] dE \quad (69)$$

and

$$d(\mathbf{k}) = \frac{1}{2} \int_{-\infty}^{\mu} [S_1(\mathbf{k}, E) - S_2(\mathbf{k}, E)] dE. \quad (70)$$

These quantities satisfy the sum rules

$$\frac{1}{N} \sum_{\mathbf{k}} n(\mathbf{k}) = n, \quad \frac{1}{N} \sum_{\mathbf{k}} d(\mathbf{k}) = nP. \quad (71)$$

In section 4 we report numerical results for all the above quantities, based on the approximate Green's function of equation (61), in the 1D case. Many of the results are compared with those of the DMRG method, both to assess the validity of the present approximation and sometimes to throw new light on the DMRG results. The application of the DMRG method to the present model has been described previously [16, 17].

4. Numerical results for ground state and spectral properties in 1D

In 1D the band energy $\gamma(\mathbf{k}) = -2\cos k$, with the lattice constant taken as 1 and the unit of energy taken as t_0 . The quantity \bar{D} which appears in the Green's function (equation (61)) can then be evaluated analytically using equations (58) and (59). The \mathbf{q} -summation is most conveniently performed as a contour integral around the unit circle. The result is

$$\bar{D}(E, n_l) = D_{lr}\theta(a_l^2 - b_l^2) - iD_{li}\theta(b_l^2 - a_l^2), \quad (72)$$

where

$$D_{lr} = \frac{1}{a_l \sqrt{1 - b_l^2/a_l^2}}, \quad D_{li} = \frac{1}{\sqrt{b_l^2 - a_l^2}} \quad (73)$$

with

$$a_l = E + \omega_0 - \frac{2n_l}{E + 2\omega_0}, \quad b_l = -\frac{2n_l}{E + 2\omega_0}. \quad (74)$$

The density of states, given by equation (64), can be evaluated similarly with the result

$$N_l(E) = N_{l1}(E) + N_{l2}(E), \quad (75)$$

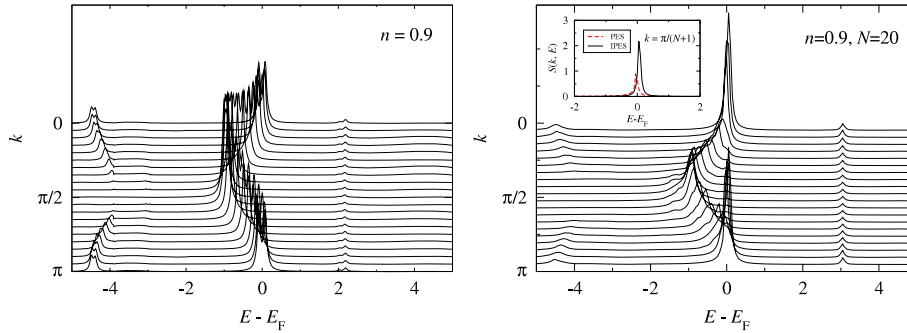


Figure 1. Zero-temperature single-particle spectral function $S(k, E)$ at $n = 0.9$ for $\omega_0 = 3$ from equation (68) (left panel) compared with the DDMRG result (right panel) obtained for a finite system with $N = 20$ sites using open boundary conditions (OBC). The inset shows the photoemission spectra (PES) and inverse photoemission spectra (IPES) near the Fermi point. E is measured with respect to the Fermi energy E_F (all energies are given in units of t_0).

(This figure is in colour only in the electronic version)

where

$$N_{11}(E) = \frac{1}{\pi} \theta(a_i^2 - b_i^2) \left[\frac{\theta(v_i^2 - u_i^2)}{\sqrt{v_i^2 - u_i^2}} + \theta(u_i^2 - v_i^2) \right. \\ \left. \times \left| \operatorname{Im} \left(\frac{1}{\sqrt{u_i(E + i\eta)^2 - v_i(E + i\eta)^2}} \right) \right| \right], \quad (76)$$

$$N_{12}(E) = \frac{\theta(b_i^2 - a_i^2)}{2\pi n_i D_{ii}} \sqrt{\frac{\sqrt{V_i^2 + 4} - |V_i|}{2|V_i|(V_i^2 + 4)}} \quad (77)$$

with

$$u_i(E) = E - 2(1 - n_i)C(E, n_i) - 2n_i D_{ir}(E), \quad (78)$$

$$v_i(E) = -2n_i D_{ir}(E), \quad (79)$$

$$V_i(E) = -\frac{E - 2(1 - n_i)C(E, n_i)}{2n_i D_{ii}(E)}. \quad (80)$$

The results presented below are for the case $\omega_0 = 3$. By comparison with the DMRG results for the ground state properties $n(k)$ and $d(k)$, and with the dynamical DMRG [24] (DDMRG) results for $S(k, E)$, it is found that this boson energy is large enough for many results of the present analytic approximation to be quite accurate.

4.1. High and low fermion density

The existence of a two-sublattice CDW state in the present model is well established at half-filling ($n = 0.5$) for sufficiently large ω_0/t_0 [15–17, 21]. However the general results of the appendix imply that a two-sublattice CDW state is always a possibility, whatever the density n . We therefore used equations (65), (66) and (75) to search for such states even in the high and low density cases of $n = 0.9$ and 0.1. In the case $n = 0.9$ with $\omega_0/t_0 = 3$ we find a self-consistent CDW state with order parameter $P = 0.063$. The flow of the iterative procedure to determine P indicates that this, not the uniform density $P = 0$ state, is the stable ground state. In the DMRG calculations convergence to the CDW solution is improved by use of suitable external fields at the boundaries with open

boundary conditions. The spectral function $S(k, E)$ calculated from the Green's function using equation (68) is compared with the DDMRG results in figure 1. The quasiparticle peaks for the Green's function decoupling scheme results (left panels) are delta-functions in the limit $\eta \rightarrow 0$, but to make them visible we have taken $\eta = 0.05$; the same value has been taken in the DDMRG data (right panel). The following main features are in good agreement: the general shape and width of the quasiparticle band crossing the Fermi level, the dispersive peaks just below $E - E_F = -4$ which vanish for $k = \pi/2$, the weak flat band at $E - E_F = 2$ in the left panel and 3 in the right one. The splitting of the quasiparticle peaks due to CDW order is clearly visible in the left panel. This splitting is not clearly resolved in the main right panel but the inset for $k = \pi/21$ shows a splitting between a peak below E_F in the photoemission spectrum (PES) and one above E_F in the inverse photoemission spectrum (IPES). The absence of the splitting for states further from E_F in the DDMRG data is presumably due to finite lifetime broadening processes which are not included in the Green's function approximation. It should be noticed that the quasiparticle states at the Fermi level are from only one of the split subbands near $k = 0$ and π , the other subband being fully occupied. This means that the Fermi wavevectors are at $\pi/10, \pi - \pi/10$ so that the hole pockets near $k = 0$ and π have the correct Fermi surface 'volume', this being twice what it would have been in the absence of the CDW ($P = 0$). Discontinuities at these wavevectors are clearly seen in figure 3 where $n(k)$ and $d(k)$, calculated from equations (69) and (70), are plotted. The agreement with the DMRG data, also plotted, is excellent. In the Green's function calculations the discontinuities are not perfectly sharp owing to the use of a finite η ($=0.0005$) near E_F . There are two contributions to $n(k)$ and $d(k)$, one arising from the coherent quasiparticle bands and the other from spectral weight further below the Fermi level. In the present case $d(k)$ arises almost entirely from the coherent contribution and the quasiparticle states have slightly more weight on the minority sublattice, hence the negative value of $d(k)$ over most of the zone. Near $k = 0$ and π , however, only the subband associated with the majority sublattice is occupied,

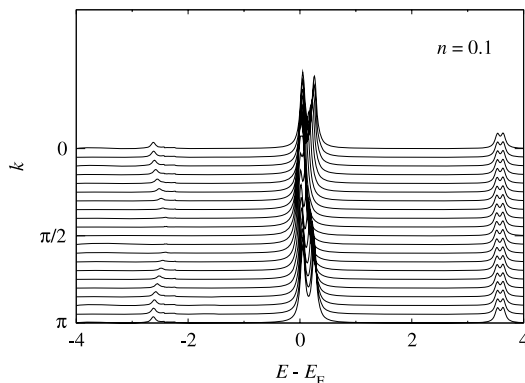


Figure 2. Single-particle spectral function $S(k, E)$ at $n = 0.1$ for $\lambda = 0$ and $\omega_0 = 3$ from equation (68).

hence the strong positive contribution. Correlations giving rise to Luttinger liquid behaviour in 1D are beyond the present Green's function approach. It should be noted that at $n = 0.9$ the CDW state is metallic, whereas at $n = 0.5$ it is an insulator, as discussed in section 4.2.

In the case $n = 0.1$ with $\omega_0/t_0 = 3$ we find a self-consistent CDW state with order parameter $P = 0.61$. The discrepancy in order of magnitude between this value and the much smaller one for $n = 0.9$ is due to the consistent use of fermion density in the definition of P (equation (66)), rather than changing to hole density for the $n = 0.9$ case. For $n = 0.1$ it has proved difficult to converge to a CDW solution in DMRG. This may indicate that the Green's function

approximation is failing in this low density case. If so, the nature of the ground state is unclear. Nevertheless in figure 2 we show results for the spectral function and in figure 3 we plot $n(k)$ and $d(k)$. The bottom of the narrow quasiparticle band near E_F is at $k = \pi/2$ and only the majority subband is occupied. Hence $d(k)$ is strongly positive near $k = \pi/2$ and almost equal to $n(k)$. Over most of the zone the only contribution is from spectral weight further below the Fermi level; this vanishes at $k = \pi/2$ and makes a negative contribution to $d(k)$ owing to more weight residing on the minority sublattice. The discontinuities in $n(k)$ and $d(k)$ at the expected values $\pi/2 \pm \pi/10$ are clearly seen.

4.2. The CDW state at half-filling

We now consider a self-consistent CDW state for the half-filled band with $n = 0.5$ and $\lambda = 0$, $\omega_0 = 3$. As before the Fermi energy E_F (or chemical potential μ at $T > 0$) and order parameter P are determined by equations (66) and (65), with the sublattice densities of states given by equation (75). For the above parameters we find $\mu = -0.211$, $P = 0.765$. E_F lies in a gap as is appropriate for an insulator.

The spectral functions calculated from the Green's function method and the DDMRG are compared in figure 4. The agreement is generally good. The Fermi level lies in a gap between two quasiparticle bands, a broad upper unoccupied one and a narrower lower occupied one. The main discrepancy is that in the DDMRG case the lower quasiparticle band is extremely narrow whereas in the Green's function method it has a significant width. This shortcoming of the Green's function approximation is discussed thoroughly

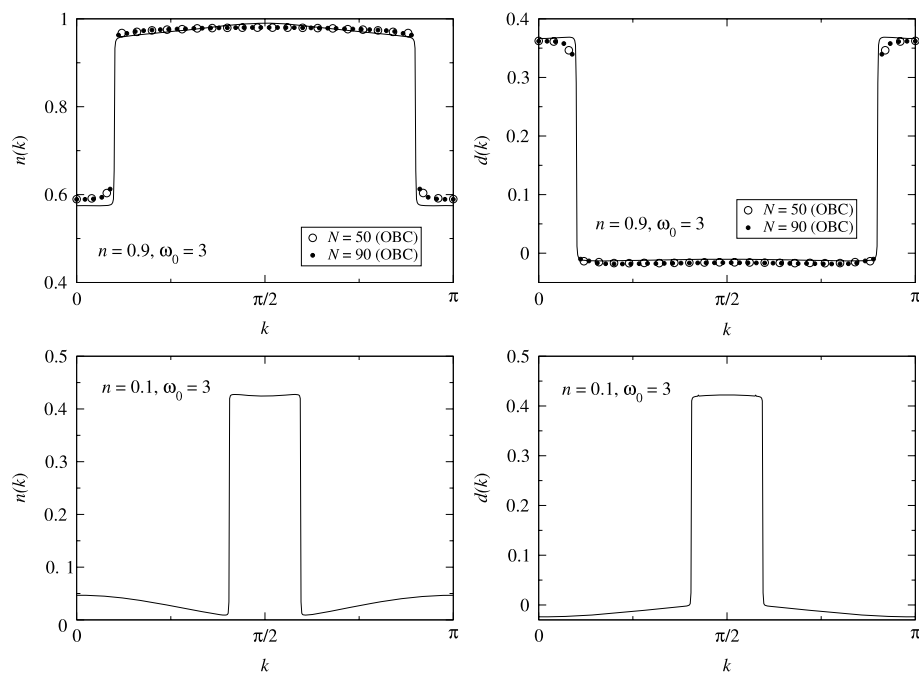


Figure 3. Bloch state occupation numbers $n(k)$ (left) and related correlation function $d(k)$ (right) for $n = 0.9$ (upper panels) and $n = 0.1$ (lower panels) at $\lambda = 0$, $\omega_0 = 3$. Analytical results (lines) are compared to numerical DMRG data (symbols).

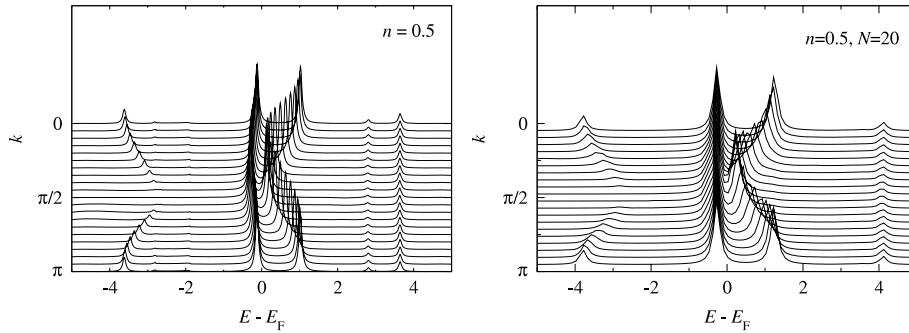


Figure 4. Single-particle spectral function $S(k, E)$ at $n = 0.5$ for $\lambda = 0, \omega_0 = 3$ from equation (68) (left panel) compared with the DDMRG result (right panel).

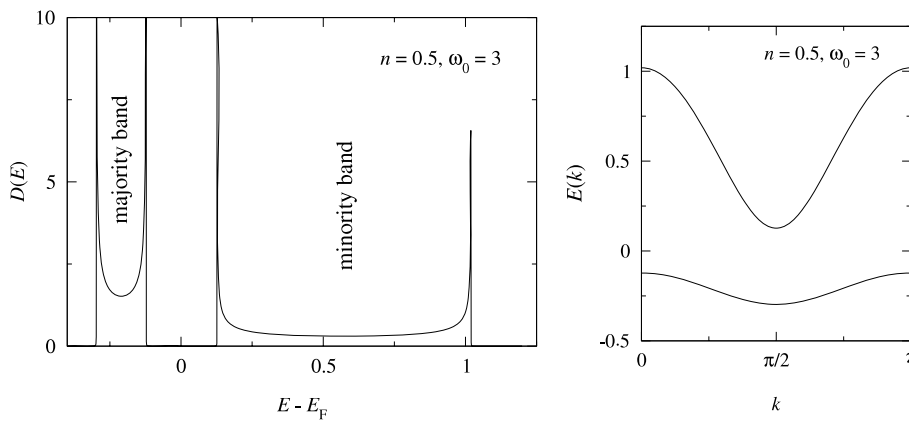


Figure 5. Density of states $D(E)$ near the Fermi level for $\lambda = 0$ at half-filling from equation (75) (left panel) and corresponding quasiparticle band dispersion $E(k)$ (right panel).

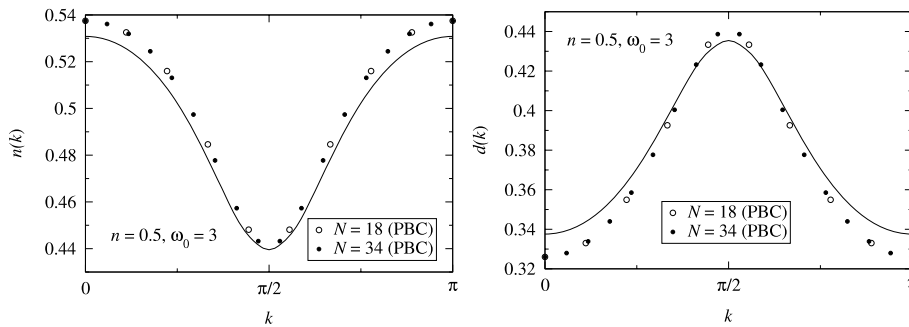


Figure 6. Bloch state occupation number $n(k)$ (left panel) and related correlation function $d(k)$ (right panel) for the half-filled band case with $\lambda = 0, \omega_0 = 3$.

in section 4.3. Figure 5 shows the density of states near the Fermi level, projected onto the majority and minority sublattices, calculated from equation (64). It is remarkable that states in the occupied quasiparticle band are entirely confined to the majority sublattice, whereas those in the unoccupied quasiparticle band reside entirely on the minority sublattice. The dispersion curves $E(k)$ of the quasiparticle bands, obtained by plotting the loci of quasiparticle peaks in

the spectral function, are shown in figure 5. The approximate Green's function therefore predicts an indirect gap, with the top of the occupied quasiparticle band at $k = 0, \pi$ and the bottom of the unoccupied band at $k = \pi/2$.

In figure 6 left and right panels we plot curves for $n(k)$ and $d(k)$, respectively, calculated from equations (69) and (70), together with points obtained by the DMRG method for finite systems of different sizes. The agreement is very

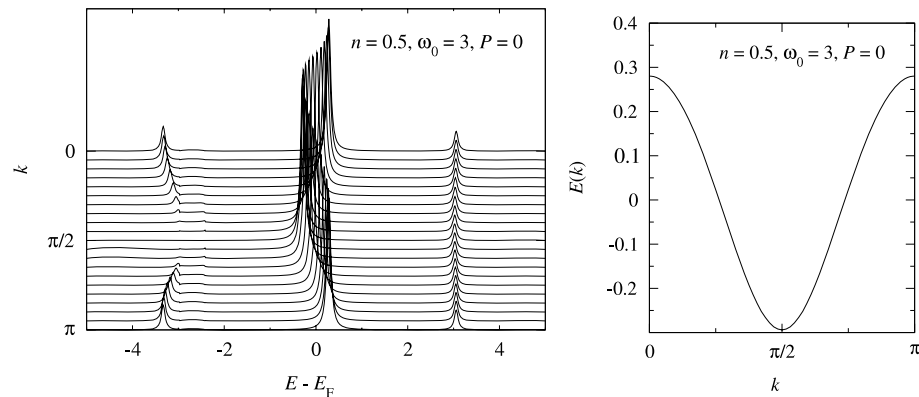


Figure 7. Single-particle spectral function (left panel) and quasiparticle band (right panel) in the high-temperature limit $P = 0$ for the half-filled band case with $\lambda = 0$, $\omega_0 = 3$.

striking, particularly since in DMRG these quantities are calculated directly from the ground state whereas in the Green's function method they are obtained as integrals over the spectral function. It should be noted that $n(\pi/2) = d(\pi/2)$ because for $k = \pi/2$ all the spectral weight of the occupied states resides in the quasiparticle peak which is entirely based on the majority sublattice. From equations (69) and (70) it is clear that the weight in this peak is $2n(\pi/2) \simeq 0.88$.

Finally in figure 7 we plot the spectral function (left panel) and quasiparticle energy (right panel) in the high-temperature limit, where all short-range order has disappeared ($P = 0$). The Fermi wavevectors are close to $\pi/4$ and $3\pi/4$ with the correct Fermi surface 'volume'. This is the state from which the CDW evolves as the temperature is lowered. Clearly the situation is quite different from the usual one in which a CDW evolves because of nesting between Fermi wavevectors at $k = \pm\pi/2$. The origin of this difference is that for $\lambda = 0$ only next-nearest-neighbour hopping, resulting in π -periodicity in k -space, occurs even in the disordered state.

4.3. Discussion

The most notable difference between the Green's function and DDMRG results lies in the width of the occupied quasiparticle band for $n = 0.5$. A very narrow band is also found in earlier calculations for $\omega_0 = 2$ using exact diagonalization where there is also no tendency for the top of the band to be at $k = 0, \pi$ rather than $\pi/2$ [15]. The band seems to be almost as narrow as one would have from the Trugman-like six-step process in a perfect CDW ($P = 1$). This is quite surprising since for $\omega_0 = 2$ the densities on the two sublattices are about 0.8 and 0.2 [16] which is far from a perfect CDW. Satellites below the main quasiparticle peak are suggestive of finite-size effects in the systems considered with 12 and 16 sites.

To gain more insight into the Green's function approximation we may consider the limit of large ω_0 where all the weight is concentrated in the two quasiparticle bands. From equation (61) it follows that these bands are given by

$$E(k) = \frac{\pm 2P + (1 \pm P) \cos(2k)}{\omega_0}, \quad (81)$$

where the upper signs (+) correspond to the upper band and the lower signs (−) to the lower band. The widths $2(1 \pm P)/\omega_0$ of these bands can be understood by inspection of the following processes, where a bullet represents a vacant site, a star represents a boson and a circle represents a fermion:



In the upper line the central site is on the majority sublattice. The diagram shows how a fermion added to the upper band, on the minority sublattice, can hop by a two-step process across an occupied majority site. The probability of the majority site being occupied is $(1 + P)/2$ so an estimate of the width of the upper band is $2(1 + P)/\omega_0$, as in equation (81). In the lower line the central site is on the minority sublattice. Clearly a hole created on the majority sublattice can hop by a two-step process across an occupied minority site. The probability of the minority site being occupied is $(1 - P)/2$ so an estimate of the width of the lower quasiparticle band is $2(1 - P)/\omega_0$ as in equation (81). The probability argument used here is equivalent to the Hartree–Fock-like approximation made in deriving the Green's function. This approximation is clearly failing in the present situation, since the width of the lower quasiparticle band is much larger than that given by the DDMRG. To expose the cause of this failure we used DMRG to calculate the three-site correlation functions $\langle n_{m-1} n_m n_{m+1} \rangle$ for a ten-site system with periodic boundary conditions and $\lambda = 0$, $\omega_0/t_0 = 3$ as usual. The correlation function takes two values 6.46062×10^{-4} and 3.90826×10^{-3} , depending on whether m is an even or odd site corresponding to the majority and minority sublattice, respectively. The simple probability argument would give respective values $P(1 - P)^2 = 0.04225$, $(1 - P)P^2 = 0.1375$ when $P = 0.765$. If a site on the minority sublattice is occupied it is clear that the probability of both neighbouring sites being occupied is only about 0.039. Thus one of these majority sublattice sites is very likely to be occupied by a hole. Hence there is a strong tendency for the minority sublattice fermions and the majority sublattice holes,

equal in number, to form bound pairs. We conclude that for $n = 0.5$ important correlations exist in the ground state which are not included in the Hartree–Fock-like approximation of the Green’s function decoupling.

5. Conclusions and outlook

Doped Mott insulators remain at the forefront of physics research largely because of their relevance to high-temperature superconductivity. In the cuprate superconductors holes in the copper oxide planes move in a background of antiferromagnetic order. In other systems of interest the background is one of alternating orbital order. The progress of a hole through such a background is hindered by the string effect. This effect has been known for a long time [8] but the string picture is central to much recent work (e.g. [25–28]). The Edwards fermion–boson model considered in this paper was introduced to describe this effect in the simplest possible way [12]. The spinless fermions correspond physically to the holes in the Mott insulator. The ordered background does not appear explicitly in the model; the essence of the string effect actually relies only on the existence of substantial short-range order without the necessity of true long-range order. Clearly the physical interest lies mainly in 2D [29], but so far most calculations for the Edwards model have been made in 1D [14–17, 21, 22]. In this paper we describe an analytical approximation to the one-fermion Green’s function which is valid in 1D, 2D and 3D. Its main limitations are that the boson energy should be fairly large ($\omega_0/t_0 > 2$) and that string relaxation is neglected ($\lambda = 0$). The principal objective of this paper is to test the accuracy of the Green’s function method, within its expected domain of validity, by comparing with numerical results obtained in 1D by the DMRG and DDRMG methods.

This comparison has been made in detail for $\omega_0 = 3$ and for various fermion densities. For the half-filled band case ($n = 0.5$) excellent agreement is obtained for ground state properties. These include the CDW order parameter, the Bloch state occupation number $n(k)$ and a related quantity $d(k)$ associated with the CDW. There is also generally good agreement for the one-fermion spectral function although the Green’s function method predicts much too wide an occupied quasiparticle band. In section 4.3 the reason for this discrepancy is traced to missing correlations in the Green’s function approximation. The Green’s function method predicts that the CDW state evolves from a high-temperature disordered state with Fermi wavevectors close to $\pi/4$ and $3\pi/4$, which is quite different from the usual case where a CDW evolves because of nesting between Fermi wavevectors at $k = \pm\pi/2$. The origin of the difference is that only next-nearest-neighbour hopping, resulting in π -periodicity in k -space, occurs even in the disordered state.

There is excellent agreement between the two methods for the dilute hole ($n = 0.9$) case with the usual parameters $\lambda = 0$, $\omega_0/t_0 = 3$. Somewhat surprisingly, there is also a two-sublattice CDW state which in this case is metallic. In the appendix it is shown how the appearance of two-sublattice CDW states is related to a symmetry property of the model

with $\lambda = 0$. The comparison between the two methods proved to be more difficult in the dilute fermion ($n = 0.1$) case. The Green’s function method again predicts a metallic CDW state but the DMRG fails to confirm this. The true nature of the ground state in this case remains unclear.

It may be concluded that the rather simple Green’s function approximation derived here is sufficiently successful in 1D, which is probably the least favourable case, to envisage future applications to the 2D t - J^z model and, with a slight extension of the model, to the t_{2g} model of alternating orbital order. The situation of physical interest will be low to moderate fermion density, the fermions corresponding to holes in the relevant Mott insulator.

Acknowledgment

This work was supported by SFB 652 of the Deutsche Forschungsgemeinschaft.

Appendix

Through the particular form of the fermion–boson hopping term at $\lambda = 0$ (cf equation (14)) the transfer of a fermion between neighbouring lattice sites coincides with a change of the number of bosons by one. As a consequence we may think of the bosons as tracking the motion of the fermions. This picture becomes exact through the identification of a conserved quantity. Let us define operators N_f^A and N_f^B which count the number of fermions on the A- or B-sites of a bipartite lattice, and similar operators N_b^A and N_b^B for bosons. Then $N_{fb} = N_f^A - N_f^B + 2(N_b^A - N_b^B)$ commutes with the Hamiltonian \tilde{H}_{Ed} , when $\lambda = 0$, and is therefore a conserved quantity. The eigenvalues of N_{fb} can be used to classify the eigenstates of the Hamiltonian. We note that N_{fb} is not conserved for $\lambda \neq 0$.

The existence of N_{fb} has two major consequences. First, fermion operators such as $f_{nA}^\dagger f_{mB}$ change N_{fb} by 2, so that in any eigenstate of the Hamiltonian the expectation value $\langle f_{nA}^\dagger f_{mB} \rangle = 0$ for arbitrary sites nA and mB on the respective sublattices. Similarly $\langle b_n \rangle = 0$. Hence quantities such as the spectral function $S(\mathbf{k}, E)$ or the momentum distribution $n(\mathbf{k})$ have the periodicity in \mathbf{k} of the reciprocal lattice of the real-space A or B sublattice, e.g. π -periodicity in the 1D case. Second, it implies that those eigenvalues of the Hamiltonian corresponding to $N_{fb} \neq 0$ are degenerate. This follows because the translation operator T commutes with H , but changes the sign of N_{fb} . The energy eigenvalue of an eigenstate $|\psi\rangle$ with $\langle \psi | N_{fb} | \psi \rangle \neq 0$ must therefore be (at least) two-fold degenerate, since the state $T|\psi\rangle$ belongs to the same energy but differs from $|\psi\rangle$ due to the change of N_{fb} . This degeneracy corresponds to a breaking of translational symmetry, as for a two-sublattice CDW state. Clearly if the ground state at $\lambda = 0$ is not such a CDW state it must have $N_{fb} = 0$.

References

- [1] Hubbard J 1963 *Proc. R. Soc. A* **276** 238
- [2] Daghofer M, Wohlfeld K, Oleś A M, Arrigoni E and Horsch P 2008 *Phys. Rev. Lett.* **100** 066403
- [3] Wohlfeld K, Daghofer M, Oleś A M and Horsch P 2008 *Phys. Rev. B* **78** 214423

- [4] Matsuno J, Okimoto K, Kawasaki M and Tokura Y 2005 *Phys. Rev. Lett.* **95** 176404
- [5] Hidaka M, Inoue K, Yamada I and Walker P J 1983 *Physica B + C* **121** 343
- [6] McLain S E, Dolglos M R, Tennant D A, Turner J F C, Barnes T, Proffen T, Sales B C and Bewley R I 2006 *Nat. Mater.* **5** 561
- [7] Chao K A, Spalek J and Oleś A M 1977 *J. Phys. C: Solid State Phys.* **10** L271
- [8] Brinkman W F and Rice T M 1970 *Phys. Rev. B* **2** 4302
- [9] Kane C L, Lee P A and Read N 1989 *Phys. Rev. B* **39** 6880
- [10] Trugman S A 1988 *Phys. Rev. B* **37** 1597
- [11] Martinez G and Horsch P 1991 *Phys. Rev. B* **44** 317
- [12] Edwards D M 2006 *Physica B* **378–380** 133
- [13] Stinchcombe R B 1973 *J. Phys. C: Solid State Phys.* **6** 2459
- [14] Alvermann A, Edwards D M and Fehske H 2007 *Phys. Rev. Lett.* **98** 056602
- [15] Wellein G, Fehske H, Alvermann A and Edwards D M 2008 *Phys. Rev. Lett.* **101** 136402
- [16] Ejima S, Hager G and Fehske H 2009 *Phys. Rev. Lett.* **102** 106404
- [17] Ejima S and Fehske H 2009 *Phys. Rev. B* **80** 155101
- [18] White S R 1992 *Phys. Rev. Lett.* **69** 2863
- [19] White S R 1993 *Phys. Rev. B* **48** 10345
- [20] Becker K W, Hübsch A and Sommer T 2002 *Phys. Rev. B* **66** 235115
- [21] Sykora S, Becker K W and Fehske H 2010 *Phys. Rev. B* **81** 195127
- [22] Alvermann A, Edwards D M and Fehske H 2010 *J. Phys. Conf. Ser.* **220** 012023
- [23] Zubarev D N 1960 *Usp. Fiz. Nauk* **71** 71
Zubarev D N 1960 *Sov. Phys. Usp.* **3** 320 (Engl. Transl.)
- [24] Jeckelmann E 2002 *Phys. Rev. B* **66** 045114
- [25] Wróbel P, Suleja W and Eder R 2008 *Phys. Rev. B* **78** 064501
- [26] Wohlfeld K, Oleś A M and Horsch P 2009 *Phys. Rev. B* **79** 224433
- [27] Berciu M 2009 *Physics* **2** 55
- [28] Wróbel P and Oleś A M 2010 *Phys. Rev. Lett.* **104** 206401
- [29] Berciu M and Fehske H 2010 *Phys. Rev. B* **82** 085116



Dynamic properties of the one-dimensional Bose-Hubbard model

S. EJIMA¹, H. FEHSKE¹ and F. GEBHARD²

¹ *Institut für Physik, Ernst-Moritz-Arndt-Universität Greifswald - D-17489 Greifswald, Germany, EU*

² *Department of Physics, Philipps-Universität Marburg - D-35032 Marburg, Germany, EU*

received 18 November 2010; accepted in final form 17 January 2011

published online 9 February 2011

PACS 03.75.Kk – Dynamic properties of condensates; collective and hydrodynamic excitations, superfluid flow

PACS 71.10.Fd – Lattice fermion models (Hubbard model, etc.)

Abstract – We use the density-matrix renormalization group method to investigate ground-state and dynamic properties of the one-dimensional Bose-Hubbard model, the effective model of ultracold bosonic atoms in an optical lattice. For fixed maximum site occupancy $n_b = 5$, we calculate the phase boundaries between the Mott insulator and the “superfluid” phase for the lowest two Mott lobes. We extract the Tomonaga-Luttinger parameter from the density-density correlation function and determine accurately the critical interaction strength for the Mott transition. For both phases, we study the momentum distribution function in the homogeneous system, and the particle distribution and quasi-momentum distribution functions in a parabolic trap. With our zero-temperature method we determine the photoemission spectra in the Mott insulator and in the “superfluid” phase of the one-dimensional Bose-Hubbard model. In the insulator, the Mott gap separates the quasi-particle and quasi-hole dispersions. In the “superfluid” phase the spectral weight is concentrated around zero momentum.

Copyright © EPLA, 2011

Introduction. – At very low temperatures, bosonic atoms which are loaded into an optical lattice become superfluid for a shallow optical potential and Mott insulators for a deep optical potential. The transition between both phases has been observed experimentally [1]; for a recent review, see [2]. The Bose-Hubbard model provides a reasonable description of the experimental situation, and its ground-state phase diagram in two and three dimensions has been determined fairly accurately by perturbation theory [3–5] and quantum Monte Carlo (QMC) calculations [6–8].

Bosons on a chain are also accessible experimentally [9] so that it is interesting to study the one-dimensional Bose-Hubbard model. The physics in one dimension is rather peculiar. For example, the state with the lowest kinetic energy is not macroscopically occupied in the “superfluid” [10] but it is characterised by an algebraic divergence of the momentum distribution; for a review, see [11]. Moreover, the Mott gap is exponentially small in the Mott insulator close to the phase transition. Therefore, it is very difficult to determine the critical interaction strength numerically. This problem also impairs the applicability of strong-coupling perturbation theory.

In one dimension and at zero temperature, the density-matrix renormalisation group (DMRG) method [12–14]

permits the calculation of ground-state properties with an excellent accuracy for large systems so that the extrapolation to the thermodynamic limit can be performed reliably. In this work, we use the density-density correlation function to calculate the Tomonaga-Luttinger parameter from which we determine the Mott transition accurately. Moreover, we obtain the momentum distribution and the particle distribution for bosons on a homogeneous chain and in the presence of a harmonic trap. Using the dynamical DMRG [15], we calculate the single-particle spectral function at zero temperature in the “superfluid” and the Mott insulating phases.

Bose-Hubbard model. – The Hamilton operator for the Bose-Hubbard model on a chain with an even number of sites L in a harmonic potential is defined by

$$\hat{\mathcal{H}} = -t \sum_j \left(\hat{b}_j^\dagger \hat{b}_{j+1} + \hat{b}_{j+1}^\dagger \hat{b}_j \right) + \frac{U}{2} \sum_j \hat{n}_j (\hat{n}_j - 1) + V_c \sum_j (j - r_c)^2 \hat{n}_j, \quad (1)$$

where \hat{b}_j^\dagger and \hat{b}_j are the creation and annihilation operators for bosons on site j , $\hat{n}_j = \hat{b}_j^\dagger \hat{b}_j$ is the boson number operator on site j , t is the tunnel amplitude between

S. Ejima *et al.*

neighbouring lattice sites, $U > 0$ denotes the strength of the on-site Coulomb repulsion, V_c parameterises the curvature of the quadratic confining potential, and $r_c = (L+1)/2$ denotes the central position of the chain. In the following, we set $U = 1$ as our energy unit, unless stated otherwise.

Constrained Bose-Hubbard model. In general, the Bose-Hubbard model cannot be solved analytically. In the low-density limit, the model reduces to the Bose gas with δ -potential interaction which was solved by Lieb and Liniger [16]. The fact that three or more bosons may occupy the same site forms the major obstacle on the way to an exact solution. Since multiple occupancies also pose technical problems in numerical approaches, the Bose-Hubbard model is usually approximated by the constraint that there is a maximal number of bosons per site, $0 \leq n_b \leq \mathcal{N} - 1$. This constrained Bose-Hubbard model has \mathcal{N} degrees of freedom per site so that it can be written in terms of spin variables with $S = (\mathcal{N} - 1)/2$. The case $\mathcal{N} = 2$ is trivial because the hard-core Bose-Hubbard model has no interaction term. It reduces to a model for free spinless fermions whose properties are known exactly [17]. The Bose-Hubbard model is recovered in the limit $\mathcal{N} \rightarrow \infty$. In general, however, the $SU(\mathcal{N})$ -Bethe Ansatz equations do not solve the constrained Bose-Hubbard model [18,19].

In our work, we study the restricted Bose-Hubbard model with $\mathcal{N} = 6$, *i.e.*, $n_b \leq 5$. Our results are representative for the original Bose-Hubbard model (1) because multiple lattice occupancies are strongly suppressed in the parameter regions of interest to us, $U/t > 2$ and fillings $\rho = N/L < n_b$.

Numerical algorithm. We adopt the DMRG method [12] as our numerical tool for the calculation of ground-state properties for constrained Bose systems [13,14]. For the spectral properties, we employ the dynamical DMRG (DDMRG) [15].

The considered lattices are large enough to permit reliable extrapolations to the thermodynamic limit for the physical quantities of interest to us. We keep up to $m = 2000$ density-matrix eigenstates, so that the discarded weight is always smaller than 1×10^{-10} .

We checked our algorithm for $n_b = 1$ against the exact result [17]. The exact ground-state energy in the thermodynamical limit and the extrapolated ground-state energy from DMRG agree to four-digit accuracy.

Ground-state phase diagram. At integer filling $\rho = N/L$, the Bose-Hubbard model in one dimension describes a Mott transition between the “superfluid” phase, characterised by a divergence of the momentum distribution at momentum $k=0$ [10], and a Mott insulating phase, characterised by a finite gap for single-particle excitations. The latter is defined by the energy difference between the chemical potentials for half band filling and one particle

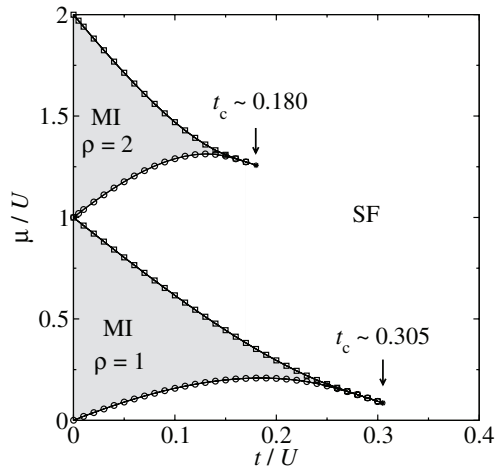


Fig. 1: Phase diagram of the one-dimensional constrained Bose-Hubbard model ($n_b \leq 5$) from DMRG with “superfluid” (SF) and Mott insulating (MI) regions. The symbols confine the regions with a finite Mott gap, $\Delta > 0$, extrapolated from $\Delta(L)$ for $L \leq 128$. The position of the Mott tips has been obtained from the Tomonaga-Luttinger parameter.

less than half filling,

$$\begin{aligned} \Delta(L) &= \mu^+(L) - \mu^-(L), \\ \mu^+(L) &= E_0(L, N+1) - E_0(L, N), \\ \mu^-(L) &= E_0(L, N) - E_0(L, N-1), \end{aligned} \quad (2)$$

where $E_0(L, N)$ is the ground-state energy for L sites and N particles. In the thermodynamical limit, $N, L \rightarrow \infty$ and $\rho = N/L$ integer, the gap is finite for the Mott insulator, $\Delta = \lim_{N, L \rightarrow \infty} \Delta(L) > 0$, so that the system becomes incompressible when we go from the “superfluid” phase to the Mott insulating phase.

The Mott transition lines in the μ - U ground-state phase diagram have been previously determined by various analytical and numerical methods, *e.g.*, strong-coupling expansions [20,21], variational cluster approach [22], QMC [23,24], and DMRG [13,14]. In fig. 1 we show the phase diagram for the first Mott lobe ($\rho=1$) and the second Mott lobe ($\rho=2$) as obtained from our DMRG calculations with system sizes up to $L = 128$.

The overall shape of the Mott lobes agrees with previous results. Here, we provide accurate data for the second Mott lobe, and the values for the critical interaction strength for the first two Mott lobes which we obtain from the Tomonaga-Luttinger parameter. At the tip of each Mott lobe, the model is in the universality class of the XY spin model so that there is a Kosterlitz-Thouless phase transition with the Tomonaga-Luttinger parameter $K_b = 1/2$, and the gap is exponentially small in the vicinity of $(t/U)_c$. In contrast, $SU(\mathcal{N})$ -Bethe Ansatz equations

predict a discontinuity of the gap at the critical interaction for $\mathcal{N} \geq 3$ [18,19].

Ground-state properties. –

Tomonaga-Luttinger parameter and critical interactions for the Mott transition. The low-energy excitations of interacting bosons in the superfluid phase are gapless linear excitations (“phonons”). As in the case of fermionic systems in one dimension [25,26], the Tomonaga-Luttinger parameter K_b determines the asymptotic behaviour of the correlation functions in the “superfluid” phase, and various correlations functions have been used to extract K_b [27–30]. Here, we employ the density-density correlation function which is defined by the ground-state expectation value

$$C(r) = \frac{1}{L} \sum_{\ell=1}^L \langle \hat{n}_{\ell+r} \hat{n}_{\ell} \rangle - \langle \hat{n}_{\ell+r} \rangle \langle \hat{n}_{\ell} \rangle. \quad (3)$$

Asymptotically, it behaves like

$$C(r \rightarrow \infty) \sim -\frac{1}{2K_b} \frac{1}{(\pi r)^2} + \frac{A\rho^2 \cos(2\pi\rho r)}{(\rho r)^{2/K_b}} + \dots \quad (4)$$

Thus, we can extract K_b from the derivative of its Fourier transformation,

$$\tilde{C}(q) = \sum_{r=1}^L e^{-iqr} C(r), \quad 0 \leq q < 2\pi, \quad (5)$$

as $q = 0$. In the thermodynamic limit one finds

$$\frac{1}{2\pi K_b} = \lim_{q \rightarrow 0} \frac{\tilde{C}(q)}{q}. \quad (6)$$

In order to treat finite systems in numerical calculations [26], we translate (6) into

$$\frac{1}{2K_b(L)} = \lim_{L \rightarrow \infty} \frac{L}{2} \tilde{C}\left(\frac{2\pi}{L}\right), \quad (7)$$

and extrapolate $K_b(L)$ to the thermodynamical limit.

In refs. [14] and [31] the transition point has been also determined from the Luttinger parameter K_b . However, these authors estimated K_b from the single-particle density matrix

$$\Gamma(r) = \langle \hat{b}_r^\dagger \hat{b}_0 \rangle \sim r^{-K_b/2} \text{ for } r \gg 1. \quad (8)$$

In their work, the extrapolation for the critical point t_c depends on the interval used for the fits to $\Gamma(r)$, see table I in ref. [14]. When we derive the Luttinger parameter from eq. (6) we can avoid this problem.

As shown in fig. 2, $K_b(L)$ can be reliably extrapolated to the thermodynamic limit using polynomial functions in $1/L$. For $\rho = 1$, we clearly have $K_b(t/U = 0.3) > 1/2$. When we extrapolate our data for up to $L = 1024$ lattice sites, we find $K_b(t/U = 0.304) > 1/2$ but $K_b(t/U = 0.306) < 1/2$. Therefore, we locate the transition point at $t_c = 0.305 \pm$

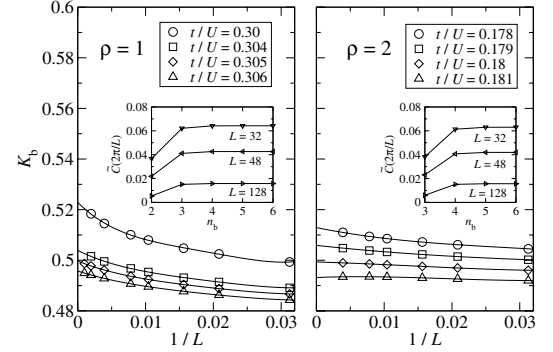


Fig. 2: Finite-size scaling for the Tomonaga-Luttinger parameter K_b in the one-dimensional constrained Bose-Hubbard model ($n_b = 5$) for the first ($\rho = 1$) and second ($\rho = 2$) Mott lobes, using the DMRG with open boundary conditions. The lines are polynomial fits. The insets give the n_b -dependence of $\tilde{C}(2\pi/L)$ for various system sizes at $t/U = 0.305$ (left panel) and $t/U = 0.18$ (right panel).

0.001 for the first Mott lobe. In the same way we find the transition point for the second Mott lobe at $t_c = 0.180 \pm 0.001$ for the restricted Bose-Hubbard model with $n_b \leq 5$. Using the same method, we have verified numerically that the values for the critical coupling $(t/U)_c$ are the same for $n_b = 4, 6$ within our extrapolation uncertainty.

Note that $K_b(t < t_c)$ is not defined because we are in the Mott insulating phase. However, $K_b(L)$ is finite and continuous over the Kosterlitz-Thouless transition because the Mott gap is exponentially small near t_c . Nevertheless, our approach remains applicable as has been shown for various fermionic models in refs. [26,32].

Previous groups located the Kosterlitz-Thouless transition for the first Mott lobe at values consistent with ours. In their DMRG work [14], Kühner *et al.* computed the Luttinger parameter using their DMRG algorithm on lattices with up to $L = 1024$ sites. From their fit to $\Gamma(r)$, eq. (8), they found $t_c = 0.297 \pm 0.01$. Based on the same correlation function, Zakrzewski and Delande [31] gave $t_c = 0.2975 \pm 0.005$ for the first and $t_c = 0.175 \pm 0.002$ for the second Mott lobe for $n_b = 6$. The determined t_c -values of such a kind significantly depend on the interval of r , which is not the case within our approach. Läuchli and Kollath [33] determined the critical point from the block entropy, by combining the recently developed quantum information theory with the DMRG. Our result is within their region of the estimated values for t_c (see fig. 2 in ref. [33]). In a combination of an exact diagonalisation study for systems with up to $L = 12$ sites and a renormalisation group approach, Kashurnikov and Svistunov found $t_c = 0.304 \pm 0.002$ [34], and their QMC calculations together with Kravasin gave $t_c = 0.300 \pm 0.005$ [24]. Another QMC calculation in combination with a renormalisation-group flow analysis of the finite-temperature data gave $t_c = 0.305(4)$ [35], in

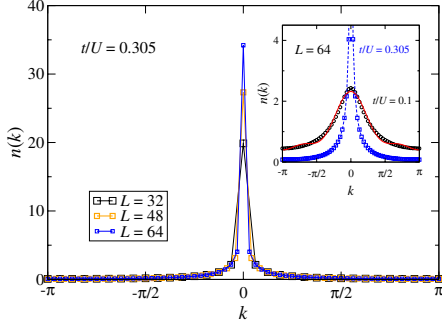


Fig. 3: (Colour on-line) Finite-size dependence of the momentum distribution function $n(k)$ for $t/U = 0.1$ (Mott insulator) and $t/U = 0.305$ (“superfluid”) in the one-dimensional Bose-Hubbard model using the DMRG with periodic boundary conditions. Inset: $n(k)$ for $L = 64$. The solid line in the inset gives the result of strong-coupling theory to third order, eq. (10) [5,37].

perfect agreement with the result of our zero-temperature study.

Momentum distribution function. Using the DMRG, the momentum distribution function $n(k)$ can be calculated by taking the Fourier transformation of the single-particle density matrix

$$n(k) = \frac{1}{L} \sum_{j,\ell=1}^L e^{ik(j-\ell)} \langle \hat{b}_j^\dagger \hat{b}_\ell \rangle, \quad (9)$$

where $k = 2\pi m/L$ for $m = -L/2 - 1, \dots, L/2$ holds for periodic boundary conditions [36]. Note that the momentum distribution function fulfils the sum rule $\sum_k n(k) = N$. In all cases of fig. 3 the numerical deviation $\xi = |N - \sum_k n(k)|$ is always small, $\xi < 1.0 \times 10^{-3}$.

The difference between the superfluid phase and the Mott insulator is most markedly seen in the momentum distribution $n(k)$ at momentum $k=0$: in the insulating phase, $n(k=0)$ remains finite whereas it diverges as a function of system size in the superfluid phase, as shown in fig. 3. At $t/U = 0.1$, $n(k=0)$ is almost independent of system size, and the momentum distribution $n(k)$ is a smooth function of momentum k . Strong-coupling perturbation theory to third order [5,37] predicts ($x = t/U$)

$$n^{[3]}(k) = 1 + 2C_1 \cos(k) + 2C_2 \cos(2k) + 2C_3 \cos(3k), \\ C_1 = 4x - 8x^3, \quad C_2 = 18x^2, \quad C_3 = 88x^3. \quad (10)$$

Our numerical results for $t/U = 0.1$ favourably compare with this expression, see the inset of fig. 3.

At $t/U = 0.305$, above the critical point, $n(k=0)$ increases rapidly with system size. In one spatial dimension there is no true superfluid with a macroscopic value for $n(k=0)$ in the thermodynamic limit [10]. Instead, we have from (8) $n(|k| \rightarrow 0) \sim |k|^{-\nu}$, $\nu = 1 - K_b/2 < 1$.

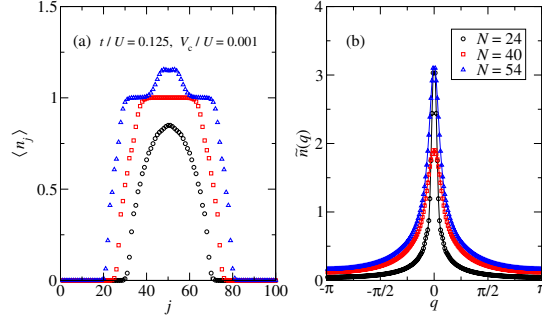


Fig. 4: (Colour on-line) Occupation probabilities in the one-dimensional constrained Bose-Hubbard model ($n_b \leq 5$) in a parabolic trap potential of strength $V_c/U = 0.001$. We show the results for $N = 24, 40, 54$ and $L = 100$ ($\rho = 0.24, 0.40, 0.54$) for $t/U = 0.125$ for (a) the local densities $\langle \hat{b}_j^\dagger \hat{b}_j \rangle$ and (b) the pseudo-momentum distribution $\tilde{n}(q)$.

Local densities for the Bose-Hubbard model in a trap.

In the presence of the confining potential V_c in the model (1), the density profile over the trap is no longer homogeneous, see, *e.g.*, ref. [38]. For an open system, we define the quasi-momentum distribution $\tilde{n}(q) = \langle \hat{b}^\dagger(q) \hat{b}(q) \rangle$ using the quasi-momentum states of particles in a box,

$$\hat{b}(q) = \sqrt{\frac{2}{L+1}} \sum_{\ell} \sin(q\ell) \hat{b}_\ell \quad (11)$$

with $q = \pi n_q/(L+1)$ for integers $1 \leq n_q \leq L$.

As demonstrated by Batrouni *et al.* [38] and Kollath *et al.* [36], the potential confines the particles in the middle of the trap. For small fillings, the local occupancies display a bell-shaped distribution, where the maximum does not reach the Mott plateau value, $\langle \hat{b}_j^\dagger \hat{b}_j \rangle (\rho = 0.24) < 1$. The quasi-momentum distribution $\tilde{n}(q)$ for this “superfluid in a trap” shows a prominent peak at $k=0$. For a larger filling, $\rho = 0.40$, there exists a Mott plateau, $\langle \hat{b}_j^\dagger \hat{b}_j \rangle (\rho = 0.40) = 1$ for $40 < j < 60$. Recall that, for $t/U = 0.125$, the homogeneous system at filling $\rho = 1$ is a Mott insulator. Correspondingly, the peak in the pseudo-momentum distribution at $k=0$ is smaller for $\rho = 0.40$ than for $\rho = 0.24$, see fig. 4(b). Finally, at filling $\rho = 0.54$, the confining potential and the bosons’ tendency to cluster overcome the repulsive potential in the middle of the trap so that local occupancies larger than unity are seen inside the trap. Correspondingly, the peak intensity of the pseudo-momentum distribution at $\rho = 0.54$ exceeds its value for $\rho = 0.40$.

Photoemission spectra. – Single-particle excitations associated with the injection or emission of a boson with wave vector q and frequency ω , $A^+(q, \omega)$ or $A^-(q, \omega)$, are described by the spectral functions

$$A^\pm(q, \omega) = \sum_n |\langle \psi_n^\pm | \hat{b}^\pm(q) | \psi_0 \rangle|^2 \delta(\omega \mp \omega_n^\pm), \quad (12)$$

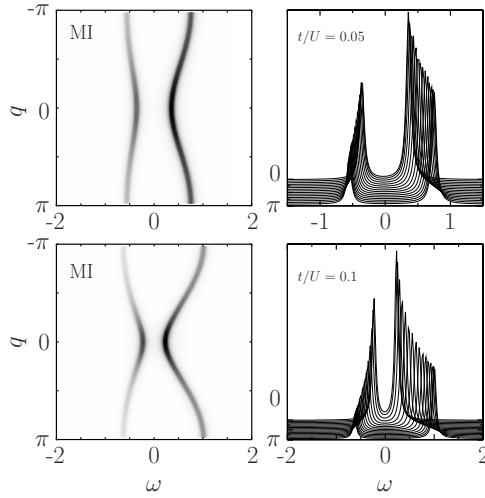


Fig. 5: Intensity (left panels) and line-shape (right panels) of the single-boson spectral functions $A(q, \omega)$ in the Mott insulating (MI) phase for $t/U = 0.05$ (upper panels) and $t/U = 0.1$ (lower panels) with system size $L = 64$ at filling $\rho = 1$ using the DDMRG technique with open boundary conditions.

where $\hat{b}^+(q) = \hat{b}^\dagger(q)$ and $\hat{b}^-(q) = \hat{b}(q)$ create/annihilate particles with pseudo-momentum q . Moreover, $|\psi_0\rangle$ is the ground state of a L -site system in the N -particle sector while $|\psi_n^\pm\rangle$ denote the n -th excited states in the $(N \pm 1)$ -particle sectors with excitation energies $\omega_n^\pm = E_n^\pm - E_0$.

So far, very few data are available for the (inverse) photoemission spectra in the one-dimensional (constrained) Bose-Hubbard model. Analytical results include the variational cluster perturbation theory [22], the random phase approximation [39], and strong-coupling theory [40]. Pippan *et al.* [41] combined QMC at low but finite temperatures with the maximum-entropy method to extract the spectral functions.

In the following we present the (inverse)-photoemission spectra at zero temperature using the numerically exact dynamical DMRG method [15,42]. We keep $m = 500$ states to obtain the ground state in the first five DMRG sweeps and take $m = 200$ states for the calculation of the various spectra from (12) by DDMRG. For a bosonic system the following sum-rules hold:

$$\int_{-\infty}^{\infty} d\omega (A^+(k, \omega) - A^-(k, \omega)) = 1, \quad (13)$$

$$\int_{-\infty}^0 d\omega (A^+(k, \omega) + A^-(k, \omega)) = n(k). \quad (14)$$

In our DDMRG calculations, both sum-rules are fulfilled with high precision.

In fig. 5 we show the results for the Mott insulator with $\rho = 1$. The spectra $A(q, \omega) = A^+(q, \omega) + A^-(q, \omega)$ for fixed q consist of two Lorentzians of width $\eta = 0.04$, the size of the broadening introduced in the DDMRG procedure. The

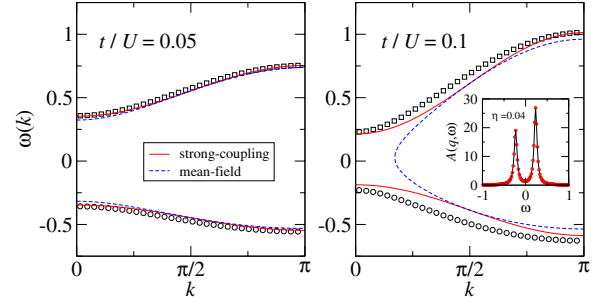


Fig. 6: (Colour on-line) Quasi-particle dispersions $\omega(k)$ in the Mott insulating phase at filling $\rho = 1$ for $t/U = 0.05$ and $t/U = 0.1$ from Lorentz fits to the spectral functions $A(q, \omega)$. For comparison, we also show the strong-coupling dispersions for the propagation of a hole and a double occupancy, $\omega_{h,p}(k)$, and the mean-field result of ref. [40]. Inset: $A(q, \omega)$ for $t/U = 0.1$ at $q = \pi/33$ with $L = 32$ (line) and $q = 2\pi/65$ with $L = 64$ (circles) demonstrating the negligible system size dependence.

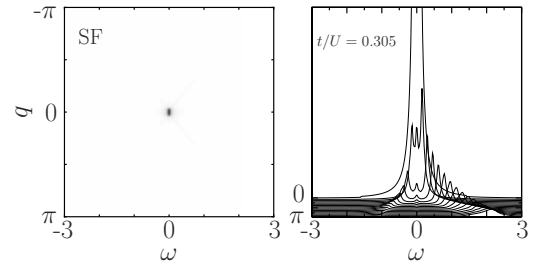


Fig. 7: Intensity (left panel) and line-shape (right panel) of the single-boson spectral functions $A(q, \omega)$ for $t_c = 0.305$ (“superfluid” phase) with system size $L = 64$ at filling $\rho = 1$ using the DDMRG technique with open boundary conditions for a broadening $\eta = 0.04$.

quality of the fits suggests that the quasi-particle life-time is very large in the Mott insulator.

In fig. 6 we show the quasi-particle dispersions for $t/U = 0.05$ and $t/U = 0.1$ which we extracted from the fits of the spectral functions to two Lorentz peaks at $\omega = \omega^\pm(k)$. For comparison, we include the mean-field result [40] and the strong-coupling result. For large interactions, each site is singly occupied in the ground state. A hole excitation can propagate freely so that the dispersion relation is given by $\omega_h(k) = -\mu + 2t \cos(k)$. Likewise, a doubly occupied site can also move freely through the system. Since either of the two bosons of the doubly occupied site can tunnel to its neighbouring sites, the dispersion relation is given by $\omega_p(k) = U - \mu - 4t \cos(k)$. These expressions for the quasi-particle dispersions are exact to leading and first order in strong-coupling perturbation theory.

In fig. 7 we show the spectral functions in the “superfluid” phase for $\rho = 1$ close to the Mott transition, $t = 0.305$. The elementary excitations concentrate around $(k = 0, \omega = 0)$. This confirms the formation of a “condensate”,

S. Ejima *et al.*

as also seen in the momentum distribution, see fig. 3. Moreover, it shows that the low-energy excitations near $k=0$ indeed dominate the spectral functions. We used this concept for the analysis of the ground-state correlation functions, see eq. (4). Note that deep inside of the Mott phase the system size dependence of the spectral functions is insignificant, see inset of fig. 6.

Conclusions. – In this work we have investigated the one-dimensional constrained Bose-Hubbard model ($n_b \leq 5$) at zero temperature. Using the density-matrix renormalisation group method we have obtained the Tomonaga-Luttinger parameter K_b from the density-density correlation function and determined the critical couplings $(t/U)_c = 0.305(1)$ for density $\rho = N/L = 1$ and $(t/U)_c = 0.180(1)$ for density $\rho = 2$ which separate the “superfluid” and Mott insulating phases.

In the “superfluid” phase, the momentum distribution diverges for small momenta, $n(|k| \rightarrow 0) \sim |k|^{-\nu} \sim L^\nu$ ($\nu = 1 - K_b/2$), and the spectral function is finite only for small frequencies and momenta. In the presence of a confining potential, we recover the Mott plateau in the particle density for filling $\rho = 0.40$ and the wedding-cake structure for filling $\rho = 0.54$.

In the Mott insulator, the momentum distribution is a continuous function. The spectral function is well described in terms of free quasi-hole and quasi-particle excitations which have a very long life-time for strong correlations. Their dispersion relation can be obtained from strong-coupling perturbation theory. A calculation of the quasi-particle bands beyond first order remains to be done.

The authors would like to thank H. FRAHM and T. GIAMARCHI for valuable discussions. SE and HF acknowledge funding by the DFG through grant SFB 652.

REFERENCES

- [1] GREINER M., MANDEL O., ESSLINGER T., HÄNSCH T. W. and BLOCH I., *Nature*, **415** (2002) 39.
- [2] BLOCH I., DALIBARD J. and ZWERGER W., *Rev. Mod. Phys.*, **80** (2008) 885.
- [3] FISHER M. P. A. *et al.*, *Phys. Rev. B*, **40** (1989) 546.
- [4] TEICHMANN N. *et al.*, *Phys. Rev. B*, **79** (2009) 224515.
- [5] FREERICKS J. K. *et al.*, *Phys. Rev. A*, **79** (2009) 053631.
- [6] CAPOGROSSO-SANSONE B., PROKOF'EV N. V. and SVISTUNOV B. V., *Phys. Rev. B*, **75** (2007) 134302.
- [7] KATO Y., ZHOU Q., KAWASHIMA N. and TRIVEDI N., *Nat. Phys.*, **4** (2008) 617.
- [8] CAPOGROSSO-SANSONE B. *et al.*, *Phys. Rev. A*, **77** (2008) 015602.
- [9] STÖFERLE T. *et al.*, *Phys. Rev. Lett.*, **92** (2004) 130403.
- [10] MORA C. and CASTIN Y., *Phys. Rev. A*, **67** (2003) 053615.
- [11] GIAMARCHI T., *Quantum Physics in One Dimension* (Oxford University Press, Oxford) 2004.
- [12] WHITE S. R., *Phys. Rev. Lett.*, **69** (1992) 2863; *Phys. Rev. B*, **48** (1993) 10345.
- [13] KÜHNER T. D. and MONIEN H., *Phys. Rev. B*, **58** (1998) R14741.
- [14] KÜHNER T. D., WHITE S. R. and MONIEN H., *Phys. Rev. B*, **61** (2000) 12474.
- [15] JECKELMANN E., *Phys. Rev. B*, **66** (2002) 045114.
- [16] LIEB E. H. and LINIGER W., *Phys. Rev.*, **130** (1963) 1605; LIEB E. H., *Phys. Rev.*, **130** (1963) 1616.
- [17] LIEB E., SCHULTZ T. and MATTIS D., *Ann. Phys. (N.Y.)*, **16** (1961) 407.
- [18] FRAHM H. and SCHADSCHNEIDER A., in *The Hubbard Model*, edited by BAERISWYL D. *et al.* (Plenum Press, New York) 1995, p. 21.
- [19] FRAHM H. and SCHADSCHNEIDER A., *J. Phys. A: Math. Gen.*, **26** (1993) 1463.
- [20] FREERICKS J. K. and MONIEN H., *Phys. Rev. B*, **53** (1996) 2691.
- [21] ELSTER N. and MONIEN H., *Phys. Rev. B*, **59** (1999) 12184.
- [22] KOLLER W. and DUPUIS N., *J. Phys.: Condens. Matter*, **18** (2006) 9525.
- [23] BATROUNI G. G. and SCALETTAR R. T., *Phys. Rev. B*, **46** (1992) 9051.
- [24] KASHURNIKOV V. A., KRASAVIN A. V. and SVISTUNOV B. V., *Pis'ma Zh. Eksp. Teor. Fiz.*, **64** (1996) 92 (*JETP Lett.*, **64** (1996) 99).
- [25] SENGUPTA P., SANDVIK A. W. and CAMPBELL D. K., *Phys. Rev. B*, **65** (2002) 155113.
- [26] EJIMA S., GEBHARD F. and NISHIMOTO S., *Europhys. Lett.*, **70** (2005) 492.
- [27] HALDANE F. D. M., *Phys. Rev. Lett.*, **47** (1981) 1840.
- [28] GIAMARCHI T., *Phys. Rev. B*, **46** (1992) 342.
- [29] MOSELEY C., FIALKO O. and ZIEGLER K., *Ann. Phys. (Berlin)*, **17** (2008) 561.
- [30] SHASHI A. *et al.*, arXiv:1010.2268.
- [31] ZAKRZEWSKI J. and DELANDE D., *AIP Conf. Proc.*, **1076** (2008) 292.
- [32] EJIMA S. and NISHIMOTO S., *Phys. Rev. Lett.*, **99** (2007) 216403.
- [33] LÄUCHLI A. M. and KOLLATH C., *J. Stat. Mech.* (2008) P05018.
- [34] KASHURNIKOV V. A. and SVISTUNOV B. V., *Phys. Rev. B*, **53** (1996) 11776.
- [35] ROMBOUTS S. M. A., VAN HOUCKE K. and POLLET L., *Phys. Rev. Lett.*, **96** (2006) 180603.
- [36] KOLLATH C. *et al.*, *Phys. Rev. A*, **69** (2004) 031601(R).
- [37] DAMSKI B. and ZAKRZEWSKI J., *Phys. Rev. A*, **74** (2006) 043609.
- [38] BATROUNI G. G. *et al.*, *Phys. Rev. Lett.*, **89** (2002) 117203.
- [39] MENOTTI C. and TRIVEDI N., *Phys. Rev. B*, **77** (2008) 235120.
- [40] VAN OOSTEN D., VAN DER STRATEN P. and STOOF H. T. C., *Phys. Rev. A*, **63** (2001) 053601.
- [41] PIPPAN P., EVERTZ H. G. and HOHENADLER M., *Phys. Rev. A*, **80** (2009) 033612.
- [42] JECKELMANN E. and FEHSKE H., *Riv. Nuovo Cimento*, **30** (2007) 259.

PHYSICAL REVIEW A **85**, 053644 (2012)

Characterization of Mott-insulating and superfluid phases in the one-dimensional Bose-Hubbard model

Satoshi Ejima and Holger Fehske

Institut für Physik, Ernst–Moritz–Arndt–Universität Greifswald, D-17489 Greifswald, Germany

Florian Gebhard and Kevin zu Münster

Fachbereich Physik, Philipps Universität Marburg, D-35032 Marburg, Germany

Michael Knap, Enrico Arrigoni, and Wolfgang von der Linden

Institute of Theoretical and Computational Physics, Graz University of Technology, A-8010 Graz, Austria

(Received 6 March 2012; published 29 May 2012)

We use strong-coupling perturbation theory, the variational cluster approach (VCA), and the dynamical density-matrix renormalization group (DDMRG) method to investigate static and dynamical properties of the one-dimensional Bose–Hubbard model in both the Mott-insulating and superfluid phases. From the von Neumann entanglement entropy we determine the central charge and the transition points for the first two Mott lobes. Our DMRG results for the ground-state energy, momentum distribution function, boson correlation function decay, Mott gap, and single-particle spectral function are reproduced very well by the strong-coupling expansion to fifth order, and by VCA with clusters up to 12 sites as long as the ratio between the hopping amplitude and onsite repulsion, t/U , is smaller than 0.15 and 0.25, respectively. In addition, in the superfluid phase VCA captures well the ground-state energy and the sound velocity of the linear phonon modes. This comparison provides an authoritative estimate for the range of applicability of these methods. In strong-coupling theory for the Mott phase, the dynamical structure factor is obtained from the solution of an effective single-particle problem with an attractive potential. The resulting resonances show up as double-peak structures close to the Brillouin zone boundary. These high-energy features also appear in the superfluid phase which is characterized by a pronounced phonon mode at small momenta and energies, as predicted by Bogoliubov and field theory. In one dimension, there are no traces of an amplitude mode in the dynamical single-particle and two-particle correlation functions.

DOI: [10.1103/PhysRevA.85.053644](https://doi.org/10.1103/PhysRevA.85.053644)

PACS number(s): 67.85.Bc, 67.85.De, 64.70.Tg

I. INTRODUCTION

The ability to place ultracold bosonic atoms in optical lattices offered new prospects in the study of quantum many-particle systems [1,2], mainly because, in contrast to solid-state realizations, the properties of the system can be manipulated in a very controlled way by tuning the particle density, the lattice depth, the trapping potential, and the interactions between the particles [3,4]. Likewise, the spatial dimension and coordination number of the optical lattice, the degree of disorder, or the coupling strength to external fields might be changed [5,6]. Hence, in these experiments, specific lattice Hamiltonians can be engineered and analyzed, including quantum phase transitions between gapped and itinerant phases. A prominent example is the transition between Mott-insulating (MI) and superfluid (SF) phases which results from the competition between the particles' kinetic energy and their mutual onsite repulsion. In this way, subtle quantum correlation effects become observable on a macroscopic scale.

The Bose-Hubbard Hamiltonian captures the essential physics of interacting bosons in optical lattices [7]. The ground-state phase diagram of this model in two and three dimensions has been determined by analytical, perturbative methods [8–10] and numerical, quantum Monte Carlo (QMC) techniques [11–15]. The one-dimensional (1D) case, which can be realized experimentally [16], is also accessible by QMC [17] and is particularly rewarding to study because the physics in 1D is normally rather peculiar [18].

On a linear chain with L sites and periodic boundary conditions (PBC) the Bose-Hubbard Hamiltonian reads

$$\hat{H} = t\hat{T} + U\hat{D}, \quad \hat{T} = -\sum_{j=1}^L (\hat{b}_j^\dagger \hat{b}_{j+1} + \hat{b}_{j+1}^\dagger \hat{b}_j),$$

$$\hat{D} = \frac{1}{2} \sum_{j=1}^L \hat{n}_j (\hat{n}_j - 1). \quad (1)$$

Here, \hat{b}_j^\dagger , \hat{b}_j , and $\hat{n}_j = \hat{b}_j^\dagger \hat{b}_j$ are the boson creation, annihilation, and particle number operators on site j .

The grand-canonical Hamiltonian is given by $\hat{K} = \hat{H} - \mu\hat{N}$ where μ is the thermodynamic chemical potential and $\hat{N} = \sum_j \hat{n}_j$ counts the total number of particles. For N particles (atoms) in the system, the (global) filling factor is $\rho = N/L$.

In Eq. (1), the hopping of the bosons between neighboring sites is characterized by the tunneling amplitude t , while U is the onsite interaction which we choose to be repulsive, $U > 0$; recently, Nägerl *et al.* investigated an unstable crystal of bosons with $U < 0$ [19]. Accordingly, the physics of the Bose-Hubbard model is governed by the ratio between kinetic energy and interaction energy, $x = t/U$. If, for a given chemical potential μ , x is larger than a critical value the bosons are “superfluid.” Below x_c , the system becomes Mott insulating, characterized by an integer filling factor ρ . In experiments, x can be varied over several orders of magnitude by modifying the depth of the lattice through quantum optical techniques

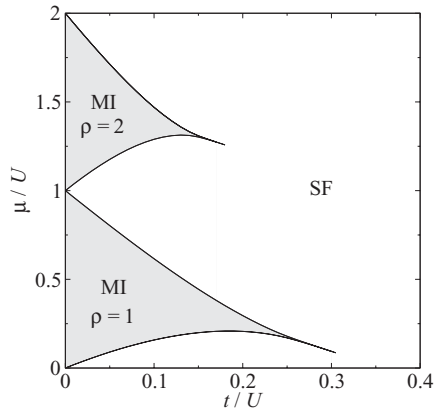


FIG. 1. Phase diagram of the 1D Bose-Hubbard model showing superfluid (SF) and Mott-insulating (MI) regions as a function of the chemical potential μ/U and the electron transfer amplitude t/U . The boundaries delimiting the first two Mott lobes were determined by DMRG, using system sizes up to $L = 128$ and open boundary conditions [20] (see text).

whereby SF and MI phases can be realized. From a theoretical point of view, the calculation of the boundaries between the SF and MI phases in the (μ, U) ground-state phase diagram is particularly demanding because quantum phase transitions in one dimension often are of Kosterlitz-Thouless type [18] with exponentially small Mott gaps in the vicinity of the transition.

The numerical density-matrix renormalization group (DMRG) method [21,22] is well suited to address one-dimensional interacting particle systems [3,23,24]. In fact, the (μ, U) ground-state phase diagram of the 1D Bose-Hubbard model has been obtained fairly accurately using this technique [20] (see Fig. 1). Since multiple occupancies pose serious technical problems, the maximal boson number per site in DMRG is constrained to be five. Note that DMRG naturally works at fixed $N, L < \infty$ (i.e., in the canonical ensemble). This leads to the definition of two chemical potentials for finite systems, $\pm\mu^\pm(L) = E_0(L, N \pm 1) - E_0(L, N)$ [24] where $E_0(L, N)$ denotes the ground-state energy. In the MI state we have a finite gap, $\Delta = \mu^+(L \rightarrow \infty) - \mu^-(L \rightarrow \infty) > 0$, whereas the chemical potential is continuous in the SF phase, $\mu = \mu^+(L \rightarrow \infty) = \mu^-(L \rightarrow \infty)$.

In one dimension, the delocalized SF state is not macroscopically occupied but rather characterized by an algebraic divergence of the momentum distribution [18,25]. The localized MI state is incompressible, as usual, and characterized by an integer particle density and a gap in the single-particle spectrum [8]. The regions in the (μ, U) phase diagram where the density ρ is pinned to integer values are termed Mott lobes. Their special shape is conditioned by the strong phase fluctuations existing in a 1D system. Close to the boundaries of the Mott lobes, the Mott gap is exponentially small. The precise position of the Mott dips can be obtained from the Tomonaga-Luttinger parameter [20,24].

A detailed theoretical understanding of the Bose-Hubbard model requires the calculations of (dynamical) correlation functions which poses a hard problem for which no exact solution exists. Recall that the 1D Bose-Hubbard model at

$U < \infty$ (soft-core bosons) is not integrable. Consequently, a large variety of approximative approaches were suggested and elaborated for the Bose-Hubbard model and its variants during the last two decades; for a recent review see Ref. [26].

In the SF phase, (weakly) interacting bosons at low energies are well described as a Tomonaga-Luttinger liquid [8,27]. However, close to the SF-to-MI transition, the precise character of the spectrum is still under debate. This particularly concerns the question of whether or not a second gapped mode besides the standard sound mode, as obtained from mean-field theory [28], can be seen in the single-particle spectral function or in the dynamical structure factor.

In the MI phase, strong-coupling expansions in $x = t/U$ give reliable analytical results. The ground-state energy of all Mott lobes was determined to second order by Freericks and Monien [29], and was improved up to order x^{14} for the lowest Mott lobe, $\rho = 1$, by Damski and Zakrzewski [30]. They also provided the series expansion for the local particle-density fluctuations to order x^{13} , a high-order series expansion for the single-particle density matrix $P(r) = O(x^r)$ for $r = 1, 2, 3$ and gave the corresponding expressions for the ground-state density-density correlation function $D(r) - 1 = O(x^{2r})$ for $r = 1, 2, 3$; for results for $r \leq 6$ and $r \leq 10$, respectively, see Ref. [9]. The Fourier transformation of $P(r)$ provides the momentum distribution $n(k)$. The result for $n(k)$ to third order in x was rederived by Freericks *et al.* [10] using a different method.

In contrast to higher dimensions, $d \geq 2$, the convergence of the strong-coupling expansion series in 1D is rather questionable. These problems become apparent, for example, in the calculation of the critical value x_c for the transition between the Mott-insulator and the superfluid phase. For example, the series expansion for the superfluid susceptibility constructed by Eckardt *et al.* [9] determines x_c very accurately in $d \geq 2$ but fails for $d = 1$ where a reentrant superfluid phase is predicted [9,23].

High-order expansions are also possible for the single-particle gap [31]. The Mott transition in one dimension is of Kosterlitz-Thouless (KT) type so that the gap becomes exponentially small close to the transition, which cannot be reproduced easily within a third-order strong-coupling expansion [29]. In order to obtain a good approximation of the critical value for the transition, Elstner and Monien [32] proposed a scaling analysis for the gap. Based on this idea, Freericks *et al.* [10] used a (6,7) Padé approximant for the square of the logarithm of the single-particle gap to find $x_c \approx 0.300(1)$ for $\rho = 1$, in good agreement with the DMRG value; for another scheme, see Heil and von der Linden [33].

In the present paper, we first refine and extend the perturbative strong-coupling approach in order to analyze the single-particle spectral function and the dynamical structure factor. For the latter quantity, we obtain higher-order corrections from the corresponding Green's function. Second, in order to relax the strong-coupling condition, we employ the variational cluster approach (VCA) that is applicable in both the Mott-insulating and the superfluid phase [34–37]. For the calculation of spectral properties in the SF phase, the VCA can be reformulated in terms of a pseudoparticle approach, whereby single-particle excitations within a cluster are approximately mapped onto particle-like excitations [36] or in terms of the self-energy functional approach [37,38].

Third, we perform large-scale DMRG calculations: (i) to access the whole parameter space of the Bose-Hubbard model and (ii) to benchmark the reliability of the used analytical strong-coupling and numerical VCA techniques. While in the past DMRG has been successfully applied to investigate the ground-state properties of the Bose-Hubbard model [3,23,24], DMRG results for dynamical properties at zero temperatures are rare (in contrast to fermionic systems), but highly desirable because superfluids in optical lattices can be studied by momentum-resolved Bragg spectroscopy [39–42].

The outline of this paper is as follows: In Sec. II we describe perturbative approaches to the Bose-Hubbard model, and present a detailed derivation of the strong-coupling results for static and dynamical quantities. Sections III and IV sketch the specifics of the VCA and DMRG, respectively, when applied to the Bose-Hubbard model. Section V contains our main results. In particular, we discuss how the von Neumann entanglement entropy can be calculated from DMRG and how it can be used to determine the KT transition point in the Mott lobes. Next, we determine the ground-state energy, the boson correlation function, and the momentum distribution function. Lastly, we analyze the photoemission spectra and dynamical structure factors. In all cases, we compare analytical and numerical results. Finally, Sec. VI summarizes our findings.

II. PERTURBATIVE APPROACHES

A. Weak-coupling limit

For weak interactions, we use the perturbative results obtained by Bogoliubov [43] (see Fetter and Walecka, Ref. [44], chap. 35), for a weakly interacting Bose gas with contact interaction and density $\rho = N/L$. From the text-book formulas we find for the 1D Bose-Hubbard Hamiltonian at $\rho = 1$,

$$\epsilon(k) = -2t[\cos(k) - 1], \quad (2)$$

$$E(k) = \sqrt{\epsilon(k)[\epsilon(k) + 2U]}, \quad (3)$$

$$\frac{N_0}{L} = 1 - \frac{1}{2L} \sum_{k \neq 0} \left(\frac{\epsilon(k) + U}{E(k)} - 1 \right), \quad (4)$$

where $\epsilon(k)$ is the bare dispersion of (1) shifted by $2t$, $E(k)$ is the dispersion of the Bogoliubov quasiparticles, and N_0 is the number of particles in the condensate. Here, $k = 2\pi m_k/L$, $m_k = 0, 1, \dots, L-1$ are the crystal momenta for PBC. The Bogoliubov ground-state energy reads

$$\frac{E_0^B(U)}{L} = -2t + \frac{U}{2} + \frac{1}{2L} \sum_{k \neq 0} [E(k) - \epsilon(k) - U]. \quad (5)$$

Two problems with the Bogoliubov theory become apparent when we consider some limits. First, we address the limit $k \rightarrow 0$ for $E(k)$, $E(k \rightarrow 0) \sim k$. Therefore, in the thermodynamic limit, the integral in Eq. (4) is logarithmically divergent, and $N_0 = 0$ in 1D results, in agreement with field theory [18]. This, however, invalidates the starting point of the Bogoliubov approximation. Second, we cannot apply the theory for large U/t because $E(k, U \gg t) \approx \sqrt{8Ut} |\sin(k/2)|$ so that

$E_0^B(U \gg t)/L \sim \sqrt{Ut}$ for large U/t , in contrast with the exact limit, $\lim_{U \rightarrow \infty} E_0(U) = 0$.

The analytical result for the ground-state energy in Bogoliubov theory is found, for example using MATHEMATICA [45], as

$$\frac{E_0^B(U)}{L} = -3t + \frac{\sqrt{2Ut}}{\pi} + \frac{U+2t}{\pi} \arccos \left(\sqrt{\frac{U}{U+2t}} \right). \quad (6)$$

The small- U expansion is

$$\frac{E_0^B(U \ll t)}{Lt} = -2 + \frac{U}{2t} - \frac{\sqrt{2}(U/t)^{3/2}}{3\pi}. \quad (7)$$

Corrections are of the order $(U/t)^{5/2}$ which is formally beyond the validity of the Bogoliubov expansion which ignores terms of order $(U/t)^2$.

B. Strong-coupling limit

1. Harris-Lange transformation

For the bosonic Hubbard model, an $x = t/U$ strong-coupling expansion easily permits the calculation of the ground state for $x \rightarrow 0$,

$$|\phi_0\rangle = \frac{1}{(\rho!)^{L/2}} \prod_i (\hat{b}_i^\dagger)^\rho |\text{vac}\rangle, \quad (8)$$

because it is nondegenerate for the Mott lobe with integer filling $\rho = N/L$. Likewise, the energy levels of a single-hole excitation, $E_h(k)$, and of a single-particle excitation, $E_p(k)$, can be determined to high order in x because the perturbation theory for these energy levels also starts from nondegenerate states; for example, for $\rho = 1$,

$$|\phi_h(k)\rangle = \sqrt{\frac{1}{L}} \sum_{l=1}^L e^{-ikl} \hat{b}_l |\phi_0\rangle, \quad (9)$$

$$|\phi_p(k)\rangle = \sqrt{\frac{1}{L}} \sqrt{\frac{1}{2!}} \sum_{l=1}^L e^{ikl} \hat{b}_l^\dagger |\phi_0\rangle. \quad (10)$$

When we employ the unitary Harris-Lange transformation [46], the strong-coupling Hamiltonian of the Bose-Hubbard model can be derived in a systematic way:

$$\hat{h} = e^{\hat{S}} \hat{H} e^{-\hat{S}} = U \hat{D} + t \sum_{r=0}^{\infty} x^r \hat{h}_r, \quad (11)$$

$$\hat{S} = -\hat{S}^\dagger = \sum_{r=1}^{\infty} x^r \hat{S}_r. \quad (12)$$

In practice, a finite order in the expansion of \hat{S} is kept. When we retain \hat{S}_r for $1 \leq r \leq n$, we denote this as the “ n th-order approximation.” In n th order we thus keep $(n-1)$ terms in the expansion for \hat{h} whose terms obey $[\hat{h}_r, \hat{D}]_- = 0$ for $0 \leq r \leq n-1$. To order $(n-1)$, the number of double occupancies is conserved by \hat{h} . This defines the construction principle for the operators \hat{S}_n .

The leading-order terms for \hat{S}_r and \hat{h}_r are given by

$$\hat{S}_1 = \sum_{D_1, D_2} \frac{\hat{P}_{D_1} \hat{T} \hat{P}_{D_2}}{D_1 - D_2}, \quad (13)$$

$$\hat{S}_2 = \sum_{D_1, D_2} \frac{-\hat{P}_{D_1} \hat{T} \hat{P}_{D_1} \hat{T} \hat{P}_{D_2} + \hat{P}_{D_1} \hat{T} \hat{P}_{D_2} \hat{T} \hat{P}_{D_2}}{(D_1 - D_2)^2} + \sum_{D_1, D_2, D_3} \frac{\hat{P}_{D_1} \hat{T} \hat{P}_{D_3} \hat{T} \hat{P}_{D_2} [D_1 - D_3 + D_2 - D_3]}{2(D_1 - D_2)(D_1 - D_3)(D_2 - D_3)}, \quad (14)$$

$$\hat{h}_0 = \sum_D \hat{P}_D \hat{T} \hat{P}_D, \quad (15)$$

$$\hat{h}_1 = \sum_{D_1, D_2} \frac{\hat{P}_{D_1} \hat{T} \hat{P}_{D_2} \hat{T} \hat{P}_{D_1}}{D_1 - D_2}, \quad (16)$$

where \hat{P}_D is the projection operator onto the subspace of eigenstate with D interactions, $\hat{D} = \sum_{D=0}^{\infty} D \hat{P}_D$. In the above sums it is implicitly understood that all indices $D_i \geq 0$ are mutually different. A compact formula for the recursive generation of higher orders can be found in Ref. [47]. In our analysis, we use a computer program to generate orders $r \geq 2$ in \hat{S}_r and \hat{h}_r [48].

For the exact ground state of the Mott insulator we have

$$\hat{H}|\psi_0\rangle = E_0|\psi_0\rangle, \quad (17)$$

where E_0 is the exact ground-state energy. Within the strong-coupling expansion we then find

$$|\psi_0\rangle = e^{\hat{S}}|\phi_0\rangle, \quad \hat{h}|\phi_0\rangle = E_0|\phi_0\rangle, \quad (18)$$

where $|\phi_0\rangle$ is the ground state of $\hat{h}_{-1} = \hat{D}$ [see Eq. (8)].

Since the Harris-Lange transformation is unitary, operators and ground-state expectation values translate according to

$$|\psi_0\rangle \mapsto |\phi_0\rangle, \quad \hat{H} \mapsto \hat{h}, \quad (19)$$

$$\hat{A} \mapsto \tilde{A} = e^{\hat{S}} \hat{A} e^{-\hat{S}}.$$

The series expansion for \hat{S} to n th order contains n powers of the kinetic energy operator \hat{T} . Therefore, local operators \hat{A}_i translate into cluster operators which involve the sites l with $|l - i| \leq n$. The range of \hat{h} scales accordingly: the strong-coupling theory generates a cluster expansion.

2. Static quantities

For fixed momentum k , the exact eigenstates of \hat{h} with one extra particle or one hole in $|\phi_0\rangle$, Eq. (8), are given by the hole and particle states defined in Eqs. (9) and (10). In this sector, we thus obtain the ground-state energy and the single-particle excitation energies from

$$E_0 = \langle \phi_0 | \hat{h} | \phi_0 \rangle, \quad (20)$$

$$E_p(k) = \langle \phi_p(k) | \hat{h} | \phi_p(k) \rangle - E_0, \quad (21)$$

$$E_h(k) = \langle \phi_h(k) | \hat{h} | \phi_h(k) \rangle - E_0. \quad (22)$$

Up to and including 6th order in x , we obtain for the ground-state energy per site

$$\frac{E_0^{[6]}}{4UL} = -x^2 + x^4 + \frac{68}{9}x^6 + O(x^8), \quad (23)$$

in agreement with Ref. [30].

The single-hole and single-particle excitation energies are

$$\frac{E_h(k)}{t} = 8x - \frac{512}{3}x^5 + \left(-2 + 12x^2 - \frac{224}{3}x^4\right)\cos(k) + \left(-4x + 64x^3 - \frac{1436}{3}x^5\right)\cos(2k) + (-12x^2 + 276x^4)\cos(3k) + (-44x^3 + 1296x^5)\cos(4k) - 180x^4\cos(5k) - 792x^5\cos(6k) + O(x^6), \quad (24)$$

and

$$\frac{E_p(k)}{t} = \frac{1}{x} + 5x - \frac{513}{20}x^3 - \frac{80139}{200}x^5 + \left(-4 + 18x^2 - \frac{137}{150}x^4\right)\cos(k) + \left(-4x + 64x^3 - \frac{426161}{1500}x^5\right)\cos(2k) + (-12x^2 + 276x^4)\cos(3k) + (-44x^3 + 1296x^5)\cos(4k) - 180x^4\cos(5k) - 792x^5\cos(6k) + O(x^6). \quad (25)$$

The single-particle gap is calculated from $\Delta = E_p(0) + E_h(0)$, which results in

$$\frac{\Delta}{U} = 1 - 6x + 5x^2 + 6x^3 + \frac{287}{20}x^4 + \frac{5821}{50}x^5 - \frac{602243}{1000}x^6 + \dots, \quad (26)$$

in agreement with Ref. [31].

3. Single-particle spectral functions

The single-particle spectral functions are obtained from

$$A^+(k, \omega) = \sum_n |\langle \phi_n | \hat{b}^\dagger(k) | \phi_0 \rangle|^2 \delta(\omega - \omega_n^+), \quad (27)$$

$$A^-(k, \omega) = \sum_n |\langle \phi_n | \hat{b}(k) | \phi_0 \rangle|^2 \delta(\omega + \omega_n^-), \quad (28)$$

where $\omega_n^\pm = E_n - E_0$ is the excitation energy of the exact eigenstates $|\phi_n\rangle$ of \hat{h} with $N = \rho L \pm 1$ bosons, measured from the ground-state energy, and

$$\hat{b}(k) = \sqrt{\frac{1}{L}} \sum_{l=1}^L e^{-ikl} \hat{b}_l, \quad \hat{b}^\dagger(k) = \sqrt{\frac{1}{L}} \sum_{l=1}^L e^{ikl} \hat{b}_l^\dagger \quad (29)$$

for PBC. Obviously, the single-particle gap Δ is obtained from $\Delta = \min_n(\omega_n^+) - \max_n(-\omega_n^-)$.

For the calculation of the spectral function, we need the weight factors

$$w_p(k) = |\langle \phi_p(k) | k_+ \rangle|^2, \quad |k_+ \rangle = \tilde{b}_k^\dagger | \phi_0 \rangle, \quad (30)$$

$$w_h(k) = |\langle \phi_h(k) | k_- \rangle|^2, \quad |k_- \rangle = \tilde{b}_k | \phi_0 \rangle. \quad (31)$$

Up to and including third order in x we find

$$w_h(k) = [1 - 4x^2 + (4x - 20x^3)\cos(k) + 14x^2\cos(2k) + 60x^3\cos(3k)]^2, \quad (32)$$

$$w_p(k) = 2\left[1 - \frac{7}{4}x^2 + \left(2x - \frac{15}{4}x^3\right)\cos(k) + 8x^2\cos(2k) + 18x^3\cos(3k)\right]^2. \quad (33)$$

The weights $w_p(k)$ and $w_h(k)$ are those of the lower and upper Hubbard bands which are energetically closest to the single-particle gap and separated by U in the atomic limit.

In higher orders of the strong-coupling expansion, secondary Hubbard bands appear in the single-particle spectral function [35,46,49,50]. This can most easily be seen from the weights which express the overlap of the exact excited eigenstates of \hat{h} with the states $|k_{\pm}\rangle$ [see Eqs. (30) and (31)]. With an amplitude of the order x^2 , the state $|k_{-}\rangle$ contains a component with two neighboring holes and one doubly occupied site in a row. This component is *not* in the original subspace with $D = 0$ and contributes to the upper Hubbard band with weight x^4 . Therefore, for the weight of the lower Hubbard band we have

$$\begin{aligned} w_{\text{LHB}}(k) &= w_h(k) + O(x^4) \\ &= 1 + (8x - 16x^3)\cos(k) + 36x^2\cos(2k) \\ &\quad + 176x^3\cos(3k) + O(x^4). \end{aligned} \quad (34)$$

The state $|k_{+}\rangle$ contains configurations with a triple occupancy and a neighboring hole to the left or right. Their amplitude up to order x^2 is $a_{\pm}(k) = \sqrt{6}[x/2 - \exp(\pm ik)x^2/3]$. They contribute to the secondary Hubbard band centered around $\omega = 3U$ to order x^2 and x^3 . Components with two double occupancies and a quadruple occupancy have an amplitude proportional to order x^2 and thus contribute to the bands centered around $\omega = 2U$ and $\omega = 6U$, respectively, with weights of the order of x^4 . Up to and including order x^3 , the secondary Hubbard band around $\omega = 3U$ has the weight

$$w_{3U}(k) = 12\left|\frac{x}{2} - \frac{x^2 e^{-ik}}{3}\right|^2 + O(x^4). \quad (35)$$

Therefore, the total weight for the upper Hubbard bands is given by $w_{\text{UHB}}(k) = w_p(k) + w_{3U}(k) = 1 + w_{\text{LHB}}(k)$, in agreement with the sum rule

$$\int_{-\infty}^{\infty} d\omega [A^{+}(k, \omega) - A^{-}(k, \omega)] = w_{\text{UHB}}(k) - w_{\text{LHB}}(k) = 1, \quad (36)$$

which follows directly from the definition of the spectral function. Another check results from the momentum distribution sum rule,

$$w_{\text{LHB}}(k) = \int_{-\infty}^{\infty} d\omega A^{-}(k, \omega) = \langle \phi_0 | \hat{b}^{\dagger}(k) \hat{b}(k) | \phi_0 \rangle = n(k). \quad (37)$$

Up to and including third order in x , our results for $n(k)$ agree with those found in Refs. [10,30].

4. Dynamical structure factor

For the density-density correlation function we focus on $\omega > 0$ so that we do not have to consider terms of the form $\langle \phi_0 | \tilde{n}_{l+r} \delta(\omega - (\hat{h} - E_0)) | \phi_0 \rangle \sim \delta(\omega)$. We define the states

$$|q\rangle = (\tilde{n}_q - \hat{n}_q) | \phi_0 \rangle, \quad (38)$$

where the density operator in momentum space is given by ($q = 2\pi m_q/L$, $m_q = 0, 1, \dots, L-1$)

$$\hat{n}(q) = \sum_{l=1}^L e^{iql} \hat{n}_l = \sum_k \hat{b}^{\dagger}(k+q) \hat{b}(k) = [\hat{n}(-q)]^{\dagger}. \quad (39)$$

Then, we can express the dynamical structure factor in the form

$$\begin{aligned} S(q, \omega > 0) &= \sum_{l=1}^L e^{-iql} S_l(\omega) \\ &= \langle q | \delta(\omega - (\hat{h} - E_0)) | q \rangle \\ &= \sum_n |\langle \Phi_n | q \rangle|^2 \delta(\omega - (\hat{h} - E_0)), \end{aligned} \quad (40)$$

where $|\Phi_n\rangle$ are the exact eigenstates of \hat{h} in the sector with $N = \rho L$ bosons.

Leading-order contribution. The dynamical structure factor was calculated analytically within mean-field theory [28], bosonization [26,51], and lowest-order strong-coupling theory [51–53].

The strong-coupling result to leading order is readily obtained from the exact eigenstates of \hat{h}_0 [Eq. (15)] in the sector with one hole and one double occupancy. The subspace ($N = L$, $D = 1$) is spanned by the $L(L-1)$ orthonormal states ($l \neq L$)

$$|q, l\rangle = \sqrt{\frac{1}{L}} \sum_{s=1}^L e^{iqs} |s, l\rangle, \quad |s, l\rangle = \sqrt{\frac{1}{2}} \hat{b}_s^{\dagger} \hat{b}_{s+l} | \phi_0 \rangle. \quad (41)$$

The states $|q, l\rangle$ obey the effective single-particle Schrödinger equation

$$\begin{aligned} \hat{h}_0 |q, l\rangle &= -(1 - \delta_{l,1})(1 + 2e^{-iq}) |q, l-1\rangle \\ &\quad - (1 - \delta_{l,L-1})(1 + 2e^{iq}) |q, l+1\rangle. \end{aligned} \quad (42)$$

As expected for a translationally invariant system, the center-of-mass momentum $q = 2\pi m_q/L$ with $m_q = 0, 1, \dots, L-1$ is conserved.

The leading-order contribution to the states $|q\rangle = \sum_{n=1}^{\infty} x^n |q^{[n]}\rangle$ from (38) is given by

$$|q^{[1]}\rangle = \sqrt{2}[(1 - e^{iq}) |q, 1\rangle + (1 - e^{-iq}) |q, L-1\rangle]; \quad (43)$$

that is, double occupancy and hole are nearest neighbors.

Equation (42) describes a single particle on an open chain with $L-1$ sites which reflects the fact that hole and double occupancy cannot be on the same site, $l \neq L$. In contrast to the fermionic case, the hard-core constraint is not sufficient to determine the phase shift between hole and double occupancy because their tunnel amplitudes differ by a factor of two. Therefore, the scattering phase shift between double occupancy and hole is not trivial [51–53]. This is in contrast to the mean-field approach [28] where the bare dispersions for hole and double occupancy enter Eq. (40).

The normalized double-occupancy–hole eigenstates are given by

$$|q; k\rangle = \sqrt{\frac{2}{L}} \sum_{l=1}^{L-1} \sin(kl) e^{i\phi(q)l} |q, l\rangle, \quad (44)$$

with $k = (\pi/L)m_k$ ($m_k = 1, 2, \dots, L-1$) where the two-particle phase shift $\phi(q)$ follows from

$$\tan[\phi(q)] = \frac{2 \sin(q)}{1 + 2 \cos(q)}. \quad (45)$$

The energies of the eigenstates $|q; k\rangle$ of $t\hat{h}_0$ are given by

$$E(q, k) = -2t \cos(k) \sqrt{5 + 4 \cos(q)}. \quad (46)$$

The overlap with the states in Eq. (43) defines the oscillator strengths in Eq. (38),

$$\langle q; k | q^{[1]} \rangle = \sqrt{2} \sqrt{\frac{2}{L}} \sin(k) [(1 - e^{iq}) e^{-i\phi(q)} - (1 - e^{-iq}) (-1)^{m_k} e^{-i\phi(q)(L-1)}], \quad (47)$$

so that, in the thermodynamic limit ($L \rightarrow \infty$), we obtain for the weights

$$w(q; k) = \left(\frac{t}{U}\right)^2 \frac{32}{L} \sin^2(k) \sin^2(q/2), \quad (48)$$

where we dropped the cross terms because their contribution to the structure factor vanishes due to the fast oscillations of $(-1)^{m_k}$.

The dynamical structure factor becomes for $\omega > 0$

$$S^{[1]}(q, \omega) = 2 \left(\frac{4t \sin(q/2)}{U} \right)^2 \times \int_0^\pi \frac{dk}{\pi} \sin^2(k) \delta(\omega - U - E(q, k)). \quad (49)$$

Finally, for $|\omega - U| \leq 2t\sqrt{5 + 4 \cos(q)}$ we obtain ($t \equiv 1$)

$$S^{[1]}(q, \omega) = \left(\frac{4 \sin(q/2)}{U} \right)^2 \frac{\sqrt{20 + 16 \cos(q) - (\omega - U)^2}}{2\pi [5 + 4 \cos(q)]} \quad (50)$$

for the dynamical structure factor to leading order [51–53].

Second- and higher-order contributions. For the next order in the (t/U) expansion we must calculate the action of $\bar{h}_1 \equiv \hat{h}_1 - E_0^{[1]}$ on the states $|q, l\rangle$, where we use $E_0 = t \sum_{n=1}^\infty x^n E_0^{[n]}$. The correction to Eq. (42) reads

$$\begin{aligned} \bar{h}_1 |q, l\rangle &= 13|q, l\rangle - 2[(1 - \delta_{l,1})(1 - \delta_{l,2})(1 + e^{-2iq})|q, l-2\rangle \\ &\quad - 2[(1 - \delta_{l,L-1})(1 - \delta_{l,L-2})(1 + e^{2iq})|q, l+2\rangle] \\ &\quad + 2\delta_{l,1} \left[\left(-\frac{1}{4} + e^{-iq} + e^{iq}\right) |q, 1\rangle \right. \\ &\quad \left. + \left(\frac{1}{4} + e^{-iq} + e^{-2iq}\right) |q, L-1\rangle \right] \\ &\quad + 2\delta_{l,L-1} \left[\left(\frac{1}{4} + e^{iq} + e^{2iq}\right) |q, 1\rangle \right. \\ &\quad \left. + \left(-\frac{1}{4} + e^{-iq} + e^{iq}\right) |q, L-1\rangle \right]. \end{aligned} \quad (51)$$

The effective single-particle problem contains an overall energy shift $13t^2/U$, a nearest-neighbor transfer $l \rightarrow (l+1)$ with amplitude $t(q) = (-t)[1 + 2 \cos(q) + 2i \sin(q)]$ as before, an additional next-nearest neighbor transfer from $l \rightarrow l+2$ with amplitude $m(q) = -2(t^2/U)[1 + \cos(2q) + i \sin(2q)]$, and a potential at the chain ends, $V_{1,1} = V_{L-1,L-1} = (t^2/U)[4 \cos(q) - 1/2]$ and $V_{1,L-1} = V_{L-1,1}^* = (2t^2/U)[1/4 + \cos(q) + \cos(2q) + i \sin(q) + i \sin(2q)]$.

Now that the potential links the two chain ends, it is computationally advantageous to treat the problem on a

ring instead of a chain. The potential is readily generalized according to Eq. (51). For a ring, the potential also contains the terms $V_{1,L-2}$ and $V_{2,L-1}$ and their complex conjugates so that the potential links four neighboring sites. Moreover, the extension of \hat{h}_0 from a chain to a ring generates corrections to $V_{1,L-1}$ and $V_{L-1,1}$.

The x^2 corrections to the states $|q\rangle$ (38) read

$$|q^{[2]}\rangle = 3\sqrt{2}[(1 - e^{2iq})|q, 2\rangle + (1 - e^{-2iq})|q, L-2\rangle]. \quad (52)$$

As the potential $V_{a,b}$, the dynamical structure factor to second order involves the four neighboring sites $l = L-2, L-1, 1, 2$.

The calculation of all eigenstates of $\hat{h}_0 + \hat{h}_1$ is not feasible in the thermodynamic limit. To calculate the dynamical structure factor we address the corresponding Green's function

$$G_{a,b}(q, z) = \langle q, a | \frac{1}{z - (\hat{h} - E_0)} | q, b \rangle. \quad (53)$$

For the structure factor in leading order, Eq. (43) requires the four Green's functions $G_{a,b}(q, \omega + i0^+)$ for $a, b = 1, L-1$. The second order requires the Green's function for $a, b = 1, 2, L-2, L-1$. This cluster principle generalizes to higher orders; that is, in n th order we have to calculate a $(2n) \times (2n)$ matrix of Green's functions for a potential which links $2n$ neighboring sites.

The Green's function of a particle in a potential of finite range is readily calculated [54]. We start from $\hat{h} = \hat{t} + \hat{V}$, where \hat{t} describes the free particle motion over the ring with dispersion relation $\varepsilon_q(k)$; up to second order we have $\varepsilon_q^{(2)}(k) = -2t[\cos(k) + 2 \cos(k-q)] + 13(t^2/U) - 4(t^2/U)[\cos(2k) + \cos(2k-2q)]$ with $0 \leq k < 2\pi$. In the thermodynamic limit, the free Green's function is readily calculated,

$$g_{a,b}(q, z) = \langle q, a | \frac{1}{z - \hat{t}} | q, b \rangle = \int_{-\pi}^\pi \frac{dk}{2\pi} \frac{e^{ik(a-b)}}{z - \varepsilon_q(k)}, \quad (54)$$

where we use the fact that the free states are plane waves. We calculate the free Green's functions for $z = \omega \pm i0^+$ with the help of the residue theorem. Therefore, their real and imaginary parts are available with high accuracy for all real frequencies $\omega > 0$.

With the help of the operator identity

$$\frac{1}{z - \hat{t} - \hat{V}} = \frac{1}{z - \hat{t}} + \frac{1}{z - \hat{t}} \hat{V} \frac{1}{z - \hat{t} - \hat{V}}, \quad (55)$$

we derive the Green's function (53) from the equation

$$G_{a,b}(q, z) = g_{a,b}(q, z) + \sum_{l,m} g_{a,l}(q, z) V_{l,m} G_{m,b}(q, z). \quad (56)$$

This matrix equation has the formal solution

$$\underline{\underline{G}}(q, z) = (\underline{\underline{1}} - \underline{\underline{g}}(q, z) \underline{\underline{V}})^{-1} \underline{\underline{g}}(q, z). \quad (57)$$

In n th-order perturbation theory, the potential and the required Green's functions have the same range $2n$ on the lattice. Therefore, the matrix problem in (57) reduces to the inversion of a $2n \times 2n$ matrix for fixed $(q, z = \omega \pm i0^+)$.

The Green's function calculation provides higher-order corrections to $S^{[1]}(q, \omega)$. In Sec. V we show results for the

dynamical structure factor to fifth order in the (t/U) expansion in the region around $\omega = U$.

The Green's function calculation does *not* cover the higher Hubbard subbands. The first contribution to the structure factor $S(q, \omega)$ beyond $\omega \approx U$ occurs around $\omega = 3U$ with intensity x^4 . In the regions where strong-coupling perturbation theory is reliable, $x \lesssim 0.15$, the secondary bands contribute only a few percent of the total weight. When we include the term to order x^4 in the frequency-integrated structure factor, the sum-rule for the structure factor is fulfilled; that is, we reproduce the terms $D(r)$ of the ground-state density-density correlation function for $r = 1, 2, 3$ [30] up to and including x^4 .

III. VARIATIONAL CLUSTER APPROACH

The basic idea of the VCA is to approximate the self-energy Σ of a strongly correlated, physical system \hat{H} by the self-energy of an exactly solvable reference system \hat{H}' [55]. Both the physical and the reference system share the same interaction but differ in their single-particle terms. The optimal self-energy is determined self-consistently from a stationary condition on the grand-canonical potential Ω ,

$$\frac{\delta \Omega}{\delta \Sigma} = 0. \quad (58)$$

To evaluate this expression, the self-energy is parametrized by the single-particle parameters of the reference system. In fact, this idea is quite general and allows to unify (cluster) dynamical mean-field theory and VCA within the same theoretical framework depending on the choice of reference system [38,56]. In the case of the VCA, the reference system is chosen to be a cluster decomposition of the physical system with modified single-particle parameters. Furthermore, the reference system is selected such that it can be solved exactly. In principle, any many-body cluster solver at hand can be used which provides the dynamic single-particle Green's function. Here, we use Lanczos exact diagonalization [35,57].

Originally, VCA was introduced for fermionic systems [55]. For correlated lattice bosons, it first has been in use to investigate the normal, Mott-insulating phase [34]. In Refs. [36,37] VCA has been extended to the superfluid phase. This extension adopts the Nambu notation and is applicable to a large class of lattice models that exhibit a condensed phase. Since VCA is in the end a form of a cluster mean-field approach, it can obviously not comprise fluctuations at length scales larger than the cluster size. This means that in the case of power-law decaying correlations as present here, these are spuriously replaced by long-range order in the VCA. This is a common issue of all mean-field like approaches. Despite this drawback, VCA still provides reliable results for many observables such as the ground-state energy, the sound velocity of the phonon excitations, and the single-particle spectral function.

Explicitly, the grand potential for bosonic systems with normal and the superfluid components is given by [36,37]

$$2\Omega = 2\Omega' - \text{Tr} \ln(-G) + \text{Tr} \ln(-G') - \text{Tr}(\underline{t} - \underline{t}') + \langle \hat{A} \rangle^\dagger [G_{(0)}]^{-1} \langle \hat{A} \rangle - \langle \hat{A} \rangle^\dagger [G'_{(0)}]^{-1} \langle \hat{A} \rangle, \quad (59)$$

where G is the interacting Green's function, \underline{t} is the single-particle Hamiltonian matrix, $\langle \hat{A} \rangle$ denotes expectation values of the Nambu boson operators consisting of both creation and

annihilation operators, and the subscript "(0)" indicates that the Green's function is evaluated at zero wave vector and zero frequency. In (59), the prime marks again reference system quantities. The first line of (59) is identical to the expression in the normal phase [34] apart from the fact that the Green's functions are considered to be in Nambu space and thus contain anomalous parts which also account for the factor 1/2. The second line takes care of the condensation of bosons, which in one dimension is an artifact of the dynamical and self-consistent mean-field treatment, as discussed above.

To obtain the results presented below, we always use the chemical potential of the reference system and a field which breaks the $U(1)$ symmetry on the level of the reference system as variational parameters. In the Mott phase we also determine the intercluster hopping and the boundary energies of the reference system self-consistently [50]. Having found the stationary point of the grand potential Ω with respect to the variational parameters, we evaluate the dynamical single-particle Green's function $G(k, \omega)$ of the physical system [36,37]. From that we calculate the single-particle spectral function $A(k, \omega) = -\text{Im}G(k, \omega)/\pi$. The static density-density correlation functions can be obtained from the Fourier transform of the momentum distribution function, as specified in Ref. [50].

IV. DENSITY MATRIX RENORMALIZATION GROUP APPROACH

The DMRG allows us to calculate static, dynamic, and spectral properties of the 1D Bose-Hubbard model with high precision for fairly large system sizes. The main obstacle is related to the fact that, in principle, each lattice site can be occupied by infinitely many bosonic particles. Therefore, one has to introduce a cutoff n_b , the maximum number of bosons per site taken into account. The DMRG results are nonetheless unbiased and numerically exact, if the dependence on n_b can be proven to be negligible and a careful finite-size extrapolation to the thermodynamic limit ($L \rightarrow \infty$) has been performed.

Within the ground-state DMRG technique [21,22] the energy functional

$$E(\psi) = \frac{\langle \psi | \hat{H} | \psi \rangle}{\langle \psi | \psi \rangle} \quad (60)$$

is minimized in a variational subspace in order to find the ground-state wave function $|\psi_0\rangle$ and energy $E_0 = E(\psi_0)$ whereby the DMRG energy error is proportional to the weight of the density-matrix eigenstates discarded in the renormalization process. Increasing the number m of density-matrix eigenstates kept, the discarded weight can be reduced systematically. Practically, the ground-state DMRG procedure consists mostly of two steps. During the infinite-system algorithm the system size is enlarged by two sites at each step and this operation has to be continued until the whole system reaches the desired system size L . Subsequently, a finite-system algorithm is used, where several sweeps through a lattice of fixed size L are performed. Thereby, the lattice is divided in two blocks with ℓ respectively $L - \ell$ sites where $1 \leq \ell \leq L - 1$. This sweeping improves the quality of the results obtained in the infinite-system algorithm. We note that this procedure is perfectly suited to compute the von Neumann entanglement entropy on the fly in the finite-system

algorithm. From this quantity, the KT transition point of the Bose-Hubbard model can be determined accurately.

The DMRG procedure can also be used to minimize the following functional [58,59]:

$$W_{A,\eta}(\omega, \psi) = \langle \psi | (E_0 + \omega - \hat{H})^2 + \eta^2 | \psi \rangle + \eta \langle A | \psi \rangle + \eta \langle \psi | A \rangle. \quad (61)$$

Here, \hat{H} is the (time-independent) Hamilton operator and \hat{A} denotes the quantum operator of the physical quantity to be analyzed; \hat{A}^\dagger is its Hermitian conjugate and $|A\rangle = \hat{A}|\psi_0\rangle$. Once this minimization has been carried out, the dynamical correlation function

$$G_{\hat{A}}(\omega + i\eta) = -\frac{1}{\pi} \langle \psi_0 | \hat{A}^\dagger \frac{1}{E_0 + \omega + i\eta - \hat{H}} \hat{A} | \psi_0 \rangle, \quad (62)$$

can be evaluated. Here, the small real number η shifts the poles of the correlation function in the complex plane; that is, η leads to a Lorentzian broadening of the peaks of the corresponding spectral function given in Lehmann representation as

$$I_{\hat{A}}(\omega + i\eta) = \text{Im} G_{\hat{A}}(\omega + i\eta) = \frac{1}{\pi} \sum_n |\langle \psi_n | \hat{A} | \psi_0 \rangle|^2 \frac{\eta}{(E_n - E_0 - \omega)^2 + \eta^2}. \quad (63)$$

Within this so-called dynamical DMRG (DDMRG) technique, the sweeps in the finite-system algorithm are repeated until both functionals, $E(\psi)$ and $W_{A,\eta}(\omega, \psi)$, take their minimal values.

Investigating the Bose-Hubbard model by DMRG, we keep up to $n_b = 5$ bosonic particles per site. Furthermore, we use $m = 2000$ density-matrix eigenstates in the DMRG runs for the ground-state expectation values. Then, the discarded weight is typically smaller than 10^{-10} . In the DDMRG calculations we keep $m = 500$ states to determine the ground state during the first five DMRG sweeps, and afterward use $m = 300$ states for the calculation of the dynamical properties.

V. RESULTS AND DISCUSSION

A. von Neumann entanglement entropy

Previously, the KT transition point between the superfluid and insulating phases has been determined from the Luttinger parameter K_b [60,61], which can be extracted from the density-density correlation function by DMRG, yielding $t_c = 0.305 \pm 0.001$ ($t_c = 0.180 \pm 0.001$) for $\rho = 1$ ($\rho = 2$) [20]. Although $K_b(t < t_c)$ is not defined in the MI, $K_b(L)$ is finite and continuous over the KT transition because the Mott gap is exponentially small. Therefore, it can be used within a DMRG finite-size extrapolation procedure.

The quantum phase transition should become manifest in the system's entanglement properties as well [62,63]. An important measure to quantify the entanglement of two subsets of an interacting quantum system is the von Neumann entanglement entropy, which shows a logarithmic scaling for critical systems [64]. To determine the critical point between a Tomonaga-Luttinger liquid and gapped (or ordered) phases for more subtle situations (e.g., for frustrated spin models, spinless fermion models with nearest-neighbor interaction, or fermion-

boson transport models), the use of the entanglement entropy difference has been demonstrated to be advantageous [65–67].

For a block of length ℓ in a periodic system of the system size L , the von Neumann entropy $S_L(\ell)$ is given by $S_L(\ell) = -\text{Tr}_\ell(\rho_\ell \ln \rho_\ell)$, with the reduced density matrix $\rho_\ell = \text{Tr}_{L-\ell}(\rho)$. One finds for PBC [68]

$$S_L(\ell) = \frac{c}{3} \ln \left[\frac{L}{\pi} \sin \left(\frac{\pi \ell}{L} \right) \right] + s_1, \quad (64)$$

where c is the central charge. When one evaluates the entropy difference $S_L(L/2) - S_{L/2}(L/4)$ using DMRG with open boundary conditions (OBC) [69], it includes the effect of the nonuniversal constant s_1 . Therefore, the values for t_c cannot be extrapolated systematically. Here, we follow the alternative scheme proposed by Nishimoto [65]. We subtract $S_L(L/2)$ from $S_L(L/2 - 1)$ to obtain

$$c^*(L) \equiv \frac{3[S_L(L/2 - 1) - S_L(L/2)]}{\ln[\cos(\pi/L)]}. \quad (65)$$

As $L \rightarrow \infty$, in the SF regime, the quantity $c^*(L)$ scales to the central charge $c = 1$ [68,70].

Figure 2 displays $c^*(L)$ for the 1D Bose-Hubbard model. Advantageously, we can use periodic boundary conditions for the calculation of this quantity. As shown in the insets, the position of the maximum in c^* can be reliably extrapolated to the thermodynamic limit. In this way we get the cone point of the Mott lobes $t_c = 0.305$ (3) for $\rho = 1$ and $t_c = 0.179$ (7) for $\rho = 2$ (in units of U), in excellent agreement with the previous estimates from the OBC finite-size scaling of K_b [20].

B. Ground-state properties

1. Ground-state energy

The ground-state energy E_0 of the 1D Bose-Hubbard model has been determined analytically in the weak- and strong-coupling cases. For weak interactions, the Bogoliubov result was given in Eq. (6), with the small- U expansion given by Eq. (7). For strong interactions, an expansion up to 14th order in $x = t/U$ was obtained by Damski and Zakrzewski [30]:

$$\begin{aligned} \frac{E_0^{[14]}}{4UL} = & -x^2 + x^4 + \frac{68}{9}x^6 - \frac{1267}{81}x^8 + \frac{44171}{1458}x^{10} \\ & - \frac{4\,902\,596}{6561}x^{12} - \frac{8\,020\,902\,135\,607}{2\,645\,395\,200}x^{14} + O(x^{16}). \end{aligned} \quad (66)$$

Figure 3 compares these perturbative results with our VCA and DMRG data. The VCA reproduces the DMRG results almost perfectly for all interaction strengths $t/U \leq 0.5$. The strong-coupling series expansion is also in accordance with the numerical exact data, surprisingly even beyond the KT transition point (i.e., for $t/U \lesssim 0.4$). Note that, in Ref. [30], the ground-state energy (67) was compared with numerical data obtained for a system with $L = 40$ sites only. Hence, in their figure, the deviation starts at about $t \approx 0.2U$. Clearly, the quality of the strong-coupling approximation improves as higher-order corrections are taken into account; cf. the 4th-, 10th-, and 14th-order results. Figure 3 also shows the range of validity of the corresponding weak-coupling approaches.

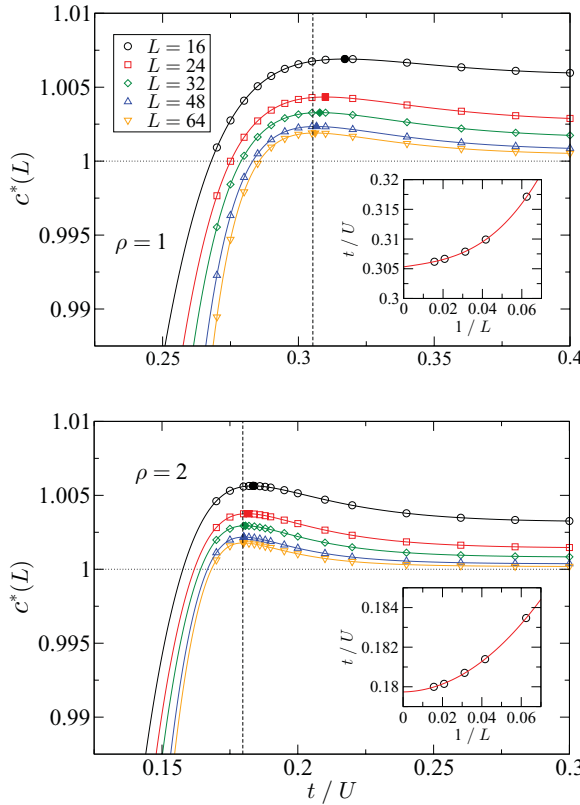


FIG. 2. (Color online) Entanglement entropy difference, c^* from Eq. (65), for the 1D Bose-Hubbard model with $\rho = 1$ (upper panel) and $\rho = 2$ (lower panel). Data are obtained by DMRG for lattices up to $L = 64$ with PBC. The closed symbols indicate the maximum value for each system size. An extrapolation of the t/U values at these maxima to the thermodynamic limit provides the Kosterlitz-Thouless transition point (see insets); here, the lines correspond to a polynomial fit. The vertical dashed lines in the main panels mark the Kosterlitz-Thouless transition point.

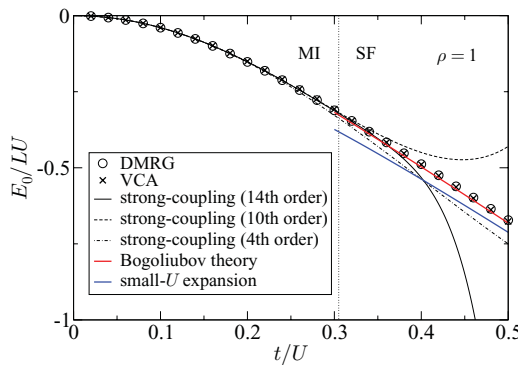


FIG. 3. (Color online) Ground-state energy $E_0/(LU)$ as a function of interaction strength t/U for $\rho = 1$. Weak- and strong-coupling results are compared with the $L \rightarrow \infty$ extrapolated DMRG data obtained from chains up to $L = 128$ with OBC. For the VCA calculations (crosses) a cluster with $L_c = 12$ ($L_c = 4$) sites is used in the MI (SF) phase.

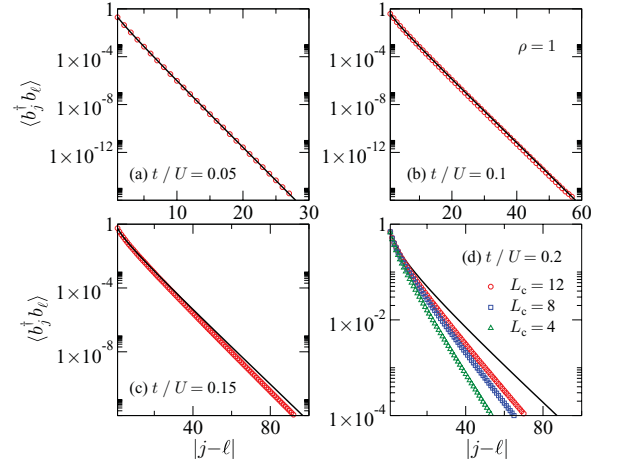


FIG. 4. (Color online) Decay of bosonic correlations in the 1D Bose-Hubbard model within the first Mott lobe ($\rho = 1$) for decreasing interaction strengths $x = 0.05$ (a), 0.1 (b), 0.15 (c), and 0.2 (d). DMRG results are obtained for a chain with $L = 128$ sites and OBC. To minimize the boundary effects we place j and ℓ symmetrically around the center of the system. The VCA data were calculated using clusters with $L_c = 4$ (green triangles), 8 (blue squares), and 12 (red circles).

Surprisingly, the Bogoliubov result is applicable up to the Mott-transition point.

2. Boson correlation function

In order to characterize the correlations in the ground state of the interacting Bose gas described by the Bose-Hubbard model, it is instructive to look at the distance dependence of the expectation values $\langle \hat{b}_j^\dagger \hat{b}_\ell \rangle$, which, with appropriate normalization, constitute the matrix elements of the one-particle density matrix [3].

In the gapless SF state, the boson single-particle correlation function

$$\langle \hat{b}_j^\dagger \hat{b}_\ell \rangle \sim |j - \ell|^{-K_b/2} \quad (67)$$

shows a power-law decay with an exponent determined by the Tomonaga-Luttinger parameter K_b [18].

In the insulating (gapped) MI, the bosonic correlations decay exponentially (at large distances), which is demonstrated by the semilogarithmic representation in Fig. 4. At very strong couplings, the excitation gap is large and therefore can be obtained very accurately within VCA. As x becomes larger (i.e., U becoming smaller at fixed t), the correlations are significant over many lattice sites. In this regime, we find noticeable deviations of the VCA results if L_c is too small [see Fig. 4(d)].

3. Momentum distribution function

The Fourier-transformed single-particle density matrix gives the momentum distribution function

$$n(k) = \frac{1}{L} \sum_{j,\ell=1}^L e^{ik(j-\ell)} \langle \hat{b}_j^\dagger \hat{b}_\ell \rangle. \quad (68)$$

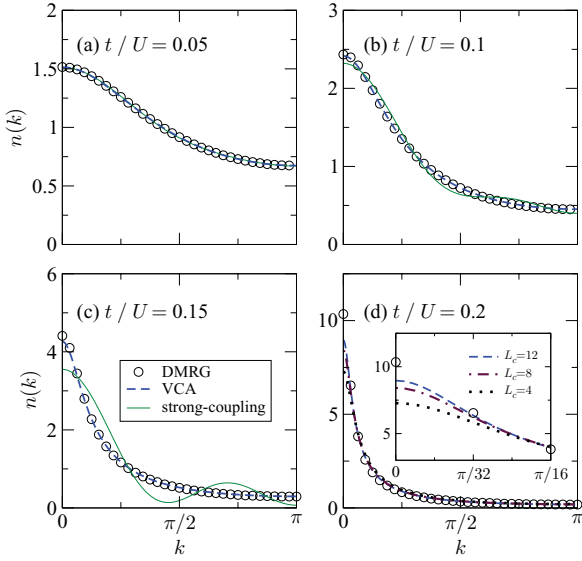


FIG. 5. (Color online) Momentum distribution function $n(k)$ within the first Mott lobe from DMRG with $L = 64$ and PBC (symbols), VCA (dashed lines), and third-order strong-coupling expansion (69) (solid lines). The inset in panel (d) shows the dependence of the VCA results on the cluster size L_c for $k \gtrsim 0$ in comparison with the DMRG data.

To third order in $x = t/U$, strong-coupling theory predicts for the first Mott lobe [10,30]

$$n^{[3]}(k) = 1 + (8x - 16x^3) \cos(k) + 36x^2 \cos(2k) + 176x^3 \cos(3k). \quad (69)$$

In Fig. 5 we compare the strong-coupling expansion (69) with the DMRG and VCA numerics.

While for $t/U = 0.05$, where the momentum distribution is rather flat indicating weak site-to-site correlations, all methods essentially agree [see Fig. 5(a)], small deviations between analytical and numerical approaches appear for $t/U \gtrsim 0.1$ [Fig. 5(b)]. The oscillations emerging for $x \sim 0.15$ in the third-order strong-coupling theory are clearly an artifact. The VCA reproduces the density distribution $n(k)$ very well. However, it fails quantitatively for $k \rightarrow 0$ and $x = 0.2$ if the cluster used is not large enough [see inset in Fig. 5(d)].

When we approach the MI-SF KT transition point by raising x , $n(k=0)$ will rapidly increase with system size. In 1D, of course, $n(k=0)$ will not attain a macroscopic value in the thermodynamic limit because no true condensate develops [25]. Instead, we have from Eq. (67)

$$n(|k| \rightarrow 0) \sim |k|^{-\nu}, \quad \nu = 1 - K_b/2 < 1. \quad (70)$$

Thus far, it is difficult to reproduce this algebraic divergence in the SF phase. However, see Ref. [71], where ν was determined by DMRG.

C. Dynamical quantities

1. Photoemission spectra and density of states

The single-particle excitations associated with the injection and emission of a boson with wave vector k and frequency ω are described by the spectral functions $A^+(k, \omega)$ and $A^-(k, \omega)$; see Eqs. (27) and (28), respectively. These quantities can be evaluated by VCA [36] and DDMRG [58,59]. For the Bose-Hubbard model the following sum rules hold [cf. Eqs. (36) and (37)]:

$$\int_{-\infty}^{\infty} d\omega [A^+(k, \omega) - A^-(k, \omega)] = 1, \quad (71)$$

$$\int_{-\infty}^{\infty} d\omega A^-(k, \omega) = n(k). \quad (72)$$

Summing over momenta k , the density of states $N(\omega)$ follows as

$$N(\omega) = A^+(\omega) - A^-(\omega), \quad (73)$$

where $A^\pm(\omega) = \sum_k A^\pm(k, \omega)/L$. Within the DDMRG framework, however, it is much more appropriate to calculate $N(\omega)$ directly, instead of performing the k summation of $A^\pm(k, \omega)$.

First, we discuss the spectral function, $A(k, \omega) = A^+(k, \omega) + A^-(k, \omega)$, and the density of states, $N(\omega)$, in the MI regime. The DDMRG spectra for fixed k consist of two Lorentzians of width $\eta = 0.04U$, which is the broadening introduced in the DDMRG procedure (cf. Sec. IV).

Figure 6 shows the quasiparticle dispersions (squares) extracted from Lorentz fits to the maxima in $A^\pm(k, \omega)$. The quality of the fits suggests that the quasiparticle lifetime is very large. Because of the large Mott gap separating single-particle and single-hole quasiparticle bands, the VCA can work with small cluster sizes and the quasiparticle spectra are in perfect agreement with the DDMRG data. The same holds for the strong-coupling results. In fact, for large interactions, each site

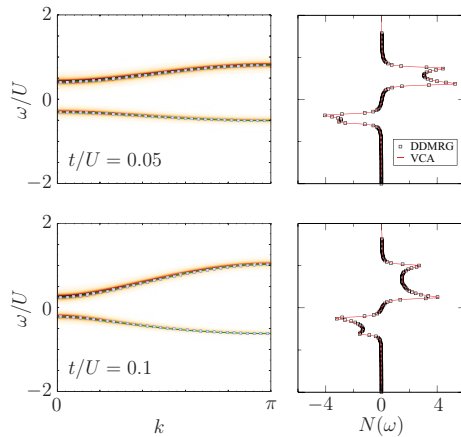


FIG. 6. (Color online) Single-particle spectral function $A(k, \omega)$ in the k - ω plane (left panels) and density of states $N(\omega)$ (right panels) for the 1D Bose-Hubbard model with $\rho = 1$ and $t/U = 0.05$ (upper panels), $t/U = 0.1$ (lower panels). We compare DDMRG data for a system with $L = 64$ and OBC (squares) with the results of VCA for $L_c = 12$ and $\eta = 0.03U$ (density plots) and strong-coupling expansions (24) and (25) (lines).

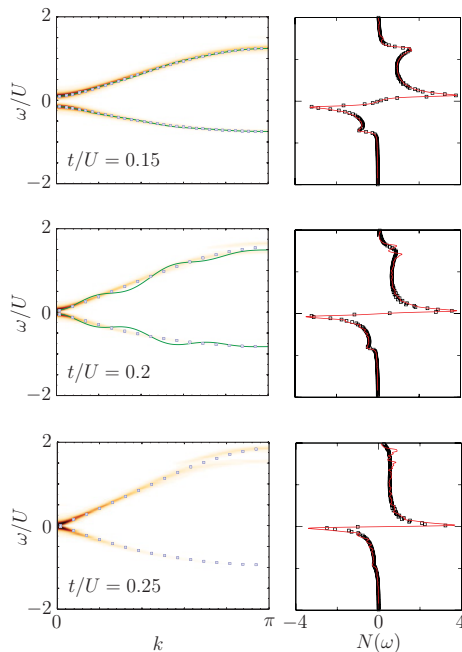


FIG. 7. (Color online) Spectral functions and density of states for intermediate couplings $t/U = 0.15$ (upper panels), $t/U = 0.2$ (middle panels) and $t/U = 0.25$ (lower panels). Notations are the same as in Fig. 6.

is singly occupied in the ground state. As a consequence, a hole or doubly occupied site can move almost freely through the system. From this consideration, the leading-order expression for the quasiparticle dispersions results [20] [see Eqs. (24) and (25)]. We note in passing that the simple mean-field approach by van Oosten *et al.* [72] fails to reproduce the quasiparticle dispersion already for $x = 0.1$ (see Ref. [20]).

As the onsite interaction further weakens, the Mott gap gradually closes; the corresponding results are depicted in Fig. 7. Obviously, strong-coupling theory becomes imprecise at $x \approx 0.2$ and completely fails at $x \gtrsim 0.25$. There also, VCA shows some artificial gap features near the Brillouin-zone boundary, which do not show up in DDMRG.

In the superfluid phase, the elementary excitations concentrate around the region ($k = 0$, $\omega = 0$) (see Fig. 7 in Ref. [20]), which indicates the formation of a “condensate.” In accordance with Bogoliubov theory and field theory [26,43], the low-energy, low-momentum excitations dominate the single-particle spectrum. As can be seen from Fig. 8, our spectral function indeed exhibits a phonon mode whose excitation energy—for a system in the thermodynamic limit—is linear in k and gapless at $k = 0$. Yet, for finite-size systems a gap is present whose magnitude is inversely proportional to the system size. Our DDMRG data demonstrate that the gap almost vanishes already for an OBC system with 64 sites. A similar behavior has been observed in QMC calculations which employ the directed-loop method [13].

Within the VCA, we find a larger gap as compared to DDMRG, due to the fact that we solve only four-site clusters exactly which are subsequently coupled perturbatively. In

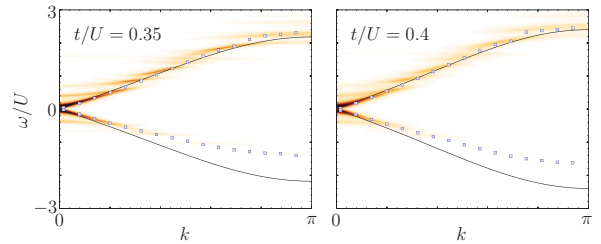


FIG. 8. (Color online) Spectral functions in superfluid phase of the 1D Bose-Hubbard model with $t/U = 0.35$ (left panel), $t/U = 0.4$ (right panel). Compared are DDMRG dispersions with VCA density plots for $L_c = 4$ and the dispersion of the condensate excitations $E(k)$ from Bogoliubov theory (black lines, other symbols are the same as in Fig. 6). See Eq. (3) with (2).

Ref. [36] we showed that the gap at $k = 0$ decreases with increasing cluster size, suggesting the correct behavior in the infinitely large cluster limit. Along the linear Goldstone modes, the spectral weight obtained by means of VCA exhibits fringes and a series of minigaps. This behavior is most likely a result of the cluster decomposition and subsequent periodization of the Green’s function [35]. However, it should be emphasized that the slopes of the phonon mode obtained by the two methods agree very well.

A universal feature of systems with broken U(1) symmetry is that, in addition to a gapless Goldstone mode, a gapped amplitude mode should be present. Whereas the Goldstone modes correspond to phase fluctuations, the amplitude modes arise from fluctuations in the magnitude of the order parameter. This behavior can be sketched by a Mexican hat potential for the order parameter [73]. It has been argued in Ref. [73] that the amplitude modes are sharp excitations in the quasiparticle sense only for dimensions $d \geq 3$ for which they were detected experimentally [74].

For $d < 3$ the decay of the amplitude modes into Goldstone modes is very efficient and, thus, the weight observed in the susceptibilities can be redistributed over a large frequency range. This renders an observation of the amplitude modes difficult. In two dimensions (2D) it was demonstrated theoretically that the coupling to the amplitude modes can be improved by evaluating susceptibilities for the kinetic energies [75] or for operators that resemble the rotationally invariant structure of the Mexican hat potential [76]. This should result in clearer signals for the amplitude modes in the respective response functions. Indeed, in setups with ultracold atoms, recent lattice modulation experiments, which couple directly to the amplitude modes, provide evidence for their existence in 2D [77].

In 1D where no true condensate exists, the spectral smearing of the amplitude modes is believed to be even more pronounced. Our numerical DMRG and VCA results for the spectral function and the dynamical structure factor, which both couple to the gapless Goldstone mode and the amplitude mode, give no indication for the latter. Therefore, we do not expect that an amplitude mode will be observed in Bragg spectroscopy experiments for bosons in one dimension. It is quite remarkable that VCA reproduces the overall character of the single-particle spectrum consisting of Goldstone modes only, despite of the fact that, technically, a spurious condensate

has to be introduced to treat the superfluid phase. See Sec. III for a detailed discussion.

2. Dynamic density-density correlations

We now turn to the dynamical density-density response function. We carry out large-scale DDMRG calculations of the dynamic structure factor $S(q, \omega)$ and compare the results with the predictions of strong-coupling theory (40) where appropriate. In strong coupling, we show results in fourth-order approximation. The agreement with the DDMRG data for $x = 0.15$ improves noticeably when we calculate expectation values with $|q\rangle \approx \sum_{n=1}^5 x^n |q^{[n]}\rangle$ from (38) (i.e., we keep the states to fifth order in x).

Since DDMRG provides $S(q, \omega)$ with a finite broadening η , it turns out to be useful to convolve the strong-coupling result with the Lorentz distribution [78],

$$S_\eta(q, \omega) = \int_{-\infty}^{\infty} d\omega' S(q, \omega') \frac{\eta}{\pi[(\omega - \omega')^2 + \eta^2]}. \quad (74)$$

Mott phase. Figure 9 illustrates the change of the intensity distribution of $S(q, \omega)$ in the q - ω plane as $x = t/U$ increases

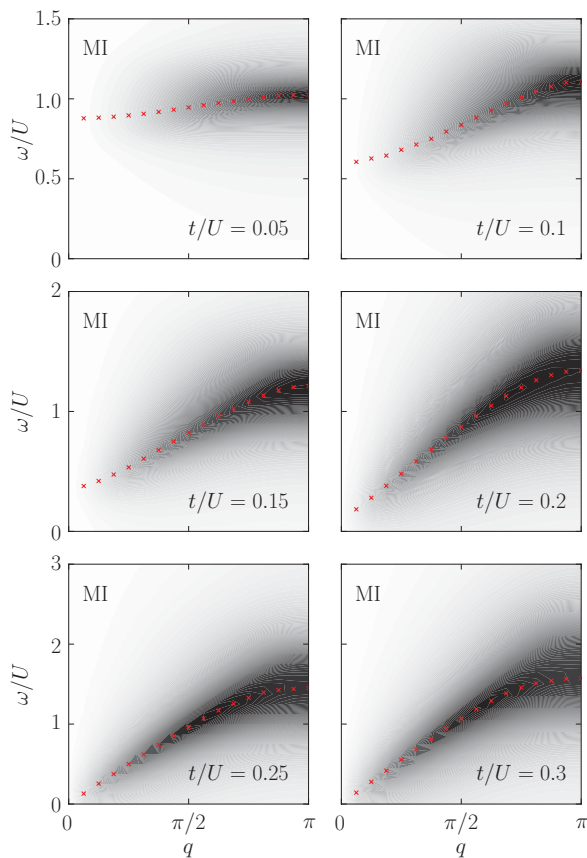


FIG. 9. (Color online) Intensity of the dynamical structure factor $S(q, \omega)$ in the MI phase of the 1D Bose-Hubbard model for different t/U where $\rho = 1$. DDMRG data were obtained for an $L = 32$ site system with PBC, using $\eta = 0.5t$. Red crosses mark the positions of the maximum in each $q = 2\pi m_q/L$ sector.

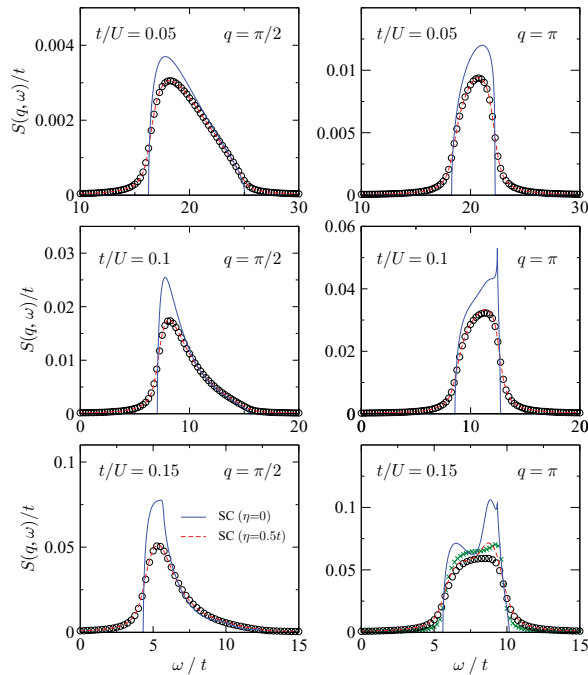


FIG. 10. (Color online) Frequency scans of the dynamical structure factor in the MI state at fixed momenta $q = \pi/2$ (left panels) and $q = \pi$ (right panels). DDMRG data (circles) were obtained for $L = 64$, PBC, and $\eta = 0.5t$; at $t/U = 0.15$ ($q = \pi$) also for $L = 128$, PBC, and $\eta = 0.2t$ (green crosses). Blue solid (red dashed) lines give the corresponding results of the strong-coupling theory with $\eta = 0$ ($\eta = 0.5t$). Please note the different scales of the ordinates.

in the MI regime. For small x , deep in the MI, the spectral weight is concentrated around $\omega \sim U$ in the region $q > \pi/2$ (cf. the upper-left panel of Fig. 9). This meets the predictions of the strong-coupling theory [53]. In this regime the structure factor is dominated by the primary band.

When x increases, the maximum of $S(q, \omega)$ acquires an appreciable dispersion; simultaneously the overall intensity of the density-density response strengthens (see the middle panels of Fig. 9 and also Fig. 10). As the system approaches the MI-SF transition point, the excitation gap closes. Concomitantly, we find a significant redistribution of the spectral weight to smaller q values (see lower panels of Fig. 9).

In Fig. 10 we show constant-moment scans of $S(q, \omega)$ at $q = \pi/2$ and $q = \pi$. For $x = 0.05$ and $x = 0.10$, the agreement between the broadened strong-coupling results and the DDMRG data for $S(q, \omega)$ is excellent. As x becomes larger than $x \approx 0.10$, the strong-coupling theory yields a double-peak structure in $S(\pi, \omega)$. When we increase the lattice size and reduce η , this feature also appears in our DDMRG data for $t/U = 0.15$. Therefore, this feature is not an artifact of the strong-coupling approach even though the strong-coupling expansion overestimates the double-peak structure for $x = 0.15$. The strong-coupling expansion solves an effective single-particle problem in a (finite range, attractive) potential. Such

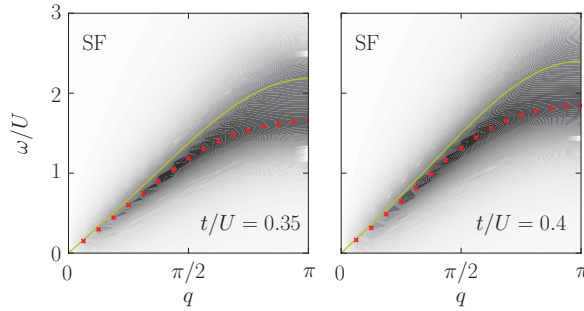


FIG. 11. (Color online) Intensity of the dynamical structure factor $S(q, \omega)$ in the superfluid phase of the Bose-Hubbard model with $\rho = 1$. Again we use $L = 32$, PBC, and $\eta = 0.5t$. The yellow line gives the Bogoliubov result (3).

a potential gives rise to a nontrivial spectrum (resonances and possibly bound states). The energy levels of the effective single-particle problem lead to nontrivial spectral signatures in the dynamical structure factor.

Superfluid phase. Figures 11 and 12 present the corresponding results for the dynamical structure factor in the SF phase. At small momenta, Bogoliubov theory gives the correct slope of the dispersion which we derive from the maximum of the DDMRG data for $S(q, \omega)$. Note that the dispersion $E(q)$ in Eq. (3) is identical to the predictions from field theory [18]. Bogoliubov's dispersion overestimates the DDMRG maxima for larger momenta and higher energies, as observed experimentally for a three-dimensional (3D) setup [41]. As compared to the MI phase, the density-density response has higher intensity in the SF state. Interestingly, we also find a shoulder in $S(\pi, \omega)$, which may form a double peak as $L \rightarrow \infty$, $\eta \rightarrow 0$ (see the right-hand panel of Fig. 12). This high-energy double peak in the SF phase resembles the structure seen in the MI phase. In our opinion, this rules out an interpretation of the second peak as signature of a massive Higgs mode [28].

VI. SUMMARY

The aim of this paper was twofold: (i) to provide extensive numerical (D)DMRG data for static and dynamical quantities of the one-dimensional Bose-Hubbard model at integer filling, mostly for $\rho = N/L = 1$; (ii) to compare the (D)DMRG

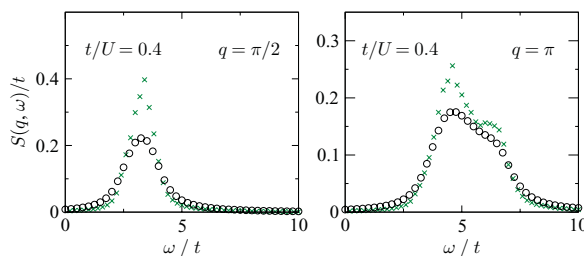


FIG. 12. (Color online) Frequency dependence of dynamical structure factor $S(q, \omega)$ at $q = \pi/2$ and $q = \pi$. Only DDMRG data are shown. Circles (crosses) mark the results for $L = 64$, PBC, and $\eta = 0.5t$ ($L = 128$, PBC, and $\eta = 0.2t$).

results with the analytical strong-coupling perturbation theory and the numerically inexpensive VCA and thereby explore their merits and limitations in the most demanding case of one dimension.

We used the DMRG to calculate the central charge from which we confirmed the critical values for the superfluid-to-Mott transition for integer fillings $\rho = 1$ and $\rho = 2$.

The ground-state energy from DMRG compares favorably with results from VCA and from perturbation theory. For static correlation functions such as the single-particle density matrix and the momentum distribution, the comparison between DMRG data and strong-coupling perturbation theory (VCA) shows that the latter are reliable for $x = t/U \lesssim 0.15$ ($x \lesssim 0.25$), for doable implementations.

We calculated dynamical quantities such as the single-particle spectral function and the dynamical structure factor. In the superfluid phase, the response at low energies is dominated by the quasicondensate, in agreement with predictions from field theory and Bogoliubov theory. The latter provides the correct result for the phonon mode despite the fact that it is based on the incorrect assumption of a true condensate. For finite interactions and at higher energies, the dynamical structure factor is broad and reflects the physics of the Mott insulator. The overall character of the single-particle spectrum and the sound velocity of the phonon modes are reproduced by VCA for larger values of x .

The strong-coupling results for the dynamical structure factor helped us to interpret our numerical DDMRG data because the latter are spectrally broadened for finite system sizes. The two-particle correlation function in the Mott phase reflects the (scattering) states of a doubly occupied site and a hole with a hard-core repulsion and a (weak) longer-ranged attraction giving rise to a double-peak structure in the dynamical structure factor near the boundary of the Brillouin zone.

Our numerical work can be compared with experiments only after the parabolic confinement potentials are taken into account. Important as it is to confine the atoms to the optical lattice, the confinement potential often is so strong that the density profile contains several Mott regions with different integer fillings and transition regions between them. In this case, the structure factor at low energies describes the dynamical response of the “wedding-cake” density profile [79,80].

There are two other directions to extend our work. The Mott gap in the Bose-Hubbard model resembles a band gap. Therefore, it is interesting to see how bound states (“excitons”) form in this gap in the presence of a nearest-neighbor attraction. A second route to extend our work is the inclusion of a disorder potential [26,81,82] so that the smearing and closing of the Mott gap as a function of the disorder can be studied. Work in this direction is in progress.

ACKNOWLEDGMENTS

The authors thank I. Danshita, G. Hager, E. Jeckelmann, H. Monien, S. Nishimoto, and W. Zwerger for valuable discussions. Financial support by the Deutsche Forschungsgemeinschaft through the SFB 652 and by the Austrian Science Fund (FWF) P24081-N16 are gratefully acknowledged.

- [1] M. Greiner, O. Mandel, T. Esslinger, T. W. Hänsch, and I. Bloch, *Nature (London)* **415**, 39 (2002).
- [2] M. Greiner, O. Mandel, T. W. Hänsch, and I. Bloch, *Nature (London)* **419**, 51 (2002).
- [3] C. Kollath, U. Schollwöck, J. von Delft, and W. Zwerger, *Phys. Rev. A* **69**, R031601 (2004).
- [4] I. Bloch, J. Dalibard, and W. Zwerger, *Rev. Mod. Phys.* **80**, 885 (2008).
- [5] G. Grynberg, P. Horak, and C. Mennerat-Robilliard, *Europhys. Lett.* **49**, 424 (2000).
- [6] P. Lugan, D. Clément, P. Bouyer, A. Aspect, M. Lewenstein, and L. Sanchez-Palencia, *Phys. Rev. Lett.* **98**, 170403 (2007).
- [7] D. Jaksch, C. Bruder, J. I. Cirac, C. W. Gardiner, and P. Zoller, *Phys. Rev. Lett.* **81**, 3108 (1998).
- [8] M. P. A. Fisher, P. B. Weichman, G. Grinstein, and D. S. Fisher, *Phys. Rev. B* **40**, 546 (1989).
- [9] N. Teichmann, D. Hinrichs, M. Holthaus, and A. Eckardt, *Phys. Rev. B* **79**, 224515 (2009).
- [10] J. K. Freericks, H. R. Krishnamurthy, Y. Kato, N. Kawashima, and N. Trivedi, *Phys. Rev. A* **79**, 053631 (2009).
- [11] W. Krauth and N. Trivedi, *Europhys. Lett.* **14**, 627 (1991).
- [12] G. G. Batrouni, V. Rousseau, R. T. Scalettar, M. Rigol, A. Muramatsu, P. J. H. Denteneer, and M. Troyer, *Phys. Rev. Lett.* **89**, 117203 (2002).
- [13] P. Pippian, H.-G. Evertz, and M. Hohenadler, *Phys. Rev. A* **80**, 033612 (2009).
- [14] B. Capogrosso-Sansone, N. V. Prokof'ev, and B. V. Svistunov, *Phys. Rev. B* **75**, 134302 (2007).
- [15] Y. Kato, Q. Zhou, N. Kawashima, and N. Trivedi, *Nat. Phys.* **4**, 617 (2008).
- [16] T. Stöferle, H. Moritz, C. Schori, M. Köhl, and T. Esslinger, *Phys. Rev. Lett.* **92**, 130403 (2004).
- [17] G. G. Batrouni, R. T. Scalettar, and G. T. Zimanyi, *Phys. Rev. Lett.* **65**, 1765 (1990).
- [18] T. Giamarchi, *Quantum Physics in One Dimension* (Oxford University Press, Oxford, 2004).
- [19] M. J. Mark, E. Haller, K. Lauber, J. G. Danzl, A. Janisch, H. P. Büchler, A. J. Daley, and H. Nägerl, [arXiv:1201.1008](https://arxiv.org/abs/1201.1008).
- [20] S. Ejima, H. Fehske, and F. Gebhard, *Europhys. Lett.* **93**, 30002 (2011).
- [21] S. R. White, *Phys. Rev. Lett.* **69**, 2863 (1992).
- [22] S. R. White, *Phys. Rev. B* **48**, 10345 (1993).
- [23] T. D. Kühner and H. Monien, *Phys. Rev. B* **58**, R14741 (1998).
- [24] T. D. Kühner, S. R. White, and H. Monien, *Phys. Rev. B* **61**, 12474 (2000).
- [25] C. Mora and Y. Castin, *Phys. Rev. A* **67**, 053615 (2003).
- [26] M. A. Cazalilla, R. Citro, T. Giamarchi, E. Orignac, and M. Rigol, *Rev. Mod. Phys.* **83**, 205301 (2011).
- [27] T. Giamarchi, *Phys. Rev. B* **46**, 342 (1992).
- [28] S. D. Huber, E. Altman, H. P. Büchler, and G. Blatter, *Phys. Rev. B* **75**, 085106 (2007).
- [29] J. K. Freericks and H. Monien, *Phys. Rev. B* **53**, 2691 (1996).
- [30] B. Damski and J. Zakrzewski, *Phys. Rev. A* **74**, 043609 (2006).
- [31] N. Elstner and H. Monien, [arXiv:cond-mat/9905367](https://arxiv.org/abs/cond-mat/9905367).
- [32] N. Elstner and H. Monien, *Phys. Rev. B* **59**, 12184 (1999).
- [33] C. Heil and W. von der Linden, [arXiv:1105.2418](https://arxiv.org/abs/1105.2418) [J. Phys.: Condens. Matter (to be published)].
- [34] W. Koller and N. Dupuis, *J. Phys.: Condens. Matter* **18**, 9525 (2006).
- [35] M. Knap, E. Arrigoni, and W. von der Linden, *Phys. Rev. B* **81**, 024301 (2010).
- [36] M. Knap, E. Arrigoni, and W. von der Linden, *Phys. Rev. B* **83**, 134507 (2011).
- [37] E. Arrigoni, M. Knap, and W. von der Linden, *Phys. Rev. B* **84**, 014535 (2011).
- [38] M. Potthoff, *Eur. Phys. J. B* **32**, 429 (2003).
- [39] D. Clément, N. Fabbri, L. Fallani, C. Fort, and M. Inguscio, *Phys. Rev. Lett.* **102**, 155301 (2009).
- [40] N. Fabbri, D. Clément, L. Fallani, C. Fort, M. Modugno, K. M. R. van der Stam, and M. Inguscio, *Phys. Rev. A* **79**, 043623 (2009).
- [41] P. T. Ernst, S. Götzke, J. S. Krauser, K. Pyka, D.-S. Lühmann, D. Pfannkuche, and K. Sengstock, *Nature Physics* **6**, 56 (2009).
- [42] X. Du, S. Wan, E. Yesilada, C. Ryu, D. J. Heinzen, Z. Liang, and B. Wu, *New J. Phys.* **12**, 083025 (2010).
- [43] N. N. Bogoliubov, *J. Phys. (USSR)* **11**, 23 (1947).
- [44] A. L. Fetter and J. D. Walecka, *Quantum Theory of Many-Particle Systems* (McGraw-Hill Publishing Company, Berlin, Heidelberg, 1971).
- [45] Wolfram Research, Inc., *Mathematica*, Version 7.0 (Wolfram Research, Inc., Champaign, 2008).
- [46] A. B. Harris and R. V. Lange, *Phys. Rev.* **157**, 295 (1967).
- [47] P. G. J. van Dongen, *Phys. Rev. B* **49**, 7904 (1994).
- [48] K. zu Münster, M.Sc. thesis, University of Marburg (2012).
- [49] S. Nishimoto, F. Gebhard, and E. Jeckelmann, *J. Phys.: Condens. Matter* **16**, 7063 (2004).
- [50] M. Knap, E. Arrigoni, and W. von der Linden, *Phys. Rev. B* **81**, 235122 (2010).
- [51] A. Iucci, M. A. Cazalilla, A. F. Ho, and T. Giamarchi, *Phys. Rev. A* **73**, 041608 (2006).
- [52] A. Tokuno and T. Giamarchi, *Phys. Rev. Lett.* **106**, 205301 (2011).
- [53] S. Ejima, H. Fehske, and F. Gebhard, [arXiv:1110.4498](https://arxiv.org/abs/1110.4498) [J. Phys.: Conf. Series (to be published)].
- [54] E. N. Economou, *Green's Functions in Quantum Physics* (Springer, Berlin, 1983).
- [55] M. Potthoff, M. Aichhorn, and C. Dahnken, *Phys. Rev. Lett.* **91**, 206402 (2003).
- [56] M. Potthoff, *Eur. Phys. J. B* **36**, 335 (2003).
- [57] M. G. Zacher, R. Eder, E. Arrigoni, and W. Hanke, *Phys. Rev. B* **65**, 045109 (2002).
- [58] E. Jeckelmann, *Phys. Rev. B* **66**, 045114 (2002).
- [59] E. Jeckelmann and H. Fehske, *Riv. Nuovo Cimento* **30**, 259 (2007).
- [60] F. D. M. Haldane, *Phys. Rev. Lett.* **47**, 1840 (1981).
- [61] C. Moseley, O. Fialko, and K. Ziegler, *Ann. Phys. (Berlin, Ger.)* **17**, 561 (2008).
- [62] L. Wang, K. S. D. Beach, and A. W. Sandvik, *Phys. Rev. B* **73**, 014431 (2006).
- [63] S. Rachel, N. Laflorencie, H. F. Song, and K. Le Hur, *Phys. Rev. Lett.* **108**, 116401 (2012).
- [64] M. A. Cazalilla, *J. Phys. B* **37**, S1 (2004).
- [65] S. Nishimoto, *Phys. Rev. B* **84**, 195108 (2011).
- [66] S. Ejima, M. J. Bhaseen, M. Hohenadler, F. H. L. Essler, H. Fehske, and B. D. Simons, *Phys. Rev. Lett.* **106**, 015303 (2011).
- [67] H. Fehske, S. Ejima, G. Wellein, and A. R. Bishop, [arXiv:1110.4486](https://arxiv.org/abs/1110.4486) [J. Phys.: Conf. Series (to be published)].
- [68] P. Calabrese and J. Cardy, *J. Stat. Mech.* (2004) P06002.

CHARACTERIZATION OF MOTT-INSULATING AND . . .

PHYSICAL REVIEW A **85**, 053644 (2012)

- [69] A. M. Läuchli and C. Kollath, *J. Stat. Mech.* (2008) P05018.
- [70] N. Laflorencie, E. S. Sørensen, M.-S. Chang, and I. Affleck, *Phys. Rev. Lett.* **96**, 100603 (2006).
- [71] M. J. Bhaseen, S. Ejima, F. H. L. Essler, H. Fehske, M. Hohenadler, and B. D. Simons, *Phys. Rev. A* **85**, 033636 (2012).
- [72] D. van Oosten, P. van der Straten, and H. T. C. Stoof, *Phys. Rev. A* **63**, 053601 (2001).
- [73] S. Sachdev, *Quantum Phase Transitions*, 2nd ed. (Cambridge University Press, Cambridge, 2011).
- [74] U. Bissbort, S. Götze, Y. Li, J. Heinze, J. S. Krauser, M. Weinberg, C. Becker, K. Sengstock, and W. Hofstetter, *Phys. Rev. Lett.* **106**, 205303 (2011).
- [75] L. Pollet and N. V. Prokof'ev, [arXiv:1204.5190](https://arxiv.org/abs/1204.5190).
- [76] D. Podolsky, A. Auerbach, and D. P. Arovas, *Phys. Rev. B* **84**, 174522 (2011).
- [77] M. Endres, T. Fukuhara, D. Pekker, M. Cheneau, P. Schauß, C. Gross, E. Demler, S. Kuhr, and I. Bloch, [arXiv:1204.5183](https://arxiv.org/abs/1204.5183).
- [78] S. Nishimoto and E. Jeckelmann, *J. Phys.: Condens. Matter* **16**, 613 (2004).
- [79] G. G. Batrouni, F. F. Assaad, R. T. Scalettar, and P. J. H. Denteneer, *Phys. Rev. A* **72**, 031601 (2005).
- [80] G. Pupillo, A. M. Rey, and G. G. Batrouni, *Phys. Rev. A* **74**, 013601 (2006).
- [81] S. Rapsch, U. Schollwöck, and W. Zwerger, *Europhys. Lett.* **46**, 559 (1999).
- [82] M. Knap, E. Arrigoni, and W. von der Linden, *Phys. Rev. A* **82**, 053628 (2010).

Dynamic density-density correlations in interacting Bose gases on optical lattices

S. Ejima¹, H. Fehske¹, and F. Gebhard²

Institut für Physik, Ernst-Moritz-Arndt-Universität Greifswald, 17489 Greifswald, Germany
 Fachbereich Physik, Philipps-Universität Marburg, 35032 Marburg, Germany

E-mail: <ejima,fehske>@physik.uni-greifswald.de

Abstract. In order to identify possible experimental signatures of the superfluid to Mott-insulator quantum phase transition we calculate the charge structure factor $S(k, \omega)$ for the one-dimensional Bose-Hubbard model using the dynamical density-matrix renormalisation group (DDMRG) technique. Particularly we analyse the behaviour of $S(k, \omega)$ by varying—at zero temperature—the Coulomb interaction strength within the first Mott lobe. For strong interactions, in the Mott-insulator phase, we demonstrate that the DDMRG results are well reproduced by a strong-coupling expansion, just as the quasi-particle dispersion. In the superfluid phase we determine the linear excitation spectrum near $k = 0$. In one dimension, the amplitude mode is absent which mean-field theory suggests for higher dimensions.

Recent experimental realisations of optical lattices make it possible to investigate the properties of ultracold dilute atoms in a new regime of strong correlations [1, 2]. Tuning the strength of the laser field, the effective interactions between the atoms can be tuned to be stronger than their kinetic energy. The competition between the Coulomb energy and the kinetic energy may even drive a quantum phase transition between superfluid (SF) and Mott insulating (MI) phases. The Bose-Hubbard model (BHM) captures the essential physics of this problem. In previous work [3] we studied the photoemission spectra of the one-dimensional (1D) BHM both in the MI and SF phases. In this contribution we extend our preceding investigations of the dynamical properties of the BHM by analysing the dynamical structure factor $S(k, \omega)$. Analytically, $S(k, \omega)$ has been determined by mean-field approaches [4, 5] and, numerically, for rather small 1D systems, by exact diagonalisation [6] or, at finite temperatures, by QMC [7]. Here, we carry out large-scale dynamical density-matrix renormalisation group (DDMRG) [8] calculations in order to examine the density-density correlations of N interacting Bose particles on L sites at zero temperature. Moreover, fixing $\rho = N/L = 1$, we set up a perturbation theory whose results can be compared with the DDMRG data in the strong-coupling limiting case.

The Hamiltonian of the 1D BHM reads

$$\hat{\mathcal{H}} = -t \sum_j (\hat{b}_j^\dagger \hat{b}_{j+1} + \hat{b}_j \hat{b}_{j+1}^\dagger) + \frac{U}{2} \sum_j \hat{n}_j (\hat{n}_j - 1), \quad (1)$$

where \hat{b}_j^\dagger and \hat{b}_j are the creation and annihilation operators for bosons on site j , $\hat{n}_j = \hat{b}_j^\dagger \hat{b}_j$ is the boson number operator on site j . The tunnel amplitude between nearest neighbour lattice sites is denoted by t , and U gives the on-site Coulomb repulsion of the Bose particles. For the DDMRG treatment of (1) we use periodic boundary conditions, take into account $n_b = 5$ bosons

per site and keep up to $m = 500$ density-matrix eigenstates, ensuring that the discarded weight is always smaller than 3×10^{-5} .

The dynamical charge structure factor is defined as

$$S(k, \omega) = \sum_n |\langle \psi_n | \hat{n}_k | \psi_0 \rangle|^2 \delta(\omega - \omega_n), \quad (2)$$

where $|\psi_0\rangle$ and $|\psi_n\rangle$ denote the ground and n -th excited state, respectively, and $\omega_n = E_n - E_0$ gives the corresponding excitation energy. $S(k, \omega)$ characterises the density-density response of the Bose gas and is directly accessible in experiment, for instance, by Bragg spectroscopy [9].

From lowest-order strong-coupling perturbation theory we find for $\rho = N/L = 1$ ($N, L \rightarrow \infty$)

$$S^{(1)}(k, \omega > 0) = \left(\frac{4t \sin(k/2)}{U} \right)^2 \int_{-\pi}^{\pi} \frac{dk}{\pi} \sin^2 k \delta(\omega - U + 2t \cos k \sqrt{5 + 4 \cos k}). \quad (3)$$

Then, for $U - 2\sqrt{5 + 4 \cos k} \leq \omega \leq U + 2\sqrt{5 + 4 \cos k}$, we have in units of t

$$S^{(1)}(k, \omega > 0) = \left[\frac{4 \sin(k/2)}{U} \right]^2 \frac{\sqrt{20 + 16 \cos k - (\omega - U)^2}}{2\pi(5 + 4 \cos k)}, \quad (4)$$

where $0 \leq k < 2\pi$. Since DDMRG provides $S(k, \omega)$ with a finite broadening η , it is useful to convolve the strong-coupling result $S^{(1)}(k, \omega)$ with the Lorentz distribution [10]: $S_\eta(k, \omega) = \int_{-\infty}^{\infty} d\omega' S(k, \omega') \eta / [\pi ((\omega - \omega')^2 + \eta^2)]$. For the 1D BHM, from Eq. (4), we thus get

$$S_\eta^{(1)}(k, \omega > 0) = \left(\frac{4 \sin(k/2)}{U} \right)^2 \frac{2}{\pi^2} \int_{-1}^1 d\lambda \frac{\eta \sqrt{1 - \lambda^2}}{(\omega - U + 2\lambda \sqrt{5 + 4 \cos k})^2 + \eta^2}. \quad (5)$$

Figure 1 illustrates the frequency and momentum dependencies of $S(k, \omega)$. Peaks in $S(k, \omega)$ assign charge excitations. For $k \simeq 0$, $S(k, \omega)$ exhibits a maximum around $\omega \approx U$ that can be attributed to excitations across the Mott gap. Within strong-coupling theory (4) this signature stays at $\omega \approx U$ for all k but becomes more pronounced as k reaches the Brillouin zone boundary.

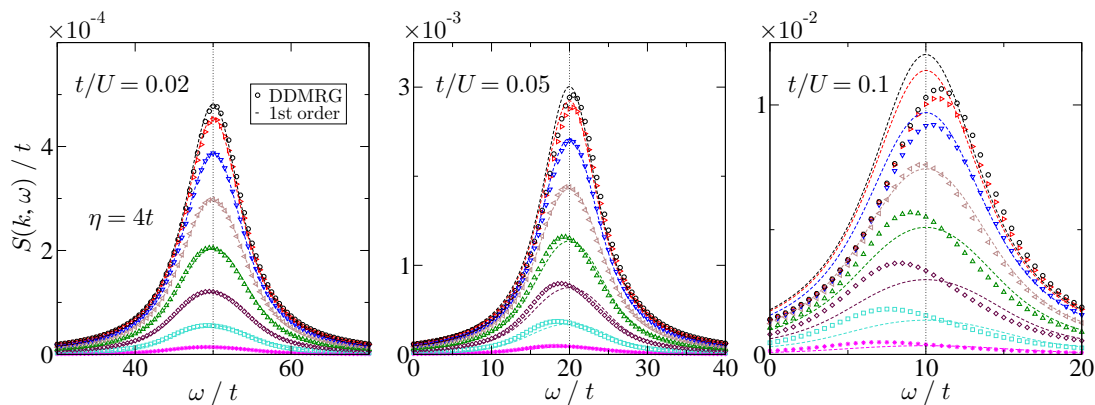


Figure 1. Frequency dependence of the dynamical charge structure factor $S(k, \omega)$ at various momenta $k = 2\pi j/L$ (for $j = 1, 2, \dots, L/2$ from bottom to top). DDMRG data (symbols) were obtained for $L = 16$; $S_\eta^{(1)}(k, \omega)$ (lines) give the corresponding first-order strong-coupling expansion results (for the same value of $\eta = 4t$). The dashed line indicates the point $\omega = U$.

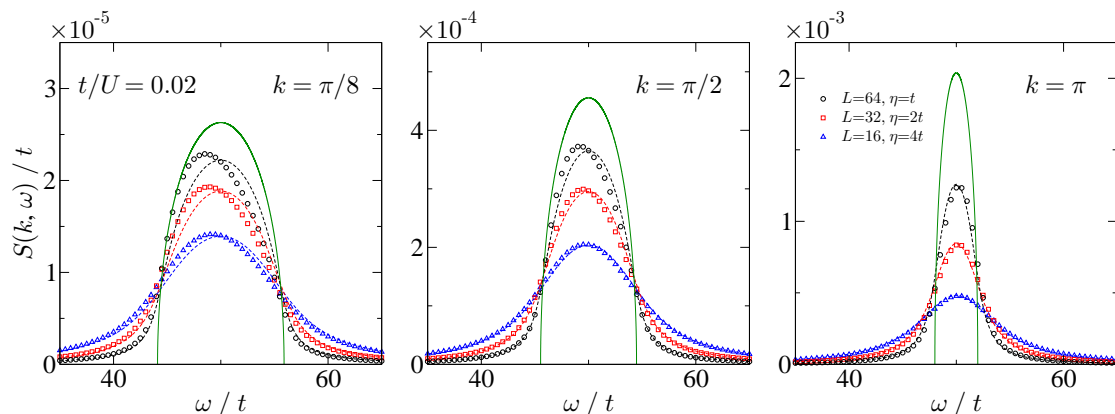


Figure 2. η -dependence of the dynamical structure factor $S(k, \omega)$. DDMRG data (symbols) are compared with the corresponding strong-coupling results (dashed lines) at various momenta k . The solid green line shows the unconvolved result of the strong-coupling expansion.

Our DDMRG data corroborate this prediction (cf. the left panel of Fig. 1 depicting the results for $t/U = 0.02$). Naturally, as U gets smaller, differences between the numerical DDMRG and the analytical strong-coupling results emerge. Most importantly, the position of the maximum in $S(k, \omega)$ varies with k : it is shifted to smaller (larger) frequencies for k values near the band centre (Brillouin zone boundary); see middle and right-hand panels of Fig. 1. We have to include higher-order t/U -corrections to reproduce this feature analytically. Note that the maximum in $S(k, \omega)$ amplifies as $k \rightarrow \pi$.

Next, we investigate the dependences of $S(k, \omega)$ on the broadening η and the system size L to scrutinise whether the DDMRG data “converge” to the unconvolved strong-coupling result (4) as $\eta \rightarrow 0$ and $L \rightarrow \infty$. Figure 2—showing $S(k, \omega)$ in the MI phase at $k = \pi/8$ (left), $\pi/2$ (middle) and π (right panel) for $L = 16, 32, 64$ $\eta = 4t, 2t, t$, respectively—demonstrates that this is indeed the case. Firstly, for $t/U = 0.02$, we see that the DDMRG results are in a satisfactory accord with $S_\eta^{(1)}(k, \omega)$, where as a matter of course for smaller system sizes a larger value of η has to be used to achieve good agreement. Secondly, $S(k, \omega)$ calculated by DDMRG approaches the curve given by (4) for increasing system size L and decreasing broadening η .

Finally, we look at the changes in the dynamical density-density response as the system crosses the MI-SF quantum phase transition with decreasing Coulomb interaction strength. Figure 3 shows the intensity distribution of $S(k, \omega)$ in the MI and SF phases as well as in the vicinity of the Kosterlitz–Thouless (KT) transition point, where the charge excitation gap closes. For large U , the spectral weight is mainly concentrated around $\omega = U$ in the region $\pi/2 \leq k \leq \pi$, in agreement with the strong-coupling prediction. As U weakens in the MI phase, the distribution of the spectral weight broadens. At the same time, the maximum value of $S(k, \omega)$ acquires a sizable dispersion (see upper-row panels). As the system reaches the MI-SF transition point we observe a significant redistribution of spectral weight to lower k values and, most notably, the excitation gap closes (see lower panels). In our previous work, we evaluated the scaling of the Tomonaga–Luttinger liquid parameter and determined the KT transition point to be located at $t/U = 0.305(1)$ [3]. In the SF phase spectra for $k \gtrsim 0$ (cf. the panel for $t/U = 0.4$), we observe an almost linear dispersion of the $S(k, \omega)$, which—in accordance with bosonization [11] and with Bogoliubov theory [12]—can be taken as a signature of the Bose condensation process. Our 1D DDMRG BHM data are unsuggestive of two distinct (gapless sound and massive) modes in the SF phase. These two phases are found in mean-field theory and may appear for dimensions $d \geq 2$ where a true condensate exists in the SF ground state.

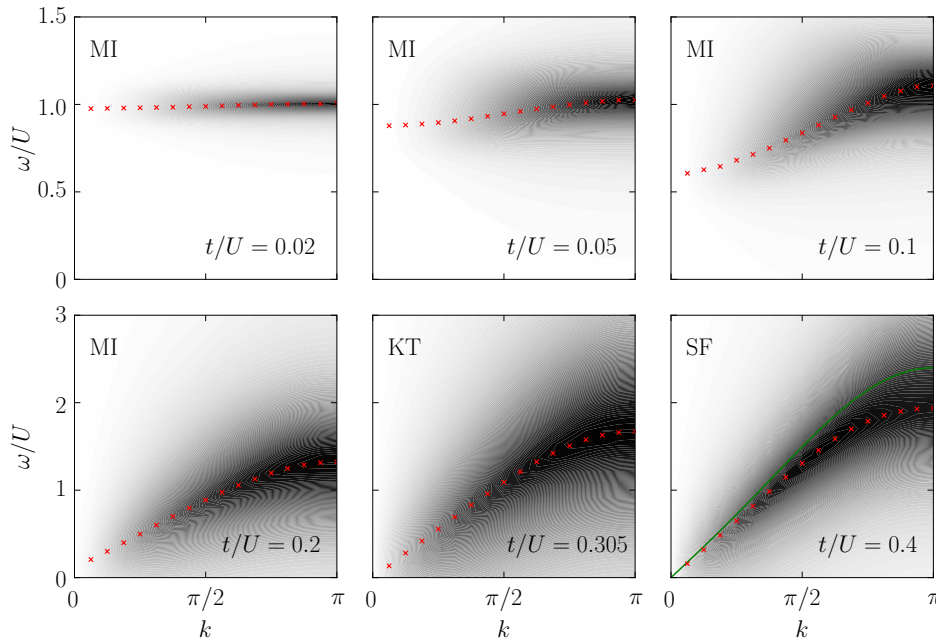


Figure 3. Intensity of the dynamical structure factor $S(k, \omega)$ in the k - ω plane for different t/U . DDMRG data were obtained for $L = 32$ system, using $\eta = 2t$ ($\eta = t$) in the MI phase and at the KT transition point (in the SF phase). The red crosses mark the positions of the maximum in each $k = 2\pi j/L$ -sector. The green line for $t/U = 0.4$ marks the field-theory/Bogoliubov result $\omega(k) = \sqrt{\epsilon_0(k)[\epsilon_0(k) + 2U]}$ with $\epsilon_0(k) = -2t(\cos k - 1)$.

To summarise, we have determined the dynamical structure factor $S(k, \omega)$ for the 1D BHM with particle density $\rho = N/L = 1$ by means of unbiased numerical DDMRG calculations. As discussed for photoemission spectra previously [3], $S(k, \omega)$ agrees with the first-order perturbation theory result in the Mott insulator phase for $U \gg t$. Naturally, as the Coulomb interaction is lowered, noticeable deviations appear between both approaches, in particular the DDMRG $S(k, \omega)$ becomes dispersive and we find a substantial redistribution of spectral weight into the small k -sector. In this regime, higher-order corrections have to be taken into account in our analytical treatment of the BHM. Approaching the SF state, the charge excitations gap closes and the maximum in $S(k, \omega)$ exhibits a linear dispersion. The quantum phase transition between MI and SF phases is located at about $t/U \simeq 0.3$ and found to be of KT type.

Acknowledgements. SE and HF acknowledge funding by DFG through SFB 652.

References

- [1] Greiner M, Mandel O, Esslinger T, Hänsch T W and Bloch I 2002 *Nature* **415** 39
- [2] Bloch I, Dalibard J and Zwerger W 2008 *Rev. Mod. Phys.* **80** 885
- [3] Ejima S, Fehske H and Gebhard F 2011 *Europhysics Letters* **93** 3002
- [4] Oosten D van *et al.* 2005 *Phys. Rev. A* **71** 021601(R)
- [5] Huber S D, Altman E, Büchler H P and Blatter G 2007 *Phys. Rev. B* **75** 085106
- [6] Roth R and Burnett K 2004 *J. Phys. B* **37** 3893
- [7] Pippan P, Evertz H G and Hohenadler M 2009 *Phys. Rev. A* **80** 033612
- [8] White S R 1992 *Phys. Rev. Lett.* **69** 2863; Jeckelmann E 2002 *Phys. Rev. B* **66** 045114
- [9] Stenger J *et al.* 1999 *Phys. Rev. Lett.* **82** 4569
- [10] Nishimoto S and Jeckelmann E 2004 *J. Phys.:Condens. Matter* **16** 613
- [11] Cazalilla M A, Citro R, Giamarchi T, Orignac E and Rigol M, 2011 *Rev. Mod. Phys.* **83** 1405
- [12] Bogoliubov N N 1947 *J. Phys. (USSR)* **11** 23

Dynamical correlation functions for the one-dimensional Bose-Hubbard insulator

Kevin zu Münster and Florian Gebhard

Fachbereich Physik, Philipps Universität Marburg, D-35032 Marburg, Germany

Satoshi Ejima and Holger Fehske

Institut für Physik, Ernst-Moritz-Arndt Universität Greifswald, D-17489 Greifswald, Germany

(Received 31 March 2014; published 27 June 2014)

We calculate the dynamical current and kinetic-energy correlation functions for the first Mott lobe of the one-dimensional Bose-Hubbard model. We employ the strong-coupling expansion up to sixth order in $x = t/U$ and the dynamical density-matrix renormalization group method on rings with 64 sites. The correlation functions are finite above the single-particle gap with a square-root onset, as also found from field theory close to the Mott transition. The correlation functions display a featureless superposition of the primary and tertiary Hubbard bands. We find very good agreement between all methods in the interaction and frequency regimes where they are applicable.

DOI: [10.1103/PhysRevA.89.063623](https://doi.org/10.1103/PhysRevA.89.063623)

PACS number(s): 67.85.Bc, 67.85.De, 64.70.Tg

I. INTRODUCTION

Ultracold atomic systems in which the atoms are trapped on an optical lattice offer a wide range of possibilities to prove the applicability of theoretical studies [1]. New experimental techniques such as the modulation of the amplitude and the phase of the lattice potential provide a variety of new possibilities, e.g., the modulation of the lattice potential can be used to introduce artificial gauge fields into the system [2,3]. Such a modulation derives an excitation of the system described by the kinetic and current correlation functions. Recently, the signature of a Higgs amplitude mode in the two-dimensional superfluid in the vicinity of a quantum phase transition to a Mott insulator has been predicted by field theory combined with quantum Monte Carlo simulations, showing a resonance-like feature in dynamical spectra [4]. Albeit this increasing attention, theoretical studies for these dynamical correlation functions in the bosonic systems are rare even in one dimension. Kühner *et al.* computed the optical conductivities in the one-dimensional Bose-Hubbard model by using the density-matrix renormalization group (DMRG) method [4]. The dynamical response due to the lattice modulation were also simulated by applying the time-dependent DMRG [5].

In this work we address the one-dimensional Bose-Hubbard model in the insulating phase when the number N of bosons equals the number of lattice sites L . The model describes a system of neutral spinless atoms trapped in an optical lattice with deep lattice potentials. The Bose-Hubbard Hamiltonian is defined by

$$\begin{aligned}\hat{H} &= -t\hat{T} + U\hat{D}, \\ \hat{T} &= \sum_{j=1}^L (\hat{b}_j^\dagger \hat{b}_{j+1} + \hat{b}_{j+1}^\dagger \hat{b}_j), \\ \hat{D} &= \frac{1}{2} \sum_{j=1}^L \hat{n}_j(\hat{n}_j - 1).\end{aligned}\quad (1)$$

Here, \hat{b}_j^\dagger , \hat{b}_j , and $\hat{n}_j = \hat{b}_j^\dagger \hat{b}_j$ are the boson creation, annihilation, and particle number operators on site j , respectively, and

periodic boundary conditions (PBCs) apply. Throughout this work, we denote the ratio of the hopping amplitude t and the local interaction strength U by $x = t/U$.

At integer filling, $\rho = N/L = 1$, the Bose-Hubbard model describes a phase transition from the Mott insulating phase to the superfluid phase at a critical interaction ratio, $x_c \approx 0.305$ [6]. The phase transition lies in the XY universality class and is of Kosterlitz-Thouless type, which results in an exponentially small band gap near the transition. In this work we restrict ourselves to the first Mott lobe: $x < x_c$.

The response of the bosons to weak phase and amplitude modulations of the lattice potential is described by the correlation functions for the current operator and the kinetic-energy operator; for a detailed discussion of the connection between measurable quantities like the energy absorption rate and correlation functions in terms of a linear response theory, see Refs. [7–9]. We define the correlation function of an operator \hat{A} as the imaginary part of the corresponding retarded Green function, which is given in frequency space by

$$\begin{aligned}\tilde{S}_A(\omega \geq 0) &= -\frac{1}{\pi} \lim_{\eta \rightarrow 0^+} \text{Im} [G_A^{\text{ret}}(\omega + i\eta)] \\ &= \frac{1}{L} \sum_n |(\Psi_n | \hat{A} | \Psi_0)|^2 \delta(\omega - (E_n - E_0)).\end{aligned}\quad (2)$$

Here, $|\Psi_0\rangle$ is the ground state of \hat{H} with energy E_0 , and $|\Psi_n\rangle$ are eigenstates of \hat{H} with energy E_n . Note that the correlation functions are positive, $\tilde{S}_A(\omega) \geq 0$. Moreover, the sum rule

$$\int_0^\infty d\omega \tilde{S}_A(\omega) = \frac{1}{L} \langle \Psi_0 | \hat{A}^2 | \Psi_0 \rangle \quad (3)$$

shows that $\tilde{S}_A(\omega \rightarrow \infty) \rightarrow 0$.

In this work, we focus on the correlation function for the kinetic energy, $\tilde{S}_T(\omega)$ with \hat{T} from Eq. (1), and define

$$\tilde{S}_T(\omega) = w_0^T \delta(\omega) + S_T(\omega), \quad (4)$$

where we extracted the δ peak at $\omega = 0$. Moreover, we address $S_J(\omega)$ with the current operator

$$\hat{J} = i \sum_l (b_{l+1}^\dagger b_l - b_l^\dagger b_{l+1}). \quad (5)$$

Note that S_J is related to the real part of the optical conductivity at zero momentum as [10]

$$S_J(\omega > 0) = \frac{\omega}{\pi} \operatorname{Re}[\sigma(q = 0, \omega)]. \quad (6)$$

Since we focus on the insulating phase, we know that $w_0^J = 0$ so that $\tilde{S}_J(\omega) = S_J(\omega)$.

Our work is organized as follows: In Sec. II we briefly discuss the dynamical DMRG (DDMRG) method and the strong-coupling expansion and give the field-theory expression for the current correlation function. In Sec. III we discuss the results for the current and kinetic-energy correlation functions in the Mott phase. Conclusions and outlook, Sec. IV, close our presentation. Some technical aspects are deferred to the Appendix.

II. METHODS

We evaluate the correlation functions with the numerical DDMRG method and the analytical strong-coupling expansion (SC). We used these methods previously [11–13] for the evaluation of single-particle and two-particle response functions such as the density correlation function $S_n(k, \omega)$. In Refs. [11,13], a detailed explanation of the methods can be found. In this section, we briefly summarize the most important aspects of both methods. For comparison, we also give the field-theoretical expression for the current correlation function. For an early application of the DMRG correction vector method [14] to the one-dimensional (extended) Bose-Hubbard model; see Ref. [4].

A. Dynamical density-matrix renormalization group

In order to simulate the Bose-Hubbard type models using the (D)DMRG technique [15–17], the maximum number n_b of bosons per site should be limited, while each lattice site can be occupied, in principle, by infinitely many bosons. Nevertheless, the (D)DMRG results are unbiased and numerically exact as long as the dependence on n_b can be verified to be negligible. In the DDMRG scheme it makes a considerable difference from the correction vector method [14] to minimize the functional [16]

$$W_{A,\eta}(\omega, \psi) = \langle \psi | (E_0 + \omega - \hat{H})^2 + \eta^2 | \psi \rangle + \eta \langle A | \psi \rangle + \eta \langle \psi | A \rangle, \quad (7)$$

where $|A\rangle = \hat{A}|\psi_0\rangle$. Then the imaginary part of the Green function can be evaluated as

$$W_{A,\eta}(\omega, \psi_{\min}) = -\pi\eta \operatorname{Im} G_A^{\text{ret}}(\omega + i\eta). \quad (8)$$

Within this DDMRG scheme we repeat the sweeps in the finite-system algorithm until the functional $W_{A,\eta}(\omega, \psi)$ takes its minimal values.

Calculating the dynamical current [$A = J$ in Eqs. (7) and (8)] and kinetic-energy [$A = T$] correlation functions in the first Mott lobe of the Bose-Hubbard model, we keep $m = 800$ states to determine the ground state during the first five DMRG sweeps, and then use $m = 400$ states for the evaluation of the dynamical properties. For a precise analysis of the dynamical properties we consider a finite system with broadening width η as small as possible. In doing so artificial peaks can appear if η is too small for fixed system size L .

Thus, one needs to find an appropriate $\eta(L)$ empirically. In order to avoid artificial peaks, in this paper we fix $\eta = 0.8t$ for $L = 64$.

B. Spectral broadening and deconvolution

The DDMRG method works with complex frequencies, i.e., instead of the real frequency ω , the calculations are done with a finite shift η into the complex plane: $\omega \rightarrow \omega + i\eta$. The shift to the complex plane introduces a Lorentzian spectral broadening of the correlation function, i.e., the DDMRG actually provides

$$S_A^\eta(\omega) = \frac{1}{\pi} \int_{-\infty}^{\infty} \frac{\eta}{(\omega - \tilde{\omega})^2 + \eta^2} S_A(\tilde{\omega}) d\tilde{\omega} \quad (9)$$

at equally spaced frequencies ω_i with high numerical accuracy. The size of the intervals $\Delta\omega = |\omega_{i+1} - \omega_i|$ is smaller than, but of the order of η . Then, without loss of accuracy, the integration over ω in Eq. (9) can be represented by a matrix multiplication,

$$S_A^\eta(\omega_i) = \sum_j \frac{1}{\pi} \frac{\eta}{(\omega_i - \omega_j)^2 + \eta^2} S_A(\omega_j),$$

$$\underline{S}_A^\eta = \underline{L}^\eta \cdot \underline{S}_A. \quad (10)$$

The derivation of the vector \underline{S}_A for the correlation function at the frequencies ω_i from the corresponding DDMRG vector \underline{S}_A^η (“deconvolution”) poses an ill-conditioned inverse problem.

There is a number of deconvolution techniques for Lorentz-broadened spectra. It was shown in Refs. [18–20] that the matrix inversion of Eq. (10) provides a simple and reliable way to deconvolve spectral functions,

$$\underline{S}_A = (\underline{L}^\eta)^{-1} \cdot \underline{S}_A^\eta. \quad (11)$$

As seen from Eq. (2), the correlation functions are positive, $S_A(\omega) \geq 0$. However, the deconvolution scheme (11) cannot guarantee this so that the deconvolved correlation functions might be negative in some regions. The width and depth of the regions with negative values of the correlation functions can be taken as a sign of the error introduced by the deconvolution technique and the finite-size and finite- η limitations in the DDMRG method. Of course, the deviations are most prominent when the correlation functions tend to zero or show narrow extrema. In the first Mott lobe of the Bose-Hubbard model, the width of the peaks is large enough to deconvolve the data by using $\eta = 0.8t$ and $L = 64$. Then, only very close to $\omega \simeq \Delta$ (with particle gap Δ) do the spectra show negative values, as we see in the following.

C. Strong-coupling expansion

In the strong-coupling expansion we use a Harris-Lange transformation [21,22] to obtain an effective Hamilton operator \hat{h} that does not mix states from different subspaces of the operator for potential energy $U\hat{D}$. Within this approach, the transformation operator \hat{S} as well as the effective Hamilton operator \hat{h} are expanded in x :

$$\hat{h} = e^{\hat{S}} \hat{H} e^{-\hat{S}} = U\hat{D} + t \sum_{r=0}^{\infty} x^r \hat{h}_r,$$

$$\hat{S} = -\hat{S}^\dagger = \sum_{r=1}^{\infty} x^r \hat{S}_r. \quad (12)$$

In m th order SC perturbation theory, the operators \hat{h}_r and \hat{S}_r are constructed iteratively whereby we enforce $[\hat{h}_r, \hat{D}]_- = 0$ for $0 \leq r \leq m$. This requires that we keep the operators up to \hat{S}_m, \hat{h}_{m-1} in the Taylor series for \hat{S} and \hat{h} .

The (nondegenerate) ground state $|\Psi_0\rangle$ for finite x is obtained from the (nondegenerate) ground state $|\Phi_0\rangle$ for $x = 0$ as

$$|\Psi_0\rangle = \exp(-\hat{S})|\Phi_0\rangle. \quad (13)$$

Note that the ground state for $t = 0$ is very simple because for $N = L$ every site is singly occupied by a boson, $|\Phi_0\rangle = \prod_j \hat{b}_j^+ |\text{vac}\rangle$. Within SC perturbation theory, the evaluation of a ground state expectation values of an operator \hat{A} reduces to

$$\begin{aligned} \langle \Psi_0 | \hat{A} | \Psi_0 \rangle &= \langle \Phi_0 | \tilde{A} | \Phi_0 \rangle, \\ \tilde{A} &= \exp(\hat{S}) \hat{A} \exp(-\hat{S}). \end{aligned} \quad (14)$$

To lowest order, it is readily deduced from Eq. (13) that the operator \hat{S}_1 generates states in $|\Phi_0\rangle$ with one doubly occupied site and a neighboring hole. In general, the states from the subspace $\mathcal{H}_1 \subset \mathcal{H}$ give rise to the primary Hubbard band in the dynamical correlation functions around $\omega \approx U$. In higher orders in Eq. (13), states from \mathcal{H}_2 and \mathcal{H}_3 appear in $|\Psi_0\rangle$ that give rise to the secondary and tertiary Hubbard bands. Therefore, as long as x is small and the spectral splitting of the Hilbert space is large, the dynamical correlation functions display contributions from energetically separated Hubbard bands. Due to sum rules and the fact that the correlation functions are non-negative, most of the spectral weight is concentrated in the primary Hubbard band. Within SC perturbation theory, the contributions from the higher Hubbard bands is fairly small.

For the primary Hubbard band in the m th-order approximation, we have to consider one double occupancy and one hole on a ring. When their relative distance is larger than m lattice sites, they do not interact with each other. For this reason, the SC problem reduces to the analytical solution of a two-particle problem with a finite-range interaction [11]. Most importantly, the interaction leads to a backscattering of the hole from the double occupancy so that an effective single-particle problem results where the hole moves on a chain with open boundary conditions.

For higher-order corrections the analytical expressions for the weights and the Hamilton operator are employed for the succeeding numerical evaluation of the correlation functions. If the states describe a single quasiparticle, Cauchy's integral formula can be used to compute the results for an infinite system [11,13] without spectral broadening, $\eta = 0^+$. The contributions originating from states with two or more quasiparticles can be obtained by a simple diagonalization of the Hamilton operator for systems large enough to set $\eta \approx 0$. However, since this perturbation theory is based on the spectral separation of the Hilbert space, it breaks down when the gap becomes exponentially small close to the Kosterlitz-Thouless-type Mott transition at $x_c \approx 0.305$. Therefore, its applicability is limited to $x \lesssim 0.10$, as we shall see below.

D. Results from field theory

Close to the Mott transition, the Bose-Hubbard model can be described by the sine-Gordon model where the dispersion of holons (h) and antiholons (\bar{h}) with momentum P is given

by $E(P) = \pm[P^2 + (\Delta/2)^2]^{1/2}$ where Δ is the (exponentially small) single-particle gap. If only one holon and antiholon is taken into account and a marginal interaction between them is assumed, the two-particle contribution to the current-current correlation function is given by [23–25] ($v = \omega/\Delta$)

$$\begin{aligned} S_{J,h,\bar{h}}(\omega) &= \frac{\Delta}{\pi} C_2(\Delta) \frac{2}{\pi} \frac{\sqrt{v^2 - 1}}{v} \Theta(v - 1) \\ &\times \exp\left(-\int_0^\infty \frac{dx}{x} \frac{1 - \cos(x\theta/\pi) \cosh x}{\exp(x/2) \cosh(x/2) \sinh x}\right), \end{aligned} \quad (15)$$

where $\theta = 2\text{arccosh}(v)$. Formula (15) is exact in the interval $\Delta \leq \omega \leq 2\Delta$. For $\omega > 2\Delta$ there are corrections to (15), which are due to multiholon and antiholon states and have a more complicated structure but can be shown to be important only at energies $\omega \gg \Delta$ [25], where the field-theory approach becomes invalid anyway.

The more general case with a relevant holon-antiholon interaction, parametrized by $1/2 < \beta^2 = K/2 < 1$, is discussed in detail in Ref. [8]; here, the parameter K in a Luttinger-model description or the parameter β^2 in the sine-Gordon model characterize the strength of the holon-antiholon interaction. As we shall see below, our DDMRG is not sufficient to determine the value β^2 for the first Mott lobe accurately but we shall see that the assumption $\beta^2 = 1$ as used in Eq. (15) provides a reasonable description of the DDMRG data for the frequency dependence of the current-current correlation function close to the gap (see below).

The current correlation function is finite only beyond the single-particle gap with a square-root onset at $\omega = \Delta$. It shows a maximum at $\omega \approx 1.24\Delta$ and a power-law decay at large frequencies. The normalization $C_2(\Delta)$ cannot be calculated analytically. To estimate the normalization $C_2(\Delta)$, we use the sum rule for the conductivity,

$$\int_0^\infty \frac{d\omega}{\pi} \text{Re}[\sigma(\omega)] = -\frac{1}{2L} \langle \Psi_0 | \hat{T} | \Psi_0 \rangle. \quad (16)$$

This quantity can be determined accurately by using the ground-state DMRG. For example, for $x = 0.20$ we find $[\Delta = 0.436t, -\langle \Psi_0 | \hat{T} | \Psi_0 \rangle / (2L) = 1.418t]$ and for $x = 0.15$ we find $[\Delta = 1.63t, -\langle \Psi_0 | \hat{T} | \Psi_0 \rangle / (2L) = 1.133t]$.

Close to the Mott transition, most of the optical weight is concentrated at low energy $\omega \sim \Delta$. Therefore, in the field-theory limit, the left-hand side of Eq. (16) can be determined from Eq. (15) because the omitted terms have a negligible contribution at low energy. This comparison provides $C_2(\Delta)$ for given x ,

$$C_2(\Delta) = -\frac{\langle \Psi_0 | \hat{T} | \Psi_0 \rangle}{2L} \frac{\pi}{F\Delta}, \quad (17)$$

with

$$\begin{aligned} F &= \frac{2}{\pi} \int_1^\infty dy \frac{\sqrt{y^2 - 1}}{y^2} \\ &\times \exp\left(-\int_0^\infty \frac{dx}{x} \frac{1 - \cos(2x\text{arccosh}(y)/\pi) \cosh x}{\exp(x/2) \cosh(x/2) \sinh x}\right) \\ &\approx 1.70, \end{aligned} \quad (18)$$

with accuracy ± 0.01 . Therefore, for $x = 0.20$, we have $C_2 = 6.01$ and, for $x = 0.15$, we find $C_2 = 1.28$.

The result from field theory is applicable in the region where the gap is (exponentially) small. Therefore, it is complementary to the DDMRG with its energy resolution $\eta \approx 12W/L$ where $W = 4t$ is the bare bandwidth. We note that the formula (15) works surprisingly well for the fermionic Hubbard model even when the gap is not exponentially small but of the order of t [26,27]. Therefore, we compare our DDMRG results for the current correlation function for $x = 0.20$ and $x = 0.15$ to those from field theory in Sec. III B.

III. CORRELATION FUNCTIONS

A. Strong-coupling result to leading order

To leading order in the SC expansion, the doubly occupied site and the hole only experience their hard-core repulsion. Otherwise, they move freely with hopping amplitudes $t_h = t$ for the hole and $t_d = -2t$ for the double occupancy. Consequently, both the current correlation function and the kinetic-energy correlation function are given by a semi-ellipse,

$$S_{J,T}^{(0)}(\omega) = \frac{4}{3\pi} \sqrt{1 - \left(\frac{\omega - U}{6t}\right)^2} \Theta\left(1 - \left(\frac{\omega - U}{6t}\right)^2\right), \quad (19)$$

where $\Theta(x)$ denotes the Heaviside step function (see also Refs. [6,7,11]). The result is qualitatively the same for the fermionic Hubbard model [26,27], where $t_d^F = -t$.

The correlation function is finite only above the single-particle gap, $\Delta \approx U - 6t$ for $x \rightarrow 0$. Moreover, the correlation function displays a square-root onset, as seen in field theory. Therefore, the square-root onset above the single-particle gap apparently is a generic feature of the correlation functions in the Mott-insulating phase.

B. Current correlation function

In Fig. 1 we show the deconvolved DDMRG data and the results from sixth-order SC theory for the current correlation function for $x = 0.05, 0.08, 0.10$, and 0.12 . For $x = 0.05$, the correlation function is almost an undisturbed semi-ellipse; see Eq. (19). Upon decreasing the interaction, the width of the primary Hubbard band increases, and spectral weight is shifted towards the lower band edge so that the current correlation function becomes asymmetric. As seen from the figure, both DDMRG and SC agree perfectly with each other up to $x = t/U = 0.08$. As discussed in Sec. II B, the slightly negative DDMRG data for the current correlation function close to the band edges are an artifact of the deconvolution scheme.

For smaller interactions, $x \geq 0.10$, the current correlation function steeply rises to its maximum value as a function of frequency and falls off monotonically beyond the maximum. The agreement of DDMRG and SC is satisfactory only at first glance because some wiggles appear in the SC results that are absent in the DDMRG data. The wiggles are more pronounced for $x = 0.12$ than for $x = 0.10$. The reason why these unphysical wiggles appear in SC is discussed in Appendix B.

For $x = 0.12$, the tertiary Hubbard band can be seen in the DDMRG data. In the SC theory this band emerges from states

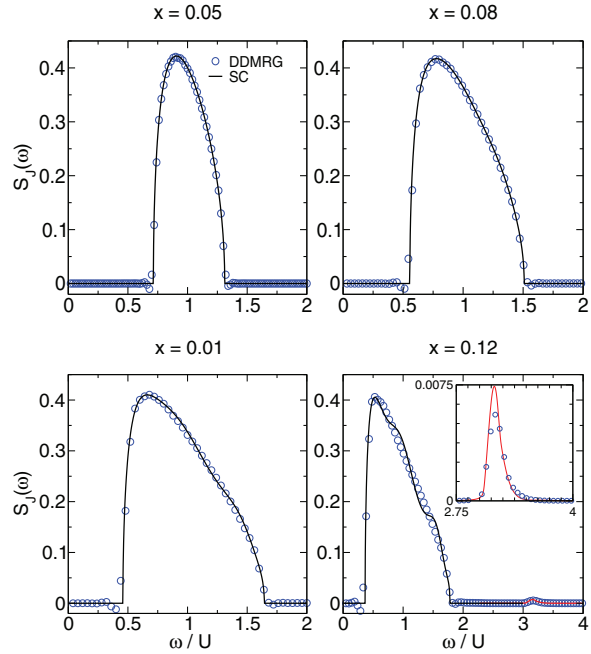


FIG. 1. (Color online) Current correlation function for interactions $x = t/U = 0.05, 0.08, 0.1, 0.12$ from top left to bottom right. The deconvolved DDMRG data (circles) were obtained for $L = 64$, PBCs, and $\eta = 0.8t$. The black solid lines give the result of the SC theory of the primary Hubbard band. The red solid lines give the result of the SC theory for the tertiary Hubbard band. A magnification of the tertiary Hubbard band is shown in the inset.

with a triple occupancy and two holes whose contributions to $|\tilde{J}|\Phi_0\rangle|^2$ are of the order $O(x^4)$. For $x = 0.12$ the weight of the primary, secondary, and tertiary Hubbard bands is given by $3.04, 1.5 \times 10^{-3}$, and 0.01 , respectively. Here, the weight of the primary Hubbard band has been approximated by a sixth-order expansion, while a third- and fourth-order expansion has been used for the secondary and tertiary Hubbard band, respectively. The secondary Hubbard band is described by two double occupancies and two holes but is not visible because its weight is only of the order $O(x^6)$; see Appendix A.

To leading order, the total weight of the correlation functions is given by $\int_0^\infty S_{J,T}^{(0)}(\omega) d\omega = 4$. For $x > 0$, the total spectral weight can be determined by the static DMRG method with great precision so that it can be used as a test for the accuracy of the SC expansion. The results for the total weight from DMRG and SC deviate by less than 3×10^{-3} up to $x \leq 0.12$. For higher values of x , the SC theory seems to overestimate the weight.

For interaction parameters $x = 0.15$ and $x = 0.20$, only the DDMRG can provide reliable results. In Fig. 2 we plot the Lorentz-broadened current correlation function $S_J^\eta(\omega)$ for $\eta = 0.8t$ and compare it to the predictions from field theory. Even up to half the width of the primary Hubbard band, the field-theory curve agrees with the DDMRG data, despite the fact that the gap is quite sizable for $x = 0.15$. For $x = 0.20$, the agreement appears to be worse than for $x = 0.15$. At $x = 0.20$,

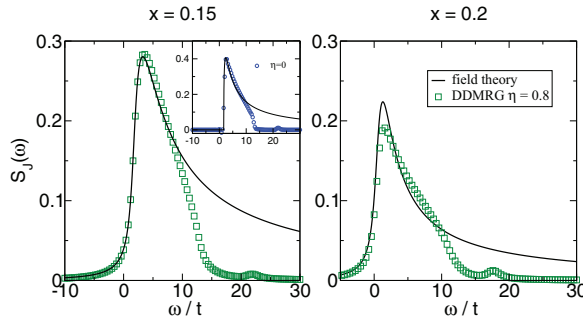


FIG. 2. (Color online) DDMRG data (squares) for $L = 64$, PBCs, and $\eta = 0.8t$ for (left panel) $x = 0.15$ and (right panel) $x = 0.2$. The solid black line gives the Lorentz-broadened field-theoretical results. The deconvolved DDMRG data (circles) and the field-theory results are shown in the inset for $x = 0.15$.

however, the DDMRG has difficulties to resolve the quite sharp maximum close to the onset of the correlation function. Here, larger system sizes and, correspondingly, smaller values for η would improve the agreement. Therefore, we show exemplarily a comparison of the deconvolved DDMRG data with the field-theory results in the inset of Fig. 2 for $x = 0.15$ and omit a further deconvolution of the DDMRG data in this parameter regime.

C. Kinetic correlation function

Before we discuss $S_T(\omega > 0)$, we briefly comment on the weight at $\omega = 0$. Within the SC expansion to sixth order, it is given by

$$\sqrt{w_0^T} = 8x - 16x^3 + \frac{529}{3}x^5 + O(x^7). \quad (20)$$

Apparently, the series converges rapidly even for $x = 0.2$. In general, the SC expansion reproduces the total weight of the kinetic-energy correlation function with an accuracy of 3.7×10^{-2} for $x \leq 0.12$. As for the current correlation function, the SC expansion seems to overestimate the weight for higher values of x .

In Fig. 3 we show the kinetic-energy correlation function for the values $x = 0.05, 0.08, 0.1$, and 0.12 . For $x \leq 0.08$ the agreement of SC and DDMRG is very good. For $x = 0.1$ and 0.12 , the sixth-order SC theory starts to develop wiggles as in the case of the current correlation functions, which are not seen in the DDMRG data. Therefore, the SC expansion cannot be used beyond $x = 0.10$. As the current correlation function, the kinetic-energy correlation function is finite above the single-particle gap with a square-root onset. In contrast to the current correlation function, the primary Hubbard band for S_T appears to remain symmetrical so that its maximum appears in the middle of the band for all interaction strengths.

The total weight of the secondary and tertiary Hubbard bands are of the order $O(x^6)$ and $O(x^2)$. For $x = 0.12$, the weight of the primary, secondary, and tertiary Hubbard bands is given by $3.3, 3.3 \times 10^{-3}$, and 0.076 , respectively. The operator \tilde{T} is symmetric under spatial inversion, so that states in which the holes are symmetrically placed to the left and the

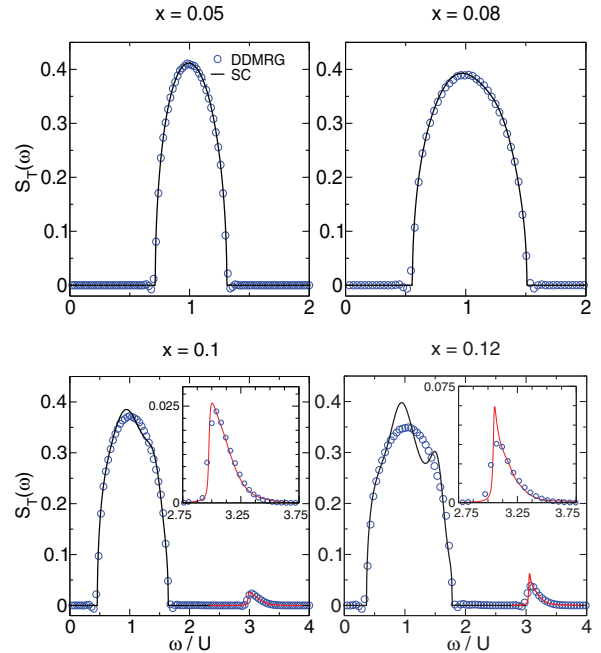


FIG. 3. (Color online) Kinetic-energy correlation function for interactions $x = 0.05, 0.08, 0.1, 0.12$ (from top left to bottom right). The deconvolved DDMRG data (circles) were obtained for $L = 64$, PBCs, and $\eta = 0.8t$. Black solid lines give the result of the SC theory of the primary Hubbard band. Red solid line gives the result of the SC theory for the tertiary Hubbard band. A magnification of the tertiary Hubbard band is shown in the insets.

right of the triple occupancy also occur in $\tilde{T}|\Phi_0\rangle$. They are the leading-order contributions to the tertiary Hubbard band. Therefore, the tertiary Hubbard band is more prominent in S_T than in S_J where the spatial antisymmetry eliminates these states; see Appendix A.

In Fig. 3, we also compare the DDMRG data with SC results for the tertiary Hubbard band. Note, however, that the calculations are quite cumbersome so that we used the weights of the tertiary Hubbard band up to fourth order and considered the action of the effective Hamiltonian on \mathcal{H}_3 in second order only. This means that we work with \hat{S}_4 and \hat{h}_1 . Given these simplifications, we obtain the SC results for the tertiary Hubbard band from an exact diagonalization of a system of $L = 128$ lattice sites and a very small spectral broadening of $\eta = 0.08$. Despite these limitations, our restricted SC approach quite accurately describes the asymmetrical shape of the tertiary Hubbard band.

The third Hubbard band shows some interesting features. For example, an attractive force acts between the two particles if they are placed next to each other. Moreover, the alignment of a hole next to the triple occupancy leads to a decrease in the potential energy. These effects induce sizable correlations between the holes and the triple occupancy which influences the shape of the correlation function.

For interaction parameters $x = 0.15$ and $x = 0.20$, only the DDMRG can provide reliable results. In Fig. 4 we plot

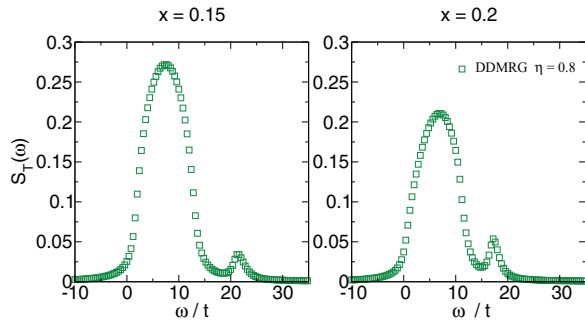


FIG. 4. (Color online) DDMRG data (squares) were obtained for $L = 64$, PBCs, and $\eta = 0.8t$ for (left panel) $x = 0.15$ and (right panel) $x = 0.2$.

the Lorentz-broadened kinetic-energy correlation function for $\eta = 0.8t$. The weight of the primary Hubbard band shrinks when we approach the transition whereas the tertiary Hubbard band gains more weight as a function of x . Therefore, the tertiary Hubbard band becomes clearly visible for $x = 0.20$.

IV. CONCLUSION AND OUTLOOK

In this work we calculated the current and kinetic-energy correlation functions for the Mott insulating regime of the one-dimensional Bose-Hubbard model at filling $\rho = N/L = 1$ using the strong-coupling (SC) expansion up to sixth order in $x = t/U$ and the dynamical density-matrix renormalization group (DDMRG) method on rings with $L = 64$ lattice sites. The DDMRG data for finite $\eta = 0.8t$ permit a reliable deconvolution of the Lorentz-broadened data so that the correlation functions can be studied in the thermodynamical limit.

A comparison of sixth-order SC and DDMRG results shows that SC is reliable up to $x = 0.10$. DDMRG on $L = 64$ sites can be used up to $x \lesssim 0.20$. For $x \gtrsim 0.20$ it becomes difficult to resolve the sharp maximum in the current correlation functions at frequency $\omega \approx 1.3\Delta$, where Δ is the single-particle gap. In any case, the exponentially small gap close to the Mott transition at $x_c \approx 0.305$ cannot be resolved by (D)DMRG for $x \gtrsim 0.25$.

The correlation functions are dominated by the primary Hubbard band around $\omega \approx U$. The primary Hubbard band starts at the single-particle gap with a characteristic square-root onset $S_{J,T}(\omega \rightarrow \Delta) \propto \sqrt{\omega - \Delta}$. This is seen in SC perturbation theory and in the deconvolved DDMRG data. It is confirmed for the current correlation function by field theory which is applicable close to the Mott transition. Apart from a maximum at low frequencies, the primary Hubbard band of the current correlation function is featureless. The primary Hubbard band of the kinetic-energy correlation function appears to be symmetric with a single maximum at the band center. For both correlation functions, the secondary Hubbard band is very small but the tertiary Hubbard band around $\omega = 3U$ becomes visible for $x \gtrsim 0.10$. The asymmetric shape is understood from SC theory which includes correlations between the quasiparticles.

For the primary Hubbard band in the one-dimensional Bose-Hubbard model, the attractive correlations between

doubly occupied site and hole are not significant enough to overcome their hard-core repulsion. Therefore, it requires a finite nearest-neighbor interaction to generate an excitonic state [4,26,27]. The situation could change in the two-dimensional Bose-Hubbard model. In recent quantum Monte Carlo studies and field-theoretical studies [28], the existence of a peak in the optical conductivity has been alluded to in the critical region above but close to the Mott transition, $x_c^{2d} - x < 1.15x_c^{2d}$. This peak is a signature of the Higgs boson in the two-dimensional superfluid which should persist as a resonance in the Mott phase.

Albeit the SC expansion is better behaved in two than in one dimension [29], it is not clear at this point whether the expansion can be carried out far enough to include such features. The SC diagrams show that higher orders in the expansion generate an attractive interaction between the quasiparticles in the primary and tertiary Hubbard band. However, it is unclear whether these interactions are sufficient to generate a resonance structure close to the transition. Moreover, the diagrammatic expansion is considerably more cumbersome in two dimensions than in one dimension. Therefore, a SC study of the two-dimensional Bose-Hubbard model remains an open problem.

ACKNOWLEDGMENTS

S.E. and H.F. gratefully acknowledge financial support by the Deutsche Forschungsgemeinschaft through SFB 652.

APPENDIX A: DIAGRAMMATIC ANALYSIS

The Taylor expansion for \hat{h} in Eq. (12) gives rise to so-called *process chains* [29–31]. They represent sequences that involve alternately the kinetic-energy operator \hat{T} and projection operators \hat{P}_D onto subspaces \mathcal{H}_D . For example, the leading-order approximations of the transformation operator \hat{S} and the effective Hamilton operator \hat{h} can be written as

$$U\hat{D} + t\hat{h}_0 = U\hat{D} + t \sum_D \hat{P}_D \hat{T} \hat{P}_D, \quad (\text{A1})$$

$$\hat{S}_1 = \sum_{D_1, D_2} \frac{\hat{P}_{D_1} \hat{T} \hat{P}_{D_2}}{D_1 - D_2}. \quad (\text{A2})$$

This example shows that each process chain must be weighted according to the number of double occupancies that occur in intermediate steps.

The application of the Baker-Campbell-Hausdorff formula to Eqs. (12) shows that \hat{h} and \hat{S} can be written in terms of nested Lie brackets. In this way, only connected hopping processes must be considered in the action of these operators onto some state. This simplification leads to an intuitive understanding of why the secondary Hubbard band has vanishingly small intensity. Its starting state consists of two double occupancies and two holes. The leading-order contribution for the secondary Hubbard band can be depicted as

$$\left[\begin{array}{|c|c|c|c|} \hline 1 & \leftarrow 1 & \rightarrow 1 & \leftarrow 1 \\ \hline \end{array} \right], \left[\begin{array}{|c|c|c|c|c|c|} \hline 1 & \leftarrow 1 & \rightarrow 1 & \leftarrow 1 & \rightarrow 1 & \leftarrow 1 \\ \hline \end{array} \right], \left[\begin{array}{|c|c|c|c|c|c|c|c|} \hline 1 & \leftarrow 1 & \rightarrow 1 & \leftarrow 1 & \rightarrow 1 & \leftarrow 1 & \rightarrow 1 & \leftarrow 1 \\ \hline \end{array} \right].$$

The actual computation of these diagrams requires the evaluation of all possible hopping processes generated by an

arbitrary time ordering of its constituents. One hopping process originates from the operator \hat{T} or \hat{J} itself while the other processes result from \hat{S}_3 so that these states are $O(x^3)$. Note that the antisymmetry of \hat{J} with respect to spatial inversion leads to a cancellation of the last two diagrams.

APPENDIX B: LIMITATIONS OF STRONG-COUPPLING EXPANSION

In the primary Hubbard band, a particle hole-pair is created in which the hole is placed n lattice sites to the right or left of the double occupancy (state $|\pm n\rangle$). In the lowest-order approximation, the hole cannot jump over the double

occupancy, so that it moves on an open chain on the remaining $L - 1$ sites. The correlation functions are a weighted sum of Green functions of the form $G_{ij}(\omega) = \langle i | \delta(\omega - (\hat{h} - E_0)) | j \rangle$.

For $x \geq 0.1$, the SC expansion shows some wiggles which can be understood as follows: In general, the Greens functions G_{jj} or G_{1j} of a particle in an open chain subject to nearest-neighbor hopping with lattice-site index j will have j extrema. The parts of the state $\hat{J}|\Phi_0\rangle$ that describe particle-hole pairs which are separated by j lattice sites thus lead to contributions in $S_j(\omega)$ which have j maxima. The wiggles naturally appear when the expansion parameter x is chosen too large so that the weight of these contributions is overestimated and not yet corrected by contributions to higher orders.

-
- [1] I. Bloch, J. Dalibard, and W. Zwerger, *Rev. Mod. Phys.* **80**, 885 (2008).
- [2] J. Dalibard, F. Gerbier, G. Juzeliūnas, and P. Öhberg, *Rev. Mod. Phys.* **83**, 1523 (2011).
- [3] J. Struck, C. Ölschläger, M. Weinberg, P. Hauke, J. Simonet, A. Eckardt, M. Lewenstein, K. Sengstock, and P. Windpassinger, *Phys. Rev. Lett.* **108**, 225304 (2012).
- [4] T. D. Kühner, S. R. White, and H. Monien, *Phys. Rev. B* **61**, 12474 (2000).
- [5] J.-W. Huo, F.-C. Zhang, W. Chen, M. Troyer, and U. Schollwöck, *Phys. Rev. A* **84**, 043608 (2011).
- [6] S. Ejima, H. Fehske, and F. Gebhard, *Europhys. Lett.* **93**, 30002 (2011).
- [7] A. Tokuno and T. Giamarchi, *Phys. Rev. Lett.* **106**, 205301 (2011); The analytic expression for the leading order of the correlation functions can already be extracted from the results presented in this work. However, our band width seems to be twice as large, which might be caused by a wrong scaling of t . Note also the different values for x_c .
- [8] A. Iucci, M. A. Cazalilla, A. F. Ho, and T. Giamarchi, *Phys. Rev. A* **73**, 041608 (2006).
- [9] C. Kollath, A. Iucci, I. P. McCulloch, and T. Giamarchi, *Phys. Rev. A* **74**, 041604 (2006).
- [10] G. D. Mahan, *Many-Particle Physics* (Kluwer, New York, 2000).
- [11] S. Ejima, H. Fehske, F. Gebhard, K. zu Münster, M. Knap, E. Arrigoni, and W. von der Linden, *Phys. Rev. A* **85**, 053644 (2012).
- [12] S. Ejima, H. Fehske, and F. Gebhard, *J. Phys.: Conf. Ser.* **391**, 012031 (2012).
- [13] S. Ejima, F. Lange, H. Fehske, F. Gebhard, and K. zu Münster, *Phys. Rev. A* **88**, 063625 (2013).
- [14] T. D. Kühner and S. R. White, *Phys. Rev. B* **60**, 335 (1999).
- [15] S. R. White, *Phys. Rev. Lett.* **69**, 2863 (1992).
- [16] E. Jeckelmann, *Phys. Rev. B* **66**, 045114 (2002).
- [17] E. Jeckelmann and H. Fehske, *Riv. Nuovo Cimento Soc. Ital. Fis.* **30**, 259 (2007).
- [18] F. Gebhard, E. Jeckelmann, S. Mahler, S. Nishimoto, and R. M. Noack, *Eur. Phys. J. B* **36**, 491 (2003).
- [19] S. Nishimoto and E. Jeckelmann, *J. Phys.: Condens. Matter* **16**, 613 (2004).
- [20] M. Paech and E. Jeckelmann, *Phys. Rev. B* **89**, 195101 (2014).
- [21] A. B. Harris and R. V. Lange, *Phys. Rev.* **157**, 295 (1967).
- [22] P. G. J. van Dongen, *Phys. Rev. B* **49**, 7904 (1994).
- [23] M. Karowski and P. Weisz, *Nucl. Phys. B* **139**, 455 (1978).
- [24] F. A. Smirnov, *Form Factors in Completely Integrable Models of Quantum Field Theory* (World Scientific, Singapore, 1992).
- [25] D. Controzzi, F. H. L. Essler, and A. M. Tsvelik, *Phys. Rev. Lett.* **86**, 680 (2001).
- [26] E. Jeckelmann, F. Gebhard, and F. H. L. Essler, *Phys. Rev. Lett.* **85**, 3910 (2000).
- [27] F. H. L. Essler, F. Gebhard, and E. Jeckelmann, *Phys. Rev. B* **64**, 125119 (2001).
- [28] L. Pollet and N. Prokofev, *Phys. Rev. Lett.* **109**, 010401 (2012).
- [29] N. Teichmann, D. Hinrichs, M. Holthaus, and A. Eckardt, *Phys. Rev. B* **79**, 224515 (2009).
- [30] A. Eckardt, *Phys. Rev. B* **79**, 195131 (2009).
- [31] B. Damski and J. Zakrzewski, *Phys. Rev. A* **74**, 043609 (2006).

PHYSICAL REVIEW A **88**, 063625 (2013)**One-dimensional Bose-Hubbard model with local three-body interactions**

Satoshi Ejima, Florian Lange, and Holger Fehske

Institut für Physik, Ernst-Moritz-Arndt-Universität Greifswald, D-17489 Greifswald, Germany

Florian Gebhard and Kevin zu Münster

Fachbereich Physik, Philipps Universität Marburg, D-35032 Marburg, Germany

(Received 17 October 2013; published 12 December 2013)

We employ the (dynamical) density-matrix renormalization-group technique to investigate the ground-state properties of the Bose-Hubbard model with nearest-neighbor transfer amplitudes t and local two-body and three-body repulsion of strength U and W , respectively. We determine the phase boundaries between the Mott-insulating and superfluid phases for the lowest two Mott lobes from the chemical potentials. We calculate the tips of the Mott lobes from the Tomonaga-Luttinger liquid parameter and confirm the positions of the Kosterlitz-Thouless points from the von Neumann entanglement entropy. We find that physical quantities in the second Mott lobe such as the gap and the dynamical structure factor scale almost perfectly in $t/(U+W)$, even close to the Mott transition. Strong-coupling perturbation theory shows that there is no true scaling but deviations from it are quantitatively small in the strong-coupling limit. This observation should remain true in higher dimensions and for not too large attractive three-body interactions.

DOI: [10.1103/PhysRevA.88.063625](https://doi.org/10.1103/PhysRevA.88.063625)

PACS number(s): 67.85.Bc, 67.85.De, 64.70.Tg

I. INTRODUCTION

The revolutionary control over ultracold atoms in optical lattices made possible the direct experimental observation of many-body states of different quantum systems [1]. Tuning two-body interactions by using Feshbach resonances or changing the strength of the lattice confinement permitted the observation of a superfluid (SF) to Mott-insulating (MI) quantum phase transition for bosonic lattice atoms [2] for integer densities. More recently, the importance of multibody interactions has been inferred from experiment [3,4]. These interactions were so far deemed negligible higher-order many-body interactions.

The minimal model to describe bosonic lattice quantum gases is the Bose-Hubbard model. On a chain with L sites, the Hamiltonian operator with local two-body and three-body interactions is given by

$$\begin{aligned}
 H &= -t\hat{T} + U\hat{D} + W\hat{W}, \\
 \hat{T} &= \sum_{j=1}^{L-1} (\hat{b}_j^\dagger \hat{b}_{j+1} + \hat{b}_{j+1}^\dagger \hat{b}_j), \\
 \hat{D} &= \frac{1}{2} \sum_{j=1}^L \hat{n}_j(\hat{n}_j - 1), \\
 \hat{W} &= \frac{1}{6} \sum_{j=1}^L \hat{n}_j(\hat{n}_j - 1)(\hat{n}_j - 2),
 \end{aligned} \tag{1}$$

where \hat{b}_j^\dagger and \hat{b}_j are the creation and annihilation operators for bosons on site j , $\hat{n}_j = \hat{b}_j^\dagger \hat{b}_j$ is the boson number operator on site j , t is the tunnel amplitude between neighboring lattice sites, and $U > 0$ ($W > 0$) denote the strength of the on-site two-body (three-body) repulsion. There are $N = \rho L$ bosons in the system.

The Bose-Hubbard model in one dimension with pure two-body interactions has been extensively studied [5–8], using the density-matrix renormalization-group (DMRG) technique [9].

SF-to-MI quantum phase transition points can be determined accurately from the finite-size scaling of the Tomonaga-Luttinger liquid (TLL) parameter K_b ; the model is in the universality class of the spin-1/2 XY model so that there exists a Kosterlitz-Thouless transition in the thermodynamic limit, $L \rightarrow \infty$, where $K_b = 1/2$.

The model including the three-body local interaction remains largely unexplored. The first Mott lobe was recently studied using DMRG [10] and the cluster expansion approach [11]. The whole ground-state phase diagram for the first and second lobes was derived from exact diagonalization results for small system sizes $L \leq 8$ [12] and DMRG data for larger system sizes [13]. Very recently, Sowiński *et al.* [14] studied the full model with attractive two-body and repulsive three-body interactions using the DMRG.

In this work, we examine the static and dynamical ground-state properties of the Bose-Hubbard model with two-body and three-body interactions using large-scale DMRG calculations. To determine the phase boundaries between MI and SF phases we compute the chemical potential, the Tomonaga-Luttinger liquid (TLL) parameter, and the von Neumann entanglement entropy. Moreover, for $\rho = 2$, we calculate the single-particle gap and the dynamical structure factor $S(q, \omega)$ using the dynamical DMRG (DDMRG) procedure [15].

We find that the three-body interaction is qualitatively irrelevant in one dimension for strong coupling. Its quantitative corrections for $\rho = 2$ for the size of the Mott lobe, the gap, and the dynamical structure factor can be incorporated almost perfectly by rescaling $t/U \rightarrow t/(U+W)$ in the results for a bare two-body interaction ($W = 0$). Strong-coupling perturbation theory shows that this rescaling is not rigorous but quantitative corrections are very small for strong interactions.

II. GROUND-STATE PHASE DIAGRAM**A. Single-particle gap**

The Mott-insulating phases are characterized by a finite gap for single-particle excitations. The chemical potential $\mu(L, N)$

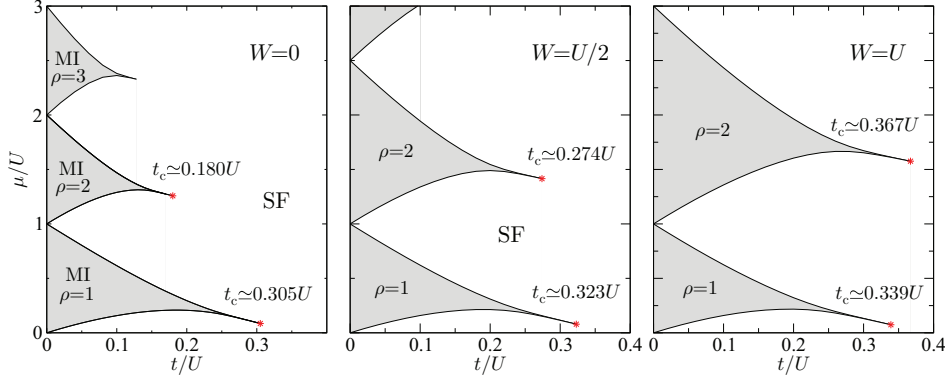


FIG. 1. (Color online) Ground-state phase diagram of the one-dimensional Bose-Hubbard model with three-body interactions for $W = 0$ (left panel), $W = U/2$ (middle panel), and $W = U$ (right panel), showing superfluid (SF) and Mott insulating (MI) regions as a function of the chemical potential μ/U and the electron transfer amplitude t/U . Results are based on DMRG data for lattices with up to $L = 128$ sites and open boundary conditions. The position of the Mott tips is obtained from the finite-size extrapolation of the Tomonaga-Luttinger parameter $K_b(L)$, Eq. (4).

gives the energy for adding the N th particle to the system with L sites in its ground state,

$$\mu(L, N) = E_0(L, N) - E_0(L, N - 1), \quad (2)$$

where $E_0(L, N)$ is the ground-state energy for N bosons on L sites. For $t = 0$, $[\mu(L, L + 1) = U, \mu(L, L) = 0]$ and $[\mu(L, 2L + 1) = 2U + W, \mu(L, 2L) = U]$ hold. The single-particle gap results from the difference between the chemical potentials for $N + 1$ and N particles,

$$\Delta(L, N) = \mu(L, N + 1) - \mu(L, N). \quad (3)$$

In the Mott insulating state, the gap remains finite in the thermodynamic limit, $\Delta(\rho) \equiv \Delta(L \rightarrow \infty, N \rightarrow \infty) > 0$ for fixed $\rho = N/L$. In the superfluid phase, the chemical potential is a continuous function of the density ρ . For $t = 0$, we have $\Delta(\rho = 1) = U$ and $\Delta(\rho = 2) = U + W$.

For integer fillings ρ and for large U/t , the Bose-Hubbard model is in its Mott insulating phase. Thus, the ground-state phase diagram in the plane $(t/U, \mu/U)$ shows superfluid and Mott-insulating regions; see Fig. 1. In the shaded regions, the particle density is constant and the gap for fixed t/U is given by the difference in the chemical potentials at the boundaries to the superfluid phases, i.e., the chemical potentials determine the phase boundaries. Unfortunately, the gaps become exponentially small close to the critical points t_c^ρ above which the Mott gap is zero. Since it is not possible to resolve such small gaps numerically, the critical points must be determined in a different manner; see Sec. II B. We obtained the ground-state phase diagram in Fig. 1 using the DMRG method with up to $L = 128$ sites and open boundary conditions (OBCs). We extrapolated the chemical potentials to the thermodynamical limit using a second-order polynomial fit in $1/L$ for $\mu(L, L + 1)$ and $\mu(L, L)$ [7,8].

In the absence of the three-body interaction (left panel), the Mott lobes become smaller with increasing density ρ , and, concomitantly, the values of the transition points t_c^ρ decrease with increasing ρ . When we switch on the three-body interaction (middle panel for $W = U/2$, right panel for $W = U$), the first Mott lobe is almost unchanged in comparison with

the result for $W = 0$, and the dependence of $t_c^{\rho=1}$ on W is rather weak, too. This is readily understood because at $t_c^{\rho=1} \simeq 0.3U$, there are few doubly occupied sites in the ground state and hardly any triply occupied sites: the Mott transition occurs at strong coupling where triple occupancies are strongly reduced for $\rho = 1$. The situation is different for $N = 2L$ particles because there are essentially double and triple occupancies present at the transition so that the three-body interaction is effective. Therefore, the size of the second Mott lobe and the value of $t_c^{\rho=2}$ substantially increase as a function of W , which also pushes up in energy the other Mott lobes.

B. Critical interactions

In order to determine the transition points, we compute the TLL parameter K_b in the superfluid phase. The Fourier transformation of the static structure factor, $S(q) = (1/L) \sum_{j,l} e^{iq(j-l)} (\langle \hat{n}_j \hat{n}_l \rangle - \langle \hat{n}_j \rangle \langle \hat{n}_l \rangle)$ at $q = 2\pi/L$, defines $K_b(L)$ [7,16],

$$\frac{1}{2\pi K_b(L)} = \frac{S(2\pi/L)}{2\pi/L}. \quad (4)$$

The TLL exponent is then obtained from the extrapolation of the DMRG data, $K_b = \lim_{L \rightarrow \infty} K_b(L)$. At the SF-MI transition point we expect that $K_b = 1/2$ [17], as in the case for the model (1) at $W = 0$ [5–7]. In this way, the transition points t_c^ρ can be determined accurately.

In the upper panels of Fig. 2 we demonstrate the finite-size scaling of the TLL parameter $K_b(L)$ for $\rho = 1$ (left panel) and $\rho = 2$ (right panel) at $U = W$, where we use the DMRG method with up to $L = 512$ sites and OBC. The transition points are determined from $\lim_{L \rightarrow \infty} K_b(L) = 0.5$ as $t_c^{\rho=1} = 0.339 \pm 0.001$ and $t_c^{\rho=2} = 0.367 \pm 0.001$. Our data improve the estimates from the exact diagonalization method [12] with up to $L = 8$ sites, $t_{c,ED}^{\rho=1}/U = 0.32$ and $t_{c,ED}^{\rho=2}/U = 0.38$.

In order to confirm the values of the critical points, we address the von Neumann entanglement entropy $S_L(\ell)$, defined as $S_L(\ell) = -\text{Tr}_\ell(\rho_\ell \ln \rho_\ell)$ with the reduced density matrix

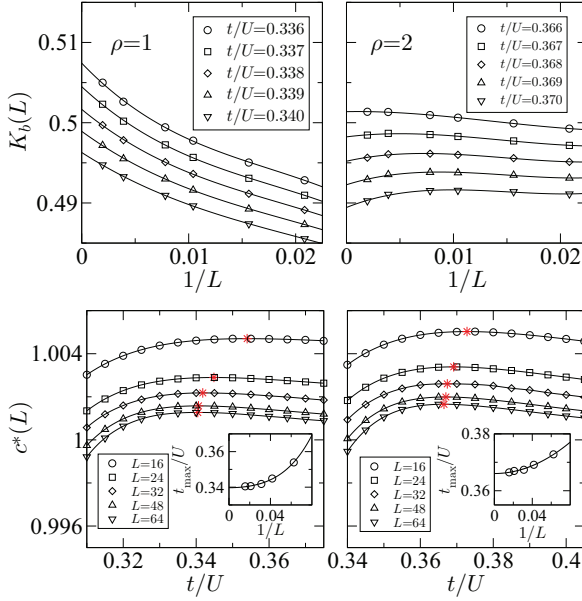


FIG. 2. (Color online) DMRG data for the Tomonaga-Luttinger liquid parameter $K_b(L)$ (upper panels) and the central charge $c^*(L)$ (lower panels) for the first (left panels) and second (right panels) Mott lobes in the model (1) for $W/U = 1$. The position of the maxima of $c^*(L)$ can be extrapolated systematically to the thermodynamic limit, as shown in the insets of the lower panels.

$\rho_\ell = \text{Tr}_{L-\ell}(\rho)$. For a system with central charge c , one finds for periodic boundary conditions (PBCs) [18]

$$S_L(\ell) = \frac{c}{3} \ln \left[\frac{L}{\pi} \sin \left(\frac{\pi \ell}{L} \right) \right] + s_1, \quad (5)$$

where s_1 is a nonuniversal constant and corrections are small, of the order $1/L$. The constant s_1 can be eliminated by subtracting $S_L(L/2)$ from $S_L(L/2 - 1)$ so that we can define the size-dependent central charge [19],

$$c^*(L) = \frac{3[S_L(L/2 - 1) - S_L(L/2)]}{\ln[\cos(\pi/L)]}. \quad (6)$$

Since the excitations of the interacting suprafluid in one dimension form a TLL with central charge $c = 1$, we can use $c^* = \lim_{L \rightarrow \infty} c^*(L)$ to locate the critical interactions.

In the lower panels of Fig. 2, we employ the DMRG method for up to $L = 64$ sites and PBCs. As in the case of the model (1) for $W/U = 0$ [8], $c^*(L)$ displays maxima as a function of the hopping amplitude t/U for fixed system size L . When we extrapolate the position of the maxima in $c^*(L)$ for $U = W$ to the thermodynamic limit, we obtain the transition points as $t_c^{\rho=1}/U = 0.340 \pm 0.002$ and $t_c^{\rho=2}/U \simeq 0.366 \pm 0.002$, in excellent agreement with our previous estimate from the TLL parameter K_b . In this way, we reliably determined the position of the tips in the Mott lobes of the ground-state phase diagram in Fig. 1.

III. SECOND MOTT LOBE

In the remainder of this work we focus on the second Mott lobe, $\rho = 2$ and $t < t_c^{\rho=2}$, where the three-body repulsion plays a significant role.

A. Gap function

For strong interactions, the gap can be calculated systematically in a power series in the particle hopping. For $N = 2L + 1$ particles, the first nontrivial order describes the free propagation of a triple occupancy so that its dispersion relation is given by $\omega^+(k) = E^+(k) - E_0(L, 2L) = W + 2U - 6t \cos(k)$. For $N = 2L - 1$ particles, the singly occupied site (a hole in the background of doubly occupied sites) has the dispersion relation $\omega^-(k) = E^-(k) - E_0(L, 2L) = -U + 4t \cos(k)$. Therefore, to leading order in t , the gap becomes $\Delta = \text{Max}_k[\omega^+(k) - \omega^-(k)]$ or

$$\frac{\Delta(t \ll U, W)}{U + W} = 1 - \frac{10t}{U + W} + \dots \quad (7)$$

To leading order, Δ is only a function of $t/(U + W)$. In the left panel of Fig. 3 we plot $\Delta/(U + W)$ as a function of $t/(U + W)$ for $t < t_c^{\rho=2}$. It is seen that the data for $W = 0, U/2, U$ essentially collapse onto a single curve, suggesting that the gap is solely a function of $U + W$. Likewise, when we plot the modified chemical potentials $\mu + W$ as a function of $t/(U + W)$ in the right panel of Fig. 3, we see that the second Mott lobes for $W = 0, U/2, U$ almost collapse onto each other. Deviations are visible only close to the transition points.

B. Dynamical structure factor

The dynamical structure factor $S(q, \omega)$ characterizes the density-density response of the Bose gas and is directly accessible by Bragg spectroscopy [20,21]. It is defined as

$$S(q, \omega) = \sum_n |(\langle \psi_n | \hat{n}(q) | \psi_0 \rangle)|^2 \delta(\omega - \omega_n), \quad (8)$$

where $\hat{n}(q) = \sum_l e^{iql} \hat{b}_l^\dagger \hat{b}_l$, $|\psi_0\rangle$ and $|\psi_n\rangle$ denote the ground state and n th excited state, respectively, and $\omega_n = E_n - E_0$ gives the corresponding excitation energy. As shown in

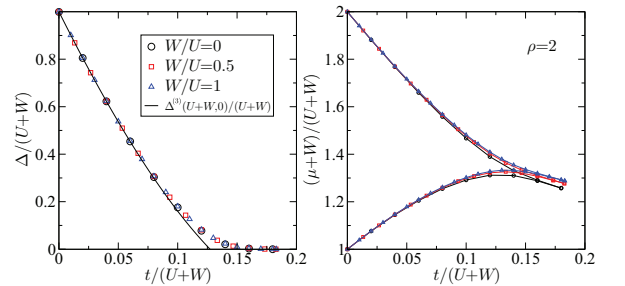


FIG. 3. (Color online) Rescaled single-particle gaps (left panel) and phase diagram (right panel) of the second Mott lobe ($\rho = 2$) in the model (1). The data for $W = 0, U/2, U$ collapse onto each other. Also shown is the third-order result for the gap $\Delta^{(3)}(U + W, 0)$ at $U = W$, Eq. (12).

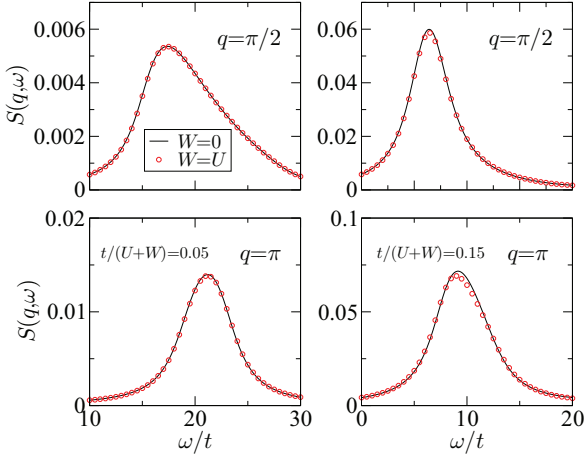


FIG. 4. (Color online) Dynamical structure factor $S_\eta(q, \omega)$ with Lorentz broadening $\eta = 2t$ at momenta $q = \pi/2$ (upper panels) and $q = \pi$ (lower panels) of the second Mott lobe in the model (1) for $t/(U+W) = 0.05$ (left panels) and $t/(U+W) = 0.15$ (right panels), as obtained from the dynamical DMRG technique for $L = 32$ sites.

Ref. [8,22], we can compute the Lorentz-broadened $S_\eta(q, \omega)$ with

$$S_\eta(q, \omega) = \int_{-\infty}^{\infty} d\omega' S(q, \omega') \frac{\eta}{\pi[(\omega - \omega')^2 + \eta^2]} \quad (9)$$

for Bose-Hubbard models using the DDMRG technique. In this work, we use $\eta = 2t$ for $L = 32$ sites with PBCs to obtain smooth curves. Note that the unbroadened dynamical quantities corresponding to the experimental measurements can be extracted from the deconvolution of the DDMRG data as demonstrated in Ref. [23].

In Fig. 4 we show $S_\eta(q, \omega)$ for $q = \pi/2$ (upper panels) and $q = \pi$ (lower panels) for $t/(U+W) = 0.05$ (left panels) and $t/(U+W) = 0.15$ (right panels) as a function of ω/t . The results for $W = U$ lie essentially on top of those for $W = 0$, apart from small deviations around $\omega = 0$ for $t/(U+W) = 0.15$ and $q = \pi$, suggesting again a scaling relation.

C. Strong-coupling perturbation theory

The strong-coupling analysis of Harris and Lange as used in [8] starts from the unperturbed Hamiltonian $\hat{H}_0 = U\hat{D}$ where \hat{D} counts the number n_D of pair interactions. The perturbation expansion for $t/U \rightarrow 0$ relies on the fact that the subspaces with $n_D = 0, 1, 2, \dots$ are well separated. In the presence of the triple interaction \hat{W} , we assume energetically separated subspaces for $\hat{H}_0 = U\hat{D} + W\hat{W}$ that have the unperturbed energies $E_0(n_D, n_W) = Un_D + Wn_W$ with two integer quantum numbers ($n_D \geq 0, n_W \geq 0$). A transfer process between neighbors with positive integer occupancies ($n_1 = \rho + m, n_2 = \rho + n$) to ($n_1 = \rho + m - 1, n_2 = \rho + n + 1$) results in an energy transfer

$$\Delta E(m, n) = (n - m + 1)[U + W(\rho - 1) + W(n + m)/2]. \quad (10)$$

For $\rho = 2$, the resulting finite-energy denominators in a perturbation expansion thus include the energies $U + W + W(n + m)/2$. Therefore, there cannot be a rigorous scaling relation, i.e., the physical quantities are not solely a function of $t/(U + W)$.

However, the lowest-order terms involve small deviations from $\rho = 2$, i.e., only $(m = 0, n = 0)$ and $(m = \pm 1, n = \mp 1)$ appear. Thus, only the energy denominator $U + W$ occurs in low-order perturbation theory in \hat{T} . Moreover, in higher orders, those terms that involve $t/(U + W)$ have a higher weight than those that are proportional to $t/(2U + W)$ or else. For these practical reasons, the results for the gap and the dynamical structure factor show fairly small deviations from a scaling behavior, apart from the region close to the MI-to-SF transition.

1. Gap

To be definite, we address the series expansion of the gap to third order. To this end, we repeat the perturbative expansion [8,24] whereby we effectively replace the energy denominators $U(n_{D,1} - n_{D,2})$ of states with $n_{D,1}$ and $n_{D,2}$ double occupancies by the appropriate energy differences $U(n_{D,1} - n_{D,2}) + W(n_{W,1} - n_{W,2})$. For $\rho = 2$ this leads to

$$\begin{aligned} \frac{\Delta^{(3)}(U, W)}{U + W} &= 1 - \frac{10t}{U + W} + \frac{2t^2(26U^2 + 57UW + 19W^2)}{(U + W)^2(2U + W)(2U + 3W)} \\ &\quad + \frac{12t^3}{(U + W)^3(2U + W)^2(2U + 3W)^2} \\ &\quad \times [40U^4 + 160U^3W + 230U^2W^2 \\ &\quad + 134UW^3 + 29W^4]. \end{aligned} \quad (11)$$

It is seen that deviations from the scaling of $\Delta/(U + W)$ with $t/(U + W)$ first occur in second order. In order to assess the quantitative effect, we use the result for $W = 0$ and define

$$\begin{aligned} \frac{\Delta^{(3,sc)}(U, W)}{U + W} &= \frac{\Delta^{(3)}(U + W, 0)}{U + W} \\ &= 1 - \frac{10t}{U + W} + \frac{13t^2}{(U + W)^2} + \frac{30t^3}{(U + W)^3}. \end{aligned} \quad (12)$$

Then, at $U = W$ we consider

$$\begin{aligned} \delta^{(3)}(U) &= \frac{|\Delta^{(3)}(U, U) - \Delta^{(3,sc)}(U, U)|}{\Delta^{(3)}(U, U)} \\ &= \frac{t^2(61t + 45U)}{2(593t^3 + 510t^2U - 750tU^2 + 150U^3)}. \end{aligned} \quad (13)$$

where, e.g., $\delta^{(3)}(t/0.15) = 0.012$. At $U = W$ we find that the relative deviation of the scaling curve for $t/U < 0.15$ is about 1% or less, a negligibly small correction. This explains the almost perfect scaling seen in Fig. 3.

2. Dynamical structure factor

As has been shown in Refs. [8,24], the dynamical structure factor in the region of the primary Hubbard band can be obtained from the solution of an effective single-particle problem on a ring that describes the propagation of a

“hole” (single occupancy for $\rho = 2$) and a “particle” (triple occupancy for $\rho = 2$) that move with total momentum q . The resulting effective single-particle problem is governed by a kinetic term and a potential whose range is proportional to the order of the expansion.

In the calculation of the structure factor, we need the eigenstates $|q; k\rangle$ of \bar{k}_0 that describes the free propagation of particles and holes,

$$\begin{aligned}\bar{k}_0|q; k\rangle &= (\beta_q e^{-ik} + \beta_q^* e^{ik})|q; k\rangle, \\ \beta_q &= -t[\rho + (\rho + 1)e^{iq}].\end{aligned}\quad (14)$$

The states $|q\rangle$ that enter the calculation of the structure factor are weighted linear combinations of the states $|q; k\rangle$. Up to second order, these weights are solely a function of $t/(U + W)$ and do not play a role for our discussion.

By definition, the states $|q; k\rangle$ are eigenstates of the kinetic contribution to all orders,

$$\begin{aligned}\bar{k}_1|q; k\rangle &= (\alpha + \gamma_q e^{-i2k} + \gamma_q^* e^{i2k})|q; k\rangle, \\ \gamma_q &= -t \frac{t\rho(\rho + 1)}{U + (\rho - 1)W} (1 + e^{i2q}), \\ \alpha &= t \frac{8t\rho(\rho + 1)}{U + (\rho - 1)W} - t \frac{2t(\rho^2 - 1)}{2U + (2\rho - 3)W} \\ &\quad - t \frac{2t\rho(\rho + 2)}{2U + (2\rho - 1)W}.\end{aligned}\quad (15)$$

For $\rho = 2$, α is not a function of $t/(U + W)$ alone but also involves terms of different analytical structure.

The same observation holds for the interaction potential. Apart from the hard-core correction that appears when we close the chain into a ring [8,24], the interaction potential contains terms between nearest neighbors and next-nearest neighbors of the form

$$\frac{V_{1,1}(q)}{t} = \frac{2t\rho(\rho + 1) \cos(q) + 2t(2\rho + 1)^2/3}{U + (\rho - 1)W}, \quad (16)$$

and

$$\begin{aligned}\frac{V_{L-1,1}(q)}{t} &= \frac{t\rho(\rho + 1)}{U + (\rho - 1)W} - \frac{t\rho(\rho + 2)}{2U + (2\rho - 1)W} \\ &\quad + \frac{t\rho(\rho + 1)e^{-iq}}{U + (\rho - 1)W} + \frac{t\rho(\rho + 1)e^{-i2q}}{U + (\rho - 1)W} \\ &\quad - \frac{t(\rho - 1)^2 e^{-i2q}}{2U + (2\rho - 3)W}.\end{aligned}\quad (17)$$

The contributions for next-nearest neighbors involve intermediate states with excitation energies that are different from $U + W$ or its multiples for $\rho = 2$. In Fig. 5 we show the resulting structure factor to second order $S^{(2)}(q, \omega)$ at $q = \pi$ as a function of ω for $U = W$, $t/U = 0.15$, and $\rho = 2$, where we give the full result to second order. For comparison we also show $S^{(2,sc)}(q, \omega)$ where we replace U by $U + W$ in the results for $W = 0$. The quantitative differences are very small so that the scaling $U \rightarrow U + W$ is almost fulfilled, as seen in the DDMRG data. Note that the result of $S(q, \omega)$ in Fig. 5 looks quantitatively different from the DDMRG data in the right lower panel of Fig. 4. This is due to the finite broadening width η in the DDMRG calculation and the limited validity of the second-order strong-coupling approach for intermediate coupling strengths.

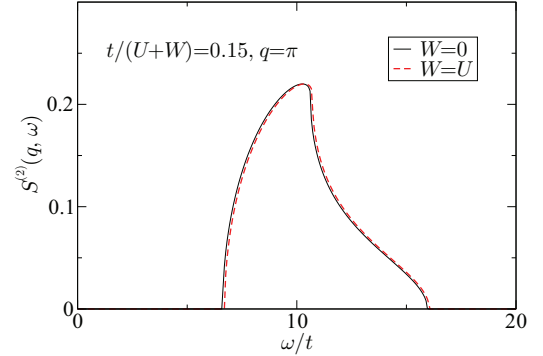


FIG. 5. (Color online) Dynamical structure factor in second-order strong-coupling perturbation theory, $S^{(2)}(q = \pi, \omega)$, for $U = W$ and $t/(U + W) = 0.15$ (full line), in comparison with the scaling result $S^{(2,sc)}(q = \pi, \omega)$ (dashed line). The differences are very small.

IV. CONCLUSIONS

In this work we used the numerically exact density-matrix renormalization-group technique to investigate the one-dimensional Bose-Hubbard model with a two-body interaction $U\hat{D}$ and a three-body interaction $W\hat{W}$. We determined the ground-state phase diagram with and without three-body repulsion for the first and second Mott lobes from the chemical potentials. The calculation of the Tomonaga-Luttinger parameter K_b close to the Kosterlitz-Thouless transitions provided accurate estimates for the tips of the Mott lobes where the gaps become exponentially small. We confirmed the results for $t_c^{\rho=1,2}$ using the von Neumann entanglement entropy. We find that $t_c^{\rho=1}(W)$ increases from $t_c^{\rho=1}(0)$ by less than 10% for $W \leq U$. Moreover, $t_c^{\rho=2}(W)$ obeys the relation $t_c^{\rho=2}(W) \approx t_c^{\rho=2}(0)(1 + W/U)$ with an accuracy of a few percent for $W \leq U$.

For the second Mott lobe, $\rho = 2$, our numerical data for the gap Δ and the Lorentz-broadened dynamical structure factor $S_\eta(q, \omega)$ showed a similarly good “scaling behavior”: the curves for different values of $W = 0, U/2, U$ almost fall on top of each other when plotted as a function of $t/(U + W)$. Our results from strong-coupling perturbation theory show that the scaling is not rigorous. However, deviations are quantitatively small because, in the Mott insulating region, interactions are strong so that the physical quantities are largely determined by particle-hole excitations with one triple occupancy and one single occupancy in the background of doubly occupied sites.

Since our observations rely on the strong-coupling picture alone, they should also hold in higher dimensions. The Bose-Hubbard model with pure two-body interactions remains qualitatively correct even in the presence of sizable local three-particle interactions. Of course, this conclusion becomes invalid for substantial attractive three-body interactions that will lead to the formation of local clusters.

ACKNOWLEDGMENTS

S.E. and H.F. gratefully acknowledge financial support by the Deutsche Forschungsgemeinschaft through SFB 652.

EJIMA, LANGE, FEHSKE, GEBHARD, AND ZU MÜNSTER

PHYSICAL REVIEW A **88**, 063625 (2013)

- [1] I. Bloch, J. Dalibard, and W. Zwerger, *Rev. Mod. Phys.* **80**, 885 (2008).
- [2] M. Greiner, O. Mandel, T. Esslinger, T. W. Hänsch, and I. Bloch, *Nature (London)* **415**, 39 (2002).
- [3] S. Will, T. Best, U. Schneider, L. Hackermüller, D.-S. Lühmann, and I. Bloch, *Nature (London)* **465**, 197 (2010).
- [4] M. J. Mark, E. Haller, K. Lauber, J. G. Danzl, A. J. Daley, and H.-C. Nägerl, *Phys. Rev. Lett.* **107**, 175301 (2011).
- [5] T. D. Kühner and H. Monien, *Phys. Rev. B* **58**, R14741 (1998).
- [6] T. D. Kühner, S. R. White, and H. Monien, *Phys. Rev. B* **61**, 12474 (2000).
- [7] S. Ejima, H. Fehske, and F. Gebhard, *Europhys. Lett.* **93**, 30002 (2011).
- [8] S. Ejima, H. Fehske, F. Gebhard, K. zu Münster, M. Knap, E. Arrigoni, and W. von der Linden, *Phys. Rev. A* **85**, 053644 (2012).
- [9] S. R. White, *Phys. Rev. Lett.* **69**, 2863 (1992).
- [10] J. Silva-Valencia and A. M. C. Souza, *Phys. Rev. A* **84**, 065601 (2011).
- [11] V. Varma and H. Monien, arXiv:1211.5664.
- [12] T. Sowiński, *Phys. Rev. A* **85**, 065601 (2012).
- [13] M. Singh, A. Dhar, T. Mishra, R. V. Pai, and B. P. Das, *Phys. Rev. A* **85**, 051604 (2012).
- [14] T. Sowiński, R. W. Chhajlany, O. Dutta, L. Tagliacozzo, and M. Lewenstein, arXiv:1304.4835.
- [15] E. Jeckelmann, *Phys. Rev. B* **66**, 045114 (2002).
- [16] S. Ejima, F. Gebhard, and S. Nishimoto, *Europhys. Lett.* **70**, 492 (2005).
- [17] T. Giamarchi, *Quantum Physics in One Dimension* (Clarendon, Oxford, 2003).
- [18] P. Calabrese and J. Cardy, *J. Stat. Mech.: Theory and Exp.* (2004) P06002.
- [19] S. Nishimoto, *Phys. Rev. B* **84**, 195108 (2011).
- [20] J. Stenger, S. Inouye, A. P. Chikkatur, D. M. Stamper-Kurn, D. E. Pritchard, and W. Ketterle, *Phys. Rev. Lett.* **82**, 4569 (1999).
- [21] P. T. Ernst, S. Götze, J. S. Krauser, K. Pyka, D.-S. Lühmann, D. Pfannkuche, and K. Sengstock, *Nat. Phys.* **6**, 56 (2009).
- [22] S. Ejima, H. Fehske, and F. Gebhard, *J. Phys. Conf. Ser.* **391**, 012031 (2012).
- [23] S. Nishimoto, F. Gebhard, and E. Jeckelmann, *J. Phys.: Condens. Matter* **16**, 7063 (2004).
- [24] K. zu Münster, M.Sc. thesis, University of Marburg, 2012.

Spectral and Entanglement Properties of the Bosonic Haldane Insulator

Satoshi Ejima, Florian Lange, and Holger Fehske

Institut für Physik, Ernst-Moritz-Arndt-Universität Greifswald, 17489 Greifswald, Germany

(Received 26 March 2014; published 8 July 2014)

We discuss the existence of a nontrivial topological phase in one-dimensional interacting systems described by the extended Bose-Hubbard model with a mean filling of one boson per site. Performing large-scale density-matrix renormalization group calculations we show that the presence of nearest-neighbor repulsion enriches the ground-state phase diagram of the paradigmatic Bose-Hubbard model by stabilizing a novel gapped insulating state, the so-called Haldane insulator, which, embedded into superfluid, Mott insulator, and density wave phases, is protected by the lattice inversion symmetry. The quantum phase transitions between the different insulating phases were determined from the central charge via the von Neumann entropy. The Haldane phase reveals a characteristic fourfold degeneracy of the entanglement spectrum. We finally demonstrate that the intensity maximum of the dynamical charge structure factor, accessible by Bragg spectroscopy, features the gapped dispersion known from the spin-1 Heisenberg chain.

DOI: 10.1103/PhysRevLett.113.020401

PACS numbers: 05.30.Jp, 03.67.-a, 64.70.Tg, 75.10.Pq

A quarter-century after Haldane's conjecture of an appearance of finite gap in the integer-spin chain [1], the so-called Haldane phase protected by the lattice inversion symmetry attracts renewed attention from a topological point of view. Such a topological protected state, characterized by symmetries and a finite bulk gap, is termed now as a symmetry-protected topological (SPT) ordered phase [2,3]. In higher dimensions, the so-called Kane-Mele topological band insulator of noninteracting fermions [4,5] exhibits a SPT state protected by $U(1)$ and time-reversal symmetries. Since particles in real materials normally interact, it is not sufficient to study SPT order for non-interacting systems. To analyze SPT states in interacting systems two main approaches have been proposed. The first is based on the definition of appropriate topological invariants within a Green function scheme [6]. It has been successfully applied to the one-dimensional Peierls-Hubbard model [7,8]. The second uses the entanglement spectrum as a fingerprint of topological order [9]. Here the lowest entanglement level reflects the degree of degeneracy corresponding to symmetries and the edge states of the system. This has been worked out for various spin chains [3,10,11].

Interestingly a hidden SPT phase was also found in interacting boson systems with long-range repulsion [12]. This phase resembles the Haldane gapped phase of the quantum spin-1 Heisenberg chain. Indeed, assuming that the site occupation of an one-dimensional extended Bose-Hubbard model (EBHM) with nearest-neighbor interaction is restricted to $n_j = 0, 1$ or 2 , the system can be described by an effective spin-1 model with $S_j^z = n_j - \rho$ for a mean boson filling factor $\rho = 1$. The Haldane insulator (HI) then appears between the conventional Mott insulator (MI) and the density wave (DW) phases at intermediate couplings

[12,13]. Field theory predicts the MI-HI transition to be in the Luttinger liquid universality class with central charge $c = 1$, whereas the HI-DW transition belongs to the Ising universality class with $c = 1/2$ [13]. Very recent quantum Monte Carlo simulations [14] reveal in addition a super-solid phase competing with the HI.

In this work, we focus on the characterization of the EBHM's ground-state and spectral properties from an entanglement point of view. Using the (dynamical) density-matrix renormalization group (DMRG) technique [15,16], we show that the lowest entanglement level in the nontrivial topological HI phase is fourfold degenerate. The universality classes of the MI-HI and HI-DW transitions are determined from the central charge in accordance with what is obtained from field theory. Most notably we demonstrate that the dynamical charge structure factor can be used to unambiguously discriminate the HI from the MI and DW phases.

The Hamiltonian of the EBHM is defined as

$$\hat{\mathcal{H}} = -t \sum_j (\hat{b}_j^\dagger \hat{b}_{j+1} + \hat{b}_j \hat{b}_{j+1}^\dagger) + U \sum_j \hat{n}_j (\hat{n}_j - 1)/2 + V \sum_j \hat{n}_j \hat{n}_{j+1}, \quad (1)$$

where \hat{b}_j^\dagger , \hat{b}_j , and $\hat{n}_j = \hat{b}_j^\dagger \hat{b}_j$ are, respectively, the boson creation, annihilation, and number operators at the lattice site j . The nearest-neighbor boson transfer amplitude is given by t ; U and V parametrize the Coulomb repulsions between bosons resting at the same and neighboring sites. While t causes the bosons to delocalize, promoting a superfluid (SF) phase at weak interactions, U (V) tends to stabilize a MI (DW) when the interaction dominates over the kinetic energy scale set by t .

In the framework of the DMRG the entanglement properties of the EBHM can be analyzed as follows. Consider the reduced density matrix $\rho_\ell = \text{Tr}_{L-\ell}[\rho]$ of a block of length ℓ out of a periodic system of size L . Then the bipartite entanglement spectrum $\{\xi_\alpha\}$ is defined as those of a fictitious Hamiltonian $\tilde{\mathcal{H}}$ defined via $\rho_\ell = e^{-\tilde{\mathcal{H}}}$. As a consequence the ξ_α can be extracted from the weights λ_α of the reduced density matrix ρ_ℓ by $\xi_\alpha = -2 \ln \lambda_\alpha$. Adding up, along the calculations, the λ_α , we have direct access to the von Neumann entropy, $S_L(\ell) = -\text{Tr}_\ell[\rho_\ell \ln \rho_\ell]$. On the other hand, from conformal field theory [17] one has $S_L(\ell) = (c/3) \ln[(L/\pi) \sin(\pi\ell/L)] + s_1$ with the nonuniversal constant s_1 . Thus we can easily determine the central charge c by DMRG. Since the most precise data for $S_L(\ell)$ were obtained when the length ℓ of the sub-block equals half the system size L , the central charge should be determined from the relation [18]

$$c^*(L) = \frac{3[S_L(L/2 - 1) - S_L(L/2)]}{\ln[\cos(\pi/L)]}, \quad (2)$$

rather than directly using the above expression for $S_L(\ell)$.

In contrast to hitherto existing open boundary DMRG studies of the EBHM [12,13,19] we use periodic boundary conditions (PBCs). As shown for the regular Bose-Hubbard model this is advantageous calculating the central charge [20,21]. Beyond that we benefit from the fact that no artificial on-site potentials at the edges will affect our results. To reach the same system sizes as with open boundary conditions (OBCs), we limit the number of bosons per site. Throughout this work we use $n_b = 2$; here the EBHM corresponds to an effective spin-1 Heisenberg model. We have convinced ourselves that at sufficiently large U the boson truncation does not alter qualitatively the results presented in the following (solely, in the weak coupling regime, the extension of the SF phase is somewhat underestimated). Let us finally note that we keep up to $m = 2400$ states in the DMRG runs, so that the discarded weight is typically smaller than 1×10^{-8} . For the dynamical DMRG calculations we take $m = 800$ states to compute the ground state during the first five DMRG sweeps, and afterwards use 400 states evaluating the dynamical properties.

As stated above the ground-state phase diagram of the EBHM (1) with $n_b = 2$ exhibits three differing insulator phases, as well as a superfluid state at weak interactions $U/t, V/t$. The stability regions of the various phases are pinpointed by Fig. 1. Let us emphasize that in the intermediate-coupling region ($3 \lesssim U \lesssim 8$), the central charge is best suited for detecting the MI-HI (HI-DW) quantum phase transition since the system becomes critical at the transition points with $c = 1$ ($1/2$).

Figure 2(a) illustrates the behavior of the central charge c^* obtained numerically as a function of V/t at fixed $U/t = 5$. With increasing system size L two sharp peaks

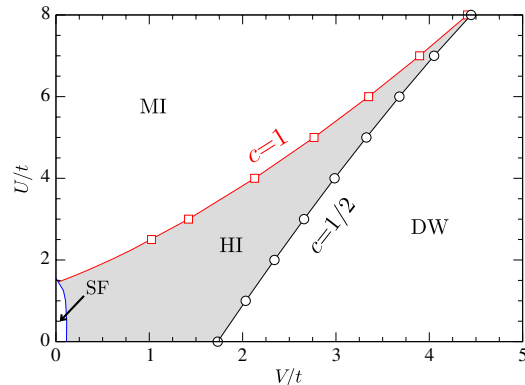


FIG. 1 (color online). DMRG phase diagram of the one-dimensional constrained extended Bose-Hubbard model with $n_b = 2$ and $\rho = 1$. Shown are the Mott insulator (MI), Haldane insulator (HI), density wave (DW), and superfluid (SF) phases. The MI-HI (squares) and HI-DW (circles) transition points are determined via the central charge $c = 1$ and $c = 1/2$, respectively, which can be extracted from the von Neumann entropy [cf. Fig. 2(b)]. MI-HI transition points are confirmed by a finite-size scaling of the two lowest energy levels with APBCs. Relaxing the boson constraint the SF region extends.

develop, indicating the MI-HI and HI-DW transition points. For $L = 128$, we found $c^* \approx 0.999$ in the former case and $c^* \approx 0.494$ in the latter case; i.e., the numerical error, $|c^*(L) - c|/c$, is about 1% if compared with the field theoretical predictions. Since the positions of the peaks only weakly depend on the system size, the transition points can be determined by extrapolating the values of the critical $V(L)$ to the thermodynamic limit $L \rightarrow \infty$. MI-HI transition points are also extracted from the level spectroscopy of two lowest-lying energies with antiperiodic boundary conditions (APBCs), $\hat{b}_{L+1}^{(\dagger)} \rightarrow -\hat{b}_1^{(\dagger)}$. This equates to the twisted boundary methods [22] with the spin operators $\hat{S}_{L+1}^x \rightarrow -\hat{S}_1^x$ and $\hat{S}_{L+1}^y \rightarrow -\hat{S}_1^y$ applied to the spin-1 XXZ chain [23], see also Ref. [24]. The obtained transition points can be linearly extrapolated to the thermodynamic limit as in the inset of Fig. 2(a), showing a perfect agreement with the critical points obtained in the main panel.

The excitation gaps behave differently in various insulating phases [12,13]: While the single-particle gap $\Delta_c = E_0(N+1) + E_0(N-1) - 2E_0(N)$ is finite in all three insulator phases, except for the MI-HI transition point, the neutral gap $\Delta_n = E_1(N) - E_0(N)$ closes both at the MI-HI and HI-DW transitions [$E_0(N)$ and $E_1(N)$ denote the energies of the ground state and first excited state of the N -particle system, respectively]. This is corroborated by Fig. 2(b). A similar behavior of the neutral gap has been observed for the SPT phases of spin-1/2 ladder systems [25]. Note that the phase boundaries obtained by our PBC DMRG calculation at intermediate and strong couplings

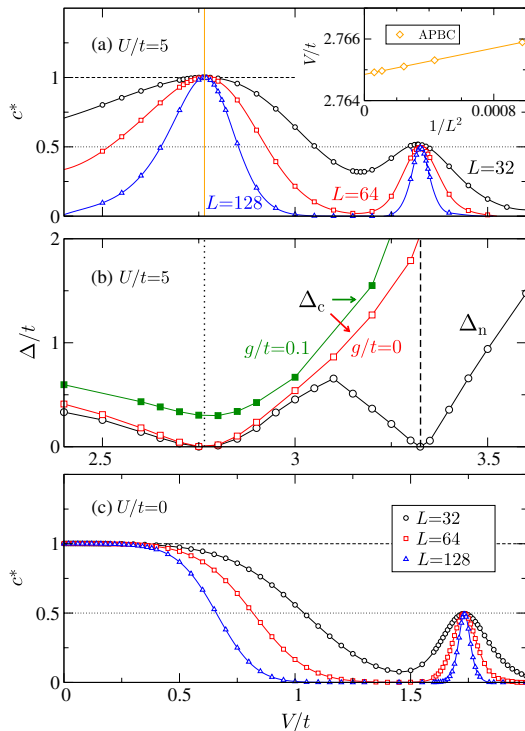


FIG. 2 (color online). Panel (a): Central charge c^* of the EBHM with $U/t = 5$, indicating the MI-HI (HI-DW) transition point with $c = 1$ ($c = 1/2$). The inset shows a finite-size scaling of the MI-HI transition points from the energy difference with APBCs. Panel (b): Extrapolated data for the charge gap Δ_c (open squares) and neutral gap Δ_n (open circles) at $U = 5t$. Vertical lines mark the transition points estimated from c^* . While Δ_n vanishes at both MI-HI and HI-DW boundaries, the charge gap Δ_c closes at the MI-HI transition only. Turning on an inversion-symmetry breaking perturbation [$g/t = 0.1$, see Eq. (3)] Δ_c stays finite $\forall V/t$ (filled squares). Panel (c): c^* at $U = 0$. Now the SF/MI-HI transition point is hardly to detect.

basically agree with very recent DMRG data for OBCs [19,26]. In the weak-coupling regime, on the other hand, our phase diagram differs from former studies due to the $n_b = 2$ restraint. Accordingly the MI-SF transition at $V = 0$ occurs at a smaller value, $U \approx 1.555t$, if compared to the critical U/t derived from the Tomonaga-Luttinger liquid parameter [27]. The appearance of the SF phase, which can be understood as a Luttinger liquid with $c = 1$ [28], together with strong finite-size effects prevents using c^* for detecting the MI-HI transition in this regime. Otherwise, as shown by Fig. 2(c), the HI-DW Ising transition can still be determined from c^* , even for $U = 0$.

On these grounds, discussing the entanglement properties of the SPT state, we consider the intermediate-coupling region hereafter. Calculating the entanglement spectrum ξ_α we divide the system in halves. Then, using DMRG with

PBCs, one of the block with $L/2$ sites possesses two edges (rather than a single edge in the semi-infinite chain used by the infinite-time evolving block-decimation algorithm [3]). In the HI phase the entanglement spectrum is expected to be at least fourfold degenerate, reflecting the broken $\mathbb{Z}_2 \times \mathbb{Z}_2$ symmetry. Figure 3 shows the DMRG data for ξ_α obtained at $U/t = 5$. While for $L = 128$ the fourfold degeneracy can be seen only deep inside of the HI phase, for $L = 512$ almost all HI states exhibit this degeneracy. By contrast, in the trivial MI and DW phases the lowest entanglement level is always nondegenerate. Obviously higher entanglement levels $\xi_\alpha > 8$ are also fourfold degenerate (cf. Fig. S2 of Ref. [24]).

We already stated that the HI phase is protected by the inversion symmetry of the lattice. This symmetry can explicitly be broken by adding to the Hamiltonian (1) an appropriate perturbation [13],

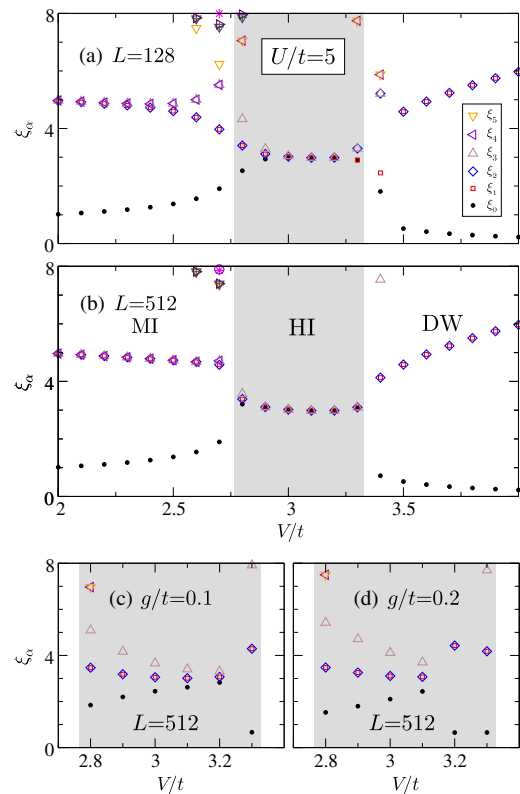


FIG. 3 (color online). Entanglement spectrum ξ_α of the EBHM with $U/t = 5$. If exciting the degeneracy of the entanglement levels becomes more perfect as the system size increases (cf. data for $L = 128$ [panel (a)] with those for 512 [panel (b)]). A perturbation (3) breaking the lattice inversion symmetry lifts the degeneracy in the HI phase. This is demonstrated by panels (c) and (d) giving ξ_α for PBCs in the primary HI regime for $g/t = 0.1$ and 0.2 , respectively.

$$\delta\hat{\mathcal{H}} = g \sum_j [(\hat{n}_j - \rho)\hat{b}_j^\dagger \hat{b}_{j+1} + \text{H.c.}]. \quad (3)$$

As a consequence the MI-HI quantum phase transition disappears [13] and the single-particle charge gap stays finite; see the filled squares in Fig. 2(b) displaying Δ_c for $g/t = 0.1$. One also expects that this perturbation lifts the degeneracy of the lowest entanglement level in the HI phase. Indeed Fig. 3(c) illustrates that any finite g dissolves the fourfold degeneracy in the HI phase, where the gap between the lowest levels increases raising g [cf. Fig. 3(d)]. That is, the entanglement spectrum substantiates the suspicion that the lattice inversion symmetry is necessary for the nontrivial topological HI state to exist.

Since the EBHM (1) can be realized by ultracold bosonic atoms loaded in optical lattices [29] it is highly desirable to study dynamical correlation functions which are accessible by experiments. For this purpose, the kinetic-energy correlations of the effective spin-1 Heisenberg chain was proposed to be a candidate detecting the HI phase and calculated on a mean-field level of approximation [12]. Here we suggest the dynamical structure factor—which can be directly measured by momentum-resolved Bragg spectroscopy [30,31]—to be indicative of a SPT state. This quantity is defined as

$$S(k, \omega) = \sum_n |\langle \psi_n | \hat{n}_k | \psi_0 \rangle|^2 \delta(\omega - \omega_n), \quad (4)$$

where $|\psi_0\rangle$ and $|\psi_n\rangle$ denote the ground state and n th excited state, respectively. The corresponding excitation energy is $\omega_n = E_n - E_0$. In the absence of the nearest-neighbor repulsion V , $S(k, \omega)$ was intensively studied by means of perturbative and dynamical DMRG techniques [20,32]. Taking V into account, in the MI, a gap opens at $k = 0$ and the spectral weight becomes concentrated in the region $k > \pi/2$, around $\omega/U \approx 1$, just as for the standard

Bose-Hubbard model. This is exemplified for $U = 5t$ and $V = t$ by Fig. 4(a). The maximum in $S(k, \omega)$ follows a cosine-dispersion which is flattened, however, near the Brillouin zone boundary for $k \geq 3\pi/4$. The situation dramatically changes when we enter the HI phase by increasing V/t , cf. Fig. 4(b) for $V/t = 3$. Now the dispersion of the maximum in $S(k, \omega)$ bends back above $k = \pi/2$, acquiring a sinus shape with (small) excitation gaps at both $k = 0$ and $k = \pi$. Also the spectral weight of the dynamical charge structure factor is concentrated at $k = \pi$ and finite but very small for $\omega \ll U$. We note that the dispersion of the maximum in the HI phase is reminiscent of those of the spin-1 Heisenberg chain. A dispersive signal persists if we allow larger n_b (see the results presented in Ref. [24] for the EBHM with $n_b = 5$). In the DW phase, the maximum of $S(k, \omega)$ is almost dispersionsless and located at $\omega \gtrsim 1.5U$ for $U/t = V/t = 5$ [see Fig. 4(c)]. The intensity is notably more confined than for the MI. Figure 4 demonstrates that the dispersion in the insulating phases barely changes if the system size is increased. In every sense, $S(k, \omega)$ behaves very differently in the MI, DW, and HI states and might therefore be used to discriminate these insulating phases.

In summary, we studied—from an entanglement point of view—the topologically nontrivial Haldane insulator, appearing in the intermediate coupling regime of the one-dimensional Bose-Hubbard model with on-site and nearest-neighbor Coulomb interactions in the midst of Mott insulator, density-wave, and superfluid phases. Using the DMRG technique, the MI-HI (HI-DW) quantum phase transition is determined with high precision from the central charge c^* that can be extracted from the von Neumann entropy. We thereby approved the universality class $c = 1$ ($c = 1/2$) predicted by field theory. We furthermore established a characteristic fourfold degeneracy of the lowest entanglement level in the SPT Haldane phase and demonstrated that any violation of the lattice

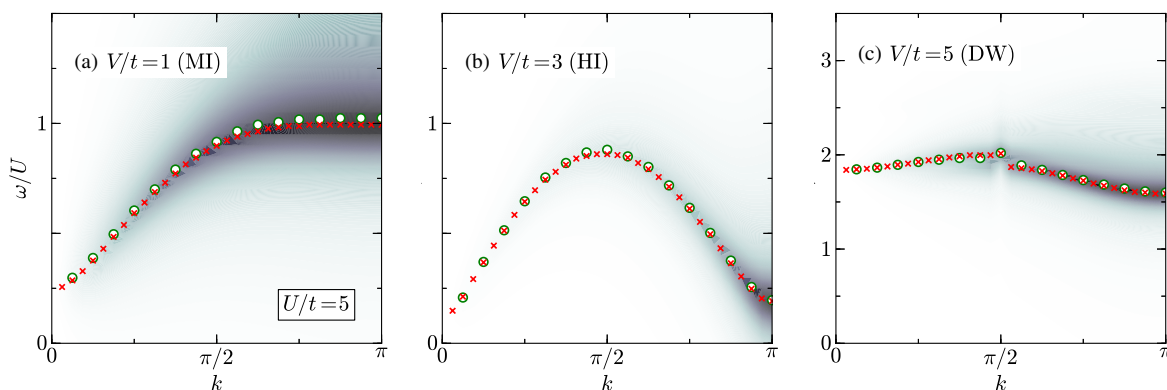


FIG. 4 (color online). Intensity plots of the dynamical structure factor $S(k, \omega)$ in the MI (a), HI (b), and DW (c) phases. Data were obtained by the dynamical DMRG technique for $L = 64$ using a broadening $\eta = 0.5t$. Crosses (circles) give the maximum value of $S(k, \omega)$ for $L = 64$ ($L = 32$ and $\eta = t$) at fixed momenta $k = 2\pi j/L$ with $j = 1, \dots, L/2$.

inversion symmetry lifts this degeneracy. With the objective to stimulate further experiments on ultracold bosonic atoms in optical lattices we analyzed the dynamical charge structure factor for the extended Bose-Hubbard model and showed that this quantity can be used to distinguish the Haldane insulator, exhibiting a gapped excitation spectrum similar to the spin-1 Heisenberg-chain model, from conventional Mott and density-wave states.

The authors would like to thank S. Nishimoto and T. Yoshida for valuable discussions. This work was supported by Deutsche Forschungsgemeinschaft through SFB 652, Project B5.

-
- [1] F. D. M. Haldane, *Phys. Rev. Lett.* **50**, 1153 (1983).
 [2] Z.-C. Gu and X.-G. Wen, *Phys. Rev. B* **80**, 155131 (2009).
 [3] F. Pollmann, E. Berg, A. M. Turner, and M. Oshikawa, *Phys. Rev. B* **85**, 075125 (2012).
 [4] C. L. Kane and E. J. Mele, *Phys. Rev. Lett.* **95**, 146802 (2005).
 [5] C. L. Kane and E. J. Mele, *Phys. Rev. Lett.* **95**, 226801 (2005).
 [6] V. Gurarie, *Phys. Rev. B* **83**, 085426 (2011).
 [7] S. R. Manmana, A. M. Essin, R. M. Noack, and V. Gurarie, *Phys. Rev. B* **86**, 205119 (2012).
 [8] T. Yoshida, R. Peters, S. Fujimoto, and N. Kawakami, *Phys. Rev. Lett.* **112**, 196404 (2014).
 [9] H. Li and F. D. M. Haldane, *Phys. Rev. Lett.* **101**, 010504 (2008).
 [10] F. Pollmann, A. M. Turner, E. Berg, and M. Oshikawa, *Phys. Rev. B* **81**, 064439 (2010).
 [11] Z.-X. Liu, Z.-B. Yang, Y.-J. Han, W. Yi, and X.-G. Wen, *Phys. Rev. B* **86**, 195122 (2012).
 [12] E. G. Dalla Torre, E. Berg, and E. Altman, *Phys. Rev. Lett.* **97**, 260401 (2006).
 [13] E. Berg, E. G. Dalla Torre, T. Giamarchi, and E. Altman, *Phys. Rev. B* **77**, 245119 (2008).
 [14] G. G. Batrouni, R. T. Scalettar, V. G. Rousseau, and B. Gréaud, *Phys. Rev. Lett.* **110**, 265303 (2013).
 [15] S. R. White, *Phys. Rev. Lett.* **69**, 2863 (1992).
 [16] E. Jeckelmann, *Phys. Rev. B* **66**, 045114 (2002).
 [17] P. Calabrese and J. Cardy, *J. Stat. Mech.* (2004) P06002.
 [18] S. Nishimoto, *Phys. Rev. B* **84**, 195108 (2011).
 [19] D. Rossini and R. Fazio, *New J. Phys.* **14**, 065012 (2012).
 [20] S. Ejima, H. Fehske, F. Gebhard, K. zu Münster, M. Knap, E. Arrigoni, and W. von der Linden, *Phys. Rev. A* **85**, 053644 (2012).
 [21] S. Ejima, M. J. Bhaseen, M. Hohenadler, F. H. L. Essler, H. Fehske, and B. D. Simons, *Phys. Rev. Lett.* **106**, 015303 (2011).
 [22] A. Kitazawa, K. Nomura, and K. Okamoto, *Phys. Rev. Lett.* **76**, 4038 (1996).
 [23] W. Chen, K. Hida, and B. C. Sanctuary, *Phys. Rev. B* **67**, 104401 (2003).
 [24] See Supplementary material at <http://link.aps.org/supplemental/10.1103/PhysRevLett.113.020401> for details on the intermediate-coupling region of the EBHM, which guarantees that our main conclusions are unaffected even in a more general case with $n_b > 2$.
 [25] S. R. Manmana, E. M. Stoudenmire, K. R. A. Hazzard, A. M. Rey, and A. V. Gorshkov, *Phys. Rev. B* **87**, 081106 (2013).
 [26] D. Rossini, M. Gibertini, V. Giovannetti, and R. Fazio, *Phys. Rev. B* **87**, 085131 (2013).
 [27] S. Ejima, H. Fehske, and F. Gebhard, *Europhys. Lett.* **93**, 30002 (2011).
 [28] T. Giamarchi, *Quantum Physics in One Dimension* (Clarendon, Oxford, 2003).
 [29] I. Bloch, J. Dalibard, and W. Zwerger, *Rev. Mod. Phys.* **80**, 885 (2008).
 [30] D. Clément, N. Fabbri, L. Fallani, C. Fort, and M. Inguscio, *Phys. Rev. Lett.* **102**, 155301 (2009).
 [31] P. T. Ernst, S. Götze, J. S. Krauser, K. Pyka, D.-S. Lühmann, D. Pfannkuche, and K. Sengstock, *Nat. Phys.* **6**, 56 (2010).
 [32] S. Ejima, H. Fehske, and F. Gebhard, *J. Phys. Conf. Ser.* **391**, 012143 (2012).

Supplementary material

Using the unbiased density matrix renormalization group (DMRG) technique with periodic boundary conditions (PBCs), in the main paper, we derived the ground-state phase diagram of the one-dimensional (1D) extended Bose-Hubbard model (EBHM), restricting the maximum number of bosons per site to be $n_b = 2$. Figure 1 showed the extent of the Haldane insulator (HI) phase, located between the conventional insulating Mott (MI) and density wave (DW) states and the superfluid (SF) phase. In the following we provide further results for the EBHM in the intermediate-coupling region, in order to guarantee that our main conclusions will be unaffected in the more general case with $n_b > 2$.

Determination of the MI-HI transition points

As stressed in the main text the 1D EBHM can be mapped onto an effective spin-1 XXZ chain model with on-site anisotropy D . Then, in the notations of Ref. [23], the three insulating MI, HI, and DW phases of the EBHM correspond to the large- D , the Haldane and the Néel phases, respectively. The Haldane phase in the spin-1 chain is described by a spin-1/2 two-leg ladder system [3, 10, 11]. As discussed in Ref. [11], with the projective representations of the symmetry group it is related to the t_0 phase of the latter system. According to Ref. [23], using Lanczos diagonalization, the large- D -Haldane phase transition points can be determined by level spectroscopy [22] of the two lowest-lying energies with twisted boundary conditions (i.e., $\hat{S}_{L+1}^x \rightarrow -\hat{S}_1^x$, $\hat{S}_{L+1}^y \rightarrow -\hat{S}_1^y$, and $\hat{S}_{L+1}^z \rightarrow \hat{S}_1^z$). Hence also the MI-HI transition points can be extracted by analyzing the two lowest-lying energies with anti-periodic boundary conditions (APBCs), i.e., $\hat{b}_{L+1}^{(\dagger)} \rightarrow -\hat{b}_1^{(\dagger)}$. As shown by

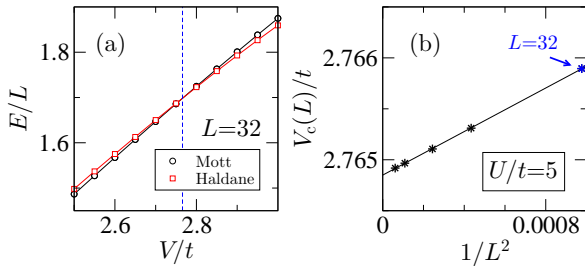


FIG. S1. (a) The V dependence of the two lowest energy eigenvalues with APBCs at $U/t = 5$ and $L = 32$. The energies of the Haldane state (squares) and the Mott insulating state (circles) cross at the MI-HI transition point. (b) The critical points $V_c(L)/t$ as extracted in the panel (a) versus inverse of the squares of the system size at $U/t = 5$ with up to $L = 128$.

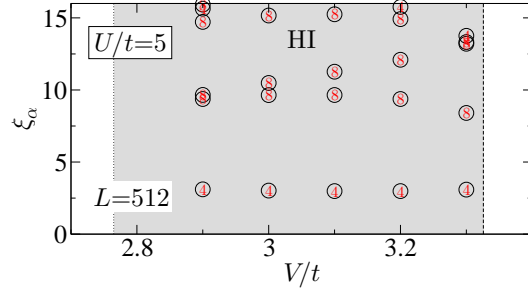


FIG. S2. Entanglement spectrum ξ_α obtained by DMRG in the HI state of the EBHM with $U/t = 5$. The dotted (dashed) line denotes the MI-HI (HI-DW) transition point extracted from the von Neumann entropy, see Fig. 2(a) of the main text. The numbers in the circles give the degree of degeneracy.

Fig. S1 (a), the Mott insulating state and the Haldane state crosses at the MI-HI transition point $V_c(L)$ for the fixed system size used at $U/t = 5$. The transition points obtained for various system sizes can be linearly extrapolated to the thermodynamic limit $L \rightarrow \infty$, see Fig. S1(b). We emphasize the perfect agreement with the critical points obtained in the main panel of Fig. 2(a).

Entanglement spectrum in the constrained EBHM

In the HI, due to the broken $\mathbb{Z}_2 \times \mathbb{Z}_2$ symmetry, the lowest entanglement level is four-fold degenerate. Since the HI phase is nontrivial protected by the lattice inversion symmetry, not only the lowest but also the entire entanglement spectrum is $4j$ -fold degenerate with $j = 1, 2, \dots$. Figure S2 visualizes the four-fold degeneracy of the higher entanglement levels in the HI phase at $U/t = 5$ for a system with $L = 512$, PBC and $n_b = 2$.

As noticed in the main text, in the weak-coupling regime the central charge $c^*(L)$ strongly depends on the system size [cf. Fig. 2 (c)]. Then the MI-HI (and likewise the SF-HI) phase transition is hard to detect. Figure S3 demonstrates that the situation is similar for the entanglement spectrum calculations at $U = 0$ with $n_b = 2$. Close to the Ising transition point ($U \approx 1.733$) the lowest entanglement level is four-fold degenerate, indicating the existence of the HI phase also at $U = 0$. Increasing the system size the HI state extends to $V \rightarrow 0$. Here a more precise finite-size-scaling is desired to pinpoint the MI/SF-HI transition.

Haldane insulator state in the full EBHM

We now demonstrate that the qualitative analysis of EBHM with $n_b = 2$ remains valid if we increase the boson cutoff. To this end we convinced ourselves that for

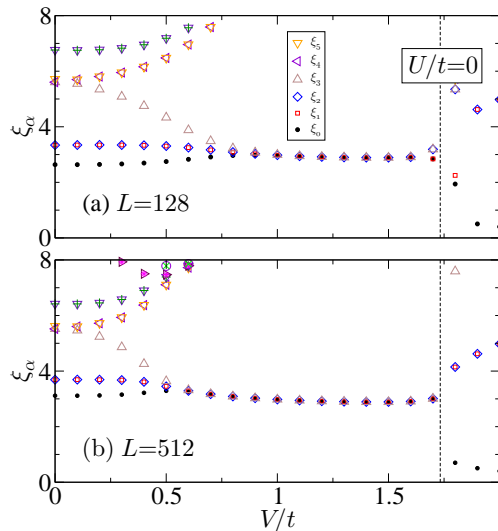


FIG. S3. Entanglement spectrum ξ_α in the weak-coupling (V/t) regime at $U/t = 0$. Data obtained by DMRG with PBCs for $L = 128$ (a) and $L = 512$ (b). The dashed line gives the HI-DW transition point extracted from the von Neumann entropy.

large enough values of U/t again both MI-HI and HI-DW phase transition points can be determined via the entanglement entropy and the level spectroscopy. For example, at $U = 5t$, the MI-HI phase transition occurs at $V/t \simeq 3.00$ with $c^* \simeq 1.0$ and the system-size dependence of maxima is very weak; see main panel of Fig. S4(a). Adopting level spectroscopy again, the MI-HI transition points can be determined (see inset), yielding excellent agreement with the values in the main panel. The Ising-like HI-DW transition shows up for large system sizes $L > 32$ at $V/t \simeq 3.55$ with $c^* \simeq 0.5$. The entanglement spectrum ξ_α with $n_b = 5$ shows a degeneracy of the lowest level deep in the HI phase for $L = 128$ as in Fig. S4(b). With increasing system size the degenerate HI state extends to the point of the MI-HI transition [Fig. S4(c)].

Finally we show that characteristic behavior of the dynamical charge structure factor $S(k, \omega)$ in the HI phase survives the inclusion of higher boson occupation numbers. Figure S5 presents dynamical DMRG results for

$S(k, \omega)$ with $n_b = 5$ deep in the HI phase (for $U/t = 5$, $V/t = 3.3$, $L = 32$ and broadening $\eta = t$). Just as for the constrained EBHM with $n_b = 2$, most of the spectral weights in $S(k, \omega)$ is concentrated around $k = \pi$ and $\omega \ll U$. The maxima of $S(k, \omega)$ follow—as a function of the momentum—the sinus-like dispersion known from the dynamical spin structure factor in the quantum spin-1 Heisenberg model. Note that the system-size dependence of the dispersion in $S(k, \omega)$ is hardly seen in Fig. 4. We conclude that our results for the dynamical structure factor in the HI phase of the constrained EBHM hold qualitatively in the full EBHM as well.

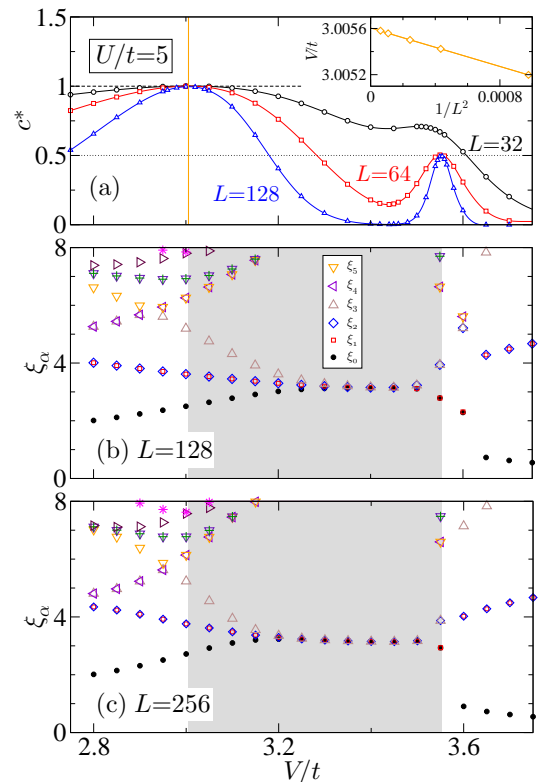


FIG. S4. (a) Central charge $c^*(L)$ at $U/t = 5$ with $n_b = 5$, indicating the MI-HI (HI-DW) transition points with $c = 1$ ($c = 1/2$). ξ_α in the 1D EBHM with $U/t = 5$ for $n_b = 5$ and $L = 128$ (b) respectively $L = 256$ (c).

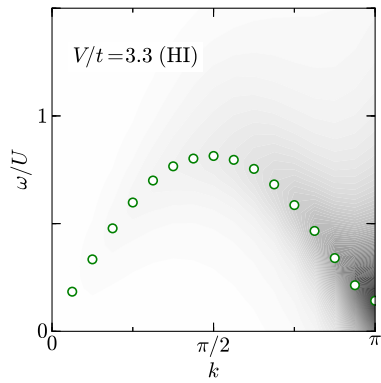


FIG. S5. Intensity plot of $S(k, \omega)$ in the EBHM with cutoff $n_b = 5$. Results were obtained for a lattice with $L = 32$ sites and PBCs, where $U/t = 5$ and $V/t = 3.3$. Within the dynamical DMRG a broadening $\eta/t = 1$ is used. Circles give the maxima in $S(k, \omega)$ for $k = 2\pi j/L$ where $j = 1, \dots, L/2$.

Entanglement properties of the nontrivial Haldane insulator in the 1D extended Bose-Hubbard model

Satoshi Ejima and Holger Fehske

Institut für Physik, Ernst-Moritz-Arndt-Universität Greifswald, 17489 Greifswald, Germany

E-mail: <ejima,fehske>@physik.uni-greifswald.de

Abstract. We investigate the entanglement properties of a nontrivial topological phase in the one-dimensional (1D) Bose-Hubbard model with additional nearest-neighbor repulsion. Employing the large-scale density-matrix renormalization group technique we show that a gapped insulating phase protected by lattice inversion symmetry, the so-called Haldane insulator, appears between the Mott and density wave phases in the intermediate-coupling regime. The phase boundaries were determined from the central charge via the von Neumann entropy. The Haldane insulator reveals a characteristic degeneracy in the entanglement spectra. Breaking the lattice inversion symmetry strongly affects the distinctive gapped dispersion of the dynamical charge response of the bosonic Haldane insulator.

1. Introduction

In the recent past, quantum spin chains, featuring rich physics in spite of their simplicity, have attracted renewed attention from a topological point of view. For example, a novel symmetry-protected topological (SPT) phase, the gapful Haldane phase [1] protected by lattice inversion symmetry, appears in one-dimensional (1D) integer-spin systems [2, 3]. Interestingly such SPT phase emerges also in interacting boson systems with long-range particle repulsion [4, 5, 6]. This is documented for the 1D extended Bose-Hubbard model (EBHM) with local and nearest-neighbor particle repulsion, and a site occupation $n_j = 0, 1$ or 2 , where the system can be mapped into an effective spin-1 model with $S_j^z = n_j - \rho$ for a mean boson filling factor $\rho = 1$. Here the so-called Haldane insulator (HI) phase, resembling the topological Haldane phase in the quantum spin-1 chain, appears between the conventional Mott insulator (MI) and the insulating density wave (DW) phases in the intermediate-coupling regime. Thereby the MI-HI transition belongs to the Tomonaga-Luttinger liquid universality class with central charge $c = 1$, while the HI-DW transition is of Ising type with $c = 1/2$ [5].

In this work we characterize the properties of the topological HI phase in the EBHM from an entanglement point of view. Utilizing the density-matrix renormalization group (DMRG) technique [7], we numerically determine the MI-HI and HI-DW quantum phase transition points via the central charge. The results appear to be in accordance with field theoretical predictions. For the nontrivial HI phase a distinctive degeneracy of the lowest entanglement levels is demonstrated. Finally, carrying out the dynamical DMRG (DDMRG) simulations [8, 9], we investigate the dynamical density structure factor in the vicinity of the quantum phase transitions to confirm the closing of the excitation gap, which is of great significance for the the SPT state.



Content from this work may be used under the terms of the [Creative Commons Attribution 3.0 licence](https://creativecommons.org/licenses/by/3.0/). Any further distribution of this work must maintain attribution to the author(s) and the title of the work, journal citation and DOI.

Published under licence by IOP Publishing Ltd

1

2. Model and Method

The Hamiltonian of the EBHM reads

$$\hat{\mathcal{H}} = -t \sum_j (\hat{b}_j^\dagger \hat{b}_{j+1} + \hat{b}_j \hat{b}_{j+1}^\dagger) + U \sum_j \hat{n}_j (\hat{n}_j - 1)/2 + V \sum_j \hat{n}_j \hat{n}_{j+1}, \quad (1)$$

where \hat{b}_j^\dagger , \hat{b}_j , and $\hat{n}_j = \hat{b}_j^\dagger \hat{b}_j$ are, respectively, the boson creation, annihilation, and number operators at lattice site j . In Eq. (1) the nearest-neighbor boson transfer amplitude is denoted by t ; U (V) parametrizes the on-site (nearest-neighbor) repulsions of bosons. The bosonic hopping amplitude t promotes a superfluid (SF) phase at weak interactions, while U (V) tends to stabilize a MI (DW) state. In what follows we take t as energy unit.

To address the topological properties of the 1D EBHM we perform an entanglement analysis in the framework of the finite-system DMRG approach. Considering the reduced density matrix $\rho_\ell = \text{Tr}_{L-\ell}[\rho]$ of a sub-block of length ℓ , the entanglement spectrum ξ_α [10] is obtained from the weights λ_α of ρ_ℓ by $\xi_\alpha = -2 \ln \lambda_\alpha$. In the nontrivial HI phase of the EBHM one expects a characteristic degeneracy of the lowest entanglement levels due to the artificial edges that appear by dividing the system into two sub-blocks during the simulation [11].

The entanglement analysis provides also valuable information about the universality class of the system. Adding up the λ_α in the course of their computation, the von Neumann entropy is obtained as $S_L(\ell) = -\text{Tr}_\ell[\rho_\ell \ln \rho_\ell]$. Exploiting the conformal field theory result $S_L(\ell) = \frac{c}{3} \ln \left[\frac{L}{\pi} \sin \left(\frac{\pi \ell}{L} \right) \right] + s_1$ (s_1 is a non-universal constant), the central charge c can be computed from the relation [12]

$$c^*(L) = \frac{3[S_L(L/2 - 1) - S_L(L/2)]}{\ln[\cos(\pi/L)]}, \quad (2)$$

and the phase boundaries follow—in a very efficient and accurate manner—from the numerically determined c^* , because the system becomes critical only at the MI-HI (HI-DW) transition points where $c = 1$ ($c = 1/2$) and c^* forms pronounced peaks as the system size increases. Quite recently this has been demonstrated for the EBHM [6].

In order to characterize the various insulating phases the excitation gaps have to be examined, which behave differently approaching the trivial-nontrivial phase transition points, where one expects the gap closing. This was also shown for the EBHM [4, 5, 6]. While the single-particle gap $\Delta_c = E_0(N+1) + E_0(N-1) - 2E_0(N)$ is finite in the MI, HI and DW phases and closes at the MI-HI transition, the neutral gap $\Delta_n = E_1(N) - E_0(N)$ closes at both the MI-HI and HI-DW transition lines. Here, $E_0(N)$ and $E_1(N)$ are the energies of the ground state and first excited state of the N -particle system, respectively, which can be easily calculated by DMRG.

Finally, calculating the dynamical charge structure factor is of particular importance since the frequency- and wave-vector-resolved density response can be directly compared with experimental results by momentum-resolved Bragg spectroscopy [13, 14]. The charge structure factor is defined as

$$S(k, \omega) = \sum_n |\langle \psi_n | \hat{n}_k | \psi_0 \rangle|^2 \delta(\omega - \omega_n), \quad (3)$$

where $|\psi_0\rangle$ ($|\psi_n\rangle$) denotes the ground state (n th excited state) and $\omega_n = E_n - E_0$ is the corresponding excitation energy. In the absence of the nearest-neighbor repulsion V , $S(k, \omega)$ was intensively studied by means of perturbation theory and the DDMRG method [15, 16]. Taking V into account, it is shown that the dispersion of $S(k, \omega)$ in the HI phase is remindful of those of the spin-1 Heisenberg chain and behaves very differently in all three insulating phases [6]. Hence $S(k, \omega)$ might be used analyzing experiments in order to discriminate the various insulator

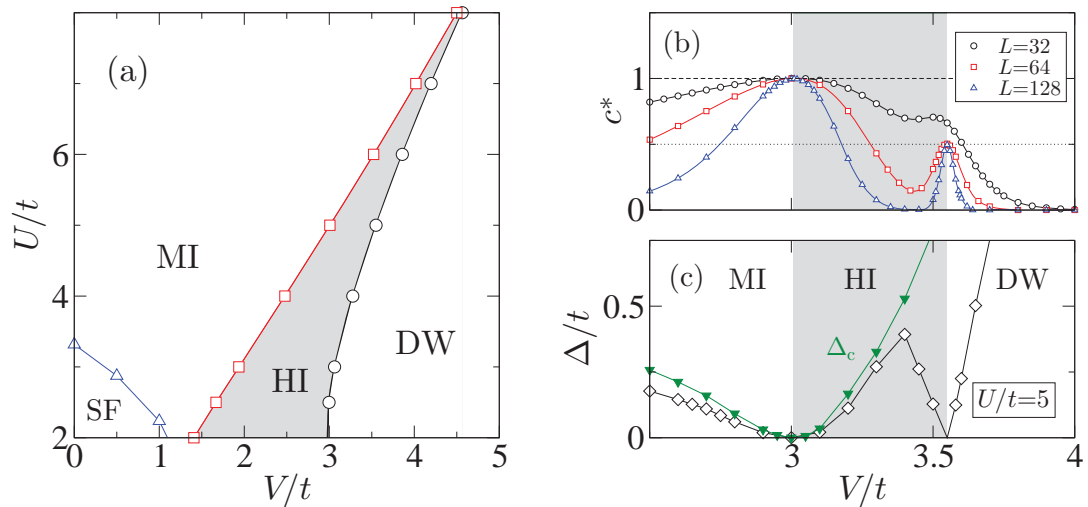


Figure 1. Ground-state phase diagram of the constrained extended Bose-Hubbard model with $n_b = 3$ and $\rho = 1$, showing the Mott insulator (MI), Haldane insulator (HI), density wave (DW) and superfluid (SF) phases. The MI-HI (squares) [HI-DW (circles)] phase transitions are determined by the central charge $c = 1$ [$c = 1/2$] exploiting the von Neumann entropy as demonstrated in panel (b) for $U/t = 5$. Panel (c) gives the corresponding ($L \rightarrow \infty$ extrapolated) data of the single-particle gap (triangles) and neutral gap (diamonds). The shaded regions in panels (b) and (c) define the HI phase.

states. Here we adapt the DDMRG method to simulate $S(k, \omega)$ in the HI phase of the EBHM, especially near MI-HI and HI-DW transition points with a focus on the gap closing.

In this work we fix the maximum number of bosons per site $n_b = 3$. Furthermore, we use periodic boundary conditions (PBC) and keep up to $m = 2400$ density matrix states in the DMRG computation, so that the discarded weight is typically smaller than 1×10^{-7} . For the DDMRG simulations we take $m = 800$ states to compute the ground state during the first five sweeps, and afterwards use 400 states evaluating dynamical quantities.

3. Numerical results

Figure 1(a) displays the DMRG ground-state phase diagram of the 1D EBHM (1) with $n_b = 3$. It exhibits three different insulating phases, besides a superfluid state in the weak-coupling region. We have shown in a preceding work that the phase boundaries between these insulating phases can be determined from the numerically calculated central charge c^* [6]. This works particularly well in the intermediate-coupling regime as demonstrated by Fig. 1(b). Obviously two maxima develop in c^* , which become more and more pronounced as the system size L increases, indicating the MI-HI and HI-DW transitions with $c = 1$ and $1/2$, respectively. This shows that the system becomes critical approaching the quantum phase transition points. Note that the estimated values of critical points in this region agree very well with other DMRG data [17]. We furthermore note that the SF-MI transition points are estimated via the Tomonaga-Luttinger exponent K_b as explained in Ref. [18].

As stressed above the various excitation gaps behave differently in the HI phase, in particular at the quantum phase transition points [4, 5]. Figure 1(c) indicates that extrapolated DMRG data of the single-particle gap Δ_c is finite in all insulating phases and closes at the MI-HI transition. By contrast the neutral gap Δ_n closes at both the MI-HI and HI-DW transitions.

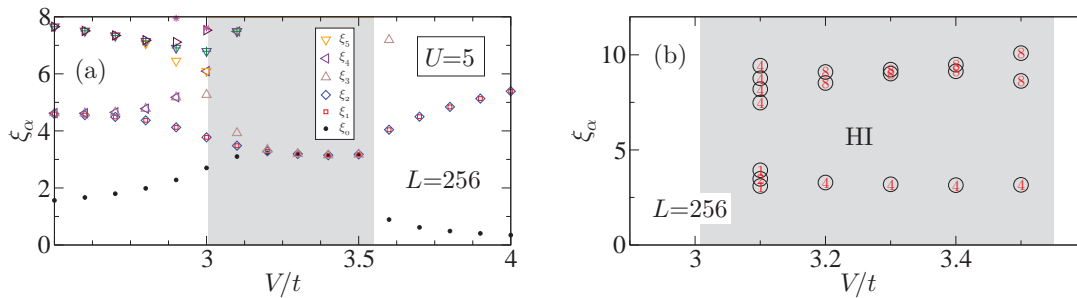


Figure 2. Entanglement spectrum ξ_α of the EBHM with $U/t = 5$, as obtained by DMRG for a system with $L = 256$. The shaded regions mark the HI phase, which shows (at least) a fourfold degeneracy of the lowest [panel (a)] and higher entanglement levels [panel (b)]. The numbers in panel (b) give the degree of degeneracy.

Let us now discuss the topological properties in terms of the entanglement spectra ξ_α within the intermediate-coupling regime ($U/t = 5$). Dividing the system in two halves, using the finite-system DMRG algorithm with PBC, one of the subblock with $L/2$ sites possesses two edges [6, 11]. This has to be contrasted with the infinite-time evolving block-decimation algorithm [3], where only a single edge emerges for the semi-infinite chain. Here we expect a fourfold degeneracy of the lowest entanglement level of the HI phase, just as for the nontrivial topological Haldane phase in the spin-1 XXZ chain. Figure 2(a) brings out this characteristic fourfold degeneracy of the lowest entanglement levels of the EBHM with $n_b = 3$ —deep in the HI phase. Since the HI phase is protected by the lattice inversion symmetry in a nontrivial way, not only the lowest but the entire spectrum shows a $4j$ -fold degeneracy with $j = 1, 2, \dots$, as can be seen from Fig. 2(b). In contrast the lowest entanglement levels of the MI and DW phases are apparently non-degenerate. Close to the MI-HI transition larger system sizes $L > 256$ are needed to reproduce the fourfold degeneracy; because of $c = 1$ the gap closes exponentially.

We finally want to take a look at the dynamical properties of EBHM within the range of the topological HI phase, and therefore consider again the intermediate-coupling regime, $U/t = 5$. It is well-known that in the Mott insulator phase a gap opens at the momentum $k = 0$ and the spectral weight becomes concentrated in the region $k > \pi/2$ for $\omega \simeq U$ [15, 16]. Increasing V the MI-HI transition occurs, whereupon the gap at $k = 0$ closes according to Fig. 1(c). At the same time the spectral weight will be concentrated at $k > 3\pi/4$ for $\omega \ll U$, as indicated by Fig. 3(a) for $V \simeq 3.01$. Deep inside the HI phase [see panel (b) for $V/t = 3.3$] the gap at $k = 0$ opens again and the dispersion of the maximum in $S(k, \omega)$ acquires a sine-shape as for the spin-1 XXZ chain [6]. Then the interesting question is whether the gap in $S(k, \omega)$ closes again at the HI-DW transition point if V is increases further. The answer is yes, but now the gap closes at momentum $k = \pi$, reflecting the lattice-period doubling within the DW phase. Accordingly, $S(k, \omega)$ follows the behavior of the neutral gap Δ_n shown in Fig. 1(c).

4. Summary

To conclude, we have analyzed the non-trivial topological Haldane insulator phase—showing up in the intermediate-coupling regime of the one-dimensional Bose-Hubbard model with long-range repulsive particle interaction—from an entanglement point of view. Performing large-scale density matrix renormalization group calculations for finite systems with periodic boundary conditions, the MI-HI and HI-DW quantum phase transition lines can be determined from the central charge c^* via the von Neumann entropy. Thereby our unbiased numerical (lattice model) results confirm the corresponding field theoretical (continuum model) predictions $c = 1$ and $1/2$.

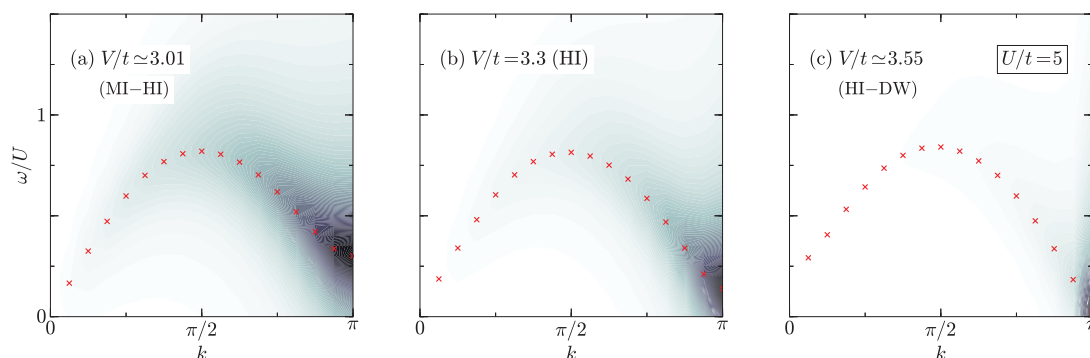


Figure 3. Intensity plots of the dynamical charge structure factor $S(k, \omega)$ at the MI-HI transition point (a), in the HI phase (b), and at the HI-DW transition point (c). Data were obtained applying the DDMRG technique to the 1D EBHM with $L = 32$, using a broadening $\eta = t$. Crosses (circles) give the maximum value of $S(k, \omega)$ at fixed momenta $k = 2\pi j/L$ where $j = 1, \dots, L/2$.

Furthermore, a characteristic fourfold degeneracy of the lowest entanglement levels in the HI phase is found, which signals the SPT state for the interacting boson model in exactly the same way as for the quantum spin-1 XXZ chain. Finally we studied the dynamical properties of the topological HI phase. Here the dynamical density structure factor is reflective of the behavior of the neutral gap: the dispersion of the maximum in $S(k, \omega)$ is gapless at both the MI-HI and HI-DW transition lines. Notably the momentum where the gap closes differs: for the MI-HI (HI-DW) phase transition the gap vanishes at $k = 0$ ($k = \pi$).

Acknowledgments

The authors would like to thank Y. Fuji and F. Pollmann for valuable discussions. This work was supported by Deutsche Forschungsgemeinschaft through SFB 652, Project B5. The computations were performed at the Regional Computing Center Erlangen.

References

- [1] Haldane F D M 1983 *Phys. Rev. Lett.* **50**(15) 1153–1156
- [2] Gu Z C and Wen X G 2009 *Phys. Rev. B* **80**(15) 155131
- [3] Pollmann F, Berg E, Turner A M and Oshikawa M 2012 *Phys. Rev. B* **85**(7) 075125
- [4] Dalla Torre E G, Berg E and Altman E 2006 *Phys. Rev. Lett.* **97** 260401
- [5] Berg E, Dalla Torre E, Giamarchi T and Altman E 2008 *Phys. Rev. B* **77** 245119
- [6] Ejima S, Lange F and Fehske H 2014 *Phys. Rev. Lett.* **113** 020401
- [7] White S R 1992 *Phys. Rev. Lett.* **69** 2863
- [8] Jeckelmann E 2002 *Phys. Rev. B* **66** 045114
- [9] Jeckelmann E and Fehske H 2007 *Rivista del Nuovo Cimento* **30** 259
- [10] Li H and Haldane F D M 2008 *Phys. Rev. Lett.* **101**(1) 010504
- [11] Ejima S and Fehske H 2015 *Phys. Rev. B* **91** 045121
- [12] Nishimoto S 2011 *Phys. Rev. B* **84** 195108
- [13] Clément D, Fabbri N, Fallani L, Fort C and Inguscio M 2009 *Phys. Rev. Lett.* **102** 155301
- [14] Ernst P T, Götze S, Krauser J S, Pyka K, Lühmann D S, Pfannkuche D and Sengstock K 2009 *Nature Physics* **6** 56
- [15] Ejima S, Fehske H, Gebhard F, zu Münster K, Knap M, Arrigoni E and von der Linden W 2012 *Phys. Rev. A* **85**(5) 053644
- [16] Ejima S, Fehske H and Gebhard F 2012 *J. Phys. Conf. Ser.* **391** 012143
- [17] Rossini D and Fazio R 2012 *New J. Phys.* **14** 065012
- [18] Ejima S, Fehske H and Gebhard F 2011 *Europhys. Lett.* **93** 30002

Comparative density-matrix renormalization group study of symmetry-protected topological phases in spin-1 chain and Bose-Hubbard models

Satoshi Ejima and Holger Fehske

Institut für Physik, Ernst-Moritz-Arndt-Universität Greifswald, 17487 Greifswald, Germany

(Received 22 July 2014; revised manuscript received 4 January 2015; published 16 January 2015)

We reexamine the one-dimensional spin-1 XXZ model with on-site uniaxial single-ion anisotropy as to the appearance and characterization of the symmetry-protected topological Haldane phase. By means of large-scale density-matrix renormalization group (DMRG) calculations the central charge can be determined numerically via the von Neumann entropy, from which the ground-state phase diagram of the model can be derived with high precision. The nontrivial gapped Haldane phase shows up in between the trivial gapped even Haldane and Néel phases, appearing at large single-ion and spin-exchange interaction anisotropies, respectively. We furthermore carve out a characteristic degeneracy of the lowest entanglement level in the topological Haldane phase, which is determined using a conventional finite-system DMRG technique with both periodic and open boundary conditions. Defining the spin and neutral gaps in analogy to the single-particle and neutral gaps in the intimately connected extended Bose-Hubbard model, we show that the excitation gaps in the spin model qualitatively behave just as for the bosonic system. We finally compute the dynamical spin structure factor in the three different gapped phases and find significant differences in the intensity maximum which might be used to distinguish these phases experimentally.

DOI: [10.1103/PhysRevB.91.045121](https://doi.org/10.1103/PhysRevB.91.045121)

PACS number(s): 75.10.Pq, 64.70.Tg, 03.67.—a

I. INTRODUCTION

One-dimensional (1D) quantum spin systems have received continued attention as paradigms for strongly correlated systems, because miscellaneous—and even exotic—phases can be realized within simple model Hamiltonians. By way of example, the exactly solvable spin-1/2 antiferromagnetic (AFM) Heisenberg chain is known to be gapless, while for integer spins a gap exists between the ground state and the first excited state, as conjectured first by Haldane [1]. Especially for the spin-1 chain, the Haldane gap was confirmed experimentally [2,3], and the dynamical spin structure factor has been observed by inelastic neutron scattering, e.g., on $\text{Ni}(\text{C}_2\text{H}_8\text{N}_2)_2\text{NO}_2\text{ClO}_4$ [4]. Affleck, Lieb, Kennedy, and Tasaki (AKLT) proposed an exactly solvable model that offers valuable clues to the physics of the spin-1 Heisenberg chain [5]. The so-called AKLT state [cf. Fig. 1(a) below] successfully describes the ground state of the Haldane phase [6]. Also for the spin-1 XXZ model, the ground-state phase diagram has been determined—even if a single-ion anisotropy is added [7]—e.g., by the Lanczos exact diagonalization (ED) technique based on the level spectroscopy method [8].

Currently, quantum integer-spin chains have attracted extraordinary interest from a topological point of view. The gapped ground states in the Haldane phase can be classified by the projective representations of the underlying symmetry group [9,10]. The odd Haldane (OH) phase in odd-integer-spin chains with two half-integer edge spins is a symmetry-protected topological (SPT) phase, because the odd- S AKLT state cannot be adiabatically connected to another trivial state without undergoing a phase transition. On the other hand, the even Haldane (EH) state in the even-integer-spin systems with integer edge spins [11–14] is a trivial state, since the even- S AKLT state is adiabatically connected to a trivial state without a bulk phase transition [15,16].

Interestingly, a hidden SPT phase analogous to the OH phase was discovered in the extended Bose-Hubbard model

(EBHM) with longer-range repulsions [17]. This Haldane-insulator (HI) phase, embedded between the Mott-insulator (MI) and the density-wave (DW) phases in the intermediate coupling regime, exhibits the characteristic degeneracy of the entanglement spectrum in the Haldane phase [18]. The excitation gaps at the quantum phase transition lines depend on their universality classes [17,19]. Beyond that, the dynamical density structure factor $S_{\text{EBHM}}(k, \omega)$ significantly differs in the MI, DW, and HI states [18].

On the basis of our recent EBHM study [18], in the present work we investigate the topological properties of the odd Haldane phase in the anisotropic spin-1 XXZ chain which, as we will show, can be taken as an effective model for the EBHM. Using the density-matrix renormalization group (DMRG) technique [20–22], first we determine the phase boundaries by exploiting the central charge. In order to confirm the closing of the excitation gap at the trivial-nontrivial phase transition points, we simulate both the spin and neutral gaps. We furthermore demonstrate the degeneracy of entanglement levels in the OH phase with both periodic (P) and open (O) boundary conditions (BC) (for the anisotropic spin-1 XXZ chain it is well known how the edge spins should be treated in the latter case). In order to experimentally detect the topological HI phase in the EBHM, various dynamical quantities have been proposed [17,18,23]. Here we will examine the dynamical spin structure factor $S^{zz}(k, \omega)$ for the spin-1 model by means of the dynamical DMRG (DDMRG) technique [24]. We will demonstrate that the intensity maximum in $S^{zz}(k, \omega)$ features a gapped dispersion in the nontrivial Haldane phase as obtained for $S_{\text{EBHM}}(k, \omega)$ in the EBHM. Since this quantity is directly accessible by inelastic neutron scattering, significant differences in $S^{zz}(k, \omega)$ could be used to detect the various gapped phases.

This paper is organized as follows. In the next section we establish the anisotropic spin-1 XXZ model and the corresponding EBHM. The physical quantities of interests are

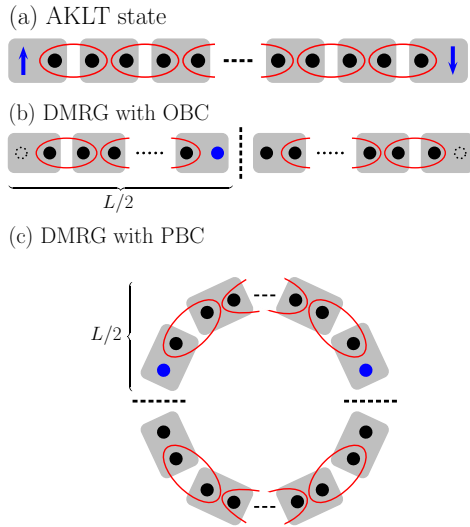


FIG. 1. (Color online) (a) Valence bond picture of the AKLT state in a spin-1 XXZ chain. Each of the two $S = 1/2$ spins connected by an ellipse form a singlet $(1/\sqrt{2})(\uparrow\downarrow - \downarrow\uparrow)$. The two free edge spins cause the fourfold degeneracy of the ground-state energy. (b) To simulate the AKLT state within OBC DMRG, the free edge spins have to be excluded from the system (dashed circles). (c) With PBC the AKLT state can be simulated without any changes, so that the lowest entanglement level exhibits a fourfold degeneracy according to the two edge spins.

introduced in Sec. III. Large-scale (D) DMRG results for the anisotropic spin-1 XXZ chain will be presented and discussed in Sec. IV. Section V contains a brief summary and our main conclusions.

II. MODEL HAMILTONIANS

In this section we introduce the anisotropic spin-1 XXZ model and get back to its established ground-state phase properties. We then define the extended Bose-Hubbard model and point out the correspondences with an effective spin-1 XXZ model.

A. Spin-1 XXZ model with single-ion anisotropy

The Hamiltonian of the 1D spin-1 XXZ model with on-site anisotropy is given by

$$\hat{\mathcal{H}} = \sum_j [J(\hat{S}_j^x \hat{S}_{j+1}^x + \hat{S}_j^y \hat{S}_{j+1}^y) + J_z \hat{S}_j^z \hat{S}_{j+1}^z] + D \sum_j (\hat{S}_j^z)^2, \quad (1)$$

where \hat{S}_j denotes a spin-1 operator. The parameter D represents the uniaxial single-ion anisotropy. The ground-state phase diagram of the model (1) exhibits various gapful and gapless phases, namely, following the conventional notations, the Haldane phase, the large- D phase, two XY phases, the ferromagnetic phase, and the Néel phase [7,25,26]. According to this, different types of phase transitions occur between these phases: (i) A gapful-gapful Gaussian phase transition

takes place between the large- D phase and the Haldane phase with the central charge $c = 1$, (ii) the Haldane-Néel transition appears to be of the Ising universality class with $c = 1/2$, and (iii) a gapless-gapful Berezinskii-Kosterlitz-Thouless (BKT) transition emerges between the XY phase and the Haldane or large- D phase. In what follows we restrict ourselves to the parameter region where $J_z > 0$ and $D > 0$. Following the notation by Kjäll *et al.* [16], we use the termini EH, OH, and AFM phases instead of the large- D , Haldane, and Néel phases, respectively. The lattice-inversion symmetry, which protects the SPT state of the Haldane phase, can be broken by adding a perturbation to the Hamiltonian (1):

$$\delta\hat{\mathcal{H}} = g \sum_j [\hat{S}_j^z (\hat{S}_j^x \hat{S}_{j+1}^x + \hat{S}_j^y \hat{S}_{j+1}^y) - \hat{S}_{j+1}^z (\hat{S}_j^x \hat{S}_{j+1}^x + \hat{S}_j^y \hat{S}_{j+1}^y) + \text{H.c.}]. \quad (2)$$

Any finite g immediately lifts the characteristic degeneracy of the lowest entanglement level in the Haldane phase [10]. As we will see later, thereby the EH-OH quantum phase transition also disappears.

B. Extended Bose-Hubbard model

In 2006, Dalla Torre *et al.* [17] discovered the HI phase in the 1D extended Bose-Hubbard model with longer-range repulsions. The HI phase features the properties of the OH phase in the spin-1 model (1). The EBHM Hamiltonian reads

$$\hat{\mathcal{H}}_{\text{EBHM}} = -t \sum_j (\hat{b}_j^\dagger \hat{b}_{j+1} + \text{H.c.}) + U \sum_j \hat{n}_j (\hat{n}_j - 1)/2 + V \sum_j \hat{n}_j \hat{n}_{j+1}, \quad (3)$$

where \hat{b}_j^\dagger (\hat{b}_j) creates (annihilates) a boson at lattice site j , and $\hat{n}_j = \hat{b}_j^\dagger \hat{b}_j$ is the corresponding boson number operator. The nearest-neighbor boson transfer amplitude is given by t and U (V) parametrizes the on-site (nearest-neighbor) particle repulsion. Assuming that the site occupation is restricted to $n_j = 0, 1, \text{ or } 2$, with $S_j^z = n_j - 1$ for a mean boson filling factor $\rho = N/L = 1$, the system can be mapped onto an effective spin-1 Hamiltonian,

$$\hat{\mathcal{H}}_{\text{EBHM}}^{\text{eff}} = \hat{\mathcal{H}} + \hat{\mathcal{H}}', \quad (4)$$

with the replacements $J \rightarrow -t$, $J_z \rightarrow V$, and $D \rightarrow U/2$ in Eq. (1). $\hat{\mathcal{H}}'$ contains further terms which breaks the particle-hole symmetry of $\hat{\mathcal{H}}$ [see Eq. (A1) of Ref. [19] for the explicit form of $\hat{\mathcal{H}}'$]. The EBHM exhibits three insulating phases, where the nontrivial HI phase appears in between the MI and DW phases for intermediate couplings. The MI, HI, and DW phases of the EBHM correspond to the EH, OH, and AFM phases of the spin-1 model (1), respectively.

III. PHYSICAL QUANTITIES OF INTEREST

In this section we assort the quantities that can be used to characterize the different phases and phase transitions in the spin-1 model (1) and accordingly in the EBHM. We furthermore explain how the quantities can be simulated using the DMRG technique.

A. Entanglement spectrum, von Neumann entropy, and central charge

After Li and Haldane's proposal [27] to characterize topological phases by the entanglement spectrum, this has become one of the most powerful tools to investigate the SPT state. Dividing a system with L sites into two subblocks and considering the reduced density matrix $\rho_\ell = \text{Tr}_{L-\ell}[\rho]$ of a subblock of arbitrarily length ℓ , the entanglement spectrum ξ_α is obtained from the weights λ_α of the reduced density matrix ρ_ℓ by

$$\xi_\alpha = -2 \ln \lambda_\alpha. \quad (5)$$

The entanglement spectrum of a subblock with $\ell = L/2$ sites can be obtained for OBC and PBC as sketched in Figs. 1(b) and 1(c), respectively. Thereby the artificial edges give rise to the characteristic degeneracy of the lowest entanglement level in the nontrivial AKLT state [displayed in Fig. 1(a)], where the degree of degeneracy depends on the boundary conditions. To determine the entanglement spectrum in the OH phase with OBC, a well-known trick is in use: One simulates a system without free edge spins by replacing the edge sites with $S = 1/2$, as shown in Fig. 1(b). One then expects a doubly degenerate lowest entanglement level in the OH phase. For PBC, on the other hand, for the same finite system, a fourfold degeneracy is expected due to two free $S = 1/2$ spins [see Fig. 1(c)], just as for the HI phase in the EBHM [18].

The entanglement analysis provides also valuable information about the criticality of the system. Adding up the λ_α during the simulation, we have direct access to the von Neumann entropy $S_L(\ell) = -\text{Tr}_\ell[\rho_\ell \ln \rho_\ell]$. From conformal field theory [28], it follows that in the case of a periodic system the von Neumann entropy takes the form

$$S_L(\ell) = \frac{c}{3} \ln \left[\frac{L}{\pi} \sin \left(\frac{\pi \ell}{L} \right) \right] + s_1, \quad (6)$$

where s_1 is a nonuniversal constant. Since the most precise data of $S_L(\ell)$ are obtained when the length ℓ of the subblock equals half the system size L , the relation [29]

$$c^*(L) \equiv \frac{3[S_L(L/2 - 1) - S_L(L/2)]}{\ln[\cos(\pi/L)]} \quad (7)$$

is much better suited for determining the central charge than directly using the above expression for $S_L(\ell)$.

For the EBHM the phase boundaries can be assigned very effectively using the (numerically determined) central charge c^* , because the system becomes critical only at the MI-HI (HI-DW) transition points where $c = 1$ ($c = 1/2$), and there c^* shows pronounced peaks [18]. Hence we adopt this method for the spin-1 model (1) as well to pinpoint the EH-OH and OH-AFM transition points.

B. Excitation gaps

Monitoring various excitation gaps for the EBHM, significant features have been found at the MI-HI and HI-DW transition points [17,19]. For example, the single-particle gap,

$$\Delta_c = E_0^{\text{EBHM}}(N+1) + E_0^{\text{EBHM}}(N-1) - 2E_0^{\text{EBHM}}(N), \quad (8)$$

is finite in all three insulating phases, except for the MI-HI transition point. By contrast, the neutral gap,

$$\Delta_n = E_1^{\text{EBHM}}(N) - E_0^{\text{EBHM}}(N), \quad (9)$$

closes at both the MI-HI and HI-DW transitions. In Eqs. (8) and (9), $E_0^{\text{EBHM}}(N)$ and $E_1^{\text{EBHM}}(N)$ denote the energies of the ground state and first excited state of the N -particle system for the EBHM, respectively.

Since adding (removing) a particle in the EBHM corresponds to raising (lowering) the spin S^z projection in a pseudospin model, we consider for the spin-1 XXZ model the spin gap

$$\Delta_s = E_0^{\text{XXZ}}(1) - E_0^{\text{XXZ}}(0), \quad (10)$$

which likewise might be finite in all three phases, except for the EH-OH transition point. As for the EBHM, the neutral gap in the spin-1 model (1) can be defined as

$$\Delta_n = E_1^{\text{XXZ}}(0) - E_0^{\text{XXZ}}(0), \quad (11)$$

where $E_0^{\text{XXZ}}(M)$ and $E_1^{\text{XXZ}}(M)$ denote the ground-state and first excited energies within the subspace $M = \sum_j S_j^z$, respectively. By analogy to the behavior of the neutral gap in the EBHM, Δ_n should vanish at the EH-OH and OH-AFM transition points for the spin-1 chain model.

C. Dynamical spin structure factor

Simulating the dynamical spin structure factor by DDMRG is of particular importance since it might be directly compared with inelastic neutron scattering experiments, e.g., on $\text{Ni}(\text{C}_2\text{H}_8\text{N}_2)_2\text{NO}_2\text{ClO}_4$ [4]. Its zz component is defined by

$$S^{zz}(k, \omega) = \sum_n |\langle \psi_n | \hat{S}_k^z | \psi_0 \rangle|^2 \delta(\omega - \omega_n), \quad (12)$$

where $|\psi_0\rangle$ and $|\psi_n\rangle$ denote the ground state and n th excited state, respectively. The corresponding excitation energy is $\omega_n = E_n - E_0$. For $D = 0$, i.e., for the isotropic Heisenberg or XXZ fix points of (1), $S^{zz}(k, \omega)$ was extensively studied by ED [30] and time-dependent DMRG [31] techniques. That is, the behavior of $S^{zz}(k, \omega)$ in the Haldane phase is well known, albeit numerical results for the EH and AFM states are rare. Taking into account the relation $S_j^z = n_j - \rho$ for the pseudospin in the effective model $\hat{\mathcal{H}}_{\text{EBHM}}^{\text{eff}}$, one expects that the spin structure factor $S^{zz}(k, \omega)$ corresponds to the dynamical density structure factor $S_{\text{EBHM}}(k, \omega)$ in the EBHM, which exhibits different behavior in the three insulating phases [18].

IV. NUMERICAL RESULTS

In this section we present our numerical (D)DMRG results for the spin-1 XXZ model with and without single-ion anisotropy. We first determine the phase boundaries and then analyze the behavior of the excitation gaps at the transitions between the nontrivial and trivial phases. Furthermore, we discuss the entanglement spectra of an odd Haldane phase. Finally, we simulate the dynamic spin structure factor and compare it with the dynamical density response in the EBHM.

In the numerics we keep up to $m = 3200$ density-matrix states for the static DMRG runs, so that the discarded weight is

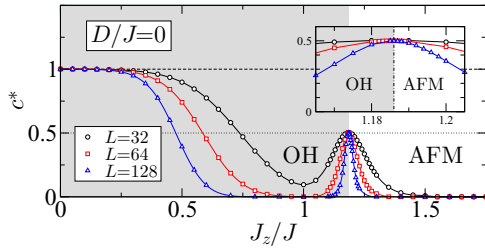


FIG. 2. (Color online) Central charge $c^*(L)$ as obtained by DMRG for the spin-1 XXZ model with $D = 0$ and PBC. The OH-AFM transition can be assigned to $J_z/J = 1.186 \pm 0.001$ with $c = 1/2$, where a pronounced peak appears [see also the magnifying inset which shows $c^*(L)$ close to the transition point].

typically smaller than 1×10^{-10} . For the DDMRG simulations we take $m = 800$, examining the ground state along the first five DMRG sweeps, and then use $m = 400$ states computing dynamical properties.

A. Phase boundaries

1. OH-AFM transition

Let us first discuss the spin-1 model (1) with $D = 0$. In this case it is known that a BKT transition occurs at $J_z = 0$ between the XY and OH phases [32]. At $J_z > 0$, only an OH-AFM transition takes place, where $c = 1/2$ is expected.

Figure 2 shows the central charge $c^*(L)$, computed from Eq. (7). If J_z/J is raised at fixed system size, the maximum in $c^*(L)$ sharpens at the OH-AFM transition point $J_{z,c1}/J$, and we deduce $c^* \simeq 0.5$. The other critical point $J_{z,c2}/J \simeq 1.185$ with $c^* \simeq 0.503$ approximates the recent infinite-system DMRG result $J_{z,c2}/J = 1.186 \pm 0.002$ [16,33] very well already for $L = 32$. The agreement becomes perfect if we increase the system size: $J_{z,c2}/J \simeq 1.186$ with $c^* \simeq 0.500$ for $L = 128$. Note that $c^*(L)$ stays equal to one in a relatively wide region (from $J_z/J = 0$ to $J_z/J \simeq 0.3$ for $L = 128$), indicating the BKT transition between the XY and the OH phases at $J_z/J = 0$ with $c = 1$.

To relate our numerical results to previous ones we include an on-site anisotropy D and compute $c^*(L)$ in the vicinity of the OH-AFM transition. For $D/J = 0.5$ the central charge $c^*(L)$ at fixed system size L develops again a pronounced maximum at the OH-AFM transition point [see Fig. 3(a)]. The

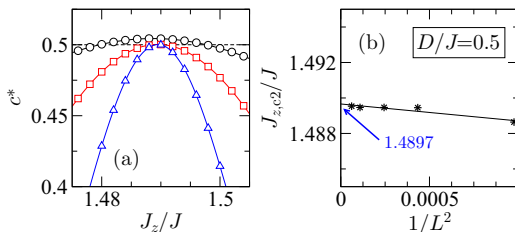


FIG. 3. (Color online) $c^*(L)$ for $D = 0.5$ near the OH-AFM transition. (b) shows that the Ising transition point $J_{z,c2}/J(L)$ obtained from $c^*(L)$ can be linearly extrapolated to the thermodynamic limit.

deduced transition point $J_{z,c1}/J(L)$ is readily extrapolated to the thermodynamic limit [Fig. 3(b)], yielding $J_{z,c2}/J \simeq 1.4897$, which is in reasonable agreement with the ED result $J_{z,c2}/J \simeq 1.536$ obtained from systems with L up to 16 [7] and confirms recent DMRG data $J_{z,c2}/J = 1.4905 \pm 0.0015$ [34].

2. EH-OH transition

We now turn to the case $D > 0$. In previous works [7,32,35,36] a Gaussian transition between the EH and OH phases has been found by employing the level spectroscopy technique to ED results obtained for small systems. Applying the twisted boundary conditions (TBC), $\hat{S}_{L+1}^x = -\hat{S}_1^x$, $\hat{S}_{L+1}^y = -\hat{S}_1^y$, and $\hat{S}_{L+1}^z = \hat{S}_1^z$ within DMRG, the two lowest energy levels can be simulated accurately for much larger system sizes than accessible to ED. Figure 4(a) demonstrates that the two lowest energies assigned to the EH and OH states cross at $J_{z,c1}/J \simeq 1.6945$ by increasing J_z/J at fixed $D/J = 1.5$ for $L = 32$ (and TBC). The critical points $J_{z,c1}/J(L)$ can be systematically extrapolated to the thermodynamic limit by a linear fit, as indicated in Fig. 4(b). For $L \rightarrow \infty$ we obtain $J_{z,c1}/J \simeq 1.6938$.

Alternatively, the EH-OH transition points can be extracted from the central charge $c^*(L)$ if compared with the field theoretical prediction $c = 1$. This is demonstrated in Fig. 4(c).

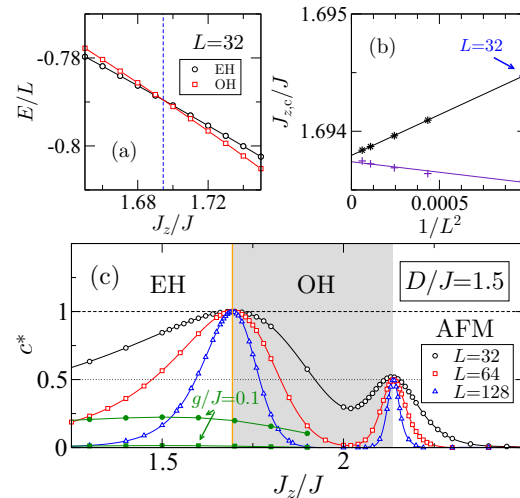


FIG. 4. (Color online) (a) J_z dependence of the two lowest energy eigenvalues at $D/J = 1.5$, using TBC and $L = 32$. Obviously the energies of the OH state (squares) and the EH state (circles) cross at the EH-OH transition point (dashed line). (b) Critical points $J_{z,c1}/J$ obtained by the level spectroscopy technique (stars) [via the central charge (pluses)] as obtained in (a) [(c)] vs the inverse of the system size squared at $D/J = 1.5$ for L up to 128. (c) Central charge c^* of the 1D spin-1 XXZ model (1) with $D/J = 1.5$, indicating the EH-OH (OH-AFM) transition point with $c = 1$ ($c = 1/2$). The solid line denotes the EH-OH transition extracted from (a) and (b), which is in accordance with the position of the maximum in $c^*(L)$. Turning on a perturbation $\delta\hat{\mathcal{H}}$ that breaks the lattice-inversion symmetry, the central charge $c^*(L)$ (solid symbols) becomes zero for large enough system sizes ($L \geq 64$).

Here the maxima of $c^*(L)$ can also be extrapolated to the thermodynamic limit [see Fig. 4(b)], where the transition point is in excellent accord with the ones via level spectroscopy in Figs. 4(a) and 4(b). We note that also the OH-AFM transition can be reliably determined from the peak at $J_{z,c2}/J \simeq 2.138$.

B. Characterization of the topological phase

In the following we analyze the signatures of the topological OH phase and of the transition between the trivial and nontrivial topological states for the model (1) in close analogy to the EBHM [18]. To this end, we simulate the excitation gaps and the entanglement spectra.

1. Excitation gaps

So far the excitation gaps of (1) have been studied mostly at the isotropic Heisenberg point with respect to the magnitude of the Haldane gap. At the trivial-nontrivial phase transition points the excitation gaps should close, as demonstrated, e.g., for the EBHM [17,19]. Here we compute the spin and neutral excitation gaps as defined in Sec. III B instead of calculating the simple first excitation gap. Thereby, we adopt PBC instead of OBC within DMRG, avoiding the use of edge spins, which have to be adapted according to the considered parameter region.

Figure 5(a) shows first the excitation gaps at $D = 0$. Upon increasing J_z/J , the gaps open exponentially, reflecting the BKT transition at $J_z/J = 0$. Δ_n and Δ_s cross each other exactly at the Heisenberg point, $J_z/J = 1$, where $\Delta_n(L) = \Delta_s(L)$ (see the discussion about the system-size dependence of the excitation gaps and the magnitude of the Haldane gap for the spin-1 Heisenberg model in the Appendix). At the OH-AFM transition ($J_{z,c}/J \simeq 1.186$), Δ_n closes linearly

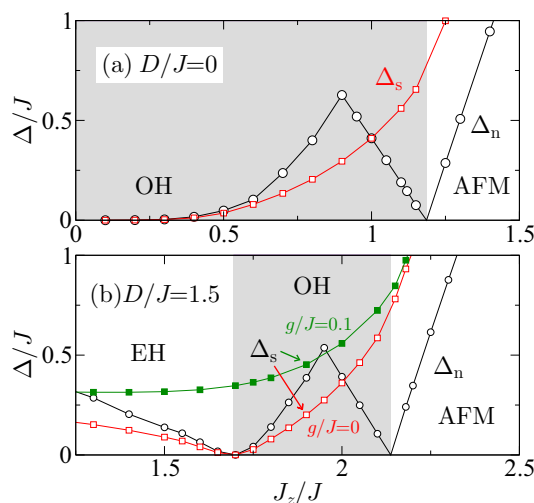


FIG. 5. (Color online) Extrapolated data for the spin gap Δ_s (squares) and neutral gap Δ_n (open circles) as a function of J_z/J for (a) $D/J = 0$ and (b) $D/J = 1.5$. The solid squares in (b) give Δ_s with a finite inversion-symmetry-breaking perturbation $g/J = 0.1$ [see Eq. (2)].

because the transition belongs to the Ising universality class, while Δ_s remains finite.

For $D/J = 1.5$ [see Fig. 5(b)], the EH-OH transition occurs at $J_{z,c1}/J \sim 1.6938$, where both spin and neutral gaps vanish. Increasing J_z/J above $J_{z,c1}/J$, only Δ_n closes at the Ising transition point $J_{z,c2}/J$, just as in the case of $D/J = 0$ [compare Figs. 5(a) and 5(b)]. If we turn on the perturbation $\delta\mathcal{H}$ [see Eq. (2)], which breaks the lattice-inversion symmetry explicitly, the EH-OH transition disappears, so that Δ_s stays finite for $g/J = 0.1$, as shown in Fig. 5(b). Thereby, owing to the loss of the criticality at the EH-OH transition, $c^*(L)$ converges to zero for large enough L , as demonstrated in Fig. 4(c).

Comparing the behavior of the excitation gaps with those of the EBHM [17,19], one sees that the spin (neutral) gap in the spin-1 model (1) takes the role of the single-particle (neutral) gap in the EBHM.

2. Entanglement spectra

Let us now analyze the entanglement properties of the topological states for intermediate single-ion anisotropy ($D/J = 1.5$), where both the EH-OH and OH-AFM transitions exist. Here Pollmann *et al.* [10] showed that the SPT state in the OH phase has a twofold degenerate lowest entanglement level for the quantum spin chain model. The infinite-time evolving block decimation procedure used by those authors gives the entanglement spectra data directly in the thermodynamic limit. In the following we show that when simulating the model (1) for a finite system by conventional DMRG, this characteristic degeneracy of the OH phase can also be obtained, but the degree of the degeneracy depends on the boundary conditions.

Figure 6 presents the entanglement spectrum ξ_α for the anisotropic spin-1 XXZ model with $D/J = 1.5$. For a small system ($L = 64$) with PBC [Fig. 6(a)] the lowest entanglement level is fourfold degenerate only deep inside the OH phase. This reflects the possession of the two edges for the subblock $L/2$. Increasing the system size, this degeneracy is observed for a larger region of the OH phase, as demonstrated by Fig. 6(b) for $L = 128$, but close to the EH-OH transition point the lowest entanglement level is still nondegenerate. To overcome this drawback we apply OBC with half-spin edges in the OH phase [cf. Fig. 1(b)]. The same procedure has been used to estimate the magnitude of the Haldane gap at the isotropic Heisenberg point. Figure 6(c) gives ξ_α for $L = 128$ and OBC, pointing out the twofold degeneracy of the lowest level in the nontrivial phase and its nondegeneracy anywhere else. The degeneracy is clearly caused by the single edge spin of subblock $L/2$.

Recently it has been demonstrated for quantum spin chains [10] and the EBHM [18] that the degeneracy of the lowest entanglement level in the OH phase might be lifted by turning on an inversion-symmetry-breaking term, such as (2). Figure 7(a) [Figure 7(c)] exemplifies that the fourfold [twofold] degeneracy with PBC [OBC] indeed dissolves for any finite g . Thereby, the gap between the lowest levels becomes larger as g increases—see Fig. 7(b) [Fig. 7(d)] for PBC [OBC]. Obviously inversion symmetry protects the Haldane phase.

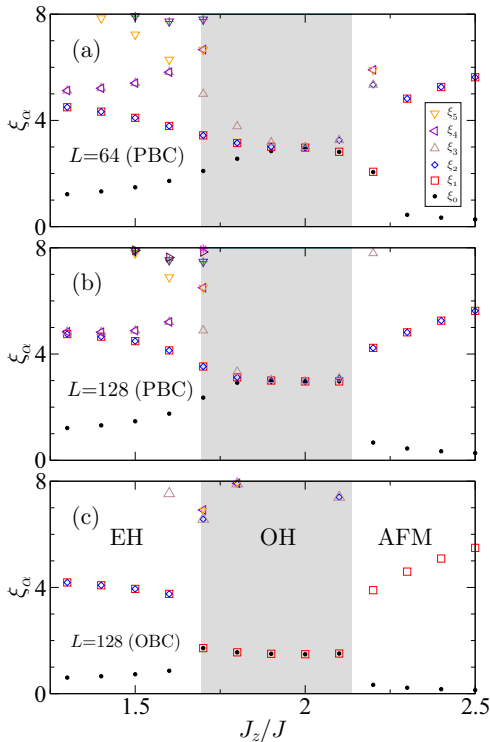


FIG. 6. (Color online) Entanglement spectrum ξ_α of the 1D spin-1 XXZ model (1) with $D = 1.5$. The fourfold degeneracy of the lowest entanglement level can be taken as an indication of a nontrivial Haldane state in the case of DMRG simulations with PBC. As the system size increases, the degeneracy appears in the whole HI phase; compare data for $L = 64$ [(a)] with those for 128 [(b)]. Using OBC and taking spins ($S = 1/2$) at the edges into account, an almost perfect double degeneracy is obtained for the OH phase even for small systems with $L = 128$, as demonstrated in (c).

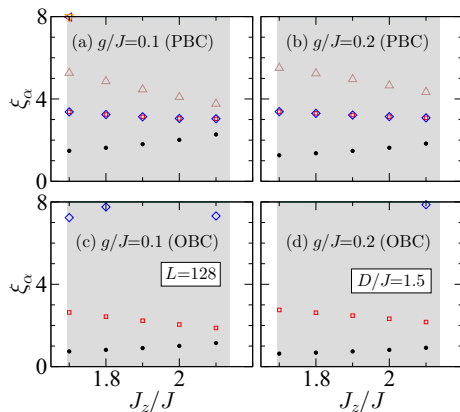


FIG. 7. (Color online) Entanglement spectrum ξ_α if an inversion-symmetry-breaking term is added to the spin-1 chain (1) with $D = 1.5$, where $g/J = 0.1$ (left panels) and 0.2 (right panels). Data obtained by DMRG with PBC (upper panels) and OBC with half-spin edges (lower panels).

3. Multicritical point and EH-AFM transition

Raising the ratios D/J and J_z/J , the EH-OH and OH-AFM critical lines merge at the multicritical point $(J_{z,mc}/J, D_{mc}/J)$. Above this point, i.e., for $J_z > J_{z,mc}$ and $D > D_{mc}$, a direct EH-AFM transition is expected to occur, as pointed out by den Nijs and Rommeles [26]. This has been confirmed numerically by ED, yielding $(J_{z,mc}, D_{mc}) \approx (3.2, 2.9)$ [7]. It is challenging to determine this multicritical point more precisely, but the entanglement analysis outlined above seems to be a powerful tool. Obviously, for fixed values $D > D_{mc}$, the lowest entanglement level is nondegenerate for the whole parameter regime of J_z/J including the EH-AFM transition point, while for $D < D_{mc}$ the lowest entanglement level should be degenerate for a very narrow but finite parameter region of J_z/J . In fact, the double degeneracy can still be observed at $D/J = 2.88$ by large-scale DMRG simulations with $L = 1024$ and OBC [see Fig. 8(a)]. If D/J is increased slightly, the degeneracy is lifted for $L = 1024$ [see Fig. 8(b) for $D/J = 2.90$], but from the results presented we cannot derive a definite conclusion about what happens for $L \rightarrow \infty$. Figure 8(c) indicates that degeneracy disappears already at $D/J = 2.92$. In this way the ED results regarding the existence of the multicritical point is corroborated by our more precise entanglement spectra analysis, yielding $(J_{z,mc}/J, D_{mc}/J) = (3.196 \pm 0.02, 2.90 \pm 0.02)$.

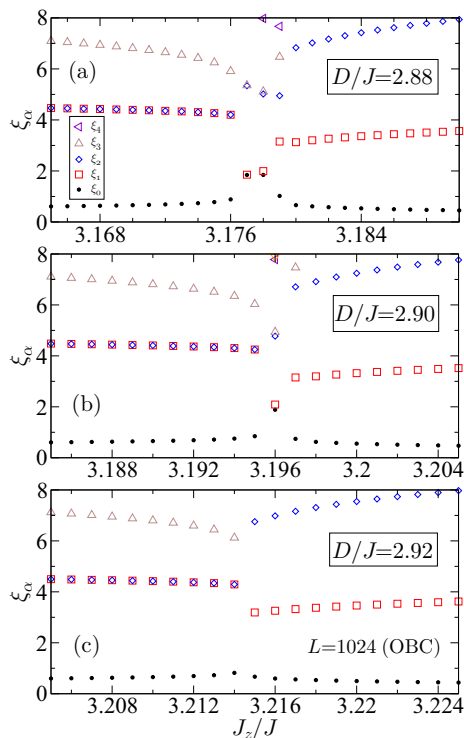


FIG. 8. (Color online) Entanglement spectrum ξ_α for (a) $D/J = 2.88$, (b) 2.90 , and (c) 2.92 close to the EH-OH-AFM multicritical point with $L = 1024$ and OBC, showing the disappearance of the double degeneracy of the lowest entanglement levels.

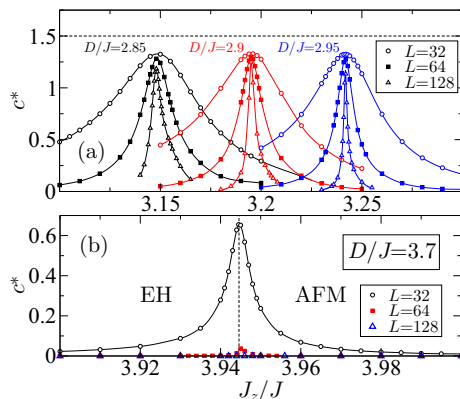


FIG. 9. (Color online) Central charge c^* of the 1D spin-1 XXZ model (1), (a) near the multicritical point D_{mc}/J and (b) across the first-order EH-AFM transition for $D/J = 3.7$. The dashed line in (b) denotes the EH-AFM transition point $D/J \simeq 3.9446$ according to Ref. [33].

Certainly it is of great interest to look at the behavior of the central charge at the multicritical point. Here the central charge might be $c = 1 + 1/2 = 3/2$ because BKT- and Ising-transition lines merge. Figure 9(a) displays the numerically obtained central charge $c^*(L)$ for fixed values of D/J in the vicinity of the multicritical point. We see that $c^*(L)$ is always smaller than $3/2$ and decreases with increasing system size L . Unfortunately, the system-size dependence of $c^*(L)$ is much stronger than those, e.g., at $D/J = 1.5$, in Fig. 4; so it turns out that even $L = 128$ is not large enough to precisely determine the value of the central charge. Maybe the use of the infinite-system DMRG [16] can resolve this problem.

Increasing D/J further, a quantum phase transition occurs between EH and AFM phases. A discontinuous staggered magnetization suggests that this transition is of first order [7]. Quite recently, this was corroborated by analyzing the energy level crossing [33]. The numerically determined central charge $c^*(L)$ at $D/J = 3.7$ yields a further signature of the first-order transition [see Fig. 9(b)]. For small system sizes ($L = 32$), c^* shows a peak at $J_z/J \simeq 3.945$, in accord with the EH-AFM transition point in Ref. [33]. With increasing the system size L , c^* decreases drastically and becomes already zero for $L = 128$, which confirms the results of former studies [7,33].

C. Ground-state phase diagram

Figure 10 displays the DMRG ground-state phase diagram of the spin-1 XXZ model with single-ion anisotropy. The EH-OH and OH-AFM phase boundaries can be derived from central charge c^* , as explained above: Again we obtain a very good agreement with former ED and DMRG data [7,34]. Most notably, the nontrivial OH phase appears in between the trivial EH and AFM phases, just as the topological HI phase develops between the MI and DW phases in the EBHM. Therefore, we have included in Fig. 10 the phase boundaries of the MI-HI and HI-DW transitions for the EBHM with $n_b = 2$ (taken from Ref. [18]). Qualitatively, the phase diagram of the spin-1 model looks quite similar to those of the EBHM, except for

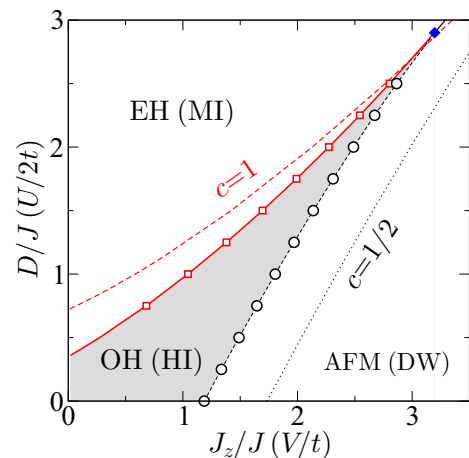


FIG. 10. (Color online) DMRG ground-state phase diagram of the 1D spin-1 XXZ model with single-ion anisotropy (1). Shown are the even Haldane (EH), odd Haldane (OH), and antiferromagnetic (AFM) phases. The EH-OH (squares) and OH-AFM (circles) transition points are determined from the central charge $c = 1$ and $c = 1/2$, respectively, which was extracted from the von Neumann entropy via Eq. (7). The EH-OH transition line was confirmed by a careful finite-size scaling of the two low-lying energy levels with TBC. The solid diamond gives the EH-OH-AFM multicritical point determined from the entanglement analysis. Error bars are smaller than symbols. The dashed (dotted) line denotes the MI-HI (HI-DW) transition in the EBHM with $n_b = 2$ bosons per site (taken from Ref. [18]).

the existence of the superfluid (SF) phase in the EBHM (not shown). Quantitatively, the topological phase of the EBHM captures a larger region in parameter space than the OH phase, however. This might be caused by the particle-hole symmetry-breaking term $\hat{\mathcal{H}}'$ in Eq. (4).

D. Dynamical structure factor

Let us finally discuss the spin dynamical properties of the spin-1 XXZ model.

Figure 11 reveals our DDMRG results for $S^{zz}(k, \omega)$ obtained for the spin-1 model (with anisotropy $D/J = 1.5$) inside the three insulating phases, as well as at the quantum phase transition points in between. In the EH phase, at $J_z/J = 1$, most of the spectral weight is concentrated in the momentum range $\pi/2 < k < \pi$ [see Fig. 11(a)]. The excitation gap appears at $k \approx 0$. The dispersion of the maximum in $S^{zz}(k, \omega)$ behaves cosinelike for small-to-intermediate momenta, and is flattened close to the Brillouin zone boundary (above $k \geq 3\pi/4$). With increasing J_z/J , the EH-OH transition occurs at $J_z/J = J_{z,c1}/J \simeq 1.694$, where the excitation gap closes at the momentum $k = 0$, as shown in Fig. 11(b). Deep in the Haldane phase, the situation changes drastically [see Fig. 11(c) for $J_z/J = 1.9$]. Now the dispersion of the maximum in $S^{zz}(k, \omega)$ takes a sinelike form. Again there are finite excitation gaps at $k = 0$ (Haldane gap) and π . This resembles the behavior found at the isotropic Heisenberg point [30]. Here the spectral weight exclusively concentrates at $k \approx \pi$ and finite but small $\omega \ll J$. We finally ask whether the gap in $S^{zz}(k, \omega)$ again

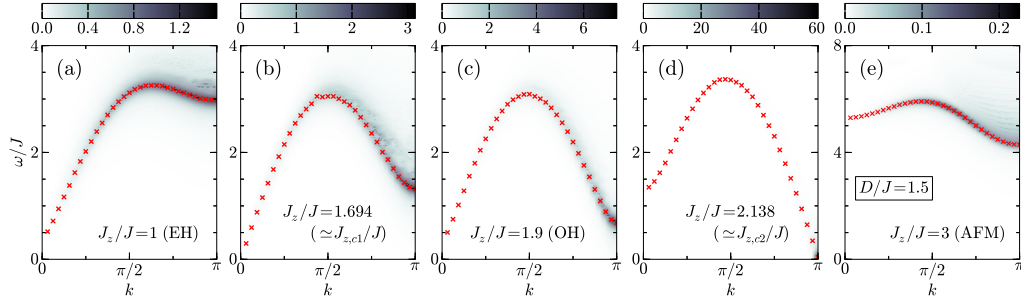


FIG. 11. (Color online) Intensity plots of the dynamical structure factor $S^{zz}(k, \omega)$ for (a) $J_z/J = 1$, (b) $J_z/J = 1.694 \simeq J_{z,c1}/J$, (c) $J_z/J = 1.9$, (d) $J_z/J = 2.138 \simeq J_{z,c2}/J$, and (e) $J_z/J = 3$. Data are obtained by the DDMRG technique for $L = 64$, using PBC and a Lorentzian broadening $\eta = 0.1t$. Crosses give the maximum value of $S^{zz}(k, \omega)$ at fixed momenta $k = 2\pi j/L$ with $j = 1, \dots, L/2$.

closes at the OH-AFM transition if J_z/J is increased further. Figure 11(d) shows that the gap indeed closes, at $J_z/J = 2.138$ ($\simeq J_{z,c2}/J$), but this time at momentum $k = \pi$, reflecting the lattice-period doubling in the AFM phase. Obviously, $S^{zz}(k, \omega)$ follows the behavior of the neutral gap Δ_n shown in Fig. 5. In the AFM phase [see Fig. 11(e) with $J_z/J = 3$], the dispersion becomes flattened with a large excitation gap that opens at $k = \pi$, however. That is, the dynamical spin structure factor shows a distinct behavior in each phase of the spin-1 model with single-ion anisotropy. Interestingly, the results obtained in the EH, OH, and AFM phases are similar to those for the MI, HI, and DW phases of the 1D EBHM [18]. This corroborates that the spin-1 model can be taken as an effective model for the EBHM with $n_b = 2$.

V. SUMMARY

We studied the topological properties of the anisotropic spin-1 XXZ model with single-ion anisotropy in close analogy to a recent investigation of the extended Bose-Hubbard model (EBHM) with a nearest-neighbor repulsion [18]. The focus was on the nontrivial Haldane phase as well. The phase boundaries between trivial phases [even Haldane (EH) and AFM phases] and nontrivial odd Haldane (OH) phase were determined numerically with high precision via the central charge. The ground-state phase diagram resembles those of the restricted EBHM with a maximum number of bosons per site $n_b = 2$, but the topological phase takes a much narrower region in the parameter space. Simulating the spin and neutral gaps, which correspond to the single-particle respectively neutral gaps in the EBHM, we confirmed the closing of the gap at the trivial-nontrivial quantum phase transition as for the EBHM.

The degeneracy of the lowest entanglement level in the OH phase could be observed by finite-system DMRG calculations with both periodic (P) and open (O) boundary conditions (BC). With PBC the lowest level in the entanglement spectrum is fourfold degenerate in the OH phase; notably, the system-size dependence of the results is much stronger than for OBC. Adopting half spins ($S = 1/2$) at the open edges, the twofold degeneracy corresponding to a single artificial edge in the entanglement calculations can be detected easily. This degeneracy will be lifted turning on a finite perturbation that

breaks the inversion symmetry of the lattice, independently from the BC used.

We furthermore used the dynamical DMRG technique to examine the dynamical spin structure $S^{zz}(k, \omega)$ which mimics the dynamical density fluctuations in the EBHM. In the topological $S = 1$ OH phase a sinus-shaped dispersion was observed for finite anisotropy D just as for the isotropic Heisenberg model and the Haldane-insulator state of the EBHM. Moreover, $S^{zz}(k, \omega)$ shows a significant different momentum and energy dependence in three different gapful phases for both the spin-1 model and the EBHM. We finally note that the influence of the particle-hole symmetry-breaking term $\tilde{\mathcal{H}}$ in Eq. (4) on the properties of the constrained EBHM is almost negligible, not only for static but also for dynamical quantities.

ACKNOWLEDGMENTS

The authors would like to thank Y. Fuji, F. Göhmann, F. Lange, S. Nishimoto, and F. Pollmann for valuable discussions. This work was supported by Deutsche Forschungsgemeinschaft (Germany), SFB 652, B5.

APPENDIX: HALDANE GAP

After Haldane's conjecture about the finite excitation gaps for integer-spin chains [1], it was a challenging issue to estimate these so-called Haldane gaps numerically (note that even the spin-1 XXZ Heisenberg chain is not integrable). White presented the first accurate DMRG results for the Haldane gap [20], and subsequently a series of more elaborated DMRG [21,38,40], quantum Monte Carlo (QMC) [37], and ED [39] studies have been performed. However, only OBC have been used within the DMRG framework so far, mainly because of the smaller computational costs. In this Appendix, we demonstrate—at least for the spin-1 Heisenberg model—that the Haldane gap can also be determined using PBC, and the system-size dependence of the gap is much smaller than those with OBC adopting the half-spin edges [cf. Fig. 1(b)]. Hence any finite-size scaling is needless.

Figure 12 presents the finite-size extrapolation of the corresponding spin and neutral excitation gaps, as defined in Sec. III B, for both OBC and PBC. The spin and neutral gaps

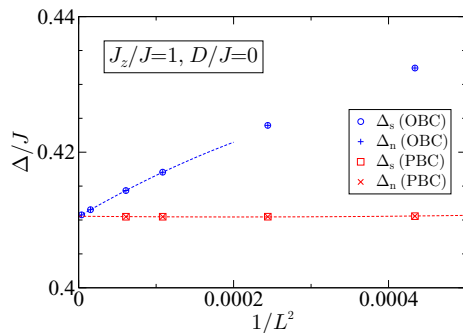


FIG. 12. (Color online) Finite-size scaling of the excitation gaps at the Heisenberg point ($D = 0$ and $J_z/J = 1$).

become equal (Δ) only at the Heisenberg point for $D = 0$ [cf. Fig. 5(a)]. Computing Δ for systems with up to $L = 512$ sites and OBC, we can extrapolate the results to the thermodynamic limit and obtain $\Delta = 0.41050(3)$ (in agreement with Ref. [38]). On the other hand, the first excitation gaps $\Delta = 0.41047924(4)$ obtained with PBC and up to $m = 4800$ density-matrix states show almost no finite-size dependence;

TABLE I. First excitation gap Δ in the spin-1 XXZ chain as obtained by QMC, ED, and DMRG for a system size L , at temperature T , using the specified boundary conditions BC.

Method	L	Δ	T	BC
QMC [37]	128	0.41048(6)	0.015625	PBC
DMRG [38]	120	0.41050(2)	0	OBC
ED [39]	24	0.41047(8)	0	TBC
DMRG [40]	2048	0.4104792485(4)	0	OBC
DMRG (this work)	96	0.4104792(7)	0	PBC
DMRG (this work)	128	0.41047924(4)	0	PBC

see also the raw data for $L = 96$ and $L = 128$ in Table I. This value is very close to the (low-temperature) QMC [37] and ED [39] results and shows a perfect agreement with the very recent non-Abelian DMRG data with OBC [40]. Let us emphasize that although the accessible system size is rather limited for PBC, Δ for PBC is always lower than for OBC. Most notably, the system-size dependence is almost negligible (for enough large L), so that sophisticated extrapolation techniques or the use of special boundary conditions [39,40] are no longer mandatory for analyzing the Haldane gap in spin-1 chains.

- [1] F. D. M. Haldane, *Phys. Rev. Lett.* **50**, 1153 (1983).
- [2] W. J. L. Buyers, R. M. Morra, R. L. Armstrong, M. J. Hogan, P. Gerlach, and K. Hirakawa, *Phys. Rev. Lett.* **56**, 371 (1986).
- [3] J. P. Renard, M. Verdaguier, L. P. Regnault, W. A. C. Erkelens, J. Rossat-Mignod, and W. G. Stirling, *Europhys. Lett.* **3**, 945 (1987).
- [4] S. Ma, C. Broholm, D. H. Reich, B. J. Sternlieb, and R. W. Erwin, *Phys. Rev. Lett.* **69**, 3571 (1992).
- [5] I. Affleck, T. Kennedy, E. H. Lieb, and H. Tasaki, *Phys. Rev. Lett.* **59**, 799 (1987).
- [6] T. Kennedy and H. Tasaki, *Phys. Rev. B* **45**, 304 (1992).
- [7] W. Chen, K. Hida, and B. C. Sanctuary, *Phys. Rev. B* **67**, 104401 (2003).
- [8] K. Nomura, *J. Phys. A* **28**, 5451 (1995).
- [9] Z.-C. Gu and X.-G. Wen, *Phys. Rev. B* **80**, 155131 (2009).
- [10] F. Pollmann, A. M. Turner, E. Berg, and M. Oshikawa, *Phys. Rev. B* **81**, 064439 (2010).
- [11] T. Tonegawa, K. Okamoto, H. Nakano, T. Sakai, K. Nomura, and M. Kaburagi, *J. Phys. Soc. Jpn.* **80**, 043001 (2011).
- [12] K. Okamoto, T. Tonegawa, H. Nakano, T. Sakai, K. Nomura, and M. Kaburagi, *J. Phys.: Conf. Ser.* **302**, 012014 (2011).
- [13] K. Okamoto, T. Tonegawa, H. Nakano, T. Sakai, K. Nomura, and M. Kaburagi, *J. Phys.: Conf. Ser.* **320**, 012018 (2011).
- [14] Y.-C. Tzeng, *Phys. Rev. B* **86**, 024403 (2012).
- [15] F. Pollmann, E. Berg, A. M. Turner, and M. Oshikawa, *Phys. Rev. B* **85**, 075125 (2012).
- [16] J. A. Kjäll, M. P. Zaletel, R. S. K. Mong, J. H. Bardarson, and F. Pollmann, *Phys. Rev. B* **87**, 235106 (2013).
- [17] E. G. Dalla Torre, E. Berg, and E. Altman, *Phys. Rev. Lett.* **97**, 260401 (2006).
- [18] S. Ejima, F. Lange, and H. Fehske, *Phys. Rev. Lett.* **113**, 020401 (2014).
- [19] E. Berg, E. G. Dalla Torre, T. Giamarchi, and E. Altman, *Phys. Rev. B* **77**, 245119 (2008).
- [20] S. R. White, *Phys. Rev. Lett.* **69**, 2863 (1992).
- [21] S. R. White, *Phys. Rev. B* **48**, 10345 (1993).
- [22] E. Jeckelmann and H. Fehske, *Riv. Nuovo Cimento* **30**, 259 (2007).
- [23] E. G. D. Torre, *J. Phys. B: At. Mol. Opt. Phys.* **46**, 085303 (2013).
- [24] E. Jeckelmann, *Phys. Rev. B* **66**, 045114 (2002).
- [25] H. J. Schulz, *Phys. Rev. B* **34**, 6372 (1986).
- [26] M. den Nijs and K. Rommelse, *Phys. Rev. B* **40**, 4709 (1989).
- [27] H. Li and F. D. M. Haldane, *Phys. Rev. Lett.* **101**, 010504 (2008).
- [28] P. Calabrese and J. Cardy, *J. Stat. Mech.* (2004) P06002.
- [29] S. Nishimoto, *Phys. Rev. B* **84**, 195108 (2011).
- [30] M. Takahashi, *Phys. Rev. B* **50**, 3045 (1994).
- [31] S. R. White and I. Affleck, *Phys. Rev. B* **77**, 134437 (2008).
- [32] A. Kitazawa, K. Nomura, and K. Okamoto, *Phys. Rev. Lett.* **76**, 4038 (1996).
- [33] G.-H. Liu, W. Li, W.-L. You, G. Su, and G.-S. Tian, *Physica B* **443**, 63 (2014).
- [34] H. Ueda, H. Nakano, and K. Kusakabe, *Phys. Rev. B* **78**, 224402 (2008).
- [35] A. Kitazawa and K. Nomura, *J. Phys. Soc. Jpn.* **66**, 3379 (1997).
- [36] A. Kitazawa and K. Nomura, *J. Phys. Soc. Jpn.* **66**, 3944 (1997).
- [37] S. Todo and K. Kato, *Phys. Rev. Lett.* **87**, 047203 (2001).
- [38] S. R. White and D. A. Huse, *Phys. Rev. B* **48**, 3844 (1993).
- [39] H. Nakano and A. Terai, *J. Phys. Soc. Jpn.* **78**, 014003 (2009).
- [40] H. Ueda and K. Kusakabe, *Phys. Rev. B* **84**, 054446 (2011).

Ising Deconfinement Transition between Feshbach-Resonant Superfluids

S. Ejima,¹ M. J. Bhaseen,² M. Hohenadler,³ F. H. L. Essler,⁴ H. Fehske,¹ and B. D. Simons²

¹*Institut für Physik, Ernst-Moritz-Arndt-Universität Greifswald, 17489 Greifswald, Germany*

²*Cavendish Laboratory, University of Cambridge, Cambridge, CB3 0HE, United Kingdom*

³*Institut für Theoretische Physik und Astrophysik, Universität Würzburg, Germany*

⁴*The Rudolf Peierls Centre for Theoretical Physics, University of Oxford, Oxford, OX1 3NP, United Kingdom*

(Received 21 September 2010; revised manuscript received 16 November 2010; published 7 January 2011)

We investigate the phase diagram of bosons interacting via Feshbach-resonant pairing interactions in a one-dimensional lattice. Using large scale density matrix renormalization group and field theory techniques we explore the atomic and molecular correlations in this low-dimensional setting. We provide compelling evidence for an Ising deconfinement transition occurring between distinct superfluids and extract the Ising order parameter and correlation length of this unusual superfluid transition. This is supported by results for the entanglement entropy which reveal both the location of the transition and critical Ising degrees of freedom on the phase boundary.

DOI: 10.1103/PhysRevLett.106.015303

PACS numbers: 67.85.Hj, 05.30.Rt, 67.85.Fg

The ability to cool atoms to low temperatures, and control their interactions, has revolutionized the study of quantum many body systems. Important achievements include realizations of Bose-Einstein condensation (BEC), Bardeen-Cooper-Schrieffer (BCS) pairing in Fermi gases, and strongly correlated Mott insulators (MIs). In this development, the BEC-BCS crossover between a gas of tightly bound molecules and weakly bound Cooper pairs has played an instrumental role, and it has been widely explored using Feshbach resonances to induce pairing. This has led to diverse studies of the condensate fraction, single-particle gap, collective excitations, and vortices, and to pioneering approaches to molecular quantum chemistry. For a review see Ref. [1].

In recent work [2–6] it has been argued that the BEC-BCS “crossover” for bosons is strikingly different from the fermionic case since the atoms as well as molecules may undergo Bose-Einstein condensation. These studies have raised the exciting possibility of an Ising quantum phase transition between distinct molecular (MC) and atomic plus molecular (AC + MC) condensates. In addition to discrete \mathbb{Z}_2 symmetry breaking, this transition has a topological character and may be viewed as a confinement-deconfinement transition for vortices.

The principal aim of this Letter is to establish the presence of such novel \mathbb{Z}_2 transitions in 1D bosonic Feshbach systems, where strong quantum fluctuations destabilize long-range superfluid order. We combine large scale density matrix renormalization group (DMRG) [7] and field theory techniques to provide compelling evidence for Ising behavior. We elucidate a full characterization of the scaling regime and the proximate phases. Our results demonstrate that an Ising transition survives at strong coupling and large densities where field theory arguments are no longer justified. For related transitions in the attractive Bose-Hubbard model with three-body losses, see

Refs. [8,9], and for analogues involving multicomponent fermions, see [10,11].

We consider the Hamiltonian [4,6,12]

$$H = \sum_{i\alpha} \epsilon_{\alpha} n_{i\alpha} - \sum_{\langle ij \rangle} \sum_{\alpha} t_{\alpha} (b_{i\alpha}^{\dagger} b_{j\alpha} + \text{H.c.}) + \sum_{i\alpha\alpha'} \frac{U_{\alpha\alpha'}}{2} : n_{i\alpha} n_{i\alpha'} : + H_F, \quad (1)$$

describing bosons $b_{i\alpha}$ hopping on a lattice with sites i , where $\alpha = a, m$ labels atoms and molecules. Here, ϵ_{α} are on-site potentials, t_{α} are hopping parameters, $\langle ij \rangle$ denotes summation over nearest neighbor bonds, and $U_{\alpha\alpha'}$ are interactions. Normal ordering yields $: n_{i\alpha} n_{i\alpha} : := n_{i\alpha}(n_{i\alpha} - 1)$ for like species and $: n_{i\alpha} n_{i\alpha'} : := n_{i\alpha} n_{i\alpha'}$ for distinct species. Molecules are formed by the Feshbach term, $H_F = g \sum_i (m_i^{\dagger} a_i a_i + \text{H.c.})$, where $m_i \equiv b_{im}$ and $a_i \equiv b_{ia}$. Atoms and molecules are not conserved, but the total, $N_T \equiv \sum_i (n_{ia} + 2n_{im})$, is preserved.

To orient the discussion, we present a section of the phase diagram in Fig. 1, with parameters chosen for comparison with previous studies [6]. In this Letter we use DMRG on a 1D system with up to $L = 512$ sites and adopt units where $t_a = 1$. We allow up to five atoms and five molecules per site and retain up to $m_{\rho} = 2400$ states in the density matrix so that the discarded weight is less than 1×10^{-10} . The phase boundaries correspond to the vanishing of the one-particle and two-particle excitation gaps, $E_{1g} \equiv \mu_{1p}(L) - \mu_{1h}(L)$ and $E_{2g} \equiv \mu_{2p}(L) - \mu_{2h}(L)$, respectively, where $\mu_{np}(L) = E_0(L, N_T + n) - E_0(L, N_T)$, $\mu_{nh}(L) = E_0(L, N_T) - E_0(L, N_T - n)$, and E_0 is the ground state energy. The diagram shows a MI with gaps for both excitations $E_{1g} \neq 0$ and $E_{2g} \neq 0$, a MC phase with a one-particle gap $E_{1g} \neq 0$ and $E_{2g} = 0$, and a coupled atomic plus molecular condensate (AC + MC) with $E_{1g} = 0$ and $E_{2g} = 0$. In contrast to the qualitative

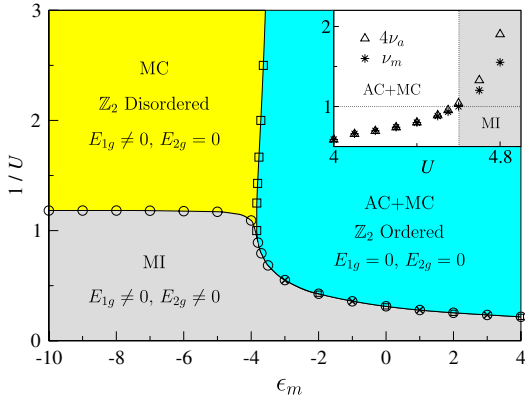


FIG. 1 (color online). Phase diagram of the 1D Hamiltonian (1) with total density $\rho_T = N_T/L = 2$, showing a Mott insulator (MI), a molecular condensate (MC), and a coupled atomic plus molecular condensate (AC + MC). We use DMRG with up to $L = 128$ and open boundaries, with $\epsilon_a = 0$, $U_{aa}/2 = U_{mm}/2 = U_{am} = g = U$, $t_a = 1$, $t_m = 1/2$. The squares and circles indicate the vanishing of the one-particle and two-particle gaps, E_{1g} and E_{2g} , as $L \rightarrow \infty$. The crosses show where the molecular correlation exponent ν_m reaches unity. Inset: AC + MC to MI transition at $\epsilon_m = 4$. The atomic and molecular exponents, ν_a and ν_m , are locked up to the MI boundary where $\nu_m = 1$, indicating the absence of an AC phase.

diagram in Ref. [6], inferred from quantum Monte Carlo simulations on smaller systems, we find no evidence for a single-component AC phase. This is in accord with expectations in higher dimensions [2]. As we will discuss, this is supported by direct evaluation of correlation functions using both DMRG and field theory. Throughout the AC + MC phase we find power laws for atoms *and* molecules with related exponents; see inset of Fig. 1. The conclusions of Ref. [6] are hampered by the slow divergence of the associated zero-momentum molecular occupation number with increasing L , close to the MI boundary. This also afflicts the molecular visibility. Here, our focus is on the transition between the MC and AC + MC superfluids. We begin with symmetry arguments and field theory predictions before comparison with DMRG.

An intuitive way to understand the origin of the proposed Ising transition between the MC and AC + MC phases is via the symmetry of the Hamiltonian (1) under $U(1) \times \mathbb{Z}_2$ transformations. This corresponds to invariance under $m \rightarrow e^{i\theta}m$ and $a \rightarrow e^{i(\theta/2 \pm \pi)}a$, where $\theta \in \mathbb{R}$. In general these symmetries may be broken independently. Before discussing the problem in 1D, where continuous $U(1)$ symmetry breaking is absent, let us first recall the situation in higher dimensions [2]. In this case, the MC phase has $\langle m \rangle \neq 0$ and $\langle a \rangle = 0$. This only breaks the $U(1)$ contribution and leaves the \mathbb{Z}_2 symmetry, $a \rightarrow -a$, intact; this corresponds to the disordered phase of an Ising model, coexisting with molecular superfluidity. On the other hand, the coupled atomic plus molecular condensate (AC + MC)

phase has $\langle m \rangle \neq 0$ and $\langle a \rangle \neq 0$. This breaks the $U(1) \times \mathbb{Z}_2$ symmetry completely and corresponds to the ordered phase of an Ising model, coexisting with atomic and molecular superfluidity. Returning to the present 1D problem, where continuous $U(1)$ symmetry breaking is absent, the spontaneous formation of expectation values $\langle a \rangle$ and $\langle m \rangle$ is prohibited. Instead, superfluid order is characterized by long-range power law correlations, and the nature of the phases and transitions in Fig. 1 requires closer inspection.

Owing to the $U(1) \times \mathbb{Z}_2$ symmetry of the Hamiltonian, the low energy Lagrangian of the MC to AC + MC transition is given by $\mathcal{L} = \mathcal{L}_\vartheta + \mathcal{L}_\phi + \mathcal{L}_{\vartheta\phi}$ [2,3], where

$$\mathcal{L}_\vartheta = \frac{K_\vartheta}{2} [c_\vartheta^{-2}(\partial_\tau \vartheta)^2 + (\partial_x \vartheta)^2] \quad (2)$$

is a $U(1)$ invariant free scalar field, and

$$\mathcal{L}_\phi = \frac{K_\phi}{2} [c_\phi^{-2}(\partial_\tau \phi)^2 + (\partial_x \phi)^2] - \eta \phi^2 + \lambda \phi^4 \quad (3)$$

is an Ising model in the soft-spin ϕ^4 representation. The coupling, $\mathcal{L}_{\vartheta\phi} = i\phi^2 \partial_\tau \vartheta / 2$, has a similar form to a Berry phase [2,3]. A similar action also emerges for quantum wires [13]. In the following we neglect $\mathcal{L}_{\vartheta\phi}$ and examine the reduced theory. Within mean field theory, $\mathcal{L}_{\vartheta\phi} \sim i\langle \phi \rangle^2 \partial_\tau \vartheta / 2$ acts like a boundary term, and this is expected to provide a good description of the proximate phases. Near the transition, this cannot be neglected *a priori*, and $\mathcal{L}_{\vartheta\phi}$ may change the behavior on very large length scales and in other regions of the phase diagram [13]. Nonetheless, we find excellent agreement with bulk properties. The parameters K_ϑ , c_ϑ , K_ϕ , c_ϕ , η , λ are related to the coefficients of H . Atoms and molecules are described by the semiclassical number-phase relations, $m \sim \sqrt{\rho_m} e^{i\vartheta}$ and $a \sim \phi e^{i\vartheta/2}$, where ρ_m is the molecular density. We will explore the consequences of this correspondence in 1D, for local observables and correlations.

Let us first gather consequences of this correspondence for local observables. Deep within the \mathbb{Z}_2 disordered MC phase, $\eta \gg 0$ and $\langle \phi(x) \rangle = 0$. However, $\phi^2(x)$ may have a nonzero average. It follows that the densities of atoms and molecules, $\langle a^\dagger(x)a(x) \rangle \sim \langle \phi^2(x) \rangle$ and $\langle m^\dagger(x)m(x) \rangle \sim \rho_m$, are generically nonzero in *both* the AC + MC and MC phases. In addition, $\langle m^\dagger(x)a(x)a(x) \rangle \sim \sqrt{\rho_m} \langle \phi^2(x) \rangle$ acquires true long-range order, even in this 1D setting; H_F locks the atomic and molecular condensates as encoded in the number-phase relations. However, this local average is naively insensitive to the \mathbb{Z}_2 transition due to invariance under $a \rightarrow -a$. Insight is better gleaned from correlations.

It follows from the relation $m \sim \sqrt{\rho_m} e^{i\vartheta}$ that the molecular correlation function $\langle m^\dagger(x)m(0) \rangle \sim \rho_m \langle e^{-i\vartheta(x)} e^{i\vartheta(0)} \rangle \sim x^{-\nu_m}$ decays like a power law, where $\nu_m = 1/2\pi K_\vartheta$ varies throughout the phase diagram. In contrast, the behavior of the atomic correlations, $\langle a^\dagger(x)a(0) \rangle \sim \langle \phi(x)\phi(0) \rangle \langle e^{-i\vartheta(x)/2} e^{i\vartheta(0)/2} \rangle \sim \langle \phi(x)\phi(0) \rangle x^{-\nu_m/4}$, depends on the Ising prefactor. We consider the disordered and ordered phases in turn.

In the \mathbb{Z}_2 disordered MC phase, the atomic correlation function decays exponentially with a power law prefactor, $\langle a^\dagger(x)a(x) \rangle \sim x^{-\nu_m/4} K_0(x/\xi) \sim x^{-1/2-\nu_m/4} e^{-x/\xi}$. Here we use the result for the hard-spin Ising model, $\langle \phi(x)\phi(0) \rangle \sim K_0(x/\xi)$, where K_0 is a modified Bessel function and ξ is the Ising correlation length [14]. On the other hand, *pairs* of atoms condense and exhibit power law correlations, $\langle a^\dagger(x)a^\dagger(x)a(0)a(0) \rangle \sim \langle \phi^2 \rangle^2 x^{-\nu_m}$, with the *same* exponent as the molecular two-point function ν_m . That is to say, the MC phase is a pairing phase of bosons without single-particle condensation [15]. In order to test these weak coupling predictions we perform DMRG on the 1D Hamiltonian (1). As predicted, this behavior is well supported by our simulations in Fig. 2(a), which reveal identical power laws for molecules and atomic bilinears, with exponential decay for atoms. This behavior extends throughout the MC phase, including the Mott boundary in the strongly coupled regime.

In contrast, in the \mathbb{Z}_2 ordered AC + MC phase, both molecules and atoms have power law correlations, $\langle m^\dagger(x)m(0) \rangle \sim x^{-\nu_m}$, $\langle a^\dagger(x)a(0) \rangle \sim \langle \phi \rangle^2 x^{-\nu_a}$, with locked exponents, $\nu_m = 4\nu_a$, that differ by a factor of 4 [2,3]. Again, these features are readily seen from our large scale DMRG simulations in Fig. 2(b) and the inset of Fig. 1. Likewise, this behavior persists into the strong coupling limit, where the field theory approach no longer strictly applies. In particular, we have checked that the molecular correlation function, $\langle m^\dagger(x)m(0) \rangle \sim x^{-\nu_m}$, remains a

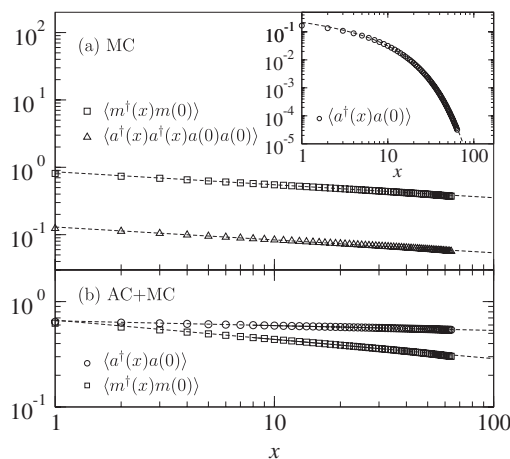


FIG. 2. Correlation functions using DMRG with $L = 128$ and open boundaries. We use the parameters in Fig. 1 with $U = 0.7$. (a) \mathbb{Z}_2 disordered MC phase with $\epsilon_m = -4$, revealing power laws for molecules and atomic bilinears with the same exponent; the fits are $y = 0.858x^{-0.1922}$ and $y = 0.130x^{-0.1909}$. Inset: Atomic correlations decay exponentially. We fit to the prediction $\langle a^\dagger(x)a(0) \rangle \sim x^{-\nu_m/4} K_0(x/\xi)$, where we input ν_m from (a) and extract $\xi \approx 9.28$. This establishes MC as a pairing phase without atomic condensation. (b) \mathbb{Z}_2 ordered AC + MC phase with $\epsilon_m = -3$. Atoms and molecules exhibit power law exponents locked by a factor of 4; the fits are $y = 0.667x^{-0.1827}$ and $y = 0.657x^{-0.0456}$.

power law throughout the AC + MC phase and close to the Mott boundary in Fig. 1. This is consistent with the absence of an AC phase [2] in contrast to Ref. [6]. The latter employ the zero-momentum occupation $n(0)$. However, the Fourier transform of $x^{-\nu}$ gives $n(0) \sim \text{const} + \text{const} L^{1-\nu}$; close to the MI where $\nu_m = 1$, one may miss the slow divergence of $n_m(0)$.

Having established a close connection between field theory and DMRG for the MC and AC + MC phases, let us now examine the transition. A key diagnostic is the central charge c , which counts critical degrees of freedom. This may be obtained from the entanglement entropy. For a block of length l in a periodic system of length L , the von Neumann entropy is given by $S_L(l) = -\text{Tr}_l(\rho_l \ln \rho_l)$, where $\rho_l = \text{Tr}_{L-l}(\rho)$ is the reduced density matrix. One obtains [16]

$$S_L(l) = \frac{c}{3} \ln \left[\frac{L}{\pi} \sin \left(\frac{\pi l}{L} \right) \right] + s_1, \quad (4)$$

where s_1 is a constant. As may be seen in Fig. 3, the numerically extracted central charge of the MC phase yields $c = 1$, as one would expect for a free boson, with coexisting gapped degrees of freedom. In addition, the AC + MC phase also has $c = 1$. Note that it is *not* $c = 2$ as would be the case

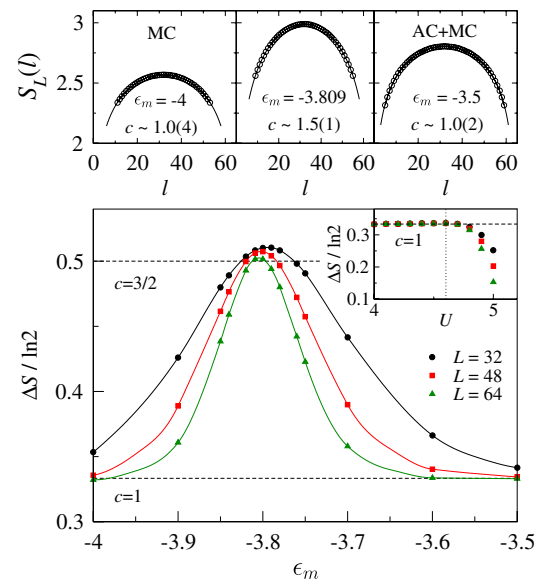


FIG. 3 (color online). Top: Entanglement entropy $S_L(l)$ obtained by DMRG in a periodic system with $L = 64$. We transit through the AC to AC + MC transition in Fig. 1 with $U = 0.7$. The fits to Eq. (4) yield $c \approx 1$ in the MC and AC + MC phases, and $c \approx 3/2$ close to the transition. This reflects additional critical \mathbb{Z}_2 degrees of freedom. Because of the asymptotic nature of Eq. (4), high quality fits are obtained from the central region away from the boundaries. Bottom: Entanglement entropy difference $\Delta S(L)$ showing an Ising transition at $\epsilon_m \approx -3.8$ for $U = 0.7$, in agreement with Fig. 1. The solid lines are spline fits. Inset: ΔS on passing through the AC + MC to MI transition at $\epsilon_m = 4$, suggesting an XY transition with $c = 1$.

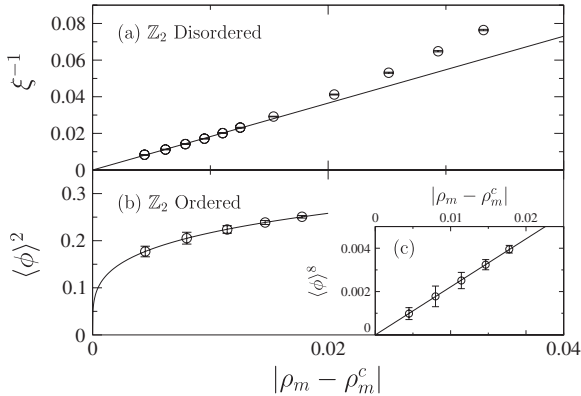


FIG. 4. DMRG with open boundaries. We use the parameters in Fig. 1 with $U = 0.7$ and transit from MC to AC + MC. \mathbb{Z}_2 disordered MC phase (a) ξ extracted from the atomic correlations with $L = 256$. $\xi^{-1} \sim |\rho_m - \rho_m^c|^\nu$, where ρ_m ($\rho_m^c \approx 0.85$) is the (critical) density of molecules and $\nu = 1$. \mathbb{Z}_2 ordered AC + MC phase (b) $\langle \phi \rangle^2$ up to a constant prefactor, obtained by finite size scaling of the atomic correlations with up to $L = 512$. (c) Replotting yields $\beta = 1/8$.

for two independent Luttinger liquids. This reflects the coupled nature of the atomic and molecular condensates in the AC + MC phase, with additional gapped Ising degrees of freedom; the Feshbach term is relevant and drives the \mathbb{Z}_2 sector massive. Close to the MC to AC + MC transition, where the anticipated Ising gap closes, one expects the central charge to increase to $c = 3/2$, due to *additional* critical Ising degrees of freedom with $c = 1/2$. This is confirmed by DMRG in Fig. 3. Further evidence is obtained from the difference [17], $\Delta S(L) \equiv S_L(L/2) - S_{L/2}(L/4) = \frac{c}{3} \times \ln(2) + \dots$, as a function of ϵ_m ; see Fig. 3. For a given L this displays a peak, whose location coincides with the MC to AC + MC transition obtained via the single-particle gap in Fig. 1. The evolution with increasing L is consistent with the passage towards $c = 1$ in the superfluid phases and $c = 3/2$ in the vicinity of the transition. Application of this method to the MI to superfluid transitions [4] yields $c = 1$ close to the MI boundary, suggesting XY behavior; see inset of Fig. 3. The absence of criticality within the MI phase is evidence against a super-Mott state [6] and correlations decay exponentially [12,18].

Having provided evidence for a \mathbb{Z}_2 superfluid transition, we now extract the Ising correlation length ξ and order parameter $\langle \phi \rangle$ via finite size scaling of the atomic and molecular correlations. Because of the absence of particle conservation, and the presence of additional superfluid degrees of freedom, these cannot be readily obtained from the energy spectra alone. Ising scaling close to the transition implies that $\xi^{-1} \sim |\mathcal{M} - \mathcal{M}_c|$ and $\langle \phi \rangle \sim |\mathcal{M} - \mathcal{M}_c|^{1/8}$, where \mathcal{M} is a mass scale parametrizing the departure from criticality. We identify the molecular density, $\mathcal{M} \sim \rho_m$, as the appropriate scaling variable. As shown in Fig. 4, the DMRG results are in excellent

agreement with Ising critical exponents. This is nontrivial since the Ising degrees of freedom are nonlocal with respect to the atoms and molecules themselves.

In summary, we have studied bosons interacting via Feshbach interactions in a 1D lattice. We provide evidence for an Ising quantum phase transition between distinct superfluids. We extract both the \mathbb{Z}_2 order parameter $\langle \phi \rangle$ and the Ising correlation length ξ . It would be interesting to see if this \mathbb{Z}_2 transition may be driven first order and the effect of higher bands [19]. One may also consider \mathbb{Z}_N transitions involving N -particle pairing.

We thank F. Assaad, S. Capponi, N. Cooper, S. Diehl, M. Garst, Z. Hadzibabic, E. Jeckelmann, M. Köhl, A. Lamacraft, A. Läuchli, C. Lobo, and A. Silver for discussions. M. J. B. and B. D. S. acknowledge EPSRC Grant No. EP/E018130/1. F. H. L. E. was supported by EP/D050952/1. S. E. and H. F. acknowledge DFG Grant No. SFB 652. M. H. was supported by DFG FG1162.

- [1] W. Ketterle and M. W. Zwierlein, in *Ultra-cold Fermi Gases*, Proceedings of the International School of Physics “Enrico Fermi,” Course CLXIV, edited by M. Inguscio, W. Ketterle, and C. Salomon (IOS Press, Amsterdam, 2007).
- [2] L. Radzihovsky, J. Park, and P. B. Weichman, *Phys. Rev. Lett.* **92**, 160402 (2004); M. W. J. Romans *et al.*, *ibid.* **93**, 020405 (2004); L. Radzihovsky *et al.*, *Ann. Phys. (N.Y.)* **323**, 2376 (2008).
- [3] Y.-W. Lee and Y.-L. Lee, *Phys. Rev. B* **70**, 224506 (2004); *Phys. Rev. A* **73**, 043606 (2006).
- [4] D. B. M. Dickerscheid *et al.*, *Phys. Rev. A* **71**, 043604 (2005); K. Sengupta and N. Dupuis, *Europhys. Lett.* **70**, 586 (2005).
- [5] V. Gurarie, *Phys. Rev. A* **73**, 033612 (2006).
- [6] V. G. Rousseau and P. J. H. Denteneer, *Phys. Rev. Lett.* **102**, 015301 (2009); *Phys. Rev. A* **77**, 013609 (2008).
- [7] S. R. White, *Phys. Rev. Lett.* **69**, 2863 (1992).
- [8] A. J. Daley *et al.*, *Phys. Rev. Lett.* **102**, 040402 (2009); **102**, 179902(E) (2009); S. Diehl *et al.*, *Phys. Rev. Lett.* **104**, 165301 (2010).
- [9] S. Diehl, M. Baranov, A. J. Daley, and P. Zoller, *Phys. Rev. B* **82**, 064509 (2010); **82**, 064510 (2010).
- [10] C. Wu, *Phys. Rev. Lett.* **95**, 266404 (2005); P. Lecheminant, E. Boulat, and P. Azaria, *Phys. Rev. Lett.* **95**, 240402 (2005).
- [11] S. Capponi *et al.*, *Phys. Rev. B* **75**, 100503(R) (2007); G. Roux *et al.*, *Eur. Phys. J. B* **68**, 293 (2008).
- [12] M. J. Bhaseen, A. O. Silver, M. Hohenadler, and B. D. Simons, *Phys. Rev. Lett.* **103**, 265302 (2009).
- [13] M. Sitte *et al.*, *Phys. Rev. Lett.* **102**, 176404 (2009).
- [14] T. T. Wu *et al.*, *Phys. Rev. B* **13**, 316 (1976).
- [15] J. G. Valatin *et al.*, *Nuovo Cimento* **10**, 37 (1958).
- [16] C. Holzhey *et al.*, *Nucl. Phys.* **B424**, 443 (1994); P. Calabrese and J. Cardy, *J. Stat. Mech.* (2004) P06002.
- [17] A. M. Läuchli *et al.*, *J. Stat. Mech.* (2008) P05018.
- [18] M. Eckholt and T. Roscilde, *Phys. Rev. Lett.* **105**, 199603 (2010).
- [19] H. P. Büchler, *Phys. Rev. Lett.* **104**, 090402 (2010).

Discrete symmetry breaking transitions between paired superfluids

M. J. Bhaseen,¹ S. Ejima,² F. H. L. Essler,³ H. Fehske,² M. Hohenadler,⁴ and B. D. Simons¹

¹*Cavendish Laboratory, University of Cambridge, Cambridge CB3 0HE, United Kingdom*

²*Institut für Physik, Ernst-Moritz-Arndt-Universität Greifswald, 17489 Greifswald, Germany*

³*The Rudolf Peierls Centre for Theoretical Physics, University of Oxford, Oxford OX1 3NP, United Kingdom*

⁴*Institut für Theoretische Physik und Astrophysik, Universität Würzburg, 97074 Würzburg, Germany*

(Received 24 November 2011; revised manuscript received 24 February 2012; published 26 March 2012)

We explore the zero-temperature phase diagram of bosons interacting via Feshbach resonant pairing interactions in one dimension. Using DMRG (density matrix renormalization group) and field theory techniques we characterize the phases and quantum phase transitions in this low-dimensional setting. We provide a broad range of evidence in support of an Ising quantum phase transition separating distinct paired superfluids, including results for the energy gaps, correlation functions, and entanglement entropy. In particular, we show that the Ising correlation length, order parameter and critical properties are directly accessible from a ratio of the atomic and molecular two-point functions. We further demonstrate that both the zero-momentum occupation numbers and the visibility are in accordance with the absence of a purely atomic superfluid phase. We comment on the connection to recent studies of boson pairing in a generalized classical XY model.

DOI: [10.1103/PhysRevA.85.033636](https://doi.org/10.1103/PhysRevA.85.033636)

PACS number(s): 67.85.Hj, 67.85.Fg, 05.30.Rt

I. INTRODUCTION

The rapid progress in manipulating ultracold atomic gases has led to new approaches to strongly interacting quantum systems. This includes the properties of highly correlated states of matter, such as Bose-Einstein condensates (BECs) [1,2], Mott insulators [3], and supersolids [4]. It also allows access to the phase transitions and crossovers between these fascinating phases. In the last few years, the BEC-BCS crossover [5–8] between a molecular BEC and a Bardeen-Cooper-Schrieffer (BCS) pairing state, has stimulated a wealth of experimental activity using fermionic atoms [9–16]. This has been achieved through the use of Feshbach resonances, which enable one to control the strength of pairing interactions using a magnetic field. This has not only opened the door to central problems in condensed matter physics, but also offers insights into the quantum chemistry of molecule formation and chemical reactions [17].

In tandem with these advances, Feshbach resonances and molecule formation have also been studied in bosonic systems [18–26]. Recent experiments have been performed both in optical traps [27–29] and in optical lattices [30]; for a review see Ref. [31]. On the theoretical side, the BEC-BCS “crossover” problem for bosons has also been investigated in the continuum limit [32–34] and on the lattice [35–40]. The problem differs markedly from the fermionic case since the carriers themselves may Bose condense. This leads to the possibility of an Ising quantum phase transition occurring between distinct paired superfluids [32–34]. The phases are distinguished by the presence or absence of carrier condensation, and the associated quantum phase transition involves discrete \mathbb{Z}_2 symmetry breaking. Closely related phases and quantum phase transitions have also been observed in multicomponent fermion systems [41–44], and in the attractive Bose-Hubbard model with a restricted three particle Hilbert space [45–51]. There are also magnetic analogs in quantum spin chains [52]. More recently, the phenomenon of boson pairing has also been explored in the context of a generalized classical XY model with two competing harmonics

in the periodic interactions [53–56]. This has led to the prediction of a novel phase diagram with unusual criticality.

Motivated by the possibility of stabilizing pairing phases of bosons [57–62] in cold atomic gases, we recently investigated the bosonic Feshbach resonance problem in one dimension (1D) [63]. We employed large scale DMRG (density matrix renormalization group) [64] and field theory techniques [63] in order to incorporate the effects of enhanced quantum fluctuations in 1D. Among our findings, we presented compelling evidence for an Ising quantum phase transition separating distinct superfluids.¹ The aim of the present manuscript is to shed further light on this novel transition, and to provide a thorough discussion of the superfluid phases in this 1D setting. In particular, we describe a variety of methods to extract the Ising characteristics from the gapless superfluid background. We also provide a quantitative finite-size scaling analysis of the zero-momentum occupation numbers and the visibility. Our results are consistent with the absence of a purely atomic superfluid phase with noncondensed molecules, in contrast to the earlier suggestions of Refs. [37,38].

The layout of this paper is as follows. In Sec. II we present the Hamiltonian under investigation and in Sec. III we discuss the phase diagram. In Sec. IV we describe the associated field theory and gather our predictions for a variety of local expectation values and correlation functions. We use these results to characterize the different phases and to establish a detailed comparison with DMRG. In Sec. V we provide a quantitative account of the finite-size scaling of the zero-momentum occupation numbers and the visibility. We contrast our results with those of Refs. [37,38]. In Sec. VI we discuss the behavior of the entanglement entropy and the emergence of Ising criticality at the transition between the distinct paired superfluids. We also discuss the behavior at the superfluid-Mott insulator transitions. In Sec. VII we

¹In this 1D setting we use the terms “superfluid” and “condensate” to indicate a phase with power-law correlations.

describe the Ising scaling regime, and discuss a variety of ways to extract the principal Ising characteristics. This includes the Ising order parameter and the correlation length using a finite-size scaling analysis of the atomic and molecular correlation functions. We also discuss the utility of a suitable ratio of the atomic and molecular two-point functions for analyzing the Ising quantum phase transition. We conclude in Sec. VIII and provide further directions for research.

II. MODEL

We consider the Hamiltonian

$$H = \sum_{i\alpha} \epsilon_{\alpha} n_{i\alpha} - \sum_i \sum_{\alpha} t_{\alpha} (b_{i\alpha}^{\dagger} b_{i+1\alpha} + \text{H.c.}) + \sum_{i\alpha\alpha'} \frac{U_{\alpha\alpha'}}{2} n_{i\alpha} (n_{i\alpha'} - \delta_{\alpha\alpha'}) + H_{\text{F}}, \quad (1)$$

describing bosons $b_{i\alpha}$ hopping on a 1D lattice with sites i , where $\alpha = a, m$ labels atoms and molecules [35–40]. Here ϵ_{α} are on-site potentials, t_{α} are nearest neighbor hopping parameters, and $U_{\alpha\alpha'}$ are interactions. We assume that molecule formation is described by the s -wave Feshbach resonance term,

$$H_{\text{F}} = g \sum_i (m_i^{\dagger} a_i a_i + \text{H.c.}), \quad (2)$$

where we denote $m_i \equiv b_{im}$ and $a_i \equiv b_{ia}$; for recent work on the p -wave problem see Refs. [65,66]. This conversion implies that the number of atoms and molecules are not separately conserved, but the total $N_{\text{T}} \equiv \sum_i (n_{ia} + 2n_{im})$ is preserved. For simplicity, in writing Eq. (1) we neglect any effects of higher Bloch bands in optical lattices [67–69]. In this respect, the Hamiltonian (1) may be regarded as a lattice regularization of the continuum models studied in Refs. [32–34]; see also Refs. [24–26]. This approach is very convenient for numerical simulations, and enables us to investigate the superfluid transitions where lattice effects are germane. It also allows us to make contact with previous quantum Monte Carlo (QMC) simulations [37,38] and to place the problem on a firmer footing. As in the original works [32–34], we neglect the effects of three-body losses and finite molecular lifetimes.

In this paper we use DMRG on 1D systems with up to $L = 512$ sites, where we set the lattice spacing to unity and adopt energy units where $t_a = 1$. We furthermore set $t_m = 1/2$ throughout. We work in the canonical ensemble with the total density $\rho_{\text{T}} = N_{\text{T}}/L = 2$ held fixed and allow up to five atoms and five molecules per site, corresponding to a large Hilbert space of dimension $(6 \times 6)^L$; for a discussion of the effects of changing the local Hilbert space dimension see Appendix. With open (periodic) boundary conditions we retain up to $m_{\rho} = 2400$ ($m_{\rho} = 3000$) states in the density matrix in order to ensure that the discarded weight is less than 1×10^{-10} (1×10^{-8}).

III. PHASE DIAGRAM

As we discussed in Ref. [63], the qualitative phase diagram of the 1D lattice Hamiltonian (1) was previously considered using QMC simulations [37,38]. In addition to delineating the Mott insulating and superfluid phase boundaries, this work led to intriguing predictions of superfluidity within the

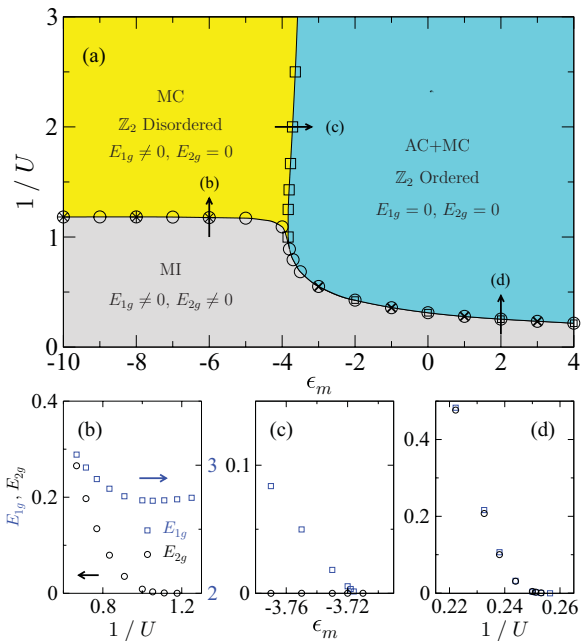


FIG. 1. (Color online) (a) Phase diagram of the 1D Hamiltonian (1) with total density $\rho_{\text{T}} = N_{\text{T}}/L = 2$, showing a Mott insulator (MI), a molecular condensate (MC), and a coupled atomic plus molecular condensate (AC + MC). We use DMRG with up to $L = 128$ sites and open boundary conditions. We choose parameters $\epsilon_a = 0$, $U_{aa}/2 = U_{mm}/2 = U_{am} = g = U$, $t_a = 1$, $t_m = 1/2$, for comparison with Ref. [37]. The squares and circles indicate the vanishing of the one-particle and two-particle gaps E_{1g} and E_{2g} , respectively, as $L \rightarrow \infty$. The stars and crosses indicate where the molecular and atomic correlation exponents ν_m and ν_a reach $1/4$ in the MC and AC + MC phases, respectively. These values correspond to a molecular KT transition and an atomic KT transition, respectively. The remaining panels (b), (c), and (d) show the variation of the extrapolated gaps E_{1g} and E_{2g} with $L \rightarrow \infty$ on passing through the phase boundaries at the corresponding points in panel (a). In particular, we provide detailed evidence for an Ising quantum phase transition occurring between the MC and AC + MC phases.

Mott phase, and an additional superfluid phase not present in mean-field theory [32–36]. Although we find very good quantitative agreement with many of the numerical results [37,38], these additional predictions are at variance with our recent findings [63] which combine field theory with DMRG. This was also suggested by our earlier studies using hardcore bosons [39,40]. It has recently been argued that the absence of particle conservation hindered the interpretation of these previous QMC simulations [70]. In this paper we will further demonstrate that the use of momentum space observables, including the zero-momentum occupation numbers and the visibility, also complicated the interpretation of these earlier finite-size QMC simulations.

In order to put the problem on a more stable platform, we present a section of the phase diagram in Fig. 1, with parameters chosen for comparison with Ref. [37]. (Note that our conventions differ from Ref. [37] by a factor of $1/2$ in the interaction terms so that double occupancy corresponds

directly to $U_{\alpha\alpha'}$. Also, ϵ_m plays the role of their detuning parameter D when $\epsilon_a = 0$.) The phase boundaries shown in Fig. 1 correspond to the vanishing of the one-particle and two-particle excitation gaps, $E_{1g} \equiv \mu_{1p}(L) - \mu_{1h}(L)$ and $E_{2g} \equiv \mu_{2p}(L) - \mu_{2h}(L)$, respectively, where the data are extrapolated to the thermodynamic limit $L \rightarrow \infty$. Here

$$\begin{aligned} \mu_{np}(L) &= [E_0(L, N_T + n) - E_0(L, N_T)] / n, \\ \mu_{nh}(L) &= [E_0(L, N_T) - E_0(L, N_T - n)] / n, \end{aligned} \quad (3)$$

where $E_0(L, N)$ is the ground state energy for a system of size L and a total number N of atoms and molecules. The phase diagram in Fig. 1 consists of three distinct phases: a Mott insulator (MI) with gaps for both excitations $E_{1g} \neq 0$ and $E_{2g} \neq 0$, a molecular condensate (MC) with a one-particle gap $E_{1g} \neq 0$ and $E_{2g} = 0$, and a coupled atomic plus molecular condensate (AC + MC) with $E_{1g} = 0$ and $E_{2g} = 0$. As we shall discuss more fully below, the MC phase may be interpreted as a pairing phase of bosons in the absence of atomic condensation. In contrast, the AC + MC phase has both molecular and atomic condensation. In comparison to the qualitative phase diagram presented in Ref. [37], inferred from QMC simulations on smaller system sizes, we find no evidence for a single-component atomic superfluid phase coexisting with noncondensed molecules. This is in accord with theoretical expectations in higher dimensions, where atomic condensation is always accompanied by molecular condensation [32–34] provided the molecules are present; in the extreme limit where $\epsilon_m \rightarrow \infty$, occurring on the boundary of the AC + MC phase, the molecules are explicitly excluded by the chemical potential as shown in Fig. 2. The conclusions of Ref. [37] have also come under scrutiny due to the additional claims of superfluidity within the Mott phase [39,70]. Here, however, our main focus is on the character of the transition between the distinct MC and AC + MC superfluids. In the subsequent discussion we will begin with symmetry arguments and field theory predictions before turning to a comparison with DMRG.

IV. FIELD THEORY DESCRIPTION

A heuristic way to understand the possibility of an Ising quantum phase transition between the distinct MC and AC + MC superfluids is via the generic number-phase relationships $a \sim \sqrt{\rho_a} e^{i\vartheta_a}$ and $m \sim \sqrt{\rho_m} e^{i\vartheta_m}$, where ρ_a and ρ_m are the average atomic and molecular densities respectively. Substituting these expressions into (1), the Feshbach term (2) takes the form [34]

$$H_F \sim 2g\rho_a\sqrt{\rho_m} \cos(\vartheta_m - 2\vartheta_a). \quad (4)$$

Minimizing this interaction locks the phases of the atomic and molecular condensates according to the relationship

$$\vartheta_m - 2\vartheta_a = \pm\pi, \quad (5)$$

where for simplicity we assume $g > 0$. We see that the phases are locked, but only modulo π , and this gives rise to the possibility of a discrete symmetry breaking \mathbb{Z}_2 transition between Feshbach coupled superfluids. Denoting $\vartheta_m \equiv \vartheta$, one

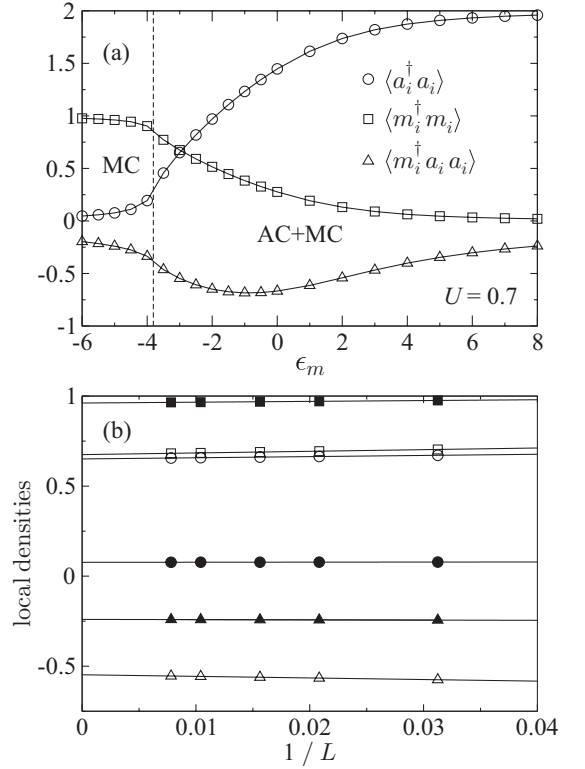


FIG. 2. (a) Local expectation values obtained by DMRG for the 1D Hamiltonian (1) with open boundaries and up to $L = 128$ sites. We use the same parameters as in Fig. 1 and set $U = 0.7$. We plot the local density of atoms $\langle a_i^\dagger a_i \rangle$ (circles), molecules $\langle m_i^\dagger m_i \rangle$ (squares), and the expectation value of the Feshbach conversion term $\langle m_i^\dagger a_i a_i \rangle$ (triangles), evaluated at the system midpoint, $i = L/2$. All of these quantities are generically nonzero on both sides of the MC to AC + MC transition as indicated by the dashed line. In the limit of large positive (negative) detuning ϵ_m we have mainly atoms (molecules) with a density determined by the canonical ensemble constraint $\rho_T = 2$. (b) Corresponding finite-size data and linear extrapolation as a function of $1/L$ for $\epsilon_m = -3$ (open) and $\epsilon_m = -5$ (filled).

may recast the number-phase relationships in the form [34]

$$m \sim \sqrt{\rho_m} e^{i\vartheta}, \quad a \sim \phi e^{i\vartheta/2}, \quad (6)$$

where the Feshbach locking is explicitly enforced and $\phi \sim \sqrt{\rho_a} e^{\mp i\pi/2}$ plays the role of an Ising degree of freedom. The decomposition (6) will play a central role in the subsequent analysis and allows one to gain a handle on the correlation functions and the principal features of the phase diagram.

An alternative way to understand the possibility of an Ising quantum phase transition between the MC and AC + MC phases is via the symmetry of the Hamiltonian (1) under $U(1) \times \mathbb{Z}_2$ transformations:

$$m \rightarrow e^{i\theta} m, \quad a \rightarrow e^{i(\theta/2 \pm \pi)} a, \quad (7)$$

where $\theta \in \mathbb{R}$. Before discussing the problem in 1D, where continuous symmetry breaking is absent, we first consider the behavior in higher dimensions [32–34]. In this case, the

molecular condensate (MC) phase has $\langle m \rangle \neq 0$ and $\langle a \rangle = 0$. This only breaks the U(1) symmetry, and leaves the \mathbb{Z}_2 symmetry $a \rightarrow -a$ unbroken. This corresponds to an Ising degree of freedom in the disordered phase, coexisting with molecular superfluidity. In contrast, the coupled atomic plus molecular condensate (AC + MC) phase has $\langle m \rangle \neq 0$ and $\langle a \rangle \neq 0$. This breaks the $U(1) \times \mathbb{Z}_2$ symmetry completely and corresponds to a \mathbb{Z}_2 ordered Ising degree of freedom, coexisting with atomic and molecular superfluidity. Returning to the present 1D problem, where continuous U(1) symmetry breaking is prohibited, the formation of expectation values for $\langle a \rangle$ and $\langle m \rangle$ is excluded. Instead, superfluidity is characterized by power-law correlations, and the nature of the phases and quantum phase transitions in Fig. 1 requires further examination.

Due to the $U(1) \times \mathbb{Z}_2$ symmetry of the Hamiltonian (1), the low energy Lagrangian of the MC to AC + MC transition is given by $\mathcal{L} = \mathcal{L}_\vartheta + \mathcal{L}_\phi + \mathcal{L}_{\vartheta\phi}$ [34,71], where

$$\mathcal{L}_\vartheta = \frac{K_\vartheta}{2} [c_\vartheta^{-2} (\partial_\tau \vartheta)^2 + (\partial_x \vartheta)^2] \quad (8)$$

is a free bosonic field and

$$\mathcal{L}_\phi = \frac{K_\phi}{2} [c_\phi^{-2} (\partial_\tau \phi)^2 + (\partial_x \phi)^2] - \mathcal{M}\phi^2 + \lambda\phi^4 \quad (9)$$

is an Ising model in the soft-spin ϕ^4 representation. The coupling between the two sectors, $\mathcal{L}_{\vartheta\phi} = i\phi^2 \partial_\tau \vartheta / 2$, has a form similar to a Berry phase [34,71]. A closely related action also arises for tunneling between quantum wires [72]. In the following we will neglect the contribution $\mathcal{L}_{\vartheta\phi}$ and explore the consequences of the reduced action. Sufficiently far away from the transition this can be justified by a mean-field decoupling $\mathcal{L}_{\vartheta\phi} \sim i\langle \phi \rangle^2 \partial_\tau \vartheta / 2$, which reduces the additional interaction to a total derivative term, which can be neglected. The simplified action is therefore expected to provide a good description of the proximate phases. Near the quantum phase transitions, this cannot be neglected *a priori*, and $\mathcal{L}_{\vartheta\phi}$ may change the behavior on very large length scales and in other regions of the phase diagram [72]. However, all of our findings are consistent with expectations based on $\mathcal{L}_\vartheta + \mathcal{L}_\phi$ only. The parameters $K_\vartheta, c_\vartheta, K_\phi, c_\phi, \eta, \lambda$, are related to the coefficients of the Hamiltonian (1), but the details need not concern us here. In this field theory approach, the atoms and molecules are described by the semiclassical number-phase relations given in Eq. (6). In the subsequent discussion we will explore the ramifications of this correspondence in 1D, both for local observables and correlation functions. For complementary work using the Bethe ansatz and bosonization see also Refs. [73,74].

A. Local expectation values

An immediate consequence of the decomposition (6) is that the densities of atoms and molecules

$$\langle m^\dagger(x)m(x) \rangle \sim \rho_m, \quad \langle a^\dagger(x)a(x) \rangle \sim \langle \phi^2 \rangle \quad (10)$$

are generically nonzero in both the MC and AC + MC phases. This is supported by our DMRG results as shown

in Fig. 2(a). These are extrapolated from the finite-size data to $L \rightarrow \infty$, as indicated in Fig. 2(b). In the limit of large positive detuning with $\epsilon_m \rightarrow \infty$ we have mainly atoms as one would naively expect and $\langle a^\dagger(x)a(x) \rangle \sim 2$. Likewise, in the limit of large negative detuning, corresponding to $\epsilon_m \rightarrow -\infty$, we have mainly molecules and $\langle m^\dagger(x)m(x) \rangle \sim 1$. These limiting densities are consistent with working in the canonical ensemble with $\rho_T = \sum_i (n_{ia} + 2n_{im}) / L = 2$ held fixed.

In addition to these local densities the local expectation value of the Feshbach conversion term

$$\langle m^\dagger(x)a(x)a(x) \rangle \sim \sqrt{\rho_m} \langle \phi^2 \rangle \neq 0 \quad (11)$$

is nonzero. It exhibits true long range order, even in this low-dimensional setting. This is a consequence of the relevance of the Feshbach term in the renormalization group sense. Our numerical results in Fig. 2 show that this quantity is indeed finite. In particular, this confirms the locking of the phases of the atomic and molecular condensates (modulo π) on *both* sides of the transition. However, due to the symmetry under $a \rightarrow -a$, the expectation value (11) is naively insensitive to the Ising transition itself, as may be seen in Fig. 2. Further insight into this quantum phase transition and the proximate phases is more readily obtained from correlation functions. We will explore this in more detail below.

B. Green's functions and pairing correlations

The nature of the MC and AC + MC phases shows up most clearly in the atomic and molecular Green's functions $\langle a^\dagger(x)a(0) \rangle$ and $\langle m^\dagger(x)m(0) \rangle$ and the pairing correlations $\langle a^\dagger(x)a^\dagger(x)a(0)a(0) \rangle$. Their spatial dependence is dictated by the correlations of the underlying Ising model in Eq. (9), and we address each phase in turn.

1. \mathbb{Z}_2 disordered MC phase

As follows from the decomposition (6), the molecular Green's function

$$\langle m^\dagger(x)m(0) \rangle \propto \langle e^{-i\vartheta(x)} e^{i\vartheta(0)} \rangle \sim \left(\frac{a_0}{x} \right)^{\nu_m} \quad (12)$$

decays as a power law, where the correlation exponent $\nu_m = 1/(2\pi K_\vartheta)$ varies throughout the phase diagram, and a_0 is a short-distance cutoff. In contrast, in the \mathbb{Z}_2 disordered MC phase, the atomic Green's function

$$\begin{aligned} \langle a^\dagger(x)a(0) \rangle &\propto \langle \phi(x) e^{-i\frac{\vartheta(x)}{2}} \phi(0) e^{i\frac{\vartheta(0)}{2}} \rangle \\ &\sim \left(\frac{a_0}{x} \right)^{\frac{\nu_m}{4}} \mathcal{K}_0(x/\xi) \end{aligned}$$

decays exponentially, where ξ is the Ising correlation length. Here we use the hard-spin fermionic representation of the Ising model to write [75]

$$\langle \phi(x)\phi(0) \rangle \sim \mathcal{K}_0(x/\xi), \quad (13)$$

where \mathcal{K}_0 is a modified Bessel function. On the other hand, *pairs* of atoms exhibit power-law correlations

$$\langle a^\dagger(x)a^\dagger(x)a(0)a(0) \rangle \sim \left(\frac{a_0}{x} \right)^{\nu_p}, \quad (14)$$

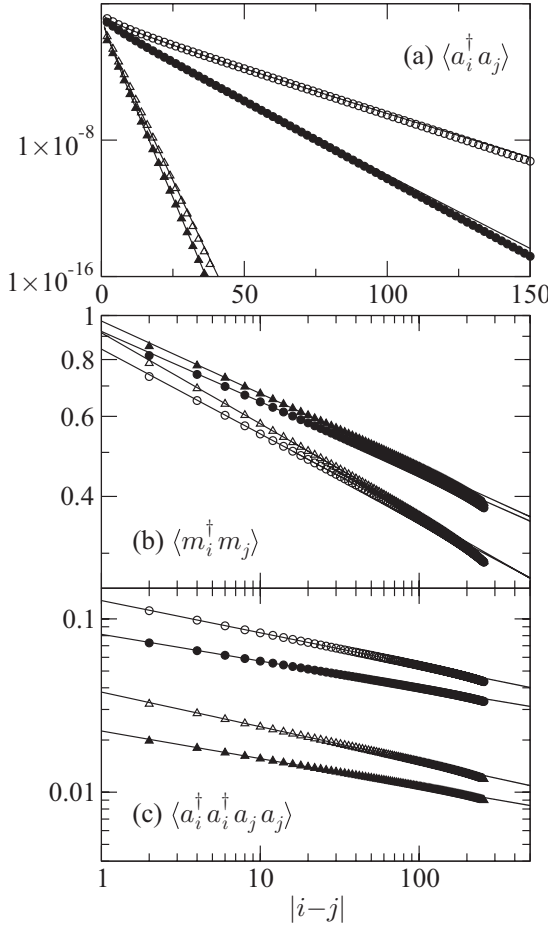


FIG. 3. Correlation functions in the \mathbb{Z}_2 disordered MC phase obtained by DMRG on the 1D Hamiltonian (1) with $L = 512$ and open boundaries. Here and throughout the paper we consider sites displaced around the system midpoint in order to minimize boundary effects. We use the same parameters as in Fig. 1 and set $U = 0.7$ (open), $U = 0.5$ (filled), $\epsilon_m = -4$ (circles), and $\epsilon_m = -6$ (triangles). (a) Atomic Green's function $\langle a_i^\dagger a_j \rangle$ showing exponential decay. (b) Molecular Green's function $\langle m_i^\dagger m_j \rangle$ showing power-law behavior. (c) Bilinears of atoms $\langle a_i^\dagger a_i^\dagger a_j a_j \rangle$ showing power-law behavior with the same exponent as the molecular Green's function in panel (b); see Fig. 4. This establishes the MC phase as a pairing phase of atoms without power-law atomic condensation.

where the exponent $\nu_b = \nu_m$ for these atomic bilinears coincides with the molecular exponent in Eq. (12). That is to say, the MC phase is a pairing phase of bosons without power-law atomic condensation [57–62].

In order to explore these field theory predictions in more detail we perform DMRG on the 1D Hamiltonian (1). The predicted behavior is well supported by our simulations in Fig. 3. The molecules and atomic bilinears show power-law behavior with the same exponent $\nu_m = \nu_b$, while the atomic two-point function shows exponential decay. Our DMRG results also indicate that this behavior persists into the regime

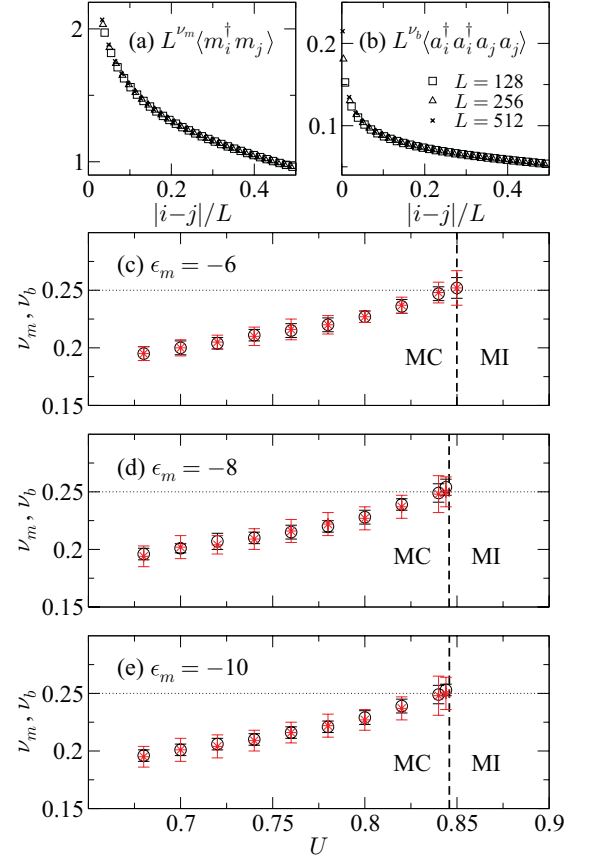


FIG. 4. (Color online) DMRG results for the two-point functions of (a) molecules and (b) atomic bilinears in the MC phase with open boundaries and up to $L = 512$. We extract the molecular and bilinear exponents ν_m and ν_b by finite-size scaling collapse of the data for different system sizes. In (c), (d), and (e) we show the resulting evolution of ν_m (circles) and ν_b (stars) for vertical scans through Fig. 1 with fixed values of ϵ_m . The vertical dashed lines correspond to the location of the MC to MI transition obtained from the gap data. The molecular exponent reaches the value of $\nu_m = 1/4$ at the MC to MI transition. This corresponds to a molecular KT transition and is analogous to the fixed density transition at the tips of the Mott lobes in the single-band Bose-Hubbard model. The critical exponent ν_b associated with the power-law decay of the atomic bilinears $\langle a_i^\dagger a_i^\dagger a_j a_j \rangle$ (stars) coincides with ν_m .

close to the Mott insulating phase boundary shown in Fig. 1. In particular, the molecular correlation exponent reaches the value of $\nu_m = 1/4$ at the MI boundary; see Fig. 4. This is consistent with a molecular Kosterlitz-Thouless (KT) [76,77] transition. It is analogous to the behavior at the tips of the Mott lobes in the single-band Bose-Hubbard model [78–80] where the Luttinger liquid parameter takes the value $K = 1/(2\pi\nu) = 2/\pi$ in the normalization conventions of Eq. (8). The latter transition takes place at constant density, and is therefore compatible with our canonical ensemble constraint $\rho_T = 2$.

We recall that in deriving the above correlation functions we have neglected the coupling term $\mathcal{L}_{\partial\phi}$ in the low-energy

Lagrangian so that the expressions factorize into independent U(1) and \mathbb{Z}_2 contributions. The good agreement with DMRG lends *a posteriori* support to this approximation within the explored region of the phase diagram.

2. \mathbb{Z}_2 ordered AC + MC phase

In the \mathbb{Z}_2 ordered phase the molecular Green's function

$$\langle m^\dagger(x)m(0) \rangle \propto \langle e^{-i\vartheta(x)} e^{i\vartheta(0)} \rangle \sim \left(\frac{a_0}{x}\right)^{\nu_m} \quad (15)$$

continues to decay as a power law. In addition, the atomic Green's function

$$\langle a^\dagger(x)a(0) \rangle \sim \langle \phi \rangle^2 \langle e^{-i\frac{\vartheta(x)}{2}} e^{i\frac{\vartheta(0)}{2}} \rangle \sim \left(\frac{a_0}{x}\right)^{\nu_a} \quad (16)$$

also decays as a power law, where the atomic correlation exponent $\nu_a = \nu_m/4$ is locked to the molecular exponent by a factor of 1/4 [71]. This is a consequence of the Feshbach coupling which ties the phases of the atomic and molecular condensates together. Note that in writing Eq. (16) we approximate the result for the two-point function of the Ising order parameter at leading order [81]:

$$\langle \phi(x)\phi(0) \rangle \sim \langle \phi \rangle^2 [1 + \pi^{-2} \mathcal{F}(x/\xi)] \approx \langle \phi \rangle^2, \quad (17)$$

where

$$\mathcal{F}(z) = z^2 [\mathcal{K}_1^2(z) - \mathcal{K}_0^2(z)] - z\mathcal{K}_0(z)\mathcal{K}_1(z) + \frac{1}{2}\mathcal{K}_0^2(z), \quad (18)$$

and $\mathcal{K}_0(z)$ and $\mathcal{K}_1(z)$ are Bessel functions. These predictions of power-law behavior, as given by Eqs. (15) and (16), are well supported by our numerical simulations as shown in Fig. 5. The locking of the atomic and molecular correlation exponents $\nu_a = \nu_m/4$ is also observed. In addition, these robust features persist into the large- U regime where field theory arguments are no longer strictly valid. In particular, the atomic and molecular correlation functions remain as power laws right up to the MI boundary shown in Fig. 1. We find that the atomic exponent ν_a reaches the value of $\nu_a = 1/4$ at the AC + MC to MI transition; see Fig. 6. This is consistent with an atomic KT transition, as occurs at the tips of the Mott lobes in the single-band Bose-Hubbard model. At the same time, the molecular exponent ν_m reaches the value of $\nu_m = 1$ due to the aforementioned exponent locking; see Fig. 6. The presence of this molecular superfluid close to the MI boundary, clearly supports the absence of a single component atomic superfluid phase in this 1D setting, in contrast to the findings of Ref. [37]. This is also compatible with mean-field theory in higher dimensions [32–34] where atomic condensation is always accompanied by molecular condensation due to the structure of the Feshbach term H_F . We will return to this issue in Sec. V in our discussion of the corresponding zero-momentum occupation numbers and the visibility.

3. Mixed correlation functions

In addition to the purely atomic or molecular Green's functions, it is also instructive to examine the mixed correlation functions involving both atoms and molecules. It follows from

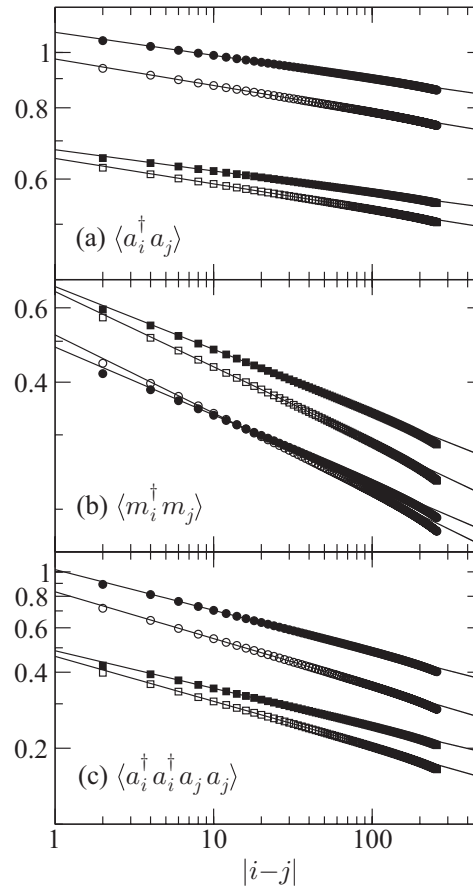


FIG. 5. Correlation functions in the \mathbb{Z}_2 ordered AC + MC phase obtained by DMRG on the 1D Hamiltonian (1) with $L = 512$ and open boundaries. We use the same parameters as in Fig. 1 and set $U = 0.7$ (open), $U = 0.5$ (filled), $\epsilon_m = -2$ (circles), and $\epsilon_m = -3$ (squares). (a) Atomic Green's function $\langle a_i^\dagger a_j \rangle$ showing power-law decay, in contrast to Fig. 3(a). (b) Molecular Green's function $\langle m_i^\dagger m_j \rangle$ showing power-law behavior; the exponent tracks the atomic exponent in panel (a) up to a factor of 4; see Fig. 6. (c) Bilinears of atoms $\langle a_i^\dagger a_i^\dagger a_j a_j \rangle$ showing power-law behavior with the same exponent as the molecular Green's function in panel (b). This establishes the AC + MC phase as a pairing phase of atoms in the presence of atomic condensation.

the decomposition (6) that

$$\langle m^\dagger(x)a(0)a(0) \rangle \sim \sqrt{\rho_m} \langle \phi \rangle^2 \left(\frac{a_0}{x}\right)^{\nu_m} \quad (19)$$

decays as a power law with the same exponent as the molecular Green's function. Once again this reflects the phase locking of the atomic and molecular condensates due to the Feshbach term, and is present in both the MC and AC + MC phases. This behavior is in very good agreement with our DMRG simulations as shown in Fig. 7. In particular, the power-law exponent tracks those displayed in Figs. 3(b) and 5(b) for $\langle m^\dagger(x)m(0) \rangle$.

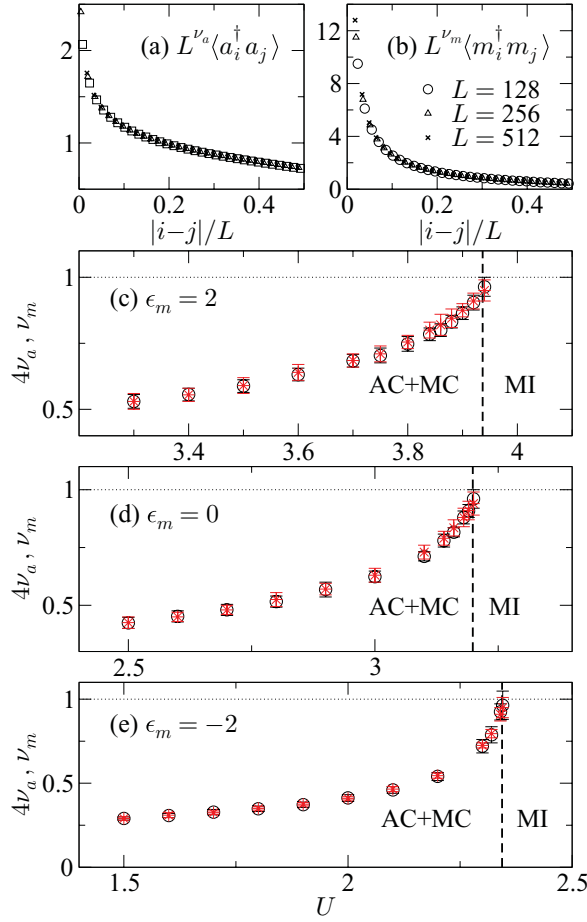


FIG. 6. (Color online) DMRG results for the two-point functions of (a) atoms and (b) molecules in the AC + MC phase with open boundaries and up to $L = 512$. We extract the atomic and molecular exponents ν_a and ν_m by finite-size scaling collapse of the data for different system sizes. In (c), (d), and (e) we show the resulting evolution of $4\nu_a$ (circles) and ν_m (stars) for vertical scans through Fig. 1 with fixed values of ϵ_m . The vertical dashed lines correspond to the location of the AC + MC to MI transition obtained from the gap data. The data confirm the locking of the atomic and molecular exponents via the relation $\nu_m = 4\nu_a$. The exponents reach the values of $\nu_a = 1/4$ and $\nu_m = 1$ at the MI boundary. This is consistent with an atomic KT transition. It is analogous to the behavior at the tips of the Mott lobes in the single-band Bose-Hubbard model.

C. Density correlation functions

Having discussed the atomic and molecular Green's functions we now turn our attention to the correlation functions of the local densities. Denoting $n_m(x) \equiv m^\dagger(x)m(x)$ and $n_a(x) \equiv a^\dagger(x)a(x)$ one obtains

$$\begin{aligned} n_m(x) &\sim \rho_m + \gamma_1 \partial_x \vartheta + \dots, \\ n_a(x) &\sim \rho_a + \gamma_2 \partial_x \vartheta + \gamma_3 : \phi^2(x) : + \dots, \end{aligned} \quad (20)$$

where ρ_m and ρ_a are the average molecular and atomic densities, and $\gamma_1, \gamma_2, \gamma_3$ are constants. Here we use the primary correspondence given in Eq. (6), and combine the

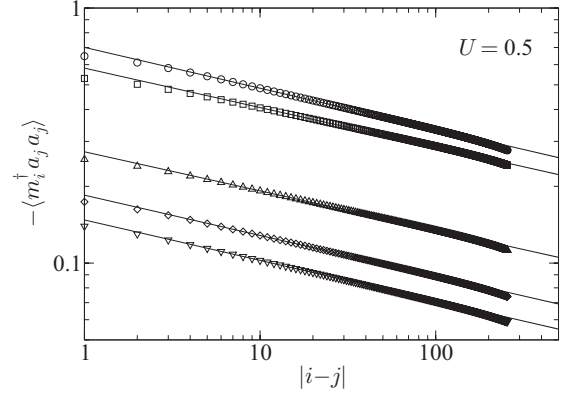


FIG. 7. DMRG results for the mixed correlation function $-\langle m_i^\dagger a_j a_j \rangle$ with $L = 512$ sites, open boundaries and $U = 0.5$. The data correspond to $\epsilon_m = -2$ (circles), $\epsilon_m = -3$ (squares), $\epsilon_m = -4$ (up triangles), $\epsilon_m = -5$ (diamonds), $\epsilon_m = -6$ (down triangles), and show power-law behavior in both the AC and AC + MC phases. As predicted by Eq. (19), the exponents agree with those of the molecular Green's function in panels (b) of Figs. 3 and 5.

exponentials by point splitting and the short distance operator product expansion. The expansion (20) incorporates the effects of density fluctuations and it follows that the density-density correlations have the same leading dependence in both the MC and AC + MC phases:

$$\langle n_\alpha(x)n_\beta(0) \rangle \simeq \rho_\alpha \rho_\beta + \frac{C_{\alpha\beta}}{x^2} + \dots, \quad (21)$$

where $\alpha, \beta \in a, m$, and $C_{\alpha\beta}$ are nonuniversal constants. This is confirmed by our DMRG results in Figs. 8 and 9.

V. MOMENTUM SPACE OBSERVABLES

In the previous section we have focused directly on the superfluid correlation functions due to the absence of continuous symmetry breaking in 1D. However, a useful diagnostic of superfluidity in higher dimensions is the divergence of the occupation number

$$n_\alpha(k) = \frac{1}{L} \sum_{i,j=1}^L e^{ik(i-j)} \langle a_{\alpha,i}^\dagger a_{\alpha,j} \rangle \quad (22)$$

at zero momentum $k = 0$. This quantity was recently used in Ref. [37], in conjunction with visibility data, to argue in favor of a single component atomic superfluid phase in the 1D system (1). In view of our results in the previous sections, which show the presence of both atomic and molecular superfluidity right up to the Mott boundary in Fig. 1, we revisit this issue here. As shown in Fig. 6, the atomic and molecular correlation functions in the AC + MC phase are power laws, $\langle m^\dagger(x)m(0) \rangle \sim x^{-\nu_m}$ and $\langle a^\dagger(x)a(0) \rangle \sim x^{-\nu_a}$, with locked exponents. Substituting these asymptotic forms into Eq. (22) suggests that the zero-momentum occupation numbers depend on system size according to [82,83]

$$n_m(0) \sim \mathcal{A}_m + \mathcal{B}_m L^{1-\nu_m}, \quad n_a(0) \sim \mathcal{A}_a + \mathcal{B}_a L^{1-\nu_a/4}, \quad (23)$$

where $\mathcal{A}_{\alpha,m}$ and $\mathcal{B}_{\alpha,m}$ are constants. In particular, since the molecular exponent ν_m only reaches unity at the Mott phase

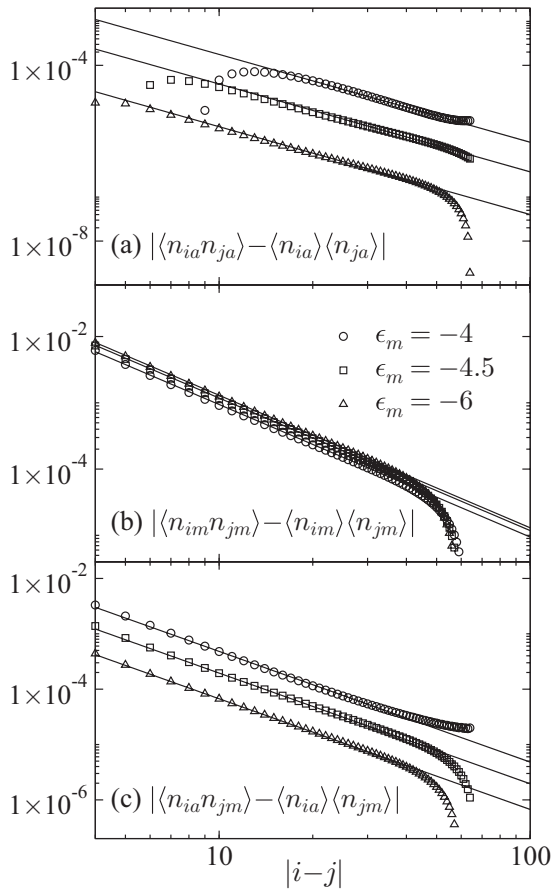


FIG. 8. DMRG results for the connected density correlation functions in the \mathbb{Z}_2 disordered MC phase for the parameters used in Fig. 1. The values of ϵ_m are indicated in panel (b). We use open boundaries with $L = 128$ and set $U = 0.7$. (a) $|\langle n_{ia} n_{ja} \rangle - \langle n_{ia} \rangle \langle n_{ja} \rangle|$. (b) $|\langle n_{im} n_{jm} \rangle - \langle n_{im} \rangle \langle n_{jm} \rangle|$. (c) $|\langle n_{ia} n_{jm} \rangle - \langle n_{ia} \rangle \langle n_{jm} \rangle|$. The results are in agreement with the leading $1/x^2$ dependence predicted by Eq. (21).

boundary (see Figs. 1 and 6) both of these zero-momentum occupation numbers are expected to diverge with increasing system size. This is supported by our DMRG results as shown in Fig. 10. However, it is evident from Eq. (23) that $n_m(0)$ diverges very slowly with increasing system size close to the MI boundary since $v_m \rightarrow 1$. In the absence of a detailed finite-size scaling analysis this may lead to the erroneous conclusion of a purely atomic superfluid. In addition, our findings suggest the absence of any change in behavior in the convergence properties of $n_m(0)$ as $L \rightarrow \infty$, which could be misinterpreted as a quantum phase transition to a purely atomic superfluid. In general, in this 1D setting, the zero-momentum occupation number is a poor diagnostic of superfluid transitions since it may simply reflect a change in the value of the critical exponent within a superfluid phase, rather than the onset of exponential correlations. Direct evaluation of the correlation functions $\langle a^\dagger(x)a(0) \rangle$ and $\langle m^\dagger(x)m(0) \rangle$ provides a clearer picture in 1D, especially in the case of a finite size system.

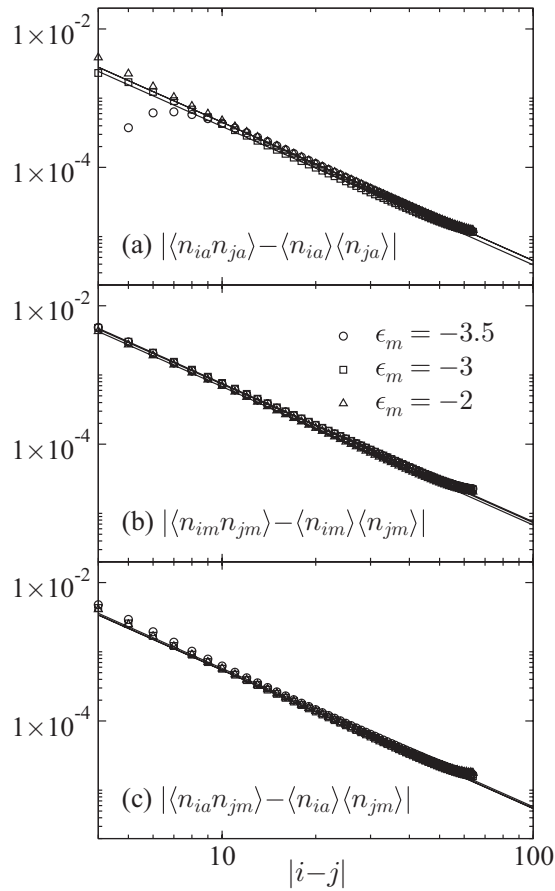


FIG. 9. DMRG results for the connected density correlation functions in the \mathbb{Z}_2 ordered AC + MC phase for the parameters used in Fig. 1. The values of ϵ_m are indicated in panel (b). We use open boundaries with $L = 128$ and set $U = 0.7$. (a) $|\langle n_{ia} n_{ja} \rangle - \langle n_{ia} \rangle \langle n_{ja} \rangle|$. (b) $|\langle n_{im} n_{jm} \rangle - \langle n_{im} \rangle \langle n_{jm} \rangle|$. (c) $|\langle n_{ia} n_{jm} \rangle - \langle n_{ia} \rangle \langle n_{jm} \rangle|$. The results are in agreement with the leading $1/x^2$ dependence predicted by Eq. (21).

Our results are fully consistent with the absence of a purely atomic superfluid phase in this region of the phase diagram. This is compatible with the predictions of mean-field theory in higher dimensions [32–34].

In addition to the zero-momentum occupation numbers, the authors of Ref. [37] also consider the visibility. The visibility is related to the momentum occupation numbers (22) via [84]

$$\mathcal{V}_\alpha \equiv \frac{n_\alpha^{\max}(k) - n_\alpha^{\min}(k)}{n_\alpha^{\max}(k) + n_\alpha^{\min}(k)}, \quad (24)$$

where n^{\max} (n^{\min}) is the maximum (minimum) in the momentum space occupation number distribution. In the present context this is identified as

$$\mathcal{V}_\alpha = \frac{n_\alpha(0) - n_\alpha(\pi)}{n_\alpha(0) + n_\alpha(\pi)}. \quad (25)$$

In a superfluid phase where $n_\alpha(0)$ diverges with increasing system size, the visibility \mathcal{V}_α approaches unity as $L \rightarrow \infty$. In Ref. [37] it was argued that the molecular visibility within

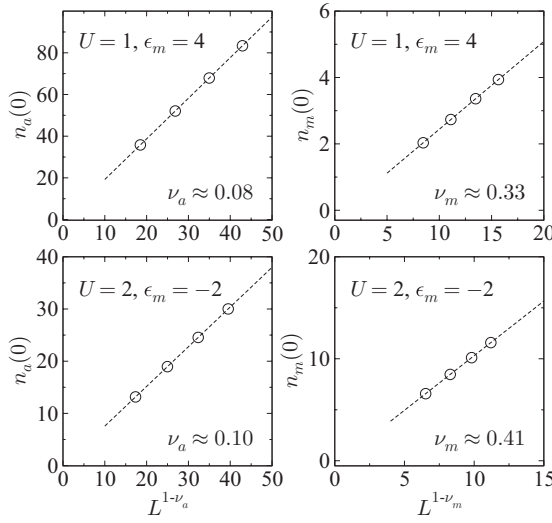


FIG. 10. DMRG results for the dependence of the zero-momentum occupation numbers $n_a(0)$ and $n_m(0)$ on system size L within the AC + MC phase shown in Fig. 1. The results are consistent with algebraic correlations for both atoms and molecules with locked exponents $\nu_m = 4\nu_a$. The presence of molecular superfluidity in the lower panels confirms the absence of an AC phase close to the MI boundary.

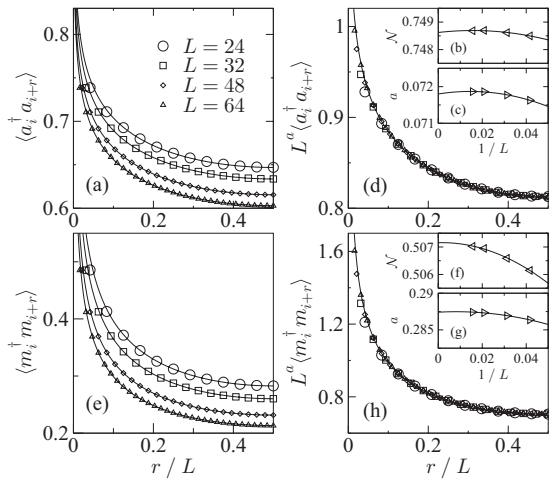


FIG. 11. Atomic and molecular correlation functions within the AC + MC phase obtained by DMRG with periodic boundary conditions. We set $\epsilon_m = -2$ and $U = 1.5$. (a) Atomic correlation function $\langle a_i^\dagger a_{i+r} \rangle$ as a function of the reduced separation r/L for different system sizes. (b) Normalization factor \mathcal{N} obtained from (a) using Eq. (26). (c) Correlation exponent a obtained from (a) using Eq. (26). (d) Rescaling the data in (a) using the extracted exponent a leads to data collapse. This confirms the applicability of the conformal result (26) within the AC + MC phase. This corresponds to power-law atomic correlations for separations $r \gtrsim 3a_0$. The remaining panels show the corresponding results for molecules.

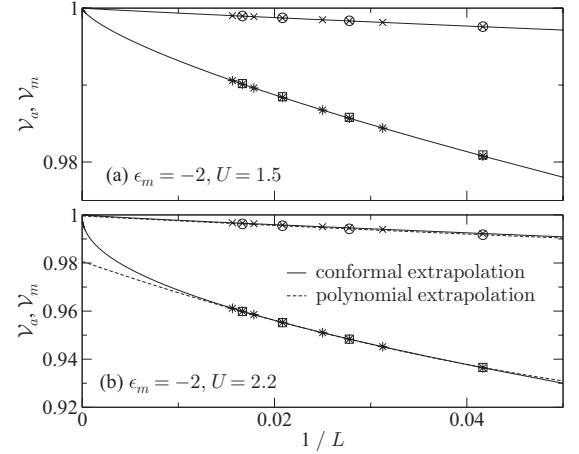


FIG. 12. Finite-size scaling of the atomic and molecular visibilities within the AC + MC phase. The circles correspond to \mathcal{V}_a and the squares to \mathcal{V}_m obtained by Fourier transformation of the correlation functions obtained by DMRG. The crosses and stars correspond to Fourier transformation of the conformal result (25) supplemented by exact DMRG results for the correlators at small separations $r \leq 3a_0$. The solid line indicates the results of conformal extrapolation (described in the text and justified by the scaling collapse in Fig. 11) supplemented by the exact DMRG results for small separations $r \leq 3a_0$. (a) With $\epsilon_m = -2$ and $U = 1.5$ both \mathcal{V}_a and \mathcal{V}_m extrapolate to unity in the thermodynamic limit. (b) Close to the MI transition with $\epsilon_m = -2$ and $U = 2.2$ both \mathcal{V}_a and \mathcal{V}_m approach unity as $L \rightarrow \infty$. This is in direct contrast to naive polynomial extrapolation (dashed) which erroneously suggests that the molecular visibility is less than unity.

the AC + MC phase failed to saturate at this value close to the MI boundary. In order to gain a quantitative handle on this issue we need to exploit the finite-size dependence of the superfluid correlations within the AC + MC phase. In a system with periodic boundary conditions the two-point function of a primary field $\mathcal{O}(r)$ at position r can be obtained by conformal transformation [85]:

$$\langle \mathcal{O}(r_1) \mathcal{O}(r_2) \rangle_L = \mathcal{N} \left[\frac{\pi}{L \sin(\frac{\pi r}{L})} \right]^a, \quad (26)$$

where a is the critical exponent in the thermodynamic limit, $r = |r_1 - r_2|$ is the separation, and \mathcal{N} is a constant prefactor. It follows that the rescaled combination $L^a \langle \mathcal{O}(r_1) \mathcal{O}(r_2) \rangle_L$ is a prescribed scaling function of the reduced separation r/L . The confirmation of this behavior for the atomic and molecular correlation functions within the AC + MC phase is shown in Fig. 11. Given this agreement we may substitute the conformal result (26) into Eq. (22) in order to obtain formal expressions for the finite-size dependence of the atomic and molecular visibilities in Eq. (24). In Fig. 12 we show the results of this conformal extrapolation, where we further incorporate the exact DMRG results for the short distance behavior with $r \leq 3a_0$, where a_0 is the lattice spacing. It is readily seen from the solid lines in Fig. 12 that both the atomic and molecular visibilities extrapolate to unity in the thermodynamic limit.

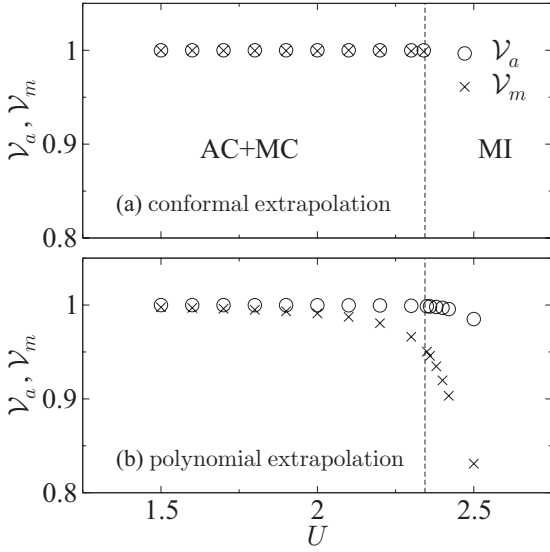


FIG. 13. (a) Atomic and molecular visibilities \mathcal{V}_a (circles) and \mathcal{V}_m (crosses) within the AC + MC phase for $\epsilon_m = -2$ obtained by DMRG with up to $L = 64$ and periodic boundaries. We use the conformal extrapolation procedure described in the text in order to obtain the asymptotic results as $L \rightarrow \infty$. Both \mathcal{V}_a and \mathcal{V}_m are unity right up to the MI boundary, indicating the presence of both atomic and molecular superfluidity. (b) Naive polynomial extrapolation erroneously suggests that the molecular visibility is less than unity in the AC + MC phase.

In particular, close to the MI boundary there are strong deviations from the results that would be obtained by naive polynomial extrapolation as indicated by the dashed lines. In Fig. 13(a) we use the conformal extrapolation procedure to track the atomic and molecular visibilities within the AC + MC phase. The results are consistent with unity right up to the MI boundary. For comparison, in Fig. 13(b) we show the results that would be inferred using a naive polynomial extrapolation. The results are in accordance with those of Ref. [37], but differ markedly from the asymptotic visibilities obtained by conformal extrapolation as shown in Fig. 13(a).

To summarize the results of this section, within the AC + MC phase the finite-size dependence of the atomic and molecular momentum space diagnostics is in complete agreement with power-law correlations for both the atoms and the molecules. This behavior persists right up to the MI boundary and provides further evidence for the absence of a purely AC phase. This is analogous to expectations in higher dimensions arising from mean-field theory analyses [32–34].

VI. ENTANGLEMENT ENTROPY

Having established good agreement between field theory and DMRG for the MC and AC + MC phases, let us now examine the quantum phase transition between them. A key diagnostic in this 1D setting is the central charge c which is a measure of the number of critical degrees of freedom. This may be obtained from the entanglement entropy. For a block of length l in a periodic system of length L , the von Neumann en-

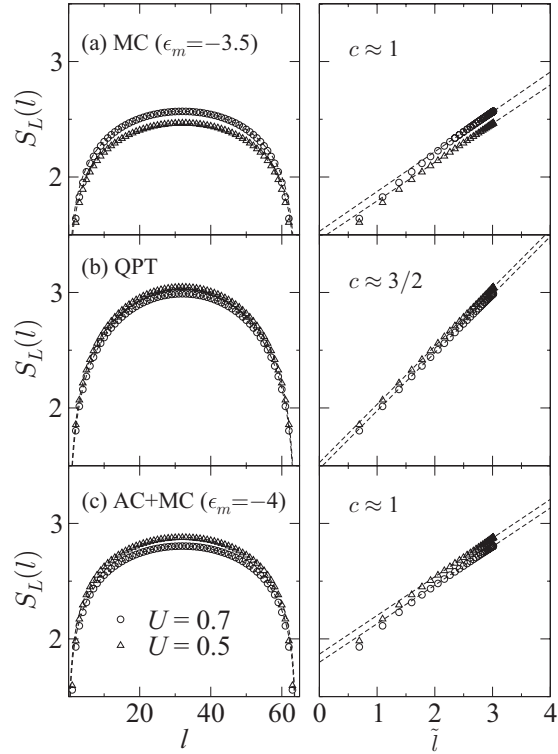


FIG. 14. Entanglement entropy $S_L(l)$ obtained by DMRG with $L = 64$ and periodic boundaries. We consider horizontal scans through Fig. 1 with $U = 0.5$ and $U = 0.7$. (a) Within the MC phase with $\epsilon_m = -3.5$ we find $c \approx 1$ corresponding to a gapless superfluid. (b) In the vicinity of the MC to AC + MC quantum phase transition we find $c \approx 3/2$. This corresponds to the presence of additional gapless Ising degrees of freedom coexisting with superfluidity. (c) Within the AC + MC phase with $\epsilon_m = -4$ we find $c \approx 1$ corresponding to an effective free boson. The panels on the right correspond to the same data as on the left, but are plotted against the conformal distance $\tilde{l} \equiv \ln[(L/\pi) \sin(\pi l/L)]$ in order to yield a linear plot with slope $c/3$. The offset between the different curves within each panel is due to the nonuniversal contribution in Eq. (27).

trophy is given by $S_L(l) = -\text{Tr}_l(\rho_l \ln \rho_l)$, where $\rho_l = \text{Tr}_{L-l}(\rho)$ is the reduced density matrix. One obtains [86,87]

$$S_L(l) = \frac{c}{3} \ln \left[\frac{L}{\pi} \sin \left(\frac{\pi l}{L} \right) \right] + s_1 + \dots, \quad (27)$$

where s_1 is a nonuniversal constant and where the corrections are small when the chord length is large [88–94]. As may be seen in Fig. 14(a), the numerically extracted central charge of the MC phase yields $c = 1$, as one would expect for a single free boson, with coexisting gapped degrees of freedom; the adjacent panel shows the same results plotted against the conformal distance $\tilde{l} \equiv \ln[(L/\pi) \sin(\pi l/L)]$ in order to yield a linear slope of $c/3$. It may be seen from Fig. 14(c) that the AC + MC phase also has $c = 1$. Note that it is *not* $c = 2$ as would be the case for two independent Luttinger liquids. This reflects the coupled nature of the atomic and molecular condensates in the AC + MC phase, with additional gapped Ising degrees of freedom; the Feshbach term is relevant and drives the \mathbb{Z}_2

sector massive. Close to the MC to AC + MC transition, where the anticipated Ising gap closes, one expects the central charge to increase to $c = 3/2$, due to *additional* critical Ising degrees of freedom with $c = 1/2$. This is confirmed by our DMRG simulations in Fig. 14(b). Further support for this \mathbb{Z}_2 transition is obtained from the difference [95]

$$\Delta S(L) \equiv S_L(L/2) - S_{L/2}(L/4) = \frac{c}{3} \ln(2) + \dots \quad (28)$$

as a function of ϵ_m . For a given system size this displays a peak, whose location coincides with the MC to AC + MC quantum phase transition obtained via the vanishing of the single-particle gap $E_{1g} = 0$, as shown in Fig. 1; see Fig. 15(a). The evolution with increasing system size is consistent

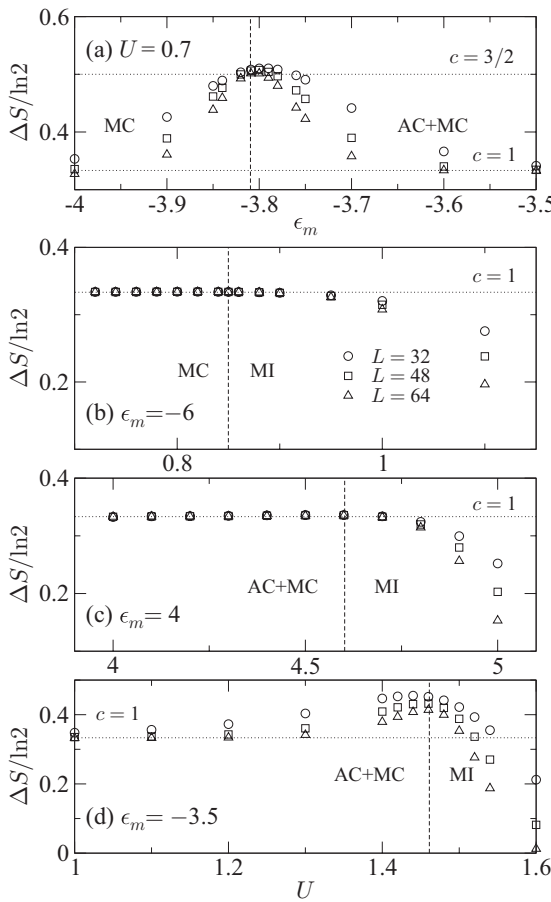


FIG. 15. Entanglement entropy difference $\Delta S(L)$ on transiting across the phase boundaries shown in Fig. 1. We use periodic boundaries with up to $L = 64$ and work away from the multicritical point. (a) The transition from MC to AC + MC yields $c \approx 3/2$ corresponding to an Ising transition coexisting with a gapless superfluid. (b) The transition from MC to MI yields $c \approx 1$ and is consistent with a molecular KT transition. (c) The transition from AC + MC to MI with $\epsilon_m = 4$ yields $c \approx 1$ and is consistent with an atomic KT transition. (d) The transition from AC + MC to MI with $\epsilon_m = -3.5$ appears to be compatible with the approach toward $c \approx 1$ with increasing L , although the finite-size effects are stronger than those in (c). (a) and (c) are adapted from Ref. [63].

with the passage toward $c = 1$ in the superfluid phases, and $c = 3/2$ in the vicinity of the transition. This behavior may be contrasted with that observed at the superfluid-MI transitions in Fig. 1, away from the multicritical point. As may be seen in Fig. 15(b), in passing from the MC phase to the MI, the central charge remains pinned at unity. This is consistent with a KT transition for the molecules. Likewise, in passing from the AC + MC phase to the MI, we find $c = 1$ again; see Fig. 15(c). This is consistent with a KT transition for the atoms. We have checked that this atomic KT behavior persists in Fig. 1 up to a value of $\epsilon_m = -3.5$; see Fig. 15(d). It is notable that the finite-size effects in Fig. 15(d) are much stronger than those in Fig. 15(c), although both are compatible with $c \approx 1$ at the MI transition. A detailed analysis of the multicritical region in Fig. 1 requires further investigation.

VII. ISING SCALING REGIME

Having provided evidence for a \mathbb{Z}_2 quantum phase transition occurring between the MC and AC + MC superfluids, we now demonstrate how to extract both the Ising order parameter $\langle \phi \rangle$ and the Ising correlation length ξ in the presence of the additional superfluid degrees of freedom with $c = 1$.

A. Ising correlation length

The Ising correlation length ξ may be obtained from the atomic and molecular correlation functions discussed in Sec. IV B. Within the \mathbb{Z}_2 disordered MC phase the atomic

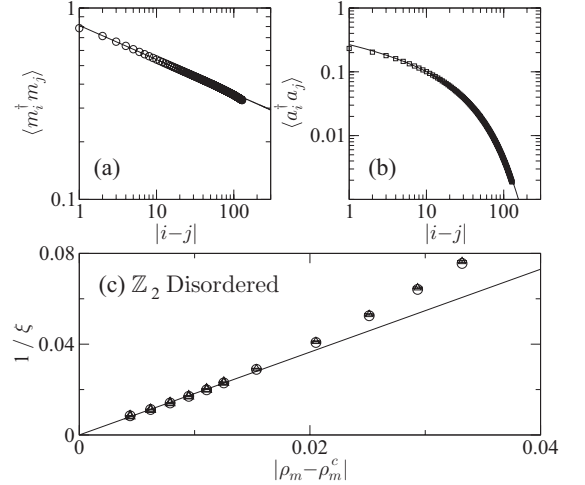


FIG. 16. DMRG results used to extract the Ising correlation length ξ within the \mathbb{Z}_2 disordered MC phase with $L = 256$ and open boundaries. (a) With $\epsilon_m = -3.85$ the molecular correlation function $\langle m_i^\dagger m_j \rangle \approx 0.81|i-j|^{-0.18}$ decays as a power law. (b) Using the previous exponent $\nu_m \approx 0.18$ we extract the Ising correlation length $\xi \approx 43.6$ from the exponential decay of $\langle a_i^\dagger a_j \rangle \sim |i-j|^{-\nu_m/4} \mathcal{K}_0(|i-j|/\xi)$. (c) Repeating the above procedure we plot ξ^{-1} (circles) vs the departure of the molecular density ρ_m from its value ρ_m^c at the MC to AC + MC transition. Close to the transition the results are in good agreement with the Ising relation $\xi^{-1} \sim |\rho_m - \rho_m^c|^\nu$ with $\nu = 1$. The triangles correspond to extracting ξ directly from the ratio $\mathcal{R}(|i-j|) \equiv \langle a_i^\dagger a_j \rangle^4 / \langle m_i^\dagger m_j \rangle \sim [\mathcal{K}_0(|i-j|/\xi)]^4$.

correlations $\langle a^\dagger(x)a(0) \rangle \sim x^{-\nu_m/4} \mathcal{K}_0(x/\xi)$ decay exponentially, while the molecular correlations $\langle m^\dagger(x)m(0) \rangle \sim x^{-\nu_m}$ decay as a power law. At a given point in parameter space we may use the molecular Green's function to determine the exponent ν_m , and thereby extract the Ising correlation length from the atomic correlations. This approach is outlined in Fig. 16. In the vicinity of an Ising quantum phase transition one expects that $\xi^{-1} \sim |\mathcal{M} - \mathcal{M}_c|^\nu$, where $\nu = 1$ is the Ising correlation length exponent and \mathcal{M} is a suitable mass scale parameterizing the departure from criticality. Unfortunately, it is nontrivial to express \mathcal{M} in terms of the microscopic parameters of the lattice model (1). A naive analysis gives $\mathcal{M} \sim \kappa_0 + \kappa_1 \rho_m + \kappa_2 \sqrt{\rho_m}$, where ρ_m is the density of molecules, and $\kappa_0 \sim \epsilon_a$, $\kappa_1 \sim U_{am}$, $\kappa_2 \sim 2g$ are constants. Expanding the square root according to $\sqrt{\rho_m} \approx \sqrt{\rho_m^c} + (\rho_m - \rho_m^c)/\sqrt{\rho_m^c}$ suggests that sufficiently close to the Ising transition

$$\xi^{-1} \propto |\rho_m - \rho_m^c|. \quad (29)$$

This Ising behavior with $\nu = 1$ is confirmed in Fig. 16.

B. Ising order parameter

In the ordered phase of the Ising model (9) we have $\langle \phi \rangle \sim |\mathcal{M} - \mathcal{M}_c|^\beta$, where $\beta = 1/8$ is the Ising magnetization critical

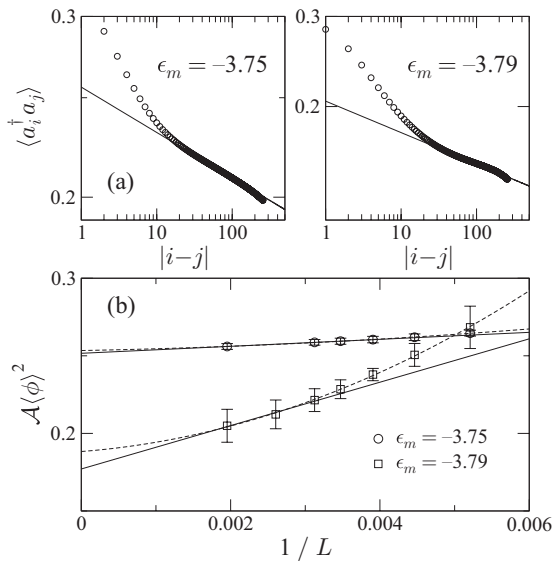


FIG. 17. (a) Atomic correlation functions within the AC + MC phase obtained by DMRG with up to $L = 512$ and open boundaries. We set $U = 0.7$ and consider $\epsilon_m = -3.75$ (left) and $\epsilon_m = -3.79$ (right). A direct fit to Eq. (31) yields $\mathcal{A}(\phi)^2$ for each value of ϵ_m , where $\langle \phi \rangle$ is the Ising order parameter and \mathcal{A} is a nonuniversal constant prefactor. Changing the fitting interval gives an estimate of the error bars. (b) Extrapolation of $\mathcal{A}(\phi)^2$ to the thermodynamic limit using linear extrapolation of the largest three system sizes is indicated by the solid line. An estimate of the error bars in the thermodynamic limit is obtained by comparing to a quadratic fit of the data shown by the dashed line. These results are plotted as a function of the molecular density in Fig. 18 in order to confirm Ising behavior with $\beta = 1/8$.

exponent. From the discussion above one thus expects that

$$\langle \phi \rangle \sim |\rho_m - \rho_m^c|^{1/8}, \quad (30)$$

where ρ_m is the density of molecules. In order to test the validity of Eq. (30), we must first extract the Ising order parameter from a finite-size scaling analysis of the atomic correlations. As follows from Eq. (16), within the \mathbb{Z}_2 ordered AC + MC phase one has

$$\langle a^\dagger(x)a(0) \rangle = \mathcal{A}(\phi)^2 x^{-\nu_m/4}, \quad (31)$$

where \mathcal{A} is a normalization amplitude. In Fig. 17(a) we show DMRG results for $\langle a^\dagger(x)a(0) \rangle$ in the vicinity of the MC to AC + MC quantum phase transition. A direct fit to Eq. (31)

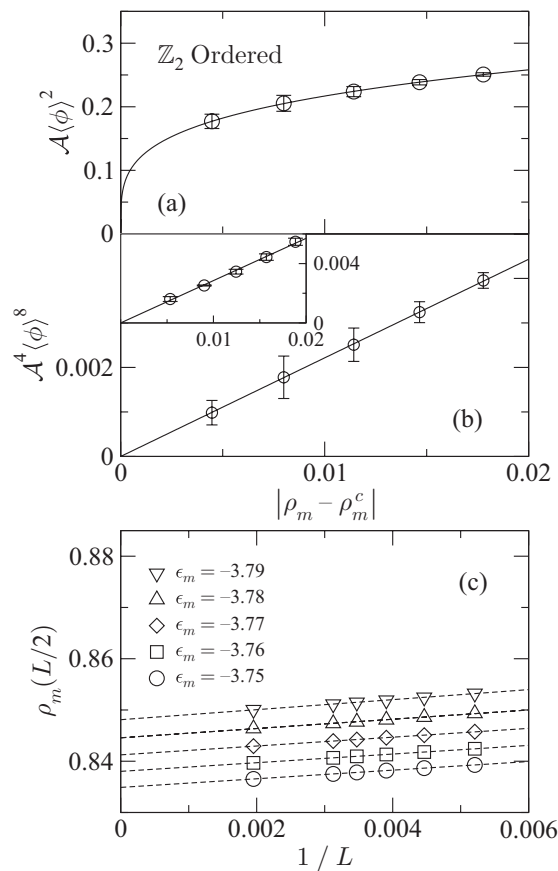


FIG. 18. DMRG results for the Ising order parameter in the \mathbb{Z}_2 ordered AC + MC phase with up to $L = 512$ and $U = 0.7$. (a) Variation of the Ising order parameter squared $\mathcal{A}(\phi)^2$ where \mathcal{A} is a constant prefactor, vs the deviation of the molecular density ρ_m from its value ρ_m^c at the MC to AC + MC quantum phase transition. (b) Variation of $\mathcal{A}^4(\phi)^8$ vs the molecular density difference. The results are in good agreement with the Ising magnetization relation $\langle \phi \rangle \sim |\rho_m - \rho_m^c|^{1/8}$ with $\beta = 1/8$. The inset shows analogous results obtained from the plateau value of $\mathcal{R}(x)$ for $L = 512$, as indicated in Fig. 19(c). The error bars are estimated from the magnitude of $|\mathcal{R}(x = 128, L = 512) - \mathcal{R}(x = 64, L = 256)|$. (c) Finite-size scaling of the thermodynamic molecular density used in (a) and (b). (a) and (b) are adapted from Ref. [63].

yields $\mathcal{A}(\phi)^2$. Repeating this procedure for different system sizes one obtains an estimate for $\mathcal{A}(\phi)^2$ in the thermodynamic limit; see Fig. 17(b). In Fig. 18 we show the variation of this order parameter with the molecular density. The results are in good agreement with the theoretical prediction in Eq. (30) and the Ising critical exponent $\beta = 1/8$.

C. Correlation function ratio

In the above discussion we have extracted the Ising correlation length and the Ising order parameter through a direct finite-size scaling analysis of the atomic and molecular correlation functions. An alternative approach is to consider the behavior of the ratio

$$\mathcal{R}(x) \equiv \frac{\langle a^\dagger(x)a(0) \rangle^4}{\langle m^\dagger(x)m(0) \rangle^4} \quad (32)$$

in analogy to the considerations of Refs. [42,43] for the confinement-deconfinement transition of Cooper pairs in 1D fermion systems.

In the \mathbb{Z}_2 disordered MC phase $\langle a^\dagger(x)a(0) \rangle \sim x^{-\nu_m/4} \mathcal{K}_0(x/\xi)$ and $\langle m^\dagger(x)m(0) \rangle \sim x^{-\nu_m}$. It follows that the

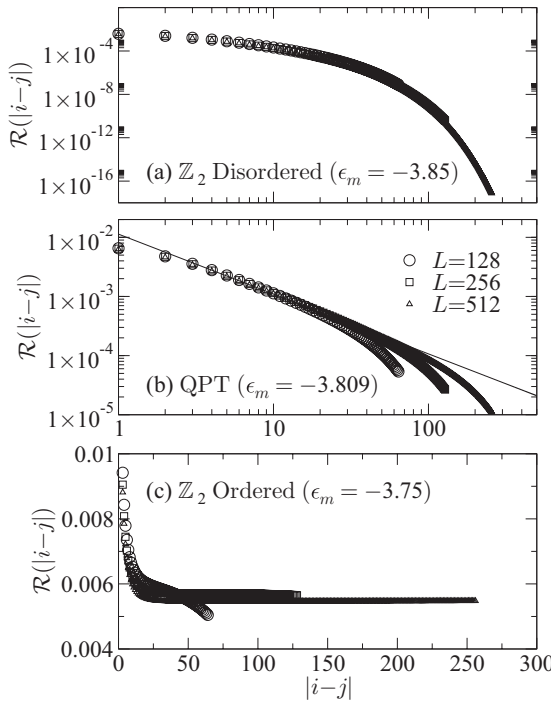


FIG. 19. Ratio $\mathcal{R}(|i-j|) \equiv \langle a_i^\dagger a_j \rangle^4 / \langle m_i^\dagger m_j \rangle^4$ of the atomic and molecular correlation functions with $U = 0.7$. (a) In the \mathbb{Z}_2 disordered MC phase with $\epsilon_m = -3.85$ the ratio $\mathcal{R}(|i-j|) \sim [\mathcal{K}_0(|i-j|/\xi)]^4$ exhibits exponential decay. (b) In the vicinity of the MC to AC + MC quantum phase transition the ratio $\mathcal{R}(|i-j|) \sim 1/|i-j|$ decays with a universal power law corresponding to the Ising critical exponent $\eta = 1/4$. The line is a fit to $\mathcal{R} = A_0|i-j|^{A_1}$ over the interval $3 \leq |i-j| \leq 48$ for $L = 512$ with $A_0 \approx 0.011$ and $A_1 \approx -1.01$. (c) In the \mathbb{Z}_2 ordered AC + MC phase with $\epsilon_m = -3.75$ the ratio $\mathcal{R}(|i-j|) \sim \langle \phi \rangle^8$ exhibits a plateau corresponding to a nonzero Ising order parameter.

power-law prefactors cancel out in this ratio:

$$\mathcal{R}(x) \sim [\mathcal{K}_0(x/\xi)]^4. \quad (33)$$

As such, this ratio should exhibit exponential decay in the MC phase. This is confirmed by our DMRG results in Fig. 19(a). A direct fit to Eq. (33) yields the Ising correlation length shown by the triangles in Fig. 16.

In the \mathbb{Z}_2 ordered AC + MC phase $\langle m^\dagger(x)m(0) \rangle \sim x^{-\nu_m}$ and $\langle a^\dagger(x)a(0) \rangle \sim \langle \phi(x)\phi(0) \rangle x^{-\nu_m/4}$ where $\langle \phi(x)\phi(0) \rangle$ is given by Eq. (17). It follows that

$$\mathcal{R}(x) \sim \langle \phi \rangle^8 [1 + \pi^{-2} \mathcal{F}(x/\xi)]^4, \quad (34)$$

where $\mathcal{F}(z)$ is given by Eq. (18). At leading order $\mathcal{R}(x) \sim \langle \phi \rangle^8$ and one thus expects $\mathcal{R}(x)$ to develop a constant plateau that is proportional to the Ising order parameter. This is confirmed by our DMRG results in Fig. 19(c).

In addition to these results for $\mathcal{R}(x)$ which are valid within the superfluid phases, one may also explore the vicinity of the quantum phase transition between them. At the Ising critical point $\langle \phi \rangle = 0$ but

$$\langle \phi(x)\phi(0) \rangle \sim \left(\frac{a_0}{x} \right)^\eta \quad (35)$$

decays as a power law where $\eta = 1/4$ is the Ising pair correlation exponent. It follows from Eqs. (6) and (35) that the atomic Green's function at criticality is given by

$$\begin{aligned} \langle a^\dagger(x)a(0) \rangle &\sim \langle \phi(x)\phi(0) \rangle \langle e^{-i\frac{\theta(x)}{2}} e^{i\frac{\theta(0)}{2}} \rangle \\ &\sim \left(\frac{a_0}{x} \right)^{\frac{1}{4}} \left(\frac{a_0}{x} \right)^{\frac{\nu_m}{4}}. \end{aligned} \quad (36)$$

On passing from the \mathbb{Z}_2 ordered AC + MC phase toward the Ising quantum phase transition, the power-law decay of the atomic Green's function is therefore enhanced by $\eta = 1/4$ due to the presence of additional critical Ising degrees of freedom. It follows that

$$\mathcal{R}(x) \sim \frac{a_0}{x} \quad (37)$$

exhibits universal power-law decay in the vicinity of the MC to AC + MC quantum phase transition. This is confirmed by our DMRG results shown in Fig. 19(b). This provides direct evidence for the Ising correlation exponent $\eta = 1/4$. These results demonstrate that the ratio $\mathcal{R}(x)$ may be used to explore both the critical and off-critical Ising behavior at the MC to AC + MC transition. The characteristic signatures of $\mathcal{R}(x)$ parallel those observed in Refs. [42,43] for the confinement-deconfinement transition of Cooper pairs in 1D fermion systems.

VIII. CONCLUSIONS

In this paper we have explored the phase diagram of bosons interacting via Feshbach resonant pairing in a 1D optical lattice. We have presented a wide variety of evidence in favor of an Ising quantum phase transition separating distinct paired superfluids. We have also provided a detailed characterization of these phases, including the behavior close to the Mott insulating phase boundary. For the investigated parameters, our DMRG results are consistent with an Ising quantum phase transition approaching both a molecular KT

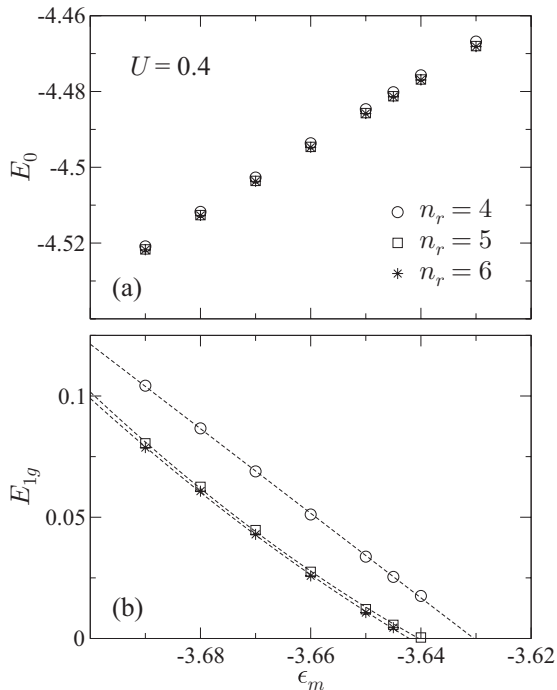


FIG. 20. DMRG results for a horizontal scan through Fig. 1 with $1/U = 2.5$. We consider up to $L = 128$ and extrapolate to the thermodynamic limit. (a) Evolution of the ground state energy E_0 with increasing local Hilbert space restriction $n_r = n_a = n_m$. (b) Evolution of the excitation gap E_{1g} with increasing n_r , showing very little change beyond $n_r = 5$.

transition and an atomic KT transition. This is compatible with mean-field theory predictions for the continuum model in higher dimensions. However, recent results for pairing phases in a 2D classical XY model suggest the possibility that the Ising transition may overextend beyond the multicritical point [53]. In view of this possibility, in a distinct but closely related model, it would be profitable to explore the multicritical region in more detail. A clear verdict on this issue for the present 1D quantum model requires further analytical and numerical investigation and we will return to this question in future work. It would also be interesting to explore the phase diagram for a broader range of parameters, with a specific focus on the choice of atomic species and experimental constraints. Even in the presence of strong three-body losses, the emergent phase diagram may exhibit notable similarities [45–51].

ACKNOWLEDGMENTS

We are grateful to E. Altman, F. Assaad, S. Capponi, N. Cooper, S. Diehl, M. Garst, Z. Hadzibabic, A. James, E. Jeckelmann, J. Kjäll, M. Köhl, A. Lamacraft, A. Läuchli, C. Lobo, J. Moore, N. Prokof'ev, A. Silver, and M. Zaletel for helpful comments and discussions. MJB and BDS acknowledge EPSRC Grant No. EP/E018130/1. FHLE by EP/I032487/1 and EP/D050952/1. SE and HF acknowledge funding by the DFG through Grant SFB 652. MH by DFG

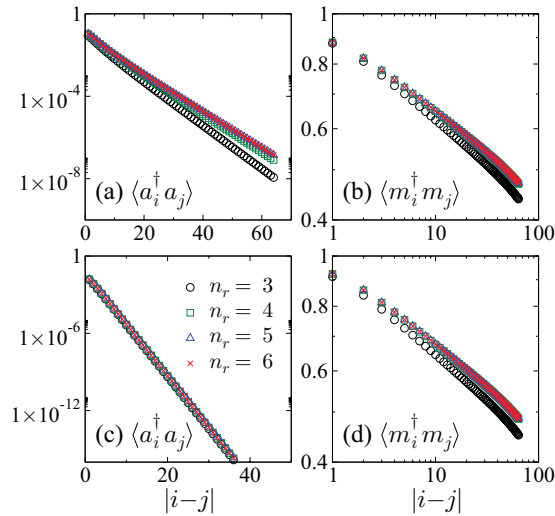


FIG. 21. (Color online) DMRG results with $L = 128$ and $U = 0.5$ within the MC phase shown in Fig. 1. We show the evolution of the atomic and molecular correlation functions with increasing local Hilbert space restriction n_r . We set $\epsilon_m = -4$ ($\epsilon_m = -6$) in the upper (lower) panels.

FG1162. Numerical calculations were performed at the URZ Greifswald.

APPENDIX: HILBERT SPACE TRUNCATION

Throughout the main text we truncate the local Hilbert space to allow up to a maximum of $n_a = 5$ atoms and $n_m = 5$ molecules per site. In the regime of large t/U , where intersite hopping is strongly favored, one should check the validity of

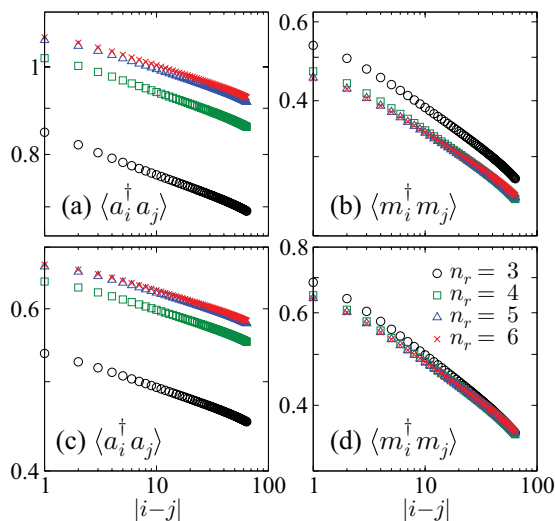


FIG. 22. (Color online) DMRG results with $L = 128$ and $U = 0.5$ within the AC + MC phase shown in Fig. 1. We show the evolution of the atomic and molecular correlation functions with increasing local Hilbert space restriction n_r . We set $\epsilon_m = -2$ ($\epsilon_m = -3$) in the upper (lower) panels.

this approximation. Here we discuss the evolution of physical observables with increasing Hilbert space restriction parameter $n_r = n_a = n_m$. For the largest value of $1/U = 2.5$ used in Fig. 1, the results converge with increasing n_r . For example, in Fig. 20(a) we show the evolution of the ground state energy E_0 with increasing n_r . The results show very little variation beyond $n_r = 5$. Likewise, in Fig. 20(b) we monitor the excitation gap E_{1g} with increasing n_r . The data again show

very little change beyond $n_r = 5$. The associated MC to AC + MC phase boundary in Fig. 1 is therefore robust to increasing n_r . In a similar fashion, in Figs. 21 and 22 we examine the evolution of the atomic and molecular correlation functions. The results show clear convergence in both the MC and AC + MC phases. The excellent agreement between our DMRG results and field theory predictions also lends *a posteriori* support for this level of Hilbert space restriction with $n_r = 5$.

-
- [1] M. H. Anderson, J. R. Ensher, M. R. Matthews, C. E. Wieman, and E. A. Cornell, *Science* **269**, 198 (1995).
- [2] K. B. Davis, M.-O. Mewes, M. R. Andrews, N. J. van Druten, D. S. Durfee, D. M. Kurn, and W. Ketterle, *Phys. Rev. Lett.* **75**, 3969 (1995).
- [3] M. Greiner, O. Mandel, T. Esslinger, T. W. Hänsch, and I. Bloch, *Nature (London)* **415**, 39 (2002).
- [4] K. Baumann, C. Guerlin, F. Brennecke, and T. Esslinger, *Nature (London)* **464**, 1301 (2010).
- [5] D. M. Eagles, *Phys. Rev.* **186**, 456 (1969).
- [6] A. J. Leggett, *J. Phys. C (Paris)* **41**, 7 (1980).
- [7] P. Nozières and S. Schmitt-Rink, *J. Low Temp. Phys.* **59**, 195 (1985).
- [8] A. J. Leggett, *Quantum Liquids: Bose Condensation and Cooper Pairing in Condensed-Matter Systems* (Oxford University Press, Oxford, 2006).
- [9] M. Greiner, C. A. Regal, and D. S. Jin, *Nature (London)* **426**, 537 (2003).
- [10] S. Jochim, M. Bartenstein, A. Altmeyer, G. Hendl, S. Riedl, C. Chin, J. Hecker Denschlag, and R. Grimm, *Science* **302**, 2101 (2003).
- [11] M. W. Zwierlein, C. A. Stan, C. H. Schunck, S. M. F. Raupach, S. Gupta, Z. Hadzibabic, and W. Ketterle, *Phys. Rev. Lett.* **91**, 250401 (2003).
- [12] C. A. Regal, M. Greiner, and D. S. Jin, *Phys. Rev. Lett.* **92**, 040403 (2004).
- [13] T. Bourdel, L. Khaykovich, J. Cubizolles, J. Zhang, F. Chevy, M. Teichmann, L. Tarruell, S. J. J. M. F. Kokkelmans, and C. Salomon, *Phys. Rev. Lett.* **93**, 050401 (2004).
- [14] M. W. Zwierlein, C. A. Stan, C. H. Schunck, S. M. F. Raupach, A. J. Kerman, and W. Ketterle, *Phys. Rev. Lett.* **92**, 120403 (2004).
- [15] M. Bartenstein, A. Altmeyer, S. Riedl, S. Jochim, C. Chin, J. H. Denschlag, and R. Grimm, *Phys. Rev. Lett.* **92**, 203201 (2004).
- [16] W. Ketterle and M. W. Zwierlein, in *Ultracold Fermi Gases*, Proceedings of the International School of Physics “Enrico Fermi”, Course CLXIV, Varenna, 2006 (2008).
- [17] S. Ospelkaus, K.-K. Ni, D. Wang, M. H. G. de Miranda, B. Neyenhuis, G. Quémener, P. S. Julienne, J. L. Bohn, D. S. Jin, and J. Ye, *Science* **327**, 853 (2010).
- [18] S. Inouye, M. R. Andrews, J. Stenger, H.-J. Miesner, D. M. Stamper-Kurn, and W. Ketterle, *Nature (London)* **392**, 151 (1998).
- [19] Ph. Courteille, R. S. Freeland, D. J. Heinzen, F. A. van Abeelen, and B. J. Verhaar, *Phys. Rev. Lett.* **81**, 69 (1998).
- [20] E. A. Donley, N. R. Claussen, S. T. Thompson, and C. E. Wieman, *Nature (London)* **417**, 529 (2002).
- [21] J. Herbig, T. Kraemer, M. Mark, T. Weber, C. Chin, H.-C. Nägerl, and R. Grimm, *Science* **301**, 1510 (2003).
- [22] S. Dürr, T. Volz, and G. Rempe, *Phys. Rev. A* **70**, 031601(R) (2004).
- [23] K. Xu, T. Mukaiyama, J.-R. Abo-Shaeer, J. K. Chin, D. E. Miller, and W. Ketterle, *Phys. Rev. Lett.* **91**, 210402 (2003).
- [24] P. D. Drummond, K. V. Kheruntsyan, and H. He, *Phys. Rev. Lett.* **81**, 3055 (1998).
- [25] E. Timmermans, P. Tommasini, M. Hussein, and A. Kerman, *Phys. Rep.* **315**, 199 (1999).
- [26] R. A. Duine and H. T. C. Stoof, *Phys. Rep.* **396**, 115 (2004).
- [27] S. B. Papp, J. M. Pino, R. J. Wild, S. Ronen, C. E. Wieman, D. S. Jin, and E. A. Cornell, *Phys. Rev. Lett.* **101**, 135301 (2008).
- [28] S. E. Pollack, D. Dries, M. Junker, Y. P. Chen, T. A. Corcovilos, and R. G. Hulet, *Phys. Rev. Lett.* **102**, 090402 (2009).
- [29] N. Navon, S. Piatecki, K. Günter, B. Rem, T. C. Nguyen, F. Chevy, W. Krauth, and C. Salomon, *Phys. Rev. Lett.* **107**, 135301 (2011).
- [30] G. Thalhammer, K. Winkler, F. Lang, S. Schmid, R. Grimm, and J. H. Denschlag, *Phys. Rev. Lett.* **96**, 050402 (2006).
- [31] C. Chin, R. Grimm, P. Julienne, and E. Tiesinga, *Rev. Mod. Phys.* **82**, 1225 (2010).
- [32] L. Radzihovsky, J. Park, and P. B. Weichman, *Phys. Rev. Lett.* **92**, 160402 (2004).
- [33] M. W. J. Romans, R. A. Duine, S. Sachdev, and H. T. C. Stoof, *Phys. Rev. Lett.* **93**, 020405 (2004).
- [34] L. Radzihovsky, P. B. Weichman, and J. I. Park, *Ann. Phys.* **323**, 2376 (2008).
- [35] D. B. M. Dickerscheid, U. Al Khawaja, D. van Oosten, and H. T. C. Stoof, *Phys. Rev. A* **71**, 043604 (2005).
- [36] K. Sengupta and N. Dupuis, *Europhys. Lett.* **70**, 586 (2005).
- [37] V. G. Rousseau and P. J. H. Denteneer, *Phys. Rev. Lett.* **102**, 015301 (2009).
- [38] V. G. Rousseau and P. J. H. Denteneer, *Phys. Rev. A* **77**, 013609 (2008).
- [39] M. J. Bhaseen, A. O. Silver, M. Hohenadler, and B. D. Simons, *Phys. Rev. Lett.* **103**, 265302 (2009).
- [40] M. Hohenadler, A. O. Silver, M. J. Bhaseen, and B. D. Simons, *Phys. Rev. A* **82**, 013639 (2010).
- [41] C. Wu, *Phys. Rev. Lett.* **95**, 266404 (2005).
- [42] P. Lecheminant, E. Boulat, and P. Azaria, *Phys. Rev. Lett.* **95**, 240402 (2005).
- [43] S. Capponi, G. Roux, P. Azaria, E. Boulat, and P. Lecheminant, *Phys. Rev. B* **75**, 100503(R) (2007).
- [44] G. Roux, S. Capponi, P. Lecheminant, and P. Azaria, *Eur. Phys. J. B* **68**, 293 (2009).
- [45] A. J. Daley, J. M. Taylor, S. Diehl, M. Baranov, and P. Zoller, *Phys. Rev. Lett.* **102**, 040402 (2009).

- [46] A. J. Daley, J. M. Taylor, S. Diehl, M. Baranov, and P. Zoller, *Phys. Rev. Lett.* **102**, 179902 (2009).
- [47] S. Diehl, M. Baranov, A. J. Daley, and P. Zoller, *Phys. Rev. Lett.* **104**, 165301 (2010).
- [48] S. Diehl, M. Baranov, A. J. Daley, and P. Zoller, *Phys. Rev. B* **82**, 064509 (2010).
- [49] S. Diehl, M. Baranov, A. J. Daley, and P. Zoller, *Phys. Rev. B* **82**, 064510 (2010).
- [50] L. Bonnes and S. Wessel, *Phys. Rev. Lett.* **106**, 185302 (2011).
- [51] L. Bonnes and S. Wessel, eprint [arXiv:1201.4117](https://arxiv.org/abs/1201.4117).
- [52] S. R. Manmana, A. M. Läuchli, F. H. L. Essler, and F. Mila, *Phys. Rev. B* **83**, 184433 (2011).
- [53] Y. Shi, A. Lamacraft, and P. Fendley, *Phys. Rev. Lett.* **107**, 240601 (2011).
- [54] S. E. Korshunov, *JETP Lett.* **41**, 263 (1985) [*Zh. Eksp. Teor. Fiz.* **41**, 216 (1985)].
- [55] D. H. Lee and G. Grinstein, *Phys. Rev. Lett.* **55**, 541 (1985).
- [56] D. B. Carpenter and J. T. Chalker, *J. Phys. Condens. Matter* **1**, 4907 (1989).
- [57] J. G. Valatin and D. Butler, *Nuovo Cimento* **10**, 37 (1958).
- [58] A. Coniglio and M. Marinaro, *Nuovo Cimento B* **48**, 249 (1967).
- [59] W. A. B. Evans and Y. Imry, *Nuovo Cimento B* **63**, 155 (1969).
- [60] P. Nozières and D. Saint James, *J. Phys. (France)* **43**, 1133 (1982).
- [61] M. J. Rice and Y. R. Wang, *Phys. Rev. B* **37**, 5893 (1988).
- [62] M. Yu. Kagan and D. V. Efremov, *Phys. Rev. B* **65**, 195103 (2002).
- [63] S. Ejima, M. J. Bhaseen, M. Hohenadler, F. H. L. Essler, H. Fehske, and B. D. Simons, *Phys. Rev. Lett.* **106**, 015303 (2011).
- [64] S. R. White, *Phys. Rev. Lett.* **69**, 2863 (1992); *Phys. Rev. B* **48**, 10345 (1993).
- [65] L. Radzihovsky and S. Choi, *Phys. Rev. Lett.* **103**, 095302 (2009).
- [66] S. Choi and L. Radzihovsky, *Phys. Rev. A* **84**, 043612 (2011).
- [67] R. B. Diener and T.-L. Ho, *Phys. Rev. A* **73**, 017601 (2006).
- [68] D. B. M. Dickerscheid, D. van Oosten, and H. T. C. Stoof, *Phys. Rev. A* **73**, 017602 (2006).
- [69] H. P. Büchler, *Phys. Rev. Lett.* **104**, 090402 (2010).
- [70] M. Eckholt and T. Roscilde, *Phys. Rev. Lett.* **105**, 199603 (2010).
- [71] Y.-W. Lee and Y.-L. Lee, *Phys. Rev. B* **70**, 224506 (2004).
- [72] M. Sitte, A. Rosch, J. S. Meyer, K. A. Matveev, and M. Garst, *Phys. Rev. Lett.* **102**, 176404 (2009).
- [73] V. Gurarie, *Phys. Rev. A* **73**, 033612 (2006); eprint [arXiv:0912.3204](https://arxiv.org/abs/0912.3204) (unpublished).
- [74] Y.-W. Lee and Y.-L. Lee, *Phys. Rev. A* **73**, 043606 (2006).
- [75] T. T. Wu, B. M. McCoy, C. A. Tracy, and E. Barouch, *Phys. Rev. B* **13**, 316 (1976).
- [76] J. M. Kosterlitz and D. J. Thouless, *J. Phys. C* **6**, 1181 (1973).
- [77] J. M. Kosterlitz, *J. Phys. C* **7**, 1046 (1974).
- [78] T. D. Kühner, S. R. White, and H. Monien, *Phys. Rev. B* **61**, 12474 (2000).
- [79] T. Giamarchi, *Phys. Rev. B* **46**, 342 (1992).
- [80] H. P. Büchler, G. Blatter, and W. Zwerger, *Phys. Rev. Lett.* **90**, 130401 (2003).
- [81] H. G. Vaidya and C. A. Tracy, *Physica A* **92**, 1 (1978).
- [82] M.-C. Cha, J.-G. Shin, and J.-W. Lee, *Phys. Rev. B* **80**, 193104 (2009).
- [83] M.-C. Cha, *J. Supercond. Novel Magn.* **23**, 725 (2010).
- [84] F. Gerbier, A. Widera, S. Fölling, O. Mandel, T. Gericke, and I. Bloch, *Phys. Rev. Lett.* **95**, 050404 (2005).
- [85] J. Cardy, *Scaling and Renormalization in Statistical Physics* (Cambridge University Press, Cambridge, 1996).
- [86] C. Holzhey, F. Larsen, and F. Wilczek, *Nucl. Phys. B* **424**, 443 (1994).
- [87] P. Calabrese and J. Cardy, *J. Stat. Mech.: Theor. Exp.* (2004) P06002.
- [88] P. Calabrese, M. Campostrini, F. H. L. Essler, and B. Nienhuis, *Phys. Rev. Lett.* **104**, 095701 (2010).
- [89] J. Cardy and P. Calabrese, *J. Stat. Mech.: Theor. Exp.* (2010) P04023.
- [90] P. Calabrese and F. H. L. Essler, *J. Stat. Mech.: Theor. Exp.* (2010) P08029.
- [91] J. C. Xavier and F. C. Alcaraz, *Phys. Rev. B* **83**, 214425 (2011).
- [92] M. Fagotti and P. Calabrese, *J. Stat. Mech.: Theor. Exp.* (2011) P01017.
- [93] E. Eriksson and H. Johannesson, *J. Stat. Mech.: Theor. Exp.* (2011) P02008.
- [94] M. Dalmonte, E. Ercolessi, and L. Taddia, *Phys. Rev. B* **84**, 085110 (2011).
- [95] A. M. Läuchli and C. Kollath, *J. Stat. Mech.: Theor. Exp.* (2008) P05018.

Magnetic properties of the second Mott lobe in pairing Hamiltonians

M. J. Bhaseen,¹ S. Ejima,² M. Hohenadler,³ A. O. Silver,¹ F. H. L. Essler,⁴ H. Fehske,² and B. D. Simons¹

¹*University of Cambridge, Cavendish Laboratory, Cambridge, CB3 0HE, United Kingdom*

²*Institut für Physik, Ernst-Moritz-Arndt-Universität Greifswald, D-17489 Greifswald, Germany*

³*Institut für Theoretische Physik und Astrophysik, Universität Würzburg, D-97074 Würzburg, Germany*

⁴*The Rudolf Peierls Centre for Theoretical Physics, University of Oxford, Oxford, OX1 3NP, United Kingdom*

(Received 29 April 2011; revised manuscript received 28 June 2011; published 29 August 2011)

We explore the Mott insulating state of single-band bosonic pairing Hamiltonians using analytical approaches and large-scale density matrix renormalization group calculations. We focus on the second Mott lobe which exhibits a magnetic quantum phase transition in the Ising universality class. We use this feature to discuss the behavior of a range of physical observables within the framework of the one-dimensional quantum Ising model and the strongly anisotropic Heisenberg model. This includes the properties of local expectation values and correlation functions both at and away from criticality. Depending on the microscopic interactions it is possible to achieve either antiferromagnetic or ferromagnetic exchange interactions and we highlight the possibility of observing the E_8 mass spectrum for the critical Ising model in a longitudinal magnetic field.

DOI: [10.1103/PhysRevA.84.023635](https://doi.org/10.1103/PhysRevA.84.023635)

PACS number(s): 03.75.Lm, 37.10.Jk, 75.10.Jm, 75.10.Pq

I. INTRODUCTION

The observation of Bose-Einstein condensation (BEC) in dilute alkali-metal gases [1,2] has led to a wealth of activity linking ultracold atom research and condensed matter physics. The precise control over atomic interactions, and the use of optical lattices, offers valuable insights into the effects of strong correlations [3]. This is exemplified by experiments on the Bose-Hubbard model which reveal the quantum phase transition from a superfluid (SF) to a Mott insulator (MI) as the depth of the optical lattice is increased [4,5]. Motivated by these advances, recent attention has been directed toward a variety of multicomponent systems, including spinor condensates [6–17] and atomic mixtures [18–23]. The possibility of novel behavior is greatly enhanced in the presence of these additional “spin” degrees of freedom, and routes to quantum magnetism have been proposed by exploiting internal hyperfine states [24] and using different atomic species [25–28]. The decoupling of the electronic and nuclear spins in alkaline-earth-metal atoms has also been suggested as a way to realize quantum spin liquids and exotic magnetism based on the $SU(N)$ groups [29–31].

In recent work some of the present authors suggested using atom-molecule mixtures as a route to the paradigmatic quantum Ising model [32,33]. Motivated by studies of the BEC-BCS transition for bosons, both in the continuum limit [34–36] and on the lattice [37–40], we investigated the rich phase diagram of bosons interacting via Feshbach resonant pairing interactions in an optical lattice. Combining exact diagonalization (ED) on small systems with analytical predictions based on the strong coupling expansion, we provided evidence for an Ising quantum phase transition in the second Mott lobe. In contrast to previous numerical studies which advocated the presence of super-Mott behavior [39,40], the Ising spectral gap indicates the absence of low-lying superfluid excitations deep within the Mott phase [32,33]. This conclusion gained further support in a recent comment [41] which shows an exponential decay of the connected correlation functions. A detailed discussion of the superfluid properties [34–36] in one dimension (1D) was also provided in Ref. [42] using

large-scale density matrix renormalization group (DMRG) [43] and field theory techniques.

In view of the broad interest in these systems, and the technical issues surrounding Refs. [39,40], we discuss the properties of the second Mott lobe in detail using analytical arguments and DMRG. To aid the comparison with these previous works we focus primarily on the homonuclear case with a single species of bosonic atom. We also begin by restricting the local Hilbert space for the atomic and molecular occupations [40]. In this reduced setting we determine both the locus of the antiferromagnetic Ising transition and the onset of superfluidity. We also investigate the atomic and molecular correlation functions within the MI and compare them directly to the predictions of the quantum Ising model. As advocated in Refs. [32,33] this provides a simple and intuitive framework in which to discuss the absence of super-Mott behavior [39–41].

Going beyond the restricted Hilbert space description we show that the same ideas apply. Interestingly, by tuning the microscopic interactions it is also possible to change the sign of the Ising exchange interaction from antiferromagnetic (AFM) to ferromagnetic (FM). In general these Ising Hamiltonians also contain an effective magnetic field [32,33] and in 1D this will act as a confinement potential for the zero-field excitations of the FM chain [44,45]. This suggests the possibility of observing the nontrivial E_8 mass spectrum of “meson” bound states for the critical FM Ising model in a longitudinal field [46–48]. As an extension of these results we also provide the magnetic Hamiltonian for Bose-Fermi mixtures.

The layout of this paper is as follows. In Secs. II and III we provide an introduction to the bosonic Feshbach Hamiltonian and discuss the mapping to the quantum Ising model. In Sec. IV we present a cross section of the phase diagram obtained by DMRG which displays both the Ising quantum phase transition and the onset of superfluidity. We confirm the Ising behavior within the Mott phase using results for the excitation gap and the entanglement entropy. In Sec. V we investigate the role of higher-order terms in the strong coupling expansion. We discuss their impact on the nonuniversal properties of the phase diagram such as the curvature of the Ising phase boundary.

In Sec. VI we examine the local expectation values within the Mott phase at and away from criticality. We move on to correlation functions in Secs. VII and VIII and discuss their relation to the Ising model. In Secs. IX and X we turn our attention to softcore bosons and demonstrate the existence of both AFM and FM Ising transitions. We comment on the closely related fermionic problem in Appendix B. We conclude in Sec. XI and provide perspectives for further research.

II. MODEL

We consider the Hamiltonian [37–40]

$$H = \sum_{i\alpha} \epsilon_\alpha n_{i\alpha} - \sum_{\langle ij \rangle} \sum_{\alpha} t_\alpha (b_{i\alpha}^\dagger b_{j\alpha} + \text{H.c.}) + \sum_{i\alpha\alpha'} \frac{U_{\alpha\alpha'}}{2} : n_{i\alpha} n_{i\alpha'} : + H_F, \quad (1)$$

describing bosons, $b_{i\alpha}$ hopping on a lattice with sites i where $\alpha = a$ and m labels atoms and molecules and $n_{i\alpha} = b_{i\alpha}^\dagger b_{i\alpha}$. Here, ϵ_α are on-site potentials, t_α are hopping parameters, $\langle ij \rangle$ denotes summation over nearest-neighbor bonds, and $U_{\alpha\alpha'}$ are interactions. We use normal ordering symbols to indicate $: n_{i\alpha} n_{i\alpha'} : = n_{i\alpha} (n_{i\alpha} - 1)$ for like species and $: n_{i\alpha} n_{i\alpha'} : = n_{i\alpha} n_{i\alpha'}$ for distinct species. For simplicity we assume that molecules are formed by s -wave Feshbach resonant interactions,

$$H_F = g \sum_i (m_i^\dagger a_i a_i + \text{H.c.}), \quad (2)$$

where $m_i \equiv b_{im}$ and $a_i \equiv b_{ia}$; for recent work on the p -wave problem see Ref. [49]. An important feature of the Feshbach interaction (2) is that atoms and molecules are not separately conserved. However, the total, $N_T \equiv \sum_i (n_{ia} + 2n_{im})$, is preserved. One may therefore work in the canonical ensemble with $\rho_T \equiv N_T/L$ held fixed, where L is the number of lattice sites. In order to make contact with the previous literature [39–41] we consider only a single-band description in Eq. (1); for a discussion of higher-band effects see Refs. [50–52]. As reported elsewhere the pairing Hamiltonian (1) has a rich phase diagram exhibiting both MI and SF phases [32–40,42]. Most notably, the system displays a discrete \mathbb{Z}_2 symmetry-breaking transition [34–36] between a paired molecular condensate (MC) and an atomic plus molecular condensate (AC + MC) phase [42]; for closely related transitions in other models see also Refs. [53–57]. Here, our main focus will be on the MI phase. In particular, we shed further light on the magnetic characteristics of the second Mott lobe [32,33]. We also discuss the connection to Ref. [41] and earlier numerical studies [39,40]. In order to facilitate our numerical simulations we consider the restricted Hamiltonian

$$H_P = \mathcal{P} H \mathcal{P}, \quad (3)$$

where the projection operator \mathcal{P} projects on to the restricted local Hilbert space with a maximum of r_a atoms and r_m molecules per site. We begin our discussion in Sec. III by setting $r_a = 2$ and $r_m = 1$ as used in Ref. [40]. As we will see, the essential characteristic features of the phase diagram are readily gleaned from this limiting case. We move on to the more general problem with canonical softcore bosons in

Secs. IX and X. Throughout this manuscript we use the value of U_{am} to set the overall energy scale; in Figs. 2, 3, and 4 and Figs. 6, 7, and 8 we set $U_{am} = 1$, and in the remaining figures we set $U_{am} = 4$ in order to descend deeper into the Mott phase.

III. SECOND MOTT LOBE

A convenient way to describe the second Mott lobe with $\rho_T = 2$ is via an effective spin model derived within the strong coupling expansion; see Fig. 1. Introducing effective spins $|\downarrow\rangle \equiv |2; 0\rangle/\sqrt{2}$ and $|\uparrow\rangle \equiv |0; 1\rangle$ in the occupation basis $|n_a; n_m\rangle$ one obtains the effective spin-1/2 quantum Ising model [32,33]

$$H \simeq J_{zz} \sum_i S_i^z S_{i+1}^z + h \sum_i S_i^z + \Gamma \sum_i S_i^x + C + \mathcal{O}(t^3), \quad (4)$$

where we work to second order in the hopping parameters. The spin operators are given by

$$S^+ = \frac{m^\dagger a a}{\sqrt{2}}, \quad S^- = \frac{a^\dagger a^\dagger m}{\sqrt{2}}, \quad S^z = \frac{(n_m - n_a)/2}{2}, \quad (5)$$

and $S^\pm \equiv S^x \pm i S^y$ where we suppress site indices. The factors of $\sqrt{2}$ arise from the action of the Bose operators on the basis states. Equivalently, since $n_a + 2n_m = 2$, one may also write $S^z = (1 - n_a)/2$ or $S^z = (2n_m - 1)/2$. As indicated in Fig. 1, the first term in Eq. (4) arises from the virtual hopping processes of atoms and molecules onto neighboring sites and corresponds to an effective magnetic exchange interaction, J_{zz} . The second term in Eq. (4) reflects the energetic detuning between atoms and molecules and corresponds to an effective longitudinal magnetic field, h . The third term in Eq. (4) corresponds directly to the Feshbach term in Eq. (2). Indeed, it is readily seen from the definition (5) that S^+ converts two atoms (\downarrow) into a molecule (\uparrow) and therefore acts like a spin raising operator. It follows that the Feshbach term (2) acts like a transverse field in the x direction with

$$\Gamma \equiv 2g\sqrt{2}. \quad (6)$$

The overall structure of the magnetic Hamiltonian (4) is generic to the second Mott lobe with $\rho_T = 2$. However, the coefficients depend on the specific Hilbert space restriction.

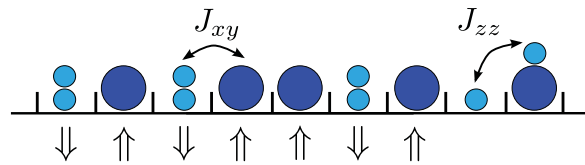


FIG. 1. (Color online) Depiction of the second Mott lobe of the Hamiltonian (1) with $\rho_T = 2$ showing either a pair of atoms or a molecule on each site. These may be regarded as an effective spin-down (\downarrow) and spin-up (\uparrow), respectively. Second-order virtual hopping processes lead to J_{zz} interactions and an effective Ising model. The XY exchange, J_{xy} , occurs at third order and involves interchanging a pair of atoms and a molecule. The Feshbach term (2) converts a pair of atoms (\downarrow) into a molecule (\uparrow) and therefore acts like a transverse field.

For the Hamiltonian (3) with restriction parameters $r_a = 2$ and $r_m = 1$ one obtains [32,33]

$$J_{zz} = \frac{4t_a^2}{U_{am} - U_{aa}} + \frac{t_m^2}{U_{am}} \quad (7)$$

and

$$h = \epsilon_m - 2\epsilon_a - U_{aa}. \quad (8)$$

The constant offset is given by

$$C = L \left(\frac{\epsilon_m}{2} + \epsilon_a + \frac{U_{aa}}{2} - \frac{zJ_{zz}}{8} \right), \quad (9)$$

where z is the cubic lattice coordination and $z = 2$ in 1D. In general there will also be additional contributions to these coefficients arising from higher-order terms in the strong coupling expansion. As we discuss in more detail below similar results also hold for canonical softcore atoms and molecules but with modified coefficients. This is due to the presence of additional intermediate states that are explored in the virtual hopping processes. Nonetheless, this truncation of the Hilbert space is useful for initial numerical simulations and is also used in Ref. [40]. In addition the principal features of the magnetic description are more readily exposed. We return to canonical softcore bosons in Secs. IX and X.

IV. PHASE DIAGRAM AND THE ANTIFERROMAGNETIC ISING TRANSITION

In Refs. [32,33] we provided a variety of evidence for an Ising quantum phase transition in the closely related heteronuclear generalization of Hamiltonian (1). However, due to the small system sizes accessible by exact diagonalization, a complete elucidation of the phase diagram was not possible. In addition correlation functions were out of reach. In particular, it was not possible to track the Ising quantum phase transition throughout the second Mott lobe or to accurately delimit the onset of superfluidity. We address this situation for the homonuclear case by using DMRG on large systems. We keep up to 3000 density matrix states so that the discarded weight is less than 10^{-10} . Following Ref. [40] we implement the model (3) as a two-leg ladder system, where the atoms and molecules reside on opposite legs of the ladder. In this representation the Feshbach term (2) corresponds to hopping along the rungs, and extreme care must be taken for small values of g . In Fig. 2 we present a cross section of the phase diagram for the Hamiltonian (3) with $r_a = 2$ and $r_m = 1$. In this approach the Hilbert space restriction parameters r_α and the interactions $U_{\alpha\alpha'}$ are treated independently. For ease of exposition we begin by setting $\epsilon_a = \epsilon_m = U_{aa} = 0$ and $U_{am} = 1$, where our choice of parameters is motivated by the simplest case with zero magnetic field as given by Eq. (8). In addition, for small hopping parameters t_a , and large U_{am} , one may set $U_{aa} = 0$ in Eq. (7) without loss of generality or conflict with the strong coupling expansion. We incorporate the effects of finite U_{aa} in our subsequent discussion.

The phase diagram in Fig. 2 contains three distinct phases. A \mathbb{Z}_2 disordered MI with vanishing staggered magnetization $\sum_i (-1)^i \langle S_i^z \rangle / L = 0$, a \mathbb{Z}_2 ordered MI with a finite staggered magnetization and long range AFM correlations, and an AC + MC superfluid with both atomic and molecular power law

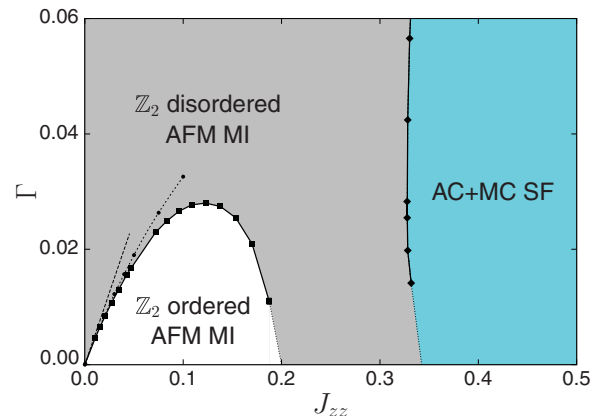


FIG. 2. (Color online) Phase diagram of the 1D Hamiltonian (3) with $\rho_T = 2$ obtained by DMRG with up to $L = 256$ sites. We restrict the local Hilbert space to a maximum of one molecule and two atoms per site with $r_m = 1$ and $r_a = 2$, and we set $\epsilon_a = \epsilon_m = 0$, $U_{aa} = 0$, and $U_{am} = 1$, corresponding to $h = 0$. We set $t_a = 2t_m = t$ and vary t to obtain different values of $J_{zz} = 17t^2/4$ corresponding to the AFM exchange. This cross section shows a \mathbb{Z}_2 ordered AFM MI, a \mathbb{Z}_2 disordered AFM MI, and an AC + MC SF. The solid squares are obtained from the vanishing of the first excitation gap, $\Delta_1 \equiv E_1 - E_0$, corresponding to an Ising quantum phase transition within the MI; the solid line is a spline fit which is extrapolated down to $\Gamma = 0$. The dashed line corresponds to the strong coupling result, $\Gamma_c = J_{zz}/2$, which follows from the Hamiltonian (4) with $h = 0$. The dotted line is obtained by ED of Hamiltonian (4) including the subleading XY exchange terms, $J_{xy} = -0.46 J_{zz}^{3/2}$, which arise at higher order in the strong coupling expansion. The diamonds are obtained from the vanishing of the two-particle gap, $E_{2g} \equiv \mu_+ - \mu_-$, where $\mu_{\pm} = \pm[E_0(L, N_T \pm 2) - E_0(L, N_T)]$, and up to $L = 128$, indicating the onset of an AC + MC superfluid.

superfluidity. The additional MC phase with only molecular superfluidity is absent in this cross section of the phase diagram due to our choice of parameters; for more details of the superfluid phases see Ref. [42]. In this manuscript our main focus is on the MI phase. In particular, we see that the magnetic phase boundary bends over quite considerably due to higher-order terms in the strong coupling expansion. Nonetheless, the quantum phase transition remains in the Ising universality class. For example, the Ising character of this transition is supported by Fig. 3 which shows the characteristic linear variation of the excitation gap [58]

$$\Delta = |\Gamma - \Gamma_c|, \quad (10)$$

on passing through the transition in the scaling regime. The Ising character is also confirmed by DMRG results for the entanglement entropy as shown in Fig. 4. For a block of length l in a system of length L , the von Neumann entropy is given by $S_L(l) = -\text{Tr}_l(\rho_l \ln \rho_l)$, where $\rho_l = \text{Tr}_{L-l}(\rho)$ is the reduced density matrix. In a critical system with periodic boundaries one obtains [59–62]

$$S_L(l) = \frac{c}{3} \ln \left[\frac{2L}{\pi} \sin \left(\frac{\pi l}{L} \right) \right] + s_1, \quad (11)$$

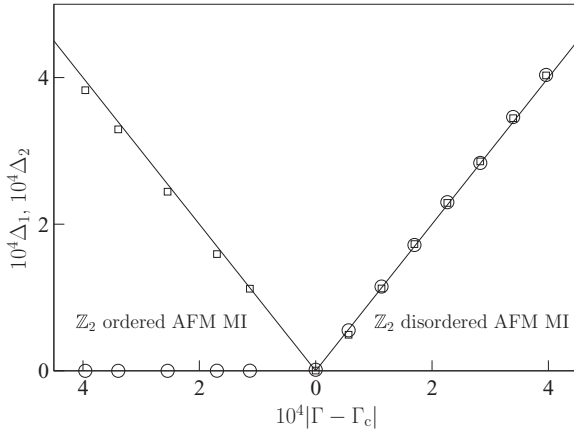


FIG. 3. DMRG results for the excitation gaps, $\Delta_1 \equiv E_1 - E_0$ (circles) and $\Delta_2 \equiv E_2 - E_0$ (squares), for the bosonic Hamiltonian (3) with open boundaries and up to $L = 256$ sites. We pass through the Ising quantum phase transition shown in Fig. 2 with $t = 0.05$ and $J_{zz} \approx 0.01$. The transition occurs at $\Gamma_c \approx 4.6 \times 10^{-3}$, which is slightly below the strong coupling result, $\Gamma_c = J_{zz}/2 \approx 5.3 \times 10^{-3}$. This reflects the curvature of the Ising transition shown in Fig. 2. The solid lines indicate the linear gap, $\Delta = |\Gamma - \Gamma_c|$, corresponding to the Ising critical exponent, $\nu = 1$.

where s_1 is a nonuniversal constant and c is the central charge. As shown in Fig. 4(a) the results are in excellent agreement with an Ising quantum phase transition with $c = 1/2$. In particular, this continues to hold further out in the Mott phase where the strong coupling analysis no longer strictly applies. Further evidence for this may be seen from the entanglement entropy difference [42,63]

$$\Delta S(L) \equiv S_L(L/2) - S_{L/2}(L/4), \quad (12)$$

which exhibits a peak on transiting through the magnetic transition as shown in Fig. 4(b). At criticality $\Delta S = \frac{c}{3} \ln 2 + \dots$ [59–62] and the peak height is in good agreement with $c = 1/2$. It is interesting to note that a naive spline fit to the currently available DMRG data for the Ising phase boundary shown in Fig. 2 terminates within the MI. This tentatively suggests that a magnetic transition may exist even in the absence of the Feshbach term (2). Unfortunately, it is difficult to gain a quantitative handle on the character of this feature, which occurs for intermediate hopping strengths and vanishing Feshbach coupling, using our current implementation of DMRG. Moreover, this $\Gamma = 0$ limit differs somewhat from other investigations of the two-component Bose-Hubbard model [64,65], since we keep the total density, $\rho_T = \sum_i (n_{ia} + 2n_{im})/L = 2$, held fixed, with two atoms and one molecule per site. It would be instructive to explore this limit in future work.

V. HIGHER-ORDER CONTRIBUTIONS IN THE STRONG COUPLING EXPANSION

In the discussion above we have presented a variety of large-scale DMRG results in favor of an Ising quantum phase transition taking place within the second Mott lobe [32,33]. In particular we have argued that the Ising character of the

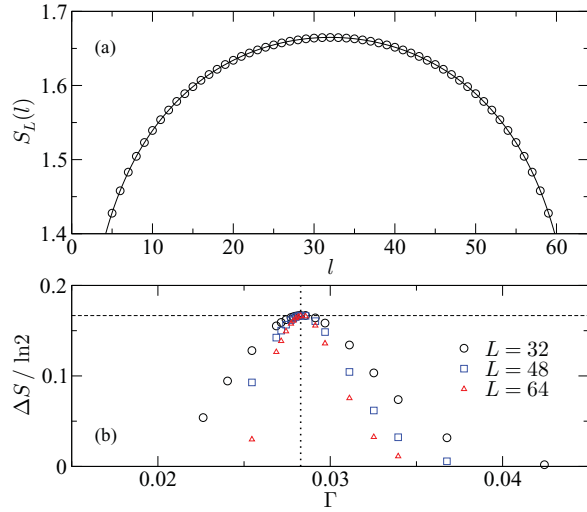


FIG. 4. (Color online) (a) DMRG results for the entanglement entropy, $S_L(t)$, at the Ising transition within the MI for a subsystem of length l in a periodic chain with $L = 64$. We use the same parameters as in Fig. 2 and set $t = 0.17$ corresponding to $J_{zz} \approx 0.12$ and $\Gamma_c \approx 0.028$. The solid line is a fit to Eq. (11). The extracted value of the central charge $c = 0.50(2)$ is consistent with a magnetic transition in the Ising universality class. (b) The entanglement entropy difference $\Delta S(L)$ for $t = 0.17$ shows a peak at the Ising transition. The peak height corresponds to $c = 1/2$ as indicated by the dashed lines.

quantum phase transition persists throughout an extended region of the phase diagram as shown in Fig. 2. Nonetheless, it is important to bear in mind that the explicit Ising Hamiltonian given in Eq. (4) is derived by means of the strong coupling, t/U , expansion. It is therefore tailored toward a quantitative description of the bosonic Hamiltonian (1) deep within the Mott lobe, as supported by our DMRG results. At larger values of the hopping parameters departures from the strong coupling result (4) are to be expected. This is evident from the deviation of the phase boundary from the asymptotic result, $\Gamma_c = J_{zz}/2$, as shown in Fig. 2. Carrying out the strong coupling expansion to third order in the hopping parameters one must supplement the Hamiltonian (4) with the additional XY exchange terms:

$$\Delta H = \frac{J_{xy}}{2} \sum_i (S_i^+ S_{i+1}^- + S_i^- S_{i+1}^+), \quad (13)$$

where $S^\pm \equiv S^x \pm iS^y$, and

$$J_{xy} = -\frac{4t_a^2 t_m}{U_{am} - U_{aa}} \left(\frac{1}{U_{am}} + \frac{1}{U_{am} - U_{aa}} \right). \quad (14)$$

One thus obtains a strongly anisotropic XXZ Heisenberg Hamiltonian in both a longitudinal and transverse field. For the parameters chosen in Fig. 2, $J_{zz} = 17t^2/4$ and $J_{xy} = -4t^3$. This yields the XXZ anisotropy parameter, $\delta \equiv J_{xy}/J_{zz} = -16t/17$, corresponding to $\delta \approx -0.46\sqrt{J_{zz}}$. Within the MI shown in Fig. 2 this gives $-0.27 \lesssim \delta < 0$. The system remains in the strongly anisotropic regime and Ising criticality is expected to persist throughout this cross section of the MI. Nonetheless, the XY contributions (13) modify the location of the Ising quantum phase transition as shown in Fig. 2. As we

discuss in Sec. VII such terms also influence the nonuniversal amplitudes in the correlation functions whilst preserving the universal critical exponents.

VI. LOCAL EXPECTATION VALUES

Having provided numerical evidence for an Ising quantum phase transition in the second Mott lobe of the Hamiltonian (1) we turn our attention to the local expectation values. The order parameter of the AFM transverse field Ising model (4) is the staggered magnetization $(-1)^i \langle S_i^z \rangle$. In the thermodynamic limit with $h = 0$ and $\Gamma < \Gamma_c$ this is given by [66,67]

$$(-1)^i \langle S_i^z \rangle = \frac{1}{2} \left[1 - \left(\frac{\Gamma}{\Gamma_c} \right)^{2\beta} \right], \quad (15)$$

where $\beta = 1/8$ is the Ising critical exponent; in the disordered phase with $\Gamma > \Gamma_c$ the order parameter vanishes. In order to verify this characteristic behavior in the bosonic Hamiltonian (3) we choose parameters deep within the Mott phase. As shown in Fig. 5(a) our DMRG results are in excellent agreement with Eq. (15). This confirms that any higher-order corrections to the Ising description (4) are small. In a similar fashion the transverse magnetization is given by [66,67]

$$\langle S_i^x \rangle = - \int_0^\pi \frac{dk}{2\pi} \frac{2\Gamma + J_{zz} \cos k}{\sqrt{4\Gamma^2 + J_{zz}^2 + 4\Gamma J_{zz} \cos k}}. \quad (16)$$

This dependence is confirmed in Fig. 5(b) both at and away from criticality. Note that at the critical point where $\Gamma = \Gamma_c$ the expectation value $\langle S_i^x \rangle = -1/\pi$ is nonvanishing due to the transverse field. We have also checked the consistency of our DMRG results by applying a small staggered field h_{st} to the bosonic Hamiltonian (3), $\Delta H_{st} = -h_{st} \sum_i (-1)^i S_i^z$, where S_i^z is given by Eq. (5). In the limit $h_{st} \rightarrow 0$ this replicates the effect of spontaneous symmetry breaking in our finite-size simulations. The results converge to the same values as for $h_{st} = 0$; see inset of Fig. 5(a).

Having established the validity of the explicit Ising Hamiltonian (4) deep within the Mott phase, it is instructive to see how this leading-order behavior is modified as one moves out toward the MI-SF boundary. In Fig. 6(a) we show the evolution of the local magnetization $\langle S_i^z \rangle$ with increasing hopping parameters within the \mathbb{Z}_2 disordered phase shown in Fig. 2. Deep within the MI, $\langle S_i^z \rangle = 0$, as one would expect for the disordered phase of the transverse field Ising model (4) with $h = 0$. However, at larger values of the hopping parameters a finite uniform magnetization develops as indicated by the plateaus in Fig. 6(a). This is due to the presence of higher-order terms in the strong coupling expansion. In general such contributions are expected to induce corrections to the leading-order coefficients, J_{zz} and C , and the magnetic field, h , given in Eqs. (7)–(9). However, it is evident from Fig. 6(b) that this uniform contribution to the magnetization remains significantly below the saturation value of $\langle S_i^z \rangle = -1/2$, indicating that the leading-order description (4) is a useful starting point in the broader phase diagram. Indeed, the staggered magnetization remains zero in the bulk of the system, as may be seen from the absence of oscillations in Fig. 6(a). As such we remain in the disordered phase of an Ising antiferromagnet, albeit in the presence of an increasing uniform effective magnetic field. More generally,

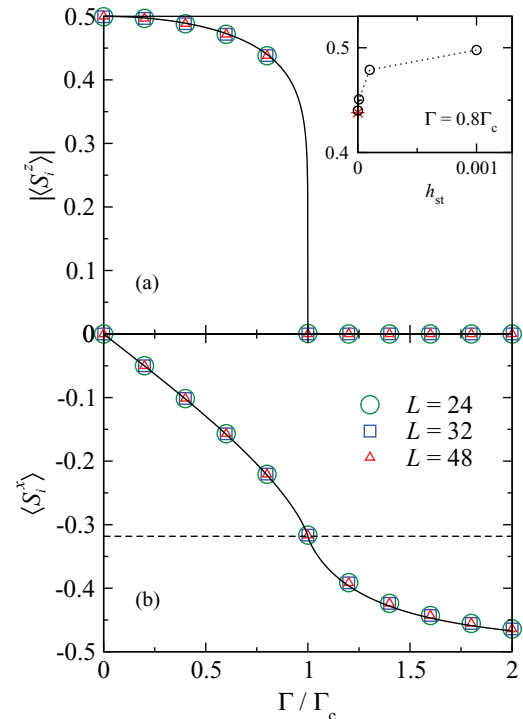


FIG. 5. (Color online) Local expectation values deep within the Mott phase obtained by DMRG for the bosonic Hamiltonian (3) with periodic boundaries and restriction parameters $r_m = 1$ and $r_a = 2$. In order to demonstrate the broader validity of our results, while suppressing higher-order terms in the strong coupling expansion, we choose parameters different from those used in Fig. 2. We set $\epsilon_a = 0$ and $\epsilon_m = U_{aa} = 3.8$, corresponding to $h = 0$, and we take $U_{am} = 4$ and $t = 0.005$. (a) Staggered magnetization $|\langle S_i^z \rangle|$. The theoretical result for the transverse field Ising model is given by Eq. (15) and is indicated by the solid line. Inset: The application of a small staggered field h_{st} yields the same results as in panel (a) in the limit $h_{st} \rightarrow 0$. (b) Transverse magnetization $\langle S_i^x \rangle$. The solid line shows the Ising behavior given by Eq. (16). The dashed line corresponds to $\langle S_i^x \rangle = -1/\pi$, which holds at criticality.

one may also transit through the \mathbb{Z}_2 ordered region shown in Fig. 2. As indicated in Figs. 6(c) and 6(d) this results in the onset of AFM oscillations in the local magnetization. In Fig. 6(e) we plot the evolution of the corresponding uniform and staggered magnetizations. The region of support of the staggered component is in agreement with the \mathbb{Z}_2 ordered phase inferred from the gap data in Fig. 2.

VII. CORRELATION FUNCTIONS

Having discussed the local expectation values we now consider correlation functions. In order to orient the discussion we first recall the expected theoretical behavior at the critical point of the AFM Ising model in a transverse field, where $\Gamma_c = J_{zz}/2$ and $h = 0$. In the absence of a longitudinal field

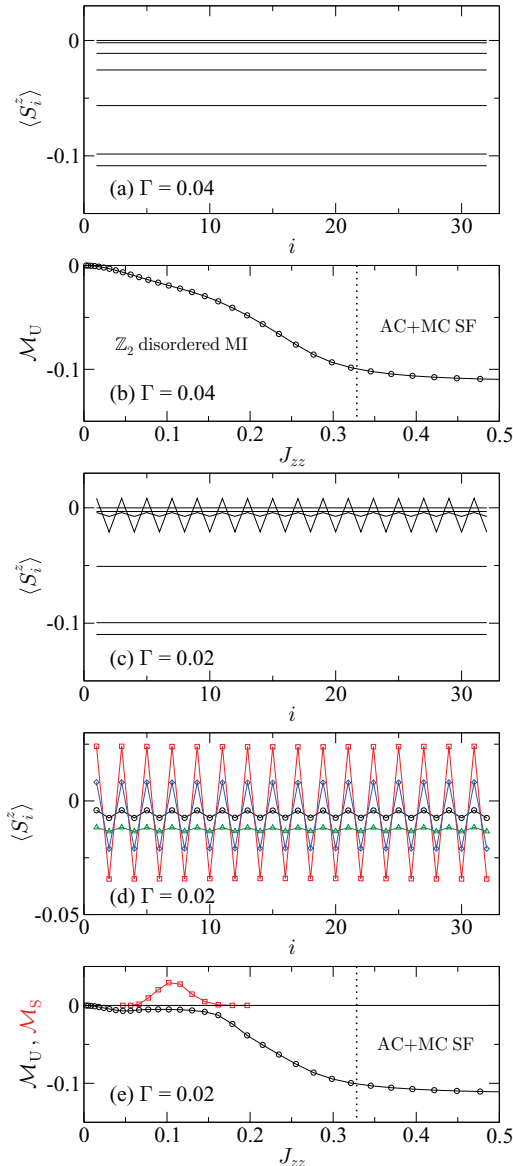


FIG. 6. (Color online) (a) DMRG results for the local magnetization $\langle S_i^z \rangle$ for the parameters used in Fig. 2 with $h = 0$ and $\Gamma = 0.04$. We set $t = 0.025, 0.075, 0.125, \dots, 0.325$ from top to bottom with $L = 32$ and periodic boundaries. The plateaus correspond to the development of a uniform magnetization while the staggered magnetization remains zero. (b) Uniform magnetization $\mathcal{M}_U = \sum_i \langle S_i^z \rangle / L$. The nonzero value is attributed to higher-order terms in the strong coupling expansion. These may modify the leading-order magnetic field given in Eq. (8). The dotted line shows the approximate location of the MI to AC + MC transition obtained from the gap data in Fig. 2. (c) We set $\Gamma = 0.02$ and use the same values of the remaining parameters as in panel (a). The oscillations correspond to the onset of the \mathbb{Z}_2 ordered phase in Fig. 2. (d) Antiferromagnetic oscillations in the \mathbb{Z}_2 ordered phase with $t = 0.125$ (circles), $t = 0.155$ (squares), $t = 0.175$ (diamonds), and $t = 0.195$ (triangles). (e) Uniform magnetization \mathcal{M}_U (circles) and staggered magnetization $\mathcal{M}_S = \sum_i (-1)^i \langle S_i^z \rangle / L$ (squares) for $\Gamma = 0.02$.

the asymptotic longitudinal correlation function decays as a power law [66],

$$\langle S_i^z S_{i+n}^z \rangle \sim (-1)^n \mathcal{B} n^{-\eta} + \dots, \quad (17)$$

where $\eta = 1/4$ is the Ising pair correlation exponent, $\mathcal{B} = \mathcal{A}^{-3} 4^{-1} 2^{1/12} e^{1/4} \simeq 0.161$ is a constant prefactor, and $\mathcal{A} \simeq 1.2824$ is the Glaisher-Kinkelin constant. In a similar fashion, the transverse correlators also exhibit power law behavior at criticality [66],

$$\langle S_i^x S_{i+n}^x \rangle \sim \langle S_i^x \rangle^2 + (2\pi n)^{-2} + \dots, \quad (18)$$

where $\langle S_i^x \rangle = -1/\pi$ at the transition and

$$\langle S_i^y S_{i+n}^y \rangle \sim -(-1)^n (\mathcal{B}/4) n^{-9/4} + \dots. \quad (19)$$

As suggested by Eq. (18), due to the finite value of $\langle S_i^x \rangle = -1/\pi$ at criticality one must consider the connected correlation function $\langle S_i^x S_{i+n}^x \rangle - \langle S_i^x \rangle \langle S_{i+n}^x \rangle$ in order to see power law behavior. To establish this dependence in the bosonic Hamiltonian (3) we perform DMRG calculations with open boundaries and up to $L = 512$ sites. As shown in Fig. 7, at $\Gamma = \Gamma_c$ the data are consistent with power law behavior in the bulk of the system away from the sample boundaries. In addition the data show long-range order in $|\langle S_i^z S_{i+n}^z \rangle|$ for $\Gamma < \Gamma_c$ and a finite correlation length for $\Gamma > \Gamma_c$. Although this provides direct evidence for a quantum phase transition, a quantitative determination of the Ising critical exponents requires a more detailed finite-size scaling analysis of the data. This is most readily achieved using periodic boundary conditions. We recall that in a finite-size critical system with periodic boundary conditions, the two-point function of a primary field \mathcal{O} may be obtained by conformal transformation of the strip geometry [68]:

$$\langle \mathcal{O}(r_1) \mathcal{O}(r_2) \rangle_L = \mathcal{N} \left[\frac{\pi}{L \sin(\frac{\pi r}{L})} \right]^a. \quad (20)$$

Here a is the critical exponent in the thermodynamic limit and \mathcal{N} is the prefactor: $\langle \mathcal{O}(r_1) \mathcal{O}(r_2) \rangle_\infty = \mathcal{N} r^{-a}$. It follows from Eq. (20) that the rescaled combination

$$L^a \langle \mathcal{O}(r_1) \mathcal{O}(r_2) \rangle_L = f_a(r/L) \quad (21)$$

is a prescribed scaling function,

$$f_a(x) = \mathcal{N} \left[\frac{\pi}{\sin(\pi x)} \right]^a, \quad (22)$$

of the reduced separation $x = r/L$. As shown in Figs. 8 and 9, the rescaled critical two-point functions,

$$\begin{aligned} \mathcal{F}_z(n/L) &\equiv L^{1/4} |\langle S_i^z S_{i+n}^z \rangle_L|, \\ \mathcal{F}_y(n/L) &\equiv L^{9/4} |\langle S_i^y S_{i+n}^y \rangle_L|, \\ \mathcal{F}_x(n/L) &\equiv L^2 [\langle S_i^x S_{i+n}^x \rangle - \langle S_i^x \rangle \langle S_{i+n}^x \rangle]_L, \end{aligned} \quad (23)$$

all show striking data collapse over the entire system length, showing clear indications of Ising criticality. Deep in the Mott phase the resulting scaling functions are in excellent agreement with the theoretical results for the lattice Ising model (4) in finite-size geometry, as indicated in Fig. 9. This includes both the universal critical exponents, a , and the non-universal amplitude prefactors, \mathcal{N} , taken from Eqs. (17), (18), and (19).

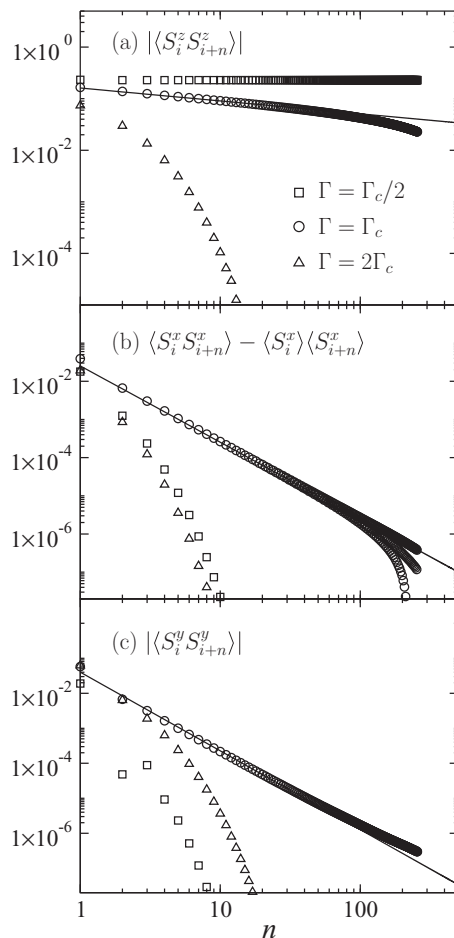


FIG. 7. Correlation functions within the second Mott lobe of the bosonic Hamiltonian (3) obtained by DMRG with $L = 512$ and open boundaries. We use the same parameters as in Fig. 3. The data are consistent with an Ising quantum phase transition between a magnetic state with long range order and a disordered state with a finite correlation length. The solid lines correspond to the critical two-point functions in Eqs. (17), (18) and (19). A quantitative demonstration of the Ising critical exponents is shown in Fig. 8 using periodic boundaries and finite-size scaling.

Further out in the Mott phase, the nonuniversal prefactors are influenced by higher-order terms in the strong coupling expansion as discussed in Sec. V, but the universal Ising exponents are robust to these perturbations; see Fig. 8.

Having confirmed the presence of a line of critical Ising correlations within the second Mott lobe of the bosonic Hamiltonian (3) we now consider the generic behavior in the MI phase. As may be seen in Fig. 7, the data reveal a finite correlation length for the connected correlation functions on either side of the transition. This is consistent with the presence of an Ising spectral gap as shown in Fig. 3. In order to place this behavior on a quantitative footing we recall the principal results for the transverse field Ising model (4) with $h = 0$. In

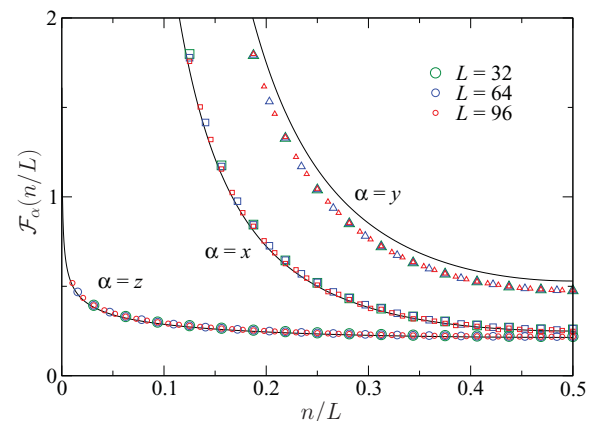


FIG. 8. (Color online) DMRG results for the rescaled bosonic correlation functions $L^{1/4}|\langle S_i^z S_{i+n}^z \rangle|$ (circles), $L^2[\langle S_i^x S_{i+n}^x \rangle - \langle S_i^x \rangle \langle S_{i+n}^x \rangle]$ (squares), and $L^{9/4}|\langle S_i^y S_{i+n}^y \rangle|$ (triangles) with periodic boundaries at criticality for the parameter set of Fig. 7 with $t = 0.05$. The data collapse over the entire system length with the Ising critical exponents. The nonuniversal prefactors differ slightly from the theoretical predictions of the lattice Ising model (4) as indicated by the solid lines. This is due to the presence of small additional XY contributions to the Ising description. By descending deeper into the Mott lobe one obtains a complete quantitative agreement including the nonuniversal prefactors as shown in Fig. 9.

the ordered phase with $\Gamma < \Gamma_c$ the leading contribution to the longitudinal correlations is given by [66]

$$\langle S_i^z S_{i+n}^z \rangle \sim (-1)^n |\langle S_i^z \rangle|^2, \quad (24)$$

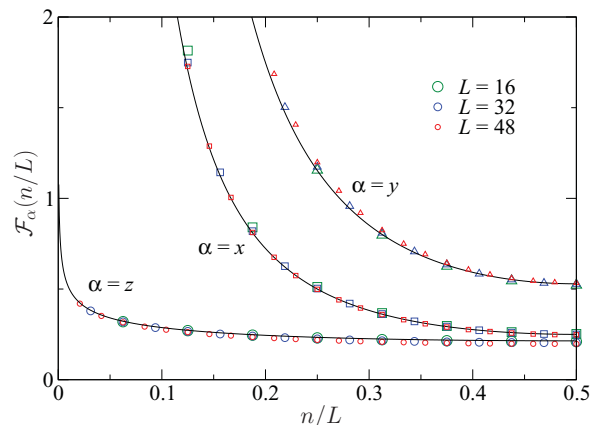


FIG. 9. (Color online) DMRG results for the rescaled bosonic correlation functions $L^{1/4}|\langle S_i^z S_{i+n}^z \rangle|$ (circles), $L^2[\langle S_i^x S_{i+n}^x \rangle - \langle S_i^x \rangle \langle S_{i+n}^x \rangle]$ (squares), and $L^{9/4}|\langle S_i^y S_{i+n}^y \rangle|$ (triangles) with periodic boundaries at criticality for the parameter set of Fig. 5 with $t = 0.005$. The data show clear scaling collapse over the entire system length. The theoretical results for the lattice Ising model (4) in a finite-size geometry are indicated by solid lines. The data are in excellent agreement with both the universal Ising critical exponents and the nonuniversal amplitudes in Eqs. (17), (18), and (19).

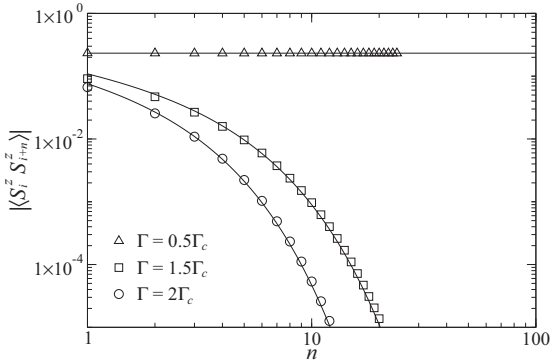


FIG. 10. Off-critical order parameter correlations $|\langle S_i^z S_{i+n}^z \rangle|$ obtained by DMRG on the 1D system (3) with $L = 48$ and periodic boundaries. We use the same parameters as in Fig. 5. The solid lines correspond to the quantum Ising model (4) and are given by Eq. (24) for $\Gamma < \Gamma_c$ and Eq. (25) for $\Gamma > \Gamma_c$. The agreement confirms the presence of long-range order for $\Gamma < \Gamma_c$ and exponential decay for $\Gamma > \Gamma_c$.

where $|\langle S_i^z \rangle|$ is the staggered magnetization corresponding to the onset of long-range AFM order as given by Eq. (15). In contrast, in the disordered phase with $\Gamma > \Gamma_c$, the correlations decay exponentially with a power law prefactor [66],

$$\langle S_i^z S_{i+n}^z \rangle \sim \frac{(-1)^n}{4} \left[1 - \left(\frac{\Gamma_c}{\Gamma} \right)^2 \right]^{-1/4} \frac{e^{-n/\xi}}{\sqrt{\pi n}}, \quad (25)$$

where $\xi^{-1} = \ln(\Gamma/\Gamma_c)$. To confirm this behavior we descend deep into the Mott phase in order to suppress the effects of the small XY terms given by Eq. (14). As shown in Fig. 10, the results are in excellent agreement with the theoretical predictions, Eqs. (24) and (25).

VIII. ATOM-MOLECULE CORRELATIONS

The above considerations are consistent with the notion that away from the Ising transition line the connected correlations decay exponentially in the MI. As advocated in Ref. [32] the absence of low-lying gapless excitations precludes the possibility of the novel super-Mott behavior proposed in Refs. [39,40]. This gained further support in a recent comment [41] which confirms the presence of exponential decay in the atom-molecule correlation functions. We discuss these observations for the bosonic Hamiltonian (3) within the framework of the Ising description.

In order to investigate the possibility of counterflow supercurrents [64,65] of atoms and molecules, the authors of Ref. [41] consider the connected correlation function

$$C_{am}(n) = \langle m^\dagger(n) a(n) a(n) a^\dagger(0) a^\dagger(0) m(0) \rangle - \langle m^\dagger(n) a(n) a(n) \rangle \langle a^\dagger(0) a^\dagger(0) m(0) \rangle. \quad (26)$$

Using the spin mapping (5) [32,33] this may be written in the equivalent form

$$C_{am}(n) = 2[\langle S^+(n) S^-(0) \rangle - \langle S^+(n) \rangle \langle S^-(0) \rangle]. \quad (27)$$

Deep within the second Mott lobe one may therefore use the Ising Hamiltonian (4) to gain a handle on the bosonic

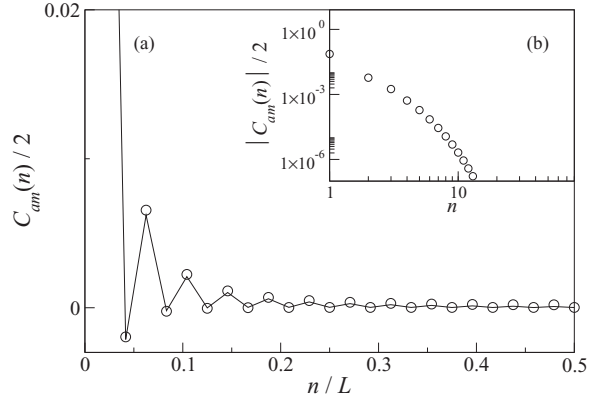


FIG. 11. Correlation function $C_{am}(n)/2$ at and away from criticality obtained by DMRG on the 1D system (3) with $L = 48$ and periodic boundaries. We use the same parameters as in Fig. 5. (a) At criticality clear oscillations are present in conformity with the Ising description. The solid line corresponds to the theoretical prediction in Eq. (31). (b) Away from the critical point with $\Gamma = 2\Gamma_c$, $C_{am}(n)$ shows a finite correlation length due to the Ising gap.

correlation function (26). To this end we may decompose the first term in Eq. (27) as

$$\langle S_i^+ S_{i+n}^- \rangle = \langle S_i^x S_{i+n}^x \rangle + \langle S_i^y S_{i+n}^y \rangle, \quad (28)$$

where the mixed component terms cancel. It follows that

$$C_{am}(n) = 2[\langle S_i^x S_{i+n}^x \rangle - \langle S_i^x \rangle \langle S_{i+n}^x \rangle + \langle S_i^y S_{i+n}^y \rangle], \quad (29)$$

where we use the fact that $\langle S_i^y \rangle = 0$ for the transverse field Ising model (4) in zero magnetic field. That is to say, $C_{am}(n)$ is the sum of the connected xx correlation function and the yy correlation function. From our previous discussion in Sec. VII these contributions generically decay exponentially, in agreement with the findings of Ref. [41]. However, along the locus of the Ising quantum phase transition one expects power law contributions. Using Eqs. (18) and (19) one obtains

$$C_{am}(n) \sim 2[(2\pi n)^{-2} - (-1)^n (\mathcal{B}/4) n^{-9/4}]. \quad (30)$$

In order to confirm this characteristic oscillatory dependence we perform DMRG on the 1D bosonic Hamiltonian (3) with $L = 96$ and periodic boundaries. Employing the finite-size result (20) obtained by conformal transformation one obtains

$$\frac{C_{am}(n)}{2} \sim \frac{1}{(2\pi)^2} \left[\frac{\pi/L}{\sin(\frac{\pi n}{L})} \right]^2 - (-1)^n \frac{\mathcal{B}}{4} \left[\frac{\pi/L}{\sin(\frac{\pi n}{L})} \right]^{9/4}. \quad (31)$$

As shown in Fig. 11 the results are in excellent agreement with the underlying Ising correlation functions.

IX. CANONICAL SOFTCORE BOSONS

Having provided a discussion of the model (3) in the reduced Hilbert space, with $r_a = 2$ and $r_m = 1$, we turn our attention to the more general problem with canonical softcore bosons. In this situation one must allow for the presence of additional virtual intermediate states in the magnetic

description. For example, in a configuration with two pairs of a atoms on neighboring sites the softcore problem allows virtual hopping to take place, in contrast to the problem with $r_a = 2$. This modifies the coefficients, J_{zz} , h , and C , but the Ising description remains valid deep within the second Mott lobe. One again obtains the effective magnetic Hamiltonian given in Eq. (4) but with the modified coefficients,

$$J_{zz} = \frac{4t_a^2}{U_{am} - U_{aa}} + \frac{t_m^2}{U_{am}} - \frac{12t_a^2}{U_{aa}} - \frac{4t_m^2}{U_{mm}} \quad (32)$$

and

$$h = \epsilon_m - 2\epsilon_a - U_{aa} + \frac{z}{2} \left(\frac{12t_a^2}{U_{aa}} - \frac{4t_m^2}{U_{mm}} \right), \quad (33)$$

together with

$$C = L \left[\frac{\epsilon_m}{2} + \epsilon_a + \frac{U_{aa}}{2} - \frac{z}{8} \left(\frac{4t_a^2}{U_{am} - U_{aa}} + \frac{t_m^2}{U_{am}} + \frac{12t_a^2}{U_{aa}} + \frac{4t_m^2}{U_{mm}} \right) \right], \quad (34)$$

as shown in Appendix A. Note in particular that the effective longitudinal magnetic field, h , now depends on the hopping parameters and is therefore already present at second order in the strong coupling expansion. In order to see the effect of these additional intermediate states it is instructive to examine the change in the ground-state energy of the bosonic Hamiltonian (3) upon increasing the local atomic Hilbert space restriction, r_a . For simplicity, we consider $U_{mm} \rightarrow \infty$, corresponding to hardcore molecules with $r_m = 1$. As shown in Fig. 12(a), the ground-state energy changes on going from $r_a = 2$ to $r_a = 3$ due to the additional hopping processes. However, increasing the atomic restriction beyond $r_a = 3$ has no further effect, since higher occupations are not explored at second order in perturbation theory within the second Mott lobe. The excellent agreement of the bosonic results with $r_a = 3$ and $r_a = 4$ therefore supports the applicability of the second-order Ising description. The solid lines shown in Fig. 12(a) correspond to the ground-state energy density of the Ising model (4) obtained by exact diagonalization with the appropriate coefficients. Our DMRG results are in excellent agreement with these predictions. As shown in Fig. 12(b) this agreement also extends to the generic softcore problem. At second order in perturbation theory around the second Mott lobe the maximum local occupation is $r_a = 3$ and $r_m = 2$. The absence of any further change in the ground-state energy on increasing the local Hilbert space justifies both the use of this truncation and the Ising description. In Fig. 13 we show the existence of an AFM Ising quantum phase transition within the second Mott lobe for these restricted softcore bosons. The entanglement entropy difference as given by Eq. (12) exhibits a peak on transiting through the magnetic transition. At criticality $\Delta S = \frac{c}{3} \ln 2 + \dots$ and the peak height is in good agreement with an Ising quantum phase transition with central charge $c = 1/2$.

X. FERROMAGNETIC ISING TRANSITION

An interesting aspect of the canonical softcore result (32) is that one may explore both AFM and FM Ising interactions

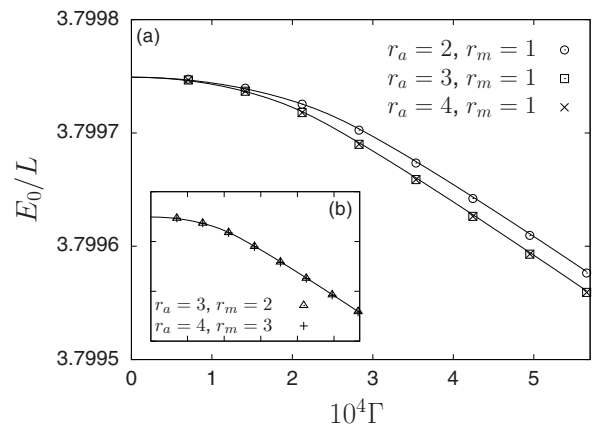


FIG. 12. Ground-state energy density of the Hamiltonian (3) obtained by DMRG with $L = 20$ (to aid comparison with ED results for the Ising model) and periodic boundaries. (a) We use the parameters in Fig. 5 and increase the local atomic Hilbert space restriction r_a , with $r_m = 1$ held fixed. The lines are results for the energy density of the Ising Hamiltonian (4) obtained by ED ($L = 20$) with $J_{zz} = 5.02 \times 10^{-4}$ and $h = 0$ for $r_a = 2$ and with $J_{zz} = 4.23 \times 10^{-4}$ and $h = 7.89 \times 10^{-5}$ for $r_a = 3$ and 4. The change from $r_a = 2$ to $r_a = 3$ is due to the presence of additional virtual states which modify the Ising model coefficients. The absence of any change beyond $r_a = 3$ is consistent with second-order perturbation theory around the second Mott lobe. (b) Ground-state energy density for the same parameters as in panel (a) with the additional interaction $U_{mm} = 4$. We increase the local Hilbert space from $r_a = 3$ and $r_m = 2$ to $r_a = 4$ and $r_m = 3$. The absence of any further change is consistent with the maximum occupancy for virtual states explored in second-order perturbation theory around the second Mott lobe. The solid line is the energy density of the Ising Hamiltonian (4) obtained by ED ($L = 20$) with $J_{zz} = 4.16 \times 10^{-4}$ and $h = 7.27 \times 10^{-5}$ as given by Eqs. (32) and (33), respectively.

due to the relative minus signs. This is readily seen by exact diagonalization on small systems using the techniques employed in Refs. [32,33,69]. As shown in Fig. 14 an Ising transition indeed persists with FM parameters and $h = 0$. This is also confirmed by DMRG results for the ground-state

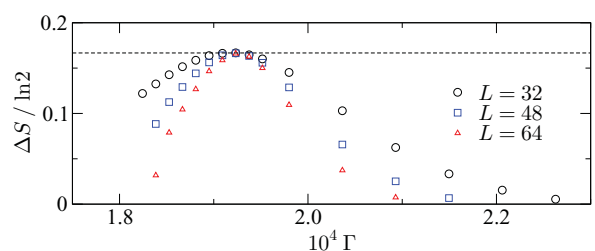


FIG. 13. (Color online) Entanglement entropy difference $\Delta S(L) \equiv S_L(L/2) - S_{L/2}(L/4)$ showing an Ising quantum phase transition within the second Mott lobe for restricted softcore bosons. We truncate the local Hilbert space to $r_a = 3$ and $r_m = 2$ which is the maximum occupancy explored at second order in perturbation theory. We use the same parameters as in Fig. 12(b) and set $t = 0.005$. The peak height corresponds to a central charge $c \approx 1/2$.

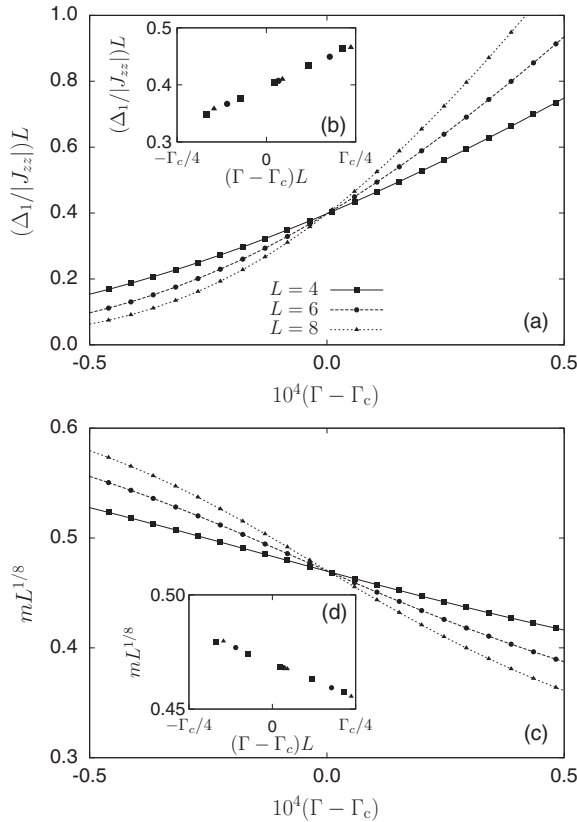


FIG. 14. ED results for the Hamiltonian (3) with hardcore molecules ($r_m = 1$) and up to three atoms ($r_a = 3$) per site. We set $\epsilon_a = 0$, $U_{aa} = 2$, $U_{am} = 4$, and $t_a = 2t_m$ and take $t_a = 0.01$ corresponding to FM exchange with $J_{zz} \simeq -3.94 \times 10^{-4}$. For simplicity we set $h = \epsilon_m - 2 + 6t_a^2 = 0$ by taking $\epsilon_m = 1.9994$. (a) The rescaled energy gap $\Delta_1 \equiv E_1 - E_0$ shows a clear intersection at $\Gamma_c \approx 1.969 \times 10^{-4} \approx 0.4997|J_{zz}|$ corresponding to a FM transition. (b) Scaling collapse with the Ising critical exponent, $\nu = 1$. (c) The rescaled pseudomagnetization $m = \langle |\sum_i S_i^z| \rangle / L$ indicates a transition at the same value of Γ_c . (d) Scaling collapse with the Ising critical exponent $\beta = 1/8$.

energy of the bosonic Hamiltonian (3) with $L = 64$ and periodic boundary conditions. In the thermodynamic limit, the ground-state energy density of the Ising model (4) is given by $E_0/L = C/L + e_\infty$ (Ref. [66]), where

$$e_\infty = -\frac{1}{4\pi} \int_0^\pi dk \sqrt{4\Gamma^2 + J_{zz}^2 + 4\Gamma J_{zz} \cos k}. \quad (35)$$

Defining $E'_0 \equiv E_0 - C$ the result for E'_0/L is in good agreement with Eq. (35) as shown in Fig. 15(a). In addition the finite-size corrections to the ground-state energy are well described by the conformal result [70,71]

$$\frac{E'_0}{L} = e_\infty - \frac{\pi c v}{6L^2} + \dots, \quad (36)$$

where $v = |J_{zz}|/2$ is the effective velocity and c is the central charge. Going beyond our $h = 0$ parameter choice, this opens up the exciting possibility of studying the celebrated E_8 mass

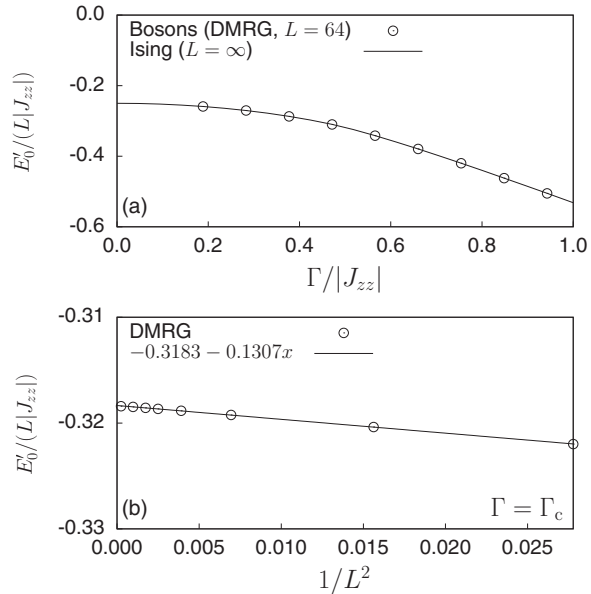


FIG. 15. (a) Rescaled ground-state energy $E'_0 \equiv E_0 - C$ of the bosonic Hamiltonian (3) with the FM parameters used in Fig. 14. The DMRG data are in good agreement with Eq. (35) for the thermodynamic limit of the Ising model. (b) The residual finite-size corrections, $E'_0/L|J_{zz}| = e_\infty/|J_{zz}| - \pi c/12L^2 + \dots$, are consistent with the central charge $c \approx 0.499$ of an Ising transition to a FM state in the absence of a longitudinal magnetic field.

spectrum of the FM Ising model in a magnetic field [46]. As exemplified by recent experiments on the quasi-1D Ising ferromagnet CoNb_2O_6 (cobalt niobate) [47,48], it would be interesting to probe the dynamical correlation functions of the 1D bosonic Hamiltonian (1) in more detail. The nontrivial excitations will manifest themselves at specific frequencies dictated by the emergent E_8 mass spectrum. Similar behavior is also expected in the AFM case in the presence of a staggered longitudinal magnetic field.

XI. CONCLUSIONS

We have investigated the Mott insulating state of bosonic pairing Hamiltonians using analytical and numerical techniques. We have described the behavior of a broad range of physical observables, including local expectation values and correlation functions, within the framework of the paradigmatic quantum Ising model. As advocated in Refs. [32,33,41] our results are consistent with the absence of super-Mott behavior within the second Mott lobe. Our results differ from those of the usual two-band Bose-Hubbard model which exhibits counterflow superfluidity [64,65] since Feshbach resonant pairing interactions favor a distinct Mott phase with either two atoms or one molecule per site. As such, XY terms generically appear at cubic order in the hopping strengths and are intrinsically suppressed. An alternative way to see this is to note that for finite Feshbach coupling, the symmetry of the Hamiltonian is reduced from $U(1) \times U(1)$ down to $U(1) \times \mathbb{Z}_2$. As such, one naively expects Ising transitions to occur in a Mott

phase with large phase fluctuations and an unbroken U(1) symmetry. Nonetheless, one cannot rule out the possibility of novel transitions in other regions of the phase diagram due to higher-order terms in the strong coupling expansion becoming appreciable. It would be interesting to explore this in more detail. In addition, we highlight the possibility of using these systems to explore the E_8 mass spectrum of the FM Ising model in a magnetic field. There are many directions for further research including the influence of higher bands and the possibility of realizing Ising transitions in Bose-Fermi mixtures; see Appendix B.

ACKNOWLEDGMENTS

We are grateful to F. Assaad, J. Oitmaa, F. Pollmann, N. Shannon, and A. Tsvelik for helpful discussions. MJB, AOS, and BDS acknowledge EPSRC Grant No. EP/E018130/1. FHLE acknowledges EPSRC Grant No. EP/D050952. SE and HF acknowledge funding by the DFG through Grant No. SFB 652. MH acknowledges funding by the DFG through Grant No. FG1162.

APPENDIX A: EFFECTIVE MAGNETIC HAMILTONIAN

To obtain the effective spin description within the second Mott lobe we perform degenerate perturbation theory. We partition the Hamiltonian as $H = H_0 + V$, where

$$H_0 = \sum_i [H'_i(1 - \mathcal{P}_{0i}) + (\epsilon_m - h_0/2)\mathcal{P}_{0i}] \quad (\text{A1})$$

and

$$V = - \sum_{(ij)\alpha} t_\alpha (b_{i\alpha}^\dagger b_{j\alpha} + \text{H.c.}) + H_F + h_0 \sum_i S_i^z \mathcal{P}_{0i}. \quad (\text{A2})$$

Here $h_0 = \epsilon_m - 2\epsilon_a - U_{aa}$, $\mathcal{P}_{0i} = |\uparrow\rangle_i \langle\uparrow|_i + |\downarrow\rangle_i \langle\downarrow|_i$, and

$$H'_i = \sum_\alpha \epsilon_\alpha n_{i\alpha} + \sum_{\alpha\alpha'} \frac{U_{\alpha\alpha'}}{2} :n_{i\alpha} n_{i\alpha'}: . \quad (\text{A3})$$

This approach is appropriate deep in the Mott lobe and in the vicinity of the transition, where g , h_0 , and t^2/U are small and V may be treated perturbatively. Up to second order in V the effective Hamiltonian is

$$H_{\text{eff}} = \mathcal{P}_0 \left(H_0 + V + V(1 - \mathcal{P}_0) \frac{1}{E_0 - H_0} (1 - \mathcal{P}_0) V \right) \mathcal{P}_0, \quad (\text{A4})$$

where $E_0 = L(\epsilon_m - h_0/2)$ and $\mathcal{P}_0 = \prod_i \mathcal{P}_{0i}$. Since the hopping terms are the only source of coupling between the degenerate subspace spanned by \mathcal{P}_0 and the remaining Hilbert space, the second-order term reduces to

$$H_{\text{eff}}^{(2)} = \sum_{(ij)\alpha} t_\alpha^2 \mathcal{P}_0 b_{i\alpha}^\dagger b_{j\alpha} \frac{1}{E_0 - H_0} b_{j\alpha}^\dagger b_{i\alpha} \mathcal{P}_0 + \text{H.c.} \quad (\text{A5})$$

This acts on two sites so within the degenerate subspace \mathcal{P}_0 , we must consider its action on four basis states. The action of $H_{\text{eff}}^{(2)}$ on sites with neighboring molecules yields

$$H_{\text{eff}}^{(2)} |\uparrow\rangle_i |\uparrow\rangle_j = - \frac{4t_m^2}{U_{mm} + h_0} |\uparrow\rangle_i |\uparrow\rangle_j, \quad (\text{A6})$$

and for an arrangement of neighboring atoms it gives

$$H_{\text{eff}}^{(2)} |\downarrow\rangle_i |\downarrow\rangle_j = - \frac{12t_a^2}{U_{aa} - h_0} |\downarrow\rangle_i |\downarrow\rangle_j. \quad (\text{A7})$$

When the neighboring species are different

$$H_{\text{eff}}^{(2)} |\uparrow\rangle_i |\downarrow\rangle_j = - \left(\frac{2t_a^2}{U_{am} - U_{aa}} + \frac{t_m^2}{2U_{am}} \right) |\uparrow\rangle_i |\downarrow\rangle_j. \quad (\text{A8})$$

In order to obtain the second-order contribution to the effective Hamiltonian we collate these terms. In addition we exploit the spin projection identities $|\uparrow\rangle_i \langle\uparrow|_i \mathcal{P}_0 = (1/2 + S_i^z) \mathcal{P}_0$ and $|\downarrow\rangle_i \langle\downarrow|_i \mathcal{P}_0 = (1/2 - S_i^z) \mathcal{P}_0$ and expand the resulting expression to leading (zeroth) order in h_0 :

$$H_{\text{eff}}^{(2)} \simeq \mathcal{P}_0 \left(J_{zz} \sum_{(ij)} S_i^z S_j^z + h_2 \sum_i S_i^z + C_2 \right) \mathcal{P}_0, \quad (\text{A9})$$

where J_{zz} is given by Eq. (32) and

$$h_2 = \frac{z}{2} \left(\frac{12t_a^2}{U_{aa}} - \frac{4t_m^2}{U_{mm}} \right). \quad (\text{A10})$$

The constant offset is given by

$$C_2 = - \frac{zL}{8} \left(\frac{4t_a^2}{U_{am} - U_{aa}} + \frac{t_m^2}{U_{am}} + \frac{12t_a^2}{U_{aa}} + \frac{4t_m^2}{U_{mm}} \right) \quad (\text{A11})$$

Inclusion of the zeroth- and first-order contributions in V yields the effective Ising Hamiltonian (4) with $h = h_0 + h_2$ and $C = E_0 + C_2$ as given by Eqs. (33) and (34). In order to obtain the effective Hamiltonian with $r_a = 2$ one must exclude the contribution from Eq. (A7) as the intermediate states involved in the perturbation do not satisfy the imposed constraint. Similarly if $r_m = 1$ the contribution from Eq. (A6) must be excluded.

APPENDIX B: BOSE-FERMI HAMILTONIAN

Throughout this manuscript we have focused exclusively on the bosonic homonuclear Hamiltonian (1) and the associated Ising description. However, it is evident from the general setup shown in Fig. 1 that similar results may also emerge with more than one atomic species. For example, this is confirmed in Refs. [32,33] for the heteronuclear bosonic case. In this Appendix we note that a similar Ising description may also apply with two-component fermionic atoms and bosonic molecules. We consider the Bose-Fermi Hamiltonian

$$H = \sum_{i\alpha} \epsilon_\alpha n_{i\alpha} - \sum_{(ij)} \sum_\alpha t_\alpha (d_{i\alpha}^\dagger d_{j\alpha} + \text{H.c.}) + H_F + \sum_{i,\alpha \neq \alpha'} \frac{U_{\alpha\alpha'}}{2} n_{i\alpha} n_{i\alpha'} + \sum_i \frac{U_{mm}}{2} n_{im} (n_{im} - 1), \quad (\text{B1})$$

where $\alpha = \downarrow, \uparrow$ are fermionic atoms, $\alpha = m$ is a bosonic molecule, $n_{i\alpha} = d_{i\alpha}^\dagger d_{i\alpha}$, and $H_F = g \sum_i (d_{im}^\dagger d_{i\downarrow} d_{i\uparrow} + \text{H.c.})$. Assuming the existence of a second Mott lobe as depicted in Fig. 1, with either two fermionic atoms or a bosonic molecule per site, one again obtains an Ising Hamiltonian (4) acting on the states $|\downarrow\rangle = d_{i\downarrow}^\dagger d_{i\downarrow} |0\rangle$ and $|\uparrow\rangle = d_{i\uparrow}^\dagger |0\rangle$. The parameters in

Eq. (4) are now given by $\Gamma = 2g$ and

$$\frac{J_{zz}}{2} = \frac{t_m^2}{U_{\uparrow m} + U_{\downarrow m}} + \frac{t_{\downarrow}^2}{U_{\downarrow m} - U_{\uparrow \downarrow}} + \frac{t_{\uparrow}^2}{U_{\uparrow m} - U_{\uparrow \downarrow}} - \frac{2t_m^2}{U_{mm}}. \quad (\text{B2})$$

The effective magnetic field is given by

$$h = \epsilon_m - (\epsilon_{\downarrow} + \epsilon_{\uparrow} + U_{\uparrow \downarrow}) - \frac{2zt_m^2}{U_{mm}}, \quad (\text{B3})$$

and the constant offset is

$$C = L \left(\epsilon_m - \frac{h}{2} + \frac{zJ}{8} - \frac{zt_m^2}{U_{mm}} \right). \quad (\text{B4})$$

In the limit $U_{mm} \rightarrow \infty$ the results (B2), (B3), and (B4) coincide with the results of Sec. III where we identify $U_{\uparrow \downarrow} = U_{aa}$ and $U_{\downarrow m} = U_{\uparrow m} = U_{am}$. In view of our findings in the bosonic problems it would be interesting to examine the Bose-Fermi mixture (B1) in more detail.

-
- [1] M. H. Anderson, J. R. Ensher, M. R. Matthews, C. E. Wieman, and E. A. Cornell, *Science* **269**, 198 (1995).
- [2] K. B. Davis, M.-O. Mewes, M. R. Andrews, N. J. van Druten, D. S. Durfee, D. M. Kurn, and W. Ketterle, *Phys. Rev. Lett.* **75**, 3969 (1995).
- [3] D. Jaksch, C. Bruder, J. I. Cirac, C. W. Gardiner, and P. Zoller, *Phys. Rev. Lett.* **81**, 3108 (1998).
- [4] M. Greiner, O. Mandel, T. Esslinger, T. W. Hänsch, and I. Bloch, *Nature (London)* **415**, 39 (2002).
- [5] M. P. A. Fisher, P. B. Weichman, G. Grinstein, and D. S. Fisher, *Phys. Rev. B* **40**, 546 (1989).
- [6] J. Stenger, S. Inouye, D. M. Stamper-Kurn, H.-J. Miesner, A. P. Chikkatur, and W. Ketterle, *Nature (London)* **396**, 345 (1998).
- [7] H.-J. Miesner, D. M. Stamper-Kurn, J. Stenger, S. Inouye, A. P. Chikkatur, and W. Ketterle, *Phys. Rev. Lett.* **82**, 2228 (1999).
- [8] D. M. Stamper-Kurn, H.-J. Miesner, A. P. Chikkatur, S. Inouye, J. Stenger, and W. Ketterle, *Phys. Rev. Lett.* **83**, 661 (1999).
- [9] A. E. Leanhardt, Y. Shin, D. Kielpinski, D. E. Pritchard, and W. Ketterle, *Phys. Rev. Lett.* **90**, 140403 (2003).
- [10] T. Ohmi and K. Machida, *J. Phys. Soc. Jpn.* **67**, 1822 (1998).
- [11] T.-L. Ho, *Phys. Rev. Lett.* **81**, 742 (1998).
- [12] E. Demler and F. Zhou, *Phys. Rev. Lett.* **88**, 163001 (2002).
- [13] A. Imambekov, M. Lukin, and E. Demler, *Phys. Rev. A* **68**, 063602 (2003).
- [14] A. Lamacraft, *Phys. Rev. Lett.* **98**, 160404 (2007).
- [15] S. Mukerjee, C. Xu, and J. E. Moore, *Phys. Rev. B* **76**, 104519 (2007).
- [16] F. H. L. Essler, G. V. Shlyapnikov, and A. M. Tsvelik, *J. Stat. Mech.* (2009) P02027.
- [17] M. Ueda and Y. Kawaguchi, e-print [arXiv:1001.2072](https://arxiv.org/abs/1001.2072).
- [18] G. Thalhammer, G. Barontini, L. De Sarlo, J. Catani, F. Minardi, and M. Inguscio, *Phys. Rev. Lett.* **100**, 210402 (2008).
- [19] M. A. Cazalilla and A. F. Ho, *Phys. Rev. Lett.* **91**, 150403 (2003).
- [20] A. Kuklov, N. Prokof'ev, and B. Svistunov, *Phys. Rev. Lett.* **92**, 050402 (2004).
- [21] A. Kleine, C. Kollath, I. P. McCulloch, T. Giamarchi, and U. Schollwöck, *Phys. Rev. A* **77**, 013607 (2008); *New J. Phys.* **10**, 045025 (2008).
- [22] S. G. Söyler, B. Capogrosso-Sansone, N. V. Prokof'ev, and B. V. Svistunov, *New J. Phys.* **11**, 073036 (2009).
- [23] M. Guglielmino, V. Penna, and B. Capogrosso-Sansone, *Phys. Rev. A* **82**, 021601 (2010).
- [24] L. M. Duan, E. Demler, and M. D. Lukin, *Phys. Rev. Lett.* **91**, 090402 (2003).
- [25] E. Altman, W. Hofstetter, E. Demler, and M. D. Lukin, *New J. Phys.* **5**, 113 (2003).
- [26] A. Hubener, M. Snoek, and W. Hofstetter, *Phys. Rev. B* **80**, 245109 (2009).
- [27] S. Powell, *Phys. Rev. A* **79**, 053614 (2009).
- [28] B. Capogrosso-Sansone, Ş. G. Söyler, N. V. Prokof'ev, and B. V. Svistunov, *Phys. Rev. A* **81**, 053622 (2010).
- [29] A. V. Gorshkov, M. Hermele, V. Gurarie, C. Xu, P. S. Julienne, J. Ye, P. Zoller, E. Demler, M. D. Lukin, and A. M. Rey, *Nat. Phys.* **6**, 289 (2010).
- [30] M. Hermele, V. Gurarie, and A. M. Rey, *Phys. Rev. Lett.* **103**, 135301 (2009).
- [31] M. A. Cazalilla, A. F. Ho, and M. Ueda, *New J. Phys.* **11**, 103033 (2009).
- [32] M. J. Bhaseen, A. O. Silver, M. Hohenadler, and B. D. Simons, *Phys. Rev. Lett.* **103**, 265302 (2009).
- [33] M. Hohenadler, A. O. Silver, M. J. Bhaseen, and B. D. Simons, *Phys. Rev. A* **82**, 013639 (2010).
- [34] L. Radzihovsky, J. Park, and P. B. Weichman, *Phys. Rev. Lett.* **92**, 160402 (2004).
- [35] M. W. J. Romans, R. A. Duine, S. Sachdev, and H. T. C. Stoof, *Phys. Rev. Lett.* **93**, 020405 (2004).
- [36] L. Radzihovsky, P. B. Weichman, and J. I. Park, *Ann. Phys.* **323**, 2376 (2008).
- [37] D. B. M. Dickerscheid, U. Al Khawaja, D. van Oosten, and H. T. C. Stoof, *Phys. Rev. A* **71**, 043604 (2005).
- [38] K. Sengupta and N. Dupuis, *Europhys. Lett.* **70**, 586 (2005).
- [39] V. G. Rousseau and P. J. H. Denteneer, *Phys. Rev. Lett.* **102**, 015301 (2009).
- [40] V. G. Rousseau and P. J. H. Denteneer, *Phys. Rev. A* **77**, 013609 (2008).
- [41] M. Eckholt and T. Roscilde, *Phys. Rev. Lett.* **105**, 199603 (2010).
- [42] S. Ejima, M. J. Bhaseen, M. Hohenadler, F. H. L. Essler, H. Fehske, and B. D. Simons, *Phys. Rev. Lett.* **106**, 015303 (2011).
- [43] S. R. White, *Phys. Rev. Lett.* **69**, 2863 (1992); *Phys. Rev. B* **48**, 10345 (1993).
- [44] B. M. McCoy and T. T. Wu, *Phys. Rev. D* **18**, 1259 (1978).
- [45] M. J. Bhaseen and A. M. Tsvelik, in *From Fields to Strings: Circumnavigating Theoretical Physics, Ian Kogan Memorial*, Vol. I, edited by M. Shifman, A. Vainshtein, and J. Wheeler (World Scientific, Singapore, 2005), pp. 661–683.
- [46] A. B. Zamolodchikov, *Int. J. Mod. Phys. A* **4**, 4235 (1989).
- [47] R. Coldea, D. A. Tennant, E. M. Wheeler, E. Wawrzynska, D. Prabhakaran, M. Telling, K. Habicht, P. Smeibidl, and K. Kiefer, *Science* **327**, 177 (2010).
- [48] J. A. Kjäll, F. Pollmann, and J. E. Moore, *Phys. Rev. B* **83**, 020407 (2011).

- [49] L. Radzihovsky and S. Choi, *Phys. Rev. Lett.* **103**, 095302 (2009); S. Choi and L. Radzihovsky, e-print arXiv:1106.5765.
- [50] R. B. Diener and T.-L. Ho, *Phys. Rev. A* **73**, 017601 (2006).
- [51] D. B. M. Dickerscheid, D. van Oosten, and H. T. C. Stoof, *Phys. Rev. A* **73**, 017602 (2006).
- [52] H. P. Büchler, *Phys. Rev. Lett.* **104**, 090402 (2010).
- [53] A. J. Daley, J. M. Taylor, S. Diehl, M. Baranov, and P. Zoller, *Phys. Rev. Lett.* **102**, 040402 (2009); **102**, 179902(E) (2009); S. Diehl, M. Baranov, A. J. Daley, and P. Zoller, *ibid.* **104**, 165301 (2010).
- [54] S. Diehl, M. Baranov, A. J. Daley, and P. Zoller, *Phys. Rev. B* **82**, 064509 (2010); **82**, 064510 (2010).
- [55] C. Wu, *Phys. Rev. Lett.* **95**, 266404 (2005); P. Lecheminant, E. Boulat, and P. Azaria, *ibid.* **95**, 240402 (2005).
- [56] S. Capponi, G. Roux, P. Azaria, E. Boulat, and P. Lecheminant, *Phys. Rev. B* **75**, 100503(R) (2007); G. Roux, S. Capponi, P. Lecheminant, and P. Azaria, *Eur. Phys. J. B* **68**, 293 (2009).
- [57] L. Bonnes and S. Wessel, *Phys. Rev. Lett.* **106**, 185302 (2011).
- [58] S. Sachdev, *Quantum Phase Transitions* (Cambridge University Press, Cambridge, UK, 1999).
- [59] C. Holzey, F. Larsen, and F. Wilczek, *Nucl. Phys. B* **424**, 443 (1994).
- [60] V. E. Korepin, *Phys. Rev. Lett.* **92**, 096402 (2004).
- [61] P. Calabrese and J. Cardy, *J. Stat. Mech.* (2004) P06002.
- [62] O. Legeza, J. Sólyom, L. Tincani, and R. M. Noack, *Phys. Rev. Lett.* **99**, 087203 (2007).
- [63] A. M. Läuchli and C. Kollath, *J. Stat. Mech.* (2008) P05018.
- [64] A. B. Kuklov and B. V. Svistunov, *Phys. Rev. Lett.* **90**, 100401 (2003).
- [65] A. Hu, L. Mathey, I. Danshita, E. Tiesinga, C. J. Williams, and C. W. Clark., *Phys. Rev. A* **80**, 023619 (2009).
- [66] P. Pfeuty, *Ann. Phys.* **57**, 79 (1970).
- [67] Y. Hieida, K. Okunishi, and Y. Akutsu, *Phys. Rev. B* **64**, 224422 (2001).
- [68] J. Cardy, *Scaling and Renormalization in Statistical Physics* (Cambridge University Press, Cambridge, UK, 1996).
- [69] J. Um, S.-I. Lee, and B. J. Kim, *J. Korean Phys. Soc.* **50**, 285 (2007).
- [70] H. W. J. Blöte, J. L. Cardy, and M. P. Nightingale, *Phys. Rev. Lett.* **56**, 742 (1986).
- [71] I. Affleck, *Phys. Rev. Lett.* **56**, 746 (1986).

PHYSICAL REVIEW B **92**, 041120(R) (2015)**Criticality at the Haldane-insulator charge-density-wave quantum phase transition**

Florian Lange, Satoshi Ejima, and Holger Fehske

Institut für Physik, Ernst-Moritz-Arndt-Universität Greifswald, 17489 Greifswald, Germany

(Received 12 June 2015; published 31 July 2015)

Exploiting the entanglement concept within a matrix-product-state based infinite density-matrix renormalization group approach, we show that the spin-density-wave and bond-order-wave ground states of the one-dimensional half-filled extended Hubbard model give way to a symmetry-protected topological Haldane state in case an additional alternating ferromagnetic spin interaction is added. In the Haldane insulator, the lowest entanglement level features a characteristic twofold degeneracy. Increasing the ratio between the nearest-neighbor and local Coulomb interaction V/U , the enhancement of the entanglement entropy, the variation of the charge, spin, and neutral gaps, and the dynamical spin and density response signal a quantum phase transition to a charge-ordered state. Below a critical point, which belongs to the universality class of the tricritical Ising model with central charge $7/10$, the model is critical with $c = 1/2$ along the transition line. Above this point, the transition between the Haldane insulator and charge-density-wave phases becomes first order.

DOI: [10.1103/PhysRevB.92.041120](https://doi.org/10.1103/PhysRevB.92.041120)

PACS number(s): 64.70.Tg

Topological phases of matter have become one of the most fascinating objects of investigation in solid state physics [1–3]. Topological states may arise from topological band structures or interactions. The order associated with these phases can be described by topological invariants that are insensitive to gradual changes of the system parameters. As a generic feature, topological ordered states contain gapless edge excitations that encode all the information of bulk topological order [4].

Symmetry-protected topological (SPT) phases are zero-temperature quantum states with a given symmetry and a finite energy gap. The Landau symmetry-breaking states belong to this class. However, there are more interesting SPT states that do not break any symmetry. For example, in higher dimensions, the Kane-Mele band insulator [5,6] is a topological state protected by $U(1)$ and time-reversal symmetries. In one dimension, a prominent representative is the Haldane phase in the spin-1 Heisenberg chain [7], which is protected by inversion, time-reversal, and dihedral symmetries [8,9]. If at least one of these symmetries is not explicitly broken, the odd- S Haldane insulator (HI) is separated from the topologically trivial state by a quantum phase transition. Relating topological order and entanglement allows for a further classification of topological states [10]. While gapped quantum systems without any symmetry split in short- and long-range entangled states, the SPT phases are always short-range entangled.

Exploring the connection between topological band structures and interacting topological states, it has been demonstrated that the topological invariants of gapped fermionic systems described by the one-dimensional half-filled Peierls-Hubbard model, deep in the Mott insulating regime, can be efficiently computed numerically by adding a ferromagnetic spin exchange [11]. On account of a topological invariant of 2, the Peierls-Hubbard model—in a certain parameter regime—possesses the same boundary states as the spin-1 Heisenberg chain. This raises the question whether the spin-density-wave (SDW) and bond-order-wave (BOW) ground states of the half-filled extended Hubbard model (EHM) [12] also disappear in favor of a SPT HI phase when a ferromagnetic spin interaction is added. If the answer is yes, one should expect

a novel quantum phase transition from the SPT state to the charge-density-wave (CDW) insulator.

In this Rapid Communication, we therefore investigate the ground-state, spectral, and dynamical properties of the EHM with additional, alternating, ferromagnetic spin coupling J , using the unbiased matrix-product-state (MPS) based infinite density-matrix renormalization group (DMRG) technique [13–16].

The Hamiltonian of the one-dimensional EHM is

$$H_{\text{EHM}} = -t \sum_{j,\sigma} \left(c_{j\sigma}^\dagger c_{j+1\sigma} + \text{H.c.} \right) + U \sum_j n_{j\uparrow} n_{j\downarrow} + V \sum_{j\sigma\sigma'} n_{j\sigma} n_{j+1\sigma'}.$$

Here, $c_{j\sigma}^\dagger$ ($c_{j\sigma}$) creates (annihilates) an electron with spin σ at site j , $n_{j\sigma} = c_{j\sigma}^\dagger c_{j\sigma}$, t is the transfer amplitude of the particles, and U (V) denotes their intrasite (intersite) Coulomb repulsion. We focus on the half-filled band case.

The ground-state phase diagram of the EHM has been worked out by various analytical [17,18] and numerical [12,19–21] techniques. In the absence of V (Hubbard model), the ground state is a quantum critical spin-density wave (SDW) with gapless spin and gapped charge excitations $\forall U > 0$ [22]. If $2V/U \lesssim 1$, the ground state resembles that at $V = 0$. For $2V/U \gtrsim 1$, the system becomes a $2k_F$ CDW state, where both spin and charge excitation spectra are gapful. The SDW and CDW phases are separated by a narrow intervening BOW phase [23,24] below the critical end point $[U_e, V_e] = [9.25t, 4.76t]$ [12], where the ground state exhibits a staggered modulation of the kinetic energy density (cf. the schematic representations included in Fig. 2 below).

Here, we consider the extended Hamilton operator

$$H = H_{\text{EHM}} + J \sum_{j=1}^{L/2} \mathcal{S}_{2j-1} \mathcal{S}_{2j}, \quad (1)$$

with $\mathcal{S}_j = (1/2) \sum_{\sigma\sigma'} c_{j\sigma}^\dagger \sigma_{\sigma\sigma'} c_{j,\sigma'}$. The nearest-neighbor Heisenberg spin interaction is assumed to be alternating and ferromagnetic, i.e., $J < 0$ on every other bond. Since the EHM

FLORIAN LANGE, SATOSHI EJIMA, AND HOLGER FEHSKE

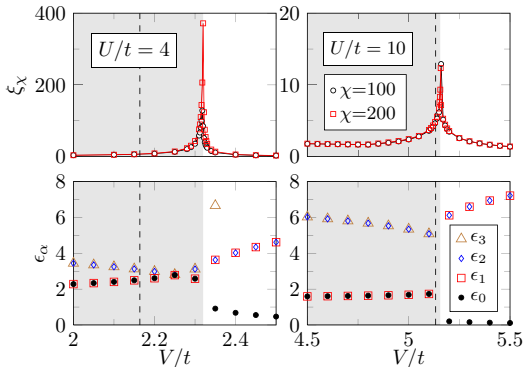
PHYSICAL REVIEW B **92**, 041120(R) (2015)

FIG. 1. (Color online) Correlation length ξ_χ (upper panels) and entanglement spectrum ϵ_α (lower panels) as a function of V/t for $U/t = 4$ (left panels) and $U/t = 10$ (right panels), where $J/t = -1.5$. Data obtained by iDMRG. Dashed lines give the BOW-CDW (SDW-CDW) transition for $U/t = 4$ ($U/t = 10$) in the EHM [12].

at large enough U/V can be thought of as a spin-1/2 chain, the second term in (1) tends to form a spin-1 moment out of two spins on sites $2j-1$ and $2j$ in this limit. Then, the resulting spin-1 antiferromagnetic chain may realize a gapped Haldane phase with zero-energy edge excitations [9].

To proceed, we perform an entanglement analysis of the model (1). The concept of entanglement is inherent in the MPS-based DMRG algorithms, too. The so-called entanglement spectrum ϵ_α characterizes topological phases [25], which can be obtained from the singular value decomposition. Dividing a system into two subblocks, $\mathcal{H} = \mathcal{H}_L \otimes \mathcal{H}_R$, and considering the reduced density matrix $\rho_L = \text{Tr}_R[\rho]$, $\epsilon_\alpha = -2 \ln \lambda_\alpha$ are given by the singular values λ_α of the reduced density matrix ρ_L . The ϵ_α spectrum also provides valuable information about the criticality of the system. Adding up the singular values λ_α , we have direct access to the entanglement entropy $S_E = -\sum_\alpha \lambda_\alpha^2 \ln \lambda_\alpha^2$. For a critical system with central charge c , the entanglement entropy S_E between the two halves of the infinite chain scales as [26,27]

$$S_E = \frac{c}{6} \ln \xi_\chi + s_0, \quad (2)$$

where s_0 is a nonuniversal constant. The correlation length ξ_χ is determined from the second largest eigenvalue of the transfer matrix for some bond dimension χ used in the infinite DMRG (iDMRG) simulation [14–16]. At the critical point the physical correlation length diverges, while ξ_χ stays finite due to the finite-entanglement cutoff. Nevertheless, ξ_χ can be used to determine the phase transition because it increases rapidly with χ near the critical point. Here, we perform iDMRG runs with χ up to 400, so that the effective correlation length at criticality is $\xi_\chi \lesssim 400$.

Let us first discuss the entanglement properties of the model (1). Figure 1 shows ξ_χ and ϵ_α in dependence on V/t and U/t for fixed $J/t = -1.5$. In the weak-to-intermediate interaction regime, $U/t = 4$, we find a pronounced peak in the correlation length at $V_c/t \simeq 2.321$, which shoots up as χ grows from 100 to 200, indicating a divergency as

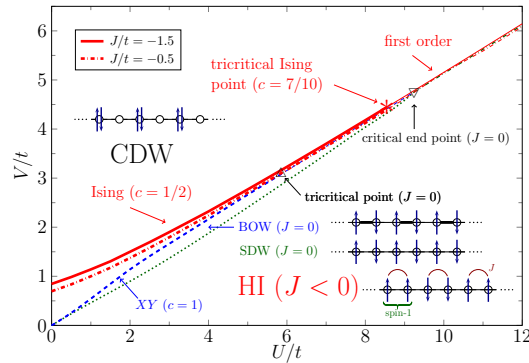


FIG. 2. (Color online) iDMRG ground-state phase diagram of the one-dimensional (half-filled) extended Hubbard model with ferromagnetic spin interaction. The red solid (dotted-dashed) lines give the HI-CDW phase boundaries for $J/t = -1.5$ (-0.5). The quantum phase transition is continuous (first order) below (above) the tricritical Ising point $[U, V]$ marked by the star symbol. For comparison, the results for the BOW-CDW (blue dashed line), SDW-BOW (green dotted line), and SDW-CDW (green double-dotted dashed line) transitions of the pure EHM were included [12].

$\xi_\chi \rightarrow \infty$. Obviously the system passes a continuous quantum phase transition. By contrast, in the strong interaction regime, $U/t = 10$, the peak height stays almost constant when χ is raised. Decreasing $|J|$, the transition points will approach those of the pure EHM, e.g., for $J/t = -0.5$ we find $V_c/t \simeq 2.242$, with a simultaneous reduction of the ξ_χ 's peak heights. The corresponding entanglement spectra denote that the nontrivial phase realized for $V < V_c$ resembles the SPT Haldane phase of the spin-1 XXZ model [28], in that the lowest entanglement level exhibits a characteristic double degeneracy [29]. For $V > V_c$, in the CDW phase, this level is nondegenerate.

According to Fig. 1, the maximum in the correlation length ξ_χ can be used to pinpoint the HI-CDW quantum phase transition, and with it map out the complete ground-state phase diagram of the EHM with ferromagnetic spin coupling (1). The outcome is given in Fig. 2, which also includes the result for the pure EHM (blue and green lines). The first striking result is that the HI phase completely replaces the SDW and BOW states. That is, the HI even survives in the weak-coupling regime until $U/t = 0$ for any finite $J < 0$ [provided that $V < V_c(U, J)$]. According to this, the itinerant model (1) behaves as a spin-1 model, even at very small U/t where double occupancy is not largely suppressed. In the intermediate-to-strong coupling regime, the HI-CDW transition approaches the BOW/SDW-CDW transition of the EHM. The transition is continuous up to a tricritical Ising point $[U_t, V_t](J)$, which converges to the tricritical point of the EHM as $J \rightarrow 0$. In the strong-coupling regime above $[U_t, V_t]$, the HI-CDW transition becomes first order. For very large U/t , the phase boundaries of the HI/SDW-CDW transitions are indistinguishable.

We now characterize the different states and the HI-CDW quantum phase transition in more detail. For this we first

041120-2

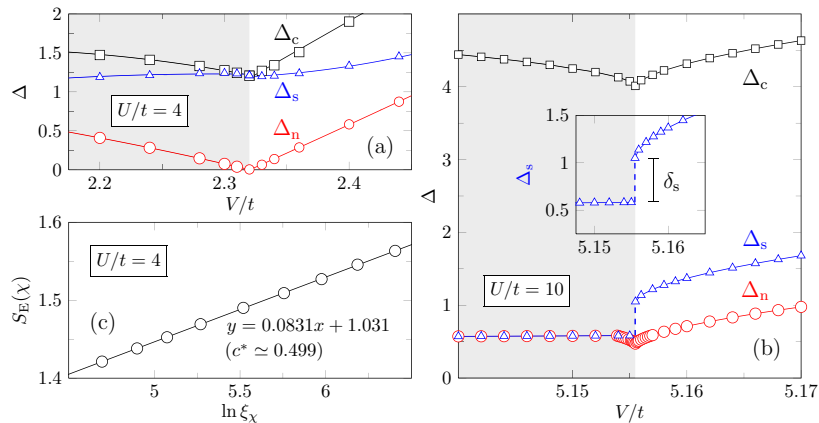


FIG. 3. (Color online) Charge (Δ_c), spin (Δ_s), and neutral (Δ_n) gaps as functions of V/t for (a) $U/t = 4$ and (b) $U/t = 10$. The HI (CDW) phase is marked in gray (white). (c) gives the scaling of the entanglement entropy $S_E(\chi)$ with the correlation length ξ_χ at the SPT-CDW transition $V_c/t \simeq 2.321$ for $U/t = 4$. The solid line is a linear fit of the data to Eq. (2), indicating an Ising phase transition with $c = 1/2$. Results shown are obtained for $J/t = -1.5$.

consider the various excitation gaps, $\Delta_c = [E_0(N+2,0) + E_0(N-2,0) - 2E_0(N,0)]/2$ [(two-particle) charge gap], $\Delta_s = E_0(N,1) - E_0(N,0)$ [spin gap], and $\Delta_n = E_1(N,0) - E_0(N,0)$ [neutral gap], where $E_0(N_e, S_{\text{tot}}^z)$ is the ground-state energy of the finite system with L sites for a given number of electrons N_e and z component of total spin S_{tot}^z , and $E_1(N_e, S_{\text{tot}}^z)$ is the corresponding energy of the first excited state. For the pure EHM, Δ_c and Δ_n vanish at the BOW-CDW transition, whereas Δ_s stays finite. Here, the excitation gaps were determined using DMRG in combination with the infinite MPS representation with “infinite boundary conditions” [30–32], where both finite-size and boundary effects are significantly reduced. Thereby, the whole lattice is divided into three parts: a window part, containing L_W sites, and two semi-infinite chains. While the L_W dependence persists, the L_W finite-size scaling is more easy to handle than the finite-size scaling in the traditional DMRG method. Figure 3 shows the variation of the different excitation gaps across the HI-CDW transition in the weak-coupling [Fig. 3(a)] and strong-coupling [Fig. 3(b)] regime. In the former case, the charge and spin gaps feature weak minima at the transition point, but stay finite. The neutral gap, on the other hand, closes [see Fig. 3(a)]. This is evocative of the Ising transition between the Haldane and antiferromagnetic phases in the spin-1 XXZ model with single-ion anisotropy [28]. For $U/t = 4$, we find $V_c/t \simeq 2.321$. In the latter case, also the neutral gap stays finite passing the phase transition [see Fig. 3(b)]. However, the jump of the spin gap $\delta_s \equiv \Delta_s(V_c^+) - \Delta_s(V_c^-)$ is striking, indicating a first-order transition. We obtain $V_c/t \simeq 5.155$ for $U/t = 10$.

Next, we ascertain the universality class of the HI-CDW quantum phase transition. When the system becomes critical, the central charge c can easily be determined from the DMRG entanglement entropy. Utilizing Eq. (2), Fig. 3(c) demonstrates that c^* indeed follows a linear fit to the DMRG data at the critical point (for $140 \leq \chi \leq 400$), provided that prior to that the transition point was determined with extremely

high precision. At $U/t = 4$ and $J/t = -1.5$, we have $c^* \simeq 0.499(1)$, suggesting the system to be in the Ising universality class where $c = 1/2$. For $U/t = 4$ and $J/t = -0.5$ (not shown), we get $c^* \simeq 0.496(3)$. From conformal field theory [26] the von Neumann entropy for a system with periodic boundary conditions takes the form $S_L(\ell) = (c/3) \ln\{(L/\pi) \sin[(\pi\ell/L)]\} + s_1$ with another nonuniversal constant s_1 . With a view of the doubled unit cell of the HI phase we slightly modify the related formula for c^* [33]:

$$c^*(L) \equiv \frac{3[S_L(L/2-2) - S_L(L/2)]}{\ln\{\cos[\pi/(L/2)]\}}. \quad (3)$$

Figure 4 displays $c^*(L)$ when moving along the HI-CDW transition line by varying U and V simultaneously. Remarkably, when U is raised, we find evidence for a crossover from

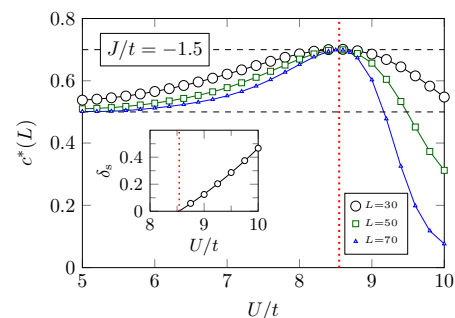


FIG. 4. (Color online) Central charge $c^*(L)$ along the HI-CDW transition line for $J/t = -1.5$. DMRG data (obtained with periodic boundary conditions) indicate the Ising universality class ($c = 1/2$) for $U < U_t$ and, most notably, a tricritical Ising point with $c = 7/10$ at U_t (red dotted line). Inset: Magnitude of the jump of the spin gap as U further increases for $U \gtrsim U_t$. The infinite MPS data—for a system with infinite boundary conditions—point to a first-order transition.

FLORIAN LANGE, SATOSHI EJIMA, AND HOLGER FEHSKE

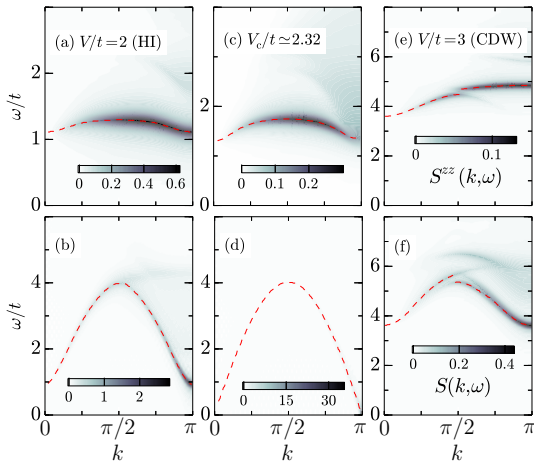
PHYSICAL REVIEW B **92**, 041120(R) (2015)

FIG. 5. (Color online) Intensity plots of the dynamical spin structure factor $S^{zz}(k, \omega)$ (top) and density structure factor $S(k, \omega)$ (bottom) in the SPT HI phase (left), at the HI-CDW transition point (middle), and in the CDW phase (right). Dashed lines connect the intensity maxima at given k . Other model parameters are $U/t = 4$ and $J/t = -1.5$.

$c^*(L) \simeq 1/2$ to $c^*(L) \simeq 7/10$, which can be taken as a sign for an emergent supersymmetry at the boundary of the SPT HI phase [34–36].

Finally, we analyze the dynamical charge (spin) structure factor of the model (1),

$$S^{(zz)}(k, \omega) = \sum_n |\langle \psi_n | \hat{O}_k | \psi_0 \rangle|^2 \delta(\omega - \omega_n), \quad (4)$$

where $\hat{O}_k = \hat{n}_k$ ($\hat{O}_k = \hat{S}^z$). In Eq. (4), $|\psi_0\rangle$ ($|\psi_n\rangle$) denotes the ground (n th excited) state, and $\omega_n = E_n - E_0$. Following Ref. [30], we first evaluate the related two-point correlation functions $\langle \psi_0 | \hat{O}_j(\tau) \hat{O}_0(0) | \psi_0 \rangle$ by way of real-time evolution of the ground-state infinite MPS $|\psi_0\rangle$. Thereby, we apply infinite boundary conditions to a finite window of sites ($L_W = 128$). After \hat{O} is applied to a given site, the system is evolved at least up to $\tau = 30/t$, where a time step $\delta\tau = 0.05/t$ is used in the fourth-order Suzuki-Trotter decomposition. Fourier transformation then gives the dynamical structure factors.

For the spin-1 chain and extended Bose-Hubbard models it has been demonstrated that the dynamical spin and density structure factor reveal distinguishing features in the SPT and topologically trivial phases [28,37,38]. Figure 5 illustrates the intensity of the dynamical wave-vector-resolved spin and density response in the k - ω plane. In the HI phase, both $S^{zz}(k, \omega)$ and $S(k, \omega)$ exhibit an essentially symmetric line shape with respect to $k = \pi/2$ and gaps at $k = 0$ and π , but the spectral weight of the excitations is higher for $k > \pi/2$; see Figs. 5(a) and 5(b). While the spin response remains unaffected at the Ising transition point [Fig. 5(c)], the gaps in the charge response closes at $k = \pi$, reflecting the doubling of the lattice period CDW phase [Fig. 5(d)]. Obviously $S(k, \omega)$

follows the behavior of the neutral gap rather than those of the charge gap [cf. Fig. 3(b)]. In the CDW phase, the overall line shape of $S^{zz}(k, \omega)$ is asymmetric with a larger excitation gap at $k = \pi$. Note that we find now two dispersive features (branches) in $S^{zz}(k, \omega)$ and $S(k, \omega)$, where a changeover of the intensity maximum takes place at $k = \pi/2$ [cf. Figs. 3(e) and 3(f)].

To summarize, exploiting the link between topological order and entanglement properties, we examined the ground-state and spectral properties of the paradigmatic one-dimensional extended Hubbard model (EHM) with alternating ferromagnetic spin coupling J by numerically exact (DMRG) techniques. We showed that any finite spin interaction $J < 0$ stabilizes a symmetry-protected topological Haldane insulator (SPT HI) that replaces the spin-density-wave and bond-order-wave ground states existing in the pure EHM below a critical ratio of nearest-neighbor (V) to intrasite (U) Coulomb interaction. The HI manifests the twofold degeneracy of the lowest entanglement level and, regarding the dynamical spin-density response, reveals a similar behavior as the SPT state of the spin-1 chain [28] and the HI of the extended Bose-Hubbard model [37,38]. Furthermore, analyzing the correlation length, entanglement spectrum, and many-body excitation gaps, we found clear evidence for a quantum phase transition from the SPT HI phase to a CDW when the V/U ratio is raised. Using iDMRG, the HI-CDW boundary and therefore the complete ground-state phase diagram could be determined with very high accuracy. In the weak-to-intermediate interaction regime, the HI-CDW transition belongs to the Ising universality class. Here, the central charge $c = 1/2$, and only the neutral gap vanishes. This is reflected in the dynamical density structure factor, where the gap closes at momentum $k = \pi$, just as for the HI-antiferromagnet transition of the spin-1 chain. In the strong interaction regime we found a first-order phase transition characterized by a jump in the spin gap. Decreasing the magnitude of J , the HI-CDW phase boundary approaches the BOW-CDW transition line in the pure EHM; thus, making the system topological, this changeover can be determined more precisely. Perhaps most interesting, tracing the central charge along the HI-CDW transition line, we detect a tricritical Ising point with $c = 7/10$ that separates the continuous and first-order transition regimes. A further field theoretical study would be highly desirable to elucidate the origin of the tricritical Ising point. In either case the EHM with additional ferromagnetic spin exchange provides valuable insights into the criticality and nontrivial topological excitations of low-dimensional correlated electron systems. Note that we applied the ferromagnetic spin exchange in order to easily realize an effective spin-1 state. Including a physically more relevant dimerization of the transfer intergrals (hopping) will also stabilize the HI phase, so that the Ising quantum phase transition occurs between the HI and CDW phases [39]. Then, in this extended Peierls-Hubbard model, the tricritical Ising point with $c = 7/10$ will separate the HI-CDW transition line into continuous and first-order lines [40].

Note added in proof. Due to the quantum-classical correspondence, D -dimensional quantum and $(D + 1)$ dimensional classical systems share important physical properties. So it is well known that the quantum spin-1 chain is related to the classical two-dimensional restricted-solid-on solid (RSOS)

041120-4

model [41]. It has been shown that a Fibonacci anyonic chain can be mapped—using the RSOS representation of the algebra—onto the tricritical Ising model with $c = 7/10$. The transitions observed in our model can be understood as transitions from a low-density phase to a high-density phase of doubly occupied sites. Interestingly in the hard squares model first and second order transitions from low to high densities also occur with a tricritical point with the same central charge $c = 7/10$, see [42] and references therein. This connects—at the tricritical

point—our model, hard squares and the so-called golden chain [43].

The authors would like to thank F. Göhmann, T. Kaneko, and A. Klümper for valuable discussions. The iDMRG simulations were performed using the ITensor library [44]. This work was supported by Deutsche Forschungsgemeinschaft (Germany) through SFB 652.

- [1] J. E. Moore, *Nature (London)* **464**, 194 (2010).
 [2] M. Z. Hazan and C. L. Kane, *Rev. Mod. Phys.* **82**, 3045 (2010).
 [3] X.-L. Qi and S.-C. Zhang, *Rev. Mod. Phys.* **83**, 1057 (2011).
 [4] B. I. Halperin, *Phys. Rev. B* **25**, 2185 (1982).
 [5] C. L. Kane and E. J. Mele, *Phys. Rev. Lett.* **95**, 146802 (2005).
 [6] C. L. Kane and E. J. Mele, *Phys. Rev. Lett.* **95**, 226801 (2005).
 [7] F. D. M. Haldane, *Phys. Rev. Lett.* **50**, 1153 (1983).
 [8] Z.-C. Gu and X.-G. Wen, *Phys. Rev. B* **80**, 155131 (2009).
 [9] F. Pollmann, E. Berg, A. M. Turner, and M. Oshikawa, *Phys. Rev. B* **85**, 075125 (2012).
 [10] X. Chen, Z.-C. Gu, Z.-X. Liu, and X.-G. Wen, *Phys. Rev. B* **87**, 155114 (2013).
 [11] S. R. Manmana, A. M. Essin, R. M. Noack, and V. Gurarie, *Phys. Rev. B* **86**, 205119 (2012).
 [12] S. Ejima and S. Nishimoto, *Phys. Rev. Lett.* **99**, 216403 (2007).
 [13] S. R. White, *Phys. Rev. Lett.* **69**, 2863 (1992).
 [14] I. P. McCulloch, [arXiv:0804.2509](https://arxiv.org/abs/0804.2509).
 [15] U. Schollwöck, *Ann. Phys.* **326**, 96 (2011).
 [16] J. A. Kjäll, M. P. Zaletel, R. S. K. Mong, J. H. Bardarson, and F. Pollmann, *Phys. Rev. B* **87**, 235106 (2013).
 [17] M. Tsuchiizu and A. Furusaki, *Phys. Rev. Lett.* **88**, 056402 (2002).
 [18] K.-M. Tam, S.-W. Tsai, and D. K. Campbell, *Phys. Rev. Lett.* **96**, 036408 (2006).
 [19] E. Jeckelmann, *Phys. Rev. Lett.* **89**, 236401 (2002).
 [20] P. Sengupta, A. W. Sandvik, and D. K. Campbell, *Phys. Rev. B* **65**, 155113 (2002).
 [21] A. W. Sandvik, L. Balents, and D. K. Campbell, *Phys. Rev. Lett.* **92**, 236401 (2004).
 [22] F. H. L. Essler, H. Frahm, F. Göhmann, A. Klümper, and V. E. Korepin, *The One-Dimensional Hubbard Model* (Cambridge University Press, Cambridge, UK, 2005).
 [23] M. Nakamura, *J. Phys. Soc. Jpn.* **68**, 3123 (1999).
 [24] M. Nakamura, *Phys. Rev. B* **61**, 16377 (2000).
 [25] H. Li and F. D. M. Haldane, *Phys. Rev. Lett.* **101**, 010504 (2008).
 [26] P. Calabrese and J. Cardy, *J. Stat. Mech.* (2004) P06002.
 [27] F. Pollmann, S. Mukerjee, A. M. Turner, and J. E. Moore, *Phys. Rev. Lett.* **102**, 255701 (2009).
 [28] S. Ejima and H. Fehske, *Phys. Rev. B* **91**, 045121 (2015).
 [29] F. Pollmann, A. M. Turner, E. Berg, and M. Oshikawa, *Phys. Rev. B* **81**, 064439 (2010).
 [30] H. N. Phien, G. Vidal, and I. P. McCulloch, *Phys. Rev. B* **86**, 245107 (2012).
 [31] A. Milsted, J. Haegeman, T. J. Osborne, and F. Verstraete, *Phys. Rev. B* **88**, 155116 (2013).
 [32] V. Zauner, M. Ganahl, H. G. Evertz, and T. Nishino, [arXiv:1207.0862](https://arxiv.org/abs/1207.0862).
 [33] S. Nishimoto, *Phys. Rev. B* **84**, 195108 (2011).
 [34] T. Grover, D. N. Sheng, and A. Vishwanath, *Science* **344**, 280 (2014).
 [35] D. Friedan, Z. Qiu, and S. Shenker, *Phys. Rev. Lett.* **52**, 1575 (1984).
 [36] D. Friedan, Z. Qiu, and S. Shenker, *Phys. Lett. B* **151**, 37 (1985).
 [37] S. Ejima, F. Lange, and H. Fehske, *Phys. Rev. Lett.* **113**, 020401 (2014).
 [38] S. Ejima and H. Fehske, *J. Phys.: Conf. Ser.* **592**, 012134 (2015).
 [39] H. Benthien, F. H. L. Essler, and A. Grage, *Phys. Rev. B* **73**, 085105 (2006).
 [40] S. Ejima *et al.* (unpublished).
 [41] K. Rommelse and M. den Nijs, *Phys. Rev. Lett.* **59**, 2578 (1987).
 [42] A. Feiguin, S. Trebst, A. W. W. Ludwig, M. Troyer, A. Kitaev, Z. Wang, and M. H. Freedman, *Phys. Rev. Lett.* **98**, 160409 (2007).
 [43] A. Klümper and P. A. Pearce, *J. Stat. Phys.* **64**, 13 (1991).
 [44] <http://itensor.org/>

Bibliography

- [1] S. R. White, Phys. Rev. Lett. **69**, 2863 (1992). 5, 7
- [2] S. R. White, Phys. Rev. B **48**, 10345 (1993). 5
- [3] E. Jeckelmann, Phys. Rev. B **57**, 11838 (1998). 7
- [4] E. R. Davidson, J. of Comp. Phys. **17**, 87 (1975). 8
- [5] E. R. Davidson and W. J. Thompson, Computers in Physics **7**(5), 519 (1993). 8
- [6] E. Jeckelmann and S. R. White, Phys. Rev. B **57**, 6376 (1998). 9
- [7] T. D. Kühner and S. R. White, Phys. Rev. B **60**, 335 (1999). 12
- [8] E. Jeckelmann, Phys. Rev. B **66**, 045114 (2002). 12
- [9] E. Jeckelmann and H. Fehske. Exact numerical methods for electron-phonon problems. In G. Iadonisi, J. Ranninger and G. De Filippis, *Polarons in Bulk Materials and Systems With Reduced Dimensionality* volume 161 of *International School of Physics Enrico Fermi* pages 247–284 Amsterdam (2006). IOS Press. 12
- [10] S. Qin, S. Liang, Z. Su and L. Yu, Phys. Rev. B **52**, 5475 (1995). 13
- [11] G. Hager, E. Jeckelmann, H. Fehske, G. Wellein and G. Hager, J. of Comp. Phys. **194**, 795 (2004). 16
- [12] H. J. Schulz, *Strongly Correlated Electronic Materials*, edited by K. S. Bedell, Z. Wang and D. E. Meltzer (Addison-Wesley, New York, 1994) p. 187; cond-mat/9412036. 17, 37
- [13] *Quantum Physics in One Dimension*, edited by T. Giamarchi (Oxford University Press, Oxford, 2004). 17, 41
- [14] H. J. Schulz, Phys. Rev. Lett. **64**, 2831 (1990). 17
- [15] H. Frahm, Physical Review B **42**, 10553–10565 (1990). 17
- [16] M. Dzierzawa, *The Hubbard Model*, edited by D. Baeriswyl, D. K. Campbell, J. M. P. Carmelo, F. Guinea and E. Louis NATO ASI Series B 343 (Plenum Press, New York, 1995) p. 327. 17
- [17] S. Ejima, F. Gebhard and S. Nishimoto, Europhys. Lett. **70**, 492 (2005). 17, 18

- [18] P. Calabrese and J. Cardy, *J. Stat. Mech.: Theor. Exp.* (**2004**), P06002. 18
- [19] A. M. Läuchli and C. Kollath, *J. Stat. Mech.* page P05018 (2008). 18
- [20] S. Nishimoto, *Phys. Rev. B* **84**, 195108 (2011). 18
- [21] H. Li and F. D. M. Haldane, *Phys. Rev. Lett.* **101**, 010504 (2008). 18, 49
- [22] F. Pollmann, A. M. Turner, E. Berg and M. Oshikawa, *Phys. Rev. B* **81**, 064439 (2010). 19, 49
- [23] F. Pollmann, E. Berg, A. M. Turner and M. Oshikawa, *Phys. Rev. B* **85**, 075125 (2012). 19, 49
- [24] Y. Wakisaka, T. Sudayama, K. Takubo, T. Mizokawa, M. Arita, H. Namatame, M. Taniguchi, N. Katayama, M. Nohara and H. Takagi, *Phys. Rev. Lett.* **103**, 026402 (2009). 21, 24
- [25] Y. Ohta, T. Shimozato, R. Eder and S. Maekawa, *Phys. Rev. Lett.* **73**, 324 (1994). 21, 23
- [26] Y. Ohta, A. Nakauchi, R. Eder, K. Tsutsui and S. Maekawa, *Phys. Rev. B* **52**, 15617 (1995). 21, 23
- [27] L. M. Falicov and J. C. Kimball, *Phys. Rev. Lett.* **22**, 997 (1969). 21
- [28] O. S. Barišić, *Phys. Rev. B* **65**, 144301 (2002). 21
- [29] C. D. Batista, J. E. Gubernatis, J. Bonča and H. Q. Lin, *Phys. Rev. Lett.* **92**, 187601 (2004). 21, 23
- [30] D. Ihle, M. Pfafferoth, E. Burovski, F. X. Bronold and H. Fehske, *Phys. Rev. B* **78**, 193103 (2008). 21
- [31] V. A. Kashurnikov and B. V. Svistunov, *Phys. Rev. B* **53**, 11776 (1996). 22
- [32] A. Damascelli, Z. Hussain and Z.-X. Shen, *RMP* **75**, 473 (2003). 27
- [33] D. N. Basov, R. D. Averitt, D. van der Marel, M. Dressel and K. Haule, *Rev. Mod. Phys.* **83**, 471 (2011). 27
- [34] H. Fehske, M. Holicki and A. Weiße. Lattice dynamical effects on the Peierls transition in one-dimensional metals and spin chains. In B. Kramer, *Advances in Solid State Physics 40* pages 235–249. Vieweg Wiesbaden (2000). 28, 29, 30
- [35] G. Wellein and H. Fehske, *Phys. Rev. B* **58**, 6208 (1998). 28, 29, 30
- [36] M. Hohenadler, G. Wellein, A. R. Bishop, A. Alvermann and H. Fehske, *Phys. Rev. B* **73**, 245120 (2006). 28, 30

- [37] R. J. Bursill, R. H. McKenzie and C. J. Hamer, Phys. Rev. Lett. **80**, 5607 (1998). 28, 30
- [38] J. E. Hirsch and E. Fradkin, Phys. Rev. B **27**, 4302 (1983). 28, 29
- [39] H. Zheng, D. Feinberg and M. Avignon, Phys. Rev. B **39**, 9405 (1989). 28
- [40] R. H. McKenzie, C. J. Hamer and D. W. Murray, Phys. Rev. B **53**, 9676 (1996). 28
- [41] S. Sykora, A. Hübsch, K. W. Becker, G. Wellein and H. Fehske, Phys. Rev. B **71**, 045112 (2005). 28, 38
- [42] J. E. Hirsch and E. Fradkin, Phys. Rev. Lett. **49**, 402 (1982). 29
- [43] H. Fehske, A. P. Kampf, M. Sekania and G. Wellein, Eur. Phys. J. B **31**, 11 (2003). 30
- [44] Y. Takada and A. Chatterjee, Phys. Rev. B **67**, 081102(R) (2003). 30
- [45] R. T. Clay and R. P. Hardikar, Phys. Rev. Lett. **95**, 096401 (2005). 30, 32, 33
- [46] R. P. Hardikar and R. T. Clay, Phys. Rev. B **75**, 245103 (2007). 30, 31, 32, 33
- [47] M. Tezuka, R. Arita and H. Aoki, Phys. Rev. Lett. **95**, 226401 (2005). 30
- [48] M. Tezuka, R. Arita and H. Aoki, Phys. Rev. B **76**, 155114 (2007). 30
- [49] H. Fehske, G. Hager and E. Jeckelmann, Europhys. Lett. **84**, 57001 (2008). 30, 32
- [50] I. P. McCulloch. Infinite size density matrix renormalization group, revisited. arXiv:0804.2509 (2008). 33, 65
- [51] U. Schollwöck, Annals of Physics **326**, 96–192 (2011). 33, 65
- [52] D. M. Edwards, Physica B **378-380**, 133 (2006). 33
- [53] A. Alvermann, D. M. Edwards and H. Fehske, Phys. Rev. Lett. **98**, 056602 (2007). 33
- [54] S. A. Trugman, Phys. Rev. B **37**, 1597 (1988). 33
- [55] G. Wellein, H. Fehske, A. Alvermann and D. M. Edwards, Phys. Rev. Lett. **101**, 136402 (2008). 34
- [56] C. Gros, K. Hamacher and W. Wenzel, Europhys. Lett. **69**, 616 (2005). 36
- [57] T. Giamarchi, *Quantum Physics in One Dimension* (Clarendon Press, Oxford, 2003). 37
- [58] K. W. Becker, A. Hübsch and T. Sommer, Phys. Rev. B **66**, 235115 (2002). 38

- [59] M. Ogata, M. U. Luchini, S. Sorella and F. F. Assaad, *Phys. Rev. Lett.* **66**, 2388 (1991). 39
- [60] A. Moreno, A. Muramatsu and S. R. Manmana, *Phys. Rev. B* **83**, 205113 (2011). 39
- [61] M. Greiner, O. Mandel, T. Esslinger, T. W. Hänsch and I. Bloch, *Nature* **415**, 39 (2002). 41
- [62] I. Bloch, J. Dalibard and W. Zwerger, *Rev. Mod. Phys.* **80**, 885 (2008). 41
- [63] T. Stöferle, H. Moritz, C. Schori, M. Köhl and T. Esslinger, *Phys. Rev. Lett.* **92**, 130403 (2004). 41
- [64] J. K. Freericks and H. Monien, *Phys. Rev. B* **53**, 2691 (1996). 41, 42, 44
- [65] N. Elster and H. Monien, *Phys. Rev. B* **59**, 12184 (1999). 41, 44
- [66] T. D. Kühner and H. Monien, *Phys. Rev. B* **58**, R14741 (1998). 41, 42, 44
- [67] T. D. Kühner, S. R. White and H. Monien, *Phys. Rev. B* **61**, 12474 (2000). 41, 42, 44
- [68] M. P. A. Fisher, P. B. Weichman, G. Grinstein and D. S. Fisher, *Phys. Rev. B* **40**, 546 (1989). 42
- [69] T. Giamarchi, *Phys. Rev. B* **46**, 342 (1992). 42
- [70] B. Damski and J. Zakrzewski, *Phys. Rev. A* **74**, 043609 (2006). 42, 43
- [71] J. K. Freericks, H. R. Krishnamurthy, Y. Kato, N. Kawashima and N. Trivedi, *Phys. Rev. A* **79**, 053631 (2009). 42
- [72] P. T. Ernst, S. Götze, J. S. Krauser, K. Pyka, D.-S. Lühmann, D. Pfannkuche and K. Sengstock, *Nature Physics* **6**, 56 (2010). 42, 48, 51
- [73] G. G. Batrouni and R. T. Scalettar, *Phys. Rev. B* **46**, 9051 (1992). 44
- [74] V. A. Kashurnikov, A. V. Krasavin and B. V. Svistuno, *Pis'ma Zh. Eksp. Teor. Fiz.* **64**, 92 (1996). 44
- [75] D. van Oosten, P. van der Straten and H. T. C. Stoof, *Phys. Rev. A* **63**, 053601 (2001). 46
- [76] N. N. Bogoliubov, *J. Phys. (USSR)* **11**, 23 (1947). 47
- [77] M. A. Cazalilla, R. Citro, T. Giamarchi, E. Orignac and M. Rigol, *Rev. Mod. Phys.* **83**, 205301 (2011). 47
- [78] S. D. Huber, E. Altman, H. P. Büchler and G. Blatter, *Phys. Rev. B* **75**, 085106 (2007). 48

- [79] F. D. M. Haldane, Phys. Rev. Lett. **50**, 1153 (1983). 49
- [80] Z.-C. Gu and X.-G. Wen, Phys. Rev. B **80**, 155131 (2009). 49
- [81] Z.-X. Liu, Z.-B. Yang, Y.-J. Han, W. Yi and X.-G. Wen, Phys. Rev. B **86**, 195122 (2012). 49
- [82] I. Affleck, T. Kennedy, E. H. Lieb and H. Tasaki, Phys. Rev. Lett. **59**, 799–802 (1987). 49
- [83] E. G. Dalla Torre, E. Berg and E. Altman, Phys. Rev. Lett. **97**(26), 260401 (2006). 49, 50
- [84] E. Berg, E. Dalla Torre, T. Giamarchi and E. Altman, Phys. Rev. B **77**(24), 245119 (2008). 50, 51
- [85] D. Clément, N. Fabbri, L. Fallani, C. Fort and M. Inguscio, Phys. Rev. Lett. **102**(15), 155301 (2009). 51
- [86] C. Chin, R. Grimm, P. Julienne and E. Tiesinga, Rev. Mod. Phys. **82**, 1225 (2010). 55
- [87] L. Radzihovsky, J. Park and P. B. Weichman, Phys. Rev. Lett. **92**, 160402 (2004). 55, 58
- [88] M. W. J. Romans, R. A. Duine, S. Sachdev and H. T. C. Stoof, Phys. Rev. Lett. **93**, 020405 (2004). 55, 58
- [89] L. Radzihovsky, P. B. Weichman and J. I. Park, Ann. Phys. **323**, 2376 (2008). 55, 58
- [90] V. G. Rousseau and P. J. H. Denteneer, Phys. Rev. Lett. **102**, 015301 (2009). 55, 56, 57, 58, 59, 61, 62
- [91] J. Cardy, *Scaling and Renormalization in Statistical Physics* (Cambridge University Press, Cambridge, 1996). 60
- [92] H. N. Phien, G. Vidal and I. P. McCulloch, Phys. Rev. B **86**(24), 245107 (2012). 66
- [93] C. Wang and T. Senthil, Phys. Rev. B **87**, 235122 (2013). 66

Erklärung

Hiermit erkläre ich, dass diese Arbeit bisher von mir weder an der Mathematisch-Naturwissenschaftlichen Fakultät der Ernst-Moritz-Arndt-Universität Greifswald noch einer anderen wissenschaftlichen Einrichtung zum Zwecke der Habilitation eingereicht wurde. Ferner erkläre ich, dass ich diese Arbeit selbständig verfasst, keine anderen als die darin angegebenen Hilfsmittel benutzt und insbesondere die wörtlich oder dem Sinne nach anderen Veröffentlichungen entnommenen Stellen kenntlich gemacht habe.

(Satoshi Ejima)

Curriculum Vitae

Satoshi Ejima

Personal

Nationality: Japanese
Family: Married, two children
Date of birth: October 12, 1977
Place of birth: Saitama, Japan
Affiliation: Institut für Physik
Ernst-Moritz-Arndt Universität Greifswald
D-17487 Greifswald, Germany
Tel.: (+49)/[0]3834/420/4765
Fax: (+49)/[0]3834/420/4701
E-mail: ejima@physik.uni-greifswald.de

Education

04/2006 Ph. D. in natural sciences, Philipps-Universität Marburg, Germany
Thesis Title: *Exact numerical and analytical results for correlated lattice electrons in one dimension*
Supervisor: Prof. Dr. F. Gebhard

05/2005 – 07/2005 Research visit, Oxford University, UK
Supervisor: Prof. Dr. F. H. L. Eßler

04/2003 – 03/2006 Ph. D. student of physics, Philipps-Universität Marburg, Germany

03/2003 Masters degree in physics, Chiba University, Japan
Thesis Title: *Anomalous physical properties associated with charge ordering in low-dimensional strongly correlated electron systems*
Supervisor: Prof. Dr. Y. Ohta

04/2001 – 03/2003 Master student of physics, Chiba University, Japan

03/2001 Bachelors degree in physics, Chiba University, Japan

04/2000 – 03/2001 Undergraduate student of physics, Chiba University, Japan

04/1999 – 03/2000 Undergraduate student of physics, Universität Göttingen, Germany

04/1996 – 03/1999 Undergraduate student of physics, Chiba University, Japan

Employment

- Since 05/2008 Postdoctoral Researcher, Ernst-Moritz-Arndt Universität Greifswald, Germany
- 04/2008 Postdoctoral Researcher, Friedrich-Alexander-Universität Erlangen-Nürnberg, Regionales RechenZentrum Erlangen
- 04/2006 – 03/2008 Postdoctoral Researcher, Philipps-Universität Marburg, Germany

Scholarships

- 04/2003 – 03/2006 Honjo International Scholarship Foundation
- 04/2003 – 03/2006 Member of the DFG International Research Training Group 790 “Electron-Electron Interactions in Solids”

Teaching Experience

- Winter Semester 2015/16 Exercise: *Fortgeschrittene Quantenmechanik*
Institut für Physik, Universität Greifswald (2 SWS)
- Winter Semester 2014/15 Exercise: *Elektrodynamik*
Institut für Physik, Universität Greifswald (2 SWS)
- Summer Semester 2013 Lecture: *Density matrix renormalization group*
Institut für Physik, Universität Greifswald (2 SWS)
- Winter Semester 2012/13 Exercise: *Fortgeschrittene Quantenmechanik*
Institut für Physik, Universität Greifswald (2 SWS)
- Winter Semester 2011/12 Exercise: *Fortgeschrittene Quantenmechanik*
Institut für Physik, Universität Greifswald (2 SWS)
- Winter Semester 2010/11 Exercise: *Fortgeschrittene Quantenmechanik*
Institut für Physik, Universität Greifswald (2 SWS)
- Winter Semester 2007/08 Exercise: *Single Particle Properties of Solids*
Fachbereich Physik, Universität Marburg
- Summer Semester 2007 Exercise: *Quantenmechanik*
Fachbereich Physik, Universität Marburg
- Winter Semester 2006/07 Exercise: *Klassische Teilchen und Felder*
Fachbereich Physik, Universität Marburg

Publications by Satoshi Ejima

Peer-reviewed articles

1. *Criticality at the Haldane-insulator charge-density-wave quantum phase transition*
F. Lange, S. Ejima and H. Fehske
Phys. Rev. B **92**, 041120 (2015).
2. *Comparative density-matrix renormalization group study of symmetry-protected topological phases in spin-1 chain and Bose-Hubbard models*
S. Ejima and H. Fehske
Phys. Rev. B **91**, 045121 (2015).
3. *Spectral and entanglement properties of the bosonic Haldane insulator*
S. Ejima, F. Lange, and H. Fehske
Phys. Rev. Lett. **113**, 020401 (2014).
4. *Dynamical correlation functions for the one-dimensional Bose-Hubbard insulator*
K. zu Münster, F. Gebhard, S. Ejima, and H. Fehske
Phys. Rev. A **89**, 063623 (2014).
5. *Order, Criticality, and Excitations in the Extended Falicov-Kimball Model*
S. Ejima, T. Kaneko, Y. Ohta, and H. Fehske
Phys. Rev. Lett. **112**, 026401 (2014).
6. *One-dimensional Bose-Hubbard model with local three-body interactions*
S. Ejima, F. Lange, H. Fehske, F. Gebhard, and K. zu Münster
Phys. Rev. A **88**, 063625 (2013).
7. *Exact-diagonalization study of exciton condensation in electron bilayers*
T. Kaneko, S. Ejima, H. Fehske, and Y. Ohta
Phys. Rev. B **88**, 035312 (2013).
8. *Anderson localization versus charge-density-wave formation in disordered electron systems*
S. Nishimoto, S. Ejima, and H. Fehske
Phys. Rev. B **87**, 045116 (2013).
9. *Phase separation in the Edwards model*
S. Ejima, S. Sykora, K. W. Becker, and H. Fehske
Phys. Rev. B **86**, 155149 (2012).
10. *Characterization of Mott-insulating and superfluid phases in the one-dimensional Bose-Hubbard model*
S. Ejima, H. Fehske, F. Gebhard, K. zu Münster, M. Knap, E. Arrigoni, and W. von der Linden
Phys. Rev. A **85**, 053644 (2012).

11. *Discrete symmetry breaking transitions between paired superfluids*
M. J. Bhaseen, S. Ejima, F. H. L. Essler, H. Fehske, M. Hohenadler, and B. D. Simons
Phys. Rev. A **85**, 033636 (2012).
12. *Magnetic properties of the second Mott lobe in pairing Hamiltonians*
M. J. Bhaseen, S. Ejima, M. Hohenadler, A. O. Silver, F. H. L. Essler, H. Fehske, and B. D. Simons
Phys. Rev. A **84**, 023635 (2011).
13. *Dynamic properties of the one-dimensional Bose-Hubbard model*
S. Ejima, H. Fehske, and F. Gebhard
EPL **93**, 30002 (2011).
14. *Ising Deconfinement Transition between Feshbach-Resonant Superfluids*
S. Ejima, M. J. Bhaseen, M. Hohenadler, F. H. L. Essler, H. Fehske, and B. D. Simons
Phys. Rev. Lett. **106**, 015303 (2011).
15. *A Green's function decoupling scheme for the Edwards fermion-boson model*
D. M. Edwards, S. Ejima, A. Alvermann and H. Fehske
J. Phys.: Condens. Matter **22**, 435601 (2010).
16. *One-dimensional quantum transport affected by a background medium: Fluctuations versus correlations*
S. Ejima and H. Fehske
Phys. Rev. B **80**, 155101 (2009).
17. *Luttinger parameters and momentum distribution function for the half-filled spinless fermion Holstein model: A DMRG approach*
S. Ejima and H. Fehske
EPL **87**, 27001 (2009).
18. *Quantum Phase Transition in a 1D Transport Model with Boson-Affected Hopping:
Luttinger Liquid versus Charge-Density-Wave Behavior*
S. Ejima, G. Hager, and H. Fehske
Phys. Rev. Lett. **102**, 106404 (2009).
19. *Random dispersion approximation for the Hubbard model*
S. Ejima, F. Gebhard, and R. M. Noack
Eur. Phys. J. B **66**, 191-200 (2008).
20. *Phase diagram of the one-dimensional half-filled extended Hubbard model*
S. Ejima and S. Nishimoto
Phys. Rev. Lett. **99**, 216403 (2007).

21. *Tomonaga-Luttinger parameters and spin excitations in the dimerized extended Hubbard model*
S. Ejima, F. Gebhard, and S. Nishimoto
Phys. Rev. B **74**, 245110 (2006).
22. *Thermodynamics of the one-dimensional half-filled Hubbard model in the spin-disordered regime*
S. Ejima, F. H. L. Essler, and F. Gebhard
J. Phys. A: Math. Gen. **39**, 4845-4857 (2006).
23. *Spin and charge excitations in the anisotropic Hubbard ladder at quarter filling with charge-ordering instability*
Y. Ohta, T. Nakaegawa, and S. Ejima
Phys. Rev. B **73**, 045101 (2006).
24. *Tomonaga-Luttinger parameters for doped Mott insulators*
S. Ejima, F. Gebhard, and S. Nishimoto
Europhys. Lett. **70**, 492 (2005).
25. *Phase diagram of the t - U - V_1 - V_2 model at quarter filling*
S. Ejima, F. Gebhard, S. Nishimoto, and Y. Ohta
Phys. Rev. B **72**, 033101 (2005).

Conference Proceedings

1. *Entanglement properties of the nontrivial Haldane insulator in the 1D extended Bose-Hubbard model*
S. Ejima and H. Fehske
J. Phys.: Conf. Ser. **592**, 012134 (2015).
2. *Charge-density-wave formation in the Edwards fermion-boson model at one-third band filling*
S. Ejima and H. Fehske
JPS Conf. Proc. **3**, 013006 (2014).
3. *Excitonic BCS-BEC crossover in double-layer systems*
T. Kaneko, S. Ejima, H. Fehske, and Y. Ohta
JPS Conf. Proc. **3**, 017006 (2014).
4. *Metal-insulator transition in the Edwards model*
H. Fehske, S. Ejima, G. Wellein, and A. R. Bishop
J. Phys.: Conf. Ser. **391**, 012152 (2012).
5. *Dynamic density-density correlations in interacting Bose gases on optical lattices*
S. Ejima, H. Fehske, and F. Gebhard
J. Phys.: Conf. Ser. **391**, 012143 (2012).

6. *DMRG analysis of the SDW-CDW crossover region in the 1D half-filled Hubbard-Holstein model*
S. Ejima and H. Fehske
J. Phys.: Conf. Ser. **200**, 012031 (2010).
7. *Ground-state properties of the one-dimensional extended Hubbard model at half filling*
S. Ejima and S. Nishimoto
Journal of Physics and Chemistry of Solids **69**, 3293-3296 (2008).
8. *Phase diagram of the one-dimensional extended Hubbard model with hopping dimerization*
S. Ejima, F. Gebhard, and S. Nishimoto
Physica C **460-462**, 1079-1080 (2007).
9. *Luttinger-liquid exponent in the vicinity of charge-density wave instabilities*
S. Ejima, F. Gebhard, and S. Nishimoto
Journal of Magnetism and Magnetic Materials **310**, 996-998 (2007).
10. *Accurate calculation of the Tomonaga-Luttinger parameter K_ρ using the density-matrix renormalization group method*
S. Ejima, F. Gebhard, and S. Nishimoto
Physica B **378-380**, 304 (2006).
11. *Interplay between Spin and Charge Excitations in the Coupled Spin-Pseudospin Systems*
Y. Ohta, S. Ejima, and T. Nakaegawa
J. Low Temp. Phys. **131**, 239 (2003).
12. *Anomalous Spin Excitations in a Coupled Spin-Pseudospin Model for Anisotropic Hubbard Ladders at Quarter Filling*
Y. Ohta, S. Ejima, Y. Shibata, and T. Nakaegawa
Physica B **329-333**, 996 (2003).
13. *Excitations in the Coupled Spin-Pseudospin Model for Quarter-Filled Ladders*
S. Ejima, T. Nakaegawa, and Y. Ohta
Physica B **328**, 105 (2003).

Summary of publications

- 25 peer-reviewed articles in international journals (5 PRLs and 3 EPLs)
- 13 contributions in international conference proceedings

Conferences, Workshops, and Seminars

2015:

1. Recent progress on DMRG method, RIKEN AICS (Kobe, Japan)
Invited talk: *Criticality at the Haldane-insulator charge-density-wave quantum phase transition*
2. International Conference on Magnetism 2015, Barcelona (Spain)
Poster: *Topological phase transitions in extended Hubbard-type models at half filling*

2014:

1. International Conference on Strongly Correlated Electron Systems, Grenoble (France)
Poster: *Entanglement properties of the nontrivial Haldane insulator phase in the one-dimensional extended Bose-Hubbard model*
2. Topology and Entanglement in Correlated Quantum Systems, Dresden (Germany)
Poster: *Spectral and entanglement properties of the bosonic Haldane insulator*

2013:

1. International Conference on Strongly Correlated Electron Systems, Tokyo (Japan)
Poster: *Phase diagram of the one-third filled Edwards fermion-boson model*
2. Korrelationstage 2013, Dresden (Germany)
Poster: *Order and criticality in the one-dimensional extended Falicov-Kimball model*

2012:

1. Ultracold Gases: Superfluidity and Strong Correlations, Tokyo (Japan)
Invited talk: *Ising Deconfinement Transition between Feshbach-Resonant Superfluids*
2. DPG-Frühjahrstagung, Berlin (Germany)
Poster: *Characterization of Mott-insulating and superfluid phases in the one-dimensional Bose-Hubbard model*
3. Seminar talk in RIKEN, Saitama (Japan)
Talk: *DMRG study on the one-dimensional bosonic systems*

2011:

1. Korrelationstage 2011, Dresden (Germany)
Talk: *Ising deconfinement transition between Feshbach resonant superfluids*
2. International Conference on Strongly Correlated Electron Systems, Cambridge (UK)
Poster: *Dynamic Density-Density Correlations in Interacting Bose Gases on Optical Lattices*
3. Seminar Many-Body Problems, Fachbereich Physik, Philipps-Universität Marburg, Marburg (Germany)
Talk: *DMRG study of Bose-Hubbard models*

2010:

1. Statistical Physics of Quantum Systems, Tokyo (Japan)
Poster: *Dynamical properties of the one-dimensional Bose-Hubbard model*

2009:

1. International Conference on Magnetism, Karlsruhe (Germany)
Poster: *DMRG analysis of the CDW-SDW crossover region in the 1D half-filled Holstein-Hubbard model*

2008:

1. Seminar Many-Body Problems, Fachbereich Physik, Philipps-Universität Marburg (Germany)
Talk: *Quantum phase transition in a one-dimensional transport model with boson-affected hopping: Luttinger-liquid versus CDW behavior*
2. Marburg-Mainz Workshop on the Physics of Strongly Correlated Electron Systems, Mainz (Germany)
Talk: *Phase diagram of the one-dimensional t - U - V model at half band-filling*
3. Seminar über Vielteilchentheorie, Fachbereich Physik, Technische Universität Kaiserslautern (Germany)
Talk: *Phase diagram of the one-dimensional half-filled extended Hubbard model*

2007:

1. Seminar zu aktuellen Problemen der Theoretischen Physik, Institut für Physik, Ernst-Moritz-Arndt Universität Greifswald (Germany)
Talk: *Phase diagram of the one-dimensional half-filled extended Hubbard model*

2. International Conference on Spectroscopies in Novel Superconductors, Sendai (Japan)
Poster: *Ground-state properties of the one-dimensional extended Hubbard model at half filling*
3. Discussion meeting Many-particle physics groups Marburg and KOMET 337 Mainz, Marburg (Germany)
Talk: *Tomonaga-Luttinger parameters in the dimerized extended Hubbard model*

2006:

1. Group Seminar Condensed Matter Theory, Fakultät für Mathematik und Physik, Leibniz Universität Hannover (Germany)
Talk: *Tomonaga-Luttinger parameters and spin excitations in the dimerized extended Hubbard model*
2. The Physical Society of Japan the Autumn Meeting, Chiba (Japan)
Talk: *Tomonaga-Luttinger parameter in doped Mott insulators*
3. International Conference on Magnetism, Kyoto (Japan)
Poster: *Luttinger-Liquid Exponent in the vicinity of charge-density-wave instabilities*
4. International Conference on Materials and Mechanisms of Superconductivity and High Temperature Superconductors, Dresden (Germany)
Poster: *Phase diagram of the one-dimensional extended Peierls-Hubbard model*
5. Evaluation workshop on “Disorder and Interactions” of the European Graduate College *Electron-Electron Interactions in Solids*, Ráckeve (Hungary)

2005:

1. Seminar of the European Graduate College *Electron-Electron Interactions in Solids*, Riezlern (Austria)
Talk: *Tomonaga-Luttinger parameters for doped Mott insulators*
2. International Conference on Strongly Correlated Electron Systems, Vienna (Austria)
Poster: *Accurate calculation of the Tomonaga-Luttinger parameter K_ρ using the density-matrix renormalization group method*
3. Workshop on “Quantum Magnetism” of the European Graduate College *Electron-Electron Interactions in Solids*, Ráckeve (Hungary)
4. Spring Meeting of the German Physical Society, Berlin (Germany)
Poster: *Tomonaga-Luttinger-liquid parameter from density-matrix renormalization group calculations*

2004:

1. Seminar of the European Graduate College *Electron-Electron Interactions in Solids*,
Ráckeve (Hungary)
Talk: *Tomonaga-Luttinger-liquid exponent near the CDW instabilities*
2. International workshop on “Recent Progress and Prospects in Density-Matrix Renormalization”, Leiden (the Netherlands)
Poster: *Luttinger-liquid parameter near the CDW instabilities*
3. Workshop on “Dynamics at Surfaces and Interfaces” of the European Graduate College *Electron-Electron Interactions in Solids*, Marburg (Germany)
4. Spring Meeting of the German Physical Society, Regensburg (Germany)
Poster: *Charge Fluctuations in the t - U - V_1 - V_2 Model*

2003:

1. Seminar of the European Graduate College *Electron-Electron Interactions in Solids*,
Riezlern (Austria)
2. Workshop on “Correlated electrons in mesoscopic systems” of the European Graduate College *Electron-Electron Interactions in Solids*, Ráckeve (Hungary)

2002:

1. International Conference on Low Temperature Physics, Hiroshima (Japan)
Poster: *Anomalous spin excitations in a coupled spin-pseudospin model for anisotropic Hubbard ladders at quarter filling*
2. The 2nd Hiroshima Workshop on Transport and Thermal Properties of Advanced Materials, Hiroshima (Japan)
Poster: *Excitations in the Coupled Spin-Pseudospin Model for Quarter-Filled Ladders*

Acknowledgments

First and foremost, I would like to gratefully thank H. Fehske for his constant guidance, understanding, patience, and support over the past eight years. His advice on my research and career has been invaluable. I would also like to sincerely acknowledge F. Gebhard and Y. Ohta for their continuing discussions and fruitful collaborations over the years.

This Habilitation thesis is based on a series of accepted papers. They would not have existed without pleasant and stimulating cooperations with my collaborators A. Alvermann, M. J. Bhaseen, D. M. Edwards, F. H. L. Essler, M. Hohenadler, T. Kaneko, K. zu Muenster, S. Nishimoto, B. D. Simons, T. Shirakawa, and S. Sykora.

I would also like to thank my colleagues in the work group members for their help and support. Especially, I am grateful to J. Schleede and T. Meyer for their technical support. My special thanks also go to F. Lange for valuable discussions and his inspiration.

Finally and most importantly, I would like to thank my wife Tomoko. Her support, encouragement, and unwavering love were essential. To my beloved daughters Juna and Lena, I would like to express my thanks for bringing their lovely smiles.